Imperial College London

RioTinto

Synthesis, Analysis and Characterisation of $CuFeS_{2(s)}$ Towards Superior, Green $Cu_{(aq)}$ Leaching

Daniel Godfrey

A thesis submitted in partial fulfilment of the requirements
for the degree of Doctor of Philosophy

Department of Chemistry
Imperial College London
September 2016

Abstract

Efforts to decrease reliance on traditional high-consumption $CuFeS_{2(s)}$ pyrometallurgy, have focused on delivering hydrometallurgic solutions to the beneficiation of sulfide ores. Ionic liquids (IL) have been proposed as a potentially higher performance and more benign alternative to conventional acid-$SO_4^{2-}{}_{(aq)}$ for $CuFeS_{2(s)}$ dissolution, although the sheer number of IL variants complicates the search for the most efficient systems. This study focuses on $Cu^{2+}{}_{(aq)}$-leaching performance in hydrogensulfate $IL_{(aq)}$-$CuFeS_{2(s)}$ systems and comparisons with equivalent acidity conventional-$SO_4^{2-}{}_{(aq)}$ references. A single commercial $CuFeS_{2(s)}$ ore source is used throughout.

A combinatorial strategy is applied to low-volume scale identification of high performance $IL_{(aq)}$ lixiviant systems. Implementation of a high performance, flexible automated workstation is presented with broad applicability to study of acidic-$CuFeS_{2(s)}$ dissolution. Electrochemical ASV is demonstrated to be an effective screening tool for $[Cu^{2+}]_{(aq)}$ extraction quantification, as verified by ICP-AES measurements throughout. Successfully ASV modifications are described; most notably a procedure for automated *in situ* electrochemical monitoring of 120 *mL*-scale $CuFeS_{2(s)}$ dissolution. High accuracy reconstructed (continuous) $Cu^{2+}{}_{(aq)}$ extraction profiles offer precise rate determinations and treatment of previously unconsidered profile features.

Application of the robotic custom instrument demonstrates high-throughput electrochemical screening of $IL_{(aq)}$ sample arrays with minimal consumption and precise $[Cu^{2+}]_{(aq)}$ measurements. Proof-of-concept screening assays find $>10^2$ difference in $IL_{(aq)}$ activities in equivalent conditions and at least 35-fold larger than sample-to sample variability. A large degree of variability in $IL_{(aq)}$ lixiviant activity is presented at nominal $[HSO_4]_{(aq)}$ and acidity for closely structurally-related ILs. Best performing $[C_nC_mim][HSO_4]_{(aq)}$ and $[NR_4{\cdot}HSO_{4(aq)}]_{(aq)}$ $IL_{(aq)}$ systems are presented, alongside the confirmation of a non-trivial $[IL]_{(aq)}$ dependence, which is a contrasting result to previous work with Cu flotation concentrates. Several ILs have been found to provide significant leaching at low acidity, 'additive-quantity' $[IL]_{(aq)}$.

Best performing $IL_{(aq)}$ systems have been scrutinised in an up-scaled tank leaching configuration for ~1 *month* leach durations. 450 $mmol{\cdot}dm^{-3}$ $NH_4{\cdot}HSO_{4(aq)}$ is demonstrated to enhance $CuFeS_{2(s)}$ dissolution compared with equivalent acidity H_2SO_4 under otherwise equal conditions. A combination of surface, bulk and solution speciation studies are untaken to obtain a global view of the $IL_{(aq)}$-$CuFeS_{2(s)}$ dissolution process, with continuous *in situ* monitoring of key physical conditions ($[M^{n+}]_{(aq)}$, $[H^+]_{(aq)}$, T, E_h). The role of surface oxygen and sulfur in $CuFeS_{2(s)}$ dissolution hindrance is examined. Experimental insights provided by consideration of the effect of $SO_4^{2-}{}_{(aq)}$ and base addition to the primitive $IL_{(aq)}$ lixiviant media has led to the proposal of a HSO_4-IL dissolution mechanism for $CuFeS_{2(s)}$.

Declaration of Originality

I hereby declare that the work presented in this thesis is my own, except where referenced. This work has not previously been submitted in any form to satisfy any degree requirement at this or any other university.



Daniel Godfrey

Copyright Declaration

The copyright of this thesis rests with the author and is made available under a Creative Commons Attribution Non-Commercial No Derivatives license. Researchers are free to copy, distribute or transmit the thesis on the condition that they attribute it, that they do not use it for commercial purposes and that they do not alter, transform or build upon it. For any reuse or redistribution. Researchers must make clear to others the license terms of this work.

Acknowledgements

I wish to thank, first and foremost, my research supervisors Dr Tim Albrecht and Professor Tom Welton for their guidance, encouragement and invaluable discussions. To Tim, who has supported me greatly throughout my project and a challenging write-up period, displaying a great deal of patient and skill in editorial work. To Tom, for his fun, informal approach to supervision that has suited me so well and for always making me laugh. You both operate in the very highest echelons of your respective fields and I remain extremely grateful for the opportunity to conduct my PhD research in the high quality research environments that you have created. It has been a great privilege to work with you. I also extend my thanks to Rio Tinto for the significant project funding they provided, in order to make this project possible.

The work presented would not have been possible without a great many contributors. My sincere thanks go to Dr Evan J. Spadafora, Dr Olga Kuzmina, Dr Emmanouil Symianakis, Thomas Arrow, Lu Qiao and Joshua Carr for participating in my research with ambition, endeavour, skill and positivity. Special thanks go to Dr James H. Bannock and Simon Turner for their technical prowess and advice, without which the creation of a safe and extremely valuable research tool could not be been possible.

Huge thanks much go to my fellow research group members, both past and present, within the Chemistry Department and also to my colleagues within the Rio Tinto Advanced Leaching project led by Dr Stephen Neethling. It has been a pleasure working with you all. I wish you all the best in your future careers.

Lastly, I wish to thank my family and friends for their unwavering support throughout my PhD. To my wonderful parents, who have given everything they have to all of their triplet children – and to my brilliant siblings, Jamie and Hannah, who both beat me to ‘Dr’ accreditation. I also extend my love and gratitude to my partner Amelia for her patience, love and support. I am indebted to all of you and love you dearly. You have each had significant supporting roles in the preparation of this document, keeping me sane and striving to complete this work.

List of Publications

Godfrey, D.; Bannock, J.H.; Kuzmina, O.; Welton, T.; Albrecht, T.; A Robotic Platform for High-Throughput Electrochemical Analysis of Chalcopyrite Leaching; *Green Chem.,* 2016,18, 1930-1937.

Kuzmina, O.; Symianakis, E.; **Godfrey, D.**; Albrecht, T.; Welton, T.; Leaching of Chalcopyrite with Ionic Liquids: Solid, Liquid and Gas Phase Studies; (submitted)

Table of Contents

Chapter 1 - The Extraction of Copper from Chalcopyrite 1-1

1.1 Copper 1-3

1.2 Chalcopyrite 1-4

1.3 Industrial Extraction Techniques 1-9

1.4 $CuFeS_{2(s)}$ Dissolution Modes 1-12

1.5 Ambient Lixiviant Systems 1-17

1.6 Kinetic Influences 1-18

1.7 Mechanistic Insights 1-33

1.8 Kinetic Hindrance of $CuFeS_{2(s)}$ Dissolution 1-37

1.9 Outlook: Chemical Leaching 1-43

1.10 Thesis Structure 1-44

1.11 References 1-48

Chapter 2 - Ionic Liquids, Materials & Methods 2-1

2.1 Introduction - Ionic Liquids 2-3

2.2 Ionic Liquids in Metallurgy 2-5

2.3 Ionic Liquid Materials, Synthesis and Properties 2-16

2.4 Advanced Consideration of $IL_{(aq)}$ *p*H 2-25

2.5 $CuFeS_{2(s)}$ Processing 2-28

2.6 Electrochemistry 2-30

2.7 Copper Quantification Techniques 2-35

2.8 Experimental Leaching Format 2-46

2.9 $CuFeS_{2(s)}$ Surface Sensitive Techniques 2-47

2.10 References 2-52

Chapter 3 - Custom Instrumentation and Programming Techniques 3-1

3.1 Introduction 3-3

3.2 Development of a Robotic Automated Platform 3-4

3.3 Platform Validation Experiments 3-17

3.4 Automated Batch Analysis 3-21

3.5 Conclusions 3-24

3.6 References 3-26

Chapter 4 - Electrochemical Monitoring of Leaching 4-1

4.1 Introduction 4-3

4.2 Extended X-Ray Absorption Fine Structure Spectroscopy (EXAFS) 4-3

4.3 Previous ASV Studies 4-10

4.4 Validity of Peak $[IL]_{(aq)}$ Lixiviant Activity 4-12

4.5 Validation and Optimisation of ASV Procedure 4-17

4.6 Automated Electrochemical Dissolution Monitoring 4-28

4.7 Conclusions 4-37

4.8 References 4-39

Chapter 5 - Up-scaled $IL_{(aq)}$ Leaching Studies 5-1

5.1 Introduction 5-3

5.2 Experiment Design 5-3

5.3 Unprocessed Data 5-4

5.4 Analysis and Discussion of Key Leaching Parameters 5-11

5.5 Surface Studies of Leached $CuFeS_{2(s)}$ Residues 5-25

5.6 Conclusions 5-39

5.7 References 5-42

Chapter 6 - $IL_{(aq)}$ Screening & Mechanistic Insights 6-1

6.1 Introduction 6-3

6.2 $IL_{(aq)}$ Screening Studies 6-3

6.3 $IL_{(aq)}$ Leaching Insights 6-10

6.4 Conclusions 6-20

6.5 References 6-24

Chapter 7 - Conclusions and Future Work 7-1

7.1 Summary of Literature Survey 7-2

7.2 Summary of Key Aims 7-3

7.3 Summary and Evaluation of Key Achievements 7-4

7.4 Suggestions for Further Work 7-7

Appendices A-1

A. Appendix 1 – Full Arduino Codes A-1

B. Appendix 2 – NI LabView VIs B-1

C. Appendix 3 – MatLab Programming for ASV C-1

D. Appendix 4 - IL Characterisation Spectra D-1

List of Figures

Chapter 1 - The Extraction of Copper from Chalcopyrite

▲ Figure 1.1 - Annual refined $Cu_{(s)}$ extraction surplus (positive %) or deficit (negative %) as a percentage of total global $Cu_{(s)}$ extraction between the years 2000-2014 1-3

▲ Figure 1.2 - (A) The sphalerite-like $CuFeS_{2(s)}$ crystal structure dimensions and atomic positions, with all the variation of Fe-S-Fe bond angles shown. (B) The opposing α/β magnetic spins of Fe atoms within the $CuFeS_{2(s)}$ structure. 1-5

▲ Figure 1.3 – (A) Electronic band structure diagram for bulk $CuFeS_{2(s)}$ describing the principal atomic orbitals contributing to occupied (shaded) and vacant (unshaded) molecular orbital bands and the location of the Fermi energy (E_{fermi}). (B) Magnification of $CuFeS_{2(s)}$ E_{Fermi} region showing VB-CB information, n-dopant energy levels (E_d) and energy levels of common aqueous oxidants. Data compiled from various sources. 1-7

▲ Figure 1.4 - Schematic overview of modern pyrometallurgic refinement of sulfidic Cu ores such as $CuFeS_{2(s)}$, ranging from initial ore concentration via flotation to casting of high-purity refined $Cu_{(s)}$. 1-10

▲ Figure 1.5 - Global annual production of refined $Cu_{(s)}$ 1960-2014 1-11

▲ Figure 1.6 - Schematic overview of solvent-extraction electrowinning (SX-EW) as an adopted industrial hydrometallurgic extraction approach for copper sulfide ores. 1-12

▲ Figure 1.7 - (A) Modes of reversible and irreversible bacterial binding at mineral interfaces. (B) Schematic of cooperative leaching of irreversibly bound 'contact-leaching' bacteria 1-16

▲ Figure 1.8 – Onset potential (E_{pp}) of reduced $CuFeS_{2(s)}$ surface reactivity as a function of $[H_2SO_4]_{(aq)}$ and lixiviant temperature, including approximate regions of active, active/passive and passive $CuFeS_{2(s)}$ reactivity. 1-29

▲ Figure 1.9 - Cu extraction profiles for $SO_4^{2-}{}_{(aq)}$ based leaching of $CuFeS_{2(s)}$ at 50 *°C* (323 *K*) for systems with and without accelerating microbial additives and/or oxidation-reduction potential (ORP) control. Reproduced from Watling *et al.* using data from Ahmadi *et al.* 1-30

▲ Figure 1.10 - (A) Schematic explaining how differential rest potentials in FeS_2-$CuFeS_{2(s)}$ create a galvanic flow to equalise E_{fermi} (B) Mineral polarisation is counteracted by enhanced solution redox activity (Fe^{2+}/Fe^{3+} couple shown) (C) Schematic of the overall galvanic effect and the localisation of enhanced redox activity on and surrounding the mineral surface. 1-32

▲ Figure 1.11 – Pourbaix diagrams applicable at 298 *K* and 373 *K* respectively for $Cu_{(aq)}$ (A-B) and $Fe_{(aq)}$ (C-D). 1-34

▲ Figure 1.12 – Mechanism for $CuFeS_{2(s)}$ dissolution as proposed by Harmer *et al*. with regard to $HClO_{4(aq)}$ leaching at initial *p*H 1 1-36

▲ Figure 1.13 – Conceptual 4-stage model for $CuFeS_{2(s)}$ dissolution 1-37

▲ Figure 1.14 – Backscattered electron micrograph of incomplete (A) and complete (B) dissolution of $CuFeS_{2(s)}$ using Galvanox® pressure-$Cl^{-}_{(aq)}$ leaching, depicting conductive porous $S^{0}_{(s)}$ overlayers. 1-40

▲ Figure 1.15 - Pourbaix diagram for the $CuFeS_{2(s)}$–H_2O system at 25 *°C*. 1-41

▲ Figure 1.16 - Pourbaix diagram (E_h-pH) showing thermodynamically prevalent species for the Fe-S-K-O-H system at 25 *°C* (298 *K*) 1-43

Chapter 2 - Ionic Liquids, Materials and Methods

▲ Figure 2.1 - (A) Selected 'discrete' IL cations with unspecified general functional groups (R) at key positions - accepted abbreviations are included. (B) Selected 'discrete' IL anions separated into (i) organic and (ii) inorganic types. 2-5

▲ Figure 2.2 - Flowchart documenting the sub-groups of acidic ionic liquids (AILs) giving exemplar structures based on the dialkylimidazolium cation 2-6

▲Figure 2.3 - Optimised geometry of the confirmed crystal structure resulting from complexation of two equivalents of $[C_2C_2ImT][Cl]$ and Pd(II) 2-8

▲ Figure 2.4 - $Cu_{(aq)}$ recovery profiles for application of $[C_4C_1im][HSO_4]_{(aq)}$ to $CuFeS_{2(s)}$ concentrate 2-9

▲ Figure 2.5 - (A) Temperature dependence for the leaching of 10 $g{\cdot}L^{-1}$ $CuFeS_{2(s)}$ by 1.1 $mol{\cdot}dm^{-3}$ (20 *%v/v*) $[C_4C_1im][HSO_4]_{(aq)}$. (B) Influence of $[IL]_{(aq)}$ on Cu and Fe recovery from $CuFeS_2$ for two differing pulp densities. 2-11

▲ Figure 2.6 - $Cu_{(aq)}$ recovery in 1 $mol{\cdot}dm^{-3}$ $H_2SO_{4(aq)}$ versus 10, 20 and 50 *%v/v* $[C_1Him][HSO_4]_{(aq)}$ (black) and $[C_4C_1im][HSO_4]_{(aq)}$ (grey) at 20 *°C* (A), 40 *°C* (B) and 60 *°C* (C). (D) Cu recovery at 60 *°C* when 10 (▲), 20 (■) or 50 *%v/v* (●) $[C_1Him][HSO_4]_{(aq)}$ is combined with neat 1 $mol{\cdot}dm^{-3}$ $H_2SO_{4(aq)}$ (◆) as a leaching additive.[65] 2-12

▲ Figure 2.7 - Cyclic voltammogram (CV) of the electrochemical window of $[C_2C_1im][NTf_2]_{(l)}$ 2-13

▲ Figure 2.8 - Photographs of the electrochemical cell used to electrodeposit $Si_xGe_{(1-x)}$, following plating procedures in $[C_4C_1pyrr][NTf_2]_{(l)}$ 2-14

▲ Figure 2.9 - Selected BAIL structures employed for $CuFeS_{2(s)}$ hydrometallurgic studies 2-16

▲ Figure 2.10 - Experimental details and synthetic routes for $[C_4C_1im][HSO_4]_{(l)}$ 2-17

▲ Figure 2.11 - Sample UV-visible spectrum for 4-nitrotoluene in neat $H_2SO_{4(l)}$ 2-22

▲ Figure 2.12 - Linear variation of IL Hammett acidity 2-22

▲ Figure 2.13 - Free $[H^+]_{(aq)}$ concentration of aqueous acid solutions recorded at 24.0 ± 0.5 *°C* 2-23

▲ Figure 2.14 - Free-$[H^+]_{(aq)}$ for $IL_{(aq)}$ as indicated by conventional electrode potential-based *p*H measurements. 2-26

▲ Figure 2.15 - Relative permittivity data for pure $[C_nC_1im]$ ILs with various alkyl chain lengths. 2-27

▲ Figure 2.16 - Simplified schematic diagram of the internal electronics of a modern potentiostat, ...2-31

▲ Figure 2.17 - Cyclic voltammograms at $Pt_{(s)}$ (black) and $CNT|CeO_2|Pt_{(s)}$ (blue) electrodes in $Ar_{(g)}$ purged 0.5 $mol{\cdot}dm^{-3}$ $H_2SO_{4(aq)}$ 2-32

▲ Figure 2.18 - Cyclic voltammogram of glassy carbon disc WE (d=3 *mm*) in 0.5 $mol{\cdot}dm^{-3}$ $H_2SO_{4(aq)}$ containing 10 $mmol{\cdot}dm^{-3}$ $CuSO_{4(aq)}$. 2-33

▲Figure 2.19 - Recorded potential response of cupric ISE probe to varied $[CuSO_4]_{(aq)}$ 2-35

▲ Figure 2.20 - (A) Schematic overview of the internal operations involved in an ICP-AES spectrometer. (B) Schematic of K electron ejection through atomic collision in high temperature plasma 2-37

▲ Figure 2.21 - Investigation of Cu (blue) and Fe (red) ICP-AES matrix effects 2-38

▲ Figure 2.22 - Typical traces for the three stages of an ASV procedure to quantify $[Cu^{2+}]_{(aq)}$ from $[CuSO_4]_{(aq)}$.....2-40

▲ Figure 2.23 - Exemplar stripping charge (Q_{strip}) determinations for three back-to-back ASV repeats 2-42

▲ Figure 2.24 - Effect of IL and solution *p*H on calculated Beer-Lambert molar extinction coefficient of $CuSO_{4(aq)}$ absorption at *p*H1 for d-d transition of $Cu^{2+}{}_{(aq)}$ centred at ~800 *nm*. 2-44

▲ Figure 2.25 - (A) Colour-coded UV-visible spectrum and (B) magnification of d-d electronic transition region displaying shifts due to *p*H changes in 450 $mol{\cdot}dm^{-3}$ $[C_4Him][HSO_4]_{(aq)}$ solution with 10 $mmol{\cdot}dm^{-3}$ $CuSO_{4(aq)}$.....2-45

▲ Figure 2.26 - Experimental designs for two 400 *mL* scale vessels for long duration (~1 *month*) $CuFeS_{2(s)}$ leaching trials.....2-47

▲ Figure 2.27 – SEM detection principle for a given probe volume of $CuFeS_{2(s)}$ 2-49

▲ Figure 2.28 – Simplified schematic representation of the stages of tof-SIMS.....2-50

Chapter 3 - Custom Instrumentation & Programming Techniques

▲ Figure 3.1 - Photographic image of the CNC robotic platform.....3-3

▲ Figure 3.2 - To-scale (overhead) technical schematic of the automated robotic platform .....
.....3-4

▲ Figure 3.3 – (left) Simplified technical schematic for a bipolar stepper motor,.....3-5

▲ Figure 3.4 - Custom-built stepper motor control box based on Arduino Uno SMD rev3® microprocessing hardware.....3-6

▲ Figure 3.5 - Flowchart summarising the Arduino© pulsed voltage signalling of four independent stepper motors for manipulation of the probe location in x, y, z dimensions 3-8

▲ Figure 3.6 – Schematic of a simple section of the PipettingRobot.vi virtual instrument.....
.....3-13

▲ Figure 3.7 – Example of an NI LabView® front panel for configuration of the robotic pipetting instrument.....3-14

▲ Figure 3.8 – Graphical coding of UVVis_Abs.vi.....3-16

▲ Figure 3.9 – Graphical coding example for 3-channel data acquisition.....3-17

▲ Figure 3.10 – (A) Linear measured R_s in response to varied $KCl_{(aq)}$ reference solution resistivity (1-50 $mmol{\cdot}dm^{-3}$) for three fabricated electrodes. (B) Measured conductivity of 1-50 $mmol{\cdot}dm^{-3}$ $CuSO_{4(aq)}$.....3-19

▲ Figure 3.11 – (A-B) ICP-AES [M] measurements on 50 standard 75 $mmol{\cdot}dm^{-3}$ H_2SO_4 samples containing the indicated $[CuSO_4]_{(aq)}$ and $[Fe_2(SO_4)_3]_{(aq)}$. (C) Associated ASV Q_{strip} measurements and (D) electrodeposition efficiency variation upon variation of $[Cu^{2+}]_{(aq)}$ and $[Fe^{3+}]_{(aq)}$. 3-20

▲ Figure 3.12 – Labelled interactive graphical outputs of semi-automated stripping peak analysis program,.....3-23

Chapter 4 - Electrochemical Monitoring of Leaching

▲ Figure 4.1 - 20 $mmol{\cdot}dm^{-3}$ $CuCl_{2(IL)}$ in eight pure ILs based on $[C_2C_1]^+$ ILs and ChCl DESs .....
.....4-4

▲ Figure 4.2 – Resolved crystallographic structure of *catena*-Poly[[[tetrakis(1-methylimidazole-κN^3)copper(II)]- μ^2-sulfato-$\kappa^2 O{:}O'$] acetonitrile hemisolvate sesquihydrate].....4-4

▲ Figure 4.3 – (A) $Cu_{(s)}$ K-shell electron attenuation coefficient upon incidence of varied X-ray photon energies, showing EXAFS region of interest at 30-1000 *eV*. (B) Fourier transformed EXAFS data φ(r) for crystalline-$Cu_{(s)}$ 4-6

▲ Figure 4.4 – Functions generated for all $Cu_{(aq)}$ samples submitted for synchrotron-EXAFS studies 4-8

▲ Figure 4.5 – Experimental EXAFS data for 10 $mmol \cdot dm^{-3}$ $CuSO_{4(aq)}$ reference solutions in various media (blue) in comparison to fitted curves for optimised $Cu(H_2O)_4(SO_4)$ coordination geometries (red). 4-9

▲ Figure 4.6 – (A) Cu recovery (72 *hr*) as a function of $[IL]_{(aq)}$ as measured by ASV in a 2-electrode configuration ($Pt_{(s)}$ WE; $Pt_{(s)}$ CE/RE). (B) Cu recovery as a function of time for 10 *%wt* $[IL]_{(aq)}$ and 75 *mM* $H_2SO_{4(aq)}$ reference. 4-11

▲ Figure 4.7 – Measured viscosity of $IL_{(aq)}$ solutions (datapoints), displayed alongside Newtonian two-component estimates 4-14

▲ Figure 4.8 – (A) Predicted variation of the diffusion coefficient for $Cu^{2+}{}_{(aq)}$ as a function of *%* $[IL]_{(aq)}$ composition. (B) Predicted total $Cu^{2+}{}_{(aq)}$ electrodeposition charge (Q_{dep}) accumulated during 300 *s* electrodeposition in $IL_{(aq)}$. 4-15

▲ Figure 4.9 – Cottrellian simulation of Q_{dep} measured during 300 *s* electrodeposition as a function of $[IL]_{(aq)}$ 4-16

▲ Figure 4.10 – Q_{dep} (A) and Q_{strip} (B) ASV calibration data 4-18

▲ Figure 4.11 – Calculated EE values 4-21

▲ Figure 4.12 – Plateaued $Cu_{(s)}$ stripping charge calibration plots for 2-vial ASV 4-22

▲ Figure 4.13 – (A) Experimental and (B) theoretical Q_{dep} data (t_{dep} = 120 s) for 1-vial ASV conducted in 450 $mmol \cdot dm^{-3}$ $[C_4Him][HSO_4]_{(aq)}$ (*p*H 1.2) with addition of indicated concentrations of $[Fe_2(SO_4)_3]_{(aq)}$ and $[CuSO_4]_{(aq)}$ 4-23

▲ Figure 4.14 – (A) Simulated q(t) curves for $Cu^{2+}{}_{(aq)}$ electrodeposition in varied strength $[C_nC_mim][HSO_4]_{(aq)}$. (B) Cottrellian plot for 10 $mmol \cdot dm^{-3}$ $[Cu^{2+}]_{(aq)}$ 4-25

▲ Figure 4.15 – Comparison of predicted Cottrellian plots (grey) with analogous plots for experimental ASV data (coloured). 4-26

▲ Figure 4.16 – Experimental apparatus for automated electrochemical monitoring of $CuFeS_{2(s)}$ dissolution 4-29

▲ Figure 4.17 – Raw *in situ* ASV data obtained during the monitoring of $CuFeS_{2(s)}$ dissolution in 450 $mmol \cdot dm^{-3}$ $NH_4 \cdot HSO_{4(aq)}$ 4-31

▲ Figure 4.18 – (A) Normalised ASV stripping charge profile for $CuFeS_{2(s)}$ dissolution in 450 *mmol·dm*$^{-3}$ $NH_4{\cdot}HSO_{4(aq)}$. (B) ASV $[Cu^{2+}]_{(aq)}$ measurements obtained from still solution 4-32

▲ Figure 4.19 - (A) Normalised ASV stripping charge profile for $CuFeS_{2(s)}$ dissolution in 450 *mmol·dm*$^{-3}$ $[C_4Him][HSO_4]_{(aq)}$. (B) ASV $[Cu^{2+}]_{(aq)}$ measurements obtained from still solution 4-33

▲ Figure 4.20 – (A) Normalised ASV stripping charge profile for $CuFeS_{2(s)}$ dissolution in 75 *mmol·dm*$^{-3}$ $H_2SO_{4(aq)}$. (B) ASV $[Cu^{2+}]_{(aq)}$ measurements obtained from still solution 4-34

▲ Figure 4.21 - (A) $Cu_{(aq)}$ stripping CV scan showing double peak feature for two independent of *in situ* ASV in 450 *mmol·dm*$^{-3}$ $[C_1C_1pz][HSO_4]_{(aq)}$. (B) all corrected ASV Q_{strip} measurements obtained at various timescales (primary y-axis), compared to ICP-AES values 4-35

Chapter 5 - Up-scaled $IL_{(aq)}$ Leaching Studies

▲ Figure 5.1 - Raw data for 400 *mL*-scale $CuFeS_{2(s)}$ dissolution in 75 *mmol·dm*$^{-3}$ $H_2SO_{4(aq)}$ over extended ~1 *month* ambient leach durations..... 5-6

▲ Figure 5.2 - Raw data for 400 *mL*-scale $CuFeS_{2(s)}$ dissolution in 450 *mmol·dm*$^{-3}$ $[C_4Him][HSO_4]_{(aq)}$ over extended ~1 *month* ambient leach durations 5-8

▲ Figure 5.3 - Variation of lixiviant E_h as a function of $[C_4C_1im][HSO_4]_{(aq)}$ concentration. 5-10

▲ Figure 5.4 - Raw data for 400-*mL* scale $CuFeS_{2(s)}$ dissolution in 450 *mmol·dm*$^{-3}$ $NH_4{\cdot}HSO_{4(aq)}$ over extended ~1 *month* ambient leach durations 5-11

▲ Figure 5.5 - Example of $[Cu]_t$ non-linear fits of raw data for $CuFeS_{2(s)}$ dissolution..... 5-13

▲ Figure 5.6 - Plots and linear fits (table 5.2) of free-$[H^+]_{(aq)}$ concentration as a function of time during ~1 *month* $CuFeS_{2(s)}$ dissolution 5-15

▲ Figure 5.7 - Plots of raw E_h data overlaid with their corresponding non-linear fits (table 5.4) as a function of time during ~1 *month* $CuFeS_{2(s)}$ dissolution..... 5-20

▲ Figure 5.8 - (A) Variation in $\log_{10}[Fe^{3+}]/[Fe^{2+}]$ and (B) associated (linear) development of free-$[Fe^{3+}]_{(aq)}$ as a function of time during ~1 *month* ambient $CuFeS_{2(s)}$ dissolution, as computed from E_h and $[Fe]_{(aq)}$ measurements..... 5-21

▲ Figure 5.9 - Plot of the fraction of $O_{2(aq)}$-assisted $CuFeS_{2(s)}$ dissolution ($xk1$) as a function of leach duration..... 5-24

▲ Figure 5.10 - High resolution SEM images of unleached $38 \leq x \leq 75$ *μm* size fractioned $CuFeS_{2(s)}$ 5-26

▲ Figure 5.11 - 30 μm^2 SEM images of a milled $CuFeS_{2(s)}$ particle following 720 *hrs* ambient dissolution in 450 $mmol \cdot dm^{-3}$ $[C_4Him][HSO_4]_{(aq)}$. (A) Primary backscattered image (B) Secondary electron image. 5-27

▲ Figure 5.12 - (A) EDX elemental surface compositions obtained at low magnification for large areas of massive $CuFeS_{2(s)}$, averaged over all samples leached in 450 $mmol \cdot dm^{-3}$ $IL_{(aq)}$ and 75 $mmol \cdot dm^{-3}$ $H_2SO_{4(aq)}$ with and (B) without inclusion of surface oxide contributions..... 5-28

▲ Figure 5.13 - High magnification EDX elemental surface compositions before and after the 30 *day* leaching of (A) 38-75 μm $CuFeS_{2(s)}$ powder and (B) 1.0x0.5x0.5 *cm* $CuFeS_{2(s)}$ samples in $IL_{(aq)}/H_2SO_{4(aq)}$ media 5-29

▲ Figure 5.14 - EDX elemental composition of non-stoichiometric moieties presented at the surface of massive $CuFeS_{2(s)}$ leached for 720 *hrs* in $IL_{(aq)}/H_2SO_{4(aq)}$, with number of corroborating spectra given in brackets.....5-30

▲ Figure 5.15 - Selected ion fragment intensity signals (static ToF-SIMS) as a function of Cs^+ ion sputter time for atmospherically oxidised yet unleached $CuFeS_{2(s)}$ 5-32

▲ Figure 5.16 - Dynamic ToF-SIMS relative surface elemental composition at the indicated sputter times (SpT) for massive $CuFeS_{2(s)}$ samples leached for 240 *hrs* in $IL_{(aq)}/H_2SO_{4(aq)}$ 5-34

▲ Figure 5.17 - Dynamic ToF-SIMS relative surface elemental composition at the indicated sputter times (SpT) for massive $CuFeS_{2(s)}$ samples leached for 720 *hrs* in $IL_{(aq)}/H_2SO_{4(aq)}$ 5-35

Chapter 6 - $IL_{(aq)}$ Screening & Mechanistic Insights

▲ Figure 6.1 - Cationic structures for N,N-dimethylpyrazolium [C_1C_1pz] and 1-methylpiperidinium [C_1pip].....6-3

▲ Figure 6.2 - Molar $Cu_{(s)}$ stripping charge suggested by normalisation of ASV data by independently verified ICP-AES $[Cu^{2+}]_{(aq)}$ measurements.....6-4

▲ Figure 6.3 - (A) ASV-determined $[Cu^{2+}]_{(aq)}$ for 10 equivalent $IL_{(aq)}$-$CuFeS_{2(s)}$ samples (4 *mL*; 450 $mmol \cdot dm^{-3}$ $NH_4 \cdot HSO_{4(aq)}$; 298 *K*; unagitated) obtained at 72 (O), 120 (□) and 216 *hrs* (△) leach durations. (B) $[Cu^{2+}]_{(aq)}$ quantification correlation plot for independent ASV and ICP-AES measurements. 6-5

▲ Figure 6.4 - (A) Colour-coded vial diagram expressing ICP-AES determined $[Cu^{2+}]_{(aq)}$ following 264 *hrs* leaching of 3 *mL* $NH_4 \cdot HSO_{4(aq)}$ samples with varied $[IL]_{(aq)}$ and mass:volume ratio. (B) Correlation plot for first repeat (■) and later repeat (○) electrochemical $[Cu^{2+}]_{(aq)}$ measurements against corresponding ICP-AES values. 6-6

▲Figure 6.5 - (A) $[Cu^{2+}]_{(aq)}$ correlation plot for ICP-AES and ASV screening of 450 *mmol·dm*$^{-3}$ $IL_{(aq)}$ solutions following 165 *hrs* ambient leaching. (B) $Cu^{2+}{}_{(aq)}$ extraction as a function of $[IL]_{(aq)}$. 6-8

▲ Figure 6.6 - (A) ICP-AES determined Cu^{2+} (blue) and Fe^{2+} recoveries (red) for screening of $NR_4{\cdot}HSO_{4(aq)}$ systems following 72 *hrs* ambient $CuFeS_{2(s)}$ leaching. (B) Associated free-$[H^+]_{(aq)}$ for screened $NR_4{\cdot}HSO_{4(aq)}$ systems 6-9

▲ Figure 6.7 - ICP-AES $Cu^{2+}{}_{(aq)}$ (blue) and $Fe^{2+}{}_{(aq)}$ (red) recoveries for 150 *hrs* ambient $CuFeS_{2(s)}$ dissolution in 450 *mmol·dm*$^{-3}$ $NR_4{\cdot}HSO_{4(aq)}$ solution....6-9

▲ Figure 6.8 - (A) ICP-AES determined $Cu^{2+}{}_{(aq)}$ (blue) and $Fe^{2+}{}_{(aq)}$ (red) following 120 *hrs* $CuFeS_{2(s)}$-leaching in 450 *mmol·dm*$^{-3}$ $[C_4Him][HSO_4]_{(aq)}$ upon addition of $Na_2SO_{4(aq)}$ with recorded leachate *p*H (□). 6-10

▲ Figure 6.9 - (A) ICP-AES determined $Cu^{2+}{}_{(aq)}$ (blue) and $Fe^{2+}{}_{(aq)}$ (red) recoveries following 331 *hrs* $CuFeS_{2(s)}$-leaching in 450 *mmol·dm*$^{-3}$ $[C_4Him][HSO_4]_{(aq)}$ with variation of added $[C_4im]$, with neat solution free-$[H^+]_{(aq)}$ shown (□). (B) Magnification of $Cu^{2+}{}_{(aq)}$ recoveries showing $Cu^{2+}{}_{(aq)}$ recovery using 450 *mmol·dm*$^{-3}$ $[C_4im]_{(aq)}$ 6-12

▲ Figure 6.10 - (A) ICP-AES determined $Cu^{2+}{}_{(aq)}$ (blue) and $Fe^{2+}{}_{(aq)}$ (red) recoveries following 120 *hrs* $CuFeS_{2(s)}$-leaching in 450 *mmol·dm*$^{-3}$ $Et_3NH{\cdot}HSO_{4(aq)}$ with variation of added $[NEt_3]$, with free-$[H^+]_{(aq)}$ shown before leaching (□). (B) Magnification of $Cu^{2+}{}_{(aq)}$ recoveries showing $Cu^{2+}{}_{(aq)}$ recovery using 450 *mmol·dm*$^{-3}$ $NEt_{3(aq)}$ 6-13

▲ Figure 6.11 - ICP-AES determined $Cu^{2+}{}_{(aq)}$ (blue) and $Fe^{2+}{}_{(aq)}$ (red) recovery following 132 *hrs* $CuFeS_{2(s)}$ dissolution in varied concentrations of (A) $[C_4Him][HSO_4]_{(aq)}$ (B) $EtNH_3{\cdot}HSO_{4(aq)}$..... 6-14

▲ Figure 6.12 - ICP-AES determined $Cu^{2+}{}_{(aq)}$ (blue) and $Fe^{2+}{}_{(aq)}$ recoveries for 450 *mmol·dm*$^{-3}$ $IL_{(aq)}$ (A) $[C_4Him][HSO_4]_{(aq)}$ - showing independent UV-visible spectroscopic $[Cu^{2+}]_{(aq)}$ measurements (□) (B) $[C_2C_1im][HSO_4]_{(aq)}$ (C) 75 *mmol·dm*$^{-3}$ $H_2SO_{4(aq)}$ (D) $EtNH_3{\cdot}HSO_{4(aq)}$..... 6-15

▲ Figure 6.13 - Mechanism for 'click' [3+2] cycloaddition of benzylazide and phenylacetylene 6-17

▲ Figure 6.14 - (A) Imidazolium-based N-heterocyclic carbene (NHC) ligands, containing bulky substituents stabilising the carbene species. (B) Ball and stick representation of NHC-Cu(I) complex (IPr)CuR]....6-17

▲ Figure 6.15 - ICP-AES $Cu^{2+}{}_{(aq)}$ (blue) and $Fe^{2+}{}_{(aq)}$ (red) metal recoveries for 120 *hrs* $CuFeS_{2(s)}$ dissolution from 450 *mmol·dm*$^{-3}$ $[C_4Him][HSO_4]_{(aq)}$ and $[EtNH_3{\cdot}HSO_4]_{(aq)}$ lixiviant solution in varied atmospheric conditions ($O_{2(g)}$ sparged; $Ar_{(g)}$ sparged; natural atmosphere) and with freshly fractured and 3 week old oxidised $CuFeS_{2(s)}$. 6-19

▲ Figure 6.16 - $Cu^{2+}_{(aq)}$ (blue) and $Fe^{2+}_{(aq)}$ (red) recoveries from 150 *hrs* of $CuFeS_{2(s)}$ leaching in (A) 450 $mmol \cdot dm^{-3}$ $IL_{(aq)}$ and (B) a selection of (partially water miscible) 450 $mmol \cdot dm^{-3}$ amine bases. 6-20

List of Tables

Chapter 1 - The Extraction of Copper from Chalcopyrite

▼ Table 1.1 – Atmospheric acidic-$SO_4^{2-}{}_{(aq)}$ related processes developed for $CuFeS_{2(s)}$ or other copper sulfide concentrates/ores: 1-18

▼ Table 1.2 – Summary of $CuFeS_{2(s)}$ dissolution kinetics studies, detailing Arrhenius parameters (rate laws, E_a, A), best fitting shrinking core model rate laws and associated kinetic conclusions 1-20

▼ Table 1.3 - Rest potentials of common relevant sulfide minerals. 1-31

Chapter 2 - Ionic Liquids, Materials and Methods

▼ Table 2.1 - Effect of $[C_4C_1im][HSO_4]_{(aq)}$ concentration on Cu extraction from $CuFeS_2$ concentrate at 70 °*C* after 24 *hrs* leaching. 2-9

▼ Table 2.2 - Measured dissolved oxygen concentrations for selected ILs at a range of temperatures. 2-10

▼ Table 2.3 - Kamlet-Taft parameters for selected ILs & molecular solvents. 2-19

▼ Table 2.4 - Physical data for selected pure $[C_nC_mim]^+$ (293 *K*) and $[NR_4]^+$ (298 *K*) Brönsted acidic ILs at atmospheric pressure. 2-24

▼ Table 2.5 - Selected viscosity measurements for validation of chosen rheological procedure in comparison to literature values. 2-25

▼ Table 2.6 - Dynamic viscosity measurements for pure $[C_nC_mim]^+$ ILs 2-25

▼ Table 2.7 – Summary of theoretical permittivity analysis of $[C_nC_mim][HSO_4]_{(aq)}$ binary solutions. 2-28

▼ Table 2.8 - ICP-AES mineral composition for independent 200 *mg* $CuFeS_{2(s)}$ samples digested in 10 *mL* aquaregia. 2-29

▼ Table 2.9 - XRF determined composition for a 51.0 *mg* sample of commercially sourced $CuFeS_{2(s)}$ 2-30

▼ Table 2.10 - Summary of ASV modes, nomenclatures and procedural details 2-43

▼ Table 2.11 – Electronic transition analysis for selected UV-visible spectra 2-46

Chapter 3 - Custom Instrumentation & Programming Techniques

▼ Table 3.1 – Summary of coding functionalities included in Arduino® firmware 3-10

▼ Table 3.2 – Summary of NI LabView sub-VIs coding functionalities 3-12

▼ Table 3.3 – Summary of NI LabView VIs 3-15

▼ Table 3.4 – Geometric factor measurements for three double-Pt disc electrodes and linear fit parameters. 3-18

▼ Table 3.5 – Summary of MatLab® coded programs for electrochemical batch analysis. 3-22

▼ Table 3.6 – Summary of MatLab® coded functions included within the ASV_ST_Analysis.m semi-automated program 3-24

Chapter 4 - Electrochemical Monitoring of Leaching

▼ Table 4.1 – Compositions of 3 *mL* samples submitted to synchrotron-EXAFS studies 4-7

▼ Table 4.2 – Summary of EXAFS structural modelling of 10 $mmol \cdot dm^{-3}$ $CuSO_{4(aq)}$ in (A) pure aqueous solution and (B) 450 $mmol \cdot dm^{-3}$ $[C_4Him][HSO_4]_{(aq)}$. 4-10

▼ Table 4.3 – $Cu_{(s)}$ stripping charge calibration parameters (linear fit) measured for conventional 3-vial ASV 4-17

▼ Table 4.4 – Linear fit parameters for ASV calibration of 1-vial and 2-vial ASV procedures 4-19

▼ Table 4.5 – Summary of simulated Cottrellian plot gradient (K) and Q_{dep} variation 4-25

▼ Table 4.6 – Summary of Cottrellian analysis 4-28

▼ Table 4.7 – Summary of effective diffusion coefficient values 4-37

Chapter 5 - Up-scaled $IL_{(aq)}$ Leaching Studies

▼ Table 5.1 - Summary of the non-linear fitting of $Cu^{2+}_{(aq)}$ extraction profiles 5-14

▼ Table 5.2 - Summary of linear fit parameters for $[H^+]_{(aq)}$ evolution in 400 *mL*-scale extended $CuFeS_{2(s)}$ dissolution experiments 5-16

▼ Table 5.3 - Summary of key measured E_h changes during ~1 *month* 400 *mL*-scale $CuFeS_{2(s)}$ ambient dissolution experiments. 5-17

▼ Table 5.4 - Summary of non-linear fitting of raw E_h profiles 5-19

▼ Table 5.5 - Linear fit parameters for evolution of $[Fe^{3+}]_{(aq)}$ as a function of time during ~1 *month* ambient $CuFeS_{2(s)}$ dissolution in $IL/H_2SO_{4(aq)}$. 5-22

Chapter 6 - $IL_{(aq)}$ Screening & Mechanistic Insights

▼ Table 6.1 – Analysis of sample-to-sample variation for 10 samples leached in parallel under equivalent conditions.....6-5

Lists of Abbreviations & Constants

The following notations are used throughout this text; defined at first use and used (unless otherwise stated) based on the recommendations of the IUPAC Commission on Electrochemistry [Parsons, R. *et al.*, *Pure Appl. Chem.*, 37, **1974**, 503].

Standard Subscripts		Standard Superscripts	
(aq)	Solubilised species in aqueous media	$\emptyset$	Assigned under standard conditions
(s)	Species in solid phase	$n+$	*n-order* positive electronic charge
(l)	Species in liquid phase	$n-$	*n-order* negative electronic charge
0	Pertaining to the initial value of a quantity	n / v_i	Rate equation molecularity
a	Pertaining to activation of a process		
CB	Pertaining to the conduction band		
d	Pertaining to an dopant species		
dep	Pertaining to electrodeposition process		
EDL	Pertaining to electric double layer		
$fermi$	Pertaining to the Fermi energy		
g	Pertaining to the electronic band gap		
h	Pertaining to solution reduction potential		
lim	Pertaining to a limiting value		
$onset$	Pertaining to the onset of a process		
$redox$	Pertaining to a redox process		
s	Pertaining to solution		
ss	Under steady state conditions		
$strip$	Pertaining to oxidative stripping process		
t	Pertaining to a measured timescale		
tot	Pertaining to the total of a variable		
VB	Pertaining to the valence band		

Roman Symbols

Symbol	Definition	Units
$[j]$	Molar concentration of species j	*mol·dm^{-3}*
A	Surface area (geometric or otherwise) / Absorbance	*cm^2 / none*
$a\{j\}$	Activity of a species j, i.e. $a\{j\} = \gamma_j \cdot b/b^{\emptyset}$	*none*
B	Magnetic field strength	*T*
b	Molality	*mol·kg^{-1}*
C	Capacitance	*F*
C_j^*	Bulk concentration of species j	*mol·dm^{-3}*
D_j	Diffusion coefficient of species j	*cm^2·s^{-1}*
E	Potential measured with respect to a reference potential / Energy	*V / J·mol^{-1}*
e	Election / elementary charge	*none / C*
F	Faraday constant, charge of one mole of electrons	*C*
f	Frequency of a sinusoidal oscillation	*Hz (s^{-1})*
i	Current / Imaginary number	*A (C·s^{-1}) / none*
I	Intensity	*Counts·s^{-1}*
j	Current density	*A·cm^{-2}*
J_j	Diffusive flux of a species j	*mol·cm^{-2}*
K	Equilibrium constant	*variable*
k	Kinetic rate constant	*variable*
l	Absorbance path length	*cm*
M	Metal atom	*none*
N_A	Avogadro constant	*mol^{-1}*
n	Number of an entity	*none*
Ox	Oxidised species of a couple: i.e. Ox + *ne$^-$* ⇆ Red	*none*
Q	Charge transferred	*C*
R	Gas constant / Resistance	*J·mol^{-1}·K^{-1} / Ω*
r	Radial distance / of a circular geometry	*m / cm*

Symbol	Definition	Units
T	Absolute temperature	*K*
t	Time / Mass	*s / tonnes*
V	Volume	*L (dm^3)*
v	Linear potential scan rate / By volume	*$mV \cdot s^{-1}$ / dm^3*
x_j	Fraction of species j as a function of molar composition	*none (%)*
X	Halogen atom	
Y	Admittance	*Ω^{-1}*
Z	Impedance	*Ω*
z	Transferred electrons in an electrochemical couple	*none*

Greek and Letter-Like Symbols

Symbol	Definition	Units
Å	Angstrom	$10^{-10} \cdot m$
α / β	Opposing atom magnetic spin state	*none*
γ_j	Activity coefficient for a species j	*none*
Δ	Difference in value between two measurements	*N/A*
ε	Molar extinction coefficient	$L \cdot mol^{-1} \cdot cm^{-1}$
η	Viscosity	$Pa \cdot s$
κ	Solution conductivity	Ω^{-1}
ρ	Resistivity	$\Omega \cdot cm$
ϕ	Phase angle separating two sinusoidal signals / Potential drop	*rad. / mV*
ω	Angular frequency of a sinusoidal oscillation: $2\pi f$	s^{-1}
λ	Wavelength	*m*
μ	Linear attenuation coefficient	m^{-1}

Standard Abbreviations

Abbreviation	Definition
AIL	Acidic ionic liquid
ASV	Anodic stripping voltammetry
at	atom
BAIL	Brönsted acidic ionic liquid
ca	*circa*
CB	Conduction band
CE	Counter electrode
cf	*conferre (compare)*
CV	Cyclic voltammetry
DES	Deep eutectic solvent
DFT	Density functional theory
EDX	Energy dispersive x-ray spectroscopy
EE	Electrodeposition efficiency
EIS	Electrochemical impedance spectroscopy
EXAFS	Extended x-ray absorption fine structure spectroscopy
IL	Ionic liquid
ISE	Ion selective electrode
PIL	Protic ionic liquid
RDS	Rate determining step
RE	Reference electrode
rpm	Revolutions per minute
SEM	Scanning electron microscopy
SHE	Standard hydrogen electrode
TSIL	Task-specific ionic liquid
ToF-SIMS	Time of flight secondary ion mass spectroscopy
UHV	Ultra-high vacuum

Abbreviation	Definition
WE	Working electrode
wt	Weight
XANES	X-ray absorption near-edge spectroscopy
XAS	X-ray absorption spectroscopy
XRD	X-ray diffraction
XRF	X-ray fluorescence
XPS	X-ray photoelectron spectroscopy

Chapter 1

The Extraction of Copper from Chalcopyrite

Contents

1.1 Copper 1-3

1.1.1 Global Copper Demand 1-3

1.1.2 Geological Origins of Copper 1-4

1.2 Chalcopyrite 1-4

1.2.1 Structural Characterisation of $CuFeS_{2(s)}$ 1-4

1.2.2 Physical Characterisation of $CuFeS_{2(s)}$ 1-5

1.2.3 Electromagnetic Characterisation of $CuFeS_{2(s)}$ 1-6

1.2.4 Chemical Characterisation of $CuFeS_2$ 1-8

1.3 Industrial Extraction Techniques 1-9

1.3.1 Pyrometallurgic Processing 1-9

1.3.2 Hydrometallurgic Processing 1-11

1.4 $CuFeS_{2(s)}$ Dissolution Modes 1-12

1.4.1 Non-Oxidative Dissolution 1-13

1.4.2 Oxidative Dissolution 1-13

1.4.3 Potential Assisted / Anodic Dissolution 1-14

1.4.4 Bioleaching 1-15

1.5 Ambient Lixiviant Systems 1-17

1.6 Kinetic Influences 1-18

1.6.1 Dissolution Rates 1-21

1.6.2 Effect of Particle Size 1-22

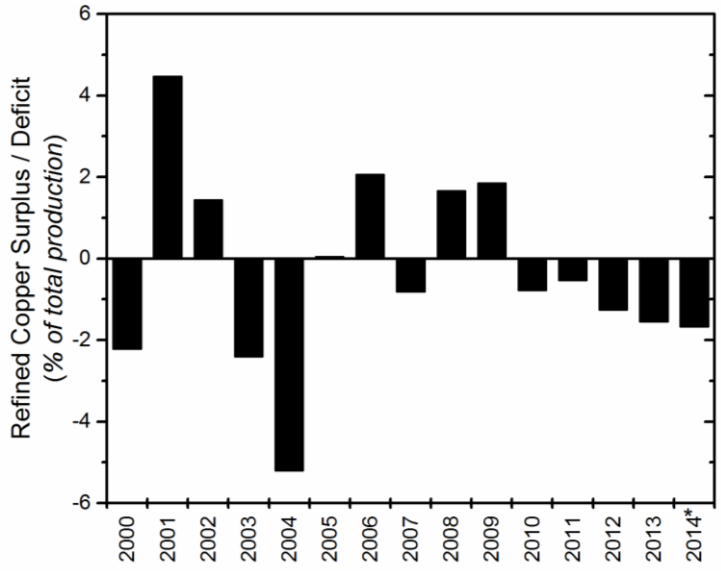
1.6.3 Effect of Agitation 1-22
1.6.4 Effect of Oxidant 1-23
1.6.5 Effect of Dissolution Enhancing Additives 1-24
1.6.6 Effect of Acid and pH 1-25
1.6.7 Effect of Temperature 1-26
1.6.8 Effect of Solution Redox Potential (E_h) 1-27
1.6.8.1 E_h Detection Principle 1-27
1.6.8.2 E_h Control 1-29
1.6.9 Effect of Galvanic Coupling 1-30
1.7 Mechanistic Insights 1-33
1.7.1 Dissolution Products 1-33
1.7.2 Mechanisms for Acidic $CuFeS_{2(s)}$ Dissolution 1-34
1.8 Kinetic Hindrance of $CuFeS_{2(s)}$ Dissolution 1-37
1.8.1 Surface Chemistry of $SO_4^{2-}{}_{(aq)}$ Leaching 1-38
1.8.2 Elemental Sulfur (S^0) 1-38
1.8.3 Metal-Deficient Sulfides (CuS_n) 1-40
1.8.4 Polysulfides (S_n^{2-}) 1-41
1.8.5 Jarosites 1-42
1.9 Outlook: Chemical Leaching 1-43
1.10 Thesis Structure 1-44
1.10.1 Aims and Objectives Statement 1-44
1.10.2 Summary of Key Aims 1-45
1.10.3 Thesis Outline 1-46
1.11 References 1-48

Synopsis: The chapter presented hereafter is intended to provide the reader with effective coverage of relevant geochemical principles and key background information from previous research efforts within the wider field of $CuFeS_{2(s)}$ processing – specifically focused on introducing the application of $acid_{(aq)}$ lixiviant systems to ambient $CuFeS_{2(s)}$ hydrometallurgy.

1.1 Copper

Copper (Cu) has remained an important economic commodity for over 10,000 years,[1] with Eurasian cast copper coins and ornaments first emerging in ~7,000 BC.[2] From these humble beginnings in the Chalcolythic period, $Cu_{(s)}$ has become increasingly prominent, generally advancing in status in line with periodic waves of scientific discoveries. The first such period was the beginning of the Bronze Age (c. 2800 BC), where material benefits of bronzed (hardened) copper-alloys saw copper usage intensify.[3]

The next major hurdle came with the Industrial Revolution (c. 1760 AD), where the electrical and magnetic discoveries of Faraday, Ampere and Ohm relied heavily on the conducting properties of copper.[3] In modern times, the scope of industrial, material and electronic applications of $Cu_{(s)}$ and its processed derivatives make for an extremely valuable economic commodity – the demand for which is ever increasing. Over its lifetime, an average residential property can consume ~200 kg of $Cu_{(s)}$,[4] where a diverse range of technological applications have been developed to benefit from intrinsic chemical stability, durability, thermal and electrical conductivity, ductility – the list goes on.



▲ Figure 1.1 - Annual refined $Cu_{(s)}$ extraction surplus (positive %) or deficit (negative %) as a percentage of total global $Cu_{(s)}$ extraction between the years 2000-2014 - *unconfirmed preliminary data for 2014.[3]

1.1.1 Global Copper Demand

It is a matter of concern that refined $Cu_{(s)}$ extraction-demand pressures have been heightened in recent years.[3-5] Annual global $Cu_{(s)}$ extraction rates are rising year-on-year[3, 4] – 2008/09: 19.99 *Mt*; 2012/13: 20.15 *Mt* (figure 1.5), with forecast data continuing to predict future refined $Cu_{(s)}$ extraction-demand shortfalls. For example, a deficit of 240 *kt* was anticipated for 2013-2014, whilst an estimated 320 *kt* was realised.[4, 6] In fact, since 2010 a total refined $Cu_{(s)}$ shortfall of 5.8 *%* has developed (figure 1.1) - a trend that needs to be addressed, especially in view of the recent sharp ~20 *%* decline in $Cu_{(s)}$ commodity valuations (2011: *8,800 US$ / tonne*; 2014: 6,900 *US$ / tonne*).[3]

With such alarming figures in evidence, it is no surprise that the industry is exploring new technologies with potentially superior $Cu_{(s)}$ recovery efficiencies.

1.1.2 Geological Origins of Copper

The principal abundant Cu bearing ores are sulfides and oxides, although copper can be found in a native state.[7-9] The geological origins of such ore bodies are a result of hydrothermal activity driving fluids out of cooling magma, causing metal-enriched metalliferous veins in large porphyry rock deposits. Alternatively, Cu bearing ores can also be formed in secondary enrichment zones of other carbonate/silicate mineral deposits or in sedimentary rock under the correct redox conditions.[7-9] Due to metallic enrichment ('ore concentration'), Cu is often found in coexistence with other precious sought-after heavy metals such as gold, silver, molybdenum, tungsten and rhenium.[10]

1.2 Chalcopyrite

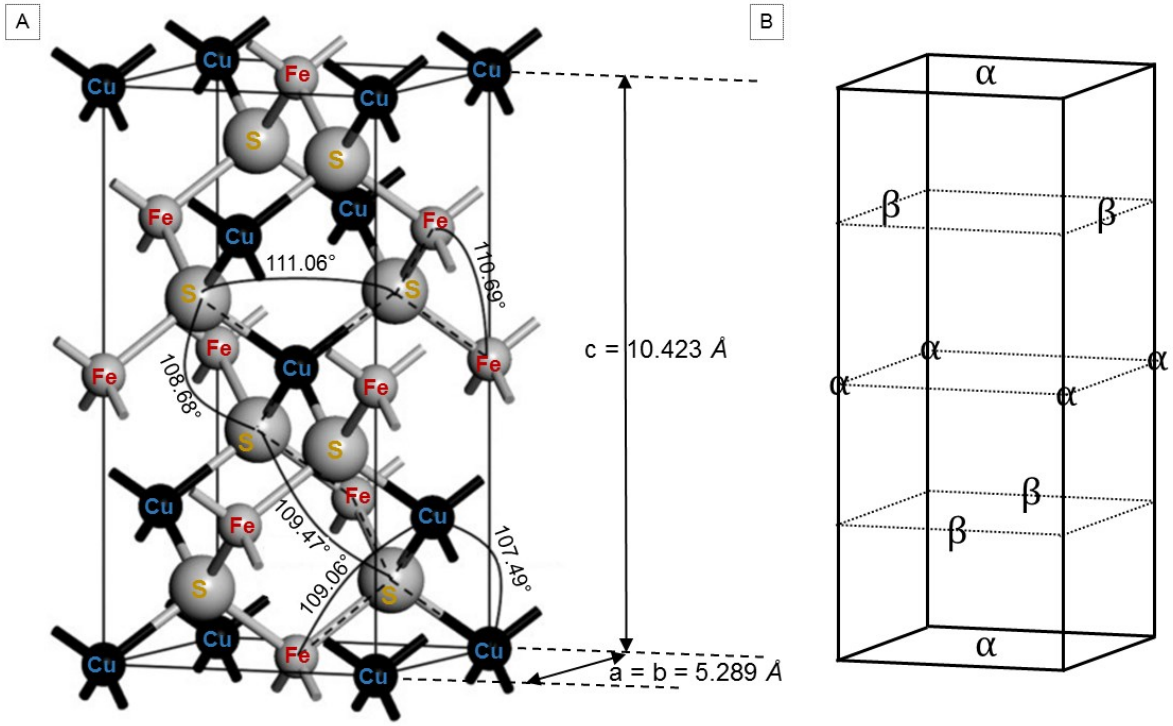
Of the above sources, chalcopyrite ($CuFeS_{2(s)}$) is the most abundant and commercially important naturally occurring source of copper, accounting for ~70% of worldwide copper reserves.[7, 11] Total identified global sources of Cu are currently estimated at 2,100 *Mt*,[3] of which 1,470 *Mt* is stored as $CuFeS_{2(s)}$. In pre-history, chalcopyrite was laid-down as part of large porphyry rock deposits, the largest known example of which is beneath the Atacama Desert in Chile (~78 km^2).[10] $CuFeS_{2(s)}$ is frequently intergrown with other common copper sulfide minerals, accounting for compositional analyses which do not represent the theoretical proportions of the empirical formula (section 5.5).[11] Au, Ag, Pt, Pb, Co, Ni, Mn, Sn and Zn can interstitially replace Cu or Fe and As or Se can replace S, however these impurities may also exist in admixture.

Previous efforts to isolate and understand Cu recovery from 'pure' $CuFeS_{2(s)}$ have explored synthetic versions of the mineral.[12] Synthetic $CuFeS_{2(s)}$ has been produced in large scale via a variety of methods – from precipitates of CuS and FeS in cold aqueous solution (25-150 ^oC),[13] via differentially heated chambers for control of pressurised sulfur sublimation (270 ^oC, 520 ^oC, <10 *Torr*)[14] or through repeated high temperature reaction in specialised quartz vessels (>600 ^oC).[15] A high volume of reduced scale hydrothermal syntheses[16, 17] have been published exploring chalcopyrite-related nanomaterials with interesting semiconductor, spintronic, ferromagnetic and thermoelectric applications.[17-19] However, the benefits of the study of such synthetic chalcopyrites are limited, since they generally compare poorly to naturally formed $CuFeS_{2(s)}$ ores in terms of both structure and reactivity.[11, 12]

1.2.1 Structural Characterisation of $CuFeS_{2(s)}$

The crystal structure of $CuFeS_{2(s)}$ was formally determined in 1917 by Burdick and Ellis using XRD studies (figure 1.2).[20] Chalcopyrite (Z = 4; 16 *atoms*; a = 5.29 *Å*; c = 10.42 *Å*) contains tetragonal coordinated atoms, the unit cell of which has a stoichiometry of 4($CuFeS_2$) accounting for an ~85

% larger cell volume than isostructural sphalerite ($ZnS_{(s)}$; Z = 4; 8 atoms; a = 5.40 *Å*) to accommodate a doubled atom count.[20, 21] As in sphalerite, crystallised $CuFeS_{2(s)}$ contains no metal-metal bonds or sulfur-sulfur bonds; each sulfur atom is coordinated to four metal atoms, providing only M-S-M tetrahedral linkages with 2 Cu and 2 Fe atoms occupying interstitial positions within the sulfur network.[11, 22] Structural refinements have revealed that Fe coordination is close to a perfect tetrahedron (109.47°),[21] however Cu and S are coordinated in distorted tetrahedra (108.68 – 111.06°),[23] with Cu–S and Fe–S bond lengths of 2.30 *Å* and 2.26 *Å* respectively.[22, 24]



▲ Figure 1.2 - (A) The sphalerite-like $CuFeS_{2(s)}$ crystal structure dimensions and atomic positions, with all the variation of Fe-S-Fe bond angles shown. (B) The opposing α/β magnetic spins of Fe atoms within the $CuFeS_{2(s)}$ structure. [sphalerite; a=b=c= 5.402 *Å*][21, 25 26]

1.2.2 Physical Characterisation of $CuFeS_{2(s)}$

Chalcopyrite is a partially-covalent copper sulfide,[24] regarded by many to formally exist in the $Cu^{+}Fe^{3+}(S^{2-})_2$ ionic state.[27-31] Given that low spin Fe is extremely unlikely within a tetrahedral lattice with weak field S^{2-} ligands, an Fe derived magnetic moment of 3.85 μB[32] suggests that bulk Fe is best represented by the $3d^5$ high-spin Fe^{3+} ion. However, this value is considered too low for a purely Fe^{3+} ionic state, with a fluctuating mixed ferric/ferrous ionic state, ~80: 20 % observed via XANES study and other related techniques.[22, 33-35] Accordingly, partial $3d^6$ high-spin Fe^{2+} character is indicated - attributed to significant covalency in M-S bonding.[21, 36, 37]

Evidence for the dominance of high-spin $3d^{10}$ Cu^{+} within $CuFeS_2$ is also compelling and generally accepted.[38, 39] Two studies[34, 40] provided evidence for Cu^{+} via XANES/XAS, having differentiated between the spectra of Cu^{+} ($3d^{10}$; 2p→4s; >932 *eV*) and Cu^{2+} ($3d^9$; 2p→3d; <931 *eV*), by probing

2p-3d electronic excitation. Additionally, further evidence falls in favour of Cu^{+} through comparison of $CuFeS_{2(s)}$ (932.4 *eV*) with reported XPS binding energy ranges for bulk Cu^{+} (932.0–932.9 *eV*) and Cu^{2+} (933.1–936.6 *eV*)[21] and through comparison to $Cu(I)_2O$ references.[37, 39] XANES K-edge spectra for Cu within $CuFeS_{2(s)}$ (2.5 *eV*) compare favourably to that of Cu^{+} standards (2.1-3.0 *eV* shift), when compared to a $Cu_{(s)}$ reference (zero shift) and Cu^{2+} standard samples (4.3-6.8 *eV* shift).[41] However, once again, a fluctuating $CuFeS_{2(s)}$ ionic is further evidenced by observation of partial Cu $3d^9$ / $3d^{10}$ character[39] - leading some researchers to hypothesise that mixed ionic states are caused by valence band (VB) hybridisation of Cu and Fe 3d orbitals, mediated by S 3p orbitals in the Fermi region (see figure 1.3).[37]

Arbitration via XPS techniques is complicated by the overlap of common Fe^{2+} (706.6–712.2 *eV*) and Fe^{3+} (708.7– 714.4 *eV*) binding energies in differing environments.[21] Conventional and synchrotron XPS Fe 2p spectra collected from $CuFeS_{2(s)}$ samples shows a strong peak ranging across this binding energy window preventing certainty (707.0–709.6 *eV*).[42-46] However, XPS of $CuFeS_{2(s)}$ intercalated with group I metals to form $LiCuFeS_2$ and $NaCuFeS_2$ reveals that the Cu 2p binding energy remains constant (932.5 *eV*), whilst Fe 2p signals reduce in energy.[30] In combination with Mössbauer spectroscopy data, decisive conclusions could be reached that Cu^{+} is retained throughout intercalation/deintercalation, with ferric-ferrous reduction/oxidation maintaining solid charge neutrality (E1.1). Overall, these works (and others[29, 37, 39]) identify the dominance of high-spin Fe^{3+} ($3d^5$), strongly indicating $Cu^{+}Fe^{3+}(S^{2-})_2$ as the prevalent ionic solid.

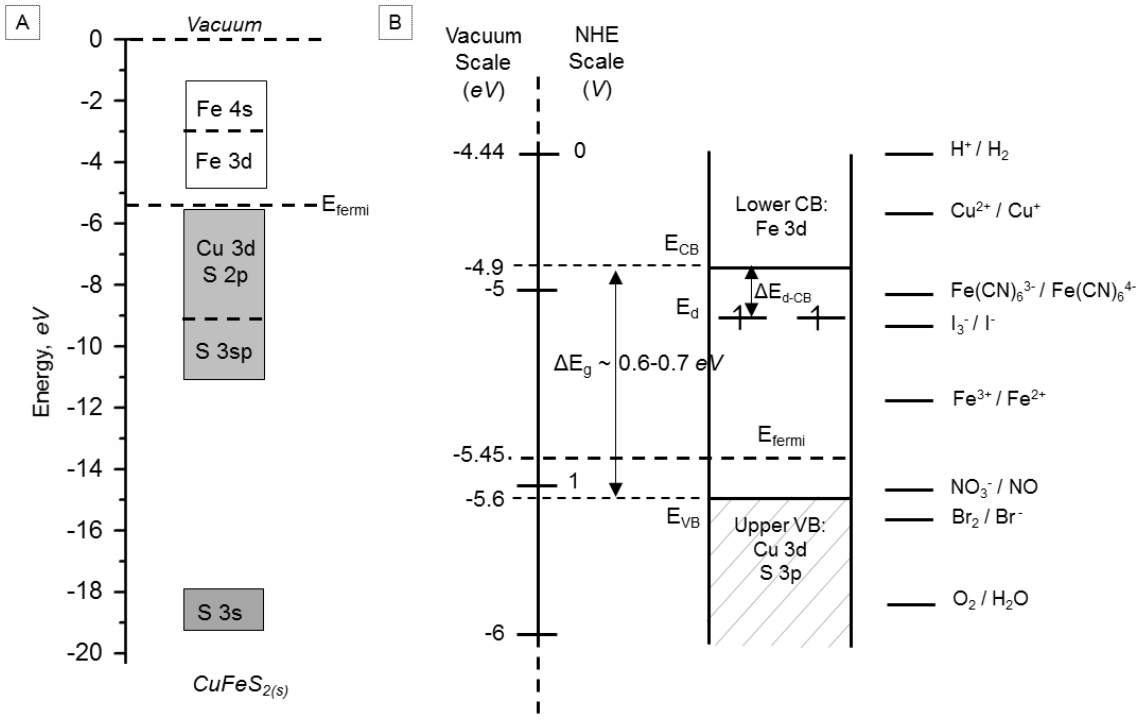
$$Cu^{+}Fe^{3+}(S^{2-})_{2\,(s)} + Li_{(s)} \rightleftharpoons Li^{+}Cu^{+}Fe^{2+}(S^{2-})_{2\,(s)} \qquad \text{E1.1}$$

Planar cleavage of the bulk $CuFeS_{2(s)}$ structure is not observed - instead fracture induces curved so-called conchoidal cleavage occuring along a mixture of cation and anion exposing planes, which is once again suggestive of M-S covalence in bulk $CuFeS_{2(s)}$ bonding. Surface analyses must therefore sample a high volume of surfaces to encompass all variations.[28, 47] The chemical evolution of $CuFeS_2$ surfaces following bulk fracture/cleavage is discussed in section 1.2.4.

1.2.3 Electromagnetic Characterisation of $CuFeS_{2(s)}$

Isostructural 'chalcopyrite' semiconductors of the form I–III–VI_2 have attracted significant attention toward applications in cells, diodes and other optoelectronic devices.[48-50]. Individual crystal grains of $CuFeS_{2(s)}$ are semiconductors with typical conductivities of 8-20 $\Omega^{-1}\cdot cm^{-1}$.[51] A narrow band gap of 0.45 – 0.6 *eV*[27, 52-54] in comparison to related compounds (e.g. $CuAlS_2$ = 3.49 *eV*),[23] means that n-type and p-type doping is accessible. Figure 1.3 shows the electronic band structure of semiconducting $CuFeS_{2(s)}$, as compiled from various sources. The ground electronic state features an empty conduction band (CB) dominated by mixing of Fe 3d – S 3p atomic orbitals and a filled valence band (VB) of mainly mixed Cu 3d - S 3p character.[27, 36, 55]

$CuFeS_{2(s)}$ generally exists as an n-type semiconductor, where the energy levels of electron-rich intercalating impurities/dopants (E_d) sit near the top-edge of the $CuFeS_{2(s)}$ band gap, providing a thermally accessible pathway ($\Delta E_{d\text{-}CB}$) to electron conduction within the delocalised $CuFeS_{2(s)}$ conduction band (E_{CB}).[56] $CuFeS_{2(s)}$ accommodates such a high level of doping that many classify $CuFeS_{2(s)}$ as 'degenerate' in nature, behaving much like a metal in terms of optoelectronic and magnetic properties.[32, 37, 57, 58] Figure 1.3 also features the energy levels of some common aqueous oxidants (Fe^{3+}, O_2, H^+, Cu^{2+}), where proximity of $E^{\ominus}_{redox}$ to the $CuFeS_{2(s)}$ valence band (E_{VB}) provides electron transfer pathways that destabilise the $CuFeS_{2(s)}$ structure - otherwise known as oxidative dissolution (section 1.4.2).[59]



▲ Figure 1.3 – (A) Electronic band structure diagram for bulk $CuFeS_{2(s)}$ describing the principal atomic orbitals contributing to occupied (shaded) and vacant (unshaded) molecular orbital bands and the location of the Fermi energy (E_{fermi}). (B) Magnification of $CuFeS_{2(s)}$ E_{Fermi} region showing VB-CB information, n-dopant energy levels (E_d) and energy levels of common aqueous oxidants. Data compiled from various sources.[23, 24, 27, 36, 42, 60]

$CuFeS_{2(s)}$ is the only magnetic semiconductor within the I–III–VI_2 class[54] and is antiferromagnetic in the range of 190 – 823 *K*, with adjacent atoms bearing opposing magnetic spins.[51] The mineral transitions to paramagnetic behaviour (magnetically polarisable) close to the $CuFeS_{2(s)}$ decomposition temperature of 830 *K*.[26, 37, 61, 62] Each Fe and Cu atom has a neutron diffraction resolved magnetic moment of 3.85 *μB* ($n_{unpaired,eff}$ ~3) and 0.2 *μB* respectively at 298 *K*,[24, 32] with net direction alternating between horizontal layers of atoms (as shown for α/β Fe - figure 1.2B). Lower magnetic moments than expected for a high spin Fe $3d^5$ ion ($n_{unpaired}$ = 5; ~5.9 *μB*) is attributed to unpaired electron involvement in covalent Fe-S bonding.[21, 32] This observation has

been corroborated by DFT simulations which calculate 3.26 effective unpaired electrons,[63] as is consistent with the aforementioned 'spin-delocalisation' theory.

1.2.4 Chemical Characterisation of $CuFeS_2$

Following cleavage, surface sulfur is found in a range of descending coordination metal-deficient states, namely sulfide (S^{2-}), disulphide (S_2^{2-}) and polysulfide (S_n^{2-}) respectively.[28, 47, 64] Increasing degree of polymerisation yields greater degree of metal-deficiency. These species can be differentiated through examination of $2p^{3/2}$ XPS spectra,[47] with a review paper providing effective comparison of existing XPS binding energy data as applied to the study of $CuFeS_{2(s)}$.[21] The formation of these dimeric (E1.2) and higher order polymeric sulfides (E1.3) has been observed during specific reconstructions of fractured surfaces alongside synchronised redox activity - during which interatomic distances can vary significantly (*e.g.* [001] surface - $S\text{-}S_{bulk}$ = 2.158 *Å*; $S\text{-}S_{recon.}$ = 1.501 *Å*).[27, 65]

$$2\,S^{2-}{}_{(s)} \rightarrow S_2^{2-}{}_{(s)} + 2e^- \qquad \text{E1.2}$$

$$n\,S_2^{2-}{}_{(s)} \rightarrow 2\,S_n^{2-}{}_{(s)} + (2n-4)e^- \qquad \text{E1.3}$$

During reconstruction processes involving physical relocation of atoms, S-S bonds are created on S-terminated surfaces,[65] M-M bonds are formed on the metal terminated surfaces and metal ions reposition to minimise angular strain.[63] These oxidative reconstruction processes seem likely to be accompanied by reduction of surface ferric ions,[21] where a pyrite-like FeS_2 compound (S-Fe-S = 93.4°; Fe-S = 2.23 *Å*) has been shown to form on $CuFeS_{2(s)}$ surfaces tracked via DFT-simulations (E1.4). Spectroscopic evidence of this pyrite-like species has been found,[63, 65, 66] with the released electron linked to the formation of copper oxides.[65] After reconstruction, the metal atoms in the exposed atomic layer lose two bonds whilst σ M–M bonds are formed through d_{xy}, d_{xz} and d_{yz} orbital overlap. The distances of these M–M bonds are found to vary from 2.45 Å to 2.67 *Å*.[63]

$$[Fe(III)(S^{2-})_2]^-_{(s)} \rightarrow Fe(II)(S^-)_{2\,(s)} + e^- \qquad \text{E1.4}$$

Upon exposure to air, freshly cleaved $CuFeS_{2(s)}$ surfaces slowly lose their lustrous appearance through oxidation. Initial oxidation produces an exposed surface of Fe(III)-O-OH,[67, 68] which overcoats a metal deficient copper sulfide layer ($Cu_{0.8}S_2$) displaying S_n^{2-} binding energies.[31, 51] Prolonged atmospheric exposure results in further transformation to sulfates,[43] carbonates, oxy-hydroxides[43] (e.g. Fe(III)-O-OH) and hydrated oxides[34] (e.g. Cu(I)-O).[67, 68] Oxidation layers composed largely of $Fe(III)_2O_3$ and Cu(II)S penetrate to depths of 1.2-4.0 *nm* upon prolonged atmospheric oxidation of $CuFeS_{2(s)}$,[31] however elsewhere Fe oxide layers have been reported with much larger thicknesses of 20–40 *nm*.[21] A modern synchrotron method also revealed that surface monosulfide evolves to ~20 % S_2^{2-} and ~20 % S_n^{2-} within 15 minutes of atmospheric oxidation.[69] These factors must be considered carefully, since atmospheric oxidation may produce diverse

surface structures that may resist subsequent aqueous oxidation.[31, 70-72] Additionally, care must be taken to treat all $CuFeS_2$ samples equivalently through milling, size fractioning and storage (section 2.4).

Upon oxygen-purged aqueous exposure, Fe(III)–O–OH is the only appreciable surface specie detected, with no apparent SO_4^{2-} or S^0.[67] However, analogous rapid oxidation of the $CuFeS_{2(s)}$ surface can occur via dissolved molecular oxygen ($O_{2(aq)}$) with an equilibrium solubility of ~8 $mg{\cdot}L^{-1}$ in pure water (0.25 $mmol{\cdot}dm^{-3}$; 298 K), which reduces with solute addition.[56] As expected, oxygenated aqueous contact with $CuFeS_{2(s)}$ leads to comparable oxidation layer thicknesses (1.5 ± 0.2 *nm*, 1 *min*) in a fraction of the exposure time required for atmospheric oxidation (1.2 ± 0.2 *nm*, 30 *mins*).[73] Final (thermodynamic) layer thicknesses are similar in each case (~3 *nm*),[74] with Fe(III)-O-OH, Cu(II)S, Cu(I)O and Cu(II)O all significant components[35, 39] and SO_4^{2-} observed only in small quantity due to high aqueous solubility.[35] Alternatively, dissolved chemical oxidants can interact with $CuFeS_{2(s)}$ surfaces, destabilising M-S bonding (figure 1.10) and ultimately leading to $CuFeS_{2(s)}$ oxidative dissolution and release of dissolved metal ions into solution (section 1.4.2). Due to more complex chemistries in aqueous media, the exact physical dimensions and moieties formed within the oxidised outer layers of $CuFeS_{2(s)}$ are subject to factors including proton concentration (*p*H), temperature and solution redox potential (E_h).

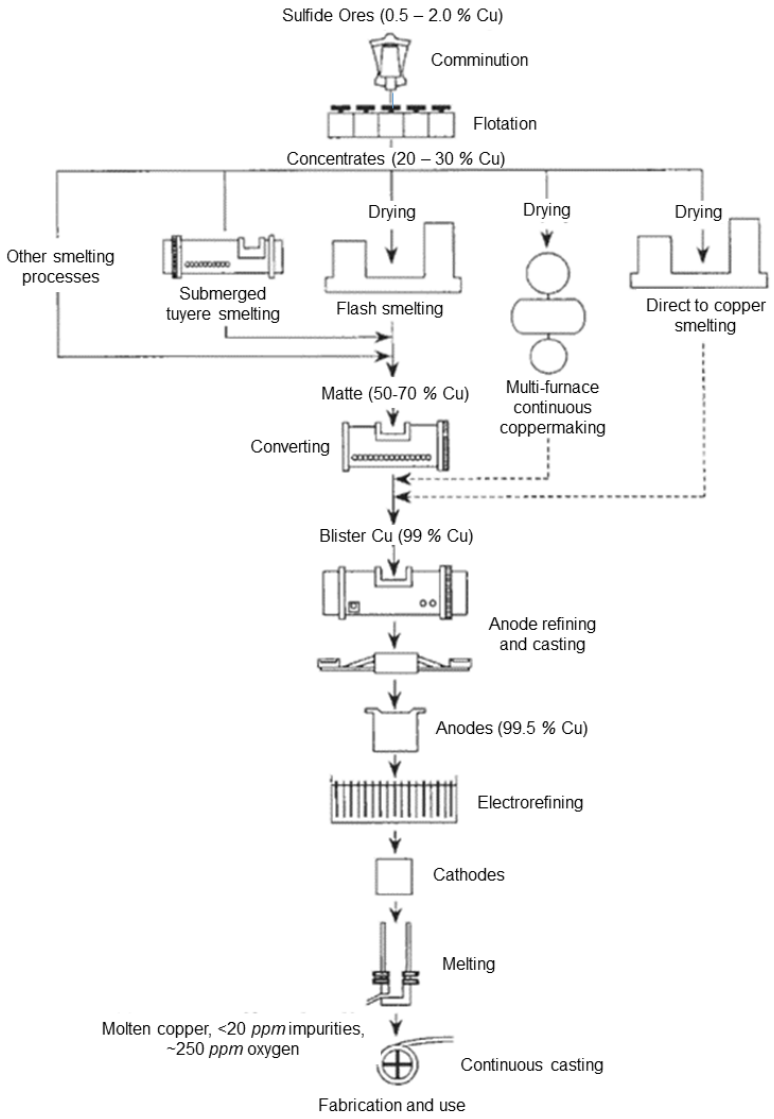
1.3 Industrial Extraction Techniques

1.3.1 Pyrometallurgic Processing

The extraction, processing and refinement of $Cu_{(s)}$ from sulfide ore is a highly energy intensive, high $CO_{2(g)}$ footprint procedure. To the present day, Cu extraction has been best achieved through smelting of high grade Cu ores converting sulfides feedstocks to oxide 'matte' – a so-called pyrometallurgy approach (figure 1.4).[7] Aside from involving expensive combustion of unsustainable fossil fuel sources, the roasting of sulfidic ores produces millions of tonnes of SO_x emissions annually.[75]

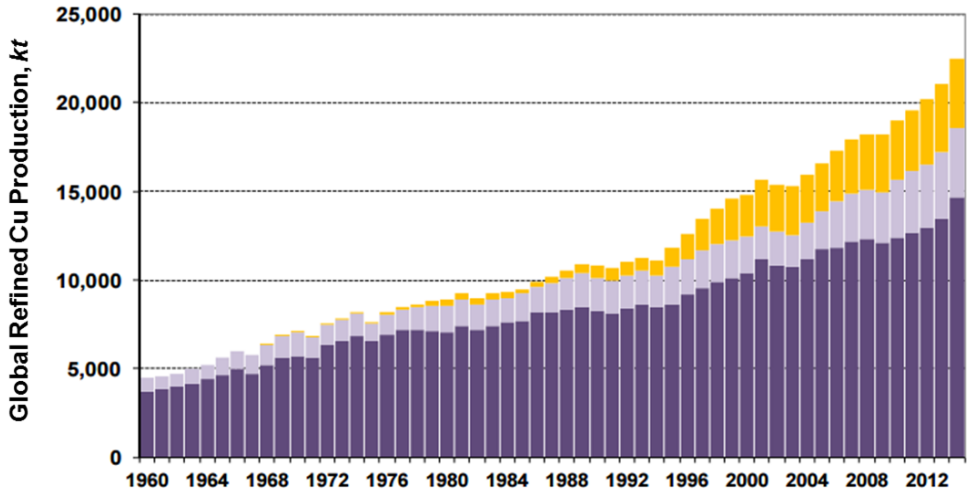
A key aspect of all copper extraction processes (including hydrometallurgy) is the beneficiation, or concentration, of the Cu containing ore feedstock. Ore is finely ground in ball-mills, followed by flotation of the ground ore to separate floatable high grade minerals from gangue material, on the basis of differential hydrophilicity. Flotation is a complex process which has been extensively reviewed in terms of 'collector' chemical additives, inert atmospheres, particle sizes, solution potential, alkaline *p*H and a range of mineral-/milling-derived galvanic interactions.[21, 76-80] Flotation concentrates typically contain ~30 *%wt* Cu and conditions must be controlled correctly to promote particle floatability and hence separation efficacy. A further high consumption stage is the electrorefining of Cu, where impurity levels are typically reduced to <20 *ppm* (figure 1.4).[7] Cast impure Cu anodes are oxidatively solubilised ($Cu^0_{(s)} \rightarrow Cu^{2+}_{(aq)} + 2e^-$), $Cu^{2+}_{(aq)}$ is electrolytically driven

to an inert cathode, where reduction results in electrodeposition of high purity $Cu^0_{(s)}$ ($Cu^{2+}_{(aq)}+2e^- \rightarrow Cu^0$).



▲ Figure 1.4 - Schematic overview of modern pyrometallurgic refinement of sulfidic Cu ores such as $CuFeS_{2(s)}$, ranging from initial ore concentration via flotation to casting of high-purity refined $Cu_{(s)}$.[7]

Figure 1.5 illustrates the divide of Cu processing approaches since 1960, with heavy reliance on energy intensive pyrometallurgy, also known as 'primary' refinement. $Cu_{(s)}$ is also refined from so-called secondary sources, referring to fire or electrolytically refined $Cu_{(s)}$ from recycled sources.[3] Figure 1.5 also details the gradual rise in industrial usage of an alternative lower consumption extraction/refinement approach named solvent extraction electrowinning (SX-EW), which was introduced in the late 1960s and at the time of writing accounts for ~17 % of total $Cu_{(s)}$ processing.[3, 7]



▲ Figure 1.5 - Global annual production of refined $Cu_{(s)}$ 1960-2014 - (purple = primary pyrometallurgic; lilac = recycled secondary refinement; yellow = SX-EW hydrometallurgy).[3]

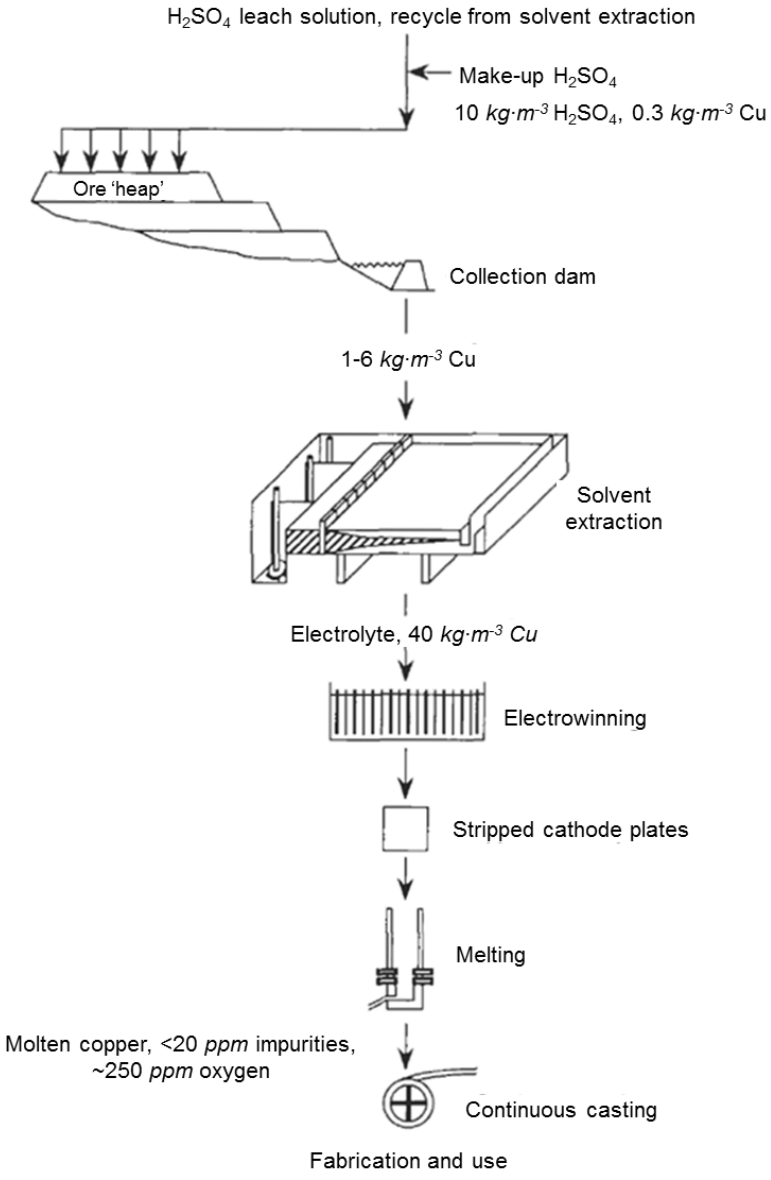
1.3.2 Hydrometallurgic Processing

The reliance of the copper industry on traditional extraction technologies is being challenged, with extraction-demand pressures driving research to explore alternative low consumption processing options, ideally with applicability to treatment of low-grade ores (lower recoverable Cu per ore mass).[81, 82] As a consequence, advances in hydrometallurgic beneficiation of sulfide ores has been sought to create a greener and more sustainable industry.[75, 83] Hydrometallurgic approaches generally employ aqueous solution-based lixiviant systems to directly leach metal ions from flotation concentrated sulfidic minerals. Hydrometallurgy has clear potential economic and environmental benefits over traditional pyrometallurgy (e.g. zero SO_x emissions), especially if future applicability to low grade copper ores can be cemented.[21, 82]

Figure 1.6 schematically details the full process of solvent extraction electrowinning (SX-EW) as a currently implemented industrial hydrometallurgy technology. Lixiviant $H_2SO_{4(aq)}$ solution is cycled between ore heap percolation and solvent-extraction processes to deliver solubilised $Cu_{(aq)}$ to the latter stages of electro-refining. Primitive hydrometallurgic lixiviant systems, developed in the 1970s, dissolve $CuFeS_{2(s)}$ in acidic solutions containing oxidants, such as $FeCl_3$, $Fe_2(SO_4)_3$ and $CuCl_2$.[84] Presently employed lixiviant systems principally use acidic ferric sulfate/chloride media to leach copper before passing the Cu-impregnated solution to a conventional SO_4^{2-}-based $Cu^{2+}_{(aq)}$ electroplating process, via a solvent extraction process if required.[3, 85]

Direct chemical leaching from $CuFeS_{2(s)}$ typically suffers from slow dissolution kinetics,[86] where dissolution is substantially incomplete after 80 days for typical 'heap' leaching conditions (250 $kg{\cdot}t^{-1}$ conc. $H_2SO_{4(aq)}$).[87] However, significant progress is being made; a recent US Bureau of Mines study revealed their work with $FeCl_3/HCl_{(aq)}$ leaching to recover 99.9 % $Cu_{(aq)}$ in 2 *hrs* from a typical $CuFeS_{2(s)}$ mill sample concentrated by flotation.[75] Such advances in direct leaching technologies

are required in order to redress the balance of $Cu_{(aq)}$ extraction in favour of hydrometallurgic approaches. It is generally thought that a better understanding of the kinetics and mechanism of $CuFeS_{2(s)}$ leaching is a key inhibition to further industrial implementation of such techniques.[70]



▲ Figure 1.6 - Schematic overview of solvent-extraction electrowinning (SX-EW) as an adopted industrial hydrometallurgic extraction approach for copper sulfide ores.

1.4 $CuFeS_{2(s)}$ Dissolution Modes

Dissolution is the process of spontaneous or activated solvation of a chemical compound into a solvent medium, often with the assistance of accelerating chemical additives. A large quantity of existing research has focused on accelerating hydrometallurgical Cu-leaching from sulfide-rich ores, containing large quantities of $CuFeS_{2(s)}$. Acidic-$SO_4^{2-}{}_{(aq)}$ dissolution has been extensively studied in terms of redox sites,[10,12-14] $CuFeS_2$-FeS_2 cooperative galvanic dissolution[88-93] and empirical rate laws.[21, 94] Many researchers have sought the origin of rate-limited ambient $CuFeS_{2(s)}$

dissolution, beyond initially slow localised 'cathodic' Fe^{3+} reduction.[95] The various modes and active molecules associated with $CuFeS_{2(s)}$ dissolution are discussed immediately below.

1.4.1 Non-Oxidative Dissolution

$$CuFeS_{2\,(s)} + 4\,H^{+}{}_{(aq)} \overset{K_{NOD1}}{\longleftrightarrow} Cu^{2+}{}_{(aq)} + Fe^{2+}{}_{(aq)} + 2\,H_2S_{(aq)} \qquad \text{E1.5}$$

$$CuFeS_{2\,(s)} + 2\,H^{+}{}_{(aq)} \overset{K_{NOD2}}{\longleftrightarrow} CuS_{(s)} + Fe^{2+}{}_{(aq)} + H_2S_{(aq)} \qquad \text{E1.6}$$

In oxygen-purged $acid_{(aq)}$, $CuFeS_{2(s)}$ undergoes a slow 'non-oxidative' dissolution process, via two possible routes (E1.5; E1.6), in which the formal oxidation state of sulfur atoms remains constant signifying no net involvement of sulfur with regard to electron flow.[21, 81, 96, 97] H_2S may later become reduced in solution (scheme E1.7), producing native sulfur and regenerating the protons consumed via non-oxidative dissolution and maintaining overall solution *p*H.

$$H_2S_{(aq)} + 2\,Fe^{3+}{}_{(aq)} \rightarrow 2\,Fe^{2+}{}_{(aq)} + S^{0}{}_{(s)} + 2\,H^{+}{}_{(aq)} \qquad \text{E1.7}$$

This reaction has been examined with respect to intermediate [H_2S], resulting in the rate dependence shown in E1.8, where k_{m,H_2S} is the H_2S mass transport factor and [H^+] is the surface proton concentration.[97] Since K_{NOD2} (2.8×10^{-3}, 308 *K*)[97] is measured as many orders of magnitude higher than K_{NOD1} (2.8×10^{-19}, 308 *K*),[97] scheme E1.6 is expected to dominate H_2S production (n=1). Subsequently, with all other conditions remaining constant, non-oxidative dissolution of $CuFeS_{2(s)}$ may be expected to proceed up to 20,000 fold faster via scheme E1.6 (n=1) over scheme E1.5 (n=2), which may explain spectroscopic observation of $CuS_{(s)}$ in $Cl^-_{(aq)}$ leaching media at low-moderate redox potentials (<600 *mV* vs. SHE).[97]

$$r_{max,H_2S} = -n\,r_{max,CuFeS_2} = k_{m,H_2S} \cdot (4K_{NOD})^{1/4}[H^+] \qquad \text{E1.8}$$

However, when purged with $N_{2(g)}$ negligible lixiviant metal recoveries are achievable in $H_2SO_{4(aq)}$ at 30 °*C* (303 *K*), even upon addition of redox active substances such as $Fe_2(SO_4)_{3(aq)}$, $FeSO_{4(aq)}$ or $CuSO_{4(aq)}$[98-100] (see later discussions).

1.4.2 Oxidative Dissolution

$$CuFeS_{2\,(s)} + 4O_{2\,(aq)} \rightarrow Cu^{2+}{}_{(aq)} + Fe^{2+}{}_{(aq)} + 2\,SO_4^{2-}{}_{(aq)} \qquad \text{E1.9}$$

The oxidative dissolution of $CuFeS_{2(s)}$ is an example of the electrochemical corrosion of a semiconductor,[101] which is very slow in non-acidic conditions (E1.9).[21] In un-purged atmospheric conditions, dissolved molecular oxygen, $O_{2(aq)}$, is a solution borne oxidant existing in dynamic equilibrium with atmospheric gaseous oxygen (E1.10). $[O_2]_{(aq)}$ can be estimated using Henry's Law (E1.11), returning 2.9×10^{-4} *mol·dm*$^{-3}$ for pure water at 298 *K*.[56] It follows that the equilibrium

constant ($K_{\equiv}$) for the dissolving of oxygen at 298 *K* is ~ 3.3 x 10^{-2} and also that $[O_2]_{(aq)}$ falls upon addition of solute to the aqueous medium, since mass density (ρ_{H2O}) will decrease.

$$O_{2\,(aq)} \overset{K_{\equiv}}{\leftrightarrow} O_{2\,(aq)} \qquad \text{E1.10}$$

$$b_{O_2} = \frac{p_{O_2}}{K_{O_2}} = \frac{21\ [kPa]}{7.9{\times}10^4\ [kPa\ kg\ mol^{-1}]} = 2.9{\times}10^{-4}\ mol\ kg^{-1}$$

$$[O_2] = b_{O_2} \cdot \rho_{H_2O} = 2.9{\times}10^{-4}[mol\ kg^{-1}] \cdot 0.99709\ [kg\ dm^{-3}] = 2.9{\times}10^{-4}\ mol\ dm^{-3} \qquad \text{E1.11}$$

Oxidative dissolution of $CuFeS_{2(s)}$ is formally a $4e^-$ oxidation process, which is most effectively mediated by high $[H^+]$ (pH ~ 1). As figure 1.3 illustrates, the VB of minerals such as $CuFeS_{2(s)}$ are vulnerable to attack from common oxidants ($H^+_{(aq)}$, $Fe^{3+}_{(aq)}$)[59] due to the close proximity of their respective reduction potentials, providing an accessible pathway to remove (covalent) $CuFeS_{2(s)}$ bonding electrons. The first such oxidants used to accelerate oxidative dissolution included $CuCl_2$, $FeCl_3$ and $Fe_2(SO_4)$ since they are inexpensive, and have solubilities and stability compatible with highly acidic environments.[84] E1.12 and E1.13 show the accepted oxidative routes to $CuFeS_{2(s)}$ dissolution, where $Fe^{3+}_{(aq)}$ oxidant is regenerated in dynamic equilibrium with leached $Fe^{2+}_{(aq)}$ (E1.14).[21, 81] The summative action of these schemes gives rise to the overall equation for $CuFeS_{2(s)}$ dissolution E1.15.

$$CuFeS_{2(s)} + 4H^+ + O_{2(aq)} \rightarrow Cu^{2+} + Fe^{2+} + 2S^0{}_{(s)} + 2H_2O \qquad \text{E1.12}$$

$$CuFeS_{2(s)} + 4Fe^{3+} \rightarrow Cu^{2+} + 5Fe^{2+} + 2S^0{}_{(s)} \qquad \text{E1.13}$$

$$4Fe^{2+} + 4H^+ + O_{2(aq)} \overset{K_{Fe}}{\leftrightarrow} 4Fe^{3+} + 2H_2O \qquad \text{E1.14}$$

$$\overline{CuFeS_{2(s)} + 4H^+ + O_{2(aq)} \rightarrow Cu^{2+} + Fe^{2+} + 2S^0{}_{(s)} + 2H_2O} \qquad \text{E1.15}$$

1.4.3 Potential Assisted / Anodic Dissolution

Oxidation of solubilised species occurs at the anode of an electrochemical cell. Thus an externally applied potential bias can establish a dissolution-driving electron flow between a bulk $CuFeS_{2(s)}$ electrode and a chosen counter electrode.[102] The anodic and cathodic processes in H_2SO_4-$Fe_2(SO_4)_{3(aq)}$ electrolyte (E1.16 & E1.17)[103] cooperate to leach, then directly electrodeposit $Cu_{(s)}$ at the cathode – a route which has become the subject of many patents.[75] Other successful studies have combined anodic dissolution with chemical leaching via acid-$Cl^-_{(aq)}$ solution as part of the 'Cymet Process' (section 1.5).[104]

$$anodic: \quad CuFeS_{2(s)} \rightarrow Cu^{2+} + Fe^{2+} + 2S^0{}_{(s)} + 4e^- \qquad \text{E1.16}$$

$$cathodic: \quad Cu^{2+} + 2e^- \rightarrow Cu^0$$

$$Fe^{3+} + e^- \rightarrow Fe^{2+} \qquad \text{E1.17}$$

$$2H^+ + 2e^- \rightarrow H_{2(g)}$$

During anodic dissolution experiments, Cu^{2+} and Fe^{2+} solute additions have a synergistic influence on solution redox potential (E_h), manipulating the prevalent surface speciation and (therefore) reactivity of $CuFeS_{2(s)}$ surfaces.[72] Additionally, cathodic pre-treatment accelerates anodic $CuFeS_{2(s)}$ dissolution since the mineral electrode is more susceptible to oxidation on account of a reduced rest potential[105] (table 1.3; figure 1.10). An anodic dissolution process is impractical on a plant scale – especially since surface passivation effects are still encountered (section 1.8), resulting in increased electron transfer resistances over time and, consequently, unacceptably high cell potentials.[105]

1.4.4 Bioleaching

Although biological leaching systems are not the focus of this work, it must be recognised that compatibility of proposed chemical leaching systems with leading examples of biologically-attained enhancements is an important consideration for all developing technological routes.[106] In fact, many of the current leading hydrometallurgic approaches (table 1.1) are set up to maximise cooperative bioleaching strategies. In future, this could allow the industry to adopt direct biochemical leaching methodologies in greater proportion with both commercial and environmental benefits.

Microorganisms have long been known to assist copper sulfide mineral dissolution from acid rock drainage (ARD) sites (E1.18).[94] Metal metabolising microbes found at such locations include strains of *Acidithiobacillus*, *Leptospirillum*, *Sulfolobus* and *Sulfobacillus* bacteria,[107] which are known to mediate the oxidation of ferrous ions and sulfurous deposits (E1.19 & E1.20).[108]

$$CuFeS_{2(s)} + 16Fe^{3+}{}_{(aq)} + 8H_2O \rightarrow Cu^{2+}{}_{(aq)} + 17Fe^{2+}{}_{(aq)} + 2SO_4^{2-}{}_{(aq)} + 16H^+{}_{(aq)} \qquad \text{E1.18}$$

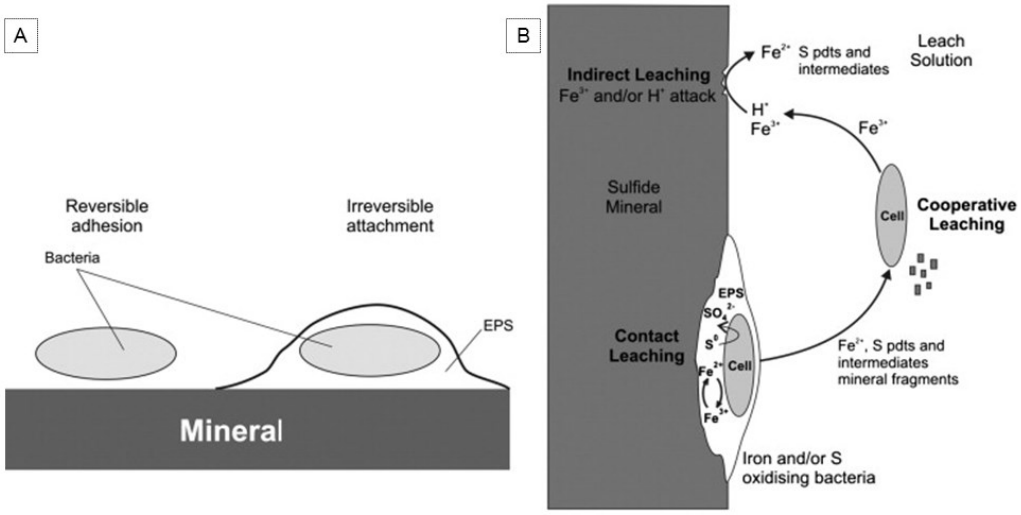
$$4Fe^{2+} + 4H^+ + O_{2(aq)} \xrightarrow{\substack{Ferrioxidans \\ activity}} 4Fe^{3+} + 2H_2O \qquad \text{E1.19}$$

$$2S^0{}_{(s)} + 3O_{2(aq)} + 2H_2O \xrightarrow{\substack{Thiooxidans \\ activity}} 2SO_4^{2-} + 2H^+ \qquad \text{E1.20}$$

Over the past ~50 years, the copper industry has developed several so-called 'bioleaching' technological models, seeking to enhance the poor kinetics of hydrometallurgic extraction via cooperative microbial activity. The current integration level for industrial scale bio-hydrometallurgic

strategies has been effectively reviewed elsewhere[106, 109] – with most attention given to heap bio-leaching (analogous to figure 1.6).[82] In such models, ideal microbial strains must remain effective under extreme conditions (50-70 *°C*; pH ~ 1; high [metal]; high [oxidant]).[21]

Unfortunately, copper oxides and 2° copper sulfides (chalcocite, covellite and pyrite) have proven to be significantly more susceptible to microbial action than $CuFeS_{2(s)}$,[110] which again exhibits poor kinetics.[82, 109, 111] It is generally recognised that microbes improve $CuFeS_{2(s)}$ dissolution kinetics via three distinct modes of action (figure 1.7B): 1) direct $CuFeS_{2(s)}$ surface contact and subsequent oxidation of surface bound Fe^{3+} and sulfidic species 2) indirect solution-bound $Fe^{2+}_{(aq)}$ oxidation, regenerating $Fe^{3+}_{(aq)}$ oxidant 3) a cooperative resource supply chain linking surface- and solution-bound bacteria.[93, 94 112-114] Therefore, it has been proposed that $CuFeS_{2(s)}$ dissolution enhancements are due to bacterial generation of $Fe^{3+}_{(aq)}$ oxidant through direct and indirect action and oxidative removal of kinetically hindering sulfidic layers.[115] High levels of bacterial attachment afford maximum effect,[107] which aligns well with microbial oxidation schemes E1.19 and E1.20.



▲ Figure 1.7 - (A) Modes of reversible and irreversible bacterial binding at mineral interfaces. (B) Schematic of cooperative leaching of irreversibly bound 'contact-leaching' bacteria releasing dissolution products to solution-borne bacteria, which metabolise to generate free $Fe^{3+}_{(aq)}$ and initiate further indirect leaching.[21, 107, 108]

Combined biochemical approaches have been proven to boost $Cu_{(aq)}$ recovery from $CuFeS_{2(s)}$ by 390 % under specific conditions (moderate thermophiles, *p*H 1.5, 50 *°C*, 600-630 *mV* vs. SHE).[116] A specific lipoprotein found in *Acidithiobacillus* strains (licanantase) has been confirmed to increase $CuFeS_{2(s)}$ dissolution rates.[117]

Despite such clear reports of bioleaching enhancements, reviewers[82, 109, 118] have highlighted the overriding importance of system control.[81, 108, 116] Consideration of additional complicating factors has proven necessary for effective bioleaching of $CuFeS_{2(s)}$, including temperature, consortia mixing,[45, 92] threshold levels of additive Fe^{2+}/Fe^{3+}, low and controlled E_h to restrict free $[Fe^{3+}]_{(aq)}$,[110, 119] reduced particle sizes[120] and bacterial nutrient additives.[21] Bioleaching is also negatively

affected by reported passivating effects, with several studies citing jarosite [$K_2Fe(III)_3(OH)_6(SO_4)_2$] precipitation on $CuFeS_{2(s)}$ surfaces as responsible for dissolution plateaus in (required) nutrient rich media (*e.g.* 9K medium).[21]

Notably, some studies reporting bacterial enhancements have been criticised for their inability to distinguish between bacterial and E_h control enhancements, the latter of which most commonly plays the dominant role (section 1.6.8).[89, 99] Overall, bacterial prosperity enhancements must be married with a complex array of chemical considerations (*e.g.* E_h control) to achieve cooperative biochemical $CuFeS_{2(s)}$ dissolution. A schematic showing typical microbial enhancement magnitudes is set out in figure 1.9.

1.5 Ambient Lixiviant Systems

Various acidic media have been found to show significant lixiviant activity, including $H_2SO_{4(aq)}$,[70, 93, 98, 121] $HCl_{(aq)}$,[85, 101, 122-124] $HNO_{3(aq)}$[125-127] and $HClO_{4(aq)}$.[42, 64] Additionally, basic $NH_4OH_{(aq)}$[43, 128, 129] has been successfully used, with significant relevance to this work as a reference for $NH_4{\cdot}HSO_{4(aq)}$ leaching and basic leaching. The accepted 'ammoniacal' scheme is given below (E1.21), in which a stable ligated ($Cu(NH_3)_4^{2+}$) species is preferentially formed.[128]

$$CuFeS_2 + 4NH_3 + 6OH^- \rightarrow Cu(NH_3)_4^{2+} + Fe(OH)_3 + \frac{1}{2}S_2O_3 + \frac{3}{2}H_2 + 7e^- \qquad \text{E1.21}$$

$H_2SO_{4(aq)}$ and $HCl_{(aq)}$ have been the most widely used lixiviants for $CuFeS_{2(s)}$,[49, 72, 130, 131] mainly for economic reasons.[7, 42] For example, despite significant promise, $NO_3^-{}_{(aq)}$ systems ultimately require high consumption conditions to effect $M_{(aq)}$ recovery and require an acid regeneration stage. Since equivalent acidities are accessible in many types of acid media, differential lixiviant activity at equal *p*H must originate from anion effects.

$SO_4^{2-}{}_{(aq)}$ lixiviants are well suited to hydrometallurgic models (*e.g.* SX-EW – figure 1.6), where the $Cu_{(aq)}$ pregnant lixiviant is directly transferred for use as electrolyte in the cathodic electrowinning process. In this process, $SO_4^{2-}{}_{(aq)}$ electrolytic media produces high quality, low impurity $Cu_{(s)}$ as sheet-deposited cathodes, with the attractive possibility of lixiviant-electrolyte $H_2SO_{4(aq)}$ recycling (labelled – figure 1.6).[7] However, free $Fe^{3+}{}_{(aq)}$ oxidant activity can become reduced through $FeSO_4^+{}_{(aq)}$ complexation in $H_2SO_{4(aq)}$ leach solutions.[132]

Acid-$Cl^-{}_{(aq)}$ media commonly displays superior dissolution rates in comparison to $SO_4^{2-}{}_{(aq)}$ of equivalent acidity,[101, 124, 133] on account of higher Fe^{3+} activity and $CuFeS_{2(s)}$-$Cl^-{}_{(aq)}$ surface adsorption.[100, 138, 144] $Cl^-{}_{(aq)}$ surface adsorption is thought to promote interfacial electron and ionic transfer, whilst also disrupting kinetically hindering sulfurous film coverage (section 1.8).[134, 135] These observations provide the accepted rationale for enhanced leaching in $HCl_{(aq)}$ over $H_2SO_{4(aq)}$ at equivalent acidities and for $FeCl_{3(aq)}$ over $Fe_2(SO_4)_{3(aq)}$ at equivalent concentration (section

1.6.4). Unfortunately, $Cl^-_{(aq)}$ media produces high impurity, powdered $Cu_{(s)}$ electrodeposits that are difficult to isolate.[42]

As highlighted by table 1.1, current best performing lixiviant systems which are approaching commercial integration exploit mixed acid systems to tune extraction kinetics, commercial viability and evolving $CuFeS_{2(s)}$ surface properties through anionic effects. Many of these advanced systems utilise extremes of pressure and temperature to aid $CuFeS_{2(s)}$ dissolution (including Galvanox®[136] and Arbiter®[133] processes). These are not discussed in detail due to their limited industrial applicability and relevance to the advancement of ambient $CuFeS_{2(s)}$ dissolution.

▼ Table 1.1 – Atmospheric acidic-$SO_4^{2-}{}_{(aq)}$ related processes developed for $CuFeS_{2(s)}$ or other copper sulfide concentrates/ores:[81] (Scale: C – commercial; D – demonstration; P – plant pilot; L – laboratory)

Process & Typical Conditions	Temp, °C	Particle Size, μm	Scale
Heap Leaching:[137] Crushed ore, stacked, irrigated with dilute $H_2SO_{4(aq)}$	Ambient	Crushed	C
Dump Leaching:[137] Unprocessed ore stacked and irrigated with dilute H_2SO_4	Ambient	Unprocessed	C
Geocoat® Process:[138] Heap SO_4^{2-} bioleaching of sulfide concentrate supported on host rock particles	Ambient	Undisclosed	D
BacTech/Mintek Process:[139, 140] Fine grind SO_4^{2-} bioleach	35–50 °C	5–10 μm	D
BioCOP™ Process:[141] High temperature SO_4^{2-} leach using archaea single cell microbial catalysts	65–80 °C	37 μm	D
Sepona Process[142] $Fe_2(SO_4)_3$ heap leach of Cu_2S using floated FeS_2 to generate required H_2SO_4	80 °C	100 μm	C
Galvanox™ Process:[143] $Fe_2(SO_4)_3$ leach with 2:1 FeS_2:$CuFeS_2$ ratio	80 °C	53–75 μm	P
NENATECH Process:[144, 145] $Fe_2(SO_4)_3$ leach of finely ground concentrate	85 °C	5–10 μm	P
Cobre Las Cruces Project:[146] $Fe_2(SO_4)_3$ generated from FeS_2 oxidation with O_2; mainly Cu_9S_5 and Cu_2S (6.2 *wt%*), minimal $CuFeS_2$	90 °C	<150 μm	C
Cuprochlor Process:[147] SO_4^{2-}/Cl^- leach with $CaCl_2$ agglomeration	Ambient	Various	C
HNO_3 Route Solvent Extraction:[127] SO_4^{2-}/NO_3^- leach of $CuFeS_2$ concentrate	90 °C	Undisclosed	L

1.6 Kinetic Influences

Several aspects of the $CuFeS_{2(s)}$ dissolution process have been suggested to be rate-determining and causal to slow chemical leaching. In kinetic studies, researchers often choose to fit rate data

from $CuFeS_{2(s)}$ dissolution experiments to the shrinking core model for geometric leaching of spherical particles. The form of a chosen best fit equation - derived under differing model conditions - provides insight in to the cause of dissolution rate limitations. The first of these proposed rate-determining steps (RDS) involves diffusion-controlled kinetics, in which the diffusion of oxidative species toward, or of dissolution products away, from the leaching interface is the RDS. In this diffusion-controlled model, a dissolution rate constant, k_d is defined as per E1.22[148, 149] – where D_s is the oxidant diffusion coefficient in the S product layer ($m^2 \cdot s^{-1}$), [ox] is the bulk oxidant concentration ($mol \cdot m^{-3}$), ρ_B is the density of chalcopyrite ($kg \cdot m^{-3}$) and r_0 is the initial radius of powdered $CuFeS_{2(s)}$ (m). Fundamentally, k_d has an inverse square relationship with respect to initial $CuFeS_{2(s)}$ particle radius (r_0).

$$k_d \cdot t = \frac{2D_S \cdot [ox]}{\rho_B \cdot r_0^2} \cdot t \qquad \text{E1.22}$$

A second rate-limitation has been reported for $CuFeS_{2(s)}$ dissolution, where the RDS is the rate of a specific surface reaction - being a mechanistic step or a redox event. E1.23[150] describes the rate constant (k_{sr}) for surface reaction controlled $CuFeS_{2(s)}$ dissolution – where m,n are reaction orders, concentrations are measured at the unleached interface and k is a rate constant. Crucially, k_{sr} has an inverse proportionality to initial $CuFeS_{2(s)}$ particle radius (r_0), providing means to distinguish between the RDS of dissolution for various lixiviant conditions. Surface reaction control is often concluded when E_a is found to be relatively high and degree of solution agitation has little influence on leaching rates - suggesting that diffusion rates are non-limiting.[151] Others have used a mixed state combining both mathematical models to describe rate behaviour.

$$k_{sr} \cdot t = k \frac{[H^+]_S^m \cdot [ox]_S^n}{\rho_B \cdot r_0} \cdot t \qquad \text{E1.23}$$

Summarised results for kinetic studies (table 1.2) show no clear consensus regarding the RDS for $CuFeS_{2(s)}$ dissolution – probably due to the diversity of conditions used and a lack of consistency in *p*H and E_h control.[21] However, the majority of studies suggest that initial stages of $CuFeS_{2(s)}$ dissolution are diffusion controlled, progressing to surface reaction control in the later stages as reflected by reported E_a values.

▼ Table 1.2 – Summary of $CuFeS_{2(s)}$ dissolution kinetics studies, detailing Arrhenius parameters (rate laws, E_a, A), best fitting shrinking core model rate laws and associated kinetic conclusions.[21]

[X = oxidised $CuFeS_{2(s)}$ mole fraction; t = leach time; k_d = diffusional RDS rate constant; k_{sr} = surface reaction RDS rate constant; k_m = mixed state RDS rate constant; k_{exp} = overall experimental rate constant]

T, ^oC	Acid [Oxidant]	Experimental Rate Findings	E_a, $kJ{\cdot}mol^{-1}$	Kinetic Conclusions
10-40	HCl [HClO]	$k_{exp} = 1.7\text{-}2.8 \times 10^{-6}\ s^{-1}$ $k_d t = \left[1-(1-X)^{2/3}\right]^2$	19.9	Diffusion through product later[152]
50-97	H_2SO_4 [$K_2Cr_2O_7$]	$k_{exp} = 5.0\text{-}15.5 \times 10^{-5}\ s^{-1}$ $k_d t = 1-\frac{2}{3}X-(1-X)^{1/3}$	24	Diffusion through a porous product layer by shrinking core model[149]
45-100	H_2SO_4 [$FeCl_3$]	$r \propto [Fe^{3+}]^{0.12}$	42	Diffusion control[153]
30-90	HCl [$FeCl_3$]	$k_{exp} = 2.63\text{-}6.93 \times 10^{-6}\ s^{-1}$ $k_{exp} = 2.3\text{-}15.9 \times 10^{-7}\ s^{-1}$	15-28	Mixed control (chemical reaction and ion diffusion through product layer)[154]
70-90	H_2SO_4 [$NaNO_3$]	$k_m t^n = -\ln(1-X)$	83	Mixed control (surface reaction and lixiviant diffusion through sulfur layer)[155]
40-95	H_2SO_4 / HCl [Fe^{3+}]	$r = 10^{1.88} e\left(\frac{-48{,}000}{RT}\right)[H^+]^{0.8}[Fe^{3+}]^{0.42}$	48 ± 10	Surface reaction control[94]
23-45	HCl [$FeCl_3$]	$r \propto \frac{[Cu^+][Fe^{3+}][Cl^-]^2}{[H^+]}$	86.4	(Not discussed)[156]
25-50	H_2SO_4 [H_2O_2]	$[H^+]^{0.3}$ $k_{sr} t = 1-(1-X)^{1/3}$	60	Surface reaction control by shrinking core model[157]
30-80	H_2SO_4 [$K_2Cr_2O_7$]	$r \propto [H^+]^{0.8-0.93}$	48-54	Chemical reaction control[158]
70-100	HCl [$FeCl_3$]	$r \propto [Fe^{3+}]^{0.38}$	93	Surface reaction control[159]
25-70	pH 1-3 HCl	$r = 10^{-5.52 \pm 0.07} exp\left(-\frac{32 \pm 5}{RT}\right)$	32 ± 5	Surface reaction control[151]
25-85	HCl [$Fe_{(s)}$]	$k_{exp} = 6.5\text{-}55.3 \times 10^{-6}\ s^{-1}$ $r \propto [H^+]^1$ $k_d t = 1-3(1-X_\delta)^{\frac{2}{3}}+2(1-X_\delta)$ $r = \frac{k_0''}{r^2} exp\left(-\frac{22{,}423}{RT}\right)$	22.4	Diffusion of protons through a product layer by shrinking core model[132]
(as above – different $CuFeS_2$ sample)		$r = \frac{k_0'}{r^2} exp\left(-\frac{33{,}880}{RT}\right)$	33.8	Diffusion of protons through a product later by shrinking core model[132]
125-150	H_2SO_4 [$O_{2(g)}$]	$r \propto \left[p_{O_2}\right]^1$ $k_{sr} t = 1-(1-0.45X)^{1/3}$	93.5	Surface chemical reaction by shrinking core model[130]
50-92	H_2SO_4 [$Fe_2(SO_4)_3$]	$k_{sr} t = 1-(1-X)^{1/3}$	79.5	Surface reaction control by shrinking core model[160]

25-75	H_2SO_4 $[H_2O_2]$	$r \propto [H_2O_2]^1$ $k_{sr}t = 1-(1-X)^{1/3}$	30	Surface reaction control by shrinking core model[161]
25-75	HCl $[Cu^{2+}]$	---	72	Surface reaction control by shrinking core model[97]
55-85	H_2SO_4 (750 *mV*; pH 1) $[Fe^{3+}]$	$k_m t = 1-(1-X)^{2/3}$ $k_m t = 1-(1-X)^{1/3}$	Cu<10hr: 21± 5 Cu>10hr: 83 ± 10	Mixed control by shrinking core model (diffusion or transport control and chemical reaction control) [162]
		$k_{sr}t = 1-(1-X)^{2/3}$	Fe: 76.1	Chemical reaction control[162]
	H_2SO_4 (750 *mV*; pH 1)	$k_{sr}t = 1-(1-X)^{1/3}$	Cu:80±10 Fe:84±10	Chemical reaction control for each[162]
30-80	H_2SO_4 $[H_2O_2]$	$r \propto [H_2O_2]^{1.45}[H^+]^{0.77}$ $k_{sr}t = 1-(1-X)^{1/3}$	39	Surface chemical reaction control[49]
50-90	$[C_4C_1im][HSO_4]$	$k_{sr}t = 1-(1-X)^{1/3}$	69.4	Electrochemical surface control[150]

1.6.1 Dissolution Rates

Many Arrhenius and shrinking core derived rate laws have been suggested for the dissolution of $CuFeS_{2(s)}$, which are also challenging to compare. In fact, some entries to table 1.2 appear to show reversed dependencies, again probably due to large variations in chosen leaching conditions. Kimball *et al.* derived an adapted Arrhenius relation applicable to $CuFeS_{2(s)}$ leach studies;[94] where A [s^{-1}] is the Arrhenius pre-exponential factor, E_a [$J \cdot mol^{-1}$] is the dissolution activation energy and m_i is the activity of each leach-active species (H^+, Cl^-, Fe^{3+}, O_2) raised to its respective molecularity n_i (E1.24).

$$r_{Arrhenius} = A \cdot exp\left(-\frac{E_a}{RT}\right) \cdot \prod_i {m_i}^{n_i} \qquad \text{E1.24}$$

$$r_{OD} = 10^{-5.52\pm0.07} \cdot exp\left(-\frac{(31 \pm 4)\times 10^3}{RT}\right) \cdot [H^+]^{0.16\pm0.04} \qquad \text{E1.25}$$

Acero *et al.*[151] derived a valuable Arrhenius rate equation (E1.26) applicable to both $SO_4^{2-}{}_{(aq)}$ and $Cl^-{}_{(aq)}$ leaching at *p*H 1-3. At *p*H 1 ($[H^+] = 10^{-1}$ $mol \cdot dm^{-3}$) typical rates of 2.1 x 10^{-6} s^{-1} (± 30 %) is expected for ambient $SO_4^{2-}{}_{(aq)}$ leaching, which is consistent with other experimental rate measurements featured in table 1.2. It is noteworthy that this analysis provides reference values for initial $CuFeS_{2(s)}$ dissolution rates, when free-$Fe^{3+}{}_{(aq)}$ oxidant levels can be assumed to be negligible. According to E1.26 and using equivalent *p*H and temperature, $H_2SO_{4(aq)}$ and $IL_{(aq)}$ lixiviant solutions should show equivalent initial leaching rates, since temperature and proton activity are indicated as the rate controlling factors.[151] As leaching progresses, $Fe_{(aq)}$ extracted into solution will equilibrate to generate Fe^{3+} which may further act as oxidant (E1.13), thus E1.26 should be considered with notable variations in molecularity and pre-exponential factor.[94]

Measured Arrhenius pre-exponential factors and activation energies will be evaluated in later discussions.

$$r_{OD} = 10^{1.88} \cdot exp\left(-\frac{48{,}100}{RT}\right) \cdot [H^+]^{0.8} \cdot [Fe^{3+}]^{0.42} \qquad \text{E1.26}$$

1.6.2 Effect of Particle Size

Choice of particle size distribution is crucial to determining the optimum process parameters for any commercial $SO_4^{2-}{}_{(aq)}$ or $Cl^-{}_{(aq)}$ hydrometallurgic process.[163] The majority of current kinetic studies (table 1.2) feature shrinking core model rate laws obtained by considering perfect uniform geometric attack of spherical $CuFeS_{2(aq)}$ particles.[163] Specific rate laws are derived from Fick's Law by imposing differing rate-limiting boundary conditions and as mentioned have fundamentally differing particle size dependencies (E1.27).[132, 152, 154, 163]

$$Diffusion\ Control: \quad k_d\ [s^{-1}] \propto \frac{1}{{r_0}^2}$$

$$Surface\ Reaction\ Control: \quad k_{sr}\ [s^{-1}] \propto \frac{1}{r_0} \qquad \text{E1.27}$$

On a single particle scale, higher recovery rates are promoted by small particle dimensions, since total reactive surface area is increased per unit mass of $CuFeS_{2(s)}$.[49, 155, 157] This effect is particularly evident in a study by Munoz *et al.*, where 58 *%* Cu was recovered over 20 *hrs* leaching from 4 *μm* sized $CuFeS_{2(s)}$ under extreme conditions (90 *°C*, 1200 *rpm*, 1.0 *mol·dm*$^{-3}$ $H_2SO_{4(aq)}$). Equivalent recoveries for 20 *μm* particles were achieved in 100 *hrs*, whereas 47 *μm* particles managed only 20 *%* in 160 *hrs*.[148] However, several other researchers have observed minimal particle size dependence[130, 153] and, as previously referred to, factors such as E_h and nature of the RDS play much more vital roles in determining $CuFeS_{2(s)}$ dissolution activity.

1.6.3 Effect of Agitation

Many agitation modes have been investigated in a commercial context, including shaking, bottle-rolling and mechanical/magnetic stirring.[121] Stirring has been principally employed in laboratory studies, with some researchers preferring (mechanical) overhead stirring, warning peers of unpredictable degrees of abrasion caused by magnetic stirring.[97] Several studies agree with the intuitive expectation that increased stirring rates result in increased leaching rates, since diffusional transport rates of active molecules/leaching products are accelerated in the vicinity of the leaching interface. Additionally, agitation is also important to aid solution reaeration to replenish consumed $[O_2]_{(aq)}$.[42]

However, further evidence for surface chemical reaction controlled kinetics is supplied by numerous similar studies identifying no observable stirring dependence or alternatively observing an optimum stirring rate.[42, 163] This phenomenon has indicated that diffusion is highly efficient under certain conditions, where high solution agitation rates can cause rate-limitations due to reduced surface-oxidant residence times.[155, 161] In one case, the extraction retarding effect of stirring in $FeCl_3/HCl_{(aq)}$ media was attributed to dispersal of $CuCl_2$ oxidant which would otherwise accumulate at the $CuFeS_{2(s)}$ interface.[164] It is noteworthy that one of the few existing $IL_{(aq)}$-$CuFeS_{2(s)}$ studies by Dong *et al.* reported a similar effect, highlighting an approximate optimum agitation rate of 600 *rpm*.[150]

It is unsurprising that the reported optimum $H_2SO_{4(aq)}$ leach agitation rates vary in the range ~400-600 *rpm*[42, 149, 150, 155] when using diverse and incomparable oxidative conditions, which are likely to exhibit higher magnitude dependence than is possible for agitation influence.[42, 152, 155, 165] In fact the study of stirring influence appears to be low on researchers' priorities, with too few agitation rates sampled under equivalent conditions for definitive conclusions be drawn and for optimum stirring rates to be verified.

1.6.4 Effect of Oxidant

A simple analysis of the overall reaction scheme (E1.15) might suggest that $CuFeS_{2(s)}$ dissolution is not promoted by excess $[Fe^{3+}]_{(aq)}$, since ferric/ferrous equilibration (E1.14) can regenerate consumed $Fe^{3+}_{(aq)}$ oxidant from product Fe^{2+} after the latter has been produced by the alternative dissolution scheme (E1.12). However, this analysis is based on the assumption that ferric/ferrous interconversion occurs at equivalent rates with respect to $CuFeS_{2(s)}$ dissolution, as a minimum requirement. If this assumption is poor, the introduction of $Fe_{(aq)}$ ions (ferric or ferrous) should lead to higher rates throughout leaching. The solubility of molecular oxygen as an oxidant and, crucially, the comparison of rates of $[O_2]_{(aq)}$ consumption during leaching (E1.12) versus $O_{2(aq)}$ reaeration rates (E1.10) are key to determining dissolution rates (chapter 6).[42]

As detailed, $CuFeS_{2(s)}$ consists of a strong lattice which is most effectively deconstructed using oxidants to extract electrons from the valence band (VB) in order to destabilise somewhat covalent $M\text{-}S^{2-}$ bonding.[42] Figure 1.3 (also figure 1.10) illustrates that the redox potentials of common oxidants can lie in close proximity to VB energies and initiate the process of 'hole formation'.[21] This M-S bond breaking process has been proposed to increase surface reactivity, creating positions that are vulnerable to further chemical attack.[165] The field has focused on $Fe^{3+}_{(aq)}$ as a cost effective oxidant partnered with $SO_4^{2-}{}_{(aq)}$ or $Cl^-_{(aq)}$ to complement the chosen acid system or to create a mixed anion system.[70, 166, 167] The accepted schemes for the dissolution of $CuFeS_{2(s)}$ in acidic-$Fe_2(SO_4)_{3(aq)}$[168] and acidic-$FeCl_{3(aq)}$[84] are shown in E1.28 and E1.29.

$$CuFeS_2 + 2\,Fe_2(SO_4)_3 \rightarrow CuSO_4 + 5\,FeSO_4 + 2\,S^0 \qquad \text{E1.28}$$

$$CuFeS_2 + 3.5\ FeCl_3 \rightarrow 0.5\ CuCl_2 + 0.5\ CuCl + 4.5\ FeCl_2 + 2\ S^0 \qquad \text{E1.29}$$

A variety of other oxidants have been utilised; ranging from mild oxidants such as $CuCl_{2(aq)}$[97, 123] and $O_{2(aq)}$ saturation,[42, 97] to highly oxidising additives such as H_2O_2[157, 161] and $Cr_2O_7^{2-}$.[149, 158] It is generally appreciated that increases in oxidant concentration lead to increased recovery,[149, 157] however reporting studies often suffer from inadequate monitoring and (ultimately) restriction of lixiviant E_h, in order to avoid $CuFeS_{2(s)}$ surface evolution to a passive state (section 1.8). A good example of this is the report of optimum exposure of leach solutions to $O_{2(aq)}$ to avoid curtailing rates,[42] since controlled $O_{2(g)}$ influx can be necessary to control and limit E_h. It is therefore a concern that any direct effect of an oxidant is shielded by the more dominant effect that their addition has on global solution E_h. This latter concern is also reinforced by the promotion of leaching with addition of $Fe^{2+}_{(aq)}$ reducing agent when E_h has been effectively controlled.[99, 100]

Some studies have quantified the empirical dependence of $[Fe^{3+}]_{(aq)}$ upon the experimental $Cu^{2+}_{(aq)}$ recovery rate (*mol·dm^{-3}·s^{-1}* - table 1.2), with temperature independent molecularities in the range of 0.12-0.42 for mixed $Fe^{3+}/H_2SO_4/HCl_{(aq)}$ leaching. However, the acceleratory influence of $Fe^{3+}_{(aq)}$ is once again debated to be highly condition dependent,[162, 169] with some studies observing no influence of $Fe^{3+}_{(aq)}$, arguing the role of Fe^{3+} is indirect in the creation of 'Goldilocks' redox conditions that best suit $CuFeS_{2(s)}$ dissolution (sections 1.6.8 and 1.7.1). It has been highlighted previously that leaches are insensitive to $[Fe^{3+}] > 0.1$ *mol·dm^{-3}*.[129] In an independent study, leaching with controlled E_h (750 *mV* vs. SHE) was carried out in an attempt to clarify the role of $Fe^{3+}_{(aq)}$.[162] However, $CuFeS_{2(s)}$ is known to show unpredictable active-passive behaviour at E_h values from ~680-800 *mV* vs. SHE (figure 1.8), which appears to have been overlooked in analysis. A study by Gomez *et al.* rather surprisingly observed a detrimental effect on chemical and biological leach rates upon $Fe^{3+}_{(aq)}$ addition when E_h was recorded as <620 *mV* vs. SHE.[119] It is possible that $Fe^{3+}_{(aq)}$ solution complexation is further clouding the issue by varying the activity of free oxidant.

Overall it is generally accepted that the requirement for control of redox conditions significantly outweighs the specific effects of solution-borne oxidants, as discussed further in section 1.6.8 below.

1.6.5 Effect of Dissolution Enhancing Additives

Many reportedly dissolution enhancing additives have been employed alongside traditional $SO_4^{2-}_{(aq)}$ leach media. Inorganic salt additives, such as NaCl[135] and $NaNO_3$,[155] have been used to create mixed anion systems - where anionic surface adsorptions and interactions influence the evolution of leached $CuFeS_{2(s)}$ surfaces.[135] Additionally, the use of Ti and Si oxides have been patented with the cause of enhancements unclear and unreported.[105]

Recently, the prospect of tuning lixiviant systems to alleviate formation of protective passivating surfaces and promotion of leaching has achieved some notable successes.[170-172] Solis-Marcial *et al*. achieved up to 3-fold increases in $Cu^{2+}_{(aq)}$ recovery using addition of 20 *%v/v* propanone or ethane-1,2-diol, with significantly reduced extraction plateaus (~2.5 $mol{\cdot}dm^{-3}$; 240 *hrs*).[170] In a later paper by the same author, 2-propanol and methanol produced similar results and it was concluded that the alcohols were contributing to stabilisation of $Cu^{2+}_{(aq)}$, promoting the formation of a copper-rich phase.[171] A rich chemical space of potentially beneficial solution and surface active species remain unexplored.

A large volume of studies have focused on the effect of Ag^{+}[173-176] and activated carbon[177, 178], which reportedly enhances $CuFeS_{2(s)}$ electrical conductivity through formation of $CuFeS_2$-Ag_2S and $CuFeS_2$-C^* galvanic couples and may also impact S^0 morphology.[179] These additives have been found to be complementary to bacterial bioleaching conditions – the details of which have been reviewed extensively elsewhere,[21] and will not be discussed in depth as these techniques are of limited relevance to the comparison of primitive $H_2SO_{4(aq)}$/$IL_{(aq)}$-based leaching. Crucially however, these results suggest that electron mobility is to some degree rate-limiting in the absence of conductivity enhancing additives.

1.6.6 Effect of Acid and pH

The anionic effect of the acid has already been discussed in terms of the favourable surface adsorptions/interactions that can result in less hindered $CuFeS_{2(s)}$ dissolution. In all other respects, at equivalent pH each acid can be considered to have an identical effect on account of equivalent proton concentration ($[H^+]_{(aq)}$) and therefore *p*H contribution to dissolution via oxidative scheme E1.12. However, the concept of *p*H, and the practicality of $IL_{(aq)}$ *p*H measurement using electrochemical probes, will be the subject of important later discussions (sections 2.3.5 and 6.3).

$$pH = -log_{10}[H^+] \qquad \text{E1.30}$$

Additionally, since a mineral dissolution process is being considered, the dissolution equilibrium for the overall $CuFeS_{2(s)}$ dissolution scheme (E1.31) identifies a fundamental *p*H dependence in the equilibrium constant ($K_{\equiv}$ - E1.32), where the activities of solids and $H_2O_{(l)}$ may be assumed to be equal to 1. From E1.32 it is expected that a rise in acidity will shift equilibrium composition in favour of the dissolved metallic ions. $[H^+]_{(aq)}$ is also reported to have an important role in maximising the solubility of surface FeOOH moieties generating additional free $Fe^{3+}_{(aq)}$ oxidant,[94] with most researchers choosing acidities below p*H* 1.5 in order to avoid FeOOH precipitation/dissolution effects.[21]

$$CuFeS_{2(s)} + 4H^+ + O_{2(aq)} \rightarrow Cu^{2+} + Fe^{2+} + 2S^0{}_{(s)} + 2H_2O \qquad \text{E1.31}$$

$$K_{\equiv} = \frac{\{Cu^{2+}\} \cdot \{Fe^{2+}\}}{\{H^{+}\}^{4} \cdot \{O_2\}} \quad \text{E1.32}$$

As table 1.2 shows, the rate dependence of $[H^+]^n$ has been resolved by several studies, where n = 0.3-1 depending on the oxidising conditions employed.[49, 94, 132, 157, 158] Increased $[H_2SO_4]_{(aq)}$ in the range 0.1-1.0 *mol·dm*$^{-3}$ has been seen to increase dissolution rates.[49, 149] However, since $[H^+]_{(aq)}$ is considerable in typical leach solutions – and is not expected to be rate limiting – control of E_h may again be the overriding factor affecting dissolution (section 1.6.8). E_h and *p*H are dependent parameters. Firstly, one must regulate E_h at high *p*H to avoid passive potentials >690 *mV* vs. SHE (figure 1.8), whilst also controlling prevalent $Cu_{(aq)}$ and $Fe_{(aq)}$ speciation at a given E_h-*p*H combination (figure 1.11). These concepts may explain the apparently contradictory findings that passivation occurs in the H_2SO_4-$H_2O_{2(aq)}$ system with acidities lower than p*H* 0.5 with efficient $CuFeS_{2(aq)}$ leaching restored under extreme concentrations (6 *mol·dm*$^{-3}$ > $[H_2SO_4]$ > 1 *mol·dm*$^{-3}$).[49, 163]

1.6.7 Effect of Temperature

Increases in thermal energy have proven responsible for up to 3 fold increases in $Cu^{2+}_{(aq)}$ extraction when leaching at 40 °*C* compared to 20 °*C*.[132, 151, 180] Leaching kinetics have also been shown to accelerate with increased temperature in acidic $SO_4^{2-}/Cl^-_{(aq)}$ media, in accordance with the conventional temperature dependence of the Arrhenius relation[129] (E1.24) – however temperature also influences other important factors such as E_h, *p*H and equilibrium compositions. For example, above 200 °*C*, surface S^0 may melt, revealing reactive metal rich surfaces.[21] Many studies have measured experimental activation enthalpies for $CuFeS_{2(s)}$ dissolution (E_a - table 1.2), which apply to the dissolution RDS (in theory). The wide ranging values recorded are likely to be a reflection of varying RDS identity, as suggested by a lack of agreement regarding the nature of the RDS across all featured studies (i.e. diffusional/surface reaction/mixed state).

One robust studies identified a low error E_a value of 72 *kJ·mol*$^{-1}$, consistent across two independent $CuFeS_{2(s)}$ flotation concentrates using a broad temperature range (25-75 °*C*).[181] However, other studies have produced E_a measurements which evenly punctuate the 24-94 *kJ·mol*$^{-1}$ range for $H_2SO_{4(aq)}$, perhaps suggesting that measured E_a is a function of oxidant type and concentration (see table 1.2 for references). Kaplun *et al*.[162] apparently confirmed this result under controlled E_h conditions (750 *mV* vs. SHE) in the absence and presence of additive $Fe^{3+}_{(aq)}$ oxidant. In $Fe^{3+}_{(aq)}$-free solution, E_a for $Cu_{(aq)}$ extraction was consistently measured as ~80 *kJ·mol*$^{-1}$ at several sampled leach durations. However, in the presence of added Fe^{3+}, two distinct E_a measurements of 21 *kJ·mol*$^{-1}$ and 83 *kJ·mol*$^{-1}$ were produced, either side of a 10 *hr* leach duration threshold. This finding provides evidence for the external oxidant accelerating initial rates through reduction of extraction activation enthalpy; an effect which tapers off as total $[Fe]_{(aq)}$ rises through the course of the reaction, leading to sufficient $Fe^{3+}_{(aq)}$ levels through ferric-ferrous equilibration.[162]

1.6.8 Effect of Solution Redox Potential (E_h)

The dissolution of $CuFeS_{2(s)}$ is a potential controlled reaction,[182] in which solution redox potential (E_h) is a crucial factor in resultant leaching rates.[162, 169] On several occasions in this text it has been noted that control of E_h is the dominant factor controlling $CuFeS_{2(s)}$ dissolution rates. Perhaps this notion is best exemplified by a reported optimum $[O_2]_{(aq)}$, with both higher and lower concentrations yielding reduced dissolution rates.[42] Referring again to E1.32, it can be seen that increased $[O_2]_{(aq)}$ should enhance dissolution, however $[O_2]_{(aq)}$ can be regarded as having a far more important influence on E_h.

1.6.8.1 E_h Detection Principle

E_h defines the oxidising power (electron affinity) of a redox active solution, in which a high potential represents a strongly oxidising medium. E_h is controlled by the Nernst equation (E1.33); where $E^{\ominus}$ is the standard reduction potential, F is the Faraday constant, n is the number of electrons transferred in the overall reaction and a_i is the activity of each redox active species present raised to the power of its stoichiometric reaction coefficient, v_i.[56]

$$E_h = E^{\ominus} - \frac{RT}{nF} ln \{\prod_i {a_i}^{v_i}\} \qquad \text{E1.33}$$

$$E^{\ominus} = -\frac{\Delta_r G^{\ominus}}{nF} \qquad \text{E1.34}$$

As the definition of $E^{\ominus}$ above illustrates, E_h is a direct measure of the spontaneity of an electrochemical process under a given set of conditions. The relevant electrochemical redox couples associated with $CuFeS_{2(s)}$ dissolution are shown below.[56]

$$anodic\ half\ cell: \quad CuFeS_2 + 4H^+ + O_2 \xrightarrow{4e^-} Cu^{2+} + Fe^{2+} + 2S^0 + 2H_2O$$

$$cathodic\ half\ cell: \quad 4Fe^{2+} + 2H_2O \xrightarrow{4e^-} 4Fe^{3+} + 4H^+ + O_2 \qquad \text{E1.35}$$

$$Overall: \quad CuFeS_2 + 4Fe^{3+} \xrightarrow{E_h, n=4} Cu^{2+} + 5Fe^{2+} + 2S^0$$

However, as many studies have pointed out, observed E_h values are more complex than might be anticipated. It is commonly assumed that E_h experienced by an inert electrode in contact with bulk solution (*e.g.* Ag/AgCl) is equivalent to the weighted so-called 'mixed potential' (E_m) experienced by the corroding mineral surface.[183-185] In fact, consideration of E_m has proven to be fundamental to the understanding of many corrosion mechanisms and rates of corrosion - directly determining the corrosion current density, i_{corr}.[184] The mixed potential of a solution is the reduction potential measured (vs. SHE with zero net current) as a result of the weighted potential contributions of all redox couples present.[186] Although simple Nernstian analysis does not strictly apply, it can be

used in conjunction with E1.15 to predict that $[Cu^{2+}]$, $[Fe^{2+}]$, $[Fe^{3+}]$, $[O_{2(aq)}]$ and $[H^{+}]$ are factors that influence E_h, and also that pH and E_h are dependent parameters (E1.36). The effect of solution composition on E_h has been studied, reflecting expectation from E1.36,[187, 188] where elsewhere some researchers have verified that E_h measurements are dominated by the Fe^{2+}: Fe^{3+} activity ratio (E1.37).[189]

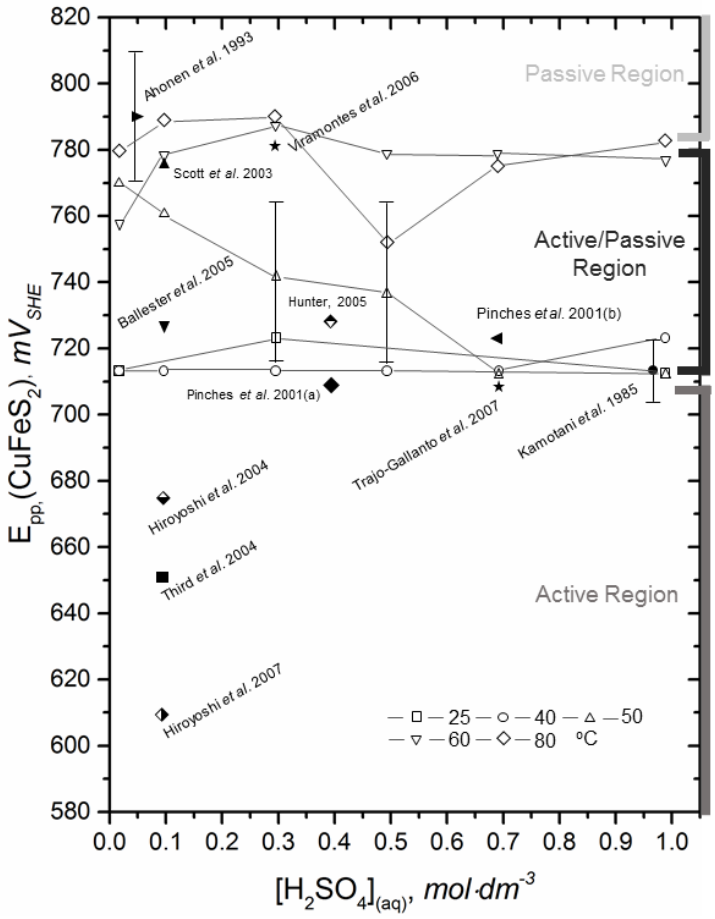
$$E_h = E^{\ominus} - \frac{RT}{4F} ln \left[\frac{\{S^0\}^2 \cdot \{H_2O\}^2}{\{CuFeS_2\}} \cdot \frac{\{Cu^{2+}\} \cdot \{Fe^{2+}\}}{\{H^+\}^4 \cdot \{O_2\}} \right] \qquad \text{E1.36}$$

$$E_h = E^{\ominus} - \frac{RT}{4F} ln \left[\frac{\{Cu^{2+}\} \cdot \{Fe^{2+}\}}{\{H^+\}^4 \cdot \{O_2\} \cdot \{Fe^{3+}\}} \right]$$

$$E_h \cong E^{\ominus} - \frac{RT}{4F} ln \left[\frac{\{Fe^{2+}\}}{\{Fe^{3+}\}} \right] \qquad \text{E1.37}$$

A case study of the leaching of chalcocite (Cu_2S) has been published, in which it was expressed that E_m for optimum leaching lies near to the anodic rest potential, particularly at low $[Fe^{3+}]_{(aq)}$.[184] Even so, conventional mixed-potential theory for dissolution does not appear to apply to $CuFeS_{2(s)}$ dissolution.[183] What is clear from existing studies for $SO_4^{2-}{}_{(aq)}$ leaching studies (figure 1.8) is that $E_{h,m}$ controls the rate of $CuFeS_{2(s)}$ oxidation and must be controlled within a relatively narrow potential window to avoid passivation effects.[183] The onset of $CuFeS_{2(s)}$ passive behaviour has been resolved as ~690 *mV* vs. SHE,[190-192] with the temperature and acidity dependence of this onset passivation potential (E_{pp}) depicted by figure 1.8.[190, 191] Under varying conditions and levels of parameter control, an optimum E_h range of 550-640 *mV* vs. SHE[106, 112, 173] has been suggested, with a consistent E_{pp} at ~710 *mV* vs. SHE. For comparative information, the Galvanox® pressure $Cl^-{}_{(aq)}$ leaching process uses an optimum E_h value of 667 *mV* vs. SHE.[143]

The physical rationale for this active/passive boundary of $CuFeS_{2(s)}$ surface reactivity is the identification of potential ranges within which the prevalent surface and solutions chemistries are compatible for dissolution. The presence of an optimum E_h range has important mechanistic consequences for $CuFeS_{2(s)}$ dissolution which will be discussed in section 1.7. Combining E1.36 and knowledge of this optimum E_h range provides an explanation for why $[O_2]_{(aq)}$ also shows an optimum level – since increased $[O_2]_{(aq)}$ increases E_h beyond the E_{pp} boundary.



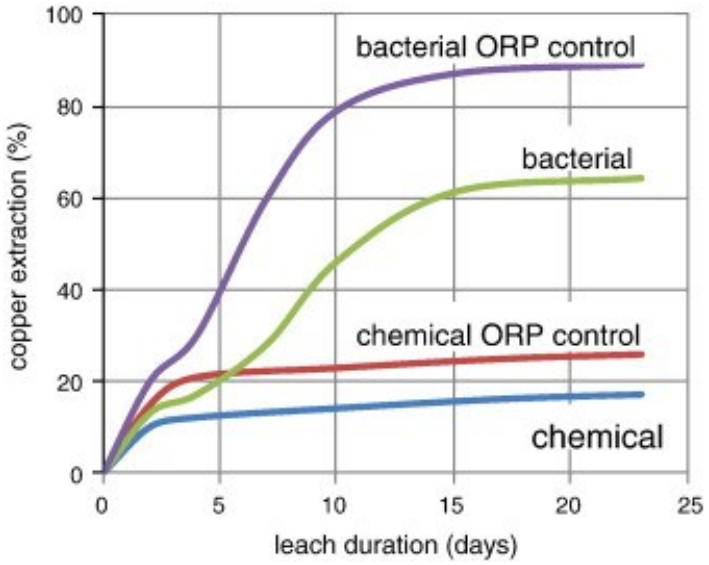
▲ Figure 1.8 – Onset potential (E_{pp}) of reduced $CuFeS_{2(s)}$ surface reactivity as a function of $[H_2SO_4]_{(aq)}$ and lixiviant temperature, including approximate regions of active, active/passive and passive $CuFeS_{2(s)}$ reactivity.[21]

1.6.8.2 E_h Control

It has been established that $CuFeS_{2(s)}$ dissolution is optimised within a given 'Goldilocks' potential window. In fact, it has been observed that $Fe^{2+}/Fe^{3+}_{(aq)}$ addition has little influence upon extraction rates when E_h is controlled.[42] E_h control is further necessary since the chemical nature of the products of $CuFeS_{2(s)}$ dissolution are highly dependent upon E_h.[95] E_h (ORP) control has been achieved via external potential application (section 1.4.3), $KMnO_4$ titration[193] and control of $[O_2]_{(g)}$ influx.[42, 182] The magnitude of enhancements achievable through E_h control and bacterial inclusion are shown in figure 1.9.

Under optimal conditions of redox control ($O_{2(g)}$ influx; 580–600 *mV* vs. SHE), 80 % $Cu_{(aq)}$ is recoverable in $Cl^-_{(aq)}$ with rates independent of particle size fraction, [Cu], [Fe], *p*H and $[Cl^-]$. This result is suggestive of transitioning to a new RDS upon application of E_h control. Elsewhere, detection of $CuS_{2(s)}$ and $CuFe_{1-x}S_{(s)}$ dominated surfaces at ≤640 *mV* vs. SHE, with $Fe_2O_{3(s)}$ and $CuO_{(s)}$ prevailing at higher potentials (640-940 *mV* vs. SHE) may provide insight into the physical reasoning for well-established $CuFeS_{2(s)}$ active/passive behaviour[194] (figure 1.8). FeS_2 was found to have an E_h controlling influence in $SO_4^{2-}{}_{(aq)}$ leaching, linked to elimination of polysulfides.[195] The specific effect of E_h on the nature of sulfurous deposits is dealt with further in section 1.8.

In summary, it is now commonly thought that $Fe_2(SO_4)_{3(aq)}$-based $CuFeS_{2(s)}$ dissolution enhancements are largely 'indirect', whereby the dominant role of Fe^{3+}:Fe^{2+} is to adjust E_h conditions, rather than via direct Fe^{3+} surface oxidation.[183] Indeed, under highly oxidising conditions leach enhancements have been achieved through addition of $FeSO_4$.[98, 99] It is possible that because of this, many leach studies have simplified their consideration of E_h to be largely accounted for by contributions of the Fe^{2+}/Fe^{3+} couple (E1.37).



▲ Figure 1.9 - Cu extraction profiles for $SO_4^{2-}{}_{(aq)}$ based leaching of $CuFeS_{2(s)}$ at 50 *ºC* (323 *K*) for systems with and without accelerating microbial additives and/or oxidation-reduction potential (ORP) control. Reproduced from Watling *et al.* using data from Ahmadi *et al.*[81, 196]

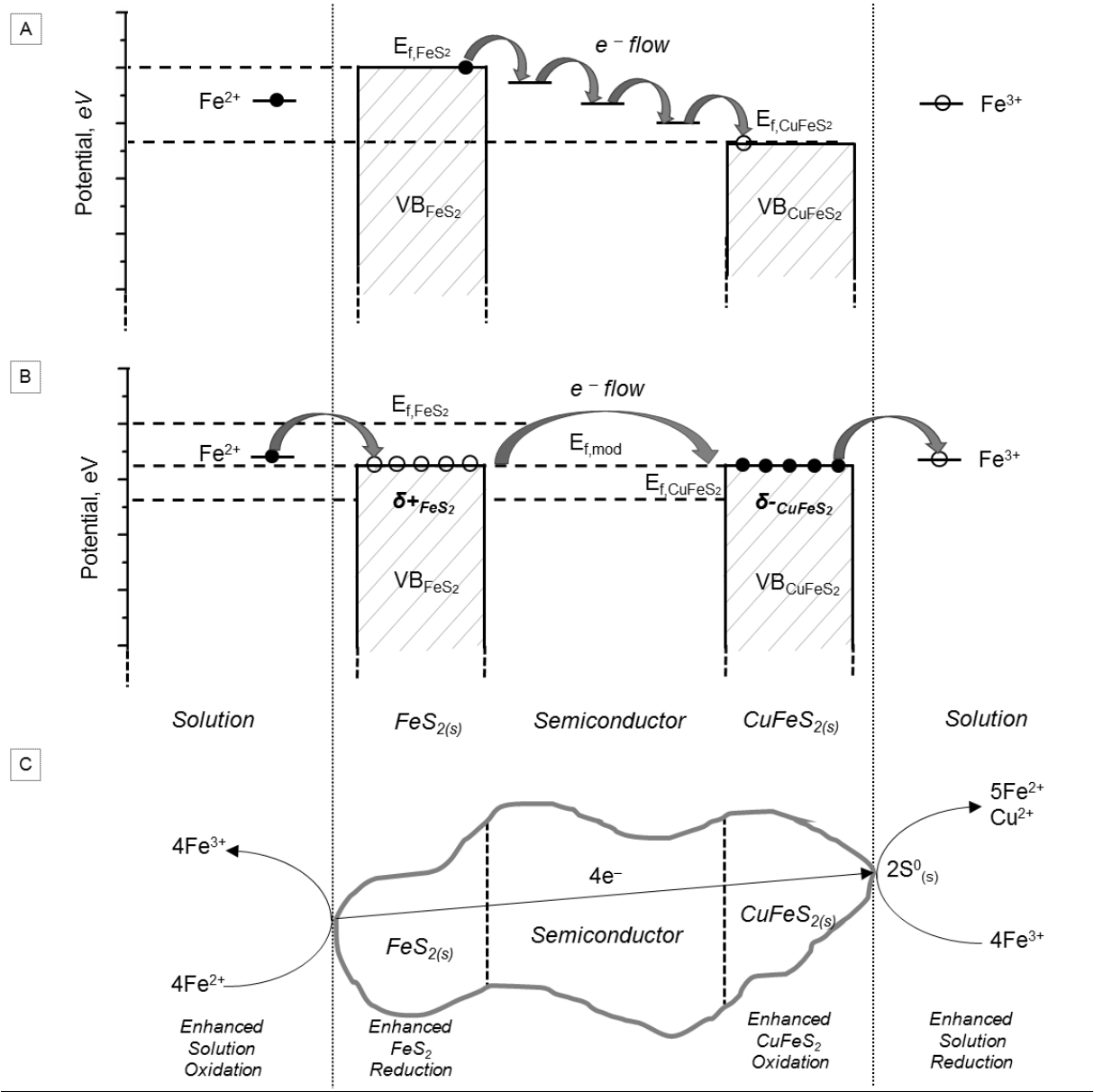
1.6.9 Effect of Galvanic Coupling

Galvanic interactions have important effects during grinding,[197] leaching,[92] flotation[198] and acid mine drainage.[89, 199] As discussed in section 1.1.2, primary sulfide ore bodies contain a wide variety of coexisting semiconducting sulfides; including significant quantities of galena (PbS), sphalerite (ZnS) and particularly pyrite (FeS_2). Table 1.3 features the rest potentials of these coexisting minerals, providing a measure of the Fermi energy of the mineral (E_{fermi} – see figure 1.3), the oxidisability of the mineral surface and explaining why $CuFeS_{2(s)}$ leaches at slower rates than related copper sulfides.[92]

▼ Table 1.3 - Rest potentials of common relevant sulfide minerals.[92]

Mineral	Chemical Formula	Rest Potential, *V* vs. SHE
Pyrite	FeS_2	0.63
Chalcopyrite	$CuFeS_2$	0.52
Chalcocite	Cu_2S	0.44
Covellite	CuS	0.42
Galena	PbS	0.28
Sphalerite	ZnS	-0.24

$CuFeS_2$: FeS_2 can be as high as 3:2 in naturally occurring ores,[200] such that each mineral shares a high proportion of fractured surface coverage.[93] $CuFeS_{2(s)}$ samples with significant FeS_2 content exhibit accelerated leach kinetics due to the formation of galvanic couples between mineral regions with distinct rest potentials.[88] Within the FeS_2-$CuFeS_{2(s)}$ galvanic couple, a net electron flow is initiated in physically contacted semiconductor minerals - flowing from the high potential mineral region (FeS_2) to the low potential region ($CuFeS_2$) driven by mineral E_{fermi} equalisation (figure 1.10A).[104, 105]



▲ Figure 1.10 - (A) Schematic explaining how differential rest potentials in FeS_2-$CuFeS_{2(s)}$ create a galvanic flow to equalise E_{fermi} (B) Mineral polarisation is counteracted by enhanced solution redox activity (Fe^{2+}/Fe^{3+} couple shown) (C) Schematic of the overall galvanic effect and the localisation of enhanced redox activity on and surrounding the mineral surface.[93]

This galvanic electron flow causes instantaneous mineral polarisation, driving solution-based reduction/oxidation to counteract electron relocation and maintain charge neutrality (figure 1.10B). Electron vacancies at the $FeS_{2(s)}$ mineral region (anode) are filled via oxidation of solution species to generate electrons (e.g. $Fe^{2+} \rightarrow Fe^{3+}$ - figure 1.10B). An excess of electron charge density at the $CuFeS_2$ mineral region (cathode) is consumed via reduction of solution species (e.g. $Fe^{3+} \rightarrow Fe^{2+}$) – thereby accelerating oxidative dissolution of the $CuFeS_2$ surface in the process.[88, 93]

Attainable enhancements are very significant, with 4-15 %[88] and up to 40 %[200] reported for 1:1 and 3:2 $CuFeS_2$:FeS_2 respectively. The galvanic effect has been confirmed by titration of 0.1 $mol \cdot dm^{-3}$ $HCl_{(aq)}$ to maintain a stable solution *p*H of 2.5 during $CuFeS_{2(s)}$ leaching, where up to 18 times

larger $[H^+]$ consumption in the presence of FeS_2 was reported to confirm dissolution enhancement.[201] For this reason, the Galvanox® process uses FeS_2:$CuFeS_{2(s)}$ ratios of up to 10,[143] with Koleini *et al*. using an optimum ratio of 4.[93] It is also noteworthy that, as expected, equivalently formed galvanic coupling to PbS and ZnS lead to reduced dissolution.[202]

1.7 Mechanistic Insights

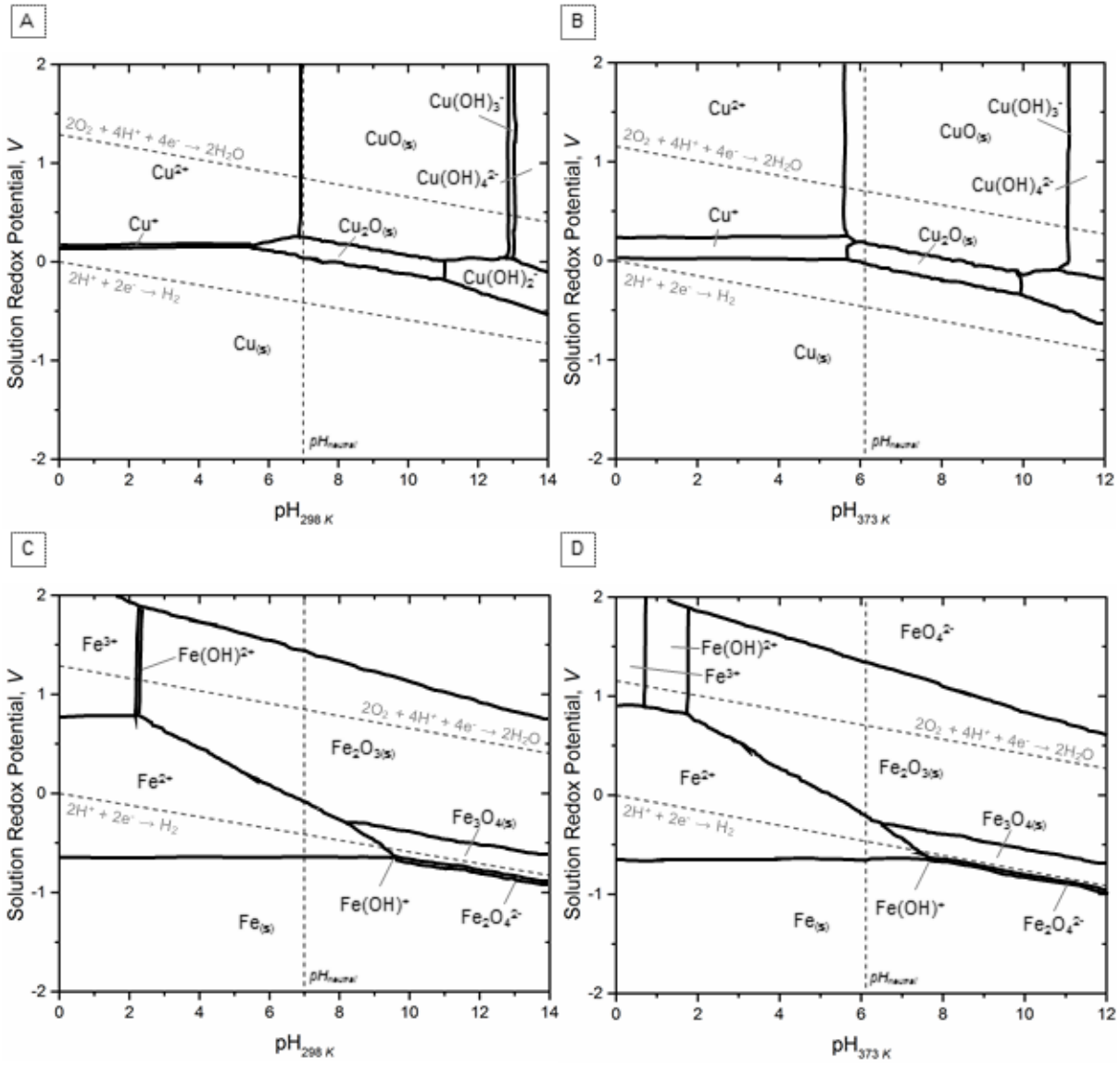
1.7.1 Dissolution Products

In section 1.2.4, it was discussed that the formal oxidation state of bulk $CuFeS_2$ is best represented by $Cu^+Fe^{3+}(S^{2-})_2$. The accepted oxidative dissolution schemes presented, all regard the products of direct chemical dissolution of $CuFeS_{2(s)}$ to be as illustrated in scheme E1.38. However, the production of only Cu^{2+}, Fe^{2+} and S^0 is clearly not realistic when considering common solid impurities, surface structure and physical variations. Additionally, when conducting an acidic leach, the $CuFeS_{2(s)}$ surface and aqueous solution speciation are functions of the specific leach conditions chosen in terms of *p*H and E_h. The consequences of dissolution can be divided into four main categories: 1) the nature of the attacked surface of $CuFeS_{2(s)}$ (as discussed in section 1.2.4); 2) the surface/solution locality of redox events; 3) the kinetic dissolution products; 4) the thermodynamic speciation of aqueous metal ions.

$$Cu^+Fe^{3+}(S^{2-})_2 \rightarrow Cu^{2+} + Fe^{2+} + 2S^0 + 4e^- \qquad \text{E1.38}$$

With respect to the latter, the predominant thermodynamic solution speciation can be judged from Pourbaix diagrams for $Cu_{(aq)}$ and $Fe_{(aq)}$. Relevant diagrams must be constructed using typical ambient leach conditions, such as in figure 1.11 ($[M]_{tot}$ = 6 $mmol{\cdot}dm^{-3}$; 298 *K*),[203, 204] where analogous plots for varied temperature (100 °*C*) can be useful to visualise temperature dependency (figure 1.11).

As discussed, the thermodynamic products of $CuFeS_{2(s)}$ dissolution are highly dependent on E_h.[95] Under typical acid-$SO_4^{2-}{}_{(aq)}$ leaching conditions (*p*H < 2; 750 > E_h > 150 *mV* vs. SHE), $Cu^{2+}{}_{(aq)}$ and $Fe^{2+}{}_{(aq)}$ have thermodynamic predominance. Furthermore, experimental ferrous/ferric activity ratios larger than 10:1 have been seen for $H_2SO_{4(aq)}$, $HClO_{4(aq)}$ and $HCl_{(aq)}$ lixiviant media (750 *mV* vs. SHE; 75 °*C*), where no $[Cu^+]_{(aq)}$ was detected for $H_2SO_{4(aq)}$.[169] A computational study predicted an E_h threshold value of 850 *mV* vs. SHE, only above which $Fe^{3+}{}_{(aq)}$ becomes the prevalent member of the Fe^{2+}/Fe^{3+} couple.[205] Consequently, there can be a high level of confidence that $Cu^{2+}{}_{(aq)}$ and $Fe^{2+}{}_{(aq)}$ are the thermodynamic products of acidic leaching of $CuFeS_{2(s)}$ and that in primitive systems E_h is largely controlled by Fe^{2+}: Fe^{3+} compositions. The speciation of S following oxidative dissolution is far more complex and vigorously debated, being the subject of discussions in section 1.8.



▲ Figure 1.11 – Pourbaix diagrams applicable at 298 *K* and 373 *K* respectively for $Cu_{(aq)}$ (A-B) and $Fe_{(aq)}$ (C-D).

1.7.2 Mechanisms for Acidic $CuFeS_{2(s)}$ Dissolution

Many researchers share the opinion that the principle hindrance to further progress in the field of $CuFeS_{2(s)}$ dissolution is limited understanding of the fundamental leaching mechanism and surface chemistries. Additionally, the drive to accelerate $CuFeS_{2(s)}$ dissolution through addition of oxidative agents has complicated the process of understanding the fundamentals of the $CuFeS_{2(s)}$ dissolution mechanism.[21]

As discussed in section 1.2.2, $CuFeS_{2(s)}$ is best represented by the $Cu^{+}Fe^{3+}(S^{2-})_2$. However, surface $Cu^{+}_{(s)}$ is reportedly readily oxidised in aqueous environments – thus exposed Cu planes may be expected to exist as both $Cu^{+}/Cu^{2+}_{(s)}$ before being released as $Cu^{2+}_{(aq)}$.[94] DFT simulation of differentially-terminated (001) $CuFeS_{2(s)}$ surfaces confirm that the Cu-terminated surface is oxidisable to Cu^{2+}, that the Fe-terminated surface is reducible to $Fe^{2+,}$ whilst the S-terminated surface can act as an electron donor or acceptor since S atomic orbitals provide both VB and CB

contributions.[27] Experimental studies have suggested that $CuFeS_{2(s)}$ M-S bonds are directly attacked by $Fe^{3+}_{(aq)}$ or $O_{2(aq)}$ oxidant forming H_2S or O_2^-, with the former reportedly directly responsible for polysulfide formation.[59, 165] However, it is difficult to reconcile direct oxidant attack with the knowledge that an optimum E_h range exists for $CuFeS_{2(s)}$ dissolution.

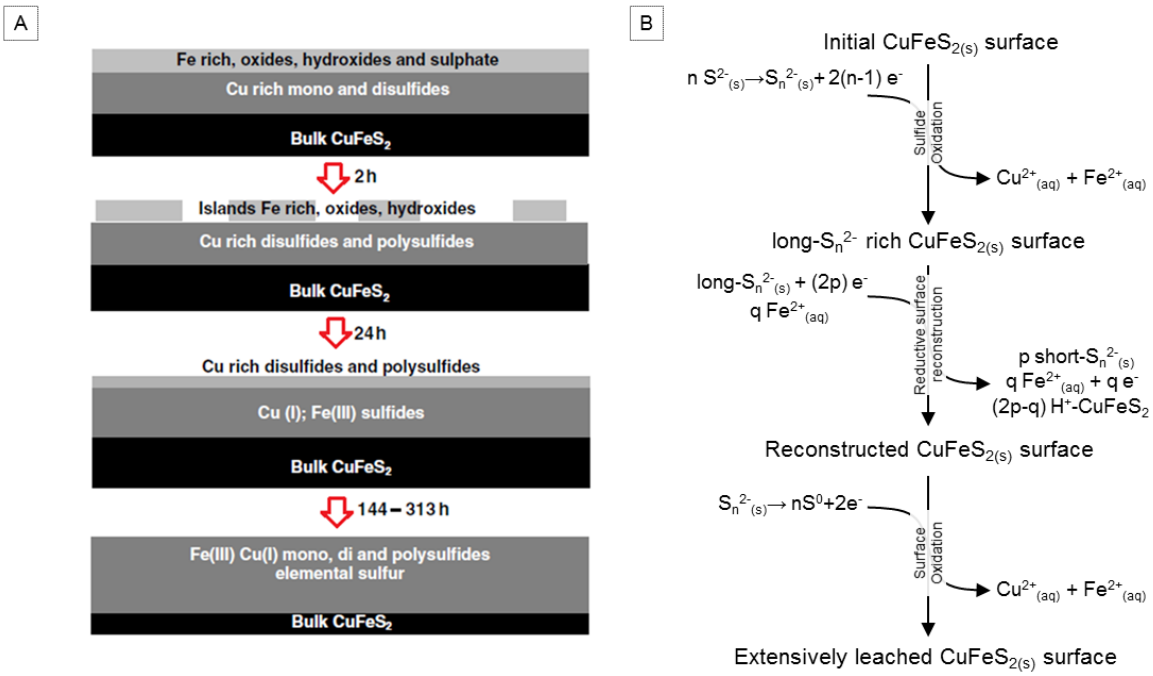
As such, overall oxidative dissolution schemes for $CuFeS_{2(s)}$ dissolution (E1.12; E1.13) can be mechanistically misleading, as those schemes appear to suggest that complete dissolution of $CuFeS_{2(s)}$ is afforded by extremes of $[Fe^{3+}]_{(aq)}$ and $[H^+]_{(aq)}$. In reality, $CuFeS_{2(s)}$ exhibits maximum leaching rates within a low E_h potential window (~640–700 *mV* vs. SHE), suggestive of competitive oxidation/reduction steps.[72, 99, 100, 188, 193] Hiroyoshi *et al*. explained the presence of this 'Goldilocks' optimum E_h, devising a mechanism which proceeds via intermediate Cu_2S (E1.39) - requiring milder oxidising dissolution conditions (lower E_h) than $CuFeS_{2(s)}$ for dissolution - before proceeding to the release of free ionic species and native S^0 (E1.40).[193, 206] This mechanism does not identify specific redox active solution species, instead creating the correct E_h conditions for these species to be present. The overall reaction equation simplifies to E1.13 also generating free $Fe^{3+}_{(aq)}$ for the direct dissolution pathway (E1.13).[98-100] E1.41 mathematically expresses the proposed basis for optimum dissolution E_h, where $E_{red(CuFeS_2)}$ is the critical potential for reduction of $CuFeS_{2(s)}$ to $Cu_2S_{(s)}$ and $E_{ox(Cu_2S)}$ is the potential for $Cu_2S_{(s)}$ oxidation to $Cu^{2+}_{(aq)}$ and each may be sensitive to changes to leach conditions.

$$CuFeS_2 + 3Cu^{2+} + 3Fe^{2+} \xrightarrow{E_{red(CuFeS_2)}} 2Cu_2S + 4Fe^{3+} \quad \text{E1.39}$$

$$Cu_2S + 4Fe^{3+} \xrightarrow{E_{ox(Cu_2S)}} 2Cu^{2+} + 3Fe^{2+} + S^0 \quad \text{E1.40}$$

$$E_{red(CuFeS_2)} > E_{h,m} > E_{ox(Cu_2S)} \quad \text{E1.41}$$

Combining time-correlated solution and surface composition studies (XPS; ToF-SIMS; SEM), Harmer *et al.*[64] devised a three-step mechanism for $HClO_{4(aq)}$ leaching (*p*H 1; 1 dm^{-3}; 280 *mM* Fe^{3+}; 380 *rpm*; 85 °*C*). The mechanism also includes competition of oxidation and reduction stages as detailed in figure 1.12B and as such also accounts for optimum E_h measurements. During the first oxidation stage, monosulfide polymerises to S_n^{2-} releasing electrons associated with subsequent ejection of $Cu^{2+}_{(aq)}$ and $Fe^{2+}_{(aq)}$ into solution. The second stage involves reductive depolymerisation, consuming electrons in the conversion of surface-bound long-S_n^{2-} into multiple short-S_n^{2-}, where electron transfer is balanced by $Fe^{2+}_{(aq)}$ oxidations and $H^+_{(aq)}$ adsorption onto $CuFeS_{2(s)}$ surface. The third stage is an oxidation of short-S_n^{2-} to crystalline $S_n{}^0_{(s)}$ releasing electrons associated with the further release of $Cu^{2+}_{(aq)}$ and $Fe^{2+}_{(aq)}$ cations. A schematic including the indication of key leaching timescales is shown in figure 1.12B.

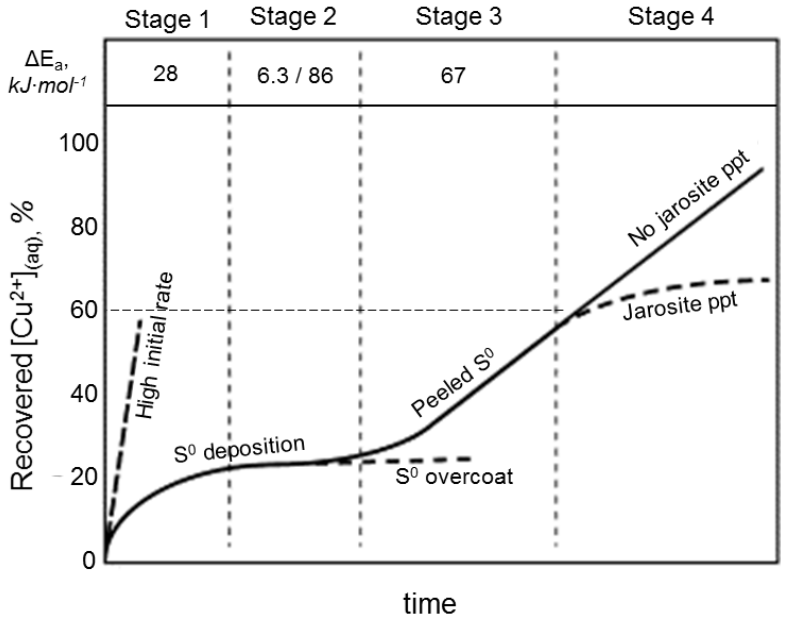


▲ Figure 1.12 – Mechanism for $CuFeS_{2(s)}$ dissolution as proposed by Harmer *et al*. with regard to $HClO_{4(aq)}$ leaching at initial *p*H 1 (1 dm^{-3}; 280 *mM* Fe^{3+}; 380 *rpm*; 85 °*C*) [64]. (A) Schematic diagram of surface changes including timescales (B) Flowchart showing key transformation in the proposed three-stage redox mechanism.

Other mechanistic studies have focused on the mechanism for $Fe_2(SO_4)_3$-$H_2SO_{4(aq)}$ leaching. In a review of many similar works, Klauber[121] introduced such a mechanistic overview, presented as a four-stage model (figure 1.13): 1) high rate, low E_a dissolution on fresh $CuFeS_{2(s)}$ surfaces; 2) reduced rates caused by high E_a associated with charge transport in thick S^0 deposits; 3) linear kinetics following removal of S^0 over-layers to reveal fresh $CuFeS_{2(s)}$ surfaces; 4) parabolic reduction in rates if conditions for jarositic surface coating precipitations are not avoided (section 1.8.5).

A similar three-stage mechanism has also been suggested for $Fe_2(SO_4)_3/H_2SO_{4(aq)}$ leaching of synthetic β-$CuFeS_{2(s)}$ (0.03 $mol{\cdot}dm^{-3}$ Fe^{3+}; *p*H 1; 80-95 °*C*; 950 *rpm*),[42, 207] giving further structural insight. $Cu^{2+}_{(aq)}$ extraction profiles show similar features to those seen in figure 1.13, also measuring equivalent variations in E_a as predicted in Klauber's four-stage model, such that numerical data has been added to figure 1.13. An initial temperature dependent stage was able to rapidly leach 20 % Cu with a low associated E_a indicating diffusion control (28 $kJ{\cdot}mol^{-1}$). After the time required for ~15 % Cu recovery, S^0 was first detected via XPS. However, by the time the second stage had commenced, with resumption of linear kinetics, no S^0 was detected on highly porous leached residues via SEM. E_a was found to be a strong function of temperature, indicating diffusion-limited rates at low temperatures (E_a = 6.3 $kJ{\cdot}mol^{-1}$) and surface reaction-limited rates above 318 *K* (E_a = 83 $kJ{\cdot}mol^{-1}$). Structural collapse initiated a third stage, in which $Cu^{2+}_{(aq)}$ recovery further increased up to ~60 % with measured E_a of 67 $kJ{\cdot}mol^{-1}$, before observed retarded rates are

correlated to increased spectroscopic levels of surface $FeOOH_{(s)}$ and $S^0_{(s)}$. Since S^0 was not detected by XRD, the authors concluded that the S^0 deposit was amorphous.



▲ Figure 1.13 – Conceptual 4-stage model for $CuFeS_{2(s)}$ dissolution displaying rational for differing extraction profile features and measured activation energies (E_a) for each stage – N.B.: stage 2 has a temperature dependent E_a of 6.3 *kJ·mol⁻¹* at low temperatures and 86 *kJ·mol⁻¹* at high temperatures.[42, 121, 207]

1.8 Kinetic Hindrance of $CuFeS_{2(s)}$ Dissolution

Commercial adoption of $Fe_2(SO_4)_3$-$H_2SO_{4(aq)}$ hydrometallurgy is ultimately limited by incomplete $CuFeS_{2(s)}$ dissolution and low ambient leaching rates. Examination of typical $Cu^{2+}_{(aq)}$ extraction profiles (*e.g.* figures 1.9 and 1.13) reveals high initial rates followed by parabolic rate reductions resulting in severely rate-limited $CuFeS_{2(s)}$ dissolution or complete plateaus. Reduction in initial rates is generally considered to be an artefact of evolving S speciation, and therefore reactivity of the leached mineral interface.[42] Since non-zero rates are generally observed at long leach durations, this process is semantically regarded as 'kinetic hindrance' (used hereafter), as opposed to 'passivation' by an overlying insulating coating. As such, kinetic hindrance takes the form of either rate-limiting surface reactions or diffusional transport of electrons or ions in the vicinity of the interface (table 1.2 and discussion in section 1.6).[148]

Many of the mechanisms featured in section 1.7, are informed by dominant S moieties observed in time-correlated surface spectroscopies, used to determine feasible S transformations and cation release mechanisms (*e.g.* figure 1.12). Although specific leaching mechanisms are still relatively uncertain, all accepted schemes for $CuFeS_{2(s)}$ dissolution pair $S^0_{(s)}$ generation with metal ion release (E1.12 & E1.13). A high volume of studies, suggest that surface-bound sulfurous species are responsible for parabolic dissolution hindrance.[70, 83, 93, 126, 168, 208] Candidate species include elemental sulfur,[42, 84, 148, 163] jarosite precipitates,[84, 94] metal-deficient sulfide[43, 67, 125] and

polysulfides.[31, 70, 96, 101, 126, 209] The spectroscopic evidence for these phases, the key conditions and mechanism precluding their formation and their kinetic influence are discussed below with reference to figure 1.13 - a conceptual four-stage model, designed to summarise kinetic hindrance effects.[121] Note that the evolution of S surfaces under non-acidic aqueous and atmospheric oxidation are reviewed above in section 1.2.4.

1.8.1 Surface Chemistry of $SO_4^{2-}{}_{(aq)}$ Leaching

In a key XPS study of $SO_4^{2-}{}_{(aq)}$ leaching with raised $O_{2(g)}$ pressure (*p*H 1; 1.4 *MPa* $O_{2(g)}$; 110 °*C*) Hackl *et al.*[70] characterised <1 *pm* thick kinetic hindering layers on $CuFeS_{2(s)}$ particles after 3 *hrs*. Whilst S^{2-}, S_2^{2-} and $Cu_{0.8}S_n$ (S_n^{2-}) were assigned in XPS spectra, the latter metal-deficient polysulfide was blamed for retarded rates with its presence appearing to be confirmed by faster initial Fe extraction rates in comparison to those of Cu. In addition, $Fe_3O_{4(s)}$, $Fe_2O_{3(s)}$ and $FeOOH_{(s)}$ were all cautiously assigned which, as mentioned, are also considered by some to be kinetic hindrance candidates.

Therefore, this single study concludes that all common kinetic hindrance candidates are formed from $SO_4^{2-}{}_{(aq)}$ leaching. However, Klauber found only S^{2-}, S_2^{2-} and S^0 sulfur species on leached $CuFeS_{2(s)}$ (*p*H 1.4-1.8; 50 °*C*; 2 *hrs*; 150 *rpm*),[209] later criticising the simplicity of XPS analysis in the assignment of both S_n^{2-} and metal-deficient sulfide.[121] Several researchers have commented that due to the overlapping nature of S signals, XPS alone is not sufficient to indicate the presence of these phases and must be combined with XRD, Raman, IR, XAFS and ToF-SIMS following published guidance on reliable assignment of S phases.[210, 211] In reality, highly soluble SO_4^{2-} is also produced by oxidation of S^0 in all of the above schemes, due to the action of molecular oxygen (section 1.2.4).[21]

1.8.2 Elemental Sulfur (S^0)

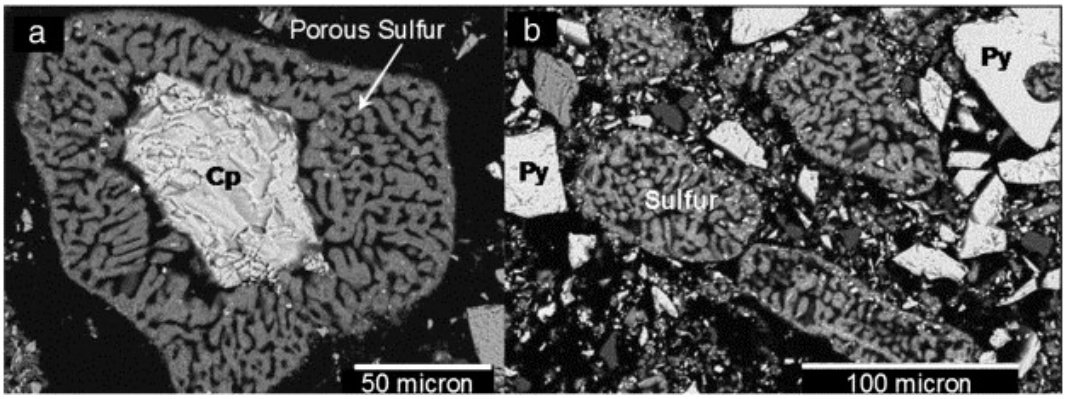
Elemental sulfur ($S^0_{(s)}$) is consistently found as a leaching product on $CuFeS_{2(s)}$ residues,[101, 125, 193] although the role, if any, of product sulfur films in limiting dissolution rates is the subject of vigorous debate[12, 84, 125, 148, 212, 213] As discussed in section 1.2.4, $S^0_{(s)}$ is formed through oxidation of exposed S_n^{2-} (n=1-6) on $CuFeS_{2(s)}$ surfaces, with accelerated transformation in low E_h conditions.[189] Concern regarding the potential significance of $S^0_{(s)}$ over-layers is justified by the observation of small leached $CuFeS_{2(s)}$ particles (<40 *μm*) completely encapsulated by a coherently layered S^0 structure.[214] Additionally, in a quantitative XPS study, Dutrizac found that surface bound S speciation is dominated by native S^0 (>90 *%*),[214] where binding energies of 163.6-164.0 *eV* are assigned to $S^0_{(s)}$ on account of sublimation losses observed under vacuum pressure (<200 *K*).[210]

Such observations, have led some to conclude that electron/ion transport through this $S^0_{(s)}$ layer is ultimately rate limiting[215] as suggested by the proximity of resolved $CuFeS_{2(s)}$ dissolution E_a

values (83.7 $kJ \cdot mol^{-1}$) to other reported measurements for electron conduction through $S^0_{(s)}$ (96.3 $kJ \cdot mol^{-1}$; *cf*. table 1.2).[148] Hirato *et al*. attribute parabolic kinetics to the development of dense $S^0_{(s)}$ on the initially rapid leaching $CuFeS_{2(s)}$ surface, followed by a later regime with increased dissolution rates, during which no significant surface $S^0_{(s)}$ was detectable – leading to the conclusion that the $S^0_{(s)}$ layer had 'peeled' away revealing a fresh reactive surface (stage 3 – figure 1.13).[216] It is worth emphasising that $S^0_{(s)}$ layers will also be depleted by the metabolic activity of bacteria, thereby posing reduced concern to a truly cooperative biochemical leaching strategy – although increased solution E_h as a result of bacterial action may require further control measures.[21]

Some doubt is cast on $S^0_{(s)}$ responsibility for kinetic retardation, since others have observed significant $S^0_{(s)}$ layers with minimal kinetic influence.[101] One particular study showed that sonication - aimed at dislodging any kinetically hindering layer - did not impact upon dissolution rates.[121] However, it is known that complex $S^0_{(s)}$ allotropy and morphologies exist in dynamic equilibrium,[158, 213] and, it is probable that the complex range of possible S^0 allotropies and solid morphologies could significantly vary predominant S^0 layer density, porosity, conductivity and tendency to agglomerate in varied conditions.[121, 214, 217] This may therefore explain the range of E_a values presented in table 1.2 measured from various experimental conditions.[216]

Regarding porosity for instance, figure 1.14 features a backscattered electron micrograph (SEM) of pressure-$Cl^-_{(aq)}$ leached $CuFeS_{2(s)}$ clearly showing $S^0_{(s)}$ to form highly porous, non-hindering agglomerates.[101, 218] It has been shown that leaching in $Cl^-_{(aq)}$ lixiviant exhibits minimal kinetic hindrance,[122, 133, 180] which is seemingly a result of higher porosity accompanying changes in S^0 morphology.[70113, 223] Similarly, in pH 1 $HClO_4$ it was found that despite significant surface S^0 compositions (78 %) no kinetic plateaus were observed.[64] Elsewhere, addition of particulate $C_{(s)}$ has been linked to heightened $S^0_{(s)}$ crystallinity and enhanced diffusional exchange rates.[167] However, it is currently unclear how the porosity and wider properties of $SO_4^{2-}{}_{(aq)}$-derived $S^0_{(s)}$ deposits compare and, as concluded in a recent influential review,[121] certain selected morphological $S^0_{(s)}$ variants are strong candidates for kinetic hindrance of $CuFeS_{2(s)}$.

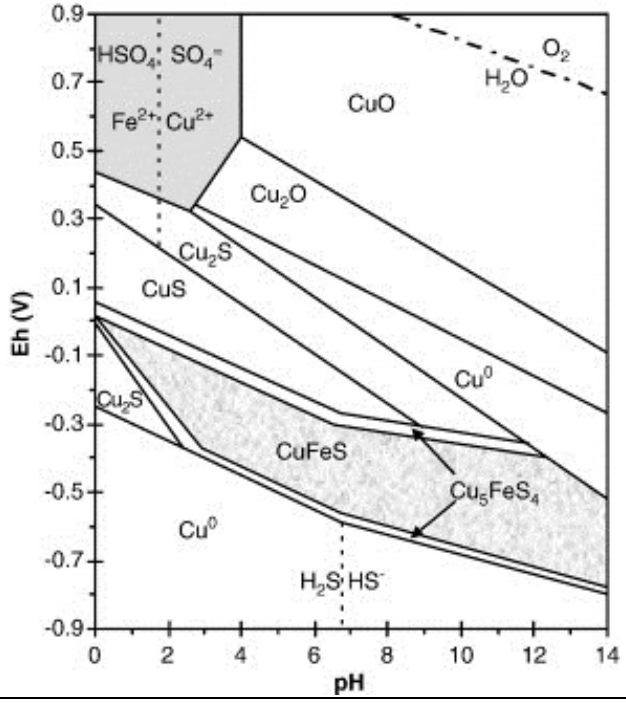


▲ Figure 1.14 – Backscattered electron micrograph of incomplete (A) and complete (B) dissolution of $CuFeS_{2(s)}$ using Galvanox® pressure-$Cl^-_{(aq)}$ leaching, depicting conductive porous $S^0_{(s)}$ overlayers.[143]

1.8.3 Metal-Deficient Sulfides (CuS_n)

Several researchers have reported initial Fe: Cu dissolution ratios in the range of 2-5,[125, 151, 213, 219] with metal-deficient sulfides forming from reconstruction of these non-stoichiometric (partially oxidised) surfaces.[43, 70] Researchers have typically assigned these phases as CuS_n (n=2-6) from surface sensitive Auger electron spectroscopy (figure 2.27) and XPS,[70] reportedly posing a barrier to diffusional transport to/from the active leaching surface.[148] A more specific surface sulfide, $Cu_{0.8}S_2$ has been reportedly detected, following 40 days of leaching in weak acid (0.2 $mol \cdot dm^{-3}$ CH_3COOH).[43]

The relevant $CuFeS_{2(s)}$ Pourbaix diagram (figure 1.15) suggests that $Cu_mS_{n(s)}$ species may be favoured in typical leach conditions when E_h is low (*p*H 1-2; <400 *mV* vs. SHE). Such surface reconstructions could theoretically be responsible for parabolic rate reduction if the reconstructed phase was less susceptible to leaching than the initial 'uniform' $CuFeS_{2(s)}$ surface, perhaps explaining high rate, low E_a for the initial period.[65, 220] The feasibility of selective initial $Fe_{(aq)}$ ionic release followed by formation of $Cu(II)S_n$ has been confirmed by 2D $CuFeS_{2(s)}$ surface simulations with enforcement of E_h control boundary conditions (600-700 *mV* vs. SHE).[192] With a lack of convincing evidence, metal-deficient sulfide has perhaps become an easily-blamed 'scapegoat' for kinetic hindrance effects, with questionable physical basis and/or significant challenges of spectroscopic assignment. Klauber largely rejected the rigour of XPS interpretations used to identify metal-deficient sulfide, favouring simpler alternative explanations for the typical spectral features observed.[121] As such, advice and guidance for correct XPS assignment of sulfurous species (particularly of S_n^{2-}) can be found for less experienced spectroscopists.[42, 220]



▲ Figure 1.15 - Pourbaix diagram for the $CuFeS_{2(s)}$–H_2O system at 25 °*C*.[221, 222]

1.8.4 Polysulfides (S_n^{2-})

Polysulfides (S_n^{2-}) are restricted length oligomers (n=2-6) which form from the reductive polymerisation of S^{2-}.[81, 121] S_n^{2-} can be characterised via XPS, showing three distinct environments (S^0, $S^{\delta-}$, $S^{(1-\delta)-}$) and negligible chain length effects[210, 220, 223] – although, with good practices in mind, an independent complementary technique should be used in conjunction to confirm observations. The use of XPS in isolation has cast doubt on some reports of S_n^{2-} detection on leached $CuFeS_{2(s)}$.[121] S_n^{2-} presence on leached $CuFeS_{2(s)}$ residues has been confirmed via several techniques, including ToF-SIMS.[211] Parker *et al.* utilised *in-situ* Raman spectroscopy following leaching (0.1 *mol·dm*$^{-3}$ $FeCl_3$-$HCl_{(aq)}$; 0.1 *mol·dm*$^{-3}$ $Fe_2(SO_4)_3$-$H_2SO_{4(aq)}$) to prove the formation of $S_n^{2-}{}_{(s)}$, which was found to be highly stable <70 *°C*.[224] However, this proposed S_n^{2-} thermodynamic stability has been questioned, with synthetic oligomeric S_n^{2-} analogues showing high conversion rates in equivalent media.

Although evidence for the formation of $S_n^{2-}{}_{(s)}$ on leached $CuFeS_{2(s)}$ surfaces is compelling,[66] evidence for it causing kinetic retardation is divided. In the absence of initial $Fe^{3+}{}_{(aq)}$ additive, both $S_n^{2-}{}_{(s)}$ and $S^0{}_{(s)}$ have been identified as significant $CuFeS_{2(s)}$ surface components for $HClO_4$/H_2SO_4/$HCl_{(aq)}$ leaches, without observation of kinetic retardation effects.[21] Interestingly, with addition of $Fe^{3+}{}_{(aq)}$ and controlled E_h (750 *mV* vs. SHE), significant surface $S_n^{2-}{}_{(s)}$ was observed on unreactive $CuFeS_{2(s)}$, at the previously discussed active/passive E_h potential boundary (figure 1.8).[162] In *p*H 1 $HCl_{(aq)}$, it was found that S_n^{2-} consisting mainly of S_2^{2-} was promoted by $FeS_{2(s)}$ presence, with $Cu_2S_{(s)}$ retained at the bulk surface with no observable reduction in leaching activity - although any retardation may have been obscured by galvanic

enhancements (section 1.6.9) which do not appear to have been considered.[45, 220] In a very recently published paper by Zhao *et al*.,[225] $FeS_{2(s)}$ was found to promote the removal of S_n^{2-} from $CuFeS_{2(s)}$ leached in $H_2SO_{4(aq)}$, via the indirect effect of controlling E_h. In addition, S_n^{2-} was reported to be responsible for kinetic limitations at low E_h, which were alleviated when E_h was increased in the presence of $FeS_{2(s)}$. Overall, $S_n^{2-}{}_{(s)}$ is considered a weak candidate for kinetic hindrance of $CuFeS_{2(s)}$ dissolution due to a current lack of evidence, however as will be discussed in section 1.8.5, it may combine with other effects.

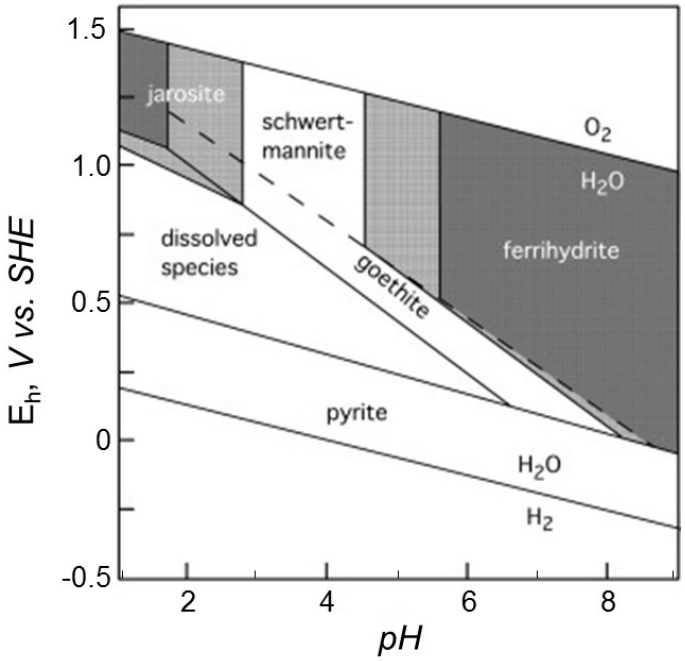
1.8.5 Jarosites

Jarosites are a group of low solubility ferric complexes, *e.g.* $Fe(III)_3(SO_4)_2(OH)_6^{2-}$, normally found with two monovalent metal cations (i.e. K_2, Na_2, Li_2). Jarosite precipitations are typically sudden and impact strongly on $CuFeS_{2(s)}$ dissolution via insulation of active $CuFeS_{2(s)}$ surfaces, preventing diffusional transport mechanisms. High $[SO_4^{2-}]_{(aq)}$ and $[M^+]_{(aq)}$ (where M = K^+, Na^+, H_3O^+, NH_4^+) are conditions that favour jarosite formation from $Fe^{3+}{}_{(aq)}$ hydrolysis,[71] as per E1.42. Since jarosites are found to coat $CuFeS_{2(s)}$ particles it has been suggested that surface bound $Fe_2(SO_4)_{3(s)}$ provides precipitation nucleation sites.

$$3Fe^{3+} + 2SO_4^{2-} + 6H_2O + 2M^+ \rightarrow M_2Fe_3(SO_4)_2(OH)_{6\,(s)} + 6H^+ \qquad \text{E1.42}$$

Jarosite precipitations are mostly problematic for ore hydrometallurgies and cooperative bioleaching strategies, where impurity levels and/or necessary nutrient rich mediums favour jarositic complexation of excess $Fe^{3+}{}_{(aq)}$. Some researchers consider jarosite formation to be inevitable when $[Fe^{3+}]_{(aq)}$ is high (i.e. long leach durations) unless controlling measures are introduced, however their formation is stifled <60 °*C* and either side of an optimum in $[H^+]_{(aq)}$ which promotes formation (*p*H~2). [82, 121] Nonetheless, in hydrometallurgic processes such as SX-EW (figure 1.6) iron reduction strategies may be necessary to control risk of jarosite formation. Sandström *et al*.[193] and Zhu *et al*.[226] highlighted that $S^0{}_{(s)}$ formed in abundance in low controlled E_h conditions (620 *mV* vs. SHE), whereas large jarosite deposits formed in high controlled E_h conditions (800 *mV*) – yet only jarosite formation was linked to dissolution plateaus. Recent studies by Yu et al.[227] also found that under E_h control (<650 *mV* vs. SHE) jarosite precipitation effects were negligible.

As the Pourbaix diagram for Fe-S-K-O-H at 25 °*C* shows (figure 1.16), jarosites are a thermodynamically prevalent species under typical leach conditions – however, at high acidities (*p*H<2) they only dominate compositions at high E_h (>1 *V* vs. SHE). The conclusive results above indicate that significant jarosite precipitations can occur far below this threshold E_h (~800 *mV* vs. SHE) and are inevitable if E_h is uncontrolled. However, jarositic effects may be rendered negligible through E_h control (~650 *mV* vs. SHE) as per section 1.6.8.



▲ Figure 1.16 - Pourbaix diagram (E_h-pH) showing thermodynamically prevalent species for the Fe-S-K-O-H system at 25 *°C* (298 *K*). E_h values have been converted to *mV* vs. SHE.[43, 228]

1.9 Outlook: Chemical Leaching

Presently, high-consumption, energy intensive pyrometallurgy remains the dominant extraction process for $CuFeS_{2(s)}$, largely due to slow ambient dissolution kinetics.[229] Efforts to decrease reliance on traditional, high-consumption pyrometallurgy from flotation concentrates (~30% Cu) have focused on enhancing hydrometallurgic beneficiation of sulfide ores.[83] SX-EW is steadily gaining ground as a hydrometallurgic alternative, however a breakthrough lixiviant system with an extraction power able to rival the recoveries available from pyrometallurgy has yet to be discovered.

Acidic-$SO_4^{2-}{}_{(aq)}$ dissolution has been widely reported and reviewed.[230] Enhancements have proven accessible using high temperatures,[70, 231-233] *in-situ* oxidants ($O_{2(aq)}$, $Fe^{3+}{}_{(aq)}$),[89] oxidant-assisting additives (Ag(I), Fe(III), FeS_2, Cl^-),[149, 157, 163, 234] ultra-fine grinding, $O_{2(g)}$ pressure-leaching[136, 202, 235, 236] and bioleaching.[106, 237] These enhancements pose limited benefit to the acceleration of ambient dissolution, which is required to further advance hydrometallurgic strategies and touted as the main barrier to further industrial applicability. Lixiviant systems must be sought in which high dissolution rates are sustained for moderate-grind $CuFeS_{2(s)}$, under low consumption (energy, $[H^+]$, [ox]), low toxicity, ambient (open air, <70 *°C*; 1 *atm*) conditions, which may also exploit cooperative bioleaching mechanisms.

Direct chemical leaching $CuFeS_{2(s)}$ strategies are currently restricted by a lack of knowledge of the fundamental $CuFeS_{2(s)}$ leaching mechanisms and an inability to avoid the poorly understood kinetic hindrances that plague dissolution rates. Overall, there is no universal agreement on the

composition of leached $CuFeS_{2(s)}$ outerlayers,[121] with the wide ranging conditions employed in studies clouding attempts to consolidate current knowledge. Capturing evidence for the passivation of $CuFeS_{2(s)}$ is fraught with additional issues, including *ex-situ* sampling, and retaining surface structure in ultra-high vacuum conditions – but probably most significantly in the human interpretation of spectral data. Independent studies are extremely difficult to compare due to insufficient control and recording of leach conditions. In a key recent review, Klauber critiqued a large number of studies with a focus on hindered $SO_4^{2-}{}_{(aq)}$ leaching of $CuFeS_{2(s)}$, during which a worrying account of misquoted (or misrepresented) findings was provided, resulting in poor spectral assignment.[121] Therefore, there is no consistent evidence across the investigations for a single hindering phase.[121, 209]

What is also clear, is that E_h control is a vital consideration from the perspective of promoting leaching via control of potentially competitive oxidation/reduction mechanistic steps and prevalent surface and solution speciation. In order to conclusively address responsibility for hindered dissolution, studies must focus future acidic-$SO_4^{2-}{}_{(aq)}$ investigation on characterising S-layers using optimum 'Goldilocks' E_h conditions, such that predominant speciation is controlled, focusing on understanding morphology, density and porosity alongside the wider probing of surface speciation.[42] Study of Fe^{2+}: Fe^{3+} ratios will be a repeated theme in this thesis, since it is crucial to the determination of E_h and thereby (indirectly) controlling wider solution/surface speciation.

Advances, such as the use of mixed $Cl^-/SO_4^{2-}{}_{(aq)}$ systems are a promising recent strategy to combat dissolution plateaus, proving successful in controlling/altering leached $CuFeS_{2(s)}$ outer layer structure and morphology. Strategies in conventional acidic-$SO_4^{2-}{}_{(aq)}$ aimed at controlling speciation at leached $CuFeS_{2(s)}$ interfaces are gaining ground slowly. However, some alternative lixiviants based on ionic liquids have recently generated promising enhancements over conventional acid-$SO_4^{2-}{}_{(aq)}$, as will be introduced in chapter 2.

1.10 Thesis Structure

1.10.1 Aims and Objectives Statement

As described, there are still many uncertainties that cloud the advancement of $CuFeS_{2(s)}$ dissolution. Throughout this introduction, it is seen that many of the phenomena curtailing the advancement of direct chemical leaching are specific to a particular system choice. For example, as has been discussed, $SO_4^{2-}{}_{(aq)}$ leaching media causes reduced $CuFeS_{2(s)}$ dissolution rates in comparison to $Cl^-{}_{(aq)}$ media, on account of specific Cl^- surface adsorptions.

Ionic liquids (ILs) are an interesting and highly diverse class of chemical, which are rapidly acquiring novel applications across the natural science and engineering fields, including several within the remit of selective metal chelation, separation and extraction technologies (section 2.2). In light of some promising initial studies regarding the lixiviant activity of acidic ILs towards

$CuFeS_{2(s)}$ flotation concentrates (section 2.2.3), the aims and objectives of this study are stated below.

The primary aim of this study is to assess whether $IL_{(aq)}$ lixiviant systems are able to provide enhancements compared to conventional $SO_4^{2-}{}_{(aq)}$ lixiviants in the dissolution of $CuFeS_{2(s)}$ ore under ambient conditions. However, as will be introduced in chapter 2, small and subtle changes to IL structure can result in large variations in physical description or chemical response of the medium. Due to the structural diversity of the IL class, a combinatorial approach to sample a maximum number of IL variants is key to the process of fairly assessing the intrinsic lixiviant activity of $IL_{(aq)}$ systems toward $CuFeS_{2(s)}$ under equivalent, ambient conditions. Screening of a significant number of potentially effective $IL_{(aq)}$ systems in equivalent conditions is a daunting task, due to the sheer size of the chemical space occupied by acidic IL variations. For this reason, high throughput screening automation is seen as an effective option, resulting in the objective of constructing a customised, flexible and programmable automated workstation, capable of screening previously untested HSO_4-$IL_{(aq)}$ systems.

$IL_{(aq)}$ lixiviant behaviour is to be assessed with reference to the ambient $CuFeS_{2(s)}$ dissolution activity of additive free equi-acidic $H_2SO_{4(aq)}$, in order to assess whether $IL_{(aq)}$ media provide any specific enhancements over conventional acid-$SO_4^{2-}{}_{(aq)}$ at nominal *p*H. In view of the aforementioned aims, a series of techniques capable of accurately assessing the extent of $CuFeS_{2(s)}$ dissolution across all studied media are investigated, validated and be integrated with the aforementioned combinatorial approach to identifying promising $IL_{(aq)}$ systems. Best performing $IL_{(aq)}$ systems are to be up-scaled and (again) compared to equivalent $H_2SO_{4(aq)}$ media with a focus on monitoring key leaching process parameters ($[H^+]_{(aq)}$, T, E_h, $[Cu]_{(aq)}$, $[Fe]_{(aq)}$). Regular solution speciation probing studies are then to be combined, where possible, with $CuFeS_{2(s)}$ surface sensitive techniques, with the aim of correlating the evolution of each and to identify and further investigate any medium-specific variations found.

Should $IL_{(aq)}$ specific enhancements be found the underlying reasons should be investigated, using analysis of recorded process data to fuel kinetic and mechanistic studies and to provide insight regarding $IL_{(aq)}$-based $CuFeS_{2(s)}$ dissolution. The proposal of a mechanism for $IL_{(aq)}$-based $CuFeS_{2(s)}$ dissolution is to be targeted specifically. To supplement this process, a series of low-volume leaching experiments will be designed on an *ad-hoc* basis, with a view to confirming/rejecting the applicability of previously reported acidic-$SO_4^{2-}{}_{(aq)}$ leaching phenomena to $IL_{(aq)}$-based $CuFeS_{2(s)}$ dissolution.

1.10.2 Summary of Key Aims

Below is a summary of the primary aims of this study; the basis of which is to assess the efficacy of $IL_{(aq)}$ lixiviant systems towards $CuFeS_{2(s)}$ hydrometallurgy and to clarify whether $IL_{(aq)}$ systems are capable of enhancements with respect to conventional acid-$SO_4^{2-}{}_{(aq)}$. Therefore, in order to

elucidate whether the promise of $IL_{(aq)}$ lixiviant activity towards future $CuFeS_{2(s)}$ hydrometallurgy is justified, the aims of this study are summarised as follows:

- Build and validate an automated screening platform capable of high throughput analysis of varied $IL_{(aq)}$-$CuFeS_{2(s)}$ systems.

- Develop anodic stripping voltammetry (ASV) as a tool for *in situ* Cu quantification applicable to $CuFeS_{2(s)}$ dissolution in aqueous/IL environments.

- Identify $IL_{(aq)}$ lead systems showing promising $CuFeS_{2(s)}$ dissolution activity and compare these observed metal recoveries with $H_2SO_{4(aq)}$ reference solutions.

- Determine whether $IL_{(aq)}$-based leaching operates with differing leach mechanisms and kinetics in comparison to $H_2SO_{4(aq)}$ reference solutions.

- Examine $IL_{(aq)}$ leaching in up-scaled conditions, monitoring key process parameters (*p*H, T, E_h).

- Examine $CuFeS_{2(s)}$ residues leached in $IL_{(aq)}$ and $H_2SO_{4(aq)}$ media using surface-sensitive SEM/EDX and ToF-SIMS in order to identify surface compositions and prevalent species.

1.10.3 Thesis Outline

Chapter 2 begins by introducing ionic liquids (ILs) with particular focus on the typical properties of acidic ionic liquids (AIL), their wide-ranging applications and previous studies aimed at determining $IL_{(aq)}$ lixiviant activity of $[C_4C_1im][HSO_4]_{(aq)}$ in comparison with existing $H_2SO_{4(aq)}$ solutions. The materials, IL and $CuFeS_2$ characterisations, leaching procedures and instrument detection principles are introduced including standardised protocols, for reference throughout the remainder of the work.

Chapter 3 presents the development of a flexible robotic screening platform used throughout this study in the high throughput screening and study of $IL_{(aq)}$ leaching. End-to-end instrument design is detailed, including custom designed electronic coding structure, testing and validation experiments. Additionally, programmatic methods used in later chapters for data-logging operations and batch analysis are documented.

Chapter 4 seeks to establish the validity of electrochemical monitoring of $CuFeS_{2(s)}$ dissolution in $IL/H_2SO_{4(aq)}$ via anodic stripping voltammetry (ASV). The speciation of $Cu^{n+}{}_{(aq)}$ leached from $CuFeS_{2(s)}$ in $IL_{(aq)}$ media is investigated using EXAFS spectroscopy in order to determine the thermodynamic product of dissolution. The rheology of selected ILs is investigated with a view to

uncovering ASV confidence limits and specifically investigating $Cu^{2+}_{(aq)}$ mass transport dynamics in $IL_{(aq)}$ using electrochemical theory in the Cottrell limit. A novel electrochemical method for the continuous monitoring of $CuFeS_{2(s)}$ leaching is introduced, with resulting extraction profiles for $CuFeS_{2(s)}$ dissolution in various $IL_{(aq)}$ and $H_2SO_{4(aq)}$ references compared and contrasted.

Chapter 5 discusses studies of the best performing $IL_{(aq)}$ systems in up-scaled leach reactions (400 *mL*) over ~1 *month* leach durations, where key system variables *p*H, temperature, E_h and ICP-AES metal contents are recorded. This experimental physical data is then combined with data obtained from the application of surface sensitive techniques to the unleached/leached $CuFeS_{2(s)}$ residues. Synchronised surface and solution speciation data are combined and analysed as parallel 'snapshots' of the progression of ambient leaching in $IL_{(aq)}$ and $H_2SO_{4(aq)}$, enabling kinetic and mechanistic comparisons to be formulated.

Chapter 6 focuses on the application of the robotic screening platform (described in chapter 3) in order to rapidly and systematically screen untested $IL_{(aq)}$ systems. *Ad-hoc* experiments are presented to examine the effect of factors such as $[IL]_{(aq)}$ influence, gaseous headspace composition, pulp density and base addition. The remainder of the chapter consolidates all key results in order to propose a mechanism for ambient $IL_{(aq)}$ $CuFeS_{2(s)}$ leaching.

Chapter 7 provides a final evaluation of the work, outlining the key conclusions derived from the study as a whole. Suggestions are given for future research directions and the implications of the work are discussed, in the context of industrial Cu hydrometallurgy.

1.11 References

1. E. G. West, *Copper and its Alloys*, Wiley, 1982.
2. M. Radivojević, T. Rehren, E. Pernicka, D. Šljivar, M. Brauns and D. Borić, *Journal of Archaeological Science*, 2010, **37**, 2775-2787.
3. *The World Copper Factbook*, International Copper Study Group (ICSG), 2015.
4. *Copper Development Association; International Copper Alliance (ICA)*, New York, USA 2012.
5. *Australian Bureau of Agricultural and Resource Economics (ABARE)*, Canberra, Australia, 2012.
6. *The World Copper Factbook*, International Copper Study Group (ICSG), 2012.
7. M. E. Schlesinger, M. J. King, K. C. Sole and W. G. Davenport, *Extractive Metallurgy of Copper*, Elsevier, Oxford, 5th edn., 2011.
8. C. H. Samans, MacMillan, 1949.
9. R. V. Dietrich and B. J. Skinner, *Rocks and Rock Minerals*, Wiley, 1979.
10. B. R. Berger, R. A. Ayuso, J. C. Wynn and R. R. Seal, *Preliminary Model of Porphyry Copper Deposits*, United States Geological Survey, 2008.
11. F. Habashi, *Chalcopyrite. It's Chemistry and Metallurgy*, McGraw-Hill, 1978.
12. J. E. Dutrizac, R. J. C. McDonald and T. R. Ingraham, *Transactions of the Society for Mining, Metallurgy, and Exploration*, 1969, **245**, 955.
13. W. M. B. Roberts, *Economic Geology*, 1963, **58**, 52-61.
14. D. B. Roberts and D. J. Williams, *Materials Research Bulletin*, 1975, **10**, 163-167.
15. J. E. Dutrizac and R. J. C. MacDonald, *Materials Research Bulletin*, 1973, **8**, 961-971.
16. W. M. Barnard and P. A. Christopher, *Economic Geology*, 1966, **61**, 897-902.
17. K.-t. Chen, C.-J. Chiang and D. Ray, *Materials Letters*, 2013, **98**, 270-272.
18. H. Ohno, D. Chiba, F. Matsukura, T. Omiya, E. Abe, T. Dietl, Y. Ohno and K. Ohtani, *Nature*, 2000, **408**, 944.
19. D. D. Awschalom and R. K. Kawakami, *Nature*, 2000, **408**, 923.
20. C. L. Burdick and J. H. Ellis, *Journal of the American Chemical Society*, 1917, **39**, 2518-2525.
21. Y. Li, N. Kawashima, J. Li, A. P. Chandra and A. R. Gerson, *Advances in Colloid and Interface Science*, 2013, **197–198**, 1-32.
22. S. R. Hall and J. M. Stewart, *Acta Crystallographica Section B*, 1973, **29**, 579-585.
23. J. Petiau, P. Sainctavit and G. Calas, *Materials Science and Engineering: B*, 1988, **1**, 237-249.
24. R. Edelbro, Å. Sandström and J. Paul, *Applied Surface Science*, 2003, **206**, 300-313.
25. R. T. Jones, PhD, University of South Australia, 2006.

26. J. C. Woolley, A. M. Lamarche, G. Lamarche, M. Quintero, I. P. Swainson and T. M. Holden, *Journal of Magnetism and Magnetic Materials*, 1996, **162**, 347-354.

27. C. de Oliveira and H. A. Duarte, *Applied Surface Science*, 2010, **257**, 1319-1324.

28. G. U. Von Oertzen, S. L. Harmer and W. M. Skinner, *Molecular Simulation*, 2006, **32**, 1207-1212.

29. D. Raj, K. Chandra and S. P. Puri, *Journal of the Physical Society of Japan*, 1968, **24**, 39-41.

30. J. Llanos, A. Buljan, C. Mujica and R. Ramírez, *Materials Research Bulletin*, 1995, **30**, 43-48.

31. Q. Yin, G. H. Kelsall, D. J. Vaughan and K. E. R. England, *Geochimica et Cosmochimica Acta*, 1995, **59**, 1091-1100.

32. G. Donnay, L. M. Corliss, J. D. H. Donnay, N. Elliott and J. M. Hastings, *Physical Review*, 1958, **112**, 1917-1923.

33. P. Sainctavit, J. Petiau, A. M. Flank, J. Ringeissen and S. Lewonczuk, *Physica B: Condensed Matter*, 1989, **158**, 623-624.

34. Y. Mikhlin, Y. Tomashevich, V. Tauson, D. Vyalikh, S. Molodtsov and R. Szargan, *Journal of Electron Spectroscopy and Related Phenomena*, 2005, **142**, 83-88.

35. E. C. Todd, D. M. Sherman and J. A. Purton, *Geochimica et Cosmochimica Acta*, 2003, **67**, 2137-2146.

36. F. K. Crundwell, *Hydrometallurgy*, 1988, **21**, 155-190.

37. M. Fujisawa, S. Suga, T. Mizokawa, A. Fujimori and K. Sato, *Physical Review B*, 1994, **49**, 7155-7164.

38. K. Karlsson, O. Gunnarsson and O. Jepsen, *Journal of Physics: Condensed Matter*, 1992, **4**, 2801.

39. C. I. Pearce, R. A. D. Pattrick, D. J. Vaughan, C. M. B. Henderson and G. van der Laan, *Geochimica et Cosmochimica Acta*, 2006, **70**, 4635-4642.

40. G. van der Laan, R. A. D. Pattrick, C. M. B. Henderson and D. J. Vaughan, *Journal of Physics and Chemistry of Solids*, 1992, **53**, 1185-1190.

41. K. Hemachandran, A. R. Chetal and G. Joshi, *physica status solidi (b)*, 1987, **141**, 441-445.

42. S. L. Harmer, Doctor of Philosophy, University of South Australia, 2002.

43. A. N. Buckley and R. Woods, *Australian Journal of Chemistry*, 1984, **37**, 2403-2413.

44. R. S. C. Smart, *Minerals Engineering*, 1991, **4**, 891-909.

45. R. G. Acres, S. L. Harmer and D. A. Beattie, *Minerals Engineering*, 2010, **23**, 928-936.

46. Y. L. Mikhlin, Y. V. Tomashevich, I. P. Asanov, A. V. Okotrub, V. A. Varnek and D. V. Vyalikh, *Applied Surface Science*, 2004, **225**, 395-409.

47. S. L. Harmer, A. R. Pratt, H. W. Nesbitt and M. E. Fleet, *American Mineralogist*, 2004, **89**, 1026–1032.

48. L. M. Liborio, C. L. Bailey, G. Mallia, S. Tomić and N. M. Harrison, *Journal of Applied Physics*, 2011, **109**, 023519.

49. A. O. Adebayo, K. O. Ipinmoroti and O. O. Ajayi, *Chemical and Biochemical Engineering Quarterly*, 2003, **17**, 213-218.

50. J. Schneider, A. Räuber and G. Brandt, *Journal of Physics and Chemistry of Solids*, 1973, **34**, 443-450.

51. K. G. Nikiforov, *Progress in Crystal Growth and Characterization of Materials*, 1999, **39**, 1-104.

52. H. Tributsch and J. C. Bennett, *Journal of Chemical Technology and Biotechnology*, 1981, **31**, 565-577.

53. F. K. Crundwell, *Hydrometallurgy*, 2003, **71**, 75-81.

54. T. Teranishi and K. Sato, *J. Phys. Colloques*, 1975, **36**, 149.

55. R. A. Serway, *Physics For Scientists & Engineers with Modern Physics*, Saunders College Publishing, 1990.

56. P. Aktins and J. de Paula, *Atkins' Physical Chemistry*, Oxford University Press, 8th edn., 2006.

57. T. Teranishi, K. Sato and K. i. Kondo, *Journal of the Physical Society of Japan*, 1974, **36**, 1618-1624.

58. H. Ohnishi and T. Teranishi, *Journal of the Physical Society of Japan*, 1961, **16**, 35-43.

59. W. Sand, T. Gehrke, P.-G. Jozsa and A. Schippers, *Hydrometallurgy*, 2001, **59**, 159-175.

60. T. Hamajima, T. Kambara, K. I. Gondaira and T. Oguchi, *Physical Review B*, 1981, **24**, 3349-3353.

61. T. Oguchi, K. Sato and T. Teranishi, *Journal of the Physical Society of Japan*, 1980, **48**, 123-128.

62. P. H. Ribbe and S. D. Scott, *Min. Soc. Am. Rev. Min.*, 1974, **1**, S1.

63. C. de Oliveira, G. F. de Lima, H. A. de Abreu and H. A. Duarte, *The Journal of Physical Chemistry C*, 2012, **116**, 6357-6366.

64. S. L. Harmer, J. E. Thomas, D. Fornasiero and A. R. Gerson, *Geochimica et Cosmochimica Acta*, 2006, **70**, 4392-4402.

65. C. Klauber, *Surface and Interface Analysis*, 2003, **35**, 415-428.

66. M. Al-Harahsheh, S. Kingman, F. Rutten and D. Briggs, *International Journal of Mineral Processing*, 2006, **80**, 205-214.

67. D. Brion, *Applications of Surface Science*, 1980, **5**, 133-152.

68. S. W. Goh, A. N. Buckley, R. N. Lamb, R. A. Rosenberg and D. Moran, *Geochimica et Cosmochimica Acta*, 2006, **70**, 2210-2228.

69. R. G. Acres, S. L. Harmer, H. W. Shui, C.-H. Chen and D. A. Beattie, *Journal of Synchrotron Radiation*, 2011, **18**, 649-657.

70. R. P. Hackl, D. B. Dreisinger, E. Peters and J. A. King, *Hydrometallurgy*, 1995, **39**, 25-48.

71. E. M. Córdoba, J. A. Muñoz, M. L. Blázquez, F. González and A. Ballester, *Minerals Engineering*, 2009, **22**, 229-235.

72. N. Hiroyoshi, S. Kuroiwa, H. Miki, M. Tsunekawa and T. Hirajima, *Hydrometallurgy*, 2004, **74**, 103-116.

73. P. Eadington, *Trans. Inst. Min. Metall.*

, 1968, C186.

74. T. Biegler and M. D. Horne, *Journal of The Electrochemical Society*, 1985, **132**, 1363-1369.

75. F. P. Haver and M. M. Wong, *JOM*, 2015, **23**, 25-29.

76. Y. Peng and S. Grano, *Electrochimica Acta*, 2010, **55**, 5470-5477.

77. Y. Peng, S. Grano, D. Fornasiero and J. Ralston, *International Journal of Mineral Processing*, 2003, **69**, 87-100.

78. X. M. Yuan, B. I. Pålsson and K. S. E. Forssberg, *International Journal of Mineral Processing*, 1996, **46**, 181-204.

79. W. J. Bruckard, G. J. Sparrow and J. T. Woodcock, *International Journal of Mineral Processing*, 2011, **100**, 1-13.

80. J. H. Ahn and J. E. Gebhardt, *International Journal of Mineral Processing*, 1991, **33**, 243-262.

81. H. R. Watling, *Hydrometallurgy*, 2013, 163.

82. N. Pradhan, K. C. Nathsarma, K. Srinivasa Rao, L. B. Sukla and B. K. Mishra, *Minerals Engineering*, 2008, **21**, 355-365.

83. S. Prasad and B. D. Pandey, *Minerals Engineering*, 1998, **11**, 763-781.

84. J. E. Dutrizac, *Metallurgical Transactions B-Process Metallurgy*, 1978, **9**, 431-439.

85. J. Liddicoat and D. Dreisinger, *Hydrometallurgy*, 2007, **89**, 323-331.

86. N. Hiroyoshi, M. Arai, H. Miki, M. Tsunekawa and T. Hirajima, *Hydrometallurgy*, 2002, **63**, 257-267.

87. D. L. Pool, D. C. Thompson and L. E. Schultze, 1989.

88. A. P. Mehta and L. E. Murr, *Biotechnology and Bioengineering*, 1982, **24**, 919-940.

89. L. Qing You, L. Heping and Z. Li, *Environmental Geology*, 2007, **52**, 11-18.

90. R. Cruz, R. M. Luna-Sánchez, G. T. Lapidus, I. González and M. Monroy, *Hydrometallurgy*, 2005, **78**, 198-208.

91. P. R. Holmes and F. K. Crundwell, *Hydrometallurgy*, 1995, **39**, 353-375.

92. A. P. Mehta and L. E. Murr, *Hydrometallurgy*, 1983, **9**, 235-256.

93. S. M. J. Koleini, V. Aghazadeh and A. Sandstrom, *Miner Eng*, 2011, **24**, 381-386.

94. B. E. Kimball, J. D. Rimstidt and S. L. Brantley, *Applied Geochemistry*, 2010, **25**, 972-983.

95. A. Ghahremaninezhad, E. Asselin and D. G. Dixon, *Electrochimica Acta*, 2010, **55**, 5041-5056.

96. A. J. Parker, R. L. Paul and G. P. Power, *Journal of Electroanalytical Chemistry and Interfacial Electrochemistry*, 1981, **118**, 305-316.

97. M. Nicol, H. Miki and L. Velásquez-Yévenes, *Hydrometallurgy*, 2010, **103**, 86-95.

98. N. Hiroyoshi, M. Hirota, T. Hirajima and M. Tsunekawa, *Hydrometallurgy*, 1997, **47**, 37-45.

99. N. Hiroyoshi, H. Miki, T. Hirajima and M. Tsunekawa, *Hydrometallurgy*, 2000, **57**, 31-38.

100. N. Hiroyoshi, H. Miki, T. Hirajima and M. Tsunekawa, *Hydrometallurgy*, 2001, **60**, 185-197.

101. A. J. Parker, R. L. Paul and G. P. Power, *Australian Journal of Chemistry*, 1981, **34**, 13-34.

102. A. E. Elsherief, *Minerals Engineering*, 2002, **15**, 215-223.

103. D. R. Nagaraj, S. Ilangovan, T. G. Prakash and K. I. Vasu, *J. Electrochem. Soc. Ind.* , 1978 11.

104. P. R. Kruesi, E. S. Allen and J. L. Lake, *Can. Min. Metall. Bull.*, 1973, 734.

105. M. Misra and M. C. Fuerstenau, *Journal*, 2004.

106. D. Dreisinger, *Hydrometallurgy*, 2006, **83**, 10-20.

107. Y. Rodríguez, A. Ballester, M. L. Blázquez, F. González and J. A. Muñoz, *Geomicrobiology Journal*, 2003, **20**, 131-141.

108. T. Rohwerder, T. Gehrke, K. Kinzler and W. Sand, *Applied Microbiology and Biotechnology*, 2003, **63**, 239-248.

109. H. R. Watling, *Hydrometallurgy*, 2006, **84**, 81-108.

110. J. Petersen and D. G. Dixon, *Hydrometallurgy*, 2006, **83**, 40-49.

111. S. C. Bouffard, *Hydrometallurgy*, 2008, **93**, 116-123.

112. V. Gautier, B. Escobar and T. Vargas, *Hydrometallurgy*, 2008, **94**, 121-126.

113. L.-m. Zhang, J.-h. Peng, M.-m. Wei, J.-n. Ding and H.-b. Zhou, *Transactions of Nonferrous Metals Society of China*, 2010, **20**, 1981-1986.

114. J. E. Dutrizac and R. J. C. McDonald, *Miner. Sci. Engng.,* , 1974, 59.

115. W. Zeng, G. Qiu, H. Zhou, X. Liu, M. Chen, W. Chao, C. Zhang and J. Peng, *Hydrometallurgy*, 2010, **100**, 177-180.

116. A. Ahmadi, M. Schaffie, J. Petersen, A. Schippers and M. Ranjbar, *Hydrometallurgy*, 2011, **106**, 84-92.

117. R. A. Bobadilla Fazzini, G. Levican and P. Parada, *Applied Microbiology and Biotechnology*, 2011, **89**, 771-780.

118. J. A. Brierley and C. L. Brierley, *Hydrometallurgy*, 2001, **59**, 233-239.

119. E. Gómez, M. L. Blázquez, A. Ballester and F. González, *Minerals Engineering*, 1996, **9**, 985-999.

120. G. J. Olson, J. A. Brierley and C. L. Brierley, *Applied Microbiology and Biotechnology*, 2003, **63**, 249-257.

121. C. Klauber, *International Journal of Mineral Processing*, 2008, **86**, 1-17.

122. E. C. Sanchez, Y. Umetsu and F. Saito, *JOURNAL OF CHEMICAL ENGINEERING OF JAPAN*, 1996, **29**, 714-716.

123. M. Lundström, J. Aromaa, O. Forsén, O. Hyvärinen and M. H. Barker, *Hydrometallurgy*, 2005, **77**, 89-95.

124. Z. Y. Lu, M. I. Jeffrey and F. Lawson, *Hydrometallurgy*, 2000, **56**, 189-202.

125. H. G. Linge, *Hydrometallurgy*, 1976, **2**, 51-64.

126. H. G. Linge, *Hydrometallurgy*, 1977, **2**, 219-233.

127. G. Bjorling, I. Faldt, E. Lindgren and I. Toromanov, 1976, 725-737.

128. I. G. Reilly and D. S. Scott, *Metallurgical Transactions B*, **15**, 726-729.

129. S. Venkatachalam, *Minerals Engineering*, 1991, **4**, 1115-1126.

130. R. Padilla, P. Pavez and M. C. Ruiz, *Hydrometallurgy*, 2008, **91**, 113-120.

131. G. Senanayake, *Hydrometallurgy*, 2009, **98**, 21-32.

132. D. Dreisinger and N. Abed, *Hydrometallurgy*, 2002, **66**, 37-57.

133. S. Prasad and B. D. Pandey, *Mineral Engineering* 1998, 763.

134. Z. Y. Lu, M. I. Jeffrey and F. Lawson, *Hydrometallurgy*, 2000, **56**, 145-155.

135. M. F. C. Carneiro and V. A. Leão, *Hydrometallurgy*, 2007, **87**, 73-82.

136. G. Nazari, D. G. Dixon and D. B. Dreisinger, *Hydrometallurgy*, 2011, **105**, 251-258.

137. E. M. Domic, in *Biomining*, eds. D. E. Rawlings and D. B. Johnson, Springer Berlin Heidelberg, Berlin, Heidelberg, 2007, DOI: 10.1007/978-3-540-34911-2_4, pp. 81-95.

138. T. J. Harvey and M. Bath, in *Biomining*, eds. D. E. Rawlings and D. B. Johnson, Springer Berlin Heidelberg, Berlin, Heidelberg, 2007, DOI: 10.1007/978-3-540-34911-2_5, pp. 97-112.

139. M. Gericke, J. W. Neale and P. W. van Staden, *J. South. Afr. Inst. Min. Metall.*, 2009, 567.

140. S. Wang, *Journal of the Minerals, Metals and Materials Society*, 2005, **57**, 48.

141. J. D. Batty and G. V. Rorke, *Hydrometallurgy*, 2006, **83**, 83-89.

142. K. Baxter, D. Dreisinger and G. Pratt, 2003.

143. D. G. Dixon, D. D. Mayne and K. G. Baxter, *Canadian Metallurgical Quarterly*, 2008, **47**, 327-336.

144. M. Hourn and D. Halbe, *The NENATECH Process: Results on Frieda River copper gold concentrates*, Randol Copper Hydrometallurgy Roundtable, 1999.

145. 1999.

146. F. Fleury, E. Delgado and N. Collao, Hamburg, Germany, 2010.

147. O. Herreros, R. Quiroz, H. Longueira, G. Fuentes and J. Viñals, *Hydrometallurgy*, 2006, **82**, 32-39.

148. P. B. Munoz, J. D. Miller and M. E. Wadsworth, *Metallurgical Transactions B*, 1979, **10**, 149-158.

149. S. Aydogan, G. Ucar and M. Canbazoglu, *Hydrometallurgy*, 2006, **81**, 45-51.

150. T. Dong, Y. Hua, Q. Zhang and D. Zhou, *Hydrometallurgy*, 2009, **99**, 33-38.

151. P. Acero, J. Cama and C. Ayora, *European Journal of Mineralogy*, 2007, **19**, 173-182.

152. D. İkiz, M. Gülfen and A. O. Aydın, *Minerals Engineering*, 2006, **19**, 972-974.

153. J. E. Dutrizac, *Metallurgical Transactions B*, 1981, **12**, 371-378.

154. N. N. Saxena and N. R. Mandre, *Hydrometallurgy*, 1992, **28**, 111-117.

155. M. D. Sokić, B. Marković and D. Živković, *Hydrometallurgy*, 2009, **95**, 273-279.

156. R. J. Orth and K. C. Liddell, *Industrial & Engineering Chemistry Research*, 1990, **29**, 1178-1183.

157. M. M. Antonijević, Z. D. Janković and M. D. Dimitrijević, *Hydrometallurgy*, 2004, **71**, 329-334.

158. M. M. Antonijević, Z. Janković and M. Dimitrijević, *Hydrometallurgy*, 1994, **35**, 187-201.

159. P. Rath, R. Paramguru and P. Jena, *Trans. Inst. Min. Metall. C*, 1988, **97**.

160. M. Al-Harahsheh, S. Kingman, N. Hankins, C. Somerfield, S. Bradshaw and W. Louw, *Minerals Engineering*, 2005, **18**, 1259-1268.

161. V. Mahajan, M. Misra, K. Zhong and M. C. Fuerstenau, *Minerals Engineering*, 2007, **20**, 670-674.

162. K. Kaplun, J. Li, N. Kawashima and A. R. Gerson, *Geochimica et Cosmochimica Acta*, 2011, **75**, 5865-5878.

163. M. M. Antonijević and G. D. Bogdanović, *Hydrometallurgy*, 2004, **73**, 245-256.

164. M. Al-Harahsheh, S. Kingman and A. Al-Harahsheh, *Hydrometallurgy*, 2008, **91**, 89-97.

165. H. Tributsch, *Hydrometallurgy*, 2001, **59**, 177-185.

166. B. L. Tiwari, J. Kolbe and H. W. Hayden, *Metallurgical Transactions B*, **11**, 89-93.

167. R. Y. Wan, J. D. Miller, J. Foley and S. Pons, *Proceedings of the International Symposium of Electrochemistry in Mineral and Metal Processing*, 1984, **84**, 391.

168. F. Barriga Mateos, I. Palencia Pérez and F. Carranza Mora, *Hydrometallurgy*, 1987, **19**, 159-167.

169. J. Li, N. Kawashima, K. Kaplun, V. J. Absolon and A. R. Gerson, *Geochimica et Cosmochimica Acta*, 2010, **74**, 2881-2893.

170. O. J. Solis-Marcíal and G. T. Lapidus, *Hydrometallurgy*, 2013, **131–132**, 120-126.

171. O. J. Solís-Marcíal and G. T. Lapidus, *Hydrometallurgy*, 2014, **147–148**, 54-58.

172. O. J. Solís-Marcial and G. T. Lapidus, *Electrochimica Acta*, 2014, **140**, 434-437.

173. C. Gómez, M. Figueroa, J. Muñoz, A. Ballester and M. L. Blázquez, *Minerals Engineering*, 1997, **10**, 111-116.

174. D. B. Johnson, N. Okibe, K. Wakeman and L. Yajie, *Hydrometallurgy*, 2008, **94**, 42-47.

175. H. Yuehua, Q. Guanzhou, W. Jun and W. Dianzuo, *Hydrometallurgy*, 2002, **64**, 81-88.

176. H. Sato, H. Nakazawa and Y. Kudo, *International Journal of Mineral Processing*, 2000, **59**, 17-24.

177. H. Nakazawa, H. Fujisawa and H. Sato, *International Journal of Mineral Processing*, 1998, **55**, 87-94.

178. C.-L. Liang, J.-L. Xia, X.-J. Zhao, Y. Yang, S.-Q. Gong, Z.-Y. Nie, C.-Y. Ma, L. Zheng, Y.-D. Zhao and G.-z. Qiu, *Hydrometallurgy*, 2010, **105**, 179-185.

179. G. Nazari, D. G. Dixon and D. B. Dreisinger, *Hydrometallurgy*, 2012, **113–114**, 177-184.

180. M. L. O'Malley and K. C. Liddell, *A rate equation for the initial stage of the leaching of $CuFeS_2$ by aqueous $FeCl_3$, HCl and NaCl;* , Metallurgical Society Inc., 1986.

181. L. V. Yévenes, H. Miki and M. Nicol, *Hydrometallurgy*, 2010, **103**, 80-85.

182. L. Velásquez-Yévenes, M. Nicol and H. Miki, *Hydrometallurgy*, 2010, **103**, 108-113.

183. M. J. Nicol and I. Lázaro, *Hydrometallurgy*, 2002, **63**, 15-22.

184. W. C. Cooper, D. B. Dreisinger, J. Li, T.-K. Zhong and M. E. Wadsworth, *Hydrometallurgy*, 1992, **29**, 47-60.

185. G. P. Power and I. M. Ritchie, *Journal of Chemical Education*, 1983, **60**, 1022.

186. G. P. Power and I. M. Ritchie, *Electrochimica Acta*, 1981, **26**, 1073-1078.

187. N. Hiroyoshi, S. Kuroiwa, H. Miki, M. Tsunekawa and T. Hirajima, *Hydrometallurgy*, 2007, **87**, 1-10.

188. N. Hiroyoshi, H. Kitagawa and M. Tsunekawa, *Hydrometallurgy*, 2008, **91**, 144-149.

189. J. Vilcáez and C. Inoue, *Minerals Engineering*, 2009, **22**, 951-960.

190. G. Viramontes-Gamboa, M. M. Peña-Gomar and D. G. Dixon, *Hydrometallurgy*, 2010, **105**, 140-147.

191. G. Viramontes-Gamboa, B. F. Rivera-Vasquez and D. G. Dixon, *Journal of The Electrochemical Society*, 2007, **154**, C299-C311.

192. G. Nazari and E. Asselin, *Hydrometallurgy*, 2009, **96**, 183-188.

193. Å. Sandström, A. Shchukarev and J. Paul, *Minerals Engineering*, 2005, **18**, 505-515.

194. P. Velásquez, H. Gómez, J. R. Ramos-Barrado and D. Leinen, *Colloids and Surfaces A: Physicochemical and Engineering Aspects*, 1998, **140**, 369-375.

195. H. Zhao, J. Wang, X. Gan, M. Hu, L. Tao, W. Qin and G. Qiu, *Hydrometallurgy*, 2016, **164**, 159–165.

196. A. Ahmadi, M. Schaffie, Z. Manafi and M. Ranjbar, *Hydrometallurgy*, 2010, **104**, 99-105.

197. T. V. Subrahmanyam and K. S. E. Forssberg, *Minerals Engineering*, 1993, **6**, 439-454.

198. Z. Ekmekçi and H. Demirel, *International Journal of Mineral Processing*, 1997, **52**, 31-48.

199. Q. Liu, H. Li and L. Zhou, *Applied Geochemistry*, 2008, **23**, 2316-2323.

200. D. Majuste, V. S. T. Ciminelli, K. Osseo-Asare and M. S. S. Dantas, *Hydrometallurgy*, 2012, **113–114**, 167-176.

201. P. K. Abraitis, R. A. D. Pattrick, G. H. Kelsall and D. J. Vaughan, *Mineralogical Magazine*, 2004, **68**, 343-351.

202. G. Nazari, D. G. Dixon and D. B. Dreisinger, *Hydrometallurgy*, 2012, **111–112**, 35-45.

203. B. Beverskog and I. Puigdomenech, *Journal of The Electrochemical Society*, 1997, **144**, 3476-3483.

204. B. Beverskog and I. Puigdomenech, *Corrosion Science*, 1996, **38**, 2121-2135.

205. D. L. Parkhurst, *User's Guide to Phreeqc a Computer Program for Speciation, Reaction-Path, Advective-Transport, And Inverse Geochemical Calculations*, U.S. Geological Survey Lakewood, Colorado, 1995.

206. A. Grizo, N. Pacović, F. Poposka and Ž. Koneska, *Hydrometallurgy*, 1982, **8**, 5-16.

207. R. C. H. Ferreira and A. R. Burkin, *Acid leaching of chalcopyrite, Leaching and Reduction in Hydrometallurgy*, IMM, London, 1975.

208. D. Maurice and J. A. Hawk, *Hydrometallurgy*, 1998, **49**, 103-123.

209. C. Klauber, A. Parker, W. van Bronswijk and H. Watling, *International Journal of Mineral Processing*, 2001, **62**, 65-94.

210. R. S. C. Smart, W. M. Skinner and A. R. Gerson, *Surface and Interface Analysis*, 1999, **28**, 101-105.

211. R. S. C. Smart, M. Jasieniak, K. E. Prince and W. M. Skinner, *Minerals Engineering*, 2000, **13**, 857-870.

212. D. L. Jones and E. Peters, *Extractive Metallurgy of Copper*, New York, 1976.

213. T. Biegler and D. A. Swift, *Journal of Applied Electrochemistry*, **6**, 229-235.

214. J. E. Dutrizac, *Canadian Metallurgical Quarterly*, 1989, **28**, 337-344.

215. J. J. McCarron, G. W. Walker and A. N. Buckley, *International Journal of Mineral Processing*, 1990, **30**, 1-16.

216. T. Hirato, H. Majima and Y. Awakura, *Metallurgical Transactions B*, 1987, **18**, 489-496.

217. C. Weisener, Ph.D., University of South Australia, 2001.

218. T. Havlík and R. Kammel, *Minerals Engineering*, 1995, **8**, 1125-1134.

219. R. I. Holliday and W. R. Richmond, *Journal of Electroanalytical Chemistry and Interfacial Electrochemistry*, 1990, **288**, 83-98.

220. A. Parker, C. Klauber, A. Kougianos, H. R. Watling and W. van Bronswijk, *Hydrometallurgy*, 2003, **71**, 265-276.

221. R. M. Garrels and C. L. Christ, *Solution, Minerals and Equilibria*, Harper & Row, New York, 1965.

222. E. M. Córdoba, J. A. Muñoz, M. L. Blázquez, F. González and A. Ballester, *Hydrometallurgy*, 2008, **93**, 81-87.

223. S. C. Termes, A. N. Buckley and R. D. Gillard, *Inorganica Chimica Acta*, 1987, **126**, 79-82.

224. G. K. Parker, R. Woods and G. A. Hope, *Colloids and Surfaces A: Physicochemical and Engineering Aspects*, 2008, **318**, 160-168.

225. H. Zhao, J. Wang, X. Gan, M. Hu, L. Tao, W. Qin and G. Qiu, *Hydrometallurgy*, 2016, **164**, 159-165.

226. W. Zhu, J.-l. Xia, Y. Yang, Z.-y. Nie, L. Zheng, C.-y. Ma, R.-y. Zhang, A.-a. Peng, L. Tang and G.-z. Qiu, *Bioresource Technology*, 2011, **102**, 3877-3882.

227. R.-l. Yu, D.-l. Zhong, L. Miao, F.-d. Wu, G.-z. Qiu and G.-h. Gu, *Transactions of Nonferrous Metals Society of China*, 2011, **21**, 1634-1640.

228. J. M. Bigham, U. Schwertmann, S. J. Traina, R. L. Winland and M. Wolf, *Geochimica et Cosmochimica Acta*, 1996, **60**, 2111-2121.

229. D. Godfrey, J. H. Bannock, O. Kuzmina, T. Welton and T. Albrecht, *Green Chemistry*, 2016, **18**, 1930-1937.

230. S. Wang, *JOM Journal of the Minerals, Metals and Materials Society*, 2005, **57**, 48-51.

231. P. Yu, C. Hansen and M. Wadsworth, *MT*, 1973, **4**, 2137-2144.

232. F. Habashi and T. Toor, *Metallurgical and Materials Transactions B*, 1979, **10**, 49-56.

233. T.-s. Qiu, G.-h. Nie, J.-f. Wang and L.-f. Cui, *Transactions of Nonferrous Metals Society of China*, 2007, **17**, 418-422.

234. B. Palmer, C. Nebo, M. Rau and M. Fuerstenau, *Metallurgical and Materials Transactions B*, 1981, **12**, 595-601.

235. R. G. McDonald and D. M. Muir, *Hydrometallurgy*, 2007, **86**, 191-205.

236. G. Nazari, D. G. Dixon and D. B. Dreisinger, *Hydrometallurgy*, 2012, **113–114**, 122-130.

237. F. Carranza, N. Iglesias, A. Mazuelos, I. Palencia and R. Romero, *Hydrometallurgy*, 2004, **71**, 413-420.

Chapter 2

Ionic Liquids, Materials & Methods

Contents

2.1 Introduction - Ionic Liquids 2-3

2.1.1 Ionic Liquid Characterisation 2-3

2.1.2 General Properties of Ionic Liquids 2-4

2.1.3 Applications of Ionic Liquids 2-4

2.2 Ionic Liquids in Metallurgy 2-5

2.2.1 Chemical Classification 2-5

2.2.2 General Metallurgy Applications 2-7

2.2.3 IL Application to $CuFeS_{2(s)}$ 2-8

2.2.4 Applications of ILs in Electrochemistry 2-12

2.2.5 Outlook: Ionic Liquids for $CuFeS_{2(s)}$ Hydrometallurgy 2-14

2.3 Ionic Liquid Materials, Synthesis and Properties 2-16

2.3.1 Selection of Lixiviant Ionic Liquids 2-16

2.3.2 Synthesis / Source of Ionic Liquids 2-17

2.3.3 Kamlet-Taft Characterisation 2-18

2.3.4 Water Uptake 2-19

2.3.5 IL Acidity 2-20

2.3.6 IL Rheology 2-24

2.4 Advanced Consideration of $IL_{(aq)}$ *p*H 2-25

2.4.1 Born Solvation Energy Theory 2-26

2.5 $CuFeS_{2(s)}$ Processing 2-28

2.5.1 $CuFeS_{2(s)}$ Mineralogical Analysis 2-28
2.6 Electrochemistry 2-30
2.6.1 Potentiostatic Electrochemistry 2-30
2.6.2 Characterisation of the Cu/Cu^{2+} Redox Couple 2-33
2.6.3 Electrochemical Impedance Spectroscopy (EIS) 2-34
2.6.4 Analogue Probes 2-34
2.7 Copper Quantification Techniques 2-35
2.7.1 Cupric Ion Selective Electrode (ISE) 2-35
2.7.2 Inductively-Coupled Plasma Atomic Emission Spectroscopy (ICP-AES) 2-36
2.7.3 Anodic Stripping Voltammetry 2-39
2.7.4 UV-Visible Spectroscopy 2-43
2.8 Experimental Leaching Format 2-46
2.8.1 Low-Volume Leaching Protocol 2-46
2.8.2 High-Volume Leaching Protocol 2-47
2.9 $CuFeS_{2(s)}$ Surface Sensitive Techniques 2-47
2.9.1 Scanning Electron Microscopy (SEM/EDX) 2-48
2.9.2 Time of Flight Secondary Ion Mass Spectroscopy (ToF-SIMS) 2-50
2.10 References 2-52

Synopsis: Herein, ionic liquids are introduced as an application-rich chemical class with existing known lixiviant behaviours. Relevant IL literature survey is accompanied by summary of the materials and standard operating procedures used throughout the remainder of the text. The chapter should be utilised as a reference point for experimental details, where not specifically discussed.

2.1 Introduction - Ionic Liquids

Ionic liquids (ILs) are by no means a new class of chemicals. As pointed out by Welton *et al.*[1] and Amarasekara,[2] the first reported ILs date to *ca.* 1900 (1888 - $(EtOH)NH_3{\cdot}NO_{3(l)}$; 1914 - $EtNH_3{\cdot}NO_{3(l)}$).[3, 4] Since publication in 1999, Welton's (and others) influential and highly cited review has prompted IL notoriety, contributing to significant advances in solvent and catalysis applications. The main reason for the prolific rise of ILs is the drive to circumvent the use of traditional volatile organic compounds (VOCs) as solvents and create greener synthetic chemistries - however, many additional benefits have been uncovered in the process (see below).

2.1.1 Ionic Liquid Characterisation

ILs are defined as pure salts or mixtures of salts, consisting of a single homogenous bulk phase with a characteristic low-temperature liquid range. Pure conventional inorganic salts present as solids at room temperature and melt at high extremes of temperature ($T_{f,KCl}$ = 776 °*C*; $T_{f,NaCl}$ = 801 °*C*).[5] Strong electrostatic forces are experienced by similarly sized, discrete ions which are able to pack closer together at low equilibrium inter-ionic separations. E2.1 expresses this strong inverse square relationship between radial separation (r_0) and electrostatic force (F_{ES}).

$$F_{ES} = \frac{1}{4\pi\varepsilon_0} \cdot \frac{q_1 q_2}{r^2} \qquad \text{E2.1}$$

ILs are commonly defined as pure salts characterised by melting points below 100 °*C*, resulting from increases in charge separation, leading to fluidity at low-moderate temperatures.[6] As such, typical IL cations and anions (see figure 2.1) are larger with higher degrees of asymmetry than their conventional salt counterparts, often with low delocalised charge densities that cause increased crystalline frustration to lower melting points.[7, 8] Figure 2.1 should be used as a reference point for the accepted structural abbreviations of the conventional discrete ILs used in this work, with a full outline of IL nomenclature conventions detailed elsewhere.[9]

However, it is noteworthy that a rich class of eutectic mixtures of Lewis/Brönsted acids and bases are now regarded as ILs. This class is referred to as deep eutectic solvents (DES; figure 2.2). DESs may contain several cationic and/or anionic structures but are commonly formed from combinations of quaternary ammonium salt ($NR_4{\cdot}X$), a metal salt (*e.g.* $AlCl_3$) and/or a hydrogen bond donor (HBD - *e.g.* urea, thiourea, oxalate) to increase charge delocalisation. A 1:2 stoichiometric combination of choline chloride and ethylene glycol stabilised by HBD urea (ethaline) was among the first reported eutectic mixtures; after which there have been many additional systems discovered.[10-15]

2.1.2 General Properties of Ionic Liquids

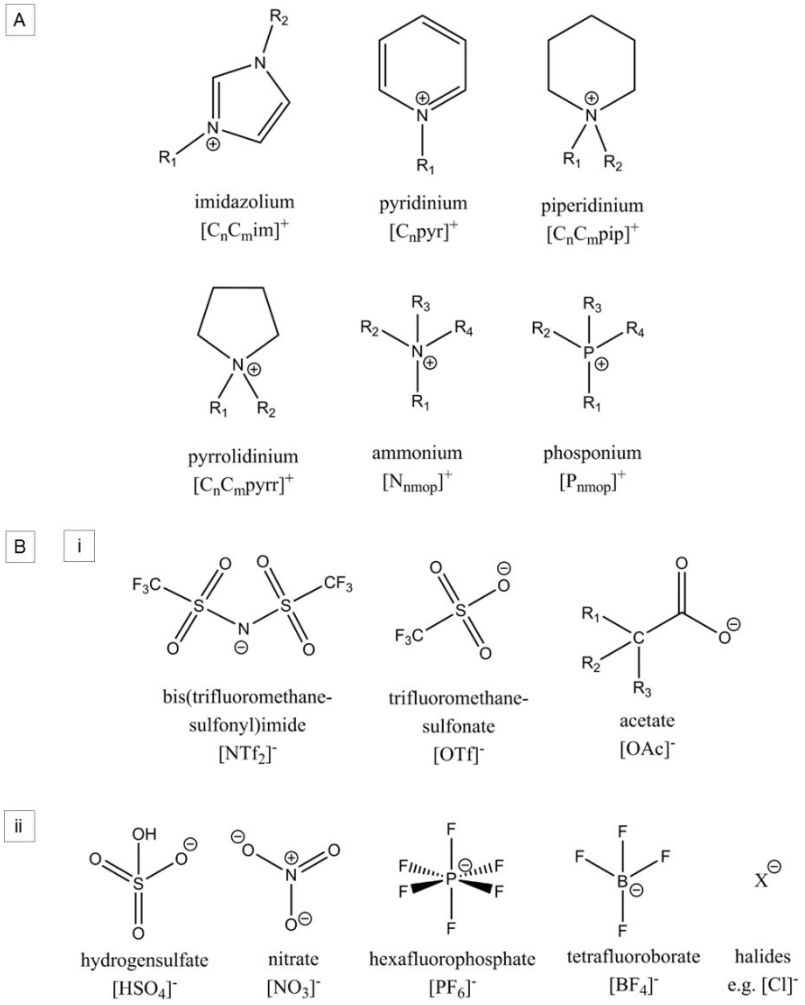
Despite weakened electrostatics, ILs remain highly networked fluids; generally displaying negligible vapour pressure, low volatility and a lack of flammability as a consequence.[16-19] This, and other properties such as low flammability,[20] high thermal (>200 °C) and electrochemical stability, mean that ILs represent a safe, low exposure, reduced waste and ultimately greener chemical class.[21, 22]

ILs are sometimes billed as 'designer solvents' that can be functionalised and modified in order to adopt specific physical properties to process requirements. Variations of functionality (e.g. $-SO_3H$, -COOH, -OH, $-NH_2$) and in the type of cation/anion creates systems with mixed physical properties, enabling tuning of factors such as aqueous/organic solvent miscibility (hydrophilicity), acidity, solute solubilisation, ionicity and hydrogen-bonding strengths. As such, creation of new biphasic IL systems[23] and designer IL-solvation of polar, ionic, inorganic and organic species[1, 24-26] has been made possible.

HSO_4-ILs are conductive and generally display wide electrochemical potential windows at ambient temperatures[27] making them well suited to electrochemical devices as discussed in section 2.1.3. However, it is noteworthy that many studies have incorrectly assigned these potential windows, generally over-estimating the true values. $IL_{(l)}$ viscosities are wide ranging, yet typically many orders of magnitude higher than that of molecular solvents (η_{H2O} = 0.89 *mPa·s*; $\eta_{[C4Him][HSO4]}$ ~ 5000 *mPa·s*, which can pose practical process issues (see section 2.3.6 and chapter 4). $IL_{(l)}$ self-diffusion, which has a key influence on medium properties such as conductivity and viscosity has been shown to exhibit non-classical behaviours - whereby ions are mobilised through discrete motions, jumping between voids formed in the medium.[28-31] Good predictions of $IL_{l)}$ mass-transport properties, deviating significantly from Stokes-Einstein behaviour, can be achieved through the modelling of low concentration solution voids, in similar fashion to consideration of ideal ionic mobility at infinite aqueous dilution ('hole theory').[28, 29]

2.1.3 Applications of Ionic Liquids

A plethora of reviews documents the constantly increasing volume of IL applications to chemical/synthetic problems.[2, 9, 10, 27, 32] For example, ILs are being used in many state-of-the-art applications in lubrication, biomass pre-treatment and deconstruction,[33, 34] fuel cell and capacitor electrolytes and dual solvent-catalysis roles in chemical synthesis (e.g. alkylation, esterification, dehydration etc.). In this thesis, review of successful applications of ILs will be limited to the field of metallurgy.



▲ Figure 2.1 - (A) Selected 'discrete' IL cations with unspecified general functional groups (R) at key positions - accepted abbreviations are included. (B) Selected 'discrete' IL anions separated into (i) organic and (ii) inorganic types.

2.2 Ionic Liquids in Metallurgy

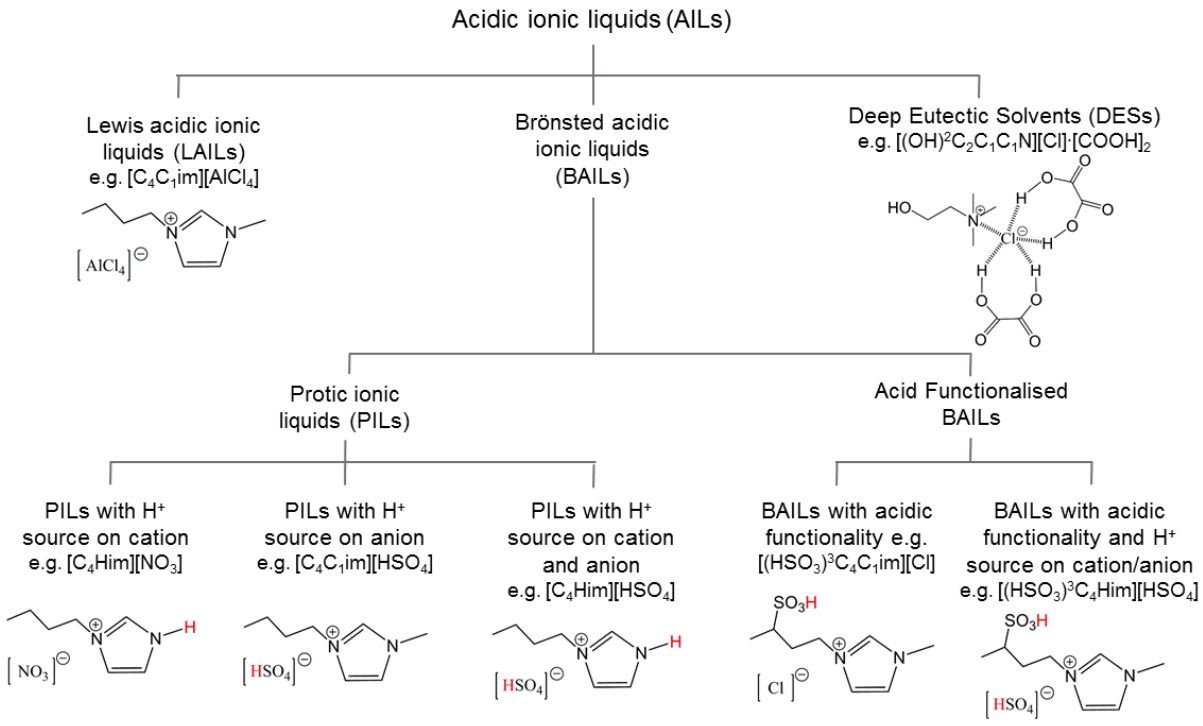
2.2.1 Chemical Classification

Under the umbrella of ionic liquids there are many sub-categories. From the perspective of hydrometallurgy methods (chapter 1), there are two overlapping sub-categories that are of particular interest to this study: namely acidic ionic liquids (AILs)[2] and room temperature ionic liquids (RTILs).[9] Advances in ILs for metallurgy coincide with broader development of task-specific ionic liquids (TSIL), where acidic ILs have been investigated as environmentally benign alternatives to replace traditional liquid acids in chemical industries.[27]

RTILs experience increasingly dynamic, transient Coulombic interactions, where cation-anion asymmetry and subsequent crystalline frustration combine to maintain a low-temperature liquid range[26, 35, 36] and melting temperatures below 25 °C by definition. Such ILs are of interest because

it is anticipated from existing ionometallurgy studies (section 2.2.2) that IL-based lixiviant activity may be maximised through application of pure $IL_{(l)}$. However, it is necessary to clarify that leaching in $IL_{(l)}$ does not necessarily represent an economic approach to $CuFeS_{2(s)}$ dissolution and addition of $H_2O_{(l)}$ significantly improves process cost efficiency (section 2.2.3).

AILs contain sources of acidity either within the cation, anion or both - be it in terms of Lewis (electron pair donation) or Brönsted acidity (free-H^+ donation).[2] Figure 2.2 illustrates the sub-classification of AILs, including the featuring of focal protic ionic liquids (PILs) and aforementioned DESs.



▲ Figure 2.2 - Flowchart documenting the sub-groups of acidic ionic liquids (AILs) giving exemplar structures based on the dialkylimidazolium cation - potentially Brönsted acidic proton sources are marked in red.

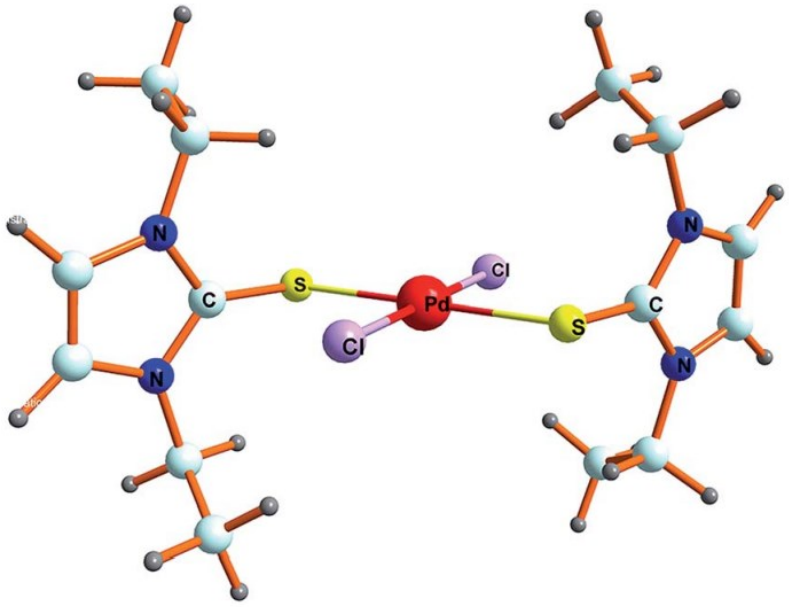
Protic ionic liquids (PILs) have received significant attention from the metallurgy research community, as their intrinsic free-[H^+] (low *p*H) can potentially be combined with 'designer' physical properties. Some have suggested that PILs may be suitable for 'dual-action' hydrometallurgy in acidic oxidative processes (section 1.4), where IL-based metal recovery enhancements may be attained through control of interfacial properties and selective M-IL interactions,[37] alongside minimised environmental impact. Additionally, Cole *et al.* were able to demonstrate that some ILs have sufficient chemical stability so as to allow >5-fold reaction cycling, without appreciable reduction in synthetic conversion rates for IL-mediated reactions.[38] Thus, IL lixiviant recycling (figure 1.6) may be a realistic possibility. Synthesis of the PILs of interest to this study is straightforward; attained through direct combination of equivalent quantities of Brönsted acid and base, which will be discussed further in section 2.3.

2.2.2 General Metallurgy Applications

Based on common hydrometallurgy and leach solution processing models (*e.g.* figure 1.6), ILs may benefit a number of different ore beneficiation stages. Firstly, ILs (including DESs) may have specific hydrometallurgic or ionometallurgic lixiviant behaviours - where the latter term has been coined in reference to the lixiviant activity of undiluted $IL_{(l)}$.[8, 10, 39-42] Secondly, ILs may favourably complex metals within metal-rich target solutions for liquid extraction purposes.[8, 41-45] Details of the specific favourable metal solvation environments created in some ILs is discussed further in section 4.2. Lastly, ILs have been found to have beneficial roles in the electrodeposition of metals, as discussed further in section 2.2.4. For reference, Ryder *et al.* provide an excellent schematic of the potential modes and processes in which ILs may benefit metallurgy.[10]

In recent years, some research efforts have explored the use of AILs as lixiviants/solvents in metal extraction applications and waste water processing.[46] The processing of rare earth metals has been particularly targeted, with some significant advances. $[C_4C_1im][HSO_4]$/NaX (*e.g.* X = Cl) systems were found to show high unselective metal extraction efficiency towards mixed Ag and Au ore (> 85 % recoveries), with 40-50 % improvements obtained with respect to $KHSO_4$ in equivalent conditions.[47] Switching to $[C_4C_1im][Cl]$ gave equivalent yet selective leaching. In a study published this year, Abbott *et al*. used ethaline (1:2; choline chloride: ethylene glycol) at 45-50 °*C* to selectively dissolve Au and Te from tellurides and sulfides, producing etched channels with measurable depth.[39] $CuFeS_{2(s)}$ dissolution was also investigated in this medium however, rates were ~1 order of magnitude lower. Elsewhere, several existing methods using DESs based upon pairings of $NR_4{\cdot}X$ and HBD molecules (ROH; NR_3; COOH) have been successful for the extraction of metals from metal oxide, benefiting from omission of metal chlorides (MX; *i.e.* component of DES), cheaper component and higher metal solubilities,[41, 42, 45] with the particular suitability of 'type III' DESs highlighted (Cat^+X^-zRZ; Z=$CONH_2$, COOH, OH).[13, 14]

Recovery of Zn and Cu with Brönsted acidic ionic liquid (BAIL; figure 2.2) lixiviant solutions is a further recent application.[48-50] In experiments concerning brass waste it was found that all Zn content could be dissolved using $[C_4C_1im][HSO_4]_{(l)}$. Resultant $Zn_{(s)}$ could be recovered by electrowinning without a purification step.[48] Elsewhere, $[N_{8880}][NTf_2]_{(l)}$ (figure 2.1) has been used for the recovery of precious metals such as Pd and Pt,[51] with a more recent paper showing $[C_2C_2im][NTf_2]_{(l)}$ forms complexes applicable to Pd-recovery from aqueous waste waters.[52] $[(EtOH)NMe_3][NTf_2]_{(l)}$ has been used for Nd leaching from NdFeB magnets, also providing benefit to later solvent extraction procedures.[53] *Whitehead et al.* have observed partially selective recovery of Au (>85 %) and Ag (>60 %) from an ore sample using a $FeCl_3/[C_4C_1im][HSO_4]$/thiourea system.[47] It is noteworthy that under the conditions studied Cu recoveries were reportedly reduced.



▲Figure 2.3 - Optimised geometry of the confirmed crystal structure resulting from complexation of two equivalents of $[C_2C_2ImT][Cl]$ and Pd(II).[52]

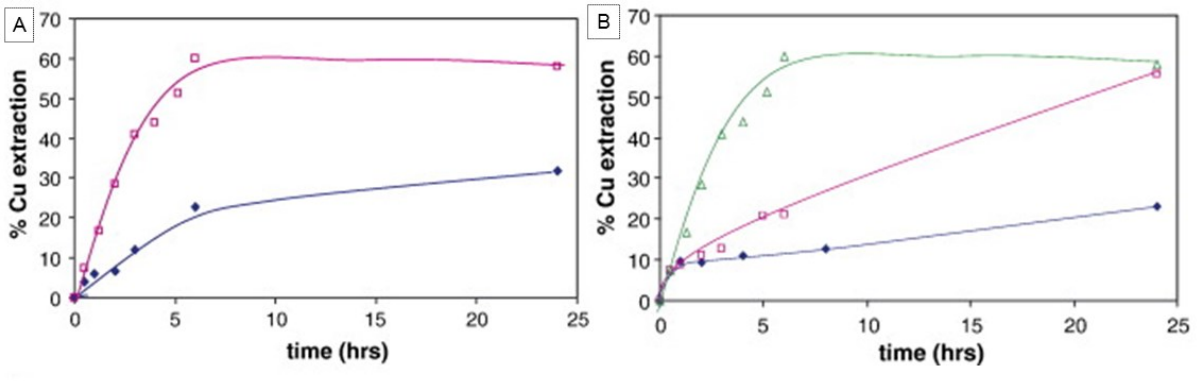
Two further key aspects of any solution-based metallurgy are the resulting metal coordination[10, 43, 44] and the required liquid-liquid extraction techniques.[54, 55] $[N_{8880}][NTf_2]$ / $[N_{8880}][NO_3]$ IL mixtures are able to extract group XIII metal ions from $HCl_{(aq)}$ solutions.[56] In similar $HCl_{(aq)}$ solutions, ILs have been used to selectively extract each of Zn^{2+}, Cd^{2+}, Cu^{2+} and Fe^{2+}, with different metal ion sensitivities for $[C_nC_mim]^+$ and $[N_{nmop}]^+$ ILs.[57] These studies exemplify the strong and often selective chelation between IL-metal ions that can be advantageous to metal recovery applications (figure 2.3).[46]

More relevantly, $[C_4C_1im][HSO_4]_{(aq)}$ has been used to solubilise $Cu_{(s)}$ from waste printed circuit boards, extracting >99 *%* under optimised conditions (70 *°C*, 2 *hrs*, 3.55 $mol{\cdot}dm^{-3}$).[58] A follow-up study revealed that a wide range of ILs achieve significant Cu leaching, however HSO_4^- AILs were more effective than SO_3H-functionalised AILs at equivalent *p*H.[59] Under typical waste water processing conditions, a variety of $[N_{nmop}]^+$ and $[P_{nmop}]^+$ ILs were able to remove 0-95 *%* Cu (amongst other metals) in 120 *min*, indicating both cation and anion effects (BA = benzoate; MTBA = 2-methylthio-benzoate; TS = thiosalicylate; $[N_{8881}][TS]$ = 95 *%*; $[P_{8881}][TS]$ = 80 *%*; $[N_{8881}][MTBA]$ = 11 *%*; $[N_{8881}][MTBA]$ ~ 0 *%*).[60]

2.2.3 IL Application to $CuFeS_{2(s)}$

IL application to $CuFeS_{2(s)}$ metallurgy is a relatively new venture, with the number and types of ILs trialled remaining restricted. To date, and to the author's knowledge, <10 works have reported the application of AILs to high grade-$CuFeS_{2(s)}$ ores or flotation concentrates. These studies all focus

on $[C_nC_mim][HSO_4]_{(aq)}$, with $[C_4C_1im][HSO_4]_{(aq)}$ the most commonly used IL system.[26, 61, 62] The promising results of these endeavours are summarised below.



▲ Figure 2.4 - $Cu_{(aq)}$ recovery profiles for application of $[C_4C_1im][HSO_4]_{(aq)}$ to $CuFeS_{2(s)}$ concentrate.[26] (A) Temperature dependence of Cu recovery in 1.1 *mol·dm*$^{-3}$ $[C_4C_1im][HSO_4]_{(aq)}$ (blue = 60 °*C*; magenta = 70 °*C*). (B) Cu recovered at 70 °*C* for 1.1 *mol·dm*$^{-3}$ and 0.55 *mol·dm*$^{-3}$ $[IL]_{(aq)}$ (green, magenta) and 1 *mol·dm*$^{-3}$ $H_2SO_{4(aq)}$ (blue).

Whitehead *et al*.[26] first applied $[C_4C_1im][HSO_4]_{(aq)}$ to a $CuFeS_{2(s)}$ flotation concentrate (Cu = 20.3 *%wt*; Fe = 34.1 *%wt*; 45-106 *µm*).[26] A significant rise in $Cu_{(aq)}$ recovery was observed between lixiviant temperatures of 60 °*C* and 70 °*C*, with 1.1 *mol·dm*$^{-3}$ $[IL]_{(aq)}$ capable of leaching ~60 *%* $Cu_{(aq)}$ within 10 *hrs* before plateauing. Further increases in [IL] to 2.8 *mol·dm*$^{-3}$ provided increased $Cu_{(aq)}$ recovery over 24 *hrs* (table 2.1), with low further enhancement (<5 *%*) beyond this concentration. The results, reproduced in figure 2.4, represent improved $Cu^{2+}_{(aq)}$ recoveries of between ~350-470 *%* versus 1 *mol·dm*$^{-3}$ $H_2SO_{4(aq)}$ benchmark solutions, over a short 24 *hr* leach period.

▼ Table 2.1 - Effect of $[C_4C_1im][HSO_4]_{(aq)}$ concentration on Cu extraction from $CuFeS_2$ concentrate at 70 °*C* after 24 *hrs* leaching.[26]

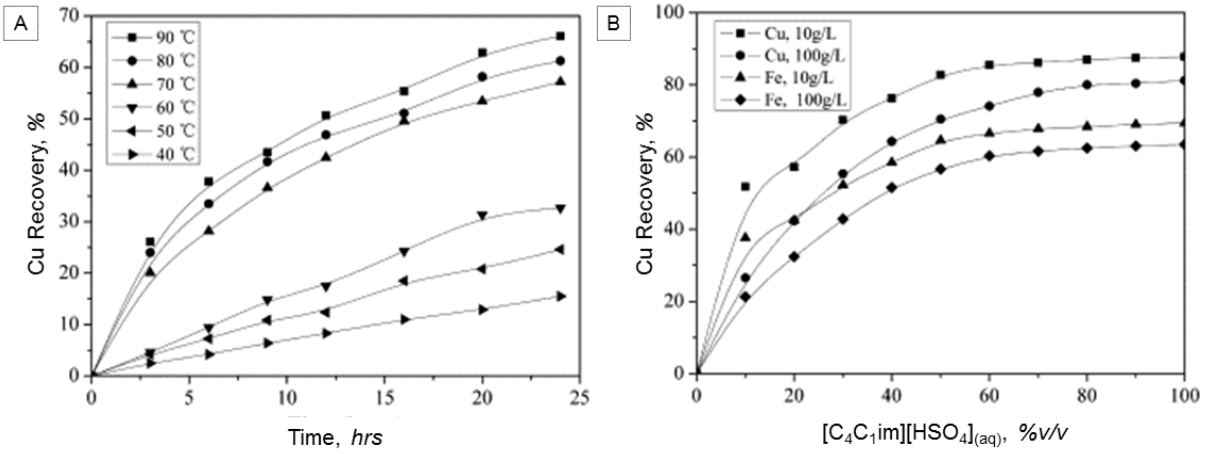
$[C_4C_1im][HSO_4]_{(aq)}$, *% w/v*	$[C_4C_1im][HSO_4]_{(aq)}$, *mol·dm*$^{-3}$	Cu Recovery, *%*
10	0.55	55.7
20	1.1	58.1
50	2.8	82.2
100	5.5	86.6
	1 *mol·dm*$^{-3}$ $H_2SO_{4(aq)}$	23.2

▼ Table 2.2 - Measured dissolved oxygen concentrations for selected ILs at a range of temperatures.[26]

$IL_{(l)}$	Temperature, °C	$[O_2]_{(aq)}$, $mg \cdot g^{-1}$	$[O_2]_{(aq)}$, $mmol \cdot dm^{-3}$	Solubility Ratio in IL: H_2O
$[C_4C_1im][BF_4]$	16.5	0.049	1.87	1.3
	60	0.039	1.47	1.3
$[C_4C_1im][HSO_4]$	35	0.042	1.67	1.2
	60	0.023	0.89	0.8
$[C_4C_1im][PF_6]$	18.5	0.067	2.89	2.1
	60	0.059	2.57	2.3
H_2O	25	0.045	1.41	
	50	0.035	1.10	

A second, more extensive study by Dong *et al*.[61] again focusing on Brönsted acidic $[C_4C_1im][HSO_4]_{(aq)}$ produced similar results for a $CuFeS_{2(s)}$ concentrate (72 *mol%* $CuFeS_2$; 18 *mol%* FeS_2; 24.8 *mol%* Cu; 30.3 *mol%* Fe; 65-74 *μm*) leached in 0.8 *atm* $air_{(g)}$ and $Ar_{(g)}$ - where the latter produced negligible leaching. Across all conditions, $Cu_{(aq)}$ recovery was found to be 10-20 *%* higher than that of $Fe_{(aq)}$. Increased pulp density (10-100 $g \cdot L^{-1}$) was found to reduce Cu recovery by 10-20 *%* across all $[IL]_{(aq)}$, being more pronounced at low $[IL]_{(aq)}$. Increased magnetic stirrer speed (200-800 *rpm*) resulted in ~30 *%* leaching enhancement, while a sharp rise in extraction was observed between 60-70 *°C* temperatures in an otherwise much weaker and Arrhenius-like dependence (figure 2.5A). This repeated feature in the temperature dependence profile suggests a high E_a value for the chemical reaction, which was measured as 69.4 $kJ \cdot mol^{-1}$.

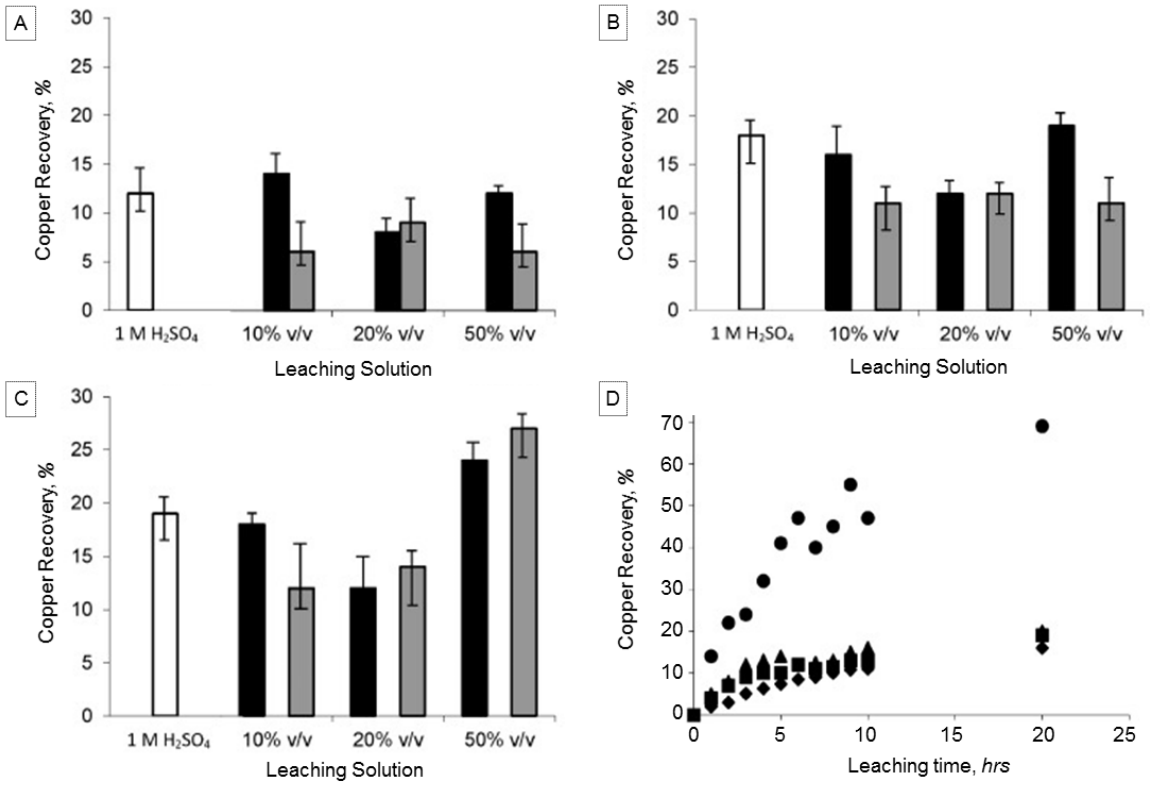
Parabolic $[IL]_{(aq)}$ dependence (0.5-5 $mol \cdot dm^{-3}$; 10-100 *%v/v*), with regard to extraction of Cu^{2+} and Fe^{2+}, was found with no significant effect of increased $[IL]_{(aq)}$ after ~60 *%v/v*. Under optimised conditions, 88 *%* Cu and ~60 *%* Fe recoveries were attainable. Representative results are summarised in figure 2.5, showing similar general physical dependences to those discussed for acid-SO_4^{2-} leaching (section 1.6) alongside significantly enhanced recovery. Somewhat surprisingly, $IL_{(aq)}$ results were not compared to traditional acid benchmark solutions, however comparisons were made to $KHSO_{4(aq)}$, as discussed further in section 2.3.4. Each of the aforementioned studies discuss the impact of improved $O_{2(aq)}$ solubility in $[IL]_{(aq)}$ in providing enhanced metal recovery at equivalent pH, although the $[O_2]_{(aq)}$ measurements used for pure IL solutions are far from conclusive (table 2.2). This conclusion would also be contrary to reports that addition of conventional solutes typically reduces $O_{2(aq)}$ solubility in aqueous environments[63] however, as discussed, ILs are generally not considered to be conventional solutes.



▲ Figure 2.5 - (A) Temperature dependence for the leaching of 10 $g{\cdot}L^{-1}$ $CuFeS_{2(s)}$ by 1.1 $mol{\cdot}dm^{-3}$ (20 *%v/v*) $[C_4C_1im][HSO_4]_{(aq)}$. (B) Influence of $[IL]_{(aq)}$ on Cu and Fe recovery from $CuFeS_2$ for two differing pulp densities.[64]

A 2016 publication by Carlesi *et al.*[65] is among the first (alongside our published work)[62] to compare the activity of two $IL_{(aq)}$ systems; namely that of $[C_1Him][HSO_4]_{(aq)}$ and $[C_4C_1im][HSO_4]_{(aq)}$. The $IL_{(aq)}$ solutions are often indicated to match/enhance dissolution compared with 1 $mol{\cdot}dm^{-3}$ $H_2SO_{4(aq)}$, however a non-trivial dependence on $[IL]_{(aq)}$ and temperature complicated matters significantly (figure 2.6). At 60 °*C*, about 30 *%* $Cu_{(aq)}$ was recovered over 20 *hrs* in agreement with analogous results in figure 2.5. Thus, it was concluded that there was no appreciable difference between the neat $IL_{(aq)}/H_2SO_{4(aq)}$ solutions; however a large 7-fold improvement was observed when 50 *%v/v* $[C_1Him][HSO_4]_{(aq)}$ was instead used as an additive to aid $SO_4^{2-}{}_{(aq)}$ leaching (1 $mol{\cdot}dm^{-3}$ $H_2SO_{4(aq)}$).

Critically, enhancement could not be explained by E_h or *p*H effects in the neat solutions - however, as will be discussed, there are some potential flaws with Carlesi *et al.'s* treatment of each quantity (sections 2.3.4 and 5.4.3). The authors concluded that the ILs may mediate conventional acid leaching by reducing 'hydrophobic charge transfer resistance' - whereby repulsion of charges species away from the interface provides an additional barrier to solution-solid charge transfer - a result that may be linked to dissolution enhancements achieved via addition of VOCs[66] (section 1.6.5). However, before this can be accepted there is a need to clarify why a reduced, proportionate enhancement is not observed for lower 'additive-level' $[IL]_{(aq)}$ quantities (section 6.3.3).

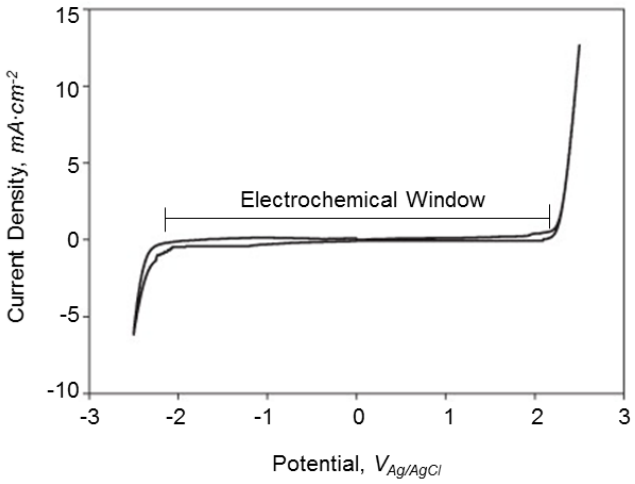


▲ Figure 2.6 - $Cu_{(aq)}$ recovery in 1 *mol·dm*$^{-3}$ $H_2SO_{4(aq)}$ versus 10, 20 and 50 *%v/v* $[C_1Him][HSO_4]_{(aq)}$ (black) and $[C_4C_1im][HSO_4]_{(aq)}$ (grey) at 20 °*C* (A), 40 °*C* (B) and 60 °*C* (C). (D) Cu recovery at 60 °*C* when 10 (▲), 20 (■) or 50 *%v/v* (●) $[C_1Him][HSO_4]_{(aq)}$ is combined with neat 1 *mol·dm*$^{-3}$ $H_2SO_{4(aq)}$ (◆) as a leaching additive.[65]

2.2.4 Applications of ILs in Electrochemistry

In addition to general chemical stability (section 2.1.2), some ILs have broad 'electrochemical windows' and high conductivity, making them suitable for use in electrolytic applications and devices.[67, 68] ILs have shown promise in applications such as rechargeable Li-ion batteries, biosensors,[69-72] actuators,[73] solvents for electrochemical devices, supercapacitors, fuel cells, dye-sensitized solar cells,[74] and polymer electrolytes.[75]

The electrochemical window indicates the electrolytic stability of an electrolyte, *i.e.* the potential range where no potential-induced solvent or electrolyte decompositions occurs. Outside of the potential window, high anodic and cathodic currents are observed. As such, ILs can be useful for electrowinning of reactive metals, thus avoiding gas evolution at the electrodes.[10, 39] Conversely, BAILs of type $[NR_4][NTf_2]_{(l)}$ can be utilised as electrolytes for $H_{2(g)}$ and $O_{2(g)}$ production at $Pt_{(s)}$ electrodes at elevated temperatures (>130 °*C*).[76] Electrochemical windows for ILs can be as large as 5.81 *V*,[77] however HSO_4^- ILs typically have a more modest value (~4.0 *V*).[78] A range of BAILs, including $[C_4C_1im][H_2PO_4]_{(l)}$ and $[C_4C_1im][HSO_4]_{(l)}$, were found to exhibit beneficial coordination effects over $HCl_{(aq)}$ in the electrochemical synthesis of polyaniline.[79]



▲ Figure 2.7 - Cyclic voltammogram (CV) of the electrochemical window of $[C_2C_1im][NTf_2]_{(l)}$ using a glassy-carbon macro-WE, Pt CE and Ag/AgCl RE at potential scan rate of 100 $mV{\cdot}s^{-1}$ and 25 °C.[77]

As discussed, pyro and hydrometallurgic (SX-EW) approaches to the refining of primary sulfides such as $CuFeS_{2(s)}$ each involves $Cu^{2+}{}_{(aq)}$ electrodeposition in some form (figures 1.4 and 1.6). For pyrometallurgy, cast impure $Cu_{(s)}$ copper anodes are oxidised into solubilised $Cu^{2+}{}_{(aq)}$ in an electrolytic acid-$SO_4^{2-}{}_{(aq)}$ medium, before transit to the inert cathode where $Cu^{2+}{}_{(aq)}$ is reduced to high purity $Cu_{(s)}$ electrodeposits. For SX-EW, $Cu^{2+}{}_{(aq)}$ may require extraction into a suitable electrolyte from the impregnated leach solution (lixiviant dependent), before electrowinning via electrodeposition from a $Cu^{2+}{}_{(aq)}$-rich solution (1-3 $mol{\cdot}dm^{-3}$; 60-200 $g{\cdot}dm^{-3}$) at analogous inert cathodes.[25]

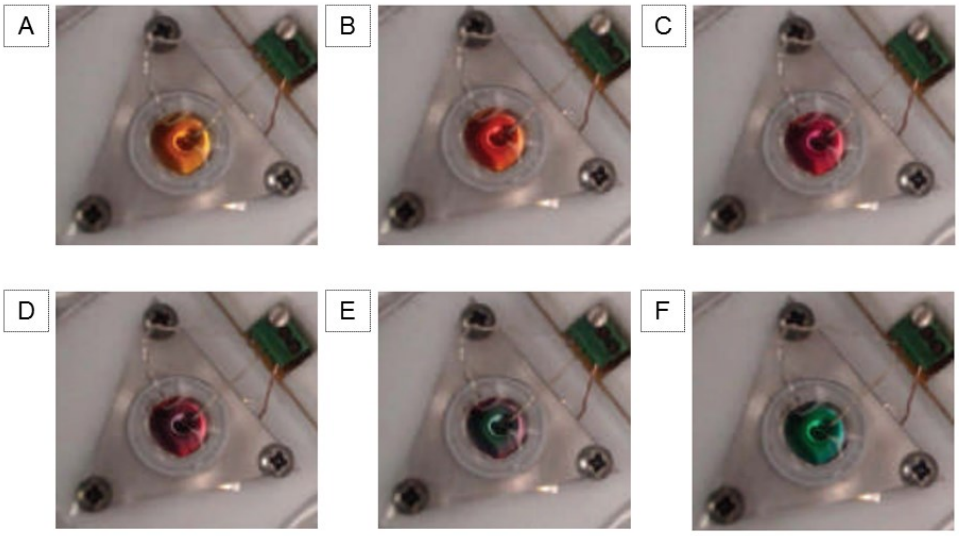
IL lixiviants could potentially offer multiple benefits to Cu refinement processes - combining provision of lixiviant activity, electroplating electrolyte and control of deposit morphology. Over the past 20 years, ILs have been the focus of most research on non-aqueous electrodeposition.[25, 80] Acidic-$SO_4^{2-}{}_{(aq)}$ electrolytes produce high quality, low impurity $Cu_{(s)}$ electrodeposits, whereas acid-$Cl^-{}_{(aq)}$ lixiviants may require extraction into $SO_4^{2-}{}_{(aq)}$ media before electrorefinement, hence reducing process efficiency.

Hence, the 'designer' properties of ILs may enable production of superior quality, low impurity cathodes, obtained directly from the leach liquor. Currently, the most common type of ionic liquids patented for electrodeposition applications are LAILs with halometallate anions with electron accepting ability (e.g. $[AlCl_4]^-$ or M = Sn, Zn).[2] However, in recent years IL/DES systems have been found to benefit the electrodeposition of the metals and alloys of Ag,[81, 82] Au,[43] Zn,[83] Al,[84, 85] and Cu[86, 87] - whereby improvements in electrodeposition can be traced to IL-dominated solution speciation, modification of redox potentials and/or control of the developing electrodeposit morphology.[10] It is noteworthy that concerted dissolution and solid-liquid separation of $Cu_{(s)}$ from complex Cu/Zn mixtures (and others) has been achieved recently using an electrocatalytic technique in ethaline (1:2; choline chloride: ethylene glycol; I_2/I^- cat.).[43]

Electrodeposition is a mature and well-understood technology enabling control of nanoscale structures and morphologies. Figure 2.8 illustrates that fine tuning of electrodeposition parameters can be used to control the electronics, structure and quantum behaviour of conductive electrodeposits such as $Si_xGe_{(1-x)}$.[88] However, it is noteworthy that that electrodeposition of $Cu^{2+}_{(aq)}$ in $[C_1py][AlCl_4]_{(l)}$ or $[C_4py][AlCl_4]_{(l)}$ environments occurs via two single electron processes (E2.2).[89, 90] Interestingly, it has also been found that there is a potential dependent absorption of $[C_4C_1im]^+$ and N-methylimidazole (base) onto a Cu electrode;[91] an interaction which may have consequences for IL-$Cu^{2+}_{(aq)}$ electrodeposition used in this study. This brief introduction to Cu electrodeposition will be extended to the theoretical principles of Cu quantification via anodic stripping voltammetry (ASV) in section 2.7.3.

$$Cu^{2+}_{(IL)} + e^- \rightleftharpoons Cu^{+}_{(IL)}$$

$$Cu^{+}_{(IL)} + e^- \rightleftharpoons Cu^{0}_{(s)} \qquad \text{E2.2}$$



▲ Figure 2.8 - Photographs of the electrochemical cell used to electrodeposit $Si_xGe_{(1-x)}$, following plating procedures in $[C_4C_1pyrr][NTf_2]_{(l)}$ at -2.62, -2.68, -2.74, -2.78, -2.83 and -2.85 *V*, in (A)-(F) respectively.[88]

2.2.5 Outlook: Ionic Liquids for $CuFeS_{2(s)}$ Hydrometallurgy

For hydrometallurgical extraction to supercede currently dominant pyrometallurgical routes, superior $Cu^{2+}_{(aq)}$ recovery kinetics, total process efficiency and reduced extraction footprint must be achieved.[92] Recent $CuFeS_{2(s)}$ leaching studies report enhanced leaching for $IL_{(aq)}$ systems, in addition to various potential '*green'* advantages to industry and the wider world. Using optimised conditions (10% *w/v* $[C_2C_1Im][HSO_4]_{(aq)}$; 10mM $FeCl_{3(aq)}$), 2-21% Cu-recovery enhancements are attainable with respect to primitive acid-sulfate industrial standards (50 $mmol{\cdot}dm^{-3}$ $H_2SO_{4(aq)}$).[26]

Elsewhere, imidazolium-based $[Im]^+$ *ILs* reportedly display Brønsted acid leaching behaviour,[93] linked to enhanced recovery for short alkyl (R) N-substituents $[C_xC_yIm]^+$.[26] Recent key advances in ionometallurgy and IL-related enhancement of metal complexation by DESs offer strategies with novel, distinct extraction pathways. However acceptable process efficiencies cannot be guaranteed at low $IL_{(l)}$ dilutions, which may ultimately limit commercial adoption.

The outlook for $IL_{(aq)}$ lixiviants is promising. State-of-the-art studies clearly mark $IL_{(aq)}$ systems as promising industrial hydrometallurgical candidates. Early-stage successful studies suggest that $IL_{(aq)}$ leaching may have the potential to significantly enhance dissolution of $CuFeS_{2(s)}$ ore with respect to conventional acid-SO_4^{2-} media - if specific IL properties can be optimised. However, little is known of the specific properties, physical conditions ([ox], [red], *p*H, T, E_h), intermolecular interactions and redox processes that promote $CuFeS_{2(s)}$ leaching by ILs. Further mechanistic insight is required regarding the isolation of the compositional evolution of key participating surface and solution species. Chosen leach systems must be subjected to multiple leaching timescales, where surface-sensitive analytical techniques, combined with $IL_{(aq)}$-$CuFeS_{2(s)}$ leachate compositional analysis, can begin to de-convolute specific leaching mechanics, kinetics, retardation effects, key chemical moieties and structure-activity relationships. Effect of $[IL]_{(aq)}$ upon lixiviant performance must be assessed since maximum aqueous dilution is key to process economy, as discussed.

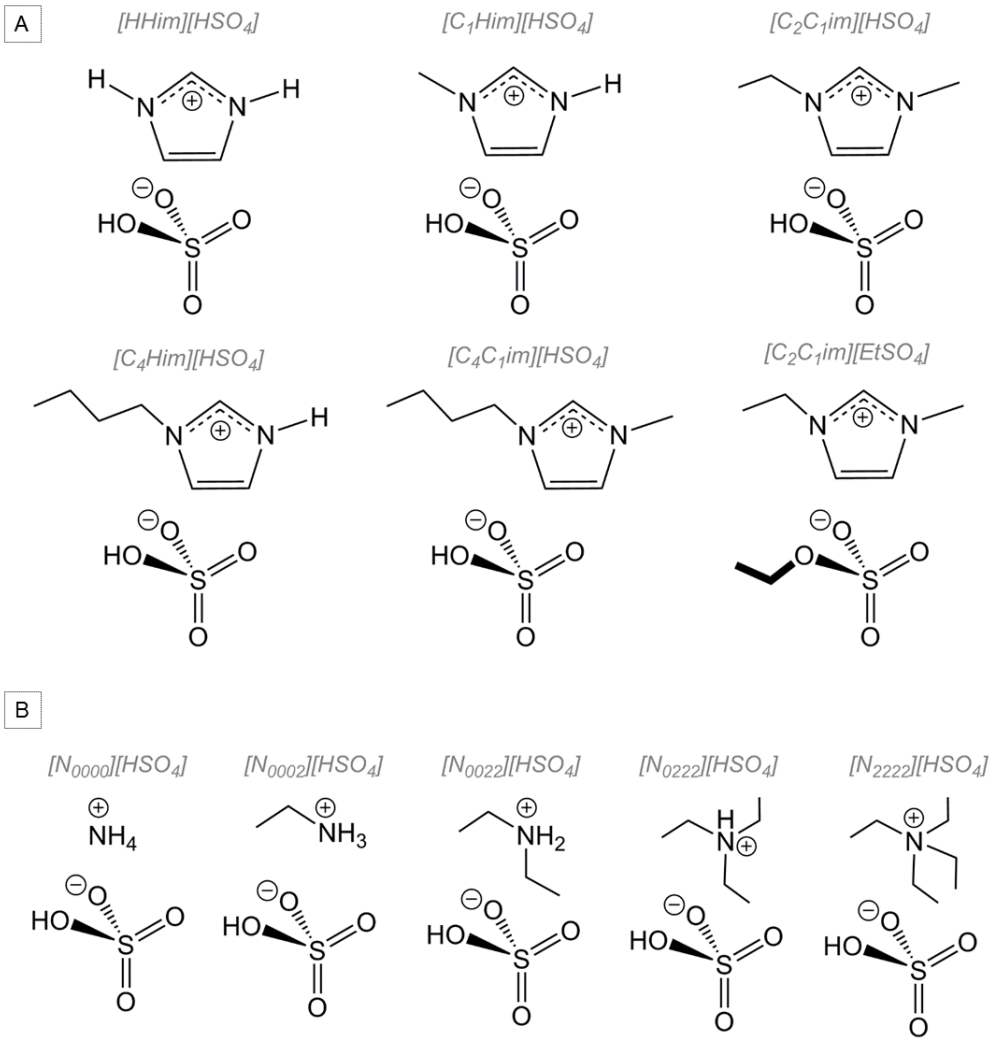
Unfortunately, the search for the best performing IL systems is complicated and most likely encompasses a vast '*chemical space*'. While it is clear that anion acidity plays an important role in IL-leaching,[61] it is also evidenced from recent findings by Carlesi *et al*.,[65] that there may be a range of complex synergistic IL effects, requiring greater understanding. Indeed, a more philosophical question that could be posed is whether the exploration of new IL systems or the greater understanding of established lead systems (such as $[C_4C_1im][HSO_4]$) should be focused upon. As discussed in the outline of the aims and objectives of this work (section 1.10.1), the author and collaborators chose a balanced approach, in which new IL systems would be explored and compared with the activity of presently known lead systems.

Effective accounting for the scope of IL structural and chemical diversity requires a systematic high-throughput analytical approach. As outlined in section 1.10, promising $IL_{(aq)}$ systems produced by combinatorial investigations, will be scaled-up into a 400 *mL*-scale reactor, so that leaching can be monitored with greater scrutiny and reference to key dissolution controlling parameters (*e.g. p*H, T, E_h, $[O_2]$ etc.). Data produced will provide mechanistic insight and IL structure-activity relationships, which will aid in the clarification of wider $IL_{(aq)}$ lixiviant performance and whether these systems have the potential to enhance $CuFeS_{2(s)}$ dissolution compared to conventional acid-$SO_4^{2-}{}_{(aq)}$.

2.3 Ionic Liquid Materials, Synthesis and Properties

2.3.1 Selection of Lixiviant Ionic Liquids

For the purposes of this work, the ILs chosen for lixiviant studies were mainly restricted to $[C_nC_mim]^+$ and $[NR_4]^+$ cations with $[HSO_4]^-$ related anions, unless otherwise stated. These selected structures are shown in figure 2.9. This choice was made in order to retain comparability with existing studies, whilst exploring the effect of substituent variations in the ethylammonium hydrogensulfate homologous series.



▲ Figure 2.9 - Selected BAIL structures employed for $CuFeS_{2(s)}$ hydrometallurgic studies from (A) the dialkylimidazolium hydrogensulfate homologous series and (B) the ethylammonium hydrogensulfate series.

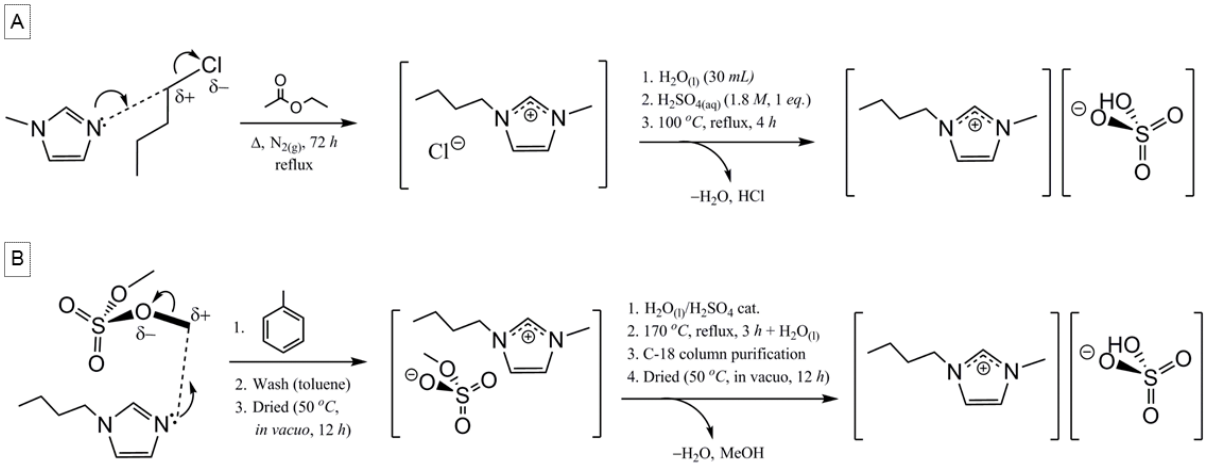
At this juncture, it is noteworthy that many BAILs are not currently synthetically cheap commodities, despite the facile appearance of the acid-base formation reactions. In fact, many peers have assessed ILs to have a low green rating and poor economies for use in industrial chemistries.[94, 95] Expensive starting materials, functionalisation of IL cations/anions and reagent/product purification are all significant sources of cost, where synthetic routes can often (ironically) involve large

quantities of molecular solvents that ILs were once billed as replacements for.[7] With these perspectives in mind, ammonium based ILs and DESs may be cheaper and greener alternatives to imidazolium ILs such as $[C_4C_1im][HSO_4]_{(l)}$, on account of high existing rates of industrial reagent production.

2.3.2 Synthesis / Source of Ionic Liquids

Synthesis of some neat $[HSO_4^-]$ ILs, of the type featured in figure 2.9, can be achieved via dropwise addition of high purity $H_2SO_{4(l)}$ to one equivalent of the distillation purified amine base, while cooled under $N_{2(g)}$.[7] A typical post-synthetic purification procedure may include vacuum drying over $CaCl_{2(s)}$ and addition of activated charcoal for decolourisation. Since many of these ILs are to be immediately mixed into aqueous lixiviant solutions, the direct synthesis of $IL_{(aq)}$ is a welcome simplified process.

Dialkylated imidazolium ILs, such as $[C_4C_1im][HSO_4]_{(l)}$, can require significantly more complex synthetic routes, where there is often a choice between several routes (figure 2.10). Some of the required ILs are available commercially, including $[C_1Him][HSO_4]_{(l)}$, $[C_2C_1im][HSO_4]_{(l)}$, $[C_2C_1im][EtSO_4]_{(l)}$, $[C_4C_1im][HSO_4]_{(l)}$ (≥95 *%*; *Sigma-Aldrich*). For convenience and since ultimate chemical purity is of little concern to the present application, wet $IL_{(aq)}$ syntheses can be used to directly synthesise high dilution $IL_{(aq)}$ solutions. Some exemplar procedures are given below, as applicable to the synthesis of $[C_4Him][HSO_4]_{(l)}$, $EtNH_3 \cdot HSO_{4(l)}$ and 500 $mmol \cdot dm^{-3}$ $[C_4Him][HSO_4]_{(aq)}$ with characterisation spectra provided in the appendices.



▲ Figure 2.10 - Experimental details and synthetic routes for $[C_4C_1im][HSO_4]_{(l)}$ as reported by (A) Whitehead *et al.*[96] and (B) Welton *et al.*[97]

Synthesis of 100 *%v/v* 3-butylimidazolium hydrogensulfate, $[C_4Him][HSO_4]_{(l)}$

Sulfuric acid (98 *%*; 1 *equiv.*; *Sigma Aldrich*) is added dropwise to an aqueous solution of distilled, recrystallized butylimidazole (1 *equiv.*) under $N_{2(g)}$ at 0 °C. The resulting mixture is stirred

overnight and the water removed via rotary evaporation, and the $IL_{(l)}$ dried *in vacuo*. IL purity and cation:anion ratio were checked by NMR (400 *MHz*, Bruker) and hygroscopic water uptake was checked using Karl-Fischer titration (*TitroLine 7500 KF Titrator*, *SI Analytics*).

δH (400 MHz; DMSO-d_6): 8.66 (1H, s, C^2H), 7.60 (1H, s, C^4H), 7.43 (1H, s, C^5H), 4.12 (2H, t, NCH_2), 1.75 (2H, m, NCH_2CH_2), 1.25 (2H, m, $NCH_2CH_2CH_2$) and 0.89 (3H, t, $NCH_2CH_2CH_2CH_3$) ppm.
δC (100 MHz; DMSO-d_6): 136.33 (C^2), 123.05 (C^4), 121.58 (C^5), 47.86 (NCH_2), 32.26 (NCH_2CH_2), 19.38 ($NCH_2CH_2CH_2$) and 13.76 ($NCH_2CH_2CH_2CH_3$) ppm.

Direct synthesis of 500 *mmol·dm^{-3}* 3-butylimidazolium hydrogensulfate, $[C_4Him][HSO_4]_{(aq)}$

1 *kg* of 10 *%wt* $[C_4Him][HSO_4]_{(aq)}$ (500 *mmol*) is synthesised directly. 1-butylimidazole (56.2 *g,* 500 *mmol, Sigma Aldrich*) is stirred overnight with $KOH_{(s)}$ and later distilled. Ultrapure water (*Ondeo Purite Purification System,* 400 *g*) is added to the weighed distillate. Sulfuric acid (97.9 *mol%,* 24.5 *mL*, 500 *mmol, Sigma Aldrich*) is combined with ultrapure water (400 *g*) and the aqueous acid added drop-wise to stirred aqueous *1-butylimidazole* at 0 *°C*, with the remaining water (99.1 *g*) added from the acid-reactant glassware.

^{1}H-NMR (400 MHz, DMSO-d_6) δ: 0.89 (3H, tt, ^3J=8 Hz, CH_3) 1.23 (2H, m, ^3J=8 Hz, CH_2CH_3) 1.77 (2H, m, ^3J=8 Hz, $CH_2CH_2CH_3$) 2.51 (d_6-DMSO) 3.69 (H_2O) 4.18 (2H, t, ^3J=8 Hz, $CH_2CH_2CH_2CH_3$) 7.63 (1H, d, ^3J=4 Hz, $HNC(H)=C(H)NCH_2$) 7.74 (1H, d, ^3J=4 Hz, $HNC(H)=C(H)NCH_2$) 9.04 (1H, s, $NC(H)N$).

Synthesis of 100 *%v/v e*thylammonium hydrogensulfate $[N_{0002}][HSO_4]_{(l)}$

As above, for $[C_4Him][HSO_4]_{(l)}$ replacing $butylimidazole_{(aq)}$ with $ethylamine_{(aq)}$.

δH (400 MHz; DMSO-d_6): 10.69 (1H, s, HSO_4), 7.64 (3H, t, NH_3), 2.80 (2H, m, CH_2), 1.12 (3H, t, CH_3) ppm.
δC (100 MHz; DMSO-d_6): 36.12 (CH_2), 12.4 (CH_3) ppm.

2.3.3 Kamlet-Taft Characterisation

Since $CuFeS_{2(s)}$ dissolution will lead to metal ion release into $IL_{(aq)}$ solution environments, it is important to understand the solvation properties of ILs. As with molecular solvents, polarity is a good guide to metal solubilities, especially since polarity has important impact on BAIL fluidity ranges, specific solute interactions and degree of hydrogen bonding.[37] For example, $NH_4{\cdot}HSO_{4(s)}$ melts just above room temperature, whereas ethylammonium derivatives are liquid and increasingly fluid at room temperature upon increased degree of substitution.

IL polarity is most effectively expressed through Kamlet-Taft parameters[98-100] for hydrogen bond donor acidity, hydrogen bond acceptor basicity and polarizability (α, β, π* respectively) - where medium dielectrics fail to explain experimental solubility data.[101] Placement within these solubility scales is defined using a series of conjugated heteroatomic dyes chosen to probe the aforementioned solvent properties (e.g. Reichardt's Dyes[101]). Table 2.3 expressed the Kamlet-Taft parameters for selected IL closely related to $[C_4C_1im][HSO_4]_{(l)}$ with lixiviant activities as introduced. However, it is noteworthy that when working in relatively high dilution in aqueous environments these parameters become less important and well-established aqueous ion interactions are expected to dominate.

▼ Table 2.3 - Kamlet-Taft parameters for selected ILs & molecular solvents.[37]

Solvent / Ionic Liquid$_{(l)}$	E^N_T	Polarizability (π^*)	Hydrogen Bond Acidity (α)	Hydrogen Bond Basicity (β)	λ_{Cu}, *nm*	ΔG^H, *kJ·mol^{-1}*
$[N_{0002}][NO_3]$	0.954	1.120	1.100	0.460	---	---
$[C_4C_1im][SbF_6]$	0.673	1.039	0.639	0.146	525.5	1069.7
$[C_4C_1im][BF_4]$	0.670	1.047	0.627	0.376	565.0	1204.5
$[C_4C_1im][PF_6]$	0.669	1.032	0.634	0.207	524.0	1158.1
$[C_4C_1im][OTf]$	0.656	1.006	0.625	0.464	577.0	1224.6
$[C_4C_1im][NTf_2]$	0.644	0.984	0.617	0.243	545.0	1187.8
$[C_4(CH_3\text{-}C^2)C_1im][BF_4]$	0.576	1.083	0.402	0.363	558.0	1204.5
$[C_4C_1py][NTf_2]$	0.544	0.954	0.427	0.252	545.0	1187.8
$[C_4(CH_3\text{-}C^2)C_1im][NTf_2]$	0.541	1.010	0.381	0.239	547.0	1187.8
H_2O	1.000	1.330	1.120	0.140	591.0	---
MeOH	0.762	0.730	1.050	0.610	589.0	---
CH_3CN	0.460	0.799	0.350	0.370	575.0	---
$(C_6H_5)CH_3$	0.100	0.532	-0.213	0.077	---	---

2.3.4 Water Uptake

Water uptake measurements are imperative for ILs since they are intrinsically hygroscopic. Anhydrous IL synthesis, leads to low water impurity levels (10s of *ppm*), however when stored in contact with atmospheric gases $H_2O_{(g)}$ is driven into $IL_{(l)}$ through gaseous/liquid equilibration (E2.3), with an IL-dependent equilibrium constant K_{H_2O}. Equilibrated water uptake into IL solution can be very significant and can reach up to 1.4 *%wt* $H_2O_{(l)}$ in even the most hydrophobic ILs,[102] modifying thermophysical properties such as acidity, density, viscosity etc. It is therefore imperative that pure IL stocks are dried and stored effectively with water contents known.

$$H_2O_{(g)} \overset{K_{H_2O}}{\longleftrightarrow} H_2O_{(g)} \qquad \text{E2.3}$$

Coulometric water content measurements (*Titroline 7500 KF, SI Analytics*) were made throughout this study to ensure accurate $[IL]_{(aq)}$ dilutions. The coulometric reagent used (*HYDRANAL®-Coulomat AF 7, Sigma-Aldrich*) contains base (imidazole), ROH (MeOH), SO_2 and I_2. Presence of $H_2O_{(l)}$ results in anodic oxidation of SO_2 by I_2 (E2.4). A constant current is driven between two electrode pairs, one of which features an ion selective membrane, blocking passage of $H_2O_{(g)}$ and nullifying E2.4. When a water-containing sample is inserted into the Coulometric reagent, differential potentials are observed for each electrode system as monitored by bipotentiometric chronopotentiometry (V-t). At the titration endpoint these potentials equalise sharply, indicating that $H_2O_{(l)}$ present in the sample has been consumed. Water content quantification is accessible via consideration of the sample mass, the required titration time and knowledge that 2 *moles* of electrons are released per *mole* of $H_2O_{(l)}$.

$$im \cdot I_2 + im \cdot SO_2 + im + H_2O \overset{2e^-}{\longrightarrow} 2\,[HHim][I] + (O_3S)im \qquad \text{E2.4}$$

2.3.5 IL Acidity

2.3.5.1 Conventional *p*H Measurement Principles

Brönsted-Lowry theory[103, 104] states that the strength of an acid is best expressed as a pK_a value (E2.5) - a constant for a given temperature, usually 298 *K* - where a low (negative) value indicates high proton lability in solution ($pK_a[H_2SO_4]$ = -2.0; $pK_a[HSO_4^-]$ = 1.99).[5] Conversely, a high pK_a value for a conjugate acid (BH^+) indicates high basicity or ability to abstract a proton from a molecule/solution (pK_a(im) = 14.5; $pK_a(NH_3)$ = 9.3). Some species, such as butylimidazole (C_4im), are termed amphoteric since they possess both acidic hydrogens and basic nitrogen atoms with a lone pair of electrons capable of proton abstraction. It is noteworthy that ILs functionalised with SO_3H can be used to increase the Brönsted acidity of an IL.[105]

$$AH + B \rightleftharpoons BH^+ + A^-$$

$$K_a = \frac{\{BH^+\}\{A^-\}}{\{B\}\{AH\}} \qquad \text{E2.5}$$

$$pK_a = -log_{10}(K_a)$$

Lewis acid/base theory introduces an alternative type of acidity. As per E2.6, a Lewis acid can accept a pair of electrons into a vacant molecular orbital donated by a Lewis base, to form an adduct. Many common IL anions are Lewis adducts and additionally imidazolium-based nitrogen may exhibit transient Lewis/Brönsted base properties.

$$PF_5 + F^- :\longrightarrow [F_5P - F]^-$$
$$BF_3 + F^- :\longrightarrow [F_3B - F]^-$$ E2.6

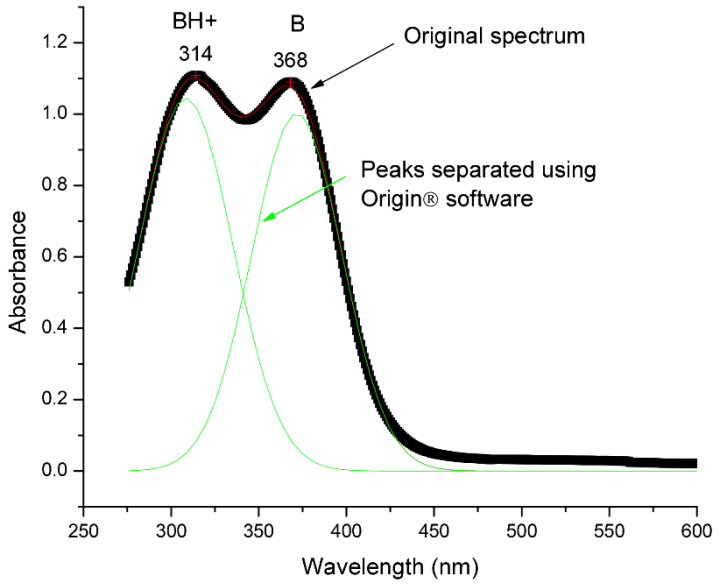
2.3.5.2 Hammett Acidity

Conventional measurement of *p*H in aqueous environments relies on proportionality of electrode potential, E(V), and proton activity. However, since the degree of solvent autoprotolysis (equilibrium free-$[H^+]_{(aq)}$) varies between solvents, *p*H values obtained for acid/base systems are not comparable across different solvents.

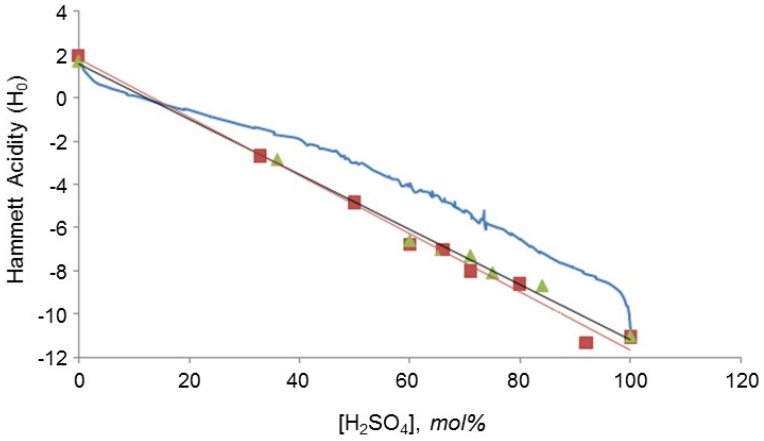
$$E(V) = E^{\ominus} + \frac{RT}{zF}\ln a_{H^+} = E^{\ominus} - \frac{2.303T}{F}pH$$ E2.7

For this reason, an alternative measurement is used for non-aqueous species, including pure and low dilution ILs, where background $[H^+]$ is unknown. The Hammett acidity function[106] (H_0 - E2.8) directly and reliably measures the acidity of the solute IL at high concentrations, using the pK_a of a base (B) and its conjugate acid (BH^+) in high dilution aqueous media for a given temperature. Nitroaniline derivatives (pK_a -11 - 1) have reduced basicity due to electron withdrawing NO_2 groups, where basicity can be varied by other ring substituents. Such bases are used to probe acidity of solutes in non-aqueous environments, remaining partially protonated in strong acid and allowing $[BH^+]/[B]$ to be measured via UV-spectroscopy and concentration referenced (Beer-Lambert) extinction coefficients in solutions of fully protonated base (ε_+), completely unprotonated base (ε_0) and base with sample (ε) (E2.8).[7]

$$H_0 = pK_{BH^+} - log_{10}\left(\frac{[BH^+]}{[B]}\right)$$
$$\frac{[BH^+]}{[B]} = \frac{\varepsilon_0 - \varepsilon}{\varepsilon - \varepsilon_+}$$ E2.8



▲ Figure 2.11 - Sample UV-visible spectrum for 4-nitrotoluene in neat $H_2SO_{4(l)}$, displaying the deconvolution of Beer-Lambert peaks due to the base in protonated (BH^+) and unprotonated (B) forms.[7]

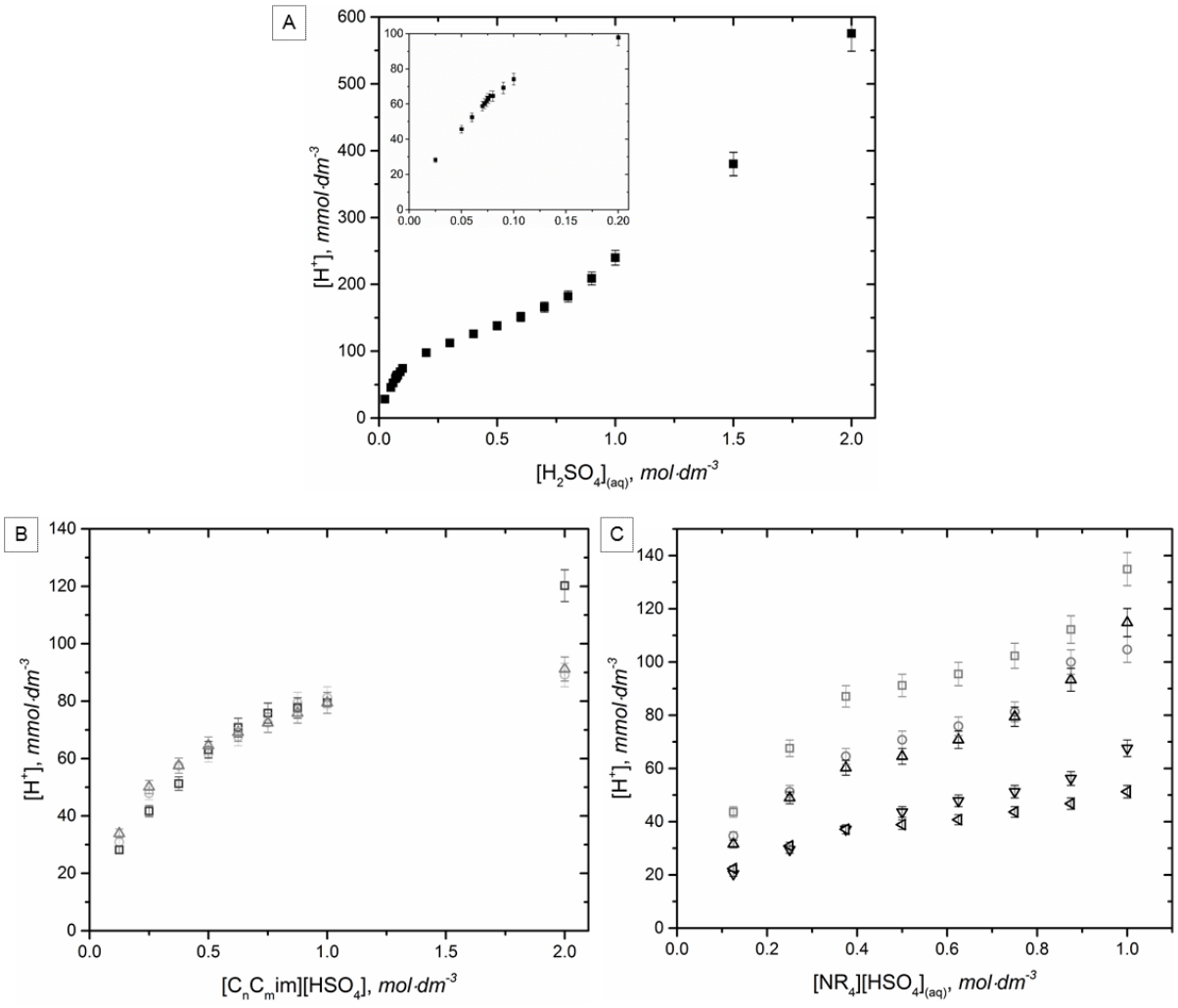


▲ Figure 2.12 - Linear variation of IL Hammett acidity of $[C_4C_1im][HSO_4]$ (■) and $[C_4Him][HSO_4]$ (▲) solutions upon addition of 0-100 *mol%* H_2SO_4, shown in comparison to the sigmoidal variation of (IL-free) $H_2SO_{4(aq)}$ solutions (blue - no markers) as a result of clustering effects.[7]

2.3.5.3 *p*H of ILs Used in this Study

For convenience, conventional electrode potential based *p*H measurements will be made during this study, however there are some important consequences of considering the true (Hammett) acidity of BAILs, and in particular that of $[C_nC_mim][HSO_4]_{(aq)}$. A key result of a doctoral research thesis, observed that the Hammett acidity of pure $[C_4C_1im][HSO_4]_{(aq)}$ (H_0 = 1.96; $[HSO_4]$ = 5.38 $mol{\cdot}dm^{-3}$) and $[C_4Him][HSO_4]_{(aq)}$ (H_0 = 1.72; $[HSO_4]$ = 5.80 $mol{\cdot}dm^{-3}$) are equivalent at equal anion concentration and vary linearly in excesses of $H_2SO_{4(aq)}$ acid or imidazole base (0-100 *mol%* - figure 2.12).[7]

The conventional *p*H-indicated free-$[H^+]_{(aq)}$ for selected ILs used and $H_2SO_{4(aq)}$ in the relevant concentration range are shown in figure 2.13. Solutions were mixed using ultra-pure water (*Purite Select Fusion 160*; *p*H 6.52) and measurements were made with a commercial *p*H meter (*Mettler Toledo SevenEasy*) following 120 *s* equilibration within a narrow ambient temperature range (24.0 ± 1.0 °*C*). Importantly, the above Hammett acidity function considerations highlight that measured variations in IL acidity at relatively high $[IL]_{(aq)}$ (2 *mol·dm*$^{-3}$; figure 2.13A) are not an accurate representation of free $[H^+]_{(aq)}$. Therefore acidity of $[C_nC_mim][HSO_4]_{(aq)}$ can be considered equivalent. Subsequently, the *p*H equivalence of 450 *mmol·dm*$^{-3}$ $[C_nC_mim][HSO_4]_{(aq)}$ and 75 *mmol·dm*$^{-3}$ $[H_2SO_4]_{(aq)}$ was determined (*p*H 1.2; ~60 *mmol·dm*$^{-3}$). The selected NR_4^+-based ILs have variable acidities at equivalent concentrations on account of the additional influence of the acidity of the protic cation (figure 2.13C), with acidities which vary by much higher magnitudes than expected for the aforementioned effect.



▲ Figure 2.13 - Free $[H^+]_{(aq)}$ concentration of aqueous acid solutions recorded at 24.0 ± 0.5 °*C* for (A) $H_2SO_{4(aq)}$ (B) $[C_nC_mim][HSO_4]_{(aq)}$ and (C) $NR_4{\cdot}HSO_{4(aq)}$. (△ $[C_4C_1im][HSO_4]$; ○ $[C_2C_1im][HSO_4]$; □ $[C_4Him][HSO_4]$; ○ $EtNH_3{\cdot}HSO_4$; □ $Et_3NH{\cdot}HSO_4$; △ $(EtOH)NH_3{\cdot}HSO_4$; ▽ $(EtOH)_3NH{\cdot}HSO_4$; ◁ $(^iPrOH)_3NH{\cdot}HSO_4$)

2.3.6 IL Rheology

The typically high viscosities of ILs (50-5000 *mPa·s*) make non-acidic ILs potentially useful as lubricants,[107] however these high viscosities can cause problems with chemical handling or when the application requires rapid microscopic transport dynamics. As such, it is often extremely important to consider the thermophysical properties of all pure ILs and their binary aqueous mixtures. Additionally, as discussed in section 2.1.2, hole theory is required to adequately model low dilution $IL_{(aq)}$ viscosities.

▼ Table 2.4 - Physical data for selected pure $[C_nC_mim]^+$ (293 *K*) and $[NR_4]^+$ (298 *K*) Brönsted acidic ILs at atmospheric pressure.[108, 109] [$u(T)$ = 0.01 *K*; $u(\rho)$ = 3x10^{-4} *g·cm*$^{-3}$; $u(\eta)$ = 0.4 *% mPa·s*; 95 *%* confidence]

BAIL	Density (ρ), *g·cm*$^{-3}$	Viscosity (η), *mPa·s*
$[(HSO_3)^3C_3C_1im][HSO_4]_{(l)}$	1.5017	1296
$[(HSO_3)^4C_4C_1im][HSO_4]_{(l)}$	1.4647	1427
$[(HSO_3)^3C_3C_4im][HSO_4]_{(l)}$	1.3469	1000
$[(HSO_3)^4C_4C_4im][HSO_4]_{(l)}$	1.3611	1592
$[Et_2NH_2][HSO_4]_{(l)}$	1.2840	34.1
$[Et_3NH][HSO_4]_{(l)}$	1.1429	235
$[Me_3NH][HSO_4]_{(l)}$	1.4676	5.1

2.3.6.1 Measurement Procedure

Rheology measurements were conducted on a TA Instruments AR-2000 Rheometer equipped with a thermocoupled plate (Peltier; +/-0.01 °*C* temperature resolution) and rotating cone geometry (d = 40 *mm*; θ = 4°; h_{trunc} = 53 *μm*). In a typical viscosity measurement, shear stress and temperature are held constant (1 *Pa*; 298 *K*) for 180 *s* to avoid sample lag effects. Experiments were conducted under a flow of dry $N_{2(g)}$ with coulometric Karl-Fischer analysis to confirm pure $IL_{(l)}$ water contents. η-T profiling was conducted for 0→80→0 °*C* with a uniform temperature ramp of 5 °*C·min*$^{-1}$. Each procedure allowed 60 *s* of initial temperature equilibration for sample pre-conditioning. The described procedure was found suitable to correctly measure the viscosity of several test samples to <1 *%* error from literature values over a wide viscosity range (table 2.5). The data presented will be discussed in reference to experimental electrochemistry and simulations in chapter 4.

▼ Table 2.5 - Selected viscosity measurements for validation of chosen rheological procedure in comparison to literature values.[5] (1 *Pa [sheer]*; 298.15 *K*; *u*(*T*) = 0.01 *K*).

BAIL	Lit. Viscosity (*η*)	Measured Viscosity (*η*), *mPa·s* ± 1 *%*,
(blank)	0	-0.012
$H_2O_{(l)}$	0.899	0.904
$(C_6H_5)CH_3$	0.550	0.542
S600 calibration oil	1273	1281

▼ Table 2.6 - Dynamic viscosity measurements for pure $[C_nC_m im]^+$ ILs to be used in lixiviant trials (1 *Pa [sheer]*; 298.15 *K*; *u*(*T*) = 0.01 *K*).

BAIL	Density (*ρ*), *g·cm⁻³*	Viscosity (*η*), *mPa·s*	Lit. Viscosity, *mPa·s* (BASF)	Water content, *% wt.*
$[C_4Him][HSO_4]_{(l)}$	1.278	5690 (± 1.2 *%*)	---	0.165 ± 0.030
$[C_2C_1im][HSO_4]_{(l)}$	1.368	1260 (± 1.4 *%*)	1650	0.169 ± 0.011
$[C_4C_1im][HSO_4]_{(l)}$	1.279	2860 (± 1.2 *%*)	4320	0.169 ± 0.030
$[C_2C_1im][EtSO_4]_{(l)}$	1.239	80.0 (± 0.5 *%*)	---	---

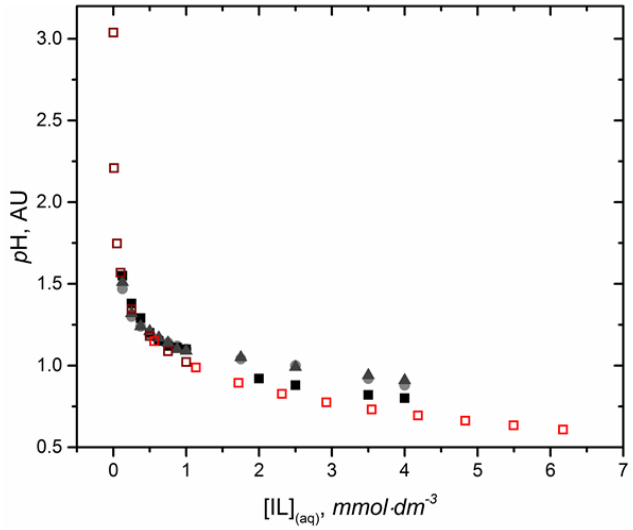
2.4 Advanced Consideration of $IL_{(aq)}$ *p*H

Hammett acidity (H_0) measurements (section 2.3.5) have revealed that there is negligible intrinsic acidity difference between equivalent $[HSO_4]$ concentrations of $[C_4Him][HSO_4]_{(aq)}$ and $[C_4C_1im][HSO_4]_{(aq)}$, since each conjugate base derived from imidazole (im; *e.g.* C_4im) is highly basic at the N position (pK_a = 18.6).[110] Therefore N-protic im^+ has negligible impact on *p*H[7] - an evaluation that can be extended to both $[C_1pip]$ and $[C_1C_1pz]$ at equivalent $[HSO_4]$ concentration. Proof of this concept, can be judged from UV-visible control experiments, which demonstrate that $[C_4Him]^+$ can have no Cu-coordinating role at low leach-typical *p*H~1, since it is fully protonated. Yet, as section 2.7.4 illustrates, Cu has important and dominant complexing interactions with its conjugate base (C_4im) at higher *p*H.

As mentioned previously, electrode potential-based *p*H measurements can misrepresent $IL_{(aq)}$ acidity - particularly at high $[IL]_{(aq)}$ as depicted by figure 2.14 for $[C_2C_1im][HSO_4]_{(aq)}$, $[C_4Him][HSO_4]_{(aq)}$ and $[C_4C_1im][HSO_4]_{(aq)}$, in comparison to *p*H measurements for $NaHSO_4$ and theoretical $[HSO_4^-]$ values computed by solving E2.10 and $K_{a,HSO4}$ = 1.99.[111]

$$K_a = \frac{[H^+] \cdot [A^-]}{[HA]} = \frac{[H^+]^2}{[HA]} = \frac{[H^+]^2}{[HA]_0 - [H^+]} \qquad \text{E2.9}$$

$$[H^+]^2 + K_a \cdot [H^+] - K_a \cdot [HA]_0 = 0 \qquad \text{E2.10}$$



▲ Figure 2.14 - Free-$[H^+]_{(aq)}$ for $IL_{(aq)}$ as indicated by conventional electrode potential-based *p*H measurements. (● $[C_4C_1im][HSO_4]$; ■ $[C_4Him][HSO_4]$; ▲ $[C_2C_1im][HSO_4]$; □ $NaHSO_4$; □ HSO_4^- (theoretical))

An analytic approach was undertaken to discover the origin of the above indicated differences in $IL_{(aq)}$ acidity at equal $HSO_4^-{}_{(aq)}$ concentration. *p*H electrodes indirectly measure proton activity a_{H+} (section 2.3.5), whereby the proton activity coefficient (γ_{H+}) is assumed constant in high dilution aqueous environments (E2.11). In actuality, γ_{H+} is a function of medium permittivity (ε_r) and analysis of the Born solvation energy can be used to evaluate whether permittivity variations are responsible for the *p*H deviations observed in figure 2.14.

$$pH = -log_{10}\{H^+\} = -log_{10}(a_{H^+}) = -log_{10}\left(\gamma_{H^+} \cdot \frac{b_{H^+}}{b^{\ominus}}\right) \approx -log_{10}(\gamma_{H^+} \cdot [H^+]) \qquad \text{E2.11}$$

2.4.1 Born Solvation Energy Theory

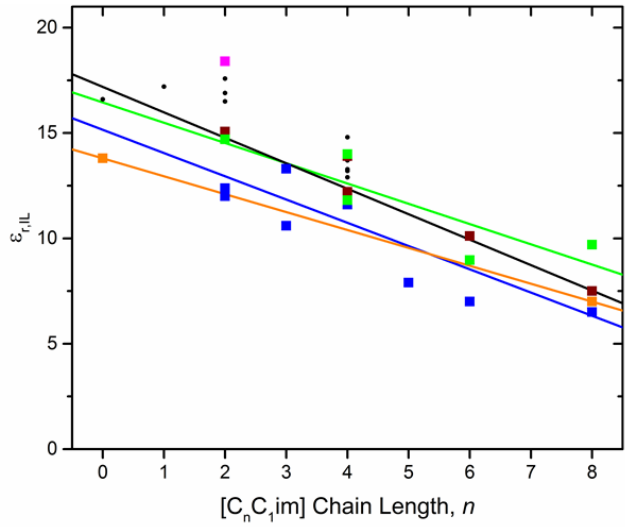
Gibbs free energy of formation ($\Delta_f G^{\ominus}$) of an ion in a given medium is a function of the properties of both the ion and solvent.[111] In the case of $H^+_{(aq)}$ in the presence of significant $IL_{(aq)}$ mole fractions, $\Delta_f G^{\ominus}$ provides a measure of the spontaneity of ion formation and therefore the effective acidity of the solution medium. Max Born derived an expression for the Gibbs free energy associated with the solvation of an ion by equating it with the electrical work done in bringing an ion from vacuum ($\varepsilon=\varepsilon_o$), into a solvent medium ($\varepsilon=\varepsilon_r \cdot \varepsilon_o$ - E2.12). Multiplying by Avogadro's constant to produce a molar quantity and computing the difference between the work done in charging the ion in each set of surroundings results in the Born equation (E2.13).

$$w = \int_0^{ze} \phi \cdot dq = \frac{1}{4\pi \cdot \varepsilon \cdot r} \cdot \int_0^{ze} q \cdot dq = \frac{{z_i}^2 \cdot e^2}{8\pi \cdot \varepsilon \cdot r_i} \qquad \text{E2.12}$$

$$\Delta_{solv}G^{\ominus} = w_{M,solvent} - w_{M,vacuum} = -\frac{{z_i}^2 \cdot e^2 \cdot N_A}{8\pi \cdot \varepsilon_0 \cdot r_i} \cdot \left(1 - \frac{1}{\varepsilon_r}\right) \quad \text{E2.13}$$

$$\Delta(\Delta_{solv}G^{\ominus}) = -\frac{{z_i}^2 \cdot e^2 \cdot N_A}{8\pi \cdot \varepsilon_0 \cdot r_i} \cdot \left(\frac{1}{\varepsilon_{r,H_2O}} - \frac{1}{\varepsilon_{r,IL_{(aq)}}}\right) \quad \text{E2.14}$$

As discussed above, a change in the Born solvation energy would indicate that the medium permittivity is causing deviation from the theoretical *p*H expected at known $[HSO_4^-]_{(aq)}$. The quantity of interest is therefore the difference in Born solvation energy, $\Delta(\Delta_{solv}G^{\ominus})$, between a purely aqueous medium and that of the high concentration $IL_{(aq)}$ solution (E2.14). Use of this expression requires relative permittivity data for the ILs of interest, where figure 2.15 illustrates the available data for related ILs. In absence of available HSO_4-IL permittivity data, the similar slopes of change in permittivity as a function of imidazolium alkyl chain length (n; $[C_nC_1im][HSO_4]$) was used to estimate permittivity values for the pure $IL_{(l)}$ ($\varepsilon_{r,pure}$; table 2.7).



▲ Figure 2.15 - Relative permittivity data for pure $[C_nC_1im]$ ILs with various alkyl chain lengths. [Data from work of H. Weingartner[112]] (■ HSO_4; ■ Cl; ■ PF_6; ■ BF_4; ■ NTf_2; ● Others)

When the proton ionic radius (r_i) is taken as 1.02 *Å*,[113] and the permittivity of binary $IL_{(aq)}$ systems are assumed to vary linearly with x_{IL}, $\Delta(\Delta_{solv}G^{\ominus})$ is on the order of 350 $J{\cdot}mol^{-1}$ (table 2.7). Despite several necessary assumptions, this treatment signifies that assumption of pure aqueous permittivity is invalid for moderate-high $[IL]_{(aq)}$. Thus, differences in ionic solvation can be concluded to be to have an influence on measured *p*H - where reported IL ion pairing effects[114, 115] further contribute to reduction in proton activity responsible for $IL_{(aq)}$ *p*H values which are larger than theoretical expectation (figure 2.14). An analytical equation was derived in order to find predicted values of $K_{a,3}$ (E2.18) which appear to converge to a solution, however, this treatment suggested low pK_a values on the order of -1>x>1, which are unreasonable values in this case therefore further treatment was abandoned.

$$H_2SO_4 \overset{K_{a,1}}{\longleftrightarrow} H^+ + HSO_4^- \quad \text{E2.15}$$

$$HSO_4 \overset{K_{a,2}}{\longleftrightarrow} H^+ + SO_4^{2-} \quad \text{E2.16}$$

$$IL^+ - H \overset{K_{a,3}}{\longleftrightarrow} H^+ + IL \quad \text{E2.17}$$

$$[H^+]^4 + \left(K_{a,1} + K_{a,3} + [HSO_4^-]_0\right) \cdot [H^+]^3 + \left(K_{a,1}K_{a,2} + K_{a,1}K_{a,3} - [HSO_4^-]_0\right) \cdot [H^+]^2 + \left(K_{a,1}K_{a,3} - K_{a,1}K_{a,2} \cdot [HSO_4^-]_0\right) \cdot [H^+] - \left(K_{a,1}K_{a,2}K_{a,3} + K_{a,3}\right) \cdot [HSO_4^-]_0 = 0 \quad \text{E2.18}$$

▼ Table 2.7 – Summary of theoretical permittivity analysis of $[C_nC_mim][HSO_4]_{(aq)}$ binary solutions. (x_{IL} = 0.05; $[IL]_{(aq)}$ ~2 *mol·dm^{-3}*; $\varepsilon_{r,H2O}$ = 78; $\Delta_{solv}G^e_{H2O}$ = -672 *kJ·mol^{-1}*)

Medium	$\varepsilon_{r,pure}$	$\varepsilon_{r,IL(aq)}$	$\Delta(\Delta_{solv}G^e)$, *J·mol^{-1}*
$[C_4C_1im][HSO_4]_{(aq)}$	16.2	74.9	353
$[C_4Him][HSO_4]_{(aq)}$	17.3	75.0	360
$[HHim][HSO_4]_{(aq)}$	20.6	75.1	332

2.5 $CuFeS_{2(s)}$ Processing

Commercially sourced $CuFeS_{2(s)}$ ore (*Alfa Aesar*) is milled manually in 20 *g* scale batches and dry-sieved to produce a 38 - 75 *μm* particle size fraction (*Endecotts*). The freshly powdered $CuFeS_{2(s)}$ is stored under purified $Ar_{(g)}$ after 30 minutes of atmospheric purging. The process is repeated whenever the atmospheric seal is broken. This measure was deemed necessary to maximise control of $CuFeS_{2(s)}$ surface oxidation, in order to gain maximum consistency in $CuFeS_{2(s)}$ surface chemistry prior to leaching (see section 1.2.4 and 6.3.6). Target masses of $CuFeS_{2(s)}$ used in experiments have been weighed with a consistent precision of +/- 0.5 *mg*. These <1 *%* mass variation uncertainties will be neglected, unless otherwise stated.

2.5.1 $CuFeS_{2(s)}$ Mineralogical Analysis

The powdered $CuFeS_{2(s)}$ sample may be completely dissolved (or 'digested') through a standard acid-attack protocol, developed by specialists within the Imperial College Earth Science and Engineering departments as compiled from literature sources.[116, 117] In the case of $CuFeS_{2(s)}$, it was found that regularly employed $HClO_4$ was unnecessary to achieve complete dissolution, thus a nitric-hydrochloric aquaregia mixture was used. 200 *mg* $CuFeS_{2(s)}$ is immersed in 10 *mL* of aquaregia (3:1 *v/v*; 69 *%wt* $HNO_{3(aq)}$: 37 *%wt* $HCl_{(aq)}$) for 24 *hrs* with agitation. The resultant media is subsequently diluted in ultra-pure H_2O and prepared for ICP-AES elemental analysis as described in section 2.7.2.2.

$CuFeS_{2(s)}$ purity is judged via the ICP-AES determined metal ion concentration in comparison to the theoretical maximum concentration. Table 2.8 displays a typical compositional analysis for commercial $CuFeS_{2(s)}$, indicating that the selected ore is stoichiometrically >90 *%* pure, with intersample variabilities up to ~5 *%*. It is noteworthy that [Fe] levels are occasionally discovered to be >100 *%* of theoretical composition, in agreement with the previous observation of Fe-rich surfaces on unleached $CuFeS_{2(s)}$ (section 1.2.4).

▼ Table 2.8 - ICP-AES mineral composition for independent 200 *mg* $CuFeS_{2(s)}$ samples digested in 10 *mL* aquaregia. Values are given as *%* of the maximum theoretical Cu and Fe concentration (109 $mmol \cdot dm^{-3}$) ± σ.

Digestion ID	ICP-AES ID	ICP-AES [Cu]	Digestion Average [Cu]	Overall Average [Cu]	ICP-AES [Fe]	Digestion Average [Fe]	Overall Average [Fe]
	#1	92.1 ± 0.1			96.3 ± 0.6		
Sample 1	#2	91.6 ± 0.4	92.1 ± 0.9		96.2 ± 1.2	96.3 ± 1.4	
	#3	92.6 ± 0.4			96.3 ± 1.5		
	#1	97.0 ± 0.3			100.9 ± 0.4		
Sample 2	#2	96.8 ± 0.2	96.9 ± 0.1	93.3 ± 3.6	100.2 ± 1.4	100.3 ± 1.1	96.9 ± 4.6
	#3	97.0 ± 0.3			99.7 ± 0.5		
	#1	91.2 ± 0.1			94.5 ± 0.7		
Sample 3	#2	90.9 ± 0.2	90.9 ± 0.5		94.5 ± 1.4	94.1 ± 1.9	
	#3	90.6 ± 0.2			93.2 ± 1.0		

An X-ray fluorescence (XRF) study, made in collaboration with colleagues, also reveals similar compositional estimates for 50 *mg* of unleached powdered $CuFeS_{2(s)}$ (table 2.9). Data shows that the constituent atoms of $CuFeS_{2(s)}$ are responsible for 89.9 *mol%* of the 50 *mg* sample studied. It is noteworthy that Cu and Fe mole fractions (*mol%*) are close to the theoretical 25 *%* for pure $CuFeS_{2(s)}$ - however (ignoring any sulfur loss from the bulk structure) it is pertinent that $CuFeS_{2(s)}$ content of this particular sample is ≤77.4 *%*, calculated by doubling sulfur mole fraction.

The data featured in this section serves to highlight that ore samples often show high variability in terms of composition and gangue material - emphasising the importance of considering sample-to-sample variation within typical leach studies (section 6.2.1). For the purposes of calculating metal recoveries, it will be assumed that $CuFeS_{2(s)}$ is pure and that $n(CuFeS_{2(s)})$ defines the maximum recoverable Cu and Fe. Additionally, since experiments were conducted using only equally processed $CuFeS_{2(s)}$ from the same large powdered batch, compositional variations within a single experiment can be largely negated and will not be discussed unless specifically relevant to the outcome of the experiment.

SEM/EDX studies are also able to offer insight into the surface composition of $CuFeS_{2(s)}$ in a variety of states. In unleached $CuFeS_{2(s)}$ studies generally indicate similar relative surface Cu, Fe and S

levels, alongside identification of common porphyry silicates and many of the trace impurities identified in table 2.9. EDX also identifies surfaces dominated by carbon and oxygen, as discussed in more detail later from the perspective of leached $CuFeS_{2(s)}$ interfaces (section 5.5).

▼ Table 2.9 - XRF determined composition for a 51.0 *mg* sample of commercially sourced $CuFeS_{2(s)}$ - analysed and reproduced with permission of former colleague, Dr E. J.Spadafora.

	Cu	Fe	S	Si	P	Ca	Al	Mg	Co
%wt	35.0	31.9	27.2	2.85	1.62	0.67	0.60	0.38	0.21
%mol	25.1	26.1	38.7	4.63	2.39	0.76	1.01	0.71	0.16

	Zn	Mn	Cl	Ni	K	Zr	Ag	Other trace:
%wt	0.16	0.1	0.08	0.08	0.05	0.03	0.03	Sr; Cd; Mo; Rb
%mol	0.16	0.08	0.10	0.06	0.06	0.02	0.01	

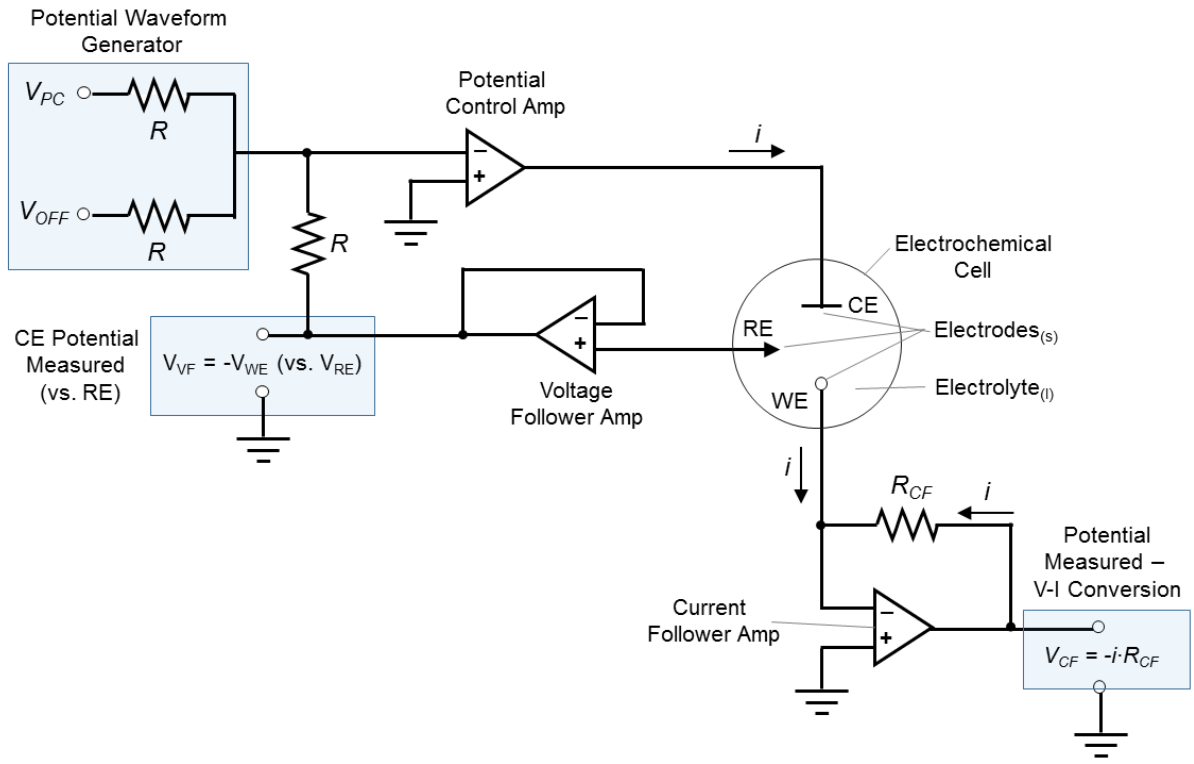
2.6 Electrochemistry

2.6.1 Potentiostatic Electrochemistry

All potentiostatic electrochemistry was carried out using two different bipotentiostatic devices (*CH Instruments 700E*; *Ivium Compacstat*) the latter of which has advantages of analogue voltammetry and programmable functionality (section 3.2). As figure 2.16 illustrates, an electrochemical cell is comprised of electrodes and electrolyte, which contains the electroactive species of interest. Potentials are applied at the counter electrode (CE) with respect to a stable reference electrode (RE). Since the working electrode is grounded, the modified potential at CE creates a potential difference whereby chemical work (W) can be done (E2.19). If there exists means of electron transfer at the electrode-electrolyte interface then a current (i) will flow, which is inversely proportional to the electrical resistance of the solution (R_s) as in E2.20. This current is measured indirectly by a V-I converter connected at the working electrode and is related to the actual potential applied (V_{VF}) to create primary 2D I-V data, which may undergo further technique-dependent processing.

$$V_{VF} = \frac{W}{Q} \qquad \text{E2.19}$$

$$i = -\frac{V_{CF}}{R_s} \qquad \text{E2.20}$$



▲ Figure 2.16 - Simplified schematic diagram of the internal electronics of a modern potentiostat, highlighting the key positions for application and subsequent measurement of potentials. (image design from instrument details)

2.6.1.1 Reference Electrode (RE)

When designing an electrochemical cell, the selection of compatible electrodes and electrolytes are key. Firstly, a suitable reference electrode is chosen with consistent composition in order to maintain a constant electrode potential. The standard hydrogen electrode (E2.21) is the benchmark for the potential scale (i.e. $E^{\theta} = 0\ V$ at 298 *K*), however it is an inconvenient choice for many applications since a{$H_{2(g)}$} must equal 1.

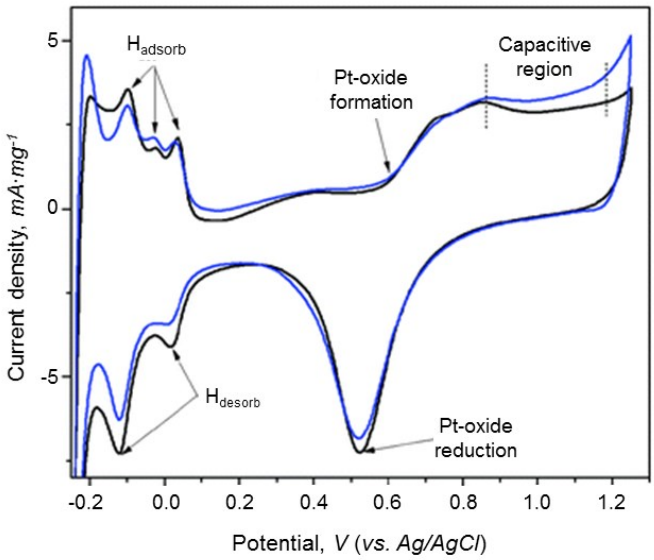
$$2H^+ + 2e^- \rightarrow H_2\ ; \qquad Pt_{(s)} \,|\, H_{2(g)} \,|\, H^+{}_{(aq)} \qquad (a = 1) \qquad E^{\theta} = 0\ V \qquad \text{E2.21}$$

When working in aqueous environments, a more convenient reference electrode is $Ag/AgCl_{(s)}$ immersed in saturated 3M $KCl_{(aq)}$ solution. This reference half-cell can be fabricated by chlorinating $H_{2(g)}$-torch annealed $Ag_{(s)}$ wire, using chronopotentiometry (1 $mol{\cdot}dm^{-3}$ $HCl_{(aq)}$; 0.5 *mA*; 30 *min*) to drive a constant oxidation current toward the $Ag_{(s)}$ anode - reversing the standard reduction reaction shown in E2.22. $AgCl_{(s)}$ has a low solubility product (low K_{sp}) and thus is sparingly soluble in water, maintaining a consistent electrode potential that does not drift appreciably over time - $AgCl_{(s)}$ is however photodegradable and therefore reference electrodes should be stored and recoated appropriately. High quality fritted Ag/AgCl REs (*IJ Cambria*) are commercially available and used throughout this work, unless otherwise stated.

$$AgCl + e^- \rightarrow Ag + Cl^- \; ; \qquad Ag_{(s)} \,|\, AgCl_{(s)} \,|sat.KCl_{(aq)} \qquad E^\theta = 0.197\,V \qquad \text{E2.22}$$

2.6.1.2 Selection of Working and Counter Electrode (WE/CE)

Selection of WE and CE is largely decided by the nature of the electrolytic medium of interest. Lixiviant solutions are highly acidic (*p*H ~1), containing high $[SO_4^{2-}]_{(aq)}$ with the expectation of moderate $[Cu^{2+}]_{(aq)}$ and $[Fe^{2+}]/[Fe^{3+}]$. $Pt_{(s)}$ is an inert conductive material, compatible with (spectator) $SO_4^{2-}{}_{(aq)}$ and able to exchange electrons directly with all aforementioned metallic$_{(aq)}$ ions, thus $Pt_{s)}$ is a suitable choice as both WE and CE. Although these electrodes are comprised of the same materials, a relatively much larger coiled-CE is often chosen with large surface area, such that current flow at CE never becomes limiting.



▲ Figure 2.17 - Cyclic voltammograms at $Pt_{(s)}$ (black) and CNT|CeO_2|$Pt_{(s)}$ (blue) electrodes in $Ar_{(g)}$ purged 0.5 *mol·dm*$^{-3}$ $H_2SO_{4(aq)}$ at scan rate of 50 *mV·s*$^{-1}$.[118]

Figure 2.17 displays example cyclic voltammetry (CV) scans for nanostructured $Pt_{(s)}$ electrodes, showing various Pt-H and Pt-O processes, which must be treated as a background signal to additional leachate-derived electrochemical processes. The high cathodic (negative) currents observed at $Pt_{(s)}$ in acid at potentials <-0.2 *V* vs Ag/AgCl are due to $H^+_{(aq)}$ reduction to $H_{2(g)}$, consuming large quantities of electrons sourced from the $Pt_{(s)}$ WE. This fact can cause issues with characterising processes that occur at similar potentials, which is discussed further in sections 2.6.2 and 4.3.

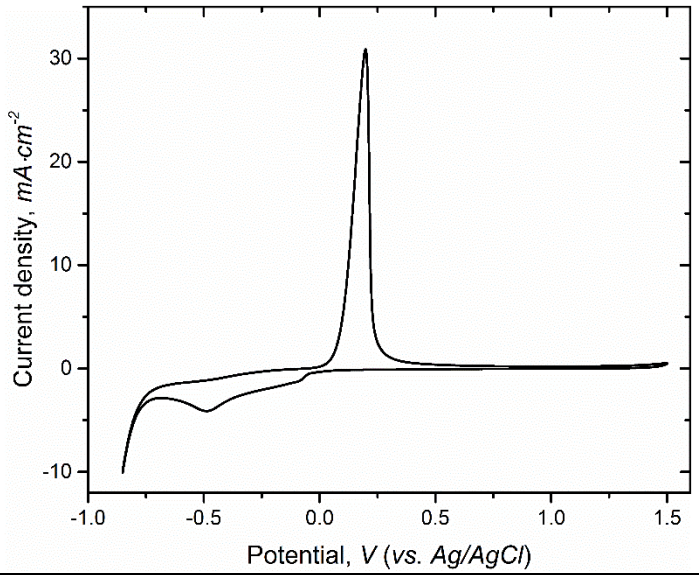
2.6.1.3 Electrode Probe Fabrication

A key challenge to WE design is the determination of active surface areas and interfacial geometry of the electrode. A flat, glass-encased double Pt disk electrode system (A_{WE} = A_{CE} = 7.85 x 10^{-3}

cm^2) is fabricated through the glass-blowing of soda glass tubes (d_{out} =5 *mm*, d_{in}=3.2 *mm*, VWR International) in a $H_{2(g)}$ flame to encase two high purity Pt wires (99.99 *%*, d=1 *mm*, *Goodfellow*). Disk electrodes are revealed using SiC paper (180/320/800 *grit*, *Struers*), with further fine-polishing prior to each use (*LaboPol-6, Struers*) using a range of alumina nanoparticle suspensions (200/100/50 nm AP-A, *Struers*). Following polishing, the electrode probe is thoroughly rinsed with distilled water and electrochemically cleaned using high potential cyclic voltammetry as outlined in section 2.7.3.2.

2.6.2 Characterisation of the Cu/Cu^{2+} Redox Couple

As E2.21 and figure 2.17 indicate, $Pt_{(s)}$ catalyses the generation of $H_{2(g)}$ at potentials < 0 *V* (vs. SHE) in acidic solutions with high $[H^+]_{(aq)}$, which can interfere with analysis of processes occurring at similar potentials. A glassy carbon WE (d = 3 *mm*, *IJ Cambria*), massive coiled-Pt CE and Ag/AgCl RE were chosen to investigate the voltammetric positioning of Cu/Cu^{2+} reduction and oxidation peaks. Glassy carbon electrodes exhibit low potential onset of $H^+/H_{2(g)}$ reduction (<0.75 *V* vs. Ag/AgCl), thus allowing for the cupric cathodic reduction (negative current) peak to be visualised alongside the associated anodic oxidation process (positive current - figure 2.18).



▲ Figure 2.18 - Cyclic voltammogram of glassy carbon disc WE (d=3 *mm*) in 0.5 *mol·dm*$^{-3}$ $H_2SO_{4(aq)}$ containing 10 *mmol·dm*$^{-3}$ $CuSO_{4(aq)}$. Average scan of six full potential cycles at 50 *mV·s*$^{-1}$ - (cathodic currents are positive).

Whilst the $Cu_{(s)}$ oxidation peak is an exhaustive process with onset at ~ 0 *V* (vs. Ag/AgCl) and terminated by 500 *mV*, the $Cu^{2+}_{(aq)}$ reduction process is broad and more complex, with onset at -50 *mV* and a peak-like $[Cu^{2+}]_{(aq)}$-dependent feature at -450 *mV*, the features of which are normally hidden in $Pt_{(s)}|Cu^{2+}_{(aq)}$ CV scans (figure 2.17).

2.6.3 Electrochemical Impedance Spectroscopy (EIS)

Electrochemical impedance spectroscopy (EIS) is a common electroanalytical tool used to determine the conductivity of solutes in aqueous solution. The interfacing conductive sample medium is modelled by the conventional series combination of an Ohmic solution resistance (R_s) and a capacitive component (C_{EDL}) representing charge phenomena associated with the electric double layer (EDL). R_s values are measured at high frequencies, where capacitive behaviour diminishes according to an inverse relation to applied frequency (E2.23), leaving resistive behaviour to dominate impedance response. An associated tendency of the phase angle towards 0 *radians* is observed in the impedance response (E2.24). Solution resistance values are related to solution conductivity (κ) via Ohm's law (E2.25) and the electrode geometric factor (GF).

$$|Z| = Z' + Z'' = R_s + \frac{1}{i\omega C_{EDL}} \qquad \text{E2.23}$$

$$\varphi = arctan\left(\frac{Z''}{Z'}\right) \qquad \text{E2.24}$$

$$R_s = GF \cdot \rho = GF.\frac{1}{\kappa} \qquad \text{E2.25}$$

Impedance spectra (5 *mV* ac, 30 sampled frequencies per logarithmic decade, 10^0-10^6 *Hz*) are recorded using the custom $Pt_{(s)}$ disc electrode (section 2.6.1.3), connecting one disc as a combined counter-reference electrode (vs. Pt CE/RE), after electrochemical $Pt_{(s)}$ cleaning and 60 *s* solution equilibration.

2.6.4 Analogue Probes

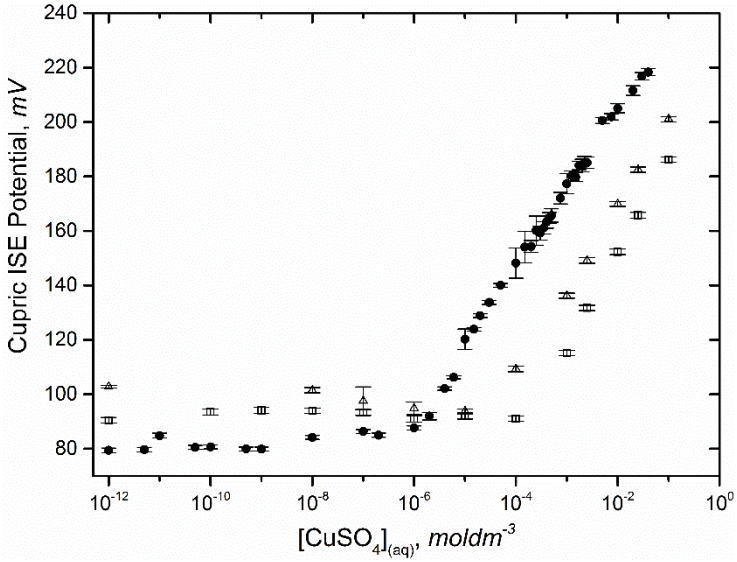
*p*H (0-14), temperature (-5 - 130 °*C*) and E_h (*V* vs. Ag/AgCl) are all measured simultaneously using an integrated double junction electrode probe (*InPro® 4800i*; *Mettler Toledo*) that is resistant to harsh chemical environments. The probe outputs three analogue current signals (0-20 *mA*) according to linear calibration ranges, which can be interpreted directly by a multi-channel sensor (*M800*; *Mettler Toledo*) allowing the output of up to six probes to be visualised. Data transfer to PC was achieved by transmitting the analogue probe signals to USB-enabled data acquisition modules (*NI cDAQ 9174; NI 9203; National Instruments*) with programmatic datalogging using *NI LabView®* (section 3.2.4).

Using similar techniques, cupric ISE output (section 2.7.1) was setup for automated datalogging. For example, results shown in figure 2.19 were produced via fully automated cycles completed on the robotic platform (section 3.2). The ground referenced analogue output (BNC - 0-20 *mA*) of the cupric ISE was transmitted to a separate BNC-enabled data acquisition device (*NI USB-6212 BNC*; *National Instruments*) before USB communication to *NI LabView®* for datalogging.

2.7 Copper Quantification Techniques

Central to lixiviant studies is the study of dissolution products, both in terms of quantification and chemical and physical characterisation. In this section, detection principles and experimental considerations of commonly employed $Cu_{(aq)}$ quantification techniques will be introduced, with reference to their advantages and disadvantages for use in this study.

2.7.1 Cupric Ion Selective Electrode (ISE)



▲Figure 2.19 - Recorded potential response of cupric ISE probe to varied $[CuSO_4]_{(aq)}$ in background 75 *mM* $[H_2SO_4]_{(aq)}$ (●), 450 *mmol·dm*$^{-3}$ $[NH_4.HSO_4]_{(aq)}$ (△) and 450 *mmol·dm*$^{-3}$ $[C_4Him][HSO_4]_{(aq)}$ (□).

A cupric ion selective electrode (ISE; *Cole Palmer*) is an attractive $Cu^{2+}{}_{(aq)}$ quantification tool for use in aqueous environments. However, the ISE was found to display significantly poorer detection capabilities in strongly coordinating $IL_{(aq)}$ media (figure 2.19). Flat-line indistinguishable sensor response was obtained for $[CuSO_4]_{(aq)}$ < 1 *µmol·dm*$^{-3}$ in 450 *mmol·dm*$^{-3}$ $IL_{(aq)}$ and ~100 *µmol·dm*$^{-3}$ Cu in 75 *mmol·dm*$^{-3}$ $H_2SO_{4(aq)}$. Above these lower $[Cu^{2+}]_{(aq)}$ detection limits, studied calibration plots exhibit near ideal Nernstian potential dependence of ~30 *mV* per $[Cu^{2+}]_{(aq)}$ decade (E2.26 - $H_2SO_{4(aq)}$ = 26.9 *mV*; $[C_4Him][HSO_4]_{(aq)}$ = 30.6 *mV*; $NH_4{\cdot}HSO_{4(aq)}$ = 31.7 *mV*). Thus, in strongly Cu-coordinating $IL_{(aq)}$ media low cupric detection limits are deemed unsuitable for the purpose of monitoring ambient $IL_{(aq)}$ leaching on timescales of <2 days.

$$\Delta E = E_2 - E_1 = \frac{RT}{zF} \cdot ln\left(\frac{a_{red,1}}{a_{red,2}} \cdot \frac{a_{ox,2}}{a_{ox,1}}\right) \approx \frac{RT}{zF} \cdot ln\left(\sim 1 \cdot \frac{a_{ox,2}}{a_{ox,1}}\right)$$

E2.26

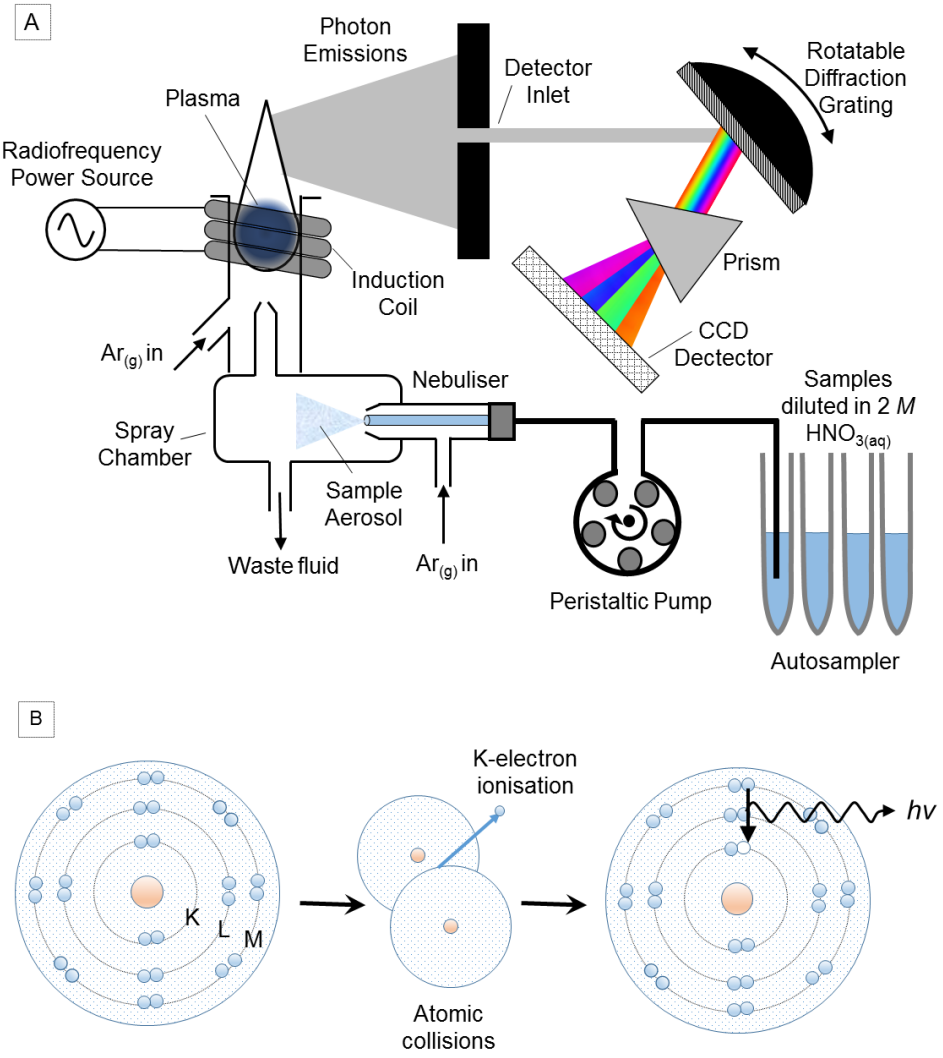
$$\Delta E = \frac{59.2 \times 10^{-3}}{z} \cdot log_{10}\left(\frac{a_{Cu^{2+},2}}{a_{Cu^{2+},1}}\right)$$

$$\Delta E_{Cu,dec} = \frac{59.2\times10^{-3}}{2} \cdot log_{10}\left(\frac{10}{1}\right) = \underline{29.6\times10^{-3}}\, V \cdot decade^{-1}$$

2.7.2 Inductively-Coupled Plasma Atomic Emission Spectroscopy (ICP-AES)

2.7.2.1 Detection Principle

ICP-AES differs from other emission spectroscopies by probing high energy photon emission resulting from nuclear collisions within a high temperature plasma (~7000 *K*). A high energy plasma state is often ignited through electromagnetic induction of $Ar_{(g)}$ using high frequency currents. Following ignition an $Ar_{(g)}$/sample mixture is nebulised to a fine droplet mist prior to injection into the plasma, where all introduced molecules become both atomised and ionised. High speed atomic collisions within the plasma eject low-lying K-shell electrons - causing the energetic relaxation of higher energy electrons to occupy the K-shell vacancies. This electronic cascade produces concomitant photon emission with energies characteristic of the element from which they originated. Elemental quantification is achieved through monitoring of photon counts rate (*cts/s*) observed at element characteristic wavelengths and with reference to count rates calibrations observed for standard solution of known analyte concentration.



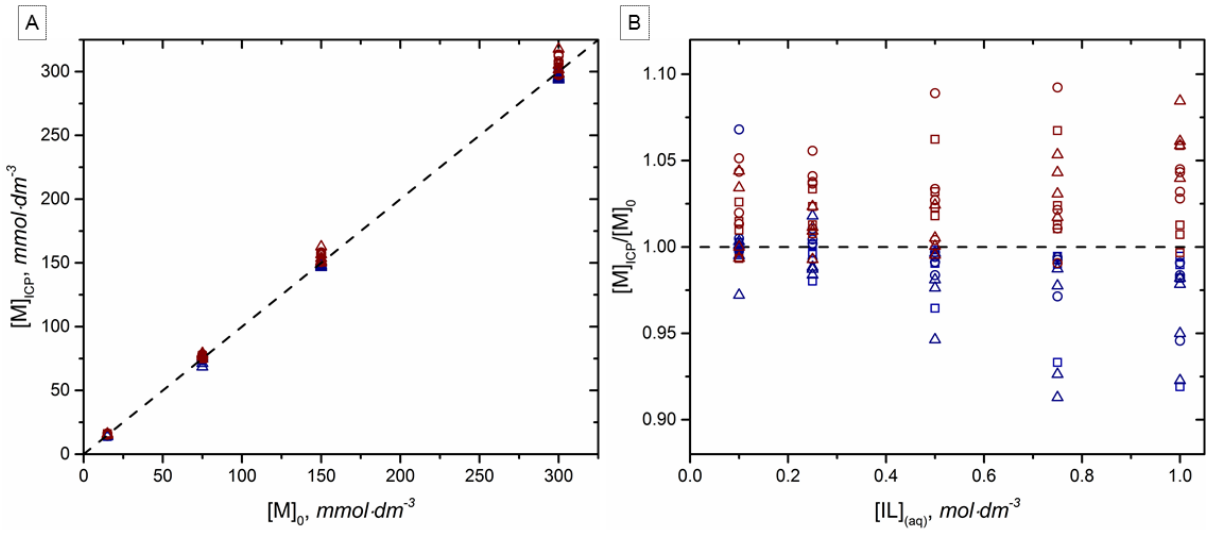
▲ Figure 2.20 - (A) Schematic overview of the internal operations involved in an ICP-AES spectrometer. (B) Schematic of K electron ejection through atomic collision in high temperature plasma (7000 *K*) followed by high energy photon (*hv*) emission from electronic relaxation to occupy K-shell vacancy.

2.7.2.2 ICP-AES Sample Preparation

Lixiviant/standard solutions are filtered (200 *nm* porous, *Acrodisc Supor*) to provide a leach completion end-point through removal of $CuFeS_{2(s)}$ and other particulate matter, before dilution onto a calibrated metal concentration range with 2 $mol{\cdot}dm^{-3}$ $HNO_{3(aq)}$. ICP-AES $[Cu]_{(aq)}$ and $[Fe]_{(aq)}$ measurements were made using non-interfering emission lines (Cu: 224.7 *nm*; Fe: 238.2 *nm*; *Thermo Scientific iCAP 7600*). Six standard solutions spanning the desired calibration range (blank - 2 $mmol{\cdot}dm^{-3}$) and each containing 2 $mol{\cdot}dm^{-3}$ $HNO_{3(aq)}$ and any IL background (to negate matrix effects - figure 2.21), were prepared from appropriate strength $[CuSO_4]_{(aq)}$ and $[Fe_2(SO_4)_3]_{(aq)}$ stock solutions. Emission count/sec calibration plots were accepted when returned with $R^2 > 0.999$.

2.7.2.3 Detection Limitations

Although, ICP-AES is an important tool for elemental quantification in solution, *ex-situ* solution sampling can be time-consuming and disruptive to leaching processes. Additionally, although operating well above the lower detection limit for these metals (5 $\mu g \cdot L^{-1}$; ~100 *nM*)[119] non-trivial calibrations and matrix effect corrections have previously been observed in complex solution environments.[120, 121] Thus it was necessary to confirm whether Cu and Fe quantification via ICP-AES was effected by the presence of ILs in ICP-AES samples. Following excellent $M_{(aq)}$ calibration (R^2 > 0.9998), 0-300 $mmol \cdot dm^{-3}$ $Cu^{2+}_{(aq)}$ and $Fe^{3+}_{(aq)}$ samples were created containing 0.1-1 $mol \cdot dm^{-3}$ $IL_{(aq)}$ - using stocks of $[C_4Him][HSO_4]_{(l)}$, $[C_4C_1im][HSO_4]_{(l)}$ and $[C_2C_1im][HSO_4]_{(l)}$.



▲ Figure 2.21 - Investigation of Cu (blue) and Fe (red) ICP-AES matrix effects in the indicated strength $[C_4Him][HSO_4]_{(aq)}$ (△), $[C_2C_1im][HSO_4]_{(aq)}$ (□) and $[C_4C_1im][HSO_4]_{(aq)}$ (○) solutions. (A) ICP-detected $[M]_{ICP}$ against nominal concentration $[M]_0$ (m_{Cu} = 0.992; m_{Fe} = 1.019). (B) Ratio of ICP-detected $[M]_{ICP}$ to formal concentration $[M]_0$.

Figure 2.21A indicates that [Cu]/[Fe] content impacts upon the absolute spread of data, where the dashed line indicates perfect detection of $[M]_{(aq)}$. A gradient <1 for $Cu_{(aq)}$ detection indicates that IL matrix effects generally lead to underestimation of [Cu] by approximately 1 %, whereas a gradient >1 indicates that IL matrix effects generally lead to the overestimation of [Fe] by ~1 %. This effect is further highlighted by figure 2.21B, where blue $Cu_{(aq)}$ markers generally fall at detection ratios <1 ($[M]_{ICP}/M_0$), whereas red $Fe_{(aq)}$ markers occupy detection ratios >1. Increases in $[IL]_{(aq)}$ can be seen to amplify spread of data in figure 2.21B, with total measurement discrepancies remaining <10 %. In order to minimise uncertainty in ICP-AES studies, calibration solutions were created containing equivalent quantities of $IL_{(aq)}$ as contained within the samples being tested.

Some solutes, such as Fe(II)$SO_{4(aq)}$ can be unstable in aqueous environments, oxidising to lower solubility ferric oxides, which can precipitate and cause poor Fe calibrations. Hence the calibration solute of choice should be highly soluble $Fe_2(SO_4)_{3(aq)}$ since Fe(III) is resistant to oxidation. Diluted ICP-AES samples may also be prone to $Fe^{2+}_{(aq)}$ oxidation since ferrous ions are a key thermodynamic end-product of $CuFeS_2$ dissolution (section 1.4). Subsequent solution oxidation may cause significant Fe losses from ICP-AES samples - therefore ICP-AES samples are always created a minimum time (ideally <6 *hrs*) prior to analysis to minimise this effect, however high acidity greatly increases $Fe^{2+}_{(aq)}$ solubility.

2.7.3 Anodic Stripping Voltammetry

Anodic/cathodic stripping voltammetry (ASV/CSV) are well-established quantification tools available to the electroanalytical scientist,[122-124] having been applied widely across many soluble metallic ions (Pb^{2+}, Cd^{2+}, Hg^{2+}, Cu^{2+} etc.) - including from the perspective of heavy metal monitoring/recovery from waste waters. ASV has many closely related procedures, which often vary in the shape of applied potential waveforms and parameter choices (e.g. square-wave[125]/differential pulse[126] stripping voltammetry).

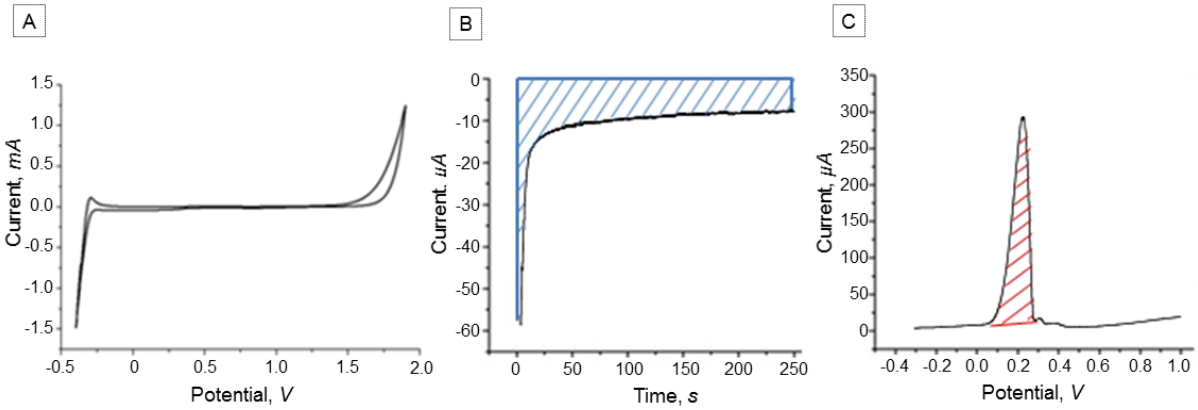
2.7.3.1 Detection Principle

In the absence of specific electrochemical processes, one would expect linear (Ohmic) i-V character in a conventional electrolyte. Upon introduction of an electroactive analyte, potential ranges will exist where electrons can be consumed/released by the analyte. As a result of modified analyte oxidation state, anodic/cathodic current peaks are observed signifying supplementary current contributions from the analyte electrochemistry (figure 2.18).

$$Q = \int_{t_1}^{t_2} i \cdot dt \qquad \text{E2.27}$$

After subtraction of background Ohmic currents and potential competing processes, the isolated peak associated with analyte electrochemistry can be further analysed. CV scan rate (e.g. 50 $mV{\cdot}s^{-1}$) allows i-V data to be transformed to i-t data, where the area under the i-t curve in the limit of the process timescale (t_1-t_2) determines the charge associated with the analyte electrochemistry (E2.27).

ASV fundamentally relies on a stable and reversible electrochemically driven WE-analyte interaction, typically consisting of the three stages schematically illustrated in figure 2.22. In theory, for a well-defined electrochemical process, quantification is possible by direct calculation of the number of moles of electrons that account for the charge transferred in a process. However, more commonly, charge values are calibrated against samples of similar solution composition with known analyte concentration.



▲ Figure 2.22 - Typical traces for the three stages of an ASV procedure to quantify $[Cu^{2+}]_{(aq)}$ from $[CuSO_4]_{(aq)}$ - (A) electrochemical $Pt_{(s)}$ WE/CE cleaning in 0.5 *mol·dm*$^{-3}$ $H_2SO_{4(aq)}$ (B) $Cu^{2+}_{(aq)}$ electrodeposition in sample medium - showing i-t integral (blue - Q_{dep}) (C) anodic $Cu_{(s)}$ stripping in electrolytic media (sample/$H_2SO_{4(aq)}$) - showing i-V integral for Q_{strip} measurement (red) .

2.7.3.2 Electrochemical Pt Cleaning

Prior to an ASV experiment, the glass encased Pt electrode is mechanically polished (*LaboPol-6, Struers*) using a range of alumina nanoparticle suspensions (200/100/50 nm AP-A, *Struers*). The electrode system is then thoroughly rinsed with distilled water, before being electrochemically cleaned via high potential vertex cyclic voltammetry (500 *mmol·dm*$^{-3}$ $H_2SO_{4(aq)}$, -0.4 – 1.9 *V* vs. Ag/AgCl, 100 *mV·s*$^{-1}$, 10 *cycles*). An exemplar trace is shown in figure 2.22B, whereby the $Pt_{(s)}$ surface is cleaned by the generation of $H_{2(g)}$, $O_{2(g)}$ and the oxidation of surface-bound contaminants at high potentials.

2.7.3.3 Heterogeneous Electrodeposition of Cu^{2+}

As discussed in sectio1.3n 1.31.31.3, the electroplating of $Cu_{(aq)}$ is a key stage in the copper refinement process. It is therefore of little surprise that heterogeneous electrodeposition of $Cu^{2+}_{(aq)}$ from $SO_4^{2-}_{(aq)}$ has been extensively studied, to include nucleation mechanisms and the effects of *p*H and cohabiting cations.[124, 127-131] As mentioned, electrodeposition from ionic liquid media is also a flourishing recent technology, where the potentials, properties and morphology of formed electrodeposits can be modified.[88, 132, 133]

$$Cu^{2+}_{(aq)} + 2e^- \rightarrow Pt - Cu^0_{(s)} \qquad E^{\theta}_{onset} \approx -0.1\,V \qquad \text{E2.28}$$

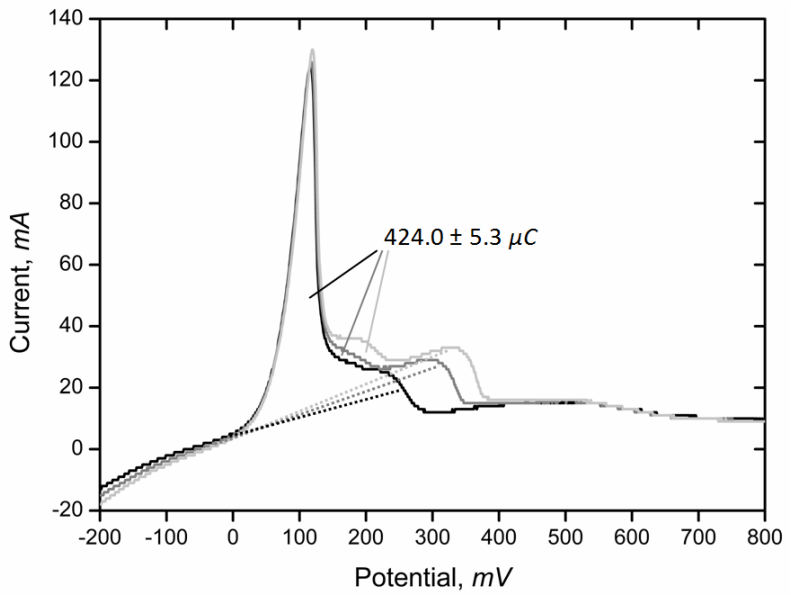
The broad reductive process onset at -50 *mV* (vs. Ag/AgCl) visualised in figure 2.18 is the heterogeneous electrodeposition of metallic $Cu_{(s)}$ (E2.28). The high current chronoamperometric data (i-t) produced during Cu^{2+} electrodeposition (120 *s*, -500 *mV* vs. Ag/AgCl) can be integrated directly (Q_{dep} - blue shaded area - figure 2.22C). Large associated charges are dominated by $H_{2(g)}$ evolution and are thus of little use for $Cu_{(aq)}$ quantification purposes, however their magnitudes can be rationalised in terms of electroactive solution composition (section 4.5).

2.7.3.4 Stripping Analysis & Charge Calibration

The relation of charge released during the $Cu_{(s)}$ stripping process to values for calibration standards is central to the quantification of $Cu^{2+}_{(aq)}$ – see chapter 4 for an exemplar calibration process. Anodic stripping peaks (figure 2.22C) form through re-oxidation of the metallic $Cu_{(s)}$ deposit, onset at ~0 *V* in the positive polarity voltammogram (E2.29). i-t peak integration is achieved by defining integration intervals (t_1-t_2) and by drawing a chord line to define background subtraction, as per figure 2.23, with software processed potential-time data conversion to account for the scan rate ($mV{\cdot}s^{-1}$).

$$Pt - Cu^{0}_{(s)} \rightarrow Cu^{2+}_{(aq)} + 2e^{-} \qquad E^{\theta}_{onset} \approx 0\ V \qquad \text{E2.29}$$

Defining t_1 is normally a facile process due to the sharp gradient change when the process onset potential is reached (E_{onset}). However, determination of t_2 can be challenging and requires experience and a high level of consistency in approach. Figure 2.23 represents an effective example of the potential issues in stripping charge (Q_{strip}) measurement for three ASV repeats in identical media. Differing I-V character of the electrode prior to the stripping event creates three independent baseline chords (dashed lines) thus defining a range of stripping event durations, ($\Delta t = t_2$-t_1). In addition, the features observed beyond the main peak can vary, complicating matters further and exposing the measurement process to human bias. It was found that repetitive charge measurements show low error (<5 %) when the variable I-V gradient prior to the event is extrapolated across the feature - a process that was difficult to reproduce in the software package. Therefore, a flexible semi-automated analysis approach programmed in *Mathworks MatLab*® was designed to benefit both consistency of peak analysis methodology and minimisation of analysis timescales (section 3.4).



▲ Figure 2.23 - Exemplar stripping charge (Q_{strip}) determinations for three back-to-back ASV repeats used to quantify Cu^{2+} leaching from $CuFeS_{2(s)}$ in 450 $mmol{\cdot}dm^{-3}$ $[NH_4][HSO_4]_{(aq)}$.

2.7.3.5 Summary of ASV Procedures

ASV is conducted in a 3-electrode configuration (vs. Ag/AgCl, *I.J. Cambria*). Sample changes and repeats are punctuated by electrochemical Pt-cleansing (500 $mmol{\cdot}dm^{-3}$ $H_2SO_{4(aq)}$; –0.4 – 1.9 *V* vs. Ag/AgCl; 100 $mV{\cdot}s^{-1}$; 10 *cyc*). Electrodeposition in the sample medium of interest (-500 *mV* vs. Ag/AgCl, 120 *s*) is followed positive polarity oxidative CV scanning (500 $mmol{\cdot}dm^{-3}$ $H_2SO_{4(aq)}$, -0.3 – 1.5 *V*, 50 $mV{\cdot}s^{-1}$, 4 *cycles*).

Adaptations are made to this (3-vial) ASV procedure as introduced in chapter 4, whereby electrochemical cleaning is removed between repeats and $Cu^{2+}_{(aq)}$ electrodeposition and $Cu_{(s)}$ stripping occur *back-to-back,* within the cupric analyte containing sample vial. Justification for use of this '1-vial' methodology is discussed during ASV procedural validation (section 4.5 and figure 4.10) with the first ASV repeat data discarded in all instances - unless otherwise stated - due to electrode conditioning effects. Table 2.10 below summarises each ASV mode, how it is referred to throughout this thesis and the experimental details involved.

Calibration plots for unagitated ASV were rapidly generated utilising a custom designed robotic platform (chapter 3), applying the ASV procedure to the appropriate strength $CuSO_{4(aq)}$ acidic/IL standard solutions. Semi-automated *Mathworks MatLab®* scripts were developed to aid the user in batch charge quantification (Q_{dep} and Q_{strip}) for high volumes of stored ASV data files. Programmatic methods are discussed further in section 3.4.

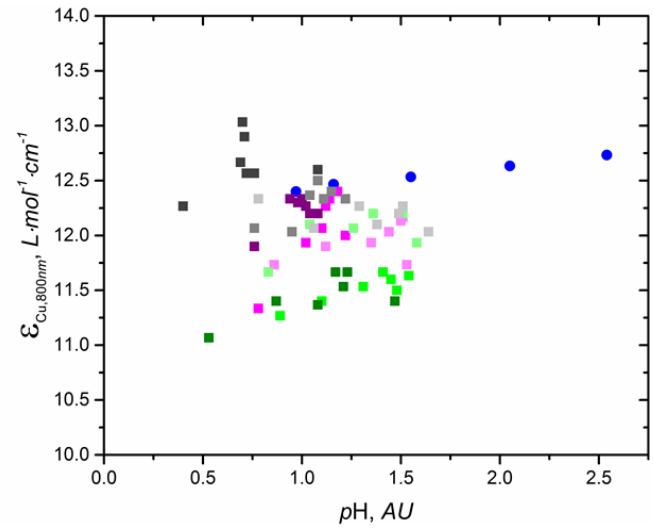
▼ Table 2.10 - Summary of ASV modes, nomenclatures and procedural details used throughout this work unless otherwise stated.

ASV Mode	Electrochemical Cleaning Details	$Cu^{2+}_{(aq)}$ Electrodeposition Details	$Cu_{(s)}$ Stripping Details
3-vial	In separate vial of 0.5 *mol·dm*$^{-3}$ $H_2SO_{4(aq)}$ After all ASV repeats (CV: -0.4 - 1.9 *V*; 10 cycles)	In sample media (CA: -500 *mV*; 120 *s*)	In separate vial of 0.5 *mol·dm*$^{-3}$ $H_2SO_{4(aq)}$ (-0.3 - 1.5 *V*; 4 cycles)
2-vial	In separate vial of 0.5 *mol·dm*$^{-3}$ $H_2SO_{4(aq)}$ After sample change only (CV: -0.4 - 1.9 *V*; 10 cycles)	(as above)	In separate vial of 0.5 *mol·dm*$^{-3}$ $H_2SO_{4(aq)}$ (-0.3 - 1.5 *V*; 4 cycles)
1-vial	In separate vial of 0.5 *mol·dm*$^{-3}$ $H_2SO_{4(aq)}$ After sample change only (CV: -0.4 - 1.9 *V*; 10 cycles)	(as above) with discard of 1st ASV repeat	In sample media with discard of 1st ASV repeat (-0.3 - 1.5 *V*; 4 cycles)
in situ	Before experiment only	(as above) with discard of 1st ASV repeat	In sample media with discard of 1st ASV repeat (-0.3 - 1.5 *V*; 4 cycles)

2.7.4 UV-Visible Spectroscopy

UV-visible spectroscopy is a well understood standard method and thus the Beer-Lambert detection principle will not be explained in detail. In a typical procedure UV-visible absorption spectra (200-1000 *nm*) are recorded using a Perkin Elmer Lambda 25 Spectrometer, monitoring leachate Cu absorption characteristics according to the Beer-Lambert Law (E2.30) in reference to $Cu^{2+}_{(aq)}$ absorption behaviour (d^8 ion- λ_{max} ~ 800-810 *nm*; ε_{max} ~ 12-13 *mol*$^{-1}$*·dm*^{3}*·cm*$^{-1}$; $E_{\Delta Oct}$ ~ 150 *kJ·mol*$^{-1}$).[5] The influence on $IL_{(aq)}$-$Cu^{2+}_{(aq)}$ solvation of $[IL]_{(aq)}$ (0.1-1 *mol·dm*$^{-3}$) and solution *p*H adjusted using $H_2SO_{4(aq)}$ was investigated for high acidity $IL_{(aq)}$-$CuSO_{4(aq)}$ reference solutions (figure 2.24). Extinction coefficients in the range 11-13 *L·mol*$^{-1}$*·cm*$^{-1}$ show that $Cu^{2+}_{(aq)}$ is solvated as a mixture of dynamic hydrates with $SO_4^{2-}{}_{(aq)}$ involvement. Using this data, the appropriate allowances and corrections can be made for changes in $[IL]_{(aq)}$ and *p*H, however for this and other practical reasons, UV-visible spectroscopy for screening was not pursued during this work. Conventional 2-beam UV-visible spectroscopy has however been used in chapter 6.

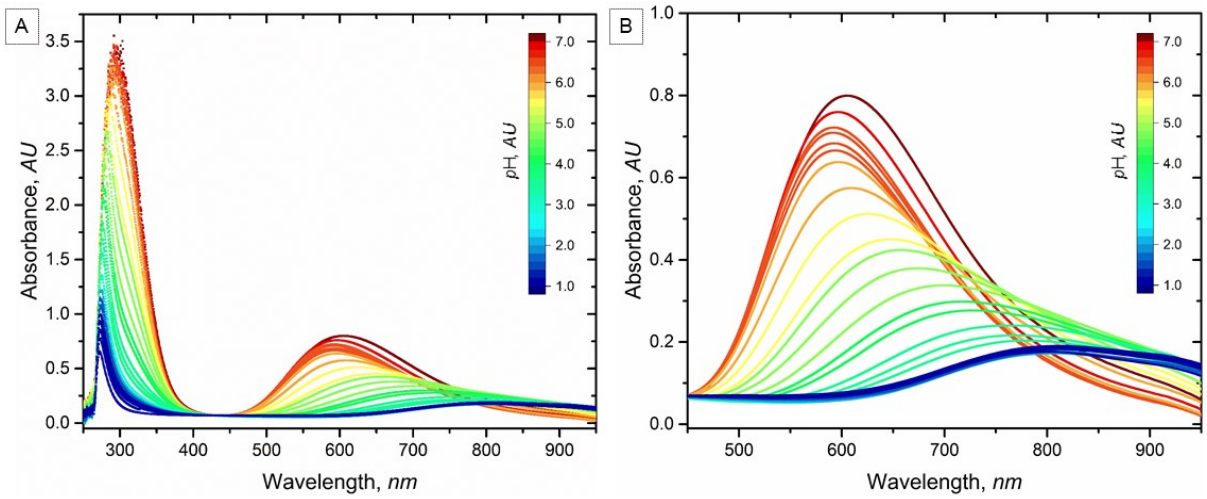
$$A = log_{10}\frac{I_0}{I} = \varepsilon \cdot c \cdot l \qquad \text{E2.30}$$



▲ Figure 2.24 - Effect of IL and solution *p*H on calculated Beer-Lambert molar extinction coefficient of $CuSO_{4(aq)}$ absorption at *p*H1 for d-d transition of $Cu^{2+}_{(aq)}$ centred at ~800 *nm*. (● $H_2O_{(l)}$; 0.1, 0.5, 1.0 *mol·dm*$^{-3}$; ■■■ $[C_2C_1im][HSO_4]_{(aq)}$; ■■■ $[C_4Him][HSO_4]_{(aq)}$; ■■■ $[C_4C_1im][HSO_4]_{(aq)}$)

UV-visible spectra were also collected for 450 *mmol·dm*$^{-3}$ $[C_4Him][HSO_4]_{(aq)}$ reference solutions containing 10 *mmol·dm*$^{-3}$ $CuSO_{4(aq)}$ in order to investigate the *p*H dependent coordination of $Cu^{2+}_{(aq)}$ by N. Figure 2.25 displays the full UV-visible spectrum for 450 *mmol·dm*$^{-3}$ $[C_4Him][HSO_4]_{(aq)}$ reference solutions containing 10 *mmol·dm*$^{-3}$ $CuSO_{4(aq)}$. *p*H was adjusted using a stock solution of $KOH_{(aq)}$ containing $[IL]_{(aq)}$ and $[Cu^{2+}]_{(aq)}$ to maintain concentrations. Clear shifts are apparent in peak wavelength and absorbance magnitudes for both the LMCT (200-400 *nm*) and d-d electronic transition (450-1000 *nm*) regions. Analysis of the $Cu^{2+}_{(aq)}$ chromophore is given in table 2.11.

As further discussed in section 4.2, at low *p*H $[Cu^{2+}]_{(aq)}$ solvation has been found to be a dynamic mixture of hydrates, where d-d transitions at ~800 *nm* with $\varepsilon_{Cu,800nm}$ is within the accepted range of 11-13 *L·mol*$^{-1}$*·cm*$^{-1}$. Upon reduction in acidity, there is a blue shift in d-d transition energy ($\Delta E_{d\text{-}d}$ = 0.52 *eV*) and ~4 fold increase in absorbance. In the LMCT region, there is a similar magnitude red shift in energy (ΔE_{LMCT} = 0.46 *eV*) accompanied by a ~5 fold increase in absorbance. Involvement of the imidazolium IL cation in $Cu^{2+}_{(aq)}$ at low acidity is confirmed by reported transitions for $Cu^{2+}_{(aq)}$ in the presence of imidazole, including charge transfer between the imidazolium π system and the metal centre (310 *nm*; $\pi(im \rightarrow Cu^{II})$; ε_{max} = 340-70 *L·mol*$^{-1}$*·cm*$^{-1}$) and relatively high energy shifted Cu^{2+} d-d transitions (621 *nm*; ε_{max} = 49-57 *L·mol*$^{-1}$*·cm*$^{-1}$).[134, 135]



▲ Figure 2.25 - (A) Colour-coded UV-visible spectrum and (B) magnification of d-d electronic transition region displaying shifts due to *p*H changes in 450 *mol·dm*$^{-3}$ $[C_4Him][HSO_4]_{(aq)}$ solution with 10 *mmol·dm*$^{-3}$ $CuSO_{4(aq)}$.

Therefore, the observed shifts are directly related to the ratio of protonated/deprotonated $[C_4Him]^+$. As *p*H is increased, the concentration of protonated $[C_4Him]^+$ tends to zero, freeing the imidazolium nitrogen to datively ligate $Cu^{2+}_{(aq)}$. The resulting blue shift of d-d transitions is due to stronger field nitrogenous ligands causing increased d orbital splitting (*cf.* O-H_2 and O-SO_3^{2-}) and increased absorbance at nominal 10 *mmol·dm*$^{-3}$ $Cu^{2+}_{(aq)}$ is likely to be due to reduced orbital symmetry upon IL involvement in complexation - increasing the intensity of symmetry 'disallowed' centrosymmetric d-d transitions.[136-138] In acidic conditions with *p*H < 3, $Cu^{2+}_{(aq)}$ complexation can be judged to be consistent, since there is sufficient free-$[H^+]_{(aq)}$ to quench the influence of KOH base addition. Hence, at typical leaching acidities (*p*H < 2) imidazolium is >99.999% fully protonated and has null influence on $Cu^{2+}_{(aq)}$ solvation. Using E2.31-E2.32 and the *p*K_a value for $[C_4Him]^+$ (7.21)[139] the concentration of free-$[C_4im]_{(aq)}$ can be computed (table 2.11), which will be discussed further later in reference to the potential action of free base in $CuFeS_{2(s)}$ leaching (section 6.3.7 and 6.4).

$$pH = pK_a + log_{10}\frac{[A^-]_t}{[HA]_t} \qquad \text{E2.31}$$

$$\frac{[A^-]_t}{[HA]_t} = \frac{[HA]_0 - [HA]_t}{[HA]_t} = \frac{[HA]_0}{[HA]_t} - 1 \qquad \text{E2.32}$$

▼ Table 2.11 – Electronic transition analysis for selected UV-visible spectra presented in figure 2.25.
(450 *mmol·dm*$^{-3}$ $[C_4Him][HSO_4]_{(aq)}$; 10 *mmol·dm*$^{-3}$ $CuSO_{4(aq)}$)

	UV-Visible Region (200-400 *nm*)				Visible Region (450-950 *nm*)				$\underline{[C_4im]}$ $[C_4Him]^+$,
*p*H	A_{max}, *AU*	λ_{max}, *nm*	ε_{max}, *L·mol*$^{-1}$*·cm*$^{-1}$	ΔE_{LMCT}, *kJ·mol*$^{-1}$	A_{max}, *AU*	λ_{max}, *nm*	ε_{max}, *L·mol*$^{-1}$*·cm*$^{-1}$	$\Delta E_{d\text{-}d}$, *kJ·mol*$^{-1}$	*%*
1.07	0.60	272	60	439.9	0.13	811	12.7	147.6	7.2 x 10^{-5}
1.32	0.90	274	90	436.7	0.16	814	15.8	147.0	1.3 x 10^{-4}
1.65	1.09	275	109	435.1	0.20	813	20.4	147.2	2.8 x 10^{-4}
1.92	1.18	275	118	435.1	0.22	809	21.6	147.9	5.1 x 10^{-4}
2.435	1.31	276	131	434.4	0.25	805	25.0	148.7	1.7 x 10^{-3}
3.35	1.45	276	145	433.6	0.27	796	27.2	150.3	1.4 x 10^{-2}
3.75	1.79	277	179	432.0	0.32	772	31.8	155.0	3.5 x 10^{-2}
3.94	1.93	278	193	431.2	0.34	763	34.3	156.8	5.4 x 10^{-2}
4.25	2.19	278	219	430.5	0.40	737	40.3	162.4	0.11
4.53	2.50	282	250	424.3	0.45	700	45.5	171.0	0.21
4.76	2.69	282	269	424.3	0.48	677	48.4	176.8	0.35
5.02	2.98	285	298	420.6	0.58	648	57.9	184.7	0.64
5.28	3.10	287	310	417.0	0.64	627	63.6	190.9	1.6
5.52	3.25	290	325	412.6	0.70	610	70.0	196.2	2.0
5.86	3.40	292	340	409.8	0.78	597	78.3	200.4	4.3
6.03	3.47	293	347	409.1	0.83	594	82.6	201.5	6.2
6.34	3.55	294	355	407.0	0.87	592	86.7	202.1	12
6.71	3.59	297	359	402.9	0.94	597	94.1	200.4	24
7.02	3.6	298	360	401.5623	0.99	606	98.9	197.5	39

2.8 Experimental Leaching Format

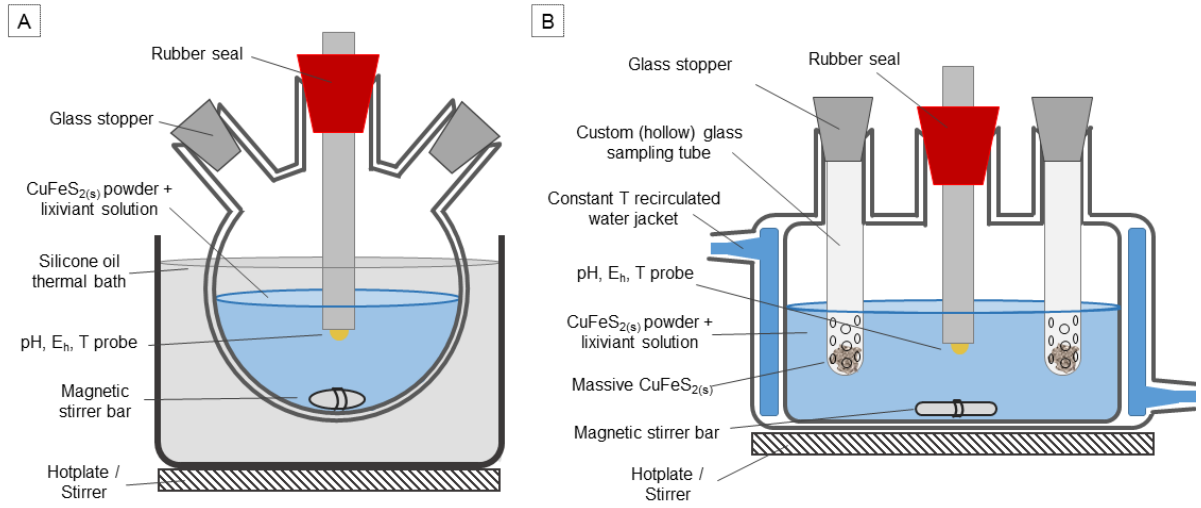
2.8.1 Low-Volume Leaching Protocol

Within the framework of the current work, a 'low volume' leaching experiment is defined as 1-5 *mL* scale. This scale of experiments will generally be used to cover a broad range of conditions to generate promising systems. Unless otherwise stated, a constant mass: volume ratio of 25 *mg·mL*$^{-1}$ (40 *mL·g*$^{-1}$) will be used – referring to mass of 35-74 *μm* diameter $CuFeS_{2(s)}$ powder and total $lixiviant_{(aq)}$ volume. Leaching timescales will be on the order of 7 *days*, at 298 *K* in still (unagitated)

conditions. Regular E_h measurements in low-volume conditions reveal that values were variable but E_h evolution is well represented by the E_h profiles obtained for 400 *mL*-scale $CuFeS_{2(s)}$ dissolution experiments. Therefore, specific consideration of E_h will be reserved for discussions in section 5.4, unless otherwise stated.

2.8.2 High-Volume Leaching Protocol

$IL_{(aq)}$ systems that exhibit interesting or promising behaviour in smaller scale testing will be termed 'lead' systems, towards leaching optimisation within the restricted scope of the work. Promising $IL_{(aq)}$ systems will be applied to ~400 *mL* scale experiments, maintaining other experimental considerations. These experiments will employ continuous *p*H, temperature and E_h monitoring throughout the leach duration, utilising data-logging equipment and the process described in sections 2.6.4 and 3.2. The two experimental designs utilised in up-scaled experiments are shown in figure 2.26. Each design contains means of thermostatic leachate temperature regulation – via a silicone oil bath and recirculated water jacket, respectively – and slow magnetic stirring (~120 *rpm*) for solution homogenisation. Figure 2.26B additionally allows for massive $CuFeS_{2(s)}$ to be interfaced with the lixiviant$_{(aq)}$ solution and easily removed for spectroscopic analyses (SEM/EDX and ToF-SIMS – see section 2.9), via perforated glass sampling tubes.



▲ Figure 2.26 - Experimental designs for two 400 *mL* scale vessels for long duration (~1 *month*) $CuFeS_{2(s)}$ leaching trials using both $H_2SO_{4(aq)}$ and $IL_{(aq)}$ lixiviant solutions. (A) 500 *mL* three-neck round-bottomed flask in thermally regulated silicone bath (B) cylindrical flat-bottomed 500 *mL* flask equipped with four perforated sampling tubes and thermally regulated (recirculated) water jacket.

2.9 $CuFeS_{2(s)}$ Surface Sensitive Techniques

In conjunction with the high volume leaching experiments described in section 2.8.2, and other investigations, a range of surface characterisation techniques were performed pre- and post-leaching, to determine key surface compositional changes. Scanning electron microscopy (SEM)

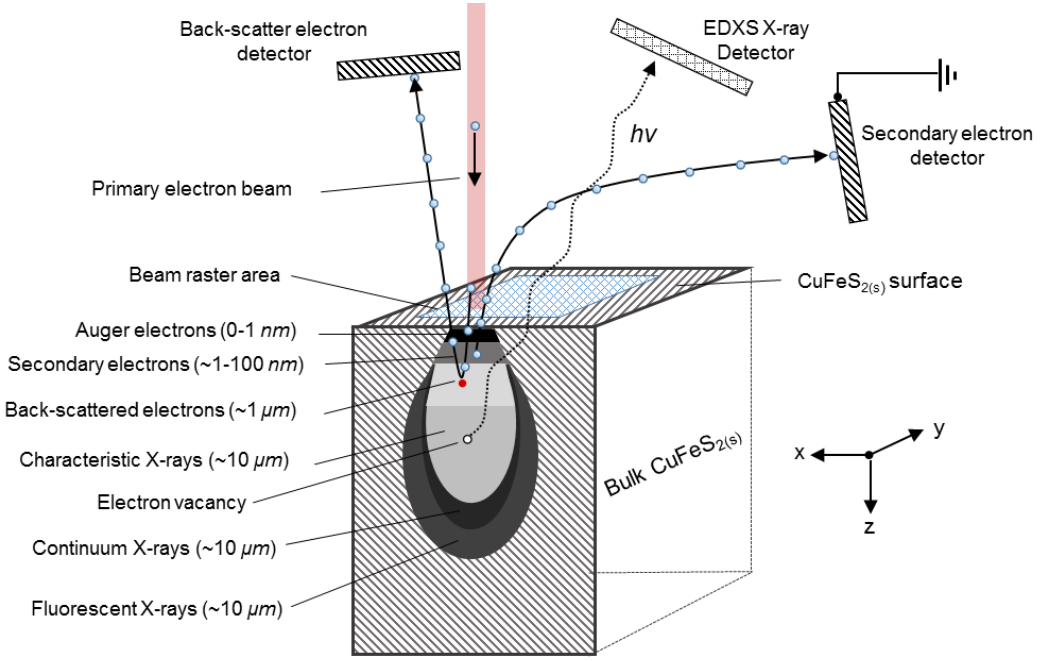
allows for high resolution imaging, which can be correlated with flexible surface element mapping and quantifications via energy dispersive X-ray spectroscopy (EDX). Time of flight secondary ion mass spectroscopy (ToF-SIMS) is a highly surface sensitive technique, ionising a few surface atomic layers for identification of key surface moieties.

2.9.1 Scanning Electron Microscopy (SEM/EDX)

2.9.1.1 Detection Principle

Scanning electron microscopy (SEM) has several imaging modes, varying in the positioning of the detectors. Electrons are released from a thermionic emitting wire (W) or crystalline cathode (LaB_6), which are then accelerated through the aperture of a ring anode. In the remainder of the microscope column the resultant electron beam passes through a series of selection apertures and electromagnetic lenses to focus the beam onto the sample, whereby the sample stage is also manoeuvrable in 3-dimensions – where working distance (WD – microscope height above sample) is crucial for image optimisation.

When an image is acquired, the electron beam is rastered across a 2D surface area, where primary electrons that are incident on the sample have several simultaneous influences (figure 2.27). Primary electrons can collide inelastically with moderate depth atoms (~0.1-1 *μm*) and be reflected at low angles to the sample normal. These 'back-scattered' electrons give crystallographic contrast, since the detected electrons suffer energy losses dependent on the incident crystallographic orientations. At lower (< 100 *μm*) probe volumes primary electrons do not escape the surface – however they cause release of low speed secondary electrons which can escape the bulk surface. Secondary electrons are delivered to the oblique detectors using an electric field, with the data used to reconstruct an image with morphological contrast. Thirdly, electrons can be 'knocked-out' of atoms at moderate solid depths (1-2 *μm*) causing electronic relaxations within the atom in analogous fashion to figure 2.20B. X-ray photons are released as a result of this relaxation, with energies characteristic of the parent atom. Photons are detected by a spatially resolved detector, where a current is induced by photon-detector collision, mapping an elemental composition to the X-ray origin (with limited spatial resolution).

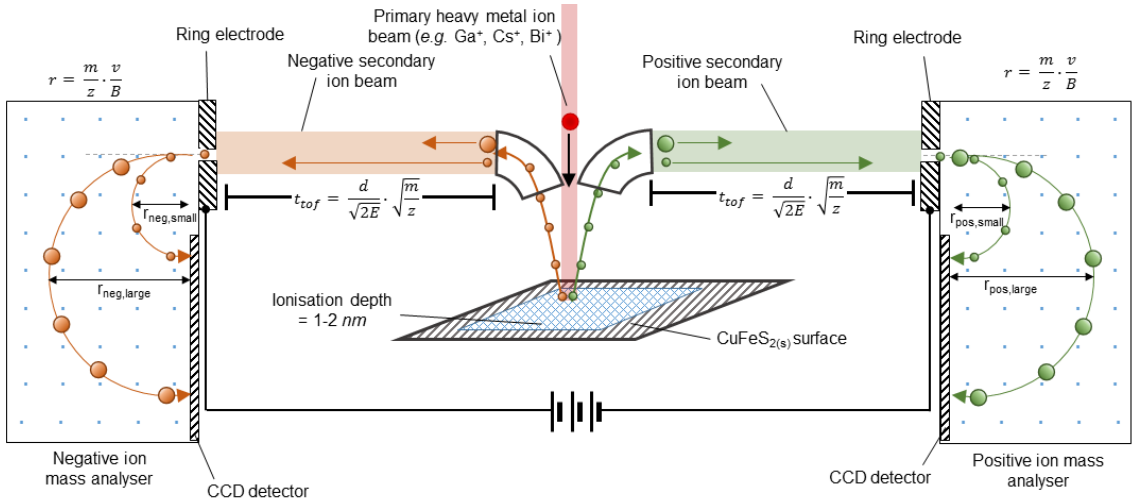


▲ Figure 2.27 – SEM detection principle for a given probe volume of $CuFeS_{2(s)}$ – displaying detection of back-scattered and secondary electrons and of characteristic X-ray photons used for EDX elemental mapping.

2.9.1.2 Sample Preparation

Energy Dispersive X-ray Spectroscopy (EDX) was performed in combination with SEM imaging (*JSM 6400*; *Jeol*; 20 *keV*) to obtain surface elemental analysis for powdered and massive $CuFeS_{2(s)}$ samples, both prior to and following various leach durations. Massive leached $CuFeS_{2(s)}$ samples were briefly washed in distilled water before drying using a low speed $N_{2(g)}$ aerosol. All samples are mounted on $C_{(s)}$ adhesive tape and loose excess powdered $CuFeS_{2(s)}$ is removed again using the $N_{2(g)}$ aerosol. It was found that chromium sputtering (5-10 *nm*) – usually undertaken to ensure sample conductivity, electrical contact to ground and to provide contrast – had little effect due to the semiconducting nature of $CuFeS_{2(s)}$ and was omitted from the procedure. Samples are introduced to the imaging chamber (typically 10^{-3}-10^{-5} Pa) before adjusting working distance (WD = 15 *mm*), lens aperture sizes, focus and EDX calibration and beam optimisations using a $Co_{(s)}$ standard. Throughout EDX quantifications carbon levels are neglected because of potential contamination arising from the use of $C_{(s)}$ adhesive tape.[140]

2.9.2 Time of Flight Secondary Ion Mass Spectroscopy (ToF-SIMS)



▲ Figure 2.28 – Simplified schematic representation of the stages of tof-SIMS, including heavy ion sputtering, secondary ion collection and m/z differentiation via acceleration in an electric field (time-of-flight) and circular motion in an orthogonal magnetic field (mass analyser).[141]

Massive samples of $CuFeS_{2(s)}$ (~50x50x50 *mm*) were submitted for ToF-SIMS analysis via an institutional service (*Dr Sarah Fearn; Department of Materials; Imperial College London*). The technique has reported probe depths of 1-2 *nm*[142] and is therefore highly surface sensitive but also with a high lateral resolution of <0.1 *μm* in imaging applications.[143, 144] In the case of ToF-SIMS, the sample is ionised by a heavy metal ion beam, which is rastered across the surface (dynamic mode) to sample wide surface areas or remains static to probe depth variations. In each case, sputtering fragments surface structure creating secondary ions, which are released into vacuum. As with all mass spectroscopy, detection relies upon a mass analyser device – where ions of differing mass: charge ratio (m/z) are differentiated between, since it decides ionic radius of curvature (r) when travelling with a velocity (*v*), perpendicular to a uniform magnetic field with magnetic field vector B (E2.33).

$$r = \frac{m}{z} \cdot \frac{v}{B} \qquad \text{E2.33}$$

However, further fine separation of ions of similar m/z ratio is possible by using 'time-of-flight' ion delivery to the mass analyser. Ions are accelerated in an electric field converting their initial potential energy (E_p) to kinetic energy (E_k) as shown in E2.34. The time (t) required for an ion to reach the mass analyser is once again dependent upon m/z, creating further differentiation via a distinct independent proportionality (E2.35). Ion separation data can be compared to libraries of references to allow for ion identification and quantification.[141]

$$E_p = zE \qquad E_k = \frac{mv^2}{2} = \frac{m \cdot d^2}{2 \cdot t^2} \tag{E2.34}$$

$$t = \frac{d}{\sqrt{2E}} \cdot \sqrt{\frac{m}{z}} = k \cdot \sqrt{\frac{m}{z}} \tag{E2.35}$$

2.10 References

1. T. Welton, *Chemical Reviews*, 1999, **99**, 2071-2084.
2. A. S. Amarasekara, *Chemical Reviews*, 2016, **116**, 6133-6183.
3. P. Walden, *Bull. Acad. Imper. Sci. (St. Petersburg)* 1914, 1800.
4. S. Gabriel and J. Weiner, *Berichte der deutschen chemischen Gesellschaft*, 1888, **21**, 2669-2679.
5. P. Atkins and J. de Paula, *Physical Chemistry*, Oxford University Press, Oxford, 8th edn., 2006.
6. T. Welton, *Coordination Chemistry Reviews*, 2004, **248**, 2459-2477.
7. T. Q. To, PhD, Imperial College of Science & Technology, 2012.
8. A. P. Abbott, G. Frisch, J. Hartley and K. S. Ryder, *Green Chemistry*, 2011, **13**, 471-481.
9. J. P. Hallett and T. Welton, *Chemical Reviews*, 2011, **111**, 3508-3576.
10. E. L. Smith, A. P. Abbott and K. S. Ryder, *Chemical Reviews*, 2014, **114**, 11060-11082.
11. H. M. A. Abood, A. P. Abbott, A. D. Ballantyne and K. S. Ryder, *Chemical Communications*, 2011, **47**, 3523-3525.
12. A. P. Abbott, G. Capper, D. L. Davies and R. Rasheed, *Inorg. Chem.*, 2004, **43**, 3447.
13. A. P. Abbott, D. Boothby, G. Capper, D. L. Davies and R. K. Rasheed, *Journal of the American Chemical Society*, 2004, **126**, 9142-9147.
14. A. P. Abbott, G. Capper, D. L. Davies, R. K. Rasheed and V. Tambyrajah, *Chemical Communications*, 2003, DOI: 10.1039/B210714G, 70-71.
15. A. P. Abbott, G. Capper, D. L. Davies, H. L. Munro, R. K. Rasheed and V. Tambyrajah, *Chem. Commun.*, 2001, **19**, 2010.
16. K. J. Baranyai, G. B. Deacon, D. R. MacFarlane, J. M. Pringle and J. L. Scott, *Australian Journal of Chemistry*, 2004, **57**, 145-147.
17. S. Chun, S. V. Dzyuba and R. A. Bartsch, *Analytical Chemistry*, 2001, **73**, 3737-3741.
18. L. C. Branco, J. N. Rosa, J. J. Moura Ramos and C. A. M. Afonso, *Chemistry – A European Journal*, 2002, **8**, 3671-3677.
19. D. M. Fox, W. H. Awad, J. W. Gilman, P. H. Maupin, H. C. De Long and P. C. Trulove, *Green Chemistry*, 2003, **5**, 724-727.
20. W. Shibayama, A. Narita, N. Matsumi and H. Ohno, *J. Organomet. Chem.*, 2009, **694**, 1642.
21. P. Anastas and N. Eghbali, *Chemical Society Reviews*, 2010, **39**, 301-312.
22. J. Shen, H. Wang, H. Liu, Y. Sun and Z. Liu, *Journal of Molecular Catalysis A: Chemical*, 2008, **280**, 24-28.
23. H. Olivier-Bourbigou, L. Magna and D. Morvan, *Applied Catalysis A: General*, 2010, **373**, 1-56.
24. J. G. Huddleston, A. E. Visser, W. M. Reichert, H. D. Willauer, G. A. Broker and R. D. Rogers, *Green Chem*, 2001, **3**, 156-164.

25. A. P. Abbott and K. J. McKenzie, *Physical Chemistry Chemical Physics*, 2006, **8**, 4265-4279.

26. J. A. Whitehead, J. Zhang, N. Pereira, A. McCluskey and G. A. Lawrance, *Hydrometallurgy*, 2007, **88**, 109-120.

27. A. R. Hajipour and F. Rafiee, *Org. Prep. Proced. Int.*, 2010, **42**, 285.

28. C. D'Agostino, L. F. Gladden, M. D. Mantle, A. P. Abbott, E. I. Ahmed, A. Y. M. Al-Murshedi and R. C. Harris, *Physical Chemistry Chemical Physics*, 2015, **17**, 15297-15304.

29. C. D'Agostino, R. C. Harris, A. P. Abbott, L. F. Gladden and M. D. Mantle, *Physical Chemistry Chemical Physics*, 2011, **13**, 21383-21391.

30. A. W. Taylor, P. Licence and A. P. Abbott, *Physical Chemistry Chemical Physics*, 2011, **13**, 10147-10154.

31. A. P. Abbott, R. C. Harris and K. S. Ryder, *The Journal of Physical Chemistry B*, 2007, **111**, 4910-4913.

32. T. L. Greaves and C. J. Drummond, *Chem. Rev.*, 2008, **108**, 206.

33. A. Brandt, M. J. Ray, T. Q. To, D. J. Leak, R. J. Murphy and T. Welton, *Green Chemistry*, 2011, **13**, 2489-2499.

34. A. Brandt, J. K. Erickson, J. P. Hallett, R. J. Murphy, A. Potthast, M. J. Ray, T. Rosenau, M. Schrems and T. Welton, *Green Chemistry*, 2012, **14**, 1079-1085.

35. K. R. Seddon, A. Stark and M. J. Torres, *Pure Appl. Chem.*, 2000, **72**, 2275–2287.

36. J. D. Holbrey, W. M. Reichert, M. Nieuwenhuyzen, S. Johnson, K. R. Seddon and R. D. Rogers, *Chemical Communications*, 2003, 1636-1637.

37. L. Crowhurst, P. R. Mawdsley, J. M. Perez-Arlandis, P. A. Salter and T. Welton, *Physical Chemistry Chemical Physics*, 2003, **5**, 2790-2794.

38. A. C. Cole, J. L. Jensen, I. Ntai, K. L. T. Tran, K. J. Weaver, D. C. Forbes and J. H. Davis, *Journal of the American Chemical Society*, 2002, **124**, 5962-5963.

39. G. R. T. Jenkin, A. Z. M. Al-Bassam, R. C. Harris, A. P. Abbott, D. J. Smith, D. A. Holwell, R. J. Chapman and C. J. Stanley, *Minerals Engineering*, 2016, **87**, 18-24.

40. A. P. Abbott and G. Frisch, in *Element Recovery and Sustainability*, The Royal Society of Chemistry, 2013, DOI: 10.1039/9781849737340-00059, pp. 59-79.

41. A. P. Abbott, G. Capper, D. L. Davies and P. Shikotra, *Mineral Processing and Extractive Metallurgy*, 2006, **115**, 15-18.

42. A. P. Abbott, G. Capper, D. L. Davies, R. K. Rasheed and P. Shikotra, *Inorganic Chemistry*, 2005, **44**, 6497-6499.

43. A. P. Abbott, R. C. Harris, F. Holyoak, G. Frisch, J. Hartley and G. R. T. Jenkin, *Green Chemistry*, 2015, **17**, 2172-2179.

44. A. P. Abbott, G. Frisch and K. S. Ryder, *Annual Reports Section "A" (Inorganic Chemistry)*, 2008, **104**, 21-45.

45. A. P. Abbott, G. Capper, D. L. Davies, K. J. McKenzie and S. U. Obi, *Journal of Chemical & Engineering Data*, 2006, **51**, 1280-1282.

46. G. c. Tian, J. Li and Y. x. Hua, *Trans. Nonferrous Met. Soc. China*, 2010, **20**, 513.

47. J. A. Whitehead, J. Zhang, A. McCluskey and G. A. Lawrance, *Hydrometallurgy*, 2009, **98**, 276-280.

48. A. Kilicarslan and M. N. Saridede, *JOM*, 2015, **67**, 2739.

49. M. Chen, J. Wang, J. Huang and H. Chen, *RSC Adv.*, 2015, **5**, 34921.

50. J. Huang, M. Chen, H. Chen, S. Chen and Q. Sun, *Waste Manage.*, 2014, **34**, 483.

51. S. Katsuta, Y. Yoshimoto, M. Okai, Y. Takeda and K. Bessho, *Ind. Eng. Chem. Res.*, 2011, **50**, 12735.

52. C. Wang, W. Lu, Y. Tong, Y. Zheng and Y. Yang, *RSC Advances*, 2014, **4**, 57009-57015.

53. D. Dupont and K. Binnemans, *Green Chem.*, 2015, **17**, 2150.

54. J.-M. Lee, *Fluid Phase Equilibria*, 2012, **319**, 30-36.

55. R. Germani, M. V. Mancini, G. Savelli and N. Spreti, *Tetrahedron Letters*, 2007, **48**, 1767-1769.

56. S. Katsuta, M. Okai, Y. Yoshimoto and Y. Kudo, *Anal. Sci.*, 2012, **28**, 1009.

57. A. P. de los Ríos, F. J. Hernández-Fernández, F. J. Alguacil, L. J. Lozano, A. Ginestá, I. García-Díaz, S. Sánchez-Segado, F. A. López and C. Godínez, *Separation and Purification Technology*, 2012, **97**, 150-157.

58. J. Huang, M. Chen, H. Chen, S. Chen and Q. Sun, *Waste Management*, 2014, **34**, 483-488.

59. M. Chen, J. Huang, O. A. Ogunseitan, N. Zhu and Y.-m. Wang, *Waste Management*, 2015, **41**, 142-147.

60. L. Fischer, T. Falta, G. Koellensperger, A. Stojanovic, D. Kogelnig, M. Galanski, R. Krachler, B. K. Keppler and S. Hann, *Water Research*, 2011, **45**, 4601-4614.

61. T. Dong, Y. Hua, Q. Zhang and D. Zhou, *Hydrometallurgy*, 2009, **99**, 33-38.

62. D. Godfrey, J. H. Bannock, O. Kuzmina, T. Welton and T. Albrecht, *Green Chemistry*, 2016, **18**, 1930-1937.

63. P. Dyson and T. Geldbach, *Metal Catalysed Reactions in Ionic Liquids*, Springer, 2010.

64. Y. Dong, Y. Nie and Q. Zhou, *Chem. Eng. Technol.*, 2013, **36**, 435.

65. C. Carlesi, E. Cortes, G. Dibernardi, J. Morales and E. Muñoz, *Hydrometallurgy*, 2016, **161**, 29-33.

66. O. J. Solis-Marcíal and G. T. Lapidus, *Hydrometallurgy*, 2013, **131–132**, 120-126.

67. R. D. Rogers and K. R. Seddon, *Ionic Liquids: Industrial Applications to Green Chemistry*, ACS, Washington DC, 2002.

68. R. Hagiwara and J. S. Lee, *Electrochemistry*, 2007, **75**, 23-34.

69. C. S. Stefan, D. Lemordant, B. C. Montigny and D. Violleau, *J. Power Sources*, 2009, **189**, 1174.

70. A. C. Franzoi, P. Migowski, J. Dupontb and I. C. Vieira, *Anal. Chim. Acta.*, 2009, **639**, 90.

71. J. W. Lee and Y. T. Yoo, *Sens. Actuators. B.*, 2009, **137**, 539.

72. V. Borgel, E. Markevich, D. Aurbach, G. Semrau and M. Schmidt, *J. Power Sources*, 2009, **189**, 331.

73. L. Larush, V. Borgel, E. Markevich, O. Haik, E. Zinigrad, D. Aurbacha, G. Semrau and M. Schmidt, *J. Power Sources*, 2009, **189**, 217.

74. S. Fang, L. Yang, J. Wang, M. Li, K. Tachibana and K. Kamijima, *Electrochim. Acta*, 2009, **17**, 4269.

75. A. L. Pont, R. Marcilla, I. D. Meatza, H. Grande and D. Mecerreyes, *J. Power Sources*, 2009, **188**, 558.

76. A. Khan, X. Lu, L. Aldous and C. Zhao, *The Journal of Physical Chemistry C*, 2013, **117**, 18334-18342.

77. M. Hayyan, F. S. Mjalli, M. A. Hashim, I. M. AlNashef and T. X. Mei, *Journal of Industrial and Engineering Chemistry*, 2013, **19**, 106-112.

78. T.-Y. Wu, S.-G. Su, Y.-C. Lin, H. P. Wang, M.-W. Lin, S.-T. Gung and I. W. Sun, *Electrochimica Acta*, 2010, **56**, 853-862.

79. B. Y. Liu, D. Q. Xu and Z. Y. Xu, *Chin. J. Chem.*, 2005, **23**, 803.

80. A. P. Abbott, G. Frisch and K. S. Ryder, *Annual Review of Materials Research*, 2013, **43**, 335-358.

81. A. P. Abbott, M. Azam, G. Frisch, J. Hartley, K. S. Ryder and S. Saleem, *Physical Chemistry Chemical Physics*, 2013, **15**, 17314-17323.

82. A. P. Abbott, K. E. Ttaib, G. Frisch, K. S. Ryder and D. Weston, *Physical Chemistry Chemical Physics*, 2012, **14**, 2443-2449.

83. A. P. Abbott, K. El Ttaib, G. Frisch, K. J. McKenzie and K. S. Ryder, *Physical Chemistry Chemical Physics*, 2009, **11**, 4269-4277.

84. A. P. Abbott, R. C. Harris, Y.-T. Hsieh, K. S. Ryder and I. W. Sun, *Physical Chemistry Chemical Physics*, 2014, **16**, 14675-14681.

85. A. P. Abbott, F. Qiu, H. M. A. Abood, M. R. Ali and K. S. Ryder, *Physical Chemistry Chemical Physics*, 2010, **12**, 1862-1872.

86. A. P. Abbott, G. Capper, D. L. Davies, R. K. Rasheed and V. Tambyrajah, *Transact. Inst. Metal Finish.*, 2001, **79**, 204.

87. Q. B. Zhang, A. P. Abbott and C. Yang, *Physical Chemistry Chemical Physics*, 2015, **17**, 14702-14709.

88. R. Al-Salman, S. Z. El Abedin and F. Endres, *Physical Chemistry Chemical Physics*, 2008, **10**, 4650-4657.

89. C. L. Hussey, L. A. King and R. A. Carpio, *Journal of The Electrochemical Society*, 1979, **126**, 1029-1034.

90. C. Nanjundiah and R. A. Osteryoung, *Journal of The Electrochemical Society*, 1983, **130**, 1312-1318.

91. Y.-X. Yuan, T.-C. Niu, M.-M. Xu, J.-L. Yao and R.-A. Gu, *Journal of Raman Spectroscopy*, 2010, **41**, 516-523.

92. A. D. Elliot and H. R. Watling, *Geochim Cosmochim Ac*, 2011, **75**, 2103-2118.

93. X. Zhou, Y. Wang, F. Meng, X. Fan, S. Qin, *Chin. J. Chem.*, 2008, **26**, 607-610.

94. M. Petkovic, K. R. Seddon, L. P. N. Rebelo and C. Silva Pereira, *Chemical Society Reviews*, 2011, **40**, 1383-1403.

95. M. Deetlefs and K. R. Seddon, *Green Chemistry*, 2010, **12**, 17-30.

96. J. A. Whitehead, G. A. Lawrance and A. McCluskey, *Green Chemistry*, 2004, **6**, 313-315.

97. O. Kuzmina, E. Symianakis, D. Godfrey, T. Albrecht and T. Welton, *Green Chem (in press)*, 2016.

98. M. J. Kamlet, J. L. Abboud and R. W. Taft, *Journal of the American Chemical Society*, 1977, **99**, 6027-6038.

99. M. J. Kamlet and R. W. Taft, *Journal of the American Chemical Society*, 1976, **98**, 377-383.

100. R. W. Taft and M. J. Kamlet, *Journal of the American Chemical Society*, 1976, **98**, 2886-2894.

101. C. Reichardt, *Chemical Reviews*, 1994, **94**, 2319-2358.

102. P. Bonhôte, A.-P. Dias, N. Papageorgiou, K. Kalyanasundaram and M. Grätzel, *Inorganic Chemistry*, 1996, **35**, 1168-1178.

103. J. N. Brönsted, *Recueil des Travaux Chimiques des Pays-Bas*, 1923, **42**, 718-728.

104. T. M. Lowry, *Chem. Ind.* , 1923, 43.

105. Y. Gu, J. Zhang, Z. Duan and Y. Deng, *Adv. Synth. Catal.*, 2005, **347**, 512.

106. L. P. Hammett and A. J. Deyrup, *Journal of the American Chemical Society*, 1932, **54**, 2721-2739.

107. A. P. Abbott, E. I. Ahmed, R. C. Harris and K. S. Ryder, *Green Chemistry*, 2014, **16**, 4156-4161.

108. N. Muhammad, Z. Man, Y. A. Elsheikh, M. A. Bustam and M. I. A. Mutalib, *Journal of Chemical & Engineering Data*, 2014, **59**, 579-584.

109. R. Umapathi, P. Attri and P. Venkatesu, *The Journal of Physical Chemistry B*, 2014, **118**, 5971-5982.

110. F. G. Bordwell, *Accounts of Chemical Research*, 1988, **21**, 456-463.

111. P. Aktins and J. de Paula, *Atkins' Physical Chemistry*, Oxford University Press, 8th edn., 2006.

112. H. Weingärtner, *Journal*, 2006, **220**, 1395.

113. R. D. Shannon and C. T. Prewitt, *Acta Cryst.*, 1969, 925.

114. J. Grasvik, J. P. Hallett, T. Q. To and T. Welton, *Chemical Communications*, 2014, **50**, 7258-7261.

115. L. M. Mihichuk, G. W. Driver and K. E. Johnson, *ChemPhysChem*, 2011, **12**, 1622-1632.

116. M. Thompson and S. Wood, in *Atomic Absorption Spectroscopy*, ed. J. I. Cantle, Elsevier, Amsterdam, 1982, pp. 261-284.

117. M. Thompson and J. N. Walsh, *A Handbook of Inductively Coupled Plasma Spectroscopy*, Blackie, New York, 1983.

118. A. Tabet-Aoul and M. Mohamedi, *Physical Chemistry Chemical Physics*, 2012, **14**, 4463-4474.

119. *Thermo Scientific iCAP 7000 ICP-OES Instrument Manual*.

120. R. M. Belchamber, D. Betteridge, A. P. Wade, A. J. Cruickshank and P. Davison, *Spectrochimica Acta Part B: Atomic Spectroscopy*, 1986, **41**, 503-505.

121. J. L. Todoli, L. Gras, V. Hernandis and J. Mora, *Journal of Analytical Atomic Spectrometry*, 2002, **17**, 142-169.

122. G. Gillain, G. Duyckaerts and A. Disteche, *Analytica Chimica Acta*, 1979, **106**, 23-37.

123. M. Lintern, A. Mann and D. Longman, *Analytica Chimica Acta*, 1988, **209**, 193-203.

124. A. Baral, C. K. Sarangi, B. C. Tripathy, I. N. Bhattacharya and T. Subbaiah, *Hydrometallurgy*, 2014, **146**, 8-14.

125. M. A. Nolan and S. P. Kounaves, *Analytical Chemistry*, 1999, **71**, 3567-3573.

126. J. C. Duinker and C. J. M. Kramer, *Marine Chemistry*, 1977, **5**, 207-228.

127. A. Kloke, C. Köhler, R. Gerwig, R. Zengerle and S. Kerzenmacher, *Advanced Materials (Deerfield Beach, Fla.)*, 2012, **24**, 2916-2921.

128. F. Qiao, B. B. O'Brien, K. A. Dunn and A. C. West, *Journal of The Electrochemical Society*, 2013, **160**, D271-D278.

129. J. Crousier and I. Bimaghra, *Electrochimica Acta*, 1989, **34**, 1205-1211.

130. I. Bimaghra and J. Crousier, *Materials Chemistry and Physics*, 1989, **21**, 109-122.

131. D. Grujicic and B. Pesic, *Electrochimica Acta*, 2002, **47**, 2901-2912.

132. F. Endres, D. MacFarlane and A. Abbott, *Electrodeposition from Ionic Liquids*, 2008.

133. W. T. Tsai and I. W. Sun, *Electrodeposition of aluminum on magnesium (Mg) alloys in ionic liquids to improve corrosion resistance*, 2013.

134. T. G. Fawcett, E. E. Bernarducci, K. Krogh-Jespersen and H. J. Schugar, *J. Am. Chem. Soc.*, 1980, 2598.

135. E. Bernarducci, W. F. Schwindinger, J. L. I. Hughey, K. Krogh- Jespersen and H. J. Schugar, *J. Am. Chem. Soc.*, 1981, 1686.

136. I. Moreno-Villoslada, F. González, M. Jofré, P. Chandía, S. Hess and B. L. Rivas, *Macromolecular Chemistry and Physics*, 2005, **206**, 1541-1548.

137. M. Ishida, Y. Naruta and F. Tani, *Dalton Transactions*, 2010, **39**, 2651-2659.

138. J. Bjerrum and B. V. Agarwala, *Acta Chem. Scand. A*, 1980, 475.

139. J. P. Hallett, personal communication.

140. D. E. Newbury, D. C. Joy, C. E. Lyman, P. Echlin, E. Lifshin, L. Sawyer and J. R. Michael, *Scanning Electron Microscopy and X-ray Microanalysis*, Springer/Plenum, New York, 3 edn., 2013.

141. H. Bubert, H. Jenett and H. F. Arlinghaus, *Surface and Thin Film Analysis - A compendium of Principles, Instrumentation and Applications*, Wiley-VCH, Weinheim, Germany 2002.

142. R. N. S. Sodhi, *Analyst*, 2004, **129**, 483-487.

143. A. Benninghoven, *Angewandte Chemie International Edition in English*, 1994, **33**, 1023-1043.

144. A. Benninghoven, F. G. Rudenauer and H. W. Werner, *Secondary Ion Mass Spectrometry: Basic Concepts, Instrumental Aspects, Applications and Trends*, John Wiley & Sons, 1987.

Chapter 3

Custom Instrumentation and Programming Techniques

Contents

3.1 Introduction 3-3

3.2 Development of a Robotic Automated Platform 3-4

3.2.1 Instrument Origins & Electronics 3-4

3.2.2 Custom Instrument Design 3-5

3.2.3 Arduino® Programming 3-7

3.2.4 NI LabView® Programming 3-10

3.3 Platform Validation Experiments 3-17

3.3.1 Conductivity Measurements 3-18

3.3.2 ASV Validation: Ferric Remediation of $Cu^{2+}_{(aq)}$ Electrodeposition 3-19

3.4 Automated Batch Analysis 3-21

3.4.1 Application to Anodic Stripping Voltammetry (ASV) 3-22

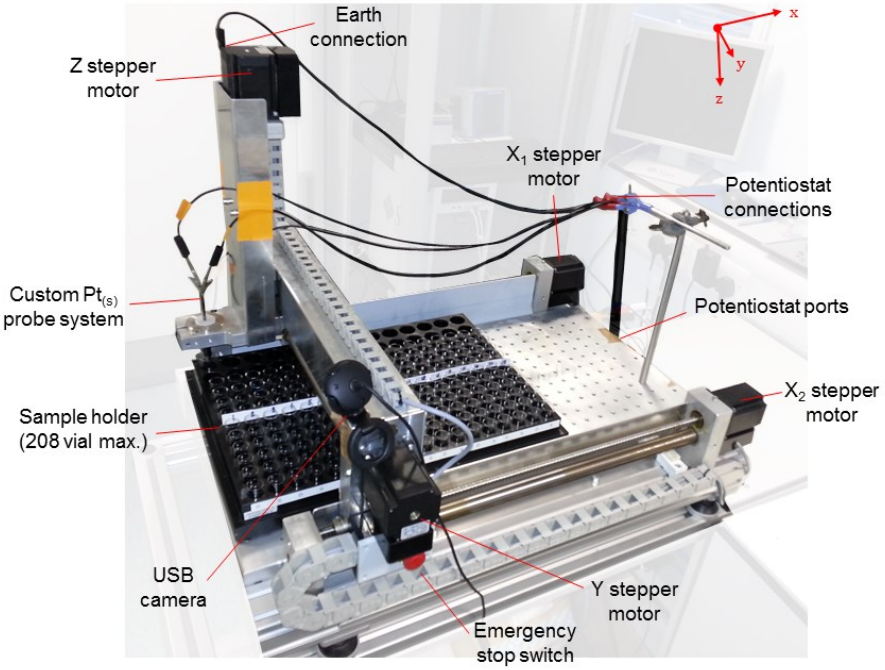
3.5 Conclusions 3-24

3.6 References 3-26

Synopsis: Herein, the design, construction, programming and validation of a flexible robotic automated platform is described. The instrument is applicable to high-throughput electrochemical screening of $IL_{(aq)}$ lixiviant activity toward $CuFeS_{2(s)}$ dissolution. Data-logging protocols are described for use in customised analogue signal transmission and recording. Additionally, methods for automated batch analysis of high volumes of electrochemical output data files are described, alongside further programming tools.

3.1 Introduction

Programming methods and custom instrumentation can offer diverse benefits. The rise in commercial availability of complex instrumentation has allowed a higher volume of research to be conducted on the nano-scale. However, many commercially available instruments suffer from restricted flexibility and automation capabilities for laborious/repetitive research activities. Aside from clear time-efficiency benefits, automation also provides subtler benefits in terms of reproducibility of experimental processes and minimisation of human error due to a 'hands-off' strategy. As such, a rapid, high-throughput combinatorial approach to the identification of promising systems is of great interest in a large number of emerging or unexplored research fields. A series of automated cycles would allow treatment of a wide variety of system variants in a minimised timescale.



▲ Figure 3.1 - Photographic image of the CNC robotic platform, equipped with a custom fabricated $Pt_{(s)}$ disc electrode probe and interfaced with a programmable potentiostat via banana plug cables.

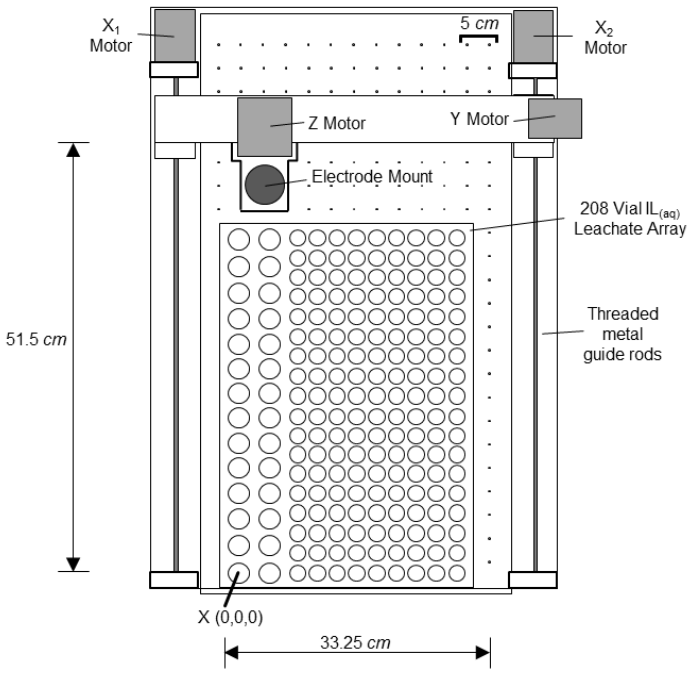
Robotic electrochemical workstations are of particular interest in the context of $CuFeS_{2(s)}$ dissolution studies. Such platforms have been custom designed, applied and reported in other scientific contexts before, namely for automated combinatorial electrochemistry in microelectrode studies on large sample arrays[1, 2] and in screening of endothelial cell NO_x excretion.[3]

3.2 Development of a Robotic Automated Platform

3.2.1 Instrument Origins & Electronics

A commercial milling platform (*CNC Technik High-Z S-400T*; *Heiz*) provided the basis for platform development (figure 3.1). The milling platform was originally operated via manufacturer software communicating with a stepper motor control box via standard USB 2.0 connectivity.

As figure 3.1 shows, the milling tool is manoeuvred in three dimensions, via control of four micro-step resolution stepper motors (200 $step \cdot rev^{-1}$; 1600 $\mu step \cdot rev^{-1}$, *Nanotec*), where two motors operate in tandem to drive motion in the x-dimension. Powered motor revolutions turn threaded metal rods (1 *rev* = 1 *cm*), with clockwise/anticlockwise turns manipulating physical probe positioning along length of each rod in each direction. The x and y dimensions of the sample bed that are accessible by the milling tool are 51.5 x 33.3 *cm*, with a maximum 30 *cm* vertical clearance from the instrument bed. Figure 3.2 shows an overhead scaled technical diagram of the platform, featuring a probe mount - which can be fitted with a flexible range of probes - and an acid resistant laser-cut sample holder (maximum 208 vials; acid resistant Acrylic; *Thompson Plastics*).

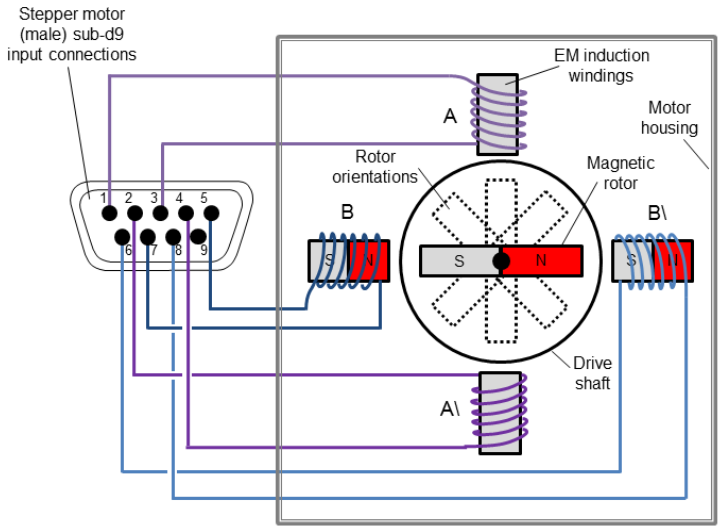


▲ Figure 3.2 - To-scale (overhead) technical schematic of the automated robotic platform, with x,y,z motors, stored reference position (X), (208-vial) sample array and electrode mount locations highlighted.

3.2.2 Custom Instrument Design

3.2.2.1 Stepper Motor Control

There are various methods of achieving commutation of stepper motors, varying in cost and precision. A common problem with low-cost motors generally surrounds a lack of control, whereby steps are gained/lost. The motors in question (200 *step·rev*$^{-1}$; 1600 *µstep·rev*$^{-1}$; *ST5918L3008-A*; *Nanotec*) - which use sinusoidal electromagnetisation of a rotor, a rotary encoder to track electric rotor positioning and closed loop current feedback current control - are high precision motors when operated within generous angular velocity limits. This type of stepper motor is a bipolar 4-wire motor, with design as per the simplified technical schematic in figure 3.3. The wiring configuration allows for 'bipolar' electromagnetisation of many coils (A, A\, B, B\) directing the orientation of a magnetic rotor. The rotor has many distinct orientations which are switched between (as indicated in figure 3.3) to induce clockwise (CW) or counter-clockwise (CCW) rotations. Additionally, current control feedback allows for power input to be regulated in real time, increasing current and thermal efficiency of motor use, with knock-on effects on precision.

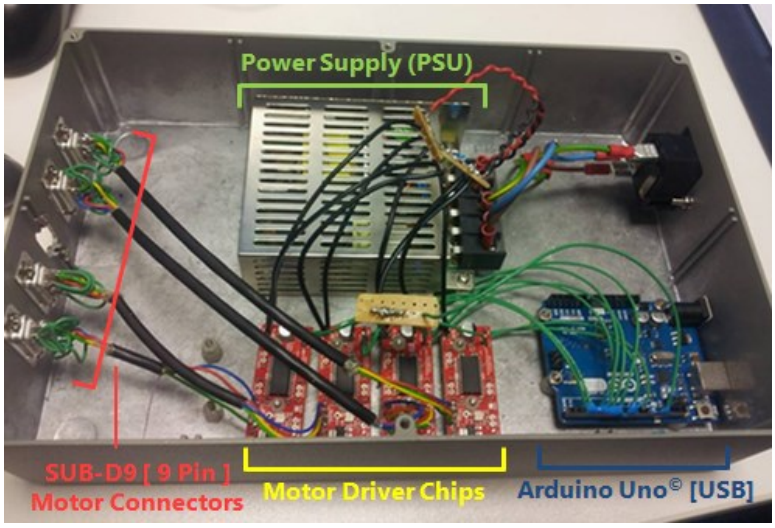


EMI Sequence		Winding Polarity			
CW	CCW	A	B	A/	B/
1	4	+	+	-	-
2	3	-	+	+	-
3	2	-	-	+	+
4	1	+	-	-	+

▲ Figure 3.3 – (left) Simplified technical schematic for a bipolar stepper motor, with sub-d9 output connections and with the distinct rotor orientations illustrated (····). (right) A table including the electromagnetic induction (EMI) sequence required to induce clockwise (CW) and counter-clockwise (CCW) magnetic rotor revolutions.

For high precision applications, stepper motors require a driver circuit board controlled by a microprocessor. The driver circuit generally receives two inputs from the microprocessor (step, direction), where ground referenced actuation (voltage) signals are converted to sinusoidal variation of current flow in the motor windings, which are pulsed in the correct sequence.

These components comprise a customised stepper motor control box with USB 2.0 connectivity (figure 3.4). The chosen printed driver circuit boards (*EasyDriver V4.5*) and microprocessor (*Arduino Uno SMD Rev3*; *ATmega328*) are cost effective and offer benefits in flexible open-source programming. Code development is discussed in section 3.2.3.



▲ Figure 3.4 - Custom-built stepper motor control box based on Arduino Uno SMD rev3® microprocessing hardware.

3.2.2.2 Safety Considerations

When implementing custom instrumentation, consideration of safety must be paramount – therefore it was deemed imperative to (at least) match the safety features of the original CNC instrument, which featured an emergency stop kill switch and magnetic limit switches for use on each axis. The instrument was enclosed by a custom-built aluminium alloy box in order to restrict access to moving parts and to protect the user in case of emergency.

The signals generated by the limit switches and stop buttons are ground referenced voltage signals, which can be interpreted digitally (I/O), allowing determination of when all motor functions should cease immediately. Arduino boards contain a reset pin, which immediately removes all uploaded firmware instructions. Delivery of a HIGH digital voltage to the reset pin thus ceasing interpretation of any further motion instructions and stopping coded signals reaching the motor driver circuit. However, in the case of an emergency a single Arduino board will not interrupt a signal transmission to send this emergency response to the reset pin. Therefore, the emergency response is 'queued' until the next main program loop, during which significant motorised motion may take place. Hence, a secondary Arduino board is required to monitor, interpret and execute the emergency response to kill the activity of the primary Arduino board. This failsafe functionality was incorporated via a fifth sub-d9 input, which is shown as

empty on figure 3.4. Full copies of the safety-ensuring code structure is provided in the appendices.

Instrument maintenance is also imperative from a safety perspective. Arduino® boards have a limited lifetime (~100,000 EEPROM read-write cycles – see below) and may require replacement over time. The dc-powering of the motor driver boards are tuned to the output power requirements of the motors (3 VDC) to maximise current efficiency and minimise heating of instrument electronics. Due to the use of volatile liquid acids, the risk of corrosion of moving metal parts is high if not properly protected, which can lead to imprecise movements or potentially mechanical locking. It was found that removal of corrosion to a base layer of metal is achieved using rust removing gel (*Hammerite*), before the most effective corrosion resistance and lubrication is afforded by use of dry PTFE lubricants (*WD-40*) and vacuum grease (*Dow Corning*).

3.2.3 Arduino® Programming

Prior to first-use, the Arduino's inbuilt microcontroller (*ATmega328*) is loaded with coded firmware instructions via USB, as developed within the Arduino IDE software. Firmware allows interpretation of received USB communications (sent by NI LabView® - section 3.2.4) and to relay the appropriate motor actuation instructions to the driver circuit for each independent motor. Within this section the full firmware coding may be useful for reference (appendices), however, key sections of code will be presented in-line with discussions.

3.2.3.1 Atmel AVR/C Programming Language

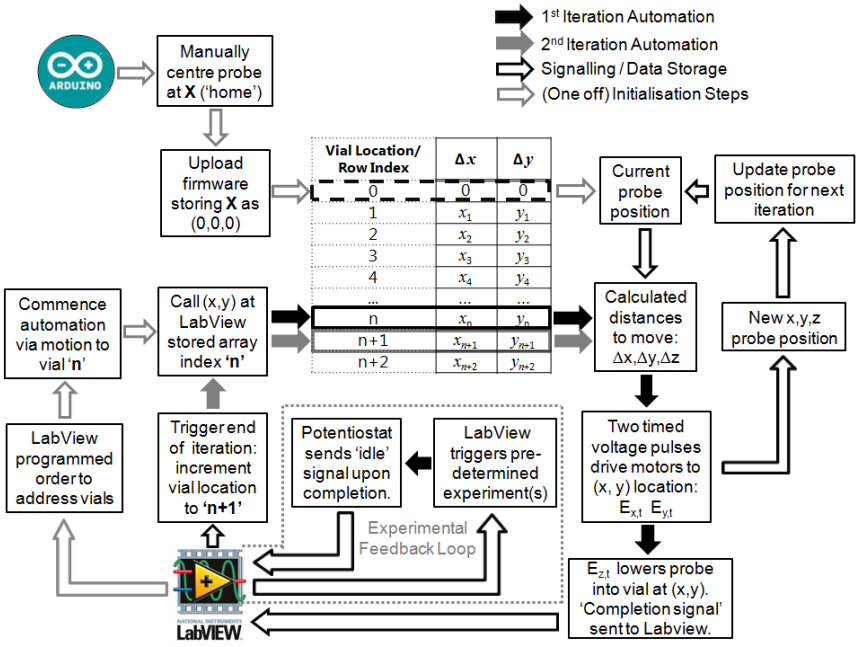
The AVC microprocessor was developed in the mid-1990s at Atmel, as one of the first microprocessors with on-chip flash memory,[4] but also containing 256 bytes (8-bit) electrically erasable programmable read-only memory (EEPROM) non-volatile memory locations. Read-only memory is necessary to repetitive cycles of programming in order to pass recorded data from one program execution loop to the next, via sequential write-read operations. A number of programming languages can be used to sketch and edit programs developed in the Arduino IDE environment, where tools can be used for conversions before upload of a code compiled in C. It was therefore convenient to directly write in the C programming language.[5]

3.2.3.2 Motor Control Coding

The key features of the full Arduino firmware code (appendices) are set out below. Figure 3.5 summarises a typical automated instrument workflow, highlighting that all vial coordinate locations can be stored and managed from a low-level LabView© virtual instrument (vi – section 3.2.4). As is standard, the code begins with a single configuration loop, in which the digital output pins are assigned and setup, thus allowing HIGH/LOW digital voltage signals to be

relayed to the motor driver circuit. Key serial communication properties (*e.g.* baud rate = 9600) and other default settings (*e.g.* revolution speed) are also initialised, including definition and storage of the current probe (x, y, z)-positioning as (0, 0, 0) in the on-chip EEPROM memory.

Software programs such as the *Arduino IDE* and *NI LabView*® transmit and receive data via USB serial communication. Figure 3.5 illustrates that when data is sent via serial communication, the microprocessor is able to read the information from the serial buffer. The main program loop of the firmware uploaded to the microprocessor is configured to read serial relayed motion commands in the form of a position to move to, *i.e.* (x, y, z). The firmware recalls the current position of the probe from EEPROM memory and calculates the required number of steps to move *i.e.* (Δx, Δy, Δz) before turning the motor until the calculated remaining steps count is equal to zero. Once all motor motions are complete, the Arduino microprocessor writes the new position of the probe to EEPROM memory (x,y,z) for use in the next probe manipulation and by way of signalling completion of motorised motion writes '1' to the serial buffer, allowing recognition of phase termination and triggering of the next electronic operation in the automated sequence.



▲ Figure 3.5 - Flowchart summarising the Arduino© pulsed voltage signalling of four independent stepper motors for manipulation of the probe location in x, y, z dimensions. LabView© commands are interfaced with the Arduino© microprocessor to exemplify the sequencing of motorised motion and potentiostatic measurement stages, with potentiostat triggering used as an example of a possible experimental stage.

3.2.3.3 Additional Functionalities

The above section summarises the key motion-inducing operations within the workflow. However, during development, several coded elements were added in order to increase

functionality and ease of use. The coded functions added are shown in table 3.1, principally relying on the serial.peak() function. When a command is sent to the Arduino serial buffer, 'reading' of that command results in the bitwise removal of information from the buffer. Serial.peak() is a function that allows for the information to be checked without being removed. Thus, if a serial transmission is begun with a specific ASCII character which is unique to a coded function, then the firmware will recognise this function and execute differing code sections, based on the identity of the initiation character. Each custom coded function is discussed briefly below.

It was often found useful to activate a 'virtual movement' of the probe, in which the EEPROM stored position of the probe was changed without physically changing the positioning of the probe. For example, the command &0,0,0 would write the current probe position as 0,0,0 and will be used to reference subsequent probe movements.

The speed of motor revolution is defined by a delay time which elapses between each single step of the motor. In micro-step mode, one step is equivalent to rotation of the rotor between two adjacent orientations out of the eight that comprise a full revolution (figure 3.3). Accessible speeds are varied by choosing a non-zero factor (v_m) within the range of 0-1, whereby a delay time (t_d) is calculated, such that the default delay time is 350 *ms* (v_m = 0.2; E3.1) and the minimum delay is 70 *ms* at the maximum (safe) motorised speed. This order of delay is required to allow for processing time, thus restricting the maximum speed of revolution. The speed factor, v_m, can easily be changed using commands initialised with the '!' character, followed by the desired double-precision value.

$$t_d = \left\| \frac{0.07}{v_m} \right\| \qquad \text{E3.1}$$

Clearly, high speeds promote reduced experimental timescales, however the motors do not supply enough torque to immediately enact high speed rotation. If too high speeds are used from rest, mechanical friction results in stalling or imprecision of motion. Therefore, high speeds are only accessible if an acceleration factor is introduced. The default acceleration (a_m) is set to 100 *steps*, whereby this integer value stipulates the number of steps over which the delay time is reduced – whereby the revolution speed is increased linearly over the chosen number of acceleration steps from a low minimum speed ($v_{m,min}$ = 0.05; $t_{d,min}$ = 1.4 *s*) up to the high revolution speeds required (e.g. v_m = 1; $t_{d,max}$ = 70 *ms*). When operating at high speeds, an equivalent deceleration process is required and is executed in analogous fashion. The number of steps over which acceleration/deceleration occurs can be adjusted using commands initiated with '?' and followed by an integer number of acceleration steps. If $2a_m$ is larger than the required number of steps for any individual motorised motion, then the unproblematic default speed (v_m = 0.2) is used to complete this manipulation before continuing to operate with the set acceleration value for larger range probe manipulation.

▼ Table 3.1 – Summary of coding functionalities included in Arduino® firmware allowing heightened accessibility and flexible use benefits.

Function / Action	Initiation Character	(Dec) ASCII Character	Command Format	Default value	Range of Values
Probe motion	n/a	n/a	X,Y,Z	0,0,0	32000,20000,9000
No movement in one axis	_	95	e.g. X,Y,_	(stored position)	(as above)
Virtual probe motion	&	38	&X,Y,Z	---	(as above)
Change revolution speed	!	33	!float	float = 0.2	0-1
Change acceleration steps	?	63	?int	int = 100	0-1000(+)
Print current position	#	35	#	---	---
Automatic probe homing	@	64	@	---	---

One challenging drawback to the EEPROM storage of probe positioning is difficulties storing and recalling negative coordinates, therefore it was necessary to choose a 0,0,0 reference position whereby all possible probe positions are positive numbers. During development stages, manual positioning of the probe to a precise set location was time-consuming and inexact. A useful function was designed to navigate to a consistent reference position of choice to be stored as (0,0,0). Use of commands initiated with '@' moves the probe to the (x,y) extremities of the accessible workspace, using the limit switch signals in order to provide feedback control to the microprocessor. The result is that the probe can be automatically moved to a precise user-defined reference position (X – figure 3.2) and the appropriate EEPROM memory locations are overwritten to become (0,0,0).

3.2.4 NI LabView® Programming

Experimental sequencing of automated operations is achieved using *NI LabView*© graphical programming interface and, more specifically, the functions contained within the virtual instrument software architecture (VISA) pallet. Graphical programming consists of the 'wiring together' of sections of pre-programmed low-level coded functions, which are represented as user-friendly icons. A user-defined 'front-panel' can be constructed to be similar in appearance to conventional software interfaces, allowing the user to feed parameter choices into the program - that is constructed in a 'block diagram' - and to view program outputs. When used in combination, the graphical block diagram and front panel are referred to as a virtual instrument (VI) and allow the user to visualise progression through a coded task. The specific use of *NI LabView*® sub-VIs in this application is to communicate with all programming-enabled devices – for example, to establish serial communication with the motor control box, actuate motions or

functions (*e.g*. table 3.1), to initialise experimental procedures or begin data-logging operations (section 3.2.4.4).

3.2.4.1 Choice of Probe

The primary envisaged purpose of the platform is as an electrochemical screening tool, requiring integration of the platform with a programmable potentiostatic device (figure 2.16). However, the described basic motorised motions can be combined for use with a number of programmable probes. Using the signal relaying equipment described in chapter 2, automated cycles to record the analogue response of the aforementioned Cu^{2+} ISE and an integrated *p*H, T and E_h probe in various chemical media has been made possible (*e.g.* figure 2.19). In addition, the required coding has been developed for the automated acquisition of UV-visible spectra using a variable path length fibre-optic spectrometer (*Ocean Optics HR2000+CG*). An exemplar sub-VI has also been developed for this purpose (UVVis_Abs.vi; table 3.2), however only test experiments have been carried out, with some practical obstacles remaining to be addressed in future work. Thus, *NI LabView*® is a highly powerful development suite allowing for flexible integration of a large number of programmable probes with the existing robotic platform.

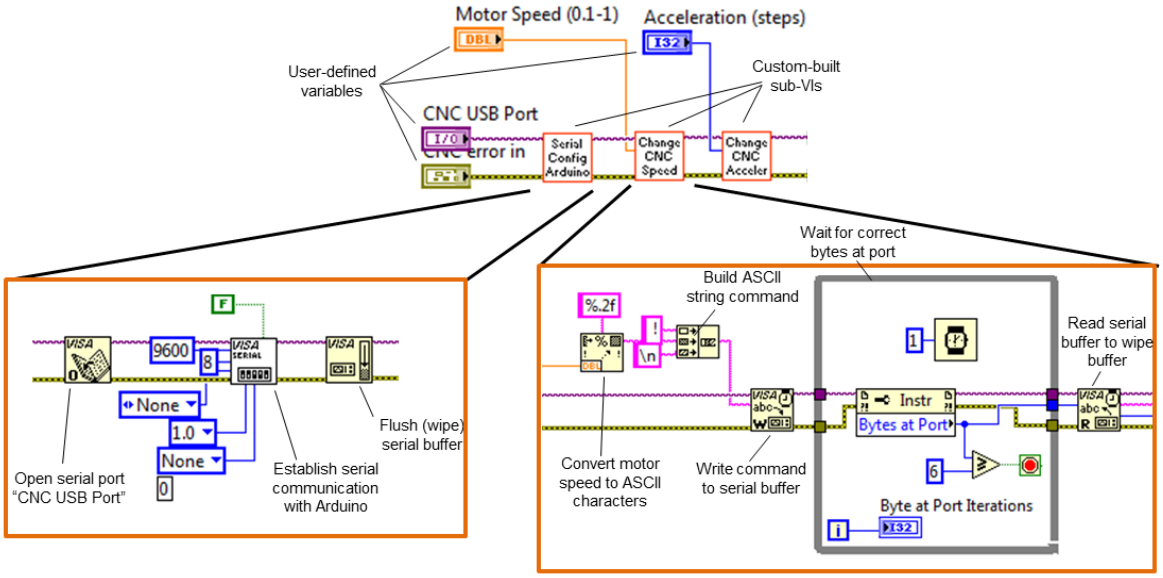
3.2.4.2 Low-level Graphical Coding (sub-VIs)

Table 3.2 shows a list of custom developed low-level sub-VIs, which are analogous to the writing of functions in a broader coding sense. Their purpose is to execute a repetitive task giving useful data outputs that are often a function of the data requirements for the function to operate (inputs). The sub-VIs are described and presented in the approximate order in which they may be sequenced during automated cycles, with exact choices allowing flexibility of experimental technique and studied samples.

Figure 3.6 gives a simplified yet crucial example of a sequence of NI LabView sub-VIs designed to establish USB serial connectivity with the Arduino microprocessor, followed by manipulation of the speed of the motor revolutions for the ensuing experiment. When establishing serial communications, the chosen buffer read-write settings must match the requirements of the device, thus explaining the choice of inputs shown in order to establish *LabView-Arduino* serial communication (9600 baud rate, 8 bits per byte packets, no flow control, no parity, stop bit = 1).

▼ Table 3.2 – Summary of NI LabView sub-VIs coding functionalities, presented in the order that they are likely to be sequenced within a typical automation program.

Sub-VI File Name	Application	Description of Function
UVVis_Ref.vi	UV-Visible Spec.	Record reference intensity file (.txt) for later calculation of absorbance for UV-visible spectroscopy with user defined settings.
UVVis_Dark.vi	UV-Visible Spec.	Record dark intensity file (.txt) for later calculation of absorbance for UV-visible spectroscopy with user defined settings.
VialDiagram.vi	Pipette	Create interactive vial diagram for choice of vials for pipetting
ConnectToIvium.vi	Potentiostat	Power up and establish connection for control of potentiostat device
CNCSerialConfig.vi	All	Establish serial communication with Arduino-based motor control box
ChangeSpeed.vi	All	Change the maximum speed of motor revolutions
ChangeAcceleration.vi	All	Change the number of steps over which acceleration to maximum speed occurs
AutomaticHoming.vi	All	Automatically move probe to X reference position and store as (0,0,0)
InitialisePipette.vi	Pipette	Establish connection to robotic pipette and set start-up settings
GoHomeandAspirate.vi	Pipette	Return to stock solution and aspirate user-defined quantity of fluid
MoveandAspirate.vi	Pipette	Move to user defined vial and deliver volume of fluid to vial
GenPipCom.vi	Pipette	Send a user defined command to the pipette (see manual for possibilities)
Z_Up.vi	All	Raise probe in Z-dimension to a safe height with clearance for XY movements
XY_Movement.vi	All	Store all vial coordinate locations and travel to a XY vial location
Z_Down.vi	All	Lower probe into a vial within the sample holder
Electrochemistry.vi	Potentiostat	Execute pre-saved Ivium (.imf) method file to generate experimental data
ReadCupricISE.vi	Cupric ISE	Read analogue input signal from cupric ISE and record in .txt file
Read_pH_T_Eh.vi	pH, T, E_h electrode	(8) Multichannel data-logging of analogue output of pH, T, E_h electrode in .txt files
UVVis_Abs.vi	UV-Visible Spec.	Displays and logs a user-defined number of UV-Vis spectra with settings choices from a fibre optic USB UV-Vis device using passed reference and dark spectra recorded previously
DeviceStatusQuery.vi	Potentiostat	Query finish of experimental procedure (wait for device idle signal)
Save.vi	Potentiostat	Save Ivium (.idf) file to predetermined location with user defined filename
CloseIvium.vi	Potentiostat	Power down routine to relinquish control of potentiostat device
ConvertAItopH_T_Eh.vi	pH, T, E_h electrode	Convert analogue input current data logged from pH, E_h, T electrode probe into physical data for pH, T and E_h



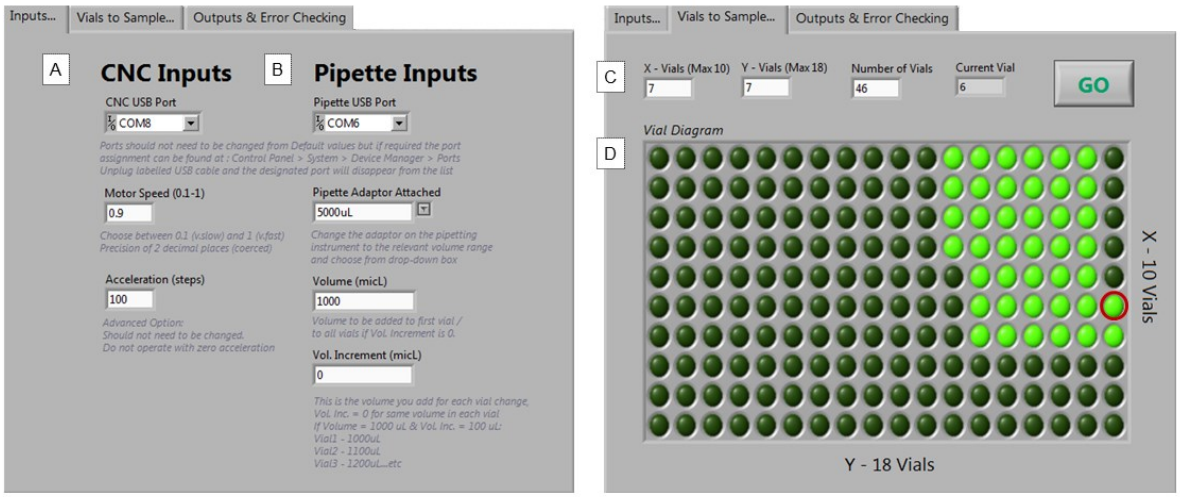
▲ Figure 3.6 – Schematic of a simple section of the PipettingRobot.vi virtual instrument (table 3.3). Square icons are sub-VIs with underlying code, producing outputs based on the treatment of variable user-defined inputs.

Having successfully initialised the platform and addressed a sample, potentiostatic electrochemistry functions (*Compactstat*; *Ivium Technologies*) are accessed and triggered in *NI LabView*® using a dynamic link library (.dll) of integrated functions. The .dll file is developed by the manufacturer and allows the user to access an *NI LabView*® library containing all key software functions required for conventional potentiostat use. *NI LabView*® has an in-built requirement for a sub-VI to complete its activity prior to the action of the next piece function within a wired chain can execute, thus making phase sequencing relatively facile. However, some specific sub-VIs are required for monitoring completion of certain phases with in-built triggering mechanisms. For example, completion of a potentiostatic operation is probed through monitoring instrument status output signals (DeviceStatusQuery.vi; table 3.2) indicating the activity of the instrument and allowing triggering of subsequent operations once the instrument becomes 'idle' due to experiment completion.

3.2.4.3 High-level Graphical Coding (VI)

High functioning VIs have been created to allow access to automated experimentation using the probes introduced in section 3.2.4.1. Table 3.3 has been constructed to summarise the virtual instrument filenames (.vi), specific function and the vial layout required for use of the technique. Due to the nature, complexity and appearance of graphical coding in *NI LabView*® it is impractical to display images of the coding involved in these VIs, however figure 3.7 displays the type of results that have been achieved. The right-hand panel of the diagram shows a tab of the (layered) front panel for PipettingRobot.vi (see table 3.3), containing a sample holder diagram for the interactive choice of vials to pipette into and real-time visual tracking of progress. A standard (NxN) grid of samples can be chosen, where mouse-clicks can be used to interactively select-

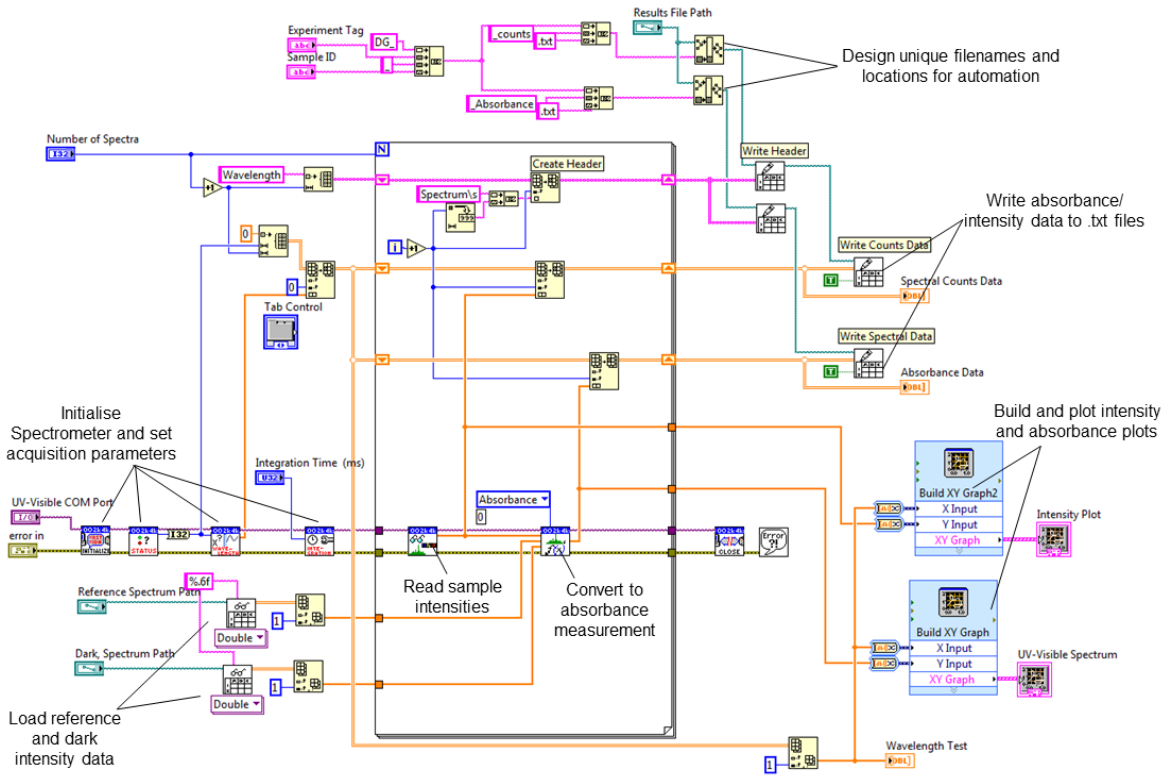
deselect further vials. Once the automation has begun, progress is tracked with a red circle around the current vial and dimming of the vial's LED indicator upon completion.



▲ Figure 3.7 – Example of an NI LabView® front panel for configuration of the robotic pipetting instrument – (A) Motor configuration - serial ports; motor speed; acceleration steps. (B) Pipetting controls - serial port; tip adapter; initial volume; volume increment. (C) User controls for number of samples - with three event controlled cooperative approaches to indicate the most time vial locations to use. (D) Interative vial diagram, auto-updating to show samples selected for pipetting (lit), current working location (○) and completed locations (dimmed).

▼ Table 3.3 – Summary of NI LabView VIs, used for user-defined sequencing of functions to create a customised automated procedure with a flexible choice of probe attachment.

VI File Name	Description of Function	Vial Layout
3_Echem_Exp.vi	Sequence (up to) three back-to-back electrochemical experiments per vial.	All samples placed at vial locations 1-180.
ASV_VI_1vial.vi	ASV in 1-vial mode where electrodeposition and stripping are conducted back-to-back with the sample vial.	Alternating row layout: cleaning sol^{n} (1-10); sample sol^{n} (11-20).
ASV_VI_2vial.vi	ASV in conventional 2-vial mode where stripping is conducted in fresh electrolytic media.	Alternating row layout: cleaning sol^{n} (1-10); samples (11-20); stripping sol^{n} (21-30).
CupricISE_SmallVials.vi	Recording of $Cu^{2+}_{(aq)}$ ISE potential output from samples placed in up to 180 small volume vials.	Alternating row layout: cleaning sol^{n} (1-10); sample sol^{n} (11-20).
CupricISE_LargeVials.vi	Recording of $Cu^{2+}_{(aq)}$ ISE potential output from samples placed in up to 28 moderate volume vials.	Alternating row layout: cleaning sol^{n} (181-194); sample sol^{n} (195-208).
GoHome.vi	Execute VI to return probe to (correctly stored) 0,0,0 coordinates.	n/a
MovementLooser.vi	Check for validation of smooth mechanical functioning, with probe repetitively moving across full workspace.	n/a
OnlineLeachingMonitor.vi	Automated scheduling of potentiostatic electrochemistry with user defined experiments and time intervals.	n/a
PipettingRobot.vi	Custom-designed procedures for automated pipetting of large numbers of samples, as per figure 3.7.	All samples placed at vial locations 1-180.
RedoxProbe_SmallVials.vi	Recording of *p*H, T and E_h current output from samples placed in up to 180 small volume vials.	Alternating row layout: cleaning sol^{n} (1-10); sample sol^{n} (11-20).
RedoxProbe_LargeVials.vi	Recording of *p*H, T and E_h current output from samples placed in up to 28 moderate volume vials.	Alternating row layout: cleaning sol^{n} (181-194); sample sol^{n} (195-208).



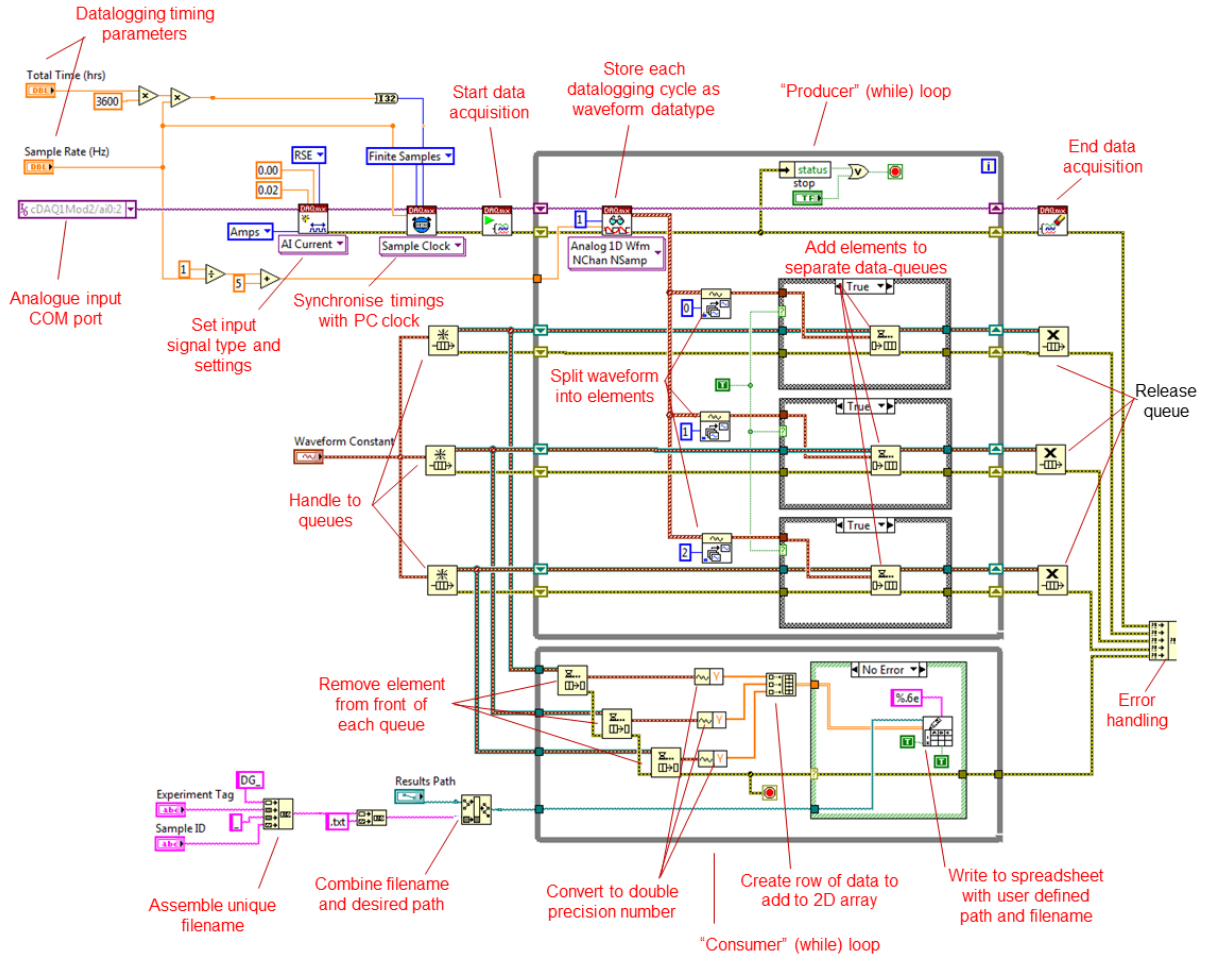
▲ Figure 3.8 – Graphical coding of UVVis_Abs.vi to allow flexible automated acquisition of UV-visible spectra from a fibre optic device.

3.2.4.4 Data-logging Operations in LabView®

Utilising the analogue readout equipment described in chapter 2, ground referenced analogue current (0-20 *mA*) or potential (0-10 *V*) signals can be transferred to PC via USB serial communication, similarly to the process described above. Visualisation of this data for single measurements is straightforward, however flexible recording of data with user defined controls over multiple data channels simultaneously is more complex, and can present programming issues. Therefore, in order to allow use of analogue probes (Cu^{2+} ISE / *p*H, T, E_h integrated electrode) in conjunction with the robotic platform (or otherwise), specific graphical coding is required.

Specifically, for N-recordings, N-channels are required for data-logging, where each data-logging channel is comprised of a so-called 'producer-consumer' loop structure (*i.e.* 3 loops for 3 parallel reactions). Figure 3.9 shows the complex coding required for this application, in which final versions of the code are further segmented into sub-VIs to simplify the appearance of block diagrams. Following input of user-defined measurement timings, PC-clock synchronised readings are obtained in a 1D-waveform data type for each cycle of the 'producer'-loop. The producer loop is unable to process waveform data while continuing to record further waveforms, hence each cycle of the 'producer' loop splits the newly recorded waveform into N recorded elements before adding N individual values to the end of N separate queue systems. The

simultaneously cycling 'consumer' accesses each 1D waveform queue, removing an element from the beginning of each queue per cycle. The waveform data is converted to numeric data (double precision; 64-bit; 8-byte) before writing values an output file in .txt format with a user-defined file-name and file-path. The key stages of the programming cycle are labelled in figure 3.9 - please note that only general (red) labels are intended to be legible for the purposes of this diagram.



▲ Figure 3.9 – Graphical coding example for 3-channel data acquisition in *NI LabView*® using a so-called "producer-consumer" loop system. Having established data acquisition settings, multiple queues of data are generated by the producer while-loop in order to retain original data ordering. For each cycle of the producer loop, the consumer loop cycles to remove an element from the beginning of the queues and writing to a .txt file.

3.3 Platform Validation Experiments

Following construction of the automated platform described in section 3.2, a series of experiments were created to test platform performance, consistency and flexibility of probe choice. The platform was employed to rapidly calibrate the readout of Cu^{2+} ISE measurements (figure 2.19). Three repeats were conducted in $CuSO_{4(aq)}$ reference solutions over a wide concentration range (10^{-12}-10^{0} $mol{\cdot}dm^{-3}$), using the CupricISE_LargeVials.vi virtual instrument described in table 3.3, with volumes of 5 *mL* chosen to minimise pipetting errors. The graphical

coding required for this application is analogous to that previously discussed in section 3.2.4.4. Since equivalent sample variation was measured at <2 *%*, this experiment was successful in discovering that Cu^{2+} ISE detection capabilities in $IL_{(aq)}$ were insufficient for monitoring of initial stages of $CuFeS_{2(s)}$ leaching (Cu < 1 *mmol·dm*$^{-3}$; t < 1 *day*), even without consideration of potential complications arising from presence/removal of semiconducting $CuFeS_{2(s)}$ when conducting measurements in real leachate samples.

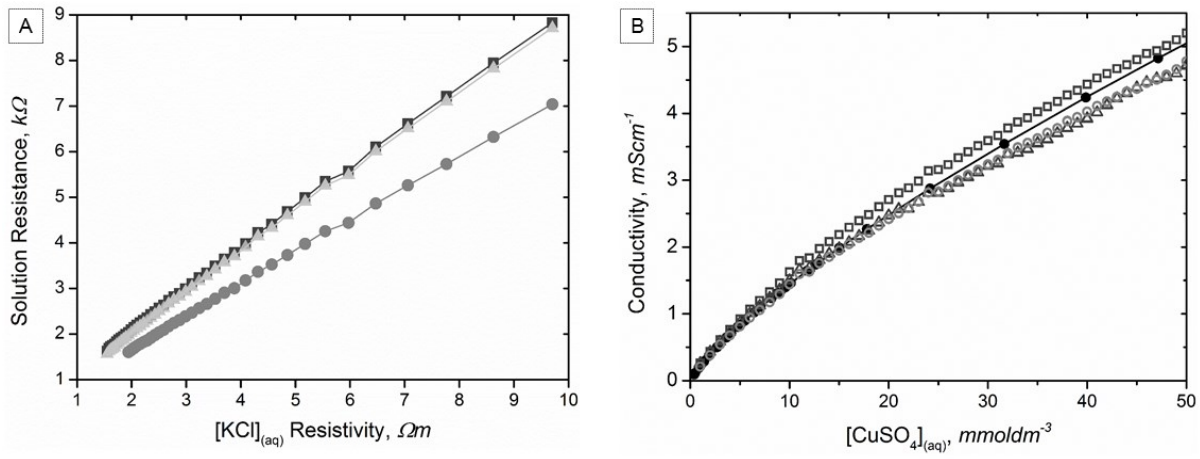
3.3.1 Conductivity Measurements

The robotic platform was used to conduct a series of automated conductivity measurements in $KCl_{(aq)}$ and $CuSO_{4(aq)}$ via EIS using an appropriately configured virtual instrument (3_Echem_Exp.vi; table 3.3). As mentioned, impedance spectra (5 *mV* ac; 10^0-10^6 *Hz*) were recorded in a two electrode configuration using a custom fabricated glass-encased double $Pt_{(s)}$ disc electrode (d = 1 *mm*), with the non-WE disc connected as a combined counter-reference electrode (vs. Pt CE/RE). This approach is appropriate since low amplitude ac fluctuations are being used, with the potential effects of reference potential drift becoming negligible.[6] When the electrode contacting electrolytic medium is modelled as outlined in chapter 2, solution resistance (R_s) measurements are obtained (figure 3.10), conducting three repeats on 50 samples in 16.5 *hrs* – a greatly reduced timescale which may be further reduced by limiting the sampled frequency range.

▼ Table 3.4 – Geometric factor measurements for three double-Pt disc electrodes and linear fit parameters.

Electrode ID	Geometric Factor, *m*$^{-1}$	R^2	Standard Error, *%*
1	888.5	0.9995	0.35
2	704.2	0.9996	0.27
3	882.2	0.9995	0.25

Rapid and accurate Ohmic geometric factor measurements (GF; table 3.4) for three fabricated electrode probes were obtained in known conductivity reference solutions (1-50 *mmol·dm*$^{-3}$ $KCl_{(aq)}$; *Sigma Aldrich*). GF estimates were then re-applied to predict the conductivity of 1-50 *mmol·dm*$^{-3}$ $CuSO_{4(aq)}$ solutions (figure 3.10B), reproducing reported data[7] with <5 *%* error and showing excellent agreement at low $CuSO_{4(aq)}$ concentrations. Low error results indicate the successful, robust automation of electrochemical methods over 100s of experiments and long experimental durations.

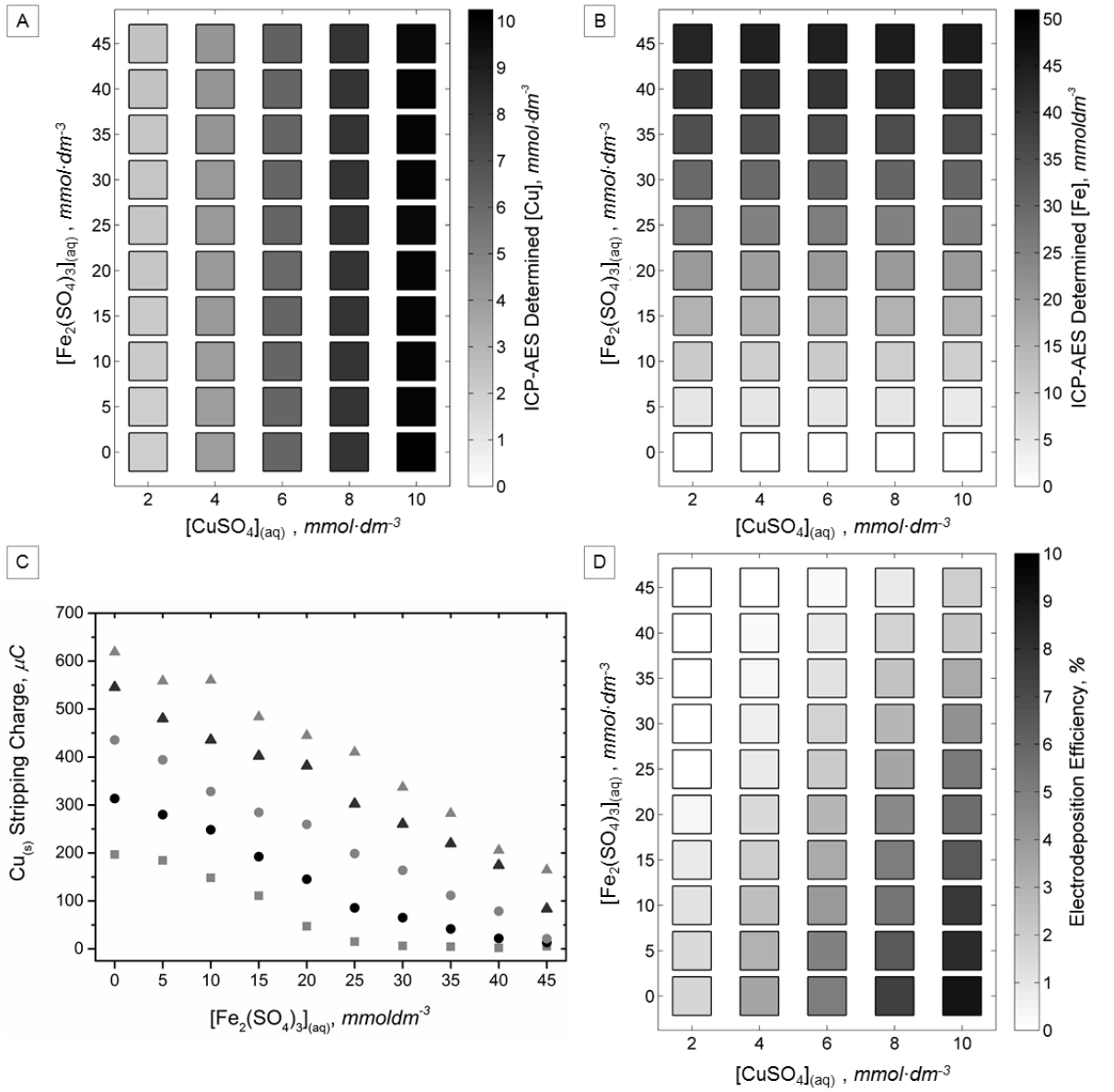


▲ Figure 3.10 – (A) Linear measured R_s in response to varied $KCl_{(aq)}$ reference solution resistivity (1-50 *mmol·dm*$^{-3}$) for three fabricated electrodes. (B) Measured conductivity of 1-50 *mmol·dm*$^{-3}$ $CuSO_{4(aq)}$ as determined using GF values (table 3.4), with all points showing <5% deviations from reported literature data.

3.3.2 ASV Validation: Ferric Remediation of $Cu^{2+}_{(aq)}$ Electrodeposition

Later, it will be established that $Cu^{2+}_{(aq)}$ is the thermodynamic product of $H_2SO_4/IL_{(aq)}$ leaching of $CuFeS_{2(s)}$ (section 4.2), evidenced by EXAFS conclusions and agreement of experimental ASV data with that of Cottrellian simulations (section 4.5.4). $Fe^{3+}_{(aq)}$ ions are a common additive oxidant for acid-sulfate chemical leaching enhancement (E1.13) and are also regenerated through the oxidation of leached $Fe^{2+}_{(aq)}$ (E1.14) in accepted reaction schemes.[8, 9] Although a strong thermodynamic prevalence of $Fe^{2+}_{(aq)}$ in equilibrated acid-$SO_{4aq)}$ leachates is established for typical leach conditions - as determined by the appropriate $Fe_{(aq)}$ Pourbaix diagram (E_h-*p*H; figure 1.11; *p*H ~1; E_h < 800 *mV* vs. SHE) - thermodynamic prevalence of Fe species has yet to be confirmed for moderate $[IL]_{(aq)}$ lixiviant solutions.

Potential presence of significant $[Fe^{3+}]_{(aq)}$ is an important electrochemical considerations, since $Fe^{3+}_{(aq)}$ has been found to curtail $Cu^{2+}_{(aq)}$ electrodeposition, lowering electrodeposition efficiency (EE; section 4.5.2) through parasitic Fe^{3+}-$Fe^{2+}_{(aq)}$ reduction currents.[10] Experiments were designed to explore the effect of $[Fe^{3+}]_{(aq)}$ on 2-vial ASV data (table 2.10) for an extreme range of possible leachate compositions in background 75 *mmol·dm*$^{-3}$ $H_2SO_{4(aq)}$ (63 *mmol·dm*$^{-3}$ $[H^+]_{(aq)}$; 0-10 *mmol·dm*$^{-3}$ $[Cu^{2+}]_{(aq)}$; 0-90 *mmol·dm*$^{-3}$ $[Fe^{3+}]_{(aq)}$), whilst also validating use of the robotic platform for complex electrochemical experimentation. Independent ICP-AES measurements were employed to confirm $[Cu^{2+}]_{(aq)}$ and $[Fe^{3+}]_{(aq)}$. As figure 3.11A-B displays, ICP-AES $[Cu^{2+}]_{(aq)}$ and $[Fe^{3+}]_{(aq)}$ were proven to show low deviations of 0.13 ± 0.11 *mmol·dm*$^{-3}$ and 0.41 ± 0.33 *mmol·dm*$^{-3}$ respectively from nominal concentration values.



▲ Figure 3.11 – (A-B) ICP-AES [M] measurements on 50 standard 75 *mmol·dm*$^{-3}$ H_2SO_4 samples containing the indicated $[CuSO_4]_{(aq)}$ and $[Fe_2(SO_4)_3]_{(aq)}$. (C) Associated ASV Q_{strip} measurements and (D) electrodeposition efficiency variation upon variation of $[Cu^{2+}]_{(aq)}$ and $[Fe^{3+}]_{(aq)}$. (■ 2; ● 4; ● 6; ▲ 8; ▲ 10 *mmol·dm*$^{-3}$ $CuSO_{4(aq)}$)

Parasitic ferric reduction currents are proven to be significant at high $[Fe^{3+}]_{(aq)}$ (figure 3.11C) where accordingly, EE is shown to be a strong function both of $[Cu^{2+}]_{(aq)}$ and $[Fe^{3+}]_{(aq)}$. In ferric-free solution, $Q_{strip,Cu}$ is increased by ~440 ± 92 *nC·mM*$^{-1}$*·s*$^{-1}$ as $[Cu^{2+}]_{(aq)}$ is increased – a value that lies within <5.5 % error of Cottrellian Q_{dep} predictions (section 4.5.4). The addition of reducible $[Fe^{3+}]_{(aq)}$ impedes cupric electrodeposition by 40 ± 15 *nC·mM*$^{-1}$*·s*$^{-1}$ at constant $[Cu^{2+}]_{(aq)}$. Returning to discussion of accepted $CuFeS_{2(s)}$ dissolution schemes (E1.12-E1.14), a 1:1 [Cu]:[Fe] ratio is accepted in the field.[8, 9, 11] If (hypothetically) 100 % $[Fe^{3+}]_{(aq)}$ was released as a result of $CuFeS_{2(s)}$ dissolution, data suggests that one would observe <10 % reduction in measured Q_{strip}. Indeed, figure 3.11D indicates that significant reductions in EE are only observed for solutions where $[Fe^{3+}]$:$[Cu^{2+}]_{(aq)}$ is ≥2.

$$pE_h = 20.1 - (2 \cdot pH) - log_{10}\left(\frac{[Fe^{2+}]}{[Fe^{3+}]}\right) \quad \text{E3.2}$$

Additionally, as discussed, since $Fe^{2+}_{(aq)}$ is thermodynamically predominant under typical leach conditions, $[Fe^{2+}]$:$[Fe^{3+}]$ would be expected to be high. This is confirmed by empirical equation E3.2,[12] estimating $[Fe^{2+}]$:$[Fe^{3+}]$ to lie within a range of 10^{11}-10^{4} for equilibrated mixtures (400-800 *mV* vs. SHE; *p*H 1.2). Since $[Fe^{3+}]_{(aq)}$ is anticipated to be extremely low and consumed by E1.13, ferric ion remediation of $Cu^{2+}_{(aq)}$ electrodeposition is expected to be an insignificant phenomenon for ASV-based monitoring of $CuFeS_{2(s)}$ leachate solutions and it can be categorically concluded that $Fe^{2+}_{(aq)}$ is the end product of leaching. The small quantities of $[Fe^{3+}]_{(aq)}$ produced by slow $Fe^{2+}_{(aq)}$ oxidation in acidic conditions is largely consumed in further $Fe^{3+}_{(aq)}$-assisted $CuFeS_{2(s)}$ oxidation via E1.13. Experimental $[Fe^{2+}]$:$[Fe^{3+}]$ within $H_2SO_{4(aq)}$/$IL_{(aq)}$ leachates will be considered further in section 5.4.4. This experiment provides a further (final) validation experiment toward the automation of high-throughput experimentation to provide large quantities of low error electrochemical data.

3.4 Automated Batch Analysis

Upon introduction of technological assistance to research activities, volumes of data requiring analysis often increases significantly. As a result, the rate-determining phase of investigations often shifts from experimental to analytical timeframes. For example, the validation experiments featured in section 3.3 generated ~1700 data files over relatively short experimental durations. Techniques such as ASV have relatively facile and repetitive analytical routines to acquire charge measures (section 2.6.3), specifically involving i-t curve integration to measure the charge transferred during each process. These operations are accomplished using device accompanying software (*IviumSoft*®), but are very time-inefficient processes when dealing with such large numbers of files. Although the analytical process must remain constant, significantly streamlined procedures and analysis flexibility benefits can be attained using customised batch analysis programs built on a suitable platform (*MatLab*®*; Mathworks*). *MatLab*® batch analysis programs are outlined below in table 3.5.

▼ Table 3.5 – Summary of MatLab® coded programs for electrochemical batch analysis.

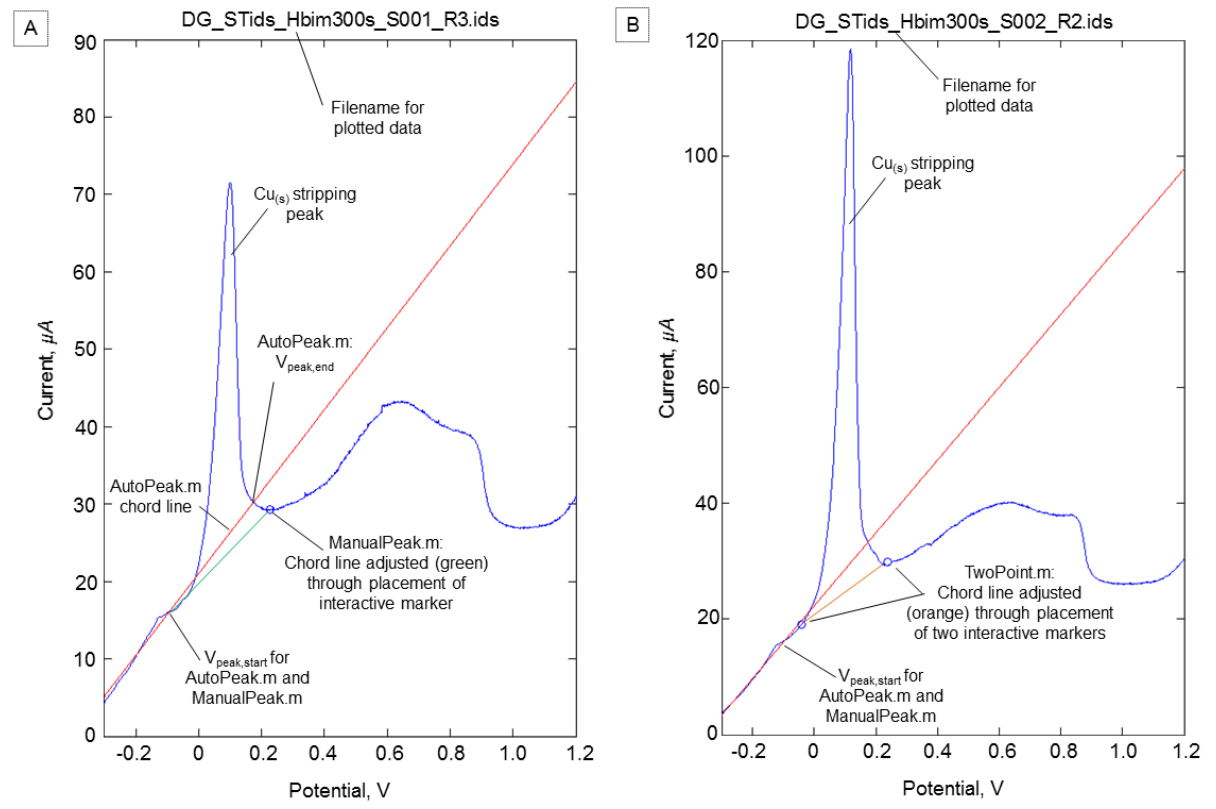
Program Filename	Program Description	Output File Formats
ASV_ED_Analysis.m	Fully automated processing of an unlimited number of (.idf) electrodeposition CA data-files producing electrolysis analysis of all files.	.txt file [File; i_{start}, i_{end}, Q_{dep}, $Q_{dep,net}$]
ASV_ST_Analysis.m	Semi-automated processing of an unlimited number of (.idf) stripping CV data-files producing peak statistics obtained from user's choice of peak-picking methodology.	.txt file [File; V_{max}, $i_{max,}$ V_{width}, A_{peak}, Q_{strip}]
ExtractandPlotIvium.m	Read and extract all electrochemical data from any Ivium (.idf, .ids), produce and save MatLab® figure for rapid visualisation and write data to file.	.fig MatLab figure .txt file [col1; col2; col3]

3.4.1 Application to Anodic Stripping Voltammetry (ASV)

In the context of automated $CuFeS_{2(s)}$ dissolution studies, ASV can generate thousands of files all requiring careful analysis. When dealing with so many files a significant proportion of the analysis timescale is wasted through the analyst executing automatable operations such as cursor movements, mouse clicks, file loading/exiting, data transfer, copy/paste operations etc. Programs such as *MatLab*® provide an ideal development suite to construct programs which rapidly access data files and load simple arrays of electrochemical data for further analysis or other operations (e.g. ExtractandPlotIvium.m - table 3.5).

$Cu^{2+}_{(aq)}$ electrodeposition i-t data is normally analysed through generation of an electrolysis report, outlining the initial current measured (i_{start}), the last current measured (i_{end}), the i-t integral (Q_{dep}) and a (rectangular) background corrected charge integral ($Q_{dep,net}$). Using ASV_ED_Analysis.m (table 3.5) an output .txt file containing this processed data is automatically generated for ~1000 files in ~5 *minutes* (*cf.* ~2 *days* manually).

Full automation of $Cu_{(s)}$ stripping analysis is not feasible for accurate Q_{strip} measurements, since the user is required to choose the integration limits ('peak-picking'). A semi-automated program was developed to rapidly load data files, visualise plotted data and to produce Q_{strip} measurements using integration boundaries determined by the user (figure 3.12). The basic data is plotted on an interactive (clickable) plot and an integration 'guideline' (red) is added. This line is added based on a linear fit of the pre-peak response of the Pt-$Cu_{(s)}$ electrode (-250 - -50 *mV*), which is assumed to be Ohmic. Theoretically, this guideline indicates the continued electrode i-V behaviour of the alloyed electrode beyond the onset of $Cu_{(s)}$ oxidation and assuming minimal influence of other electrochemical processes.



▲ Figure 3.12 – Labelled interactive graphical outputs of semi-automated stripping peak analysis program, showing interactively added points (blue circle) and baseline cords. (A) AutoPeak.m method uses -0.1 *V* and the intersection of data and (red) cord 'guideline' for integration limits. ManualPeak.m method uses -0.1 *V* and one interactively clicked point to define integration boundaries through an adjusted background cord line (green). (B) TwoPoint.m method uses two user-defined (clicked) points to define a new cord (orange) and integration limits.

The user is given a choice of three peak-picking methodologies (table 3.6) for each loaded spectrum with the additional choice to integrate multiple peaks per data file. The AutoPeak.m method is 'hands-off', using integration boundaries determined by closest data point to the intersections of the red 'guideline' before (-0.1 *V*) and after the $Cu_{(s)}$ stripping peak. The ASV_ST_Analysis.m script can be modified to use AutoPeak.m for all files - becoming an automated technique to rapidly generate Q_{strip} approximations, which can be useful.

However, the discussed red Ohmic guideline rarely provides a satisfactory measure of the limits of integration, due to non-linearity of pre-peak i-V data or peak formation variations. Figure 3.12, shows how alternative 1-point (ManualPeak.m; panel A) and 2-point (TwoPoint.m; panel B) peak-picking methodologies can be used to define alternative integration boundaries by defining adjusted cord baselines. The user is provided opportunity to visualise and review the placement of interactively placed markers and to adapt if necessary. The peak is integrated using a standard numeric method (trapezium; ΔV = 1 *mV*) with subtraction of the background trapezium area defined by the chosen baseline cord, integration boundaries and the x-axis.

Using this program, a precise and flexible approach to Q_{strip} measurement can be conducted in minimised timescales – processing hundreds of data files per hour (*cf.* ~1 day) since each data file can be processed accurately in <20 *s*. As with the previous script, all results data is automatically recorded in .txt format to avoid copy and paste operations.

▼ Table 3.6 – Summary of MatLab® coded functions included within the ASV_ST_Analysis.m semi-automated program (table 3.5) offering the user flexible choice of peak integration methodology.

Function Filename	Function Description
AutoPeak.m	Utilises experimental data point at -0.1 *V* (pre-peak) and closest data point to the point of intersection between red Ohmic guideline and experimental data (post-peak). Pre- and post-peak potential values are used to define i-t integration limits and the trapezoidal background for subtraction.
ManualPeak.m	Utilises current data point at -0.1 *V* (pre-peak). User chooses an i-V coordinate and an extrapolated linear cord line is drawn between -0.1V and the clicked position. The closest data point to the point of intersection between the adjusted cord line and experimental data is chosen (post-peak). Pre- and post-peak potential values are used to define i-t integration limits and the trapezoidal background for subtraction.
TwoPoint.m	User chooses two i-V coordinate, one pre-peak and one post-peak. An extrapolated linear cord line is drawn between the two clicked positions and the closest data points to the points of intersection either side of the peak are selected. These pre- and post-peak potential values are used to define i-t integration limits and the trapezoidal background for subtraction.

3.5 Conclusions

Throughout this chapter a range of automated research aids have been introduced and developed to directly benefit the study of $CuFeS_{2(s)}$ dissolutions. A highly flexible robotic platform has been presented and integrated with a wide range of devices (potentiostat, analogue probes, UV-visible spectroscopy, pipetting robot) all focused on investigating $lixiviant_{(aq)}$ activity towards $CuFeS_{2(s)}$ dissolution. Overhaul of the original device was found to be cost-effective, incurring costs of under £200. Crucially, successful electrochemical experiments have been conducted in order to confirm the automation power of the instrument, including ASV validation where the potential negative effect of $[Fe^{3+}]_{(aq)}$ on $Cu^{2+}{}_{(aq)}$ electrodeposition has been assessed. It was found that $[Fe^{3+}]_{(aq)}$ in leachate typical quantities ($[Fe^{2+}]/[Fe^{3+}] > 10^4$) will have negligible influence on $[Cu^{2+}]_{(aq)}$ quantification via ASV.

For any screening application, it is crucial to ensure samples are tested at equivalent time points, therefore minimising experimental timeframes becomes highly important. The custom instrumentation and programming techniques presented above offer a highly attractive combination of time-efficient automated investigations with equal sample treatment benefits. In this sense, the presented instrument provides an ideal platform for high throughput *in-situ* electrochemical screening of $IL_{(aq)}$ lixiviant activity, aiming to employ ASV $[Cu^{2+}]_{(aq)}$ determinations for identification of promising $[IL]_{(aq)}$ systems. This achievement is particularly valuable since the use of calibrated Cu^{2+} ISE output has highlighted significant detection

limitations ([Cu] > 1 *mmol·dm*$^{-3}$; t > 1 *day*) in strongly coordinating $IL_{(aq)}$ media, accompanied by difficulties in comparing analysed output for diverse $IL_{(aq)}$ systems.

In anticipation of a data analysis 'bottleneck', a series of time efficient, flexible and precise automated and semi-automated batch analysis methods have been presented to aid with minimisation of ASV data analysis durations. The user is offered a choice of three distinct 'peak-picking' methods and opportunity to record several peaks per data file.

3.6 References

1. C. A. Briehn, M.-S. Schiedel, E. M. Bonsen, W. Schuhmann and P. Bäuerle, *Angewandte Chemie International Edition*, 2001, 4680.

2. T. Erichsen, S. Reiter, W. Märkle, C. Tittel, V. Ryabova, E. M. Bonsen, G. Jung, B. Speiser and W. Schuhmann, *Review Scientific Instruments*, 2005, 062204.

3. S. Borgmann, I. Radtke, T. Erichsen, A. Blöchl, R. Heumann and W. Schuhmann, *ChemBioChem*, 2006, 669.

4. *AVR Enhanced RISC Microcontrollers Data Book*, ATMEL Corporation, 1996.

5. B. W. Kernighan and D. M. Ritchie, *The C Programming Language*, Prentice Hall, 1978

6. A. J. Bard and L. R. Faulkner, *Electrochemical Methods: Fundamentals and Applications*, Wiley, New York, 2nd edn., 2001.

7. B. B. Owen and R. W. Gurry, *Journal of the American Chemical Society*, 1938, 3074.

8. H. R. Watling, *Hydrometallurgy*, 2013, **140**, 163-180.

9. C. Klauber, *International Journal of Mineral Processing*, 2008, **86**, 1-17.

10. T. L. Hatfield and D. T. Pierce, *Journal of Applied Electrochemistry*, 1998, **28**, 397-403.

11. Y. Li, N. Kawashima, J. Li, A. P. Chandra and A. R. Gerson, *Advances in Colloid and Interface Science*, 2013, **197–198**, 1-32.

12. P. C. Singer and W. Stumm, *Oxygenation of Ferrous Iron: The Rate-Determining Step in the Formation of Acidic Mine Drainage*, Harvard University, 1968.

Chapter 4

Electrochemical Monitoring of Leaching

Contents

4.1 Introduction....4-3

4.2 Extended X-Ray Absorption Fine Structure Spectroscopy (EXAFS)....4-3

4.2.1 Motivation for EXAFS Studies....4-3

4.2.2 Detection Principle....4-5

4.2.3 Sample Submission....4-6

4.2.4 EXAFS Insights....4-8

4.2.5 Cu Speciation Modelling....4-8

4.3 Previous ASV Studies....4-10

4.4 Validity of Peak $[IL]_{(aq)}$ Lixiviant Activity....4-12

4.4.1 Background to Approach....4-12

4.4.2 Rheology Theory....4-13

4.4.3 Viscosity Data....4-13

4.4.4 $Cu^{2+}_{(aq)}$ Diffusion Coefficient....4-14

4.4.5 Implications for ASV Confidence Limits....4-16

4.5 Validation and Optimisation of ASV Procedure....4-17

4.5.1 Comparison of 1-vial and 2-vial ASV Procedures....4-17

4.5.2 Efficiency of the Electrodeposition Process....4-19

4.5.3 Control of Electrodeposition Timescale....4-21

4.5.4 Cottrellian Electrodeposition Analysis....4-22

4.6 Automated Electrochemical Dissolution Monitoring....4-28

4.6.1 Experimental Procedure 4-28
4.6.2 *In* situ ASV Data Processing 4-29
4.6.3 *In situ* Electrochemical Cu Extraction Profiles 4-31
4.6.4 Summary of *in situ* ASV Approach 4-36
4.7 Conclusions 4-37
4.8 References 4-39

Synopsis: Herein, are presented studies to establish the validity of, and optimum techniques for, electrochemical monitoring of $CuFeS_{2(s)}$ dissolution. Simulations using Cottrell theory are used to establish confidence limits of ASV charge measurements. Additionally, precise *in situ* $Cu^{2+}_{(aq)}$ extraction profiling is introduced as a novel ASV methodology for automated tracking of dissolution profiles, allowing full $Cu^{2+}_{(aq)}$ extraction reconstruction.

4.1 Introduction

Electrochemistry has provided the basis for a series of techniques offering insight into dissolution of $CuFeS_{2(s)}$ (section 2.5) and has additionally enhanced dissolution of $CuFeS_{2(s)}$ semiconducting electrodes through anodic dissolution (section 1.4.3). However, it is perhaps surprising that electrochemical monitoring of $CuFeS_{2(s)}$ has not been a more prominent thrust in past studies.

This chapter will seek to establish the feasibility of monitoring $CuFeS_{2(s)}$ leaching via ASV, towards application in an $IL_{(aq)}$ screening methodology and a novel *in situ* approach to $Cu_{(aq)}$ measurement to track progress of $CuFeS_{2(s)}$ dissolution. The stages of conventional ASV will be investigated with respect to these goals.

However, firstly the fundamental compatibility of electrodeposition in HSO_4-$IL_{(aq)}$ will be examined. Having previously outlined the probable division of $Fe^{2+}{}_{(aq)}$:$Fe^{3+}{}_{(aq)}$ (>10^4; section 3.3.2), one key aspect is to establish the speciation of solvated $Cu_{(aq)}$ following $CuFeS_{2(s)}$ dissolution in $IL_{(aq)}$ via EXAFS studies and through ASV simulations using Cottrellian theory. Simulations will later be used to uncover the confidence levels with which ASV data should be treated, requiring $IL_{(aq)}$ rheological studies to provide input data.

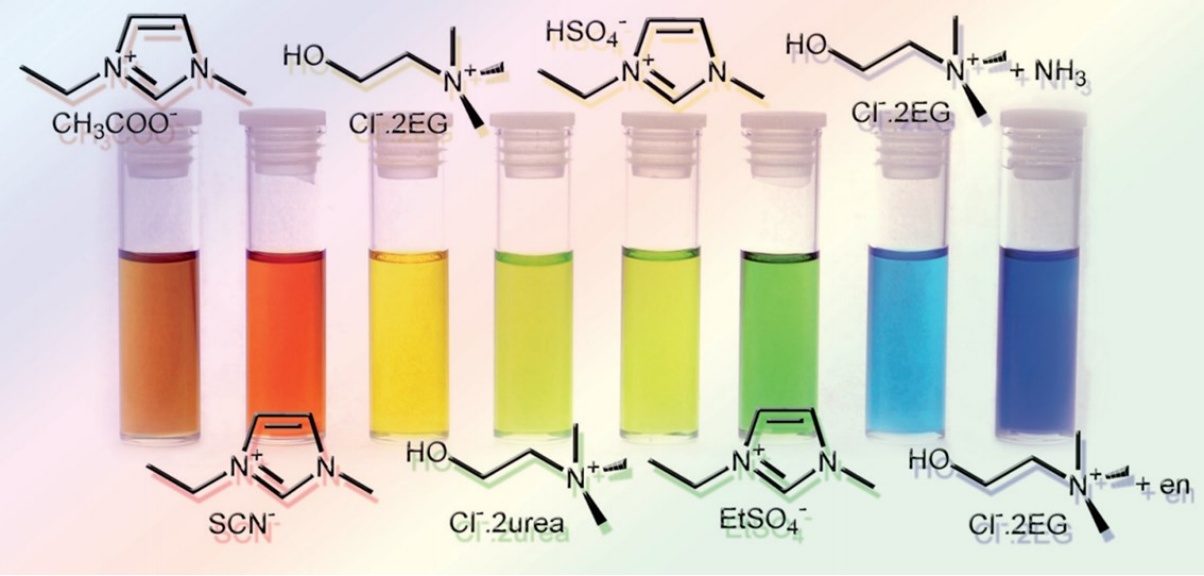
4.2 Extended X-Ray Absorption Fine Structure Spectroscopy (EXAFS)

4.2.1 Motivation for EXAFS Studies

This EXAFS investigation seeks to establish the $Cu_{(aq)}$ thermodynamic speciation resulting from $IL_{(aq)}$-$CuFeS_{2(s)}$ dissolution. Detection of IL participation in $Cu_{(aq)}$ bulk solution coordination may affect the electrochemical ASV considerations for $Cu^0/Cu^+/Cu^{2+}$ with possibility of $E^{\emptyset}$ shifts, but may also be suggestive of an IL-specific Cu extraction mechanism. Several papers since the millennium have resolved crystal structures involving favourable coordination of Cu cations by imidazole base (im), coordinating via dative N:-Cu linkages (e.g. figure 4.2).[1, 2] Similar potential dependent absorption of $[C_4C_1im]^+$ and C_1im has been observed at $Cu_{(s)}$ electrode and colloidal interfaces via Raman spectroscopy (SERS) at *p*H > 5.6 [3, 4] Additionally, further structures have been resolved showing formation of N-heterocyclic carbenes (NHCs) involving the imidazolium-C^2 position, where Cu(I)-coordinated examples have been reported (section 6.3.5).[5, 6]

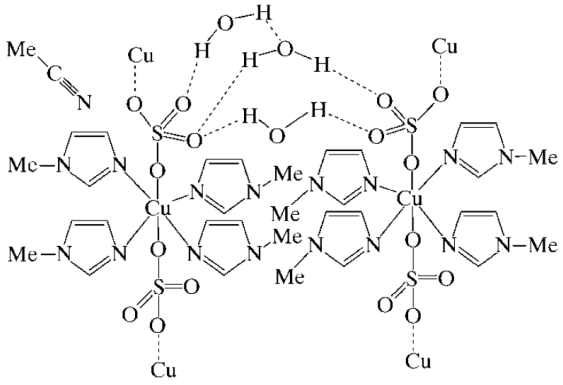
In an existing review of IL-metal complexations, EXAFS study of $CuCl_{2(IL)}$ speciation was investigated for a range of DESs and $[C_nC_mim]^+$-based ILs.[7] Figure 4.1 clearly indicates changes to Cu inner-sphere ligation in each IL, as visualised by energy shifts in d-d electronic transitions. No inherent difference was found discrete $[C_2C_1im]^+$ based ILs and ChCl based DESs in terms of Cu complexation. As anticipated, IL anions were found to dominate inner sphere metal coordination, shifting d-d transitions on the basis of their position in the spectrochemical series.

Murtomaki *et al*. also produced similar conclusions from an electrochemical study of the Cu^{2+}/Cu^{+} redox couple in DES (section 4.5).



▲ Figure 4.1 - 20 *mmol·dm*$^{-3}$ $CuCl_{2(IL)}$ in eight pure ILs based on $[C_2C_1]^+$ ILs and ChCl DESs, with structures and stoichiometries as indicated.[8]

In summary of current understanding, discussions in section 2.6.4 and figure 2.25 appear to show that nitrogen ligation of Cu can dominate at high *p*H. At high acidities, it is the IL anion which dominates metal speciation in IL, since any (basic) nitrogenous species (i.e. $C_n$im/$[C_nC_m$im$]^+$) would be expected to be protonated. Additionally, cation-cation interactions would clearly be electrostatically unfavourable. EXAFS studies may allow determination of metal coordination in the typical $IL_{(aq)}$ systems chosen and whether this complexation is best represented by aqueous or IL contributions.



▲ Figure 4.2 – Resolved crystallographic structure of *catena*-Poly[[[tetrakis(1-methylimidazole-κN^3)copper(II)]-μ^2-sulfato-$\kappa^2 O:O'$] acetonitrile hemisolvate sesquihydrate].[1]

4.2.2 Detection Principle

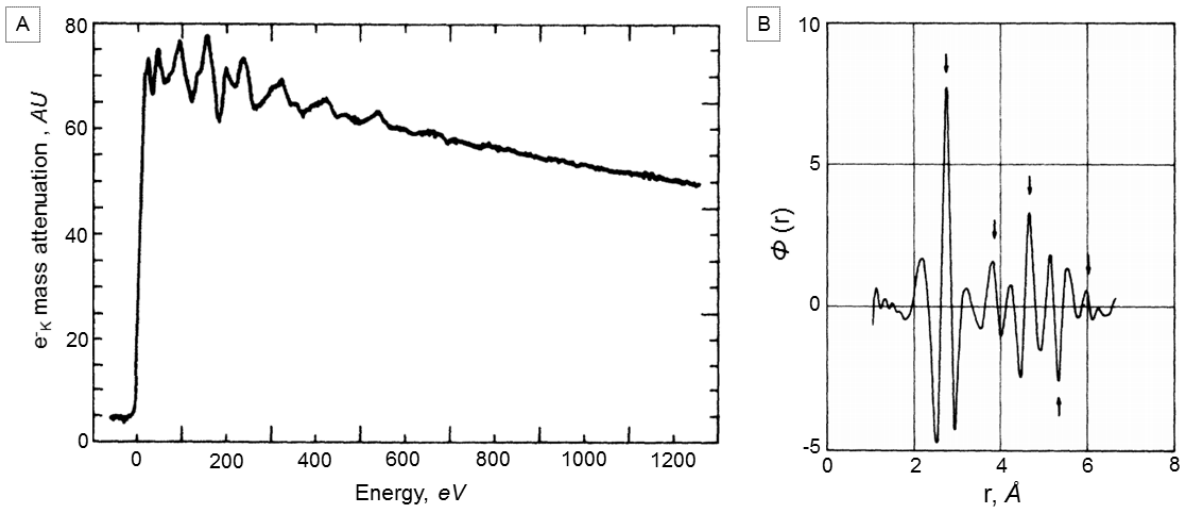
X-ray absorption spectroscopy (XAS) is a technique concerning the attenuation of x-rays in sampled chemical environments.[9] As E4.1 illustrates, the intensity of x-ray photons transmitted through a sample thickness (x) from a 1D beam decays exponentially with respect to the incident x-ray intensity (I_0) and a decay constant known as the x-ray linear attenuation coefficient (μ).

$$I = I_0 e^{-\mu x} \quad \leftrightarrow \quad \mu = -\ln\left(\frac{I}{I_0}\right) \cdot \frac{1}{x} \qquad \text{E4.1}$$

X-ray attenuation occurs due to photon absorptions, to energise electronic excitation in sample molecules. Low-lying K-shell electrons (figure 2.20B) are promoted to higher energy levels. The attenuation caused by K-shell electrons in crystalline-$Cu_{(s)}$ are shown in figure 4.3A, revealing that μ is a function of incident x-ray photon energy. The onset energy at which x-ray attenuation begins is element specific; correlated to the discrete energy differences between K-shell and vacant acceptor orbital. The extreme increase in attenuation beyond this onset is referred to as an 'edge', which for $Cu_{(aq)}$ occurs at ~9000 *eV* (figure 4.4A) but may be presented as normalised to 0 *eV* (figure 4.3A).

In the region 30-1000 *eV* above the edge, the attenuation function has a complex, waveform-like appearance referred to as 'fine structure'. The origin of this waveform complexity is the interference of the promoted photoelectronic wavefunction with backscattered waves from the chemical environment of the excited molecule - resulting in fluctuation of x-ray attenuation and the 'fine structure' modulations observed in the EXAFS region of the XAS spectrum (figure 4.3A).

Sayers *et al.* were among the first to report Fourier analysis (deconstruction of a time signal into its composite frequencies) of x-ray attenuation data, realising the value of obtaining a radial structure function.[10] Figure 4.3B shows the Fourier transform of x-ray attenuation data for crystalline-$Cu_{(s)}$, revealing the radial distance of 'shells' of nearest neighbour atoms within the crystalline lattice and indicating Cu-Cu bond lengths. EXAFS is therefore a connectivity sensitive technique, probing lattice structure in solids and speciation 'snapshots' for solution environments.[11-14]



▲ Figure 4.3 – (A) $Cu_{(s)}$ K-shell electron attenuation coefficient upon incidence of varied X-ray photon energies, showing EXAFS region of interest at 30-1000 *eV*. (B) Fourier transformed EXAFS data φ(r) for crystalline-$Cu_{(s)}$ as a function of radial distance from atomic centre, displaying layered shells of atoms (labelled ↑↓) showing peak interaction with incident X-rays.[14]

EXAFS analysis relies on the following series of equations, where X_{tot} is the sum of radial paths surrounding an excitation centre. Functions can also be produced in terms of the imaginary k wave-vector in reciprocal space ($Å^{-1}$).[12-14] Although complex, E4.3 is the fit function composed in k-space and contains free parameters used to optimise simulated functions to match experimental data – where N_i is the path degeneracy, ΔR is the change in half-path length, E_0 is the energy shift, S_0^2 is the passive electron reduction factor and σ_i^2 is the mean square displacement. These optimisation parameters require initial guesses, generated from libraries of trial structures and element references, where the former are crystallographically confirmed (table 4.2) such that complex waveforms may be combined or contributions deconvoluted.[11]

$$\chi_{tot}(k) = \sum_{i=1}^{n} \chi_i(k) \qquad \text{E4.2}$$

$$\chi_i(k) = \frac{N_i \cdot S_0^2 \cdot F_i(k)}{k \cdot R_i^2} \cdot \sin\{2kR_i + \varphi_i(k)\} \cdot e^{-2\cdot\sigma_i^2\cdot k^2} \cdot e^{\frac{-2\cdot R_i}{\lambda(k)}} \qquad \text{E4.3}$$

$$R_i = R_0 + \Delta R\,; \qquad k^2 = \frac{4\pi \cdot m_e \cdot (E - E_0)}{h} \qquad \text{E4.4}$$

4.2.3 Sample Submission

High quality EXAFS studies require a high power, coherent x-ray source. 3 *mL* unleached $CuSO_{4(aq)}$ references and leached samples were prepared in varied $[IL]_{(aq)}$ media (table 4.1) and submitted for synchrotron-EXAFS studies (*Diamond Light Source*, *Oxfordshire*), with

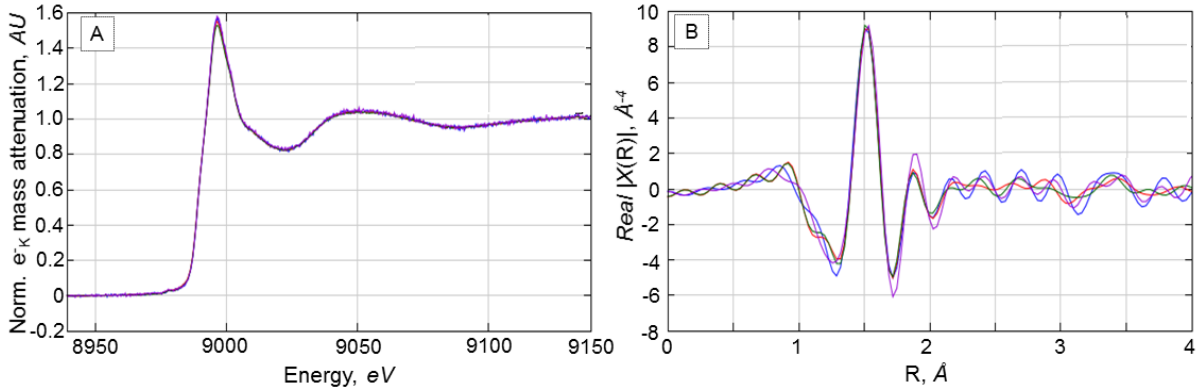
spectroscopy and analysis (*Artemis*) carried out by EXAFS specialist Dr Bao Nyugen (*University of Leeds*).[15] As table 4.1 reveals, there was considerable inaccuracy and imprecision in conventional ASV quantification of $[Cu]_{(aq)}$, which is the subject of later discussion in this chapter (section 4.5). It is also noteworthy that no stripping peak was observed in 100 *%* $[IL]_{(aq)}$ even when electrodeposition timescales were extended to 5 *mins*, where diffusion of Cu is expected to be too slow for ASV application to $IL_{(l)}$. Spectra obtained for $CuSO_4$ in pure $[C_4Him][HSO_4]_{(aq)}$ gave the expected result of solely Cu-O-SO_3 linkages, which were not analysed any further. However, no significant Cu was detected from $[C_4Him][HSO_4]_{(l)}$-leached samples.

▼ Table 4.1 – Compositions of 3 *mL* samples submitted to synchrotron-EXAFS studies for speciation studies and structural modelling.

ID	Sample Description	$[C_4Him][HSO_4]_{(aq)}$, *mmol·dm^{-3}*	$[CuSO_4]_{(aq)}$, *mmol·dm^{-3}*	t_{leach}, *hrs*	$[Cu]_{(aq)}$, *mmol·dm^{-3}*	
					ASV	ICP-AES
A.1 A.2	75 *mmol·dm^{-3}* $H_2SO_{4(aq)}$ with $CuSO_{4(aq)}$	---	10	---	---	9.8
B.1 B.2	10 *%wt* $[C_4Him][HSO_4]_{(aq)}$ with $CuSO_{4(aq)}$	450	5	---	---	4.9
B.3 B.4		450	10	---	---	10.1
B.5 B.6		450	15	---	---	15.3
C.1 C.2	1 day leaching: 150 *mg* $CuFeS_{2(s)}$ with 10 *%wt* $[C_4Him][HSO_4]_{(aq)}$	450	---	24	2.2 ± 2.2	2.0
C.3 C.4	2 day leaching: 150 *mg* $CuFeS_{2(s)}$ with 10 *%wt* $[C_4Him][HSO_4]_{(aq)}$	450	---	48	6.8 ± 3.2	3.1
C.5 C.6	3 day leaching: 150 *mg* $CuFeS_{2(s)}$ with 10 *%wt* $[C_4Him][HSO_4]_{(aq)}$	450	---	72	5.7 ± 0.8	4.2
D.1 D.2	3 day leaching: 150 *mg* $CuFeS_{2(s)}$ with 5 *%wt* $[C_4Him][HSO_4]_{(aq)}$	225	---	72	13.6 ± 1.0	2.3
E.1 E.2	3 day leaching: 150 *mg* $CuFeS_{2(s)}$ with 15 *%wt* $[C_4Him][HSO_4]_{(aq)}$	675	---	72	7.0 ± 1.6	5.0

4.2.4 EXAFS Insights

Spectra obtained for all $[C_4Him][HSO_4]_{(aq)}$ sample variants were remarkable in their close similarly (*e.g.* figure 4.5). There were few detectable spectral changes upon variation of $[IL]_{(aq)}$ in the 0-675 $mmol{\cdot}dm^{-3}$ range (samples C, D, E), where no IL-Cu interaction was observed or required accounting for. Additionally, the spectra of IL-$CuSO_{4(aq)}$ references (A) and leached IL-$CuFeS_{2(s)}$ spectra (C) were almost identical, indicating very similar speciation in each medium. Cu(I) species normally display a distinctive pre-edge feature, which was not detected in any submitted samples, indicating that $Cu^{2+}{}_{(aq)}$ is the Cu-related thermodynamic product of $CuFeS_{2(s)}$ dissolution. Further evidence for the absence of $Cu^{+}{}_{(aq)}$ is provided by observation of distinct dominant coordination geometries for Cu^{2+} (MCl_4^{2-}) and Cu^{+} (MCl_2^{-}, MCl_3^{2-}) in pure diol-based DES.[7]



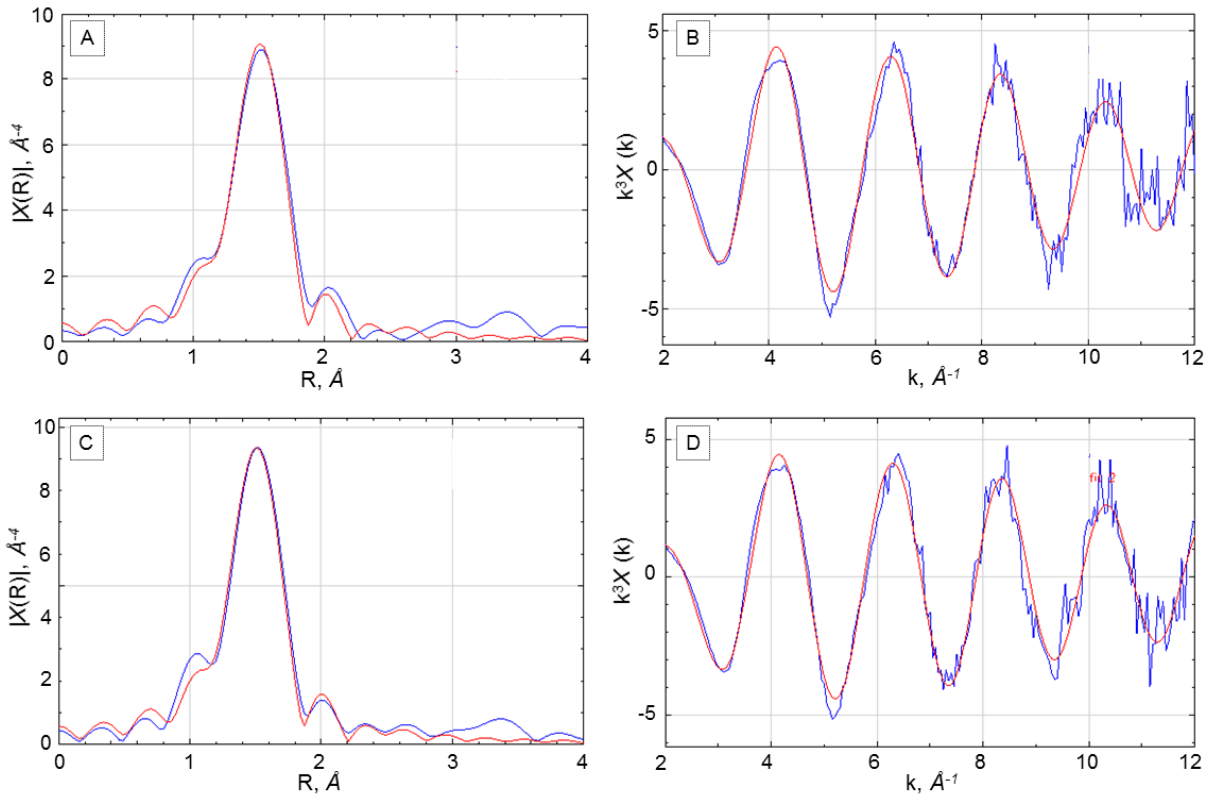
▲ Figure 4.4 – Functions generated for all $Cu_{(aq)}$ samples submitted for synchrotron-EXAFS studies (table 4.1) (A) Normalised x-ray attenuation curves as a function of incident photon energy. (B) Overlayed plots of the real component of photoelectronic wavefunction.

Some minor variability was observed in the radial distance presentation of data, corresponding to small changes in first shell hydrate coordination number for $[Cu(H_2O)_n]^{2+}{}_{(aq)}$ (figure 4.4B).[15] Interestingly, the magnitude of the peak centred at ~1.5 *Å* decreased as $[CuSO_4]_{(aq)}$ increased, possibly reflecting variation of the water availability to the $Cu^{2+}{}_{(aq)}$ solvation sphere.

4.2.5 Cu Speciation Modelling

Due to the similarity of the spectra, only IL·$CuSO_{4(aq)}$ reference samples (A, B) were used for speciation modelling. The starting point for trial coordination geometries (3D-optimised) are stored online in the Cambridge Crystallographic Data Centre (CCDC) compound library. The structures used were square pyramidal $Cu(H_2O)_4(SO_4)$, trans-octahedral $[Cu(H_2O)_4(SO_4)_2]^{2-}$, octahedral $Cu(H_2O)_5(SO_4)$ and octahedral $[Cu(H_2O)_6]^{2+}$ in both elongated Jahn-Teller and regular form. Structures were fitted in R-space (1-3 *Å*) and k-space (2-12 $Å^{-1}$; k_{weight} = 1, 2) to include only the first coordination shell. Selected optimised parameters from E4.3 are summarised in table 4.2. Low and relatively constant k-space (7.9-8.8 x 10^{-4}) and R-space uncertainties (1.6-1.8

x 10^{-3}) were received for all fits and the number of independent fit points used was held constant (~12.4).



▲ Figure 4.5 – Experimental EXAFS data for 10 *mmol·dm*$^{-3}$ $CuSO_{4(aq)}$ reference solutions in various media (blue) in comparison to fitted curves for optimised $Cu(H_2O)_4(SO_4)$ coordination geometries (red). Fits are presented in radial (R) and reciprocal space (k) for $CuSO_{4(aq)}$ in (A-B) 75 *mmol·dm*$^{-3}$ $H_2SO_{4(aq)}$ and (C-D) 450 *mmol·dm*$^{-3}$ $[C_4Him][HSO_4]_{(aq)}$.

E_0 is considered to have an acceptable value in the range of ±10 *eV*, whilst S_0^2 has been previously reported as 0.92[16] and |ΔR| should remain low in magnitude.[15] Referring to the fit summary in table 4.2 and despite good fits for all structure, $Cu(H_2O)_5(SO_4)$, $Cu(H_2O)_4(SO_4)$ (figure 4.5) and trans-$[Cu(H_2O)_4(SO_4)_2]^{2-}$ were indicated as strong candidates for inner sphere $Cu^{2+}_{(aq)}$ coordination, with regular and Jahn-Teller $[Cu(H_2O)_6]^{2+}$ structures largely rejected. The overall similarity of the spectra and the good fits with various structures suggests a dynamic mixture of hydrates, as previously indicated for $Cu^{2+}_{(aq)}$ formed from $Cu(ClO_4)_2{\cdot}6H_2O$.[17]

In summary, no interaction between the $Cu^{2+}_{(aq)}$ cation and the IL cation was suggested or required for fitting, with all evidence suggesting a dynamic mixture of $Cu^{2+}_{(aq)}$-hydrates. Cu-O coordination numbers of between 5-6, Cu-OH_2 bond length in the vicinity of 1.92 *Å* and elongated Cu-OSO_3 bond lengths of 2.3-2.5 *Å* were measured. Finally, yet crucially, the thermodynamic product of $CuFeS_{2(s)}$ dissolution has been shown to be equivalent for acid-$SO_4^{2-}{}_{(aq)}$ and $IL_{(aq)}$ leaching when 0-675 *mmol·dm*$^{-3}$ $IL_{(aq)}$ is present. Observation of water dominated $Cu^{2+}_{(aq)}$

solvation with no detection of $Cu^{+}_{(aq)}$ has important implications for correct charge measurement, calibrations and therefore the monitoring of $CuFeS_{2(s)}$ dissolution via ASV.

▼ Table 4.2 – Summary of EXAFS structural modelling of 10 *mmol·dm*$^{-3}$ $CuSO_{4(aq)}$ in (A) pure aqueous solution and (B) 450 *mmol·dm*$^{-3}$ $[C_4Him][HSO_4]_{(aq)}$.

Model Structure$_{(aq)}$	Structure; CCDC Ref.	ID	Selected Fit Parameters				Bond Length, *Å*		Fit Summary	
			N_i	E_0, *eV*	S_0^2	ΔR	Cu-OH_2	Cu-OSO_3	X^2_{red}	R-factor
$Cu(H_2O)_5(SO_4)$	Oct; WEJXIE	A	6	10.9	0.76	0.26	1.92	2.43	21.1	$1.9x10^{-3}$
		B	6	10.9	0.76	0.29	1.92	2.47	26.2	$1.9x10^{-3}$
$[Cu(H_2O)_4(SO_4)_2]^{2-}$	trans-Oct; BEVKUJ	A	6	12.5	0.83	-0.33	1.93	2.34	23.8	$2.1x10^{-3}$
		B	6	12.6	0.82	-0.33	1.93	2.36	28.8	$2.1x10^{-3}$
$Cu(H_2O)_4(SO_4)$	Sq-Py; EVAQIB	A	6	11.4	0.76	-0.14	1.92	2.34	30.5	$2.7x10^{-3}$
		B	6	11.3	0.75	-0.12	1.92	2.34	40.9	$2.9x10^{-3}$
$[Cu(H_2O)_6]^{2+}$ (crystal structure)	Jahn-Teller Oct; NAYGUR	A	6	13.8	0.87	0.01	2.80	---	40.3	$3.5x10^{-3}$
		B	5	12.3	0.58	0.51	1.93	2.31	204	$1.7x10^{-2}$
$[Cu(H_2O)_6]^{2+}$ (ideal octahedron)	Oct; NAYGUR	A	4	11.5	0.47	0.01	---	---	17.0	$3.3x10^{-3}$
		B	4	11.6	0.47	0.01	---	---	22.2	$3.6x10^{-3}$

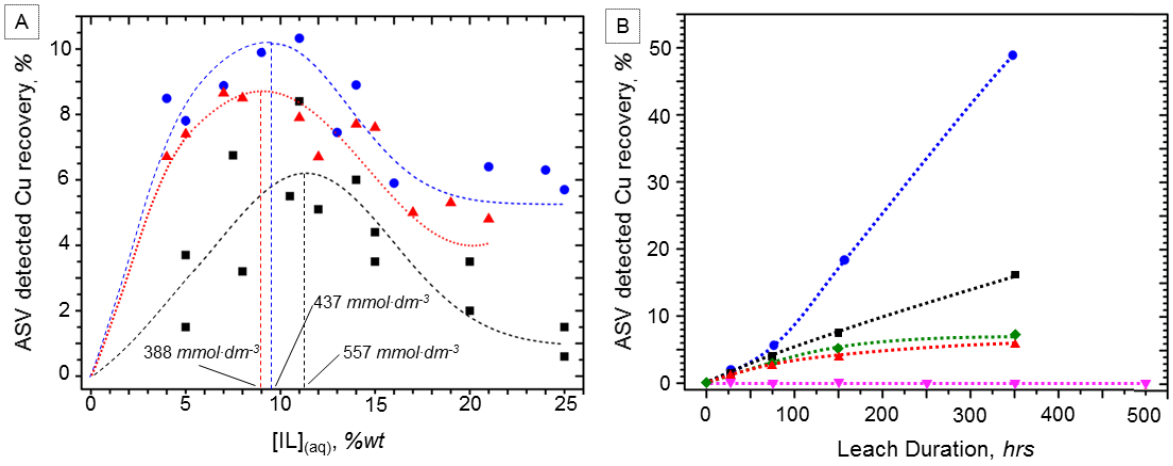
4.3 Previous ASV Studies

This section will briefly introduce the key outcomes of previous electrochemical studies in the Albrecht and Welton groups. This currently unpublished work must be introduced, since it provides the foundation to later work presented in this chapter. Experiments featured in section 4.3 were conducted in collaboration with former colleagues Dr E. J. Spadafora and Y. Choi, with grateful acknowledgement of their work and initial guidance.

Ambient, unagitated $CuFeS_{2(s)}$ dissolution (100 *mg*) was conducted in 2 *mL* volumes of $[C_nC_mim][HSO_4]_{(aq)}$. Following a leach duration of 72 *hrs*, $[Cu^{2+}]_{(aq)}$ measurements were obtained using 3-vial ASV in a two electrode configuration (t_{dep} = 300 *s*; $Pt_{(s)}$ WE; $Pt_{(s)}$ CE/RE). The resulting electrochemical $[Cu^{2+}]_{(aq)}$ measurements appear to reveal a low optimum $[C_nC_mim][HSO_4]_{(aq)}$ concentration for maximum $CuFeS_{2(s)}$ dissolution (figure 4.6A), with the indicated optimum $[IL]_{(aq)}$ dispersed about ~500 *mmol·dm*$^{-3}$.

Figure 4.6B also presents data acquired in an analogous fashion for equivalent ambient leaching over 350 *hrs*, conducted in 10 *%wt* $[C_nC_mim][HSO_4]_{(aq)}$. Based on ASV measurements as a function of time, 10 *%wt* $[C_4Him][HSO_4]_{(aq)}$ is shown to significant outperform closely related

$[C_nC_mim][HSO_4]_{(aq)}$ media of equivalent acidity (*p*H 1.2; figure 2.13B). This lixiviant medium is suggested to achieve a 3-fold enhancement in comparison to $[C_2C_1im][HSO_4]_{(aq)}$ as the next-best performing 10 *%wt* IL and a remarkable 10-fold enhancement over equivalent acidity 75 *mmol·dm*$^{-3}$ $H_2SO_{4(aq)}$ (figure 2.13A). These results reflect similar indications from figure 4.6A across a broad range of $[IL]_{(aq)}$. In contrast, $[C_2C_1im][EtSO_4]_{(aq)}$ exhibits effectively zero lixiviant behaviour, as one may expect for an IL with a non-acidic organic anion.



▲ Figure 4.6 – (A) Cu recovery (72 *hr*) as a function of $[IL]_{(aq)}$ as measured by ASV in a 2-electrode configuration ($Pt_{(s)}$ WE; $Pt_{(s)}$ CE/RE). (B) Cu recovery as a function of time for 10 *%wt* $[IL]_{(aq)}$ and 75 *mM* $H_2SO_{4(aq)}$ reference. (■ $[C_2C_1im][HSO_4]$; ● $[C_4Him][HSO_4]$; ▲ $[C_4C_1im][HSO_4]$; ◆ H_2SO_4; ▼ $[C_2C_1im][EtSO_4]$)

Although a promising result, the presence of an optimum $[IL]_{(aq)}$ for leaching has not been observed previously and begs some significant questions regarding validity, in the absence of independent corroboration by ICP-AES (unavailable). Firstly, and most strikingly, it is unclear why such small $[C_nC_mim][HSO_4]$ structural variations appear to have such a large influence on $CuFeS_{2(s)}$ dissolution at approximately equivalent *p*H. Also, E_h values for IL reference solutions suggest no significant different in neat solution E_h. As is illustrated in figure 4.6A, IL *%wt* is not the ideal concentration measure for these studies, especially since the 10 *%w/w* aqueous solutions used in figure 4.6B represent different concentrations for each IL - $[C_2C_1im][HSO_4]$ = 493 *mmol·dm*$^{-3}$; $[C_4Him][HSO_4]$ = 460 *mmol·dm*$^{-3}$; $[C_4C_1im][HSO_4]$ = 432 *mmol·dm*$^{-3}$. It is noteworthy also that $[IL]_{(aq)}$ of optimum leaching power appears to show significant separation on both *%wt* and *mol·dm*$^{-3}$ concentration scales (figure 4.6A).

Also of concern, is the use of a 2-electrode configuration when working over high potential ranges. A combined CE/RE is potentially susceptible to potential drift effects, since the flux of charge across the CE/RE may alter the referenced electrode potential.[18] Thus, one cannot that indicated WE potentials are accurate and they may have been determined according to a fluctuating potential reference. This effect has an unpredictable and complex effect on i-V behaviour observed during ASV and may impact upon $[Cu^{2+}]_{(aq)}$ quantification.

A final concern with regard to data shown in figure 4.6A is the use of a single set of $Cu_{(s)}$ calibration parameters (10 *%wt* $IL_{(aq)}$) in order to quantify $[Cu^{2+}]_{(aq)}$ via ASV. As described in section 4.5.1, ASV electrochemical traces and charge measurements are expected to show medium dependent character, with $Cu_{(s)}$ stripping calibration coefficients ranging widely for these $[C_nC_mim][HSO_4]_{(aq)}$ ILs in this ASV mode (60-220 $\mu C \cdot mM^{-1}$). Therefore, concerns are raised regarding the comparative $Cu^{2+}{}_{(aq)}$ mass transport rates in $IL_{(aq)}/H_2SO_{4(aq)}$ media. It is noteworthy that further calibrations could be recorded in order to remove uncertainty. However, work to establish the confidence limits of ASV $[Cu^{2+}]_{(aq)}$ measurements and definition of the range of $[IL]_{(aq)}$ over which a single set of calibration parameters could be applied with minimal incurred error was considered a better strategy. As section 4.4 will discuss, results in figure 4.6 have been largely validated by this approach, however an analogous experiment has been reported later in order to examine the effect of $[IL]_{(aq)}$ in greater detail (section 6.3.3).

4.4 Validity of Peak $[IL]_{(aq)}$ Lixiviant Activity

4.4.1 Background to Approach

$[C_nC_mim][HSO_4]_{(l)}$ RTILs are high viscosity fluids, on the order of several thousand *centi-Poise* (*cP* ≡ *mPa.s*). It has also been discussed that pure $IL_{(l)}$ exhibit unique mass transport properties; which deviate significantly from Stokes-Einstein behaviour and require application of hole theory in order to adequately reproduce trends (section 2.1.2). Others has noted that these IL-unique mass transport properties become apparent at IL mole fractions > 0.2 (x_{IL}).[19] Hence concerns were raised that peak leaching activities observed at moderate $[IL]_{(aq)}$ with $[Cu^{2+}]_{(aq)}$ quantification via ASV (figure 4.6A) may be an artefact of reduced analyte mass transport rates and electrodeposition efficiency at raised $[IL]_{(aq)}$.

An approach was designed to determine whether $Cu^{2+}{}_{(aq)}$ mass transport in 0-2 $mol \cdot dm^{-3}$ $[C_nC_mim][HSO_4]_{(aq)}$ becomes sufficiently reduced in order to form a 'peak-like' artefact at ~500 $mmol \cdot dm^{-3}$ $[IL]_{(aq)}$ - a concentration which is ~2 orders of magnitude lower than solution water content. This strategy required $IL_{(aq)}$ rheology measurements and ASV simulations based on Cottrellian theory.

$$D = \frac{k_B \cdot T}{6\pi \cdot a \cdot \eta} \qquad \text{E4.5}$$

Mass transport in non-convective aqueous environments is driven by a diffusive flux of species, according to Fick's law with a Stokes-Einstein diffusion coefficient (E4.5). Therefore, rate of mass transport is a function of temperature, hydrodynamic radius (a) and medium viscosity (η). Since EXAFS studies have indicated that inner-sphere $Cu^{2+}{}_{(aq)}$ speciation is equivalent in $IL/H_2SO_{4(aq)}$ media, viscosity variation is investigated as the most likely cause of any significant reduction in $Cu^{2+}{}_{(aq)}$ mass transport rate at increased $[IL]_{(aq)}$.

4.4.2 Rheology Theory

When a force is applied to a fluid - in a given direction (F_x) over a given fluid contact area (A) - a flow velocity is established in the fluid (v_x). Viscosity describes a fluid's resistance to flow. A high fluid viscosity leads to a shortening of the fluid depth (z) which experiences F_x, thus non-zero fluid flow is observed over lower fluid penetration depths (E4.6).

The viscosity of many pure and $[IL]_{(aq)}$ solutions were examined in order to identify confidence levels for the use of an ASV procedure. As reported in table 2.6, pure $IL_{(l)}$ show fairly poor agreement with BASF literature viscosity data for pure ILs. The reasoning for this discrepancy is unclear, however it is clear that low water contents cannot explain this magnitude of discrepancy. One possibility is that the ILs were likely synthesised via differing chemical processing techniques. However, since the instrumental procedure was validated, providing accurate measurement of reference solution over a broad viscosity range (0-1300 *cP*; table 2.5), there is high confidence that the viscosity measurements are representative of the tested $IL_{(l)}$/$IL_{(aq)}$ solutions.

$$\frac{F_x}{A} = \eta \cdot \frac{dv_x}{dz} \qquad \text{E4.6}$$

$$log\langle \eta \cdot V_M \rangle_{IL_{(aq)}} = x_{IL} \cdot log\langle \eta_{0,IL} \cdot V_{M,0,IL} \rangle + x_{H_2O} \cdot log\langle \eta_{H_2O} \cdot V_{M,0,H_2O} \rangle \qquad \text{E4.7}$$

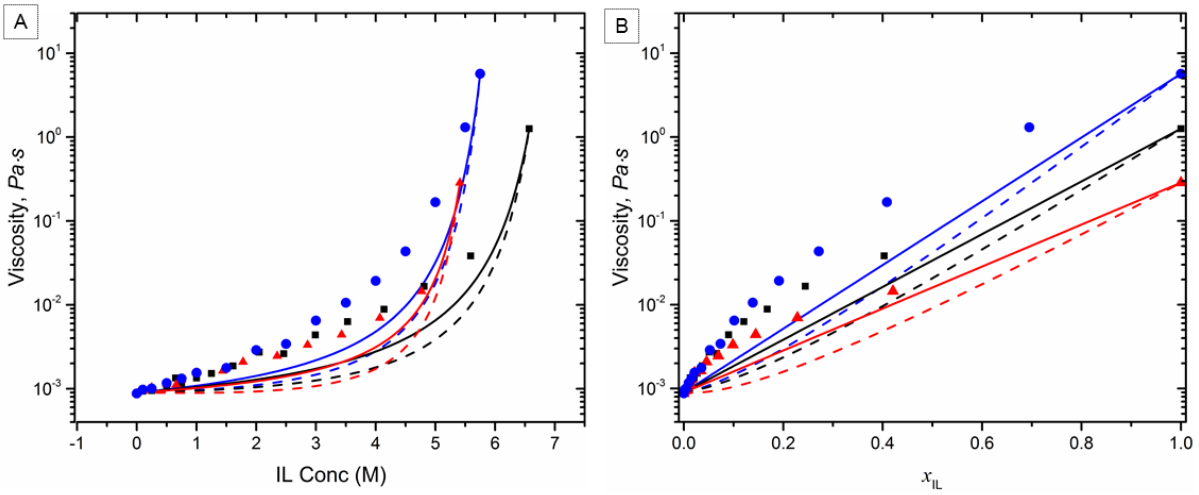
$$log\langle \eta \rangle_{IL_{(aq)}} = x_{IL} \cdot log\langle \eta_{0,IL} \rangle + x_{H_2O} \cdot log\langle \eta_{H_2O} \rangle \qquad \text{E4.8}$$

Measured viscosities for two-component Newtonian fluid mixtures can be estimated using E4.7,[20] where V_M is the molar volume of the respective solution/component. A further less accurate estimation approach, uses the (flawed) approximation that V_M is equal for all components and solutions (E4.8). This model will be compared to experimental $IL_{(aq)}$ viscosity data in the following section.

4.4.3 Viscosity Data

Figure 4.7 compares the experimental variation of η for binary $IL_{(aq)}$ mixtures with the aforementioned theoretical predictions. Low KF water contents measurements for 100 % $IL_{(l)}$ samples is provided in table 2.6 (~0.17 %). As one might expect, measured viscosity functions are as expected not in good agreement with the proposed Newtonian fluid models; requiring consideration of hole theory (section 2.1.2). This feat has not been attempted as it is beyond the scope of the objectives of this study (section 1.10). It is important to point out that the positioning of the model fit lines is flawed, since the model relies on the pure $IL_{(l)}$ exhibiting close to ideal viscosity. Hence, disagreement between the model and experimental viscosity data is, in itself,

indicative of the discussed unique $IL_{(l)}$ viscosities. Interestingly, data in figure 4.7 appears to agree with the finding that high deviations from classical viscosity theory begin above x_{IL}~0.2.



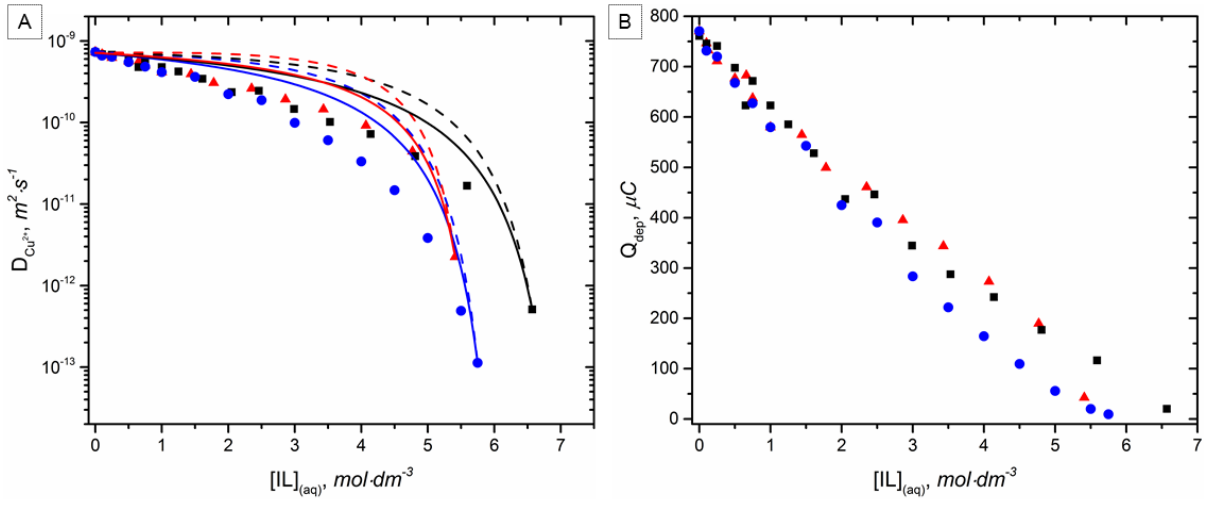
▲ Figure 4.7 – Measured viscosity of $IL_{(aq)}$ solutions (datapoints), displayed alongside Newtonian two-component estimates, with (- - - -) and without (——) incorporation of molar volume (V_M) considerations. $[C_4Him][HSO_4]_{(aq)}$ (●), $[C_2C_1im][HSO_4]_{(aq)}$ (■) and $[C_4C_1im][HSO_4]_{(aq)}$ (▲).

Within the 0-1 *mol·dm*$^{-3}$ $IL_{(aq)}$ concentration range of interest, solution viscosity displays an approximately linear increase with increased $[IL]_{(aq)}$, ranging between measured values of 0.9-2.0 *mPa·s* for all $[C_nC_mim][HSO_4]_{(aq)}$ ILs studied. It is noteworthy that the introduction of $CuSO_{4(aq)}$ (10-30 *mmol·dm*$^{-3}$) into these $IL_{(aq)}$ solutions to form a typical leachate compositions resulted in significant up to ~35 % reduction in measured viscosity. At low $IL_{(aq)}$, highest magnitude viscosity reduction is achieved at 10 *mmol·dm*$^{-3}$ $CuSO_{4(aq)}$, with further solute addition giving rise to increased viscosity. At higher $IL_{(aq)}$, viscosity reductions were more gradual and predictable over the 10-30 *mmol·dm*$^{-3}$ $CuSO_{4(aq)}$ range. For example, data indicates that 10 *mmol·dm*$^{-3}$ $CuSO_{4(aq)}$ contained in 500 *mmol·dm*$^{-3}$ *mol·dm*$^{-3}$ $[C_nC_mim][HSO_4]_{(aq)}$, results in a fluid viscosity that is <7 % larger than pure water viscosity (0.899 *mPa·s*). The latter result indicates that peak artefact produced by reduction in $Cu^{2+}_{(aq)}$ mass transport is highly unlikely. This result makes the likelihood of mass-transport related peak artefact highly unlikely.

4.4.4 $Cu^{2+}_{(aq)}$ Diffusion Coefficient

Analysis of the variation of the $Cu^{2+}_{(aq)}$ diffusion coefficient (E4.5) upon increased $[IL]_{(aq)}$ is achieved through the above viscosity measurements and the diffusion coefficient for $Cu^{2+}_{(aq)}$ in pure aqueous solution (7.14 x 10^{-10} *m*^{2}*·s*$^{-1}$).[21] According to E4.5, the hydrodynamic radius of hydrated $Cu^{2+}_{(aq)}$ is indicated as 3.4 *Å*, where previously discussed EXAFS studies conclude that hydrodynamic radius is unlikely to vary greatly in $IL_{(aq)}$ media, since IL-specific interactions do not have a role in inner-sphere $Cu^{2+}_{(aq)}$ solvation. On this basis, figure 4.8A presents the predicted variation in $Cu^{2+}_{(aq)}$ diffusion coefficient as a function of IL mole fraction, alongside the theoretical

predictions from the models discussed earlier. Accordingly, D_{Cu} is predicted to vary over 3-4 orders of magnitude over each full $[IL]_{(aq)}$ range. However, the D_{Cu} reduction over the 0-1 *mol·dm*$^{-3}$ $[IL]_{(aq)}$ range of interest is much less significant (22-43 *%*).



▲ Figure 4.8 – (A) Predicted variation of the diffusion coefficient for $Cu^{2+}_{(aq)}$ as a function of *%* $[IL]_{(aq)}$ composition. (B) Predicted total $Cu^{2+}_{(aq)}$ electrodeposition charge (Q_{dep}) accumulated during 300 *s* electrodeposition in $IL_{(aq)}$. $[C_4Him][HSO_4]_{(aq)}$ (●), $[C_2C_1im][HSO_4]_{(aq)}$ (■) and $[C_4C_1im][HSO_4]_{(aq)}$ (▲).

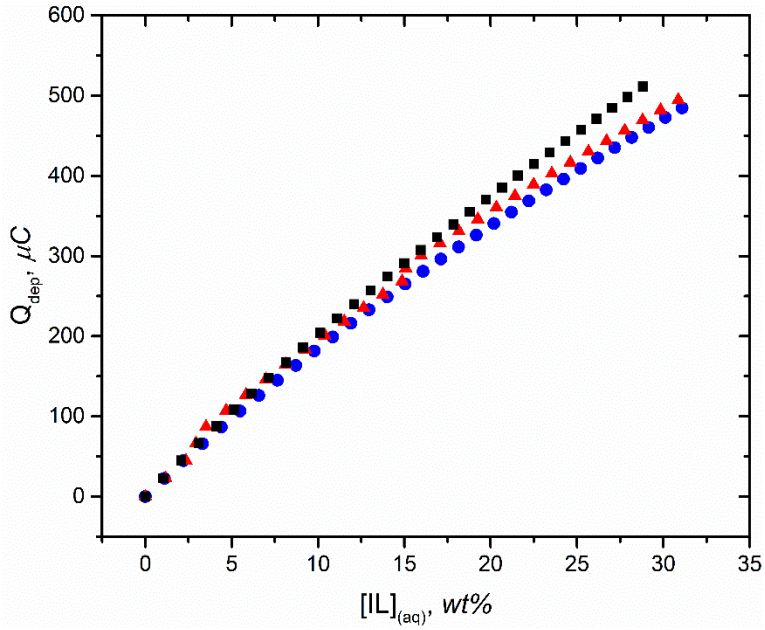
$Cu^{2+}_{(aq)}$ diffusion coefficient measurements are further used to predict chronoamperometric i(t) curves for 300 *s* electrodeposition in $IL_{(aq)}$ with 10 *mmol·dm*$^{-3}$ $CuSO_{4(aq)}$ present. It is important to note that these simulations only strictly represent the mass transport-limited scenario being examined. Choice of 10 *mmol·dm*$^{-3}$ $Cu^{2+}_{(aq)}$ is relatively arbitrary, but is typical of the leachate $[Cu^{2+}]_{(aq)}$ compositions featured in figure 4.6 where the optimum $[IL]_{(aq)}$ result was observed. I(t) curves are constructed using the Cottrell equation (E4.9; n=2; C^*_0 ~ $[Cu^{2+}]_{(aq)}$ = 1 x 10^{-5} *mol·cm*$^{-3}$; A = [*cm*^{2}]; D = [*cm*^{2}·*s*$^{-1}$]; t = 300 *s*), which is derived from a diffusion-limited model of analyte transport to a planar electrode reduction site.[18, 22]

$$i(t) = \frac{nFA \cdot \sqrt{D} \cdot C_0^*}{\sqrt{\pi}} \cdot \frac{1}{\sqrt{t}} = K \cdot \frac{1}{\sqrt{t}} \qquad \text{E4.9}$$

Integration of these Cottrellian i(t) curves gives predictions for charge transfer during the electrodeposition process (Q_{dep}; figure 4.8B), where high $[IL]_{(aq)}$ is observed to reduce Q_{dep} by an order of magnitude. Q_{dep} is a function of t_{dep}, C_0^*, α and *η*. However, the assumption that α_{Cu} remains constant across the $[IL]_{(aq)}$ range of interest (0-1 *mol·dm*$^{-3}$) is justified by IL-free inner-sphere $Cu^{2+}_{(aq)}$ coordination indicated by previously discussed EXAFS studies (section 4.2). The implications of data in figure 4.8 are discussed in the following section.

4.4.5 Implications for ASV Confidence Limits

Using all data acquired in section 4.4, a plot mimicking figure 4.6A was produced to confirm ASV confidence limits and assess the likelihood of peak artefact formation in $Cu_{(s)}$ stripping data. Figure 4.9 displays predicted Q_{dep} when considering $Cu^{2+}_{(aq)}$ to be the only redox active specie, such that Q_{dep} becomes a direct prediction of Q_{strip} data. Curve simulation for 0-1.5 *mol·dm*$^{-3}$ $[IL]_{(aq)}$ (0-30 *wt%*) were achieved using E4.9 and a realistic linear $Cu^{2+}_{(aq)}$ extraction rate of 6 *mmol·dm*$^{-3}$ per molar $[IL]_{(aq)}$. Comparing figures 4.6A and 4.9 and having assessed justification for key assumptions, it can be concluded that $Cu^{2+}_{(aq)}$ mass transport limitations at increased $[IL]_{(aq)}$ are not complicit in the formation of a 'false positive' peak artefact. The presence of a real optimum $[IL]_{(aq)}$ for $CuFeS_{2(s)}$ is an exciting, non-trivial result requiring repetition and further investigations, to include independent ICP-AES corroboration (section 6.3.3).



▲ Figure 4.9 – Cottrellian simulation of Q_{dep} measured during 300 *s* electrodeposition as a function of $[IL]_{(aq)}$ (0-1.5 *mol·dm*$^{-3}$) with a constant $[Cu^{2+}]_{(aq)}$ increase of 6 *mmol·dm*$^{-3}$ per mole $[IL]_{(aq)}$ – providing theoretical Q_{strip} measurement data. $[C_4Him][HSO_4]_{(aq)}$ (●), $[C_2C_1im][HSO_4]_{(aq)}$ (■) and $[C_4C_1im][HSO_4]_{(aq)}$ (▲).

Using constant 10 *mmol·dm*$^{-3}$ $[Cu^{2+}]_{(aq)}$, predicted Q_{dep} variations across 0-1.5 *mol·dm*$^{-3}$ $IL_{(aq)}$ (figure 4.8B) provides a good approach to assess ASV charge measurement confidence limits. Introduction of an exaggerated ±10 % uncertainty in $[IL]_{(aq)}$ produces low charge measurement error of ±2.6 % distributed about the mean charge - which can be factored up or down for other $[IL]_{(aq)}$ uncertainty magnitudes due to the ~linear form of figure 4.8B. Since $Cu_{(s)}$ stripping calibration plots are commonly ~linear, this error can be extrapolated appropriately to broader $[IL]_{(aq)}$ concentration ranges. For example, ±50 % change of a nominal $[IL]_{(aq)}$ within the 0-1.5 *mol·dm*$^{-3}$ is predicted to induce just ±12-13 % variation in ASV charge measurement (Q_{dep}/Q_{strip}).

However, it is crucial to note that this model cannot account for some potential IL-specific effects. As mentioned, IL presence has been determined to modify analyte redox potentials ($E^{\emptyset}$),[23] whereby increased $[IL]_{(aq)}$ may adversely impact on the appropriateness of chosen electrodeposition potential. Thus, with inclusion of a second independent $[Cu^{2+}]_{(aq)}$ measurement technique for verification purposes, a single set of ASV calibration parameters to be applied across significant changes in $[IL]_{(aq)}$ with acceptable initial estimation errors on the order of ~10 %. Verified application of a single set of ASV calibration parameters to wide ranging $[IL]_{(aq)}$ is a convenient approach used later (section 6.2.2).

4.5 Validation and Optimisation of ASV Procedure

This section will focus on validation of an appropriate ASV procedure design for $[Cu^{2+}]_{(aq)}$ quantification and optimisation for the study of $CuFeS_{2(s)}$ dissolution. As mentioned previously, all ASV experiments were conducted in a 3-electrode configuration (with the exception of those in section 4.3), since use of a 2-electrode configuration was deemed to provide insufficient potential control (of the WE). Table 4.3 summarises $Cu_{(s)}$ stripping calibration parameters recorded in a 2-electrode configuration, where standard errors of the slope ($\sigma_{stand.}$) and regression coefficients (R^2) appear reasonable. However, the spread in the data is high and can be significantly improved upon, especially given the simple nature of the standard solutions initially under examination. Table 2.10 provides a summary of all ASV procedures used in this work and serves as a useful reference for section 4.5. Changes made are primarily simplifying in nature and are discussed below with respect to control experiments.

▼ Table 4.3 – $Cu_{(s)}$ stripping charge calibration parameters (linear fit) measured for conventional 3-vial ASV (2-electrode; t_{dep} = 300 *s*) using 1-10 *mmol·dm*$^{-3}$ $CuSO_{4(aq)}$ in the given $IL_{(aq)}$ electrolytic medium. ($y = a \cdot x + b$)

Electrolytic Medium (10 *%wt*)	a, *µC·mM*$^{-1}$ ($\pm \sigma_{stand.}$)	b, *µC* ($\pm \sigma_{stand.}$)	R^2
$[C_4C_1im][HSO_4]_{(aq)}$	252 ± 5.6 %	-209 ± 37 %	0.964
$[C_2C_1im][HSO_4]_{(aq)}$	93.5 ± 9.1 %	-10.8 ± 370 %	0.895
$[C_4Him][HSO_4]_{(aq)}$	65.0 ± 7.6 %	-2.2 ± 1460 %	0.945

4.5.1 Comparison of 1-vial and 2-vial ASV Procedures

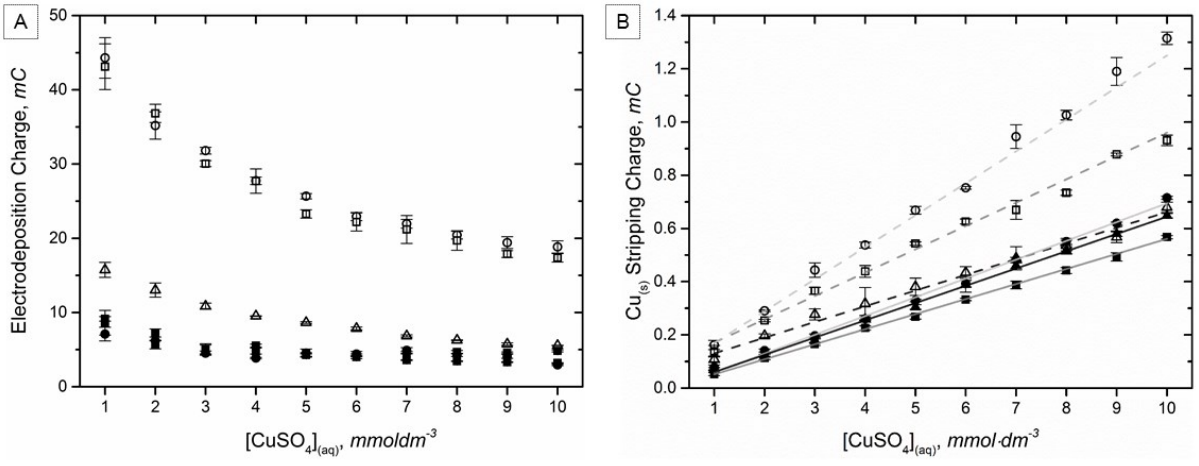
In a conventional ASV procedure it is typical to require three separate solutions for each ASV sample (i.e. '3-vial' ASV) - one solution for electrochemical cleaning of the WE, one sample solution containing the electroactive analyte and a third solution of neat electrolytic media for oxidative $M_{(s)}$ stripping. For many of the leaching studies presented here, and particularly the automation of ASV, this format is not ideal from several perspectives, including contamination via fluid transfer, net removal of analyte species from the sample solution, increased automation

timescales and increased number of error sources. Since all studies $IL_{(aq)}/H_2SO_{4(aq)}$ lixiviant solutions are highly conductive acidic electrolytes, control experiments were conducted to confirm that the aforementioned separate vial for $M_{(s)}$ stripping could be omitted without significant negative impact on data. Indeed, this simplification to a '2 vial' approach lead to a reduction of experimental error in ASV $[Cu^{2+}]_{(aq)}$ measurements.

The ASV procedure can be further simplified and automation timescales minimised through assessment of the regularity and necessity of electrochemical WE cleaning. The present section discusses the comparison of this '2-vial' ASV procedure – with electrochemical cleaning between all ASV repeats - in comparison to a preferable '1-vial' ASV procedure - with ASV repeats conducted *back-to-back* in the sample vial and electrochemical cleaning between sample changes only (table 2.10). Figure 4.10 compares Q_{dep} and Q_{strip} measurements for 1-10 *mmol·dm*$^{-3}$ $CuSO_{4(aq)}$ reference solutions in these configurations, with table 4.4 summarising the resulting $Cu_{(s)}$ stripping calibration parameters for use with E4.10.

$$Q_{strip} = m \cdot [Cu^{2+}] + c \qquad \text{E4.10}$$

It is important to note that the term '1-vial ASV' (also '*in situ ASV*' - section 4.6) is used hereafter to refer to ASV data following the discard of first repeat data, which is observed to be systematically different from subsequent *back-to-back* repeats. The extents of deviations can be visualised by the large difference between 2-vial ASV (unfilled markers) and 1-vial ASV data (solid markers - figure 4.10). Similar deviations are observed between first repeat data and all subsequent repeats for both 1-vial/*in situ* ASV procedures and is therefore not a consequence of the use of an electrochemical WE cleansing phase - instead being a result of electrode 'pre-conditioning' effects during the first (discarded) ASV repeat, as discussed below.



▲ Figure 4.10 – Q_{dep} (A) and Q_{strip} (B) ASV calibration data (3-electrode; t_{dep} = 120 *s*), in a 2-vial (unfilled markers) and 1-vial configuration (solid markers), with procedures varying in electrochemical cleaning regularity. (75 *mmol·dm*$^{-3}$ $H_2SO_{4(aq)}$ - ●○; 450 *mmol·dm*$^{-3}$ $[C_4Him][HSO_4]_{(aq)}$ - ▲△; 450 *mmol·dm*$^{-3}$ $NH_4{\cdot}HSO_{4(aq)}$ - ■□)

Using 2-vial ASV (unfilled markers – figure 4.10), highly medium-dependent i(t) data sets are obtained for $IL_{(aq)}$ and $H_2SO_{4(aq)}$ media. In contrast, 1-vial ASV data for equivalent samples results in largely medium-independent i(t) behaviour, up to 5-fold reduction in Q_{dep} (table 4.4). Rigorous electrochemical cleaning is known to produce more electrochemically active $Pt_{(s)}$ surfaces.[18, 22] Regarding the observed reductions in measurement error for 1-vial ASV, it is intuitive that there may be higher variability in to the activity of electrochemically cleaned $Pt_{(s)}$ (2-vial) than for a stripped $Pt_{(s)}$ surface which is immediately reused (1-vial). It is later shown that 1-vial ASV Q_{dep} magnitudes can be rationalised via ASV simulations (section 4.5.4), with further discussion of the possible rationale for large Q_{dep} measurements in 2-vial ASV mode and other unexplained observations.

Despite uncertainty over the origins, it is clear that these adaptations are beneficial to the automation of ASV-based $[Cu^{2+}]_{(aq)}$ quantification. The duration of experiments is reduced by up to 40 % by removal of unnecessary cleaning cycles and reproducibility of ASV repeats is significantly increased (table 4.4). Although R^2 vales are all equally high, the standard errors of the fit ($\sigma_{stand.}$), with regards to slope and intercept, are significantly reduced. For example, y-intercept (b) is now equal to zero within experimental error, as per theoretical expectation ($Q_{strip} \propto [Cu^{2+}]_{(aq)}$ - E4.12). Despite differences in electrolyte concentration and *p*H, the slopes of calibration plot slopes - typical of those used throughout - are remarkably similar, now varying in the range 56-71 *μC·mM*$^{-1}$ with <2 % standard error. Extension of these adaptations to allow automated *in situ* monitoring of real time $CuFeS_{2(s)}$ dissolution is presented in section 4.6.

▼ Table 4.4 – Linear fit parameters for ASV calibration of 1-vial and 2-vial ASV procedures (t_{dep} = 120 *s*), conducted in 1-10 *mmol·dm*$^{-3}$ $CuSO_{4(aq)}$ standard solutions, varying in electrochemical cleaning regularity.

Electrolytic Medium	E-chem Clean Regularity	Fig.4.10 Key	a, *μC·mM*$^{-1}$ ($\pm \sigma_{stand.}$)	b, *μC* ($\pm \sigma_{stand.}$)	R^2
75 *mmol·dm*$^{-3}$ $H_2SO_{4(aq)}$	2-vial	○ - - -	120.1 ± 2.2 (1.9 %)	49.3 ± 8.2 (17 %)	0.997
	1-vial	● ——	70.6 ± 1.4 (2.0 %)	-11.3 ± 9.5 (84 %)	0.998
450 *mmol·dm*$^{-3}$ $[C_4Him][HSO_4]_{(aq)}$	2-vial	△ - - -	59.0 ± 2.0 (3.3 %)	71.9 ± 9.2 (12 %)	0.996
	1-vial	▲ ——	65.0 ± 1.1 (1.7 %)	-4.5 ± 5.3 (120 %)	0.998
450 *mmol·dm*$^{-3}$ $NH_4{\cdot}HSO_{4(aq)}$	2-vial	□ - - -	87.6 ± 2.2 (2.5 %)	84.0 ± 13 (15 %)	0.991
	1-vial	■ ——	56.6 ± 0.6 (1.0 %)	-4.47 ± 3.1 (70 %)	0.999

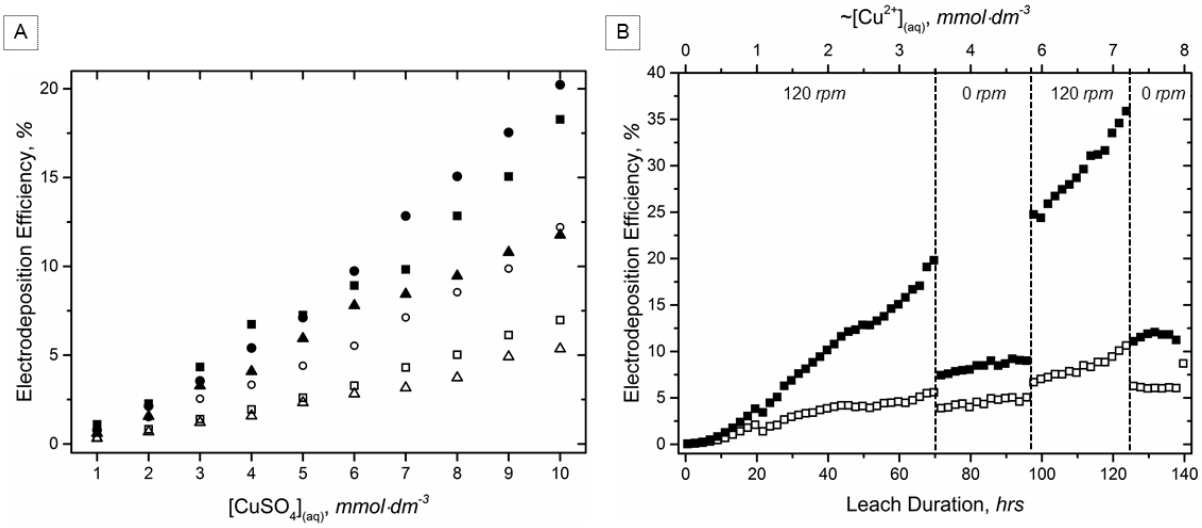
4.5.2 Efficiency of the Electrodeposition Process

Electrodeposition efficiencies (EE) of close to 100 % have previously been achieved in some ILs.[23] Throughout this work, electrodeposition efficiency (EE) is defined as the charge ratio (%)

of measured $Cu_{(s)}$ stripping charge to total electrodeposition charge, i.e. $Q_{strip,Cu}$ / Q_{dep}. It is noteworthy here, that Q_{dep} is not corrected to remove Faradaic, non-deposition reactions. Figure 4.11A displays the electrodeposition efficiencies corresponding to 2-vial and 1-vial ASV data featured in figure 4.10. 1-vial ASV is shown to achieve a maximum EE of ~20 %, representing 1.3-2.8 fold increased EE with respect to 2-vial ASV for the media studied (75 *mmol·dm*$^{-3}$ $H_2SO_{4(aq)}$; 450 *mmol·dm*$^{-3}$ $[C_4Him][HSO_4]_{(aq)}$; 450 *mmol·dm*$^{-3}$ $NH_4{\cdot}HSO_{4(aq)}$), providing a key diagnostic for enhanced 1-vial ASV reproducibility. As a result, desirable analyte reduction comprises a significantly larger proportion of total consumed charge (Q_{dep}). 1-vial ASV is therefore judged to be ~2-3 fold more sensitive to $[Cu^{2+}]_{(aq)}$ under equivalent conditions The possible origin of these EE enhancements are discussed further in section 4.6.

Typical EE values achieved in actively-leaching $IL_{(aq)}$-$CuFeS_{2(s)}$ samples will now be examined. Figure 4.11B shows EE data obtained for *in situ* ASV conducted during active $CuFeS_{2(s)}$ leaching (section 4.6), involves intermittent 120 *rpm* stirring, as labelled. In still, unstirred conditions, EE values are remarkably similar in magnitude (EE ~12-15 %; 7-8 *mmol·dm*$^{-3}$ $[Cu^{2+}]_{(aq)}$), where EE loses might intuitively be expected due to inevitable increased quantities of solubilised (reducible) impurities from $CuFeS_{2(s)}$. As mentioned, *in situ* ASV also exhibits electrode 'pre-conditioning' effects. Again in still solutions, similar ~1.9 fold improved EE values are achieved for ASV repeats 2-4 (■ - figure 4.11B) with respect to discarded first repeat data (□), in good agreement with EE data for reference solutions above.

120 *rpm* stirring increases the magnitude of the aforementioned EE shift to ~3.6 fold between latter and first repeat ASV data, reaching a maximum EE of ~36 %. Since Q_{dep} is proportional to $(D_{Cu})^{1/2}$ with all else equal (E4.12), EE changes at the dashed time boundaries in figure 4.11B predict 63-85 % and 15-30 % increases in effective diffusion coefficient when stirring for latter and first repeat data respectively.

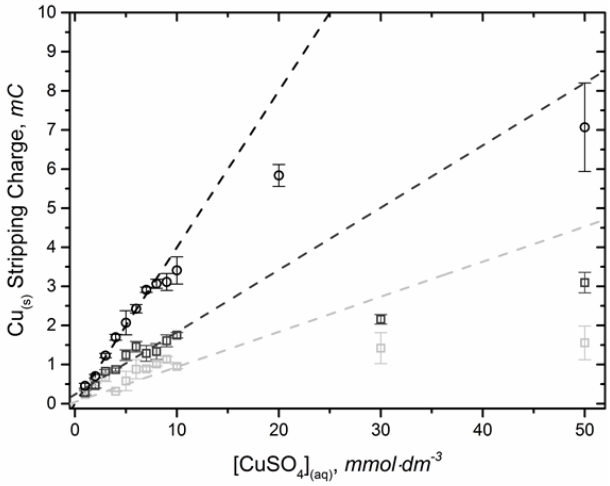


▲ Figure 4.11 – Calculated EE values obtained for (A) 1-vial ASV (unfilled markers) and 2-vial ASV data (solid markers) featured in figure 4.10 for 0-10 *mmol·dm*$^{-3}$ $CuSO_{4(aq)}$ reference samples. (B) Calculated EE values for *in situ* ASV monitoring of $CuFeS_{2(s)}$ dissolution in 450 *mmol·dm*$^{-3}$ $NH_4{\cdot}HSO_{4(aq)}$ as shown in figure 4.18. The upper X-axis displays approximate ICP-AES $[Cu^{2+}]_{(aq)}$ as a function of time (figure 4.18B).
(75 *mmol·dm*$^{-3}$ $H_2SO_{4(aq)}$ ●; 450 *mmol·dm*$^{-3}$ $[C_4Him][HSO_4]$ ▲; 450 *mmol·dm*$^{-3}$ $NH_4.HSO_{4(aq)}$ ■).

4.5.3 Control of Electrodeposition Timescale

It was found that ASV $Cu_{(s)}$ stripping calibration plots may exhibit significant non-linear, plateau-forming behaviour – usually when using inappropriately long t_{dep} and/or high $[Cu^{2+}]_{(aq)}$. For example, at high $[Cu^{2+}]_{(aq)}$ calibration plots may display charge plateaus with high magnitude error bars and plots which are unsuitable for $[Cu^{2+}]_{(aq)}$ quantification. Figure 4.12 exemplifies this behaviour in water (○) and two concentrations of $HNEt_3{\cdot}HSO_{4(aq)}$ (225 *mM* □, 450 *mM* □). ASV $[Cu^{2+}]_{(aq)}$ sensitivity is shown to decrease for $[Cu^{2+}]_{(aq)}$ > 10 *mmol·dm*$^{-3}$ due to an asymptotic dependence on $[Cu^{2+}]_{(aq)}$ and so does the measurement reproducibility. $Cu_{(s)}$ stripping charges and t_{dep} must maintained within an appropriate predetermined range which translates to near-linear response to unit variation of $[Cu^{2+}]_{(aq)}$, in order to maximise $[Cu^{2+}]_{(aq)}$ measurement sensitivity.

Quantification via electrodeposition, to some extent, relies upon linear diffusion to/from a planar electrode.[22] It is conceivable that the formation of a large electrodeposit at high $[Cu^{2+}]_{(aq)}$ and moderate electrodeposition times may result in a large protruding $Cu_{(s)}$ electrodeposit, where increased radial diffusion results in proportionately thinner (but wider) 'hemi-spherical' electrodeposits. 'Non-linear' stripping of the described electrodeposit may provide a feasible explanation. However, verification would be required, since other possibilities may exist.



▲ Figure 4.12 – Plateaued $Cu_{(s)}$ stripping charge calibration plots for 2-vial ASV (3-electrode; t_{dep} = 300 *s*) conducted in 1-50 *mmol·dm*$^{-3}$ $CuSO_{4(aq)}$, with linear fit lines shown to extrapolate behaviour within the 1-10 *mmol·dm*$^{-3}$ region. (□ 450 *mmol·dm*$^{-3}$ $EtNH_3{\cdot}HSO_{4(aq)}$; □ 225 *mmol·dm*$^{-3}$ $EtNH_3{\cdot}HSO_{4(aq)}$; **O** H_2O)

4.5.4 Cottrellian Electrodeposition Analysis

Q_{dep} can be analysed using the Anson equation (E4.12), the time integral of the Cottrell equation (E4.9), where t_{dep} is the electrodeposition time. As mentioned, E4.12 suggests proportionality between analyte concentration and Q_{dep}, in contrast to electrodeposition data featured in figure 4.10A. The Cottrell equation is derived from Fick's laws of diffusion (E4.11) to a planar macro-electrode, and as such is modelled for a diffusion-limited case.[18] One key assumption of the derivation is that the electrode area does not grow significantly during the deposition process, which is clearly a function of the chosen electrodeposition timescale. This assumption is generally justified for macro-electrodes and relatively low and appropriate t_{dep}. In this section, it will also be assumed that D_{Cu} is only a strong function of solution viscosity (η) and that hydrodynamic radius (α_{Cu}) remains constant – an assumption that is justified by the conclusions of EXAFS studies at moderate $[IL]_{(aq)}$ (section 4.2) and the validity of this assumption will be assessed below for varied $[IL]_{(aq)}$ and identity.

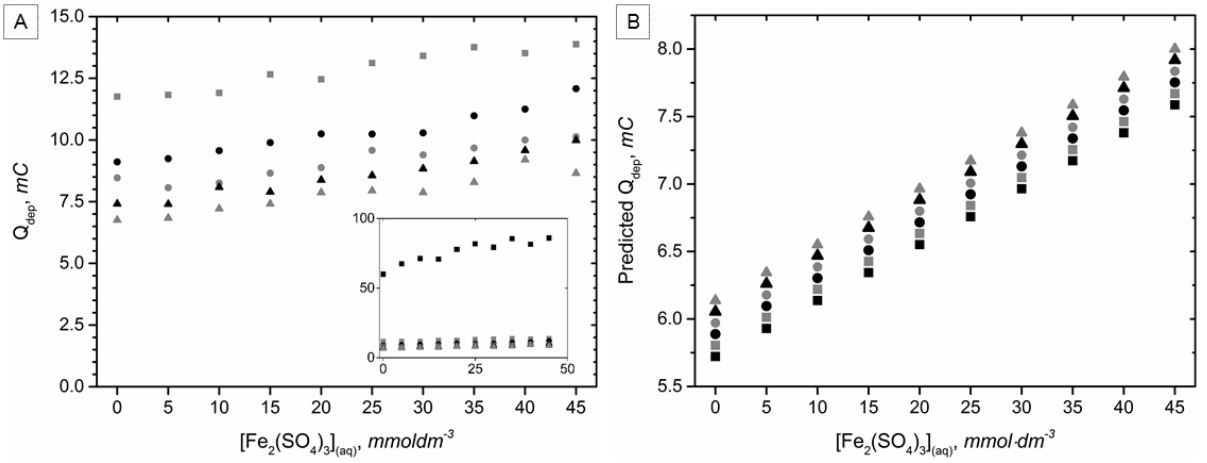
$$J = \frac{\partial c}{\partial t} = D \cdot \frac{\partial^2 c}{\partial x^2} \qquad \text{E4.11}$$

$$Q_{dep} = \int_0^{t_{dep}} i(t) \cdot dt = \left[\frac{2nFA \cdot \sqrt{D} \cdot C_0^*}{\sqrt{\pi}} \cdot \sqrt{t} \right]_0^{t_{dep}} = \frac{2nFA \cdot \sqrt{D} \cdot C_0^*}{\sqrt{\pi}} \cdot \sqrt{t_{dep}} \qquad \text{E4.12}$$

4.5.4.1 Predicted Electrodeposition Charge

Rigorous analysis of Q_{dep} must incorporate consideration of all reducible species potentially present in the acidic-lixiviant solution. Simulated Q_{dep} measurements were obtained using E4.12

(t_{dep} = 120 *s*) combined with viscosity data (section 4.4) for the $IL_{(aq)}/H_2SO_{4(aq)}$ solution compositions represented in figure 3.11 (0-10 *mmol·dm*$^{-3}$ $[Cu^{2+}]_{(aq)}$; 0-90 *mmol·dm*$^{-3}$ $[Fe^{3+}]_{(aq)}$; $[H^+]_{(aq)}$ = 63 *mmol·dm*$^{-3}$; $D_{H+,298K}$ = 9.3 x 10^{-9} $m^2 \cdot s^{-1}$; $D_{Fe3+,298K}$ = 1.2 x 10^{-9} $m^2 \cdot s^{-1}$).[24] The reduction of 0.29 *mmol·dm*$^{-3}$ $O_{2(aq)}$ estimated to be present was not considered since the reduction potential used (V_{dep} = -500 *mV* vs. Ag/AgCl) is more positive than the required oxygen reduction potential ($O_2 + e^- \rightarrow O_2^-$; E(V) = -780 *mV* vs. Ag/AgCl).[9] Figure 4.13 compares simulated Q_{dep} measurements to experimental ASV-measured Q_{dep} data obtained in 450 *mmol·dm*$^{-3}$ $[C_4Him][HSO_4]_{(aq)}$, which is theoretically independent of electrolyte medium at constant *p*H.



▲ Figure 4.13 – (A) Experimental and (B) theoretical Q_{dep} data (t_{dep} = 120 s) for 1-vial ASV conducted in 450 *mmol·dm*$^{-3}$ $[C_4Him][HSO_4]_{(aq)}$ (*p*H 1.2) with addition of indicated concentrations of $[Fe_2(SO_4)_3]_{(aq)}$ and $[CuSO_4]_{(aq)}$. The inset plot in panel A has equivalent axes and shows the larger scale of 0 *mmol·dm*$^{-3}$ $[Cu^{2+}]_{(aq)}$. (■ 0 *mM* $[Cu^{2+}]$; ■ 2 *mM* $[Cu^{2+}]$; ● 4 *mM* $[Cu^{2+}]$; ● 6 *mM* $[Cu^{2+}]$; ▲ 8 *mM* $[Cu^{2+}]$; ▲ 10 *mM* $[Cu^{2+}]$).

The predicted charge sensitivities are 41.5 *µC·mM*$^{-1}$ and 20.8 *µC·mM*$^{-1}$ for $Cu^{2+}_{(aq)}$ and $Fe^{3+}_{(aq)}$ respectively. A slope of 1.87 *mC* across the 0-45 *mmol·dm*$^{-3}$ $[Fe_2(SO_4)_3]_{(aq)}$ range is an excellent representation of the analogous slopes observed in real ASV data, with the dataset in combination with 10 *mmol·dm*$^{-3}$ $Cu^{2+}_{(aq)}$ showing near-perfect correlation to theory. At lower $[Cu^{2+}]_{(aq)}$ however, experimental ASV data shows a clear shift of the parallel trend to higher order charges - a reversal of the expected $[Cu^{2+}]_{(aq)}$ dependency, which has been previously highlighted (section 4.5.1). In summary, 1-vial ASV Q_{dep} charge measurements show a good correlation to theory at high metal concentrations, thus the challenge becomes to explain the higher magnitude Q_{dep} measurements for 2-vial ASV.

The trend is judged to not be derived from parasitic ferric-ferrous reduction, since data is unaffected by $[Fe^{3+}]_{(aq)}$, with overpotentials being too low for significant electrolysis (-1.23 *V* vs. SHE).[9] $Pt_{(s)}$ surfaces are known to electrocatalyse H^+ reduction to $H_{2(g)}$,[e.g.25-27] producing high Q_{dep} measurements in analyte-free solution (figure 4.13A - inset). Accordingly, a proposed explanation is provided for the aforementioned shift of Q_{dep} to higher values at low $[Cu^{2+}]_{(aq)}$, based upon catalytic $H^+_{(aq)}$ reduction at the $Pt_{(s)}$ WE.

When there is no $Cu^{2+}_{(aq)}$ analyte present in solution the $Pt_{(s)}$ surface is free to catalyse $H_{2(g)}$ evolution and observed currents are extremely high (60-90 *mC*). Alloyed Pt-$Cu_{(s)}$ is proposed to catalyse $H_{2(g)}$ evolution to a lesser extent, where assuming diffusion-limited electrodeposition, the time required ($t_{Pt\text{-}Cu}$) to develop a non-catalytically active Pt-$Cu_{(s)}$ surface may be expressed via a rearrangement of the i-t integral of the Cottrell equation (E4.13). E4.13 indicates that $t_{Pt\text{-}Cu}$ will vary with the inverse square of $[Cu^{2+}]_{(aq)}$ concentration. This influence acts to reverse the theoretical trend, with measured Q_{dep} data displaying an ~inverse square relation to $[Cu^{2+}]_{(aq)}$ (figures 4.10A and 4.13). Further, somewhat compelling evidence for this postulate is provided by Q_{dep} measurements on the order of 6-8 *mC* in base neutralised solutions (*p*H 7.0 ± 10 %) in excellent agreement with model predictions.

$$t_{Pt-Cu} = \frac{{Q_{dep}}^2 \cdot \pi}{(2nFA)^2 \cdot D_{Cu}} \cdot \frac{1}{C_0^{*2}} \qquad \text{E4.13}$$

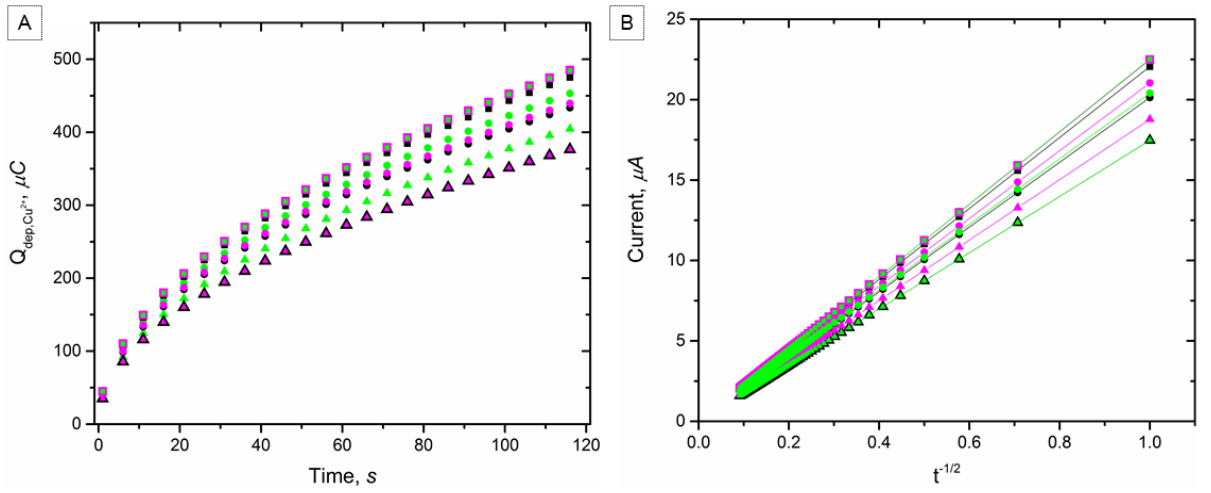
The underlying reasons why 1-vial ASV calibration plots show a lack of medium dependence are unclear and will not be speculated upon - however, it is likely that there are implications that arise from the proposed effect.

4.5.4.2 Simulation of Electrodeposition in the Cottrell-limit

Simulated Cottrellian i(t) curves agree well with experimental data (*cf.* figure 2.22B), as can be judged by agreement of Q_{dep} measurements. E4.12 has been used to examine the influence of $[IL]_{(aq)}$ on electrodeposition via production of q(t) curves (figure 4.14A). Judging by the indicated variation of D_{Cu} for 0.1-1 *mol·dm*$^{-3}$ $[C_nC_mim][HSO_4]_{(aq)}$ (figure 4.8), a maximum variation of ±1.2-4.2 % is predicted based on IL-dependent viscosity-related suppression of $Cu^{2+}_{(aq)}$ diffusion rates (figure 4.14A). These low variabilities quantify the small influence of $Cu^{2+}_{(aq)}$ mass transport variability and further emphasise figure 4.6A as reliable evidence for an optimum $[IL]_{(aq)}$ for $CuFeS_{2(s)}$ dissolution.

Linear Cottrellian plots (i(t) vs. $t^{-1/2}$; figure 4.14B) are predicted for electrodeposition in $IL_{(aq)}/H_2SO_{4(aq)}$, with a medium-specific (±1.2-4.2 %) gradient which absorbs the influence of $[IL]_{(aq)}$ (K - E4.9). Theory additionally predicts a zero y-intercept (*i.e.* $i(t\rightarrow\infty)=0$) for Cottrellian plots, corresponding to zero current following reduction of all reducible species reached following an infinite electrodeposition timescale (t_{dep}; E4.14). It is noteworthy that since K is predicted to be proportional to $[Cu^{2+}]_{(aq)}$, further simulated Cottrellian gradients can be easily calculated. Key simulated parameters for 10 *mmol·dm*$^{-3}$ $[Cu^{2+}]_{(aq)}$ electrodeposition are numerically summarised in table 4.5 for later discussions.

$$t^{-1/2} = \frac{1}{\sqrt{t_{dep}}} = 0 \quad \Leftrightarrow \quad t_{dep} = \frac{1}{(t^{-1/2})^2} \quad \Leftrightarrow \quad \lim_{t^{-1/2}\rightarrow 0}\left(t_{dep}\right) = \infty \qquad \text{E4.14}$$



▲ Figure 4.14 – (A) Simulated q(t) curves for $Cu^{2+}_{(aq)}$ electrodeposition in varied strength $[C_nC_mim][HSO_4]_{(aq)}$. (B) Cottrellian plot for 10 *mmol·dm*$^{-3}$ $[Cu^{2+}]_{(aq)}$ in 100 (■), 500 (●) and 1000 *mmol·dm*$^{-3}$ (▲) $[C_nC_mim][HSO_4]_{(aq)}$. (■ $[C_2C_1im][HSO_4]_{(aq)}$; ■ $[C_4C_1im][HSO_4]_{(aq)}$; ■ $[C_4Him][HSO_4]_{(aq)}$)

▼ Table 4.5 – Summary of simulated Cottrellian plot gradient (K) and Q_{dep} variation (t_{dep} = 120 *s*) for 10 *mmol·dm*$^{-3}$ $[Cu^{2+}]_{(aq)}$ in varied $[C_nC_mim][HSO_4]_{(aq)}$ media.

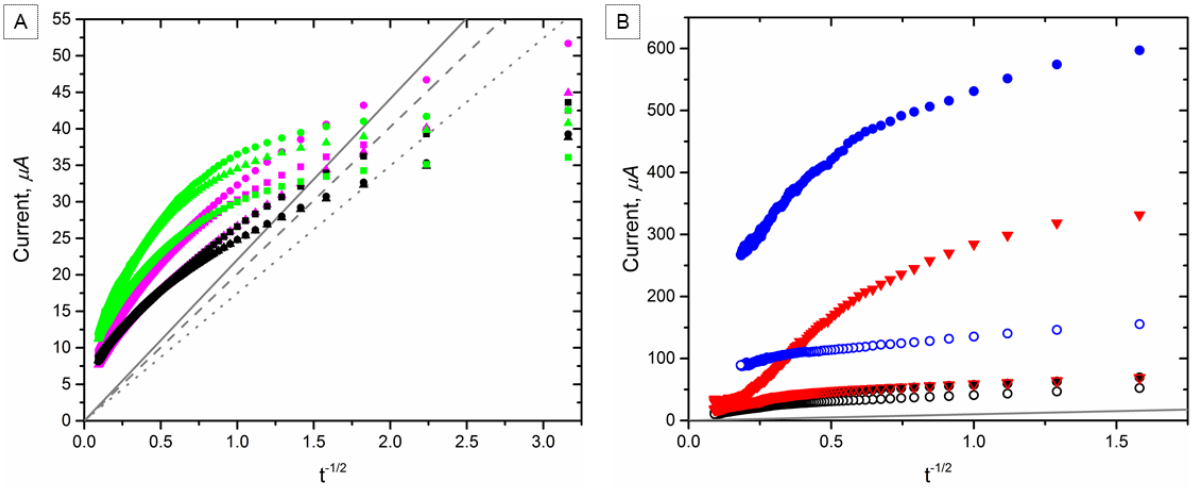
$[IL]_{(aq)}$, *mmol·dm*$^{-3}$	Electrolytic Medium	Predicted Q_{dep}, *μC*	Constant $[IL]_{(aq)}$ Q_{dep}, *μC* (± σ)	Diffusion-limited K, *μA·s*$^{1/2}$	Constant $[IL]_{(aq)}$ K_{av}, *μA·s*$^{1/2}$ (± σ)
	$[C_4Him][HSO_4]$	483		22.1	
100	$[C_4C_1im][HSO_4]$	492	490 (± 1.1 %)	22.5	22.4 (± 1.1 %)
	$[C_2C_1im][HSO_4]$	493		22.5	
	$[C_4Him][HSO_4]$	441		20.1	
500	$[C_4C_1im][HSO_4]$	461	450 (± 2.3 %)	20.4	20.5 (± 2.3 %)
	$[C_2C_1im][HSO_4]$	412		21.0	
	$[C_4Him][HSO_4]$	383		17.5	
1000	$[C_4C_1im][HSO_4]$	447	392 (± 4.2 %)	17.5	17.9 (± 4.2 %)
	$[C_2C_1im][HSO_4]$	383		18.8	

4.5.4.3 Comparison with Measured $Cu^{2+}_{(aq)}$ i(t) Curves

Cottrellian plots are often examined for deviation from linearity.[18] Deviations from linearity are anticipated at short and long electrodeposition timescales due to capacitive charging and convection, respectively.[22] However, non-linearity may also indicate non-diffusion limited kinetics, specific interactions at the electrode or involvement of unconsidered species in the redox event.[18] Figure 4.15 displays Cottrellian plots for experimental electrodeposition of

$CuFeS_{2(s)}$ dissolution relevant $[Cu^{2+}]_{(aq)}$ in $H_2SO_4/IL_{(aq)}$ media of varied concentration, alongside the appropriately simulated Cottrellian curves (section 4.5.4.2) for the $Cu^{2+}_{(aq)}$-bearing solution compositions studied. Data in figure 4.15A was obtained using application of a 2-vial ASV procedure on 10 $mmol{\cdot}dm^{-3}$ $[Cu^{2+}]_{(aq)}$ contained within selected $[C_nC_mim][HSO_4]_{(aq)}$ solutions of 100, 500 and 1000 $mmol{\cdot}dm^{-3}$. Table 4.6 summarises the features of the Cottrellian plots as described below.

As anticipated from the above discussion, plots for 2-vial ASV in $[C_nC_mim][HSO_4]_{(aq)}$ (figure 4.15A) are non-linear over short, initial electrodeposition timescales (t_0 < 4 *s*) with a medium specific initial slope (K_0) of 1.4-6.1 $\mu A{\cdot}s^{1/2}$ that only persists over ~1 *s*. Following this initial period, plots for all $IL_{(aq)}$ solutions are linear over the remainder of the experiment, with good agreement with the expected diffusion limited $K_{t=\infty}$ values in table 4.6 (*cf.* 18-23 $\mu A{\cdot}s^{1/2}$; table 4.5). Plots feature a significant non-zero y-intercept (i(t→∞)) on the order of 7.1-10.4 μA (table 4.6). However, as discussed above, prediction of i(t→∞)=0 is only valid under the assumption that analyte $[Cu^{2+}]_{(aq)}$ reduction occurs in isolation. Consideration of IL *p*H variation as a function of $[IL]_{(aq)}$ (figure 2.13) fully accounts for the magnitudes of i(t→∞) curve offset for each $[IL]_{(aq)}$. Crucially, this agreement of experimental and theoretical curves (after correction) confirms that α_{Cu2+} is well represented by 3.4 *Å* in the 0.1-1.0 $mol{\cdot}dm^{-3}$ $[C_nC_mim][HSO_4]_{(aq)}$ concentration range.



▲ Figure 4.15 – Comparison of predicted Cottrellian plots (grey) with analogous plots for experimental ASV data (coloured). (A) 2-vial ASV experimental data for 10 $mmol{\cdot}dm^{-3}$ $CuSO_{4(aq)}$ in 100, 450, 1000 $mmol{\cdot}dm^{-3}$ $IL_{(aq)}$. (■●▲ $[C_2C_1im][HSO_4]$; ■●▲ $[C_4C_1im][HSO_4]$; ■●▲ $[C_4Him][HSO_4]$; ·····; - - -; — Cottrell Sims.). (B) *in situ* ASV data obtained during $CuFeS_{2(s)}$ leaching in for 450 $mmol{\cdot}dm^{-3}$ $IL_{(aq)}$ / 75 $mmol{\cdot}dm^{-3}$ $H_2SO_{4(aq)}$ with 5 $mmol{\cdot}dm^{-3}$ (± 5 %) $[Cu^{2+}]_{(aq)}$ (via ICP-AES). First repeat ASV data (solid markers) is separated from subsequent repeats (unfilled markers). (●○ $[C_4Him][HSO_4]$; ●○ $NH_4{\cdot}HSO_4$; ▼▽ H_2SO_4; — Cottrell Sim.)

Figure 4.15B presents analogous Cottrellian plots for *in situ* ASV (section 4.6) conducted in approximately equivalent acidity $IL_{(aq)}/H_2SO_{4(aq)}$, where $[Cu^{2+}]_{(aq)}$ was independently assessed as 5.0 $mmol{\cdot}dm^{-3}$ ± 5 % via ICP-AES (75 $mmol{\cdot}dm^{-3}$ $H_2SO_{4(aq)}$; 450 $mmol{\cdot}dm^{-3}$ $[C_4Him][HSO_4]_{(aq)}$;

450 *mmol·dm*$^{-3}$ $NH_4{\cdot}HSO_{4(aq)}$). In comparison to 2-vial ASV, the *in situ* electrodeposition approach is indicated to be non-Cottrellian, presenting none of the behaviours discussed above and showing very poor agreement with far lower magnitude Cottrellian prediction for 5 *mmol·dm*$^{-3}$ $[Cu^{2+}]_{(aq)}$ (figure 4.15B). However, the duration of the initial non-diffusion limited regime is indicated to be ~3-fold longer in the case of undiscarded *in situ* ASV data in comparison to the discarded first repeat and data obtained using 2-vial ASV (table 4.6).

Longer initial periods of non-diffusion limited analyte electrodeposition is likely to be the source of the electrodeposition enhancements seen throughout this study. Building on the aforementioned hypothesis of $Pt_{(s)}$-catalysed $H^+_{(aq)}$ reduction, significantly more $Cu_{(s)}$ is deposited during the early non-diffusion limited stages of 1-vial/*in situ* ASV such that an electrode displaying Pt-$Cu_{(s)}$ non-catalytic behaviour is established in less time ($t_{Pt\text{-}Cu}$; E4.13). Interestingly, EE values (section 4.5.2) are also in line with these arguments. Although the origins of non-Cottrellian electrodeposition requires further examination, the presented hypothesis satisfactorily explains the electrodeposition phenomena observed.

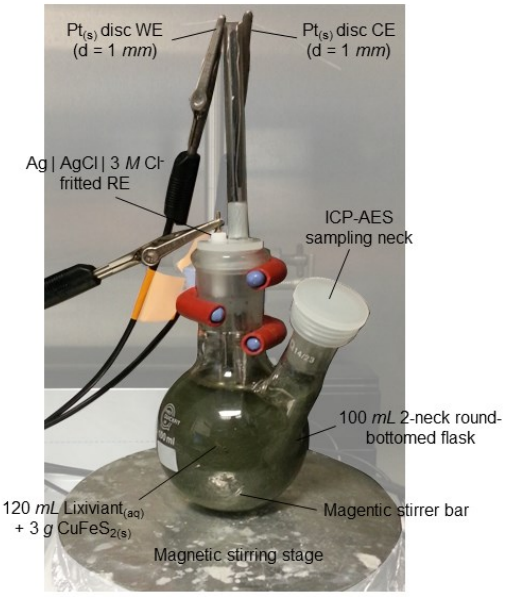
▼ Table 4.6 – Summary of Cottrellian analysis – i(t) vs. $t^{-1/2}$. Details of Cottrellian simulations versus real electrodeposition in typical $H_2SO_4/IL_{(aq)}$ lixiviant solution with known $[Cu^{2+}]_{(aq)}$.

Electrolytic Medium	[Electrolyte], *mmol·dm^{-3}*	$[Cu^{2+}]_{(aq)}$, *mmol·dm^{-3}*	Experiment ID (fig.4.15 key)	K_0, *μA·s$^{1/2}$*	t_{Kzero}, *s*	K_∞, *μA·s$^{1/2}$*	$i(t\rightarrow\infty)$, *μA*
[C4Him][HSO4]	100	10	2-vial ASV ■	6.1	≤ 0.4	20.2	7.2
	500		2-vial ASV ●	5.4	≤ 0.4	21.0	7.1
	1000		2-vial ASV ▲	5.3	≤ 0.4	14.7	10.6
[C4C1im][HSO4]	100	10	2-vial ASV ■	2.9	≤ 0.2	23.5	8.9
	500		2-vial ASV ●	5.4	≤ 0.2	28.2	7.2
	1000		2-vial ASV ▲	5.1	≤ 0.2	19.1	7.6
[C2C1im][HSO4]	100	10	2-vial ASV ■	1.7	≤ 0.4	26.4	9.4
	500		2-vial ASV ●	1.4	≤ 0.4	33.1	10.4
	1000		2-vial ASV ▲	1.7	≤ 0.4	36.7	8.9
H_2SO_4	75	5	*in situ* R1 ●	136	≤ 1.4	84.2	20.4
			in situ R2-5 ○	22.4	≤ 7.8	106	4.4
[C4Him][HSO4]	450	5	*in situ* R1 ■	21.3	≤ 3.0	70.1	6.8
			in situ R2-5 □	20.2	≤ 5.6	66.2	9.0
$NH_4{\cdot}HSO_4$	450	5	*in situ* R1 ■	160	≤ 2.2	476	181
			in situ R2-5 □	40.3	≤ 6.6	116	68

4.6 Automated Electrochemical Dissolution Monitoring

4.6.1 Experimental Procedure

Several key conclusions from section 4.5 indicate that an adapted and simplified ASV procedure has a positive impact on both $[Cu^{2+}]_{(aq)}$ quantification and time efficiency. More specifically, it has been shown that omission of fresh electrolytic stripping media and regular electrochemical cleaning of the $Pt_{(s)}$ WE/CE provides ~3-fold higher sensitivity to $[Cu^{2+}]_{(aq)}$ in the conditions studied. These findings point toward the possibility of *in situ* monitoring of $[Cu^{2+}]_{(aq)}$ with a static $Pt_{(s)}$ probe via a modified *in situ* ASV approach, whereby data acquisition cycles can be automated at user-defined intervals. Note that, although the plot is first featured in section 4.5.4.3, data shown in figure 4.15B is a product of the *in situ* ASV approach described hereafter.



▲ Figure 4.16 – Experimental apparatus for automated electrochemical monitoring of $CuFeS_{2(s)}$ dissolution by $IL_{(aq)}$ in comparison to conventional $H_2SO_{4(aq)}$ leaching.

Freshly milled $CuFeS_{2(s)}$ (3 *g*; 32 ≤ x ≤ 75 *μm*) was leached in 120 *mL* of 450 *mmol·dm*$^{-3}$ $IL_{(aq)}$ with reference to equi-acidic 75 *mmol·dm*$^{-3}$ $H_2SO_{4(aq)}$ at room temperature, with intermittent 120 *rpm* magnetic stirring (figure 4.16). Prior to insertion, the electrode probe was prepared in the usual manner, before subjecting the probe to five ASV repetitions in a 10 *mmol·dm*$^{-3}$ $CuSO_{4(aq)}$ standard solution in the relevant IL/acid medium for 'pre-conditioning' purposes. Following the addition of the $CuFeS_{2(s)}$ the stirred lixiviant solution, *in situ* ASV repeats (table 2.10) were scheduled after 30 *mins* and then at subsequent 2 *hr* intervals using a custom automated *LabView*® program (OnlineLeachingMonitor.vi; table 3.3).

Beginning with an electrodeposition time of 300 *s*, electrodeposition times were subsequently lowered at user-defined intervals, so that $Cu_{(s)}$ stripping charges remained <1 *mC*. This threshold value was chosen since, in the author's experience, plateau-formations can occur immediately beyond this value (*cf.* 1.5 *mC*; figure 4.12). Periodically, 2 *mL* samples were removed for ICP-AES analysis and replaced with fresh lixiviant solution. Stirring was intermittently switched off to allow extended periods of ASV data acquisition in still solution, such that electrochemical $[Cu^{2+}]_{(aq)}$ could be produced for direct comparison to spectroscopic ICP-AES $[Cu^{2+}]_{(aq)}$ measures. As discussed in section 3.4, Q_{dep} and Q_{strip} measurements were rapidly produced using a custom batch analysis program, with a flexible choice of pick-picking methodology (table 3.5).

4.6.2 *In* situ ASV Data Processing

Unprocessed *in situ* ASV data for the monitoring of $CuFeS_{2(s)}$ dissolution by 450 *mmol·dm*$^{-3}$ $NH_4{\cdot}HSO_{4(aq)}$ is presented in figure 4.17. Similar to discussions in previous sections, Q_{dep}

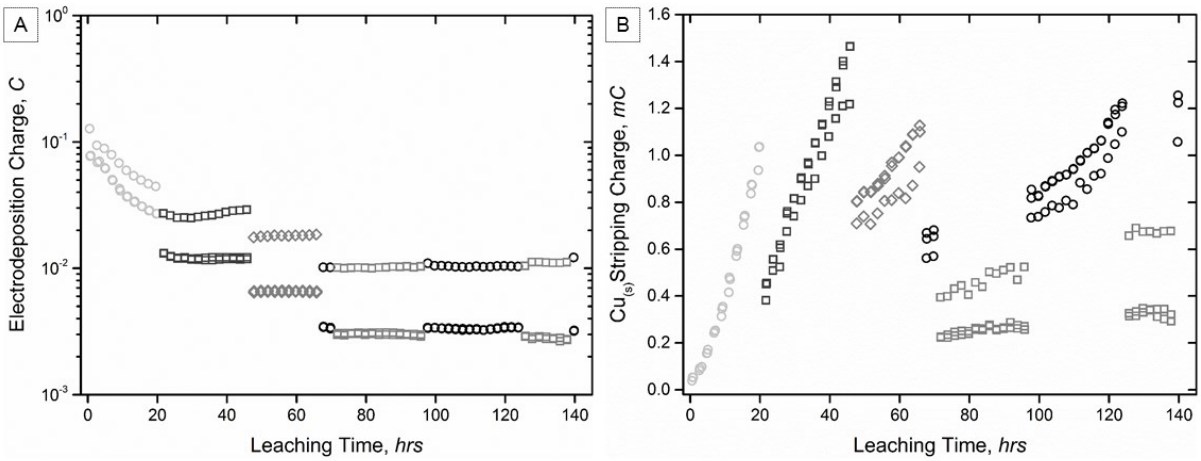
measurements reduce as $[Cu^{2+}]_{(aq)}$ increases, with up to an order of magnitude deviation between charges measured in the first ASV repeat and subsequent ASV repeats (figure 4.17A). As discussed in section 4.5.1, these effects are observed despite the omission of a $Pt_{(s)}$ electrochemical cleaning phase. These effects have been extensively discussed elsewhere and will not be commented upon in this section, unless otherwise stated.

As expected, analogous deviations are carried through to *in situ* ASV Q_{strip} measurements (figure 4.17B), producing some seemingly counter-intuitive effects. However, the EE measurements for this experiment (figure 4.11B) are a good way to visualise the uniform increase of EE correlated to approximately linear $[Cu^{2+}]_{(aq)}$ extraction rates (figure 4.18). EE reaches respective maximum values of ~15 % and ~40 % for still and stirred conditions respectively, as discussed in further detail in section 4.5.2.

According to the Cottrellian analysis of the charge transferred during a given electrodeposition time (t_{dep}; E4.12), Q_{dep} is proportional to the square root of the electrodeposition time, provided that D_{Cu} and C^*_0 remain constant. Therefore, upon lowering of electrodeposition time, $Cu_{(s)}$ stripping data should decrease by a factor of $\Delta(t^{1/2})$ (E4.15), which correlates very well with experimental data. Therefore, estimates for D_{Cu} can be computed using ICP-AES $[Cu^{2+}]_{(aq)}$ measurements, complimented by adjacent ASV data obtained with different t_{dep}. Effective $Cu^{2+}_{(aq)}$ diffusion coefficients ($D_{eff,120rpm}$; $D_{eff,0rpm}$; E4.16) are also computed in order to investigate whether accurate, continuous $[Cu^{2+}]_{(aq)}$ extraction profiles can be formed by normalising Q_{strip} measurements by the agitation speed and electrodeposition time at which ASV data is acquired. It is noteworthy that, (in theory) diffusion coefficients are independent of agitation, however these D_{eff} values absorb the changing thickness of the diffusion layer and thus have limited relation to the physical diffusion rate of the analyte.

$$\Delta Q_{dep} = Q_{dep,t_1} - Q_{dep,t_2} = 2K \cdot \left[\sqrt{t_{dep,1}} - \sqrt{t_{dep,2}}\right] \quad \text{E4.15}$$

$$D_{eff} = \frac{2K \cdot \sqrt{\pi}}{2nFA \cdot C^*_{0,t}} \quad \text{E4.16}$$



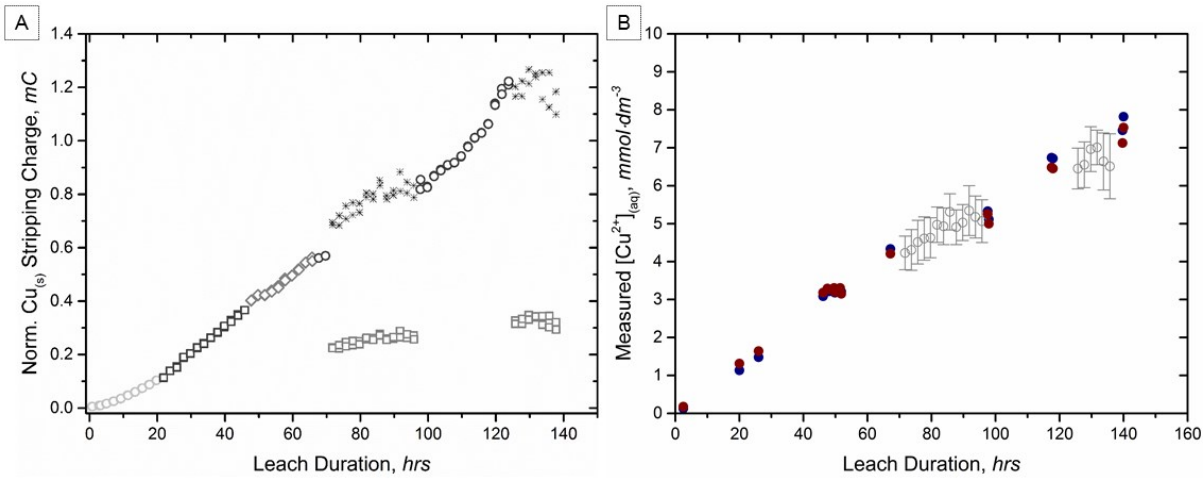
▲ Figure 4.17 – Raw *in situ* ASV data obtained during the monitoring of $CuFeS_{2(s)}$ dissolution in 450 *mmol·dm*$^{-3}$ $NH_4{\cdot}HSO_{4(aq)}$, displaying (A) total $Cu^{2+}{}_{(aq)}$ electrodeposition charge and (B) measured $Cu_{(s)}$ stripping charge for varied electrodeposition times (300 *s* ○, 120 *s* □, 60 *s* ◇, 30 *s* ○, 30 *s* [unstirred] □).

Using the shortest t_{dep} and calculated $D_{Cu,eff}$, (E4.12), Q_{strip} measurements are normalised to a single electrodeposition time and agitation rate. Continuous $CuFeS_{2(s)}$ dissolution profiles are produced (panel A - figures 4.18-4.20) where ASV data in unstirred conditions can be easily calibrated to estimate $[Cu^{2+}]_{(aq)}$. Electrochemical and ICP-AES $[Cu^{2+}]_{(aq)}$ measurements agree excellently throughout (panel B - figures 4.18-4.20). Continuous Q_{strip} profiles are therefore a detailed, accurate representation of the $[Cu^{2+}]_{(aq)}$ extraction profile and a single (verified) ICP-AES $[Cu^{2+}]_{(aq)}$ measurement can be used to construct a continuous $[Cu^{2+}]_{(aq)}$ extraction profile (not shown). Specific insights obtained from *in situ* electrochemical monitoring of $CuFeS_{2(s)}$ dissolution in 75 *mmol·dm*$^{-3}$ $H_2SO_{4(aq)}$ and 450 *mmol·dm*$^{-3}$ $IL_{(aq)}$ ($NH_4{\cdot}HSO_{4(aq)}$; $[C_4Him][HSO_4]_{(aq)}$; $[C_1C_1pz][HSO_4]_{(aq)}$) are discussed below.

4.6.3 *In situ* Electrochemical Cu Extraction Profiles

4.6.3.1 450 *mmol·dm*$^{-3}$ $NH_4{\cdot}HSO_{4(aq)}$

Figure 4.18 displays processed *in situ* ASV data when conducting a 140 *hr* $CuFeS_{2(s)}$ dissolution experiment in 450 *mmol·dm*$^{-3}$ $NH_4{\cdot}HSO_{4(aq)}$. Significant $Cu^{2+}{}_{(aq)}$ leaching is detected at short leaching timescales (<2 *hrs*) in the first data acquisition cycles and data suggests near-linear extraction over extended leach durations (figure 4.18A), with a ~1.9-fold increase in rate observed with 120 *rpm* stirring. When Q_{strip} is normalised ($t_{dep,norm}$ = 30 *s*; D_{eff} = table 4.7), reconstruction of a near-perfect continuous ASV charge profile is possible (✳; figure 4.18A). Electrochemical $[Cu^{2+}]_{(aq)}$ measurements in still solution (□ - figure 4.18A-B) prove to be an excellent representation of independent $[Cu^{2+}]_{(aq)}$ measurements by ICP-AES, further validating the charge profile.

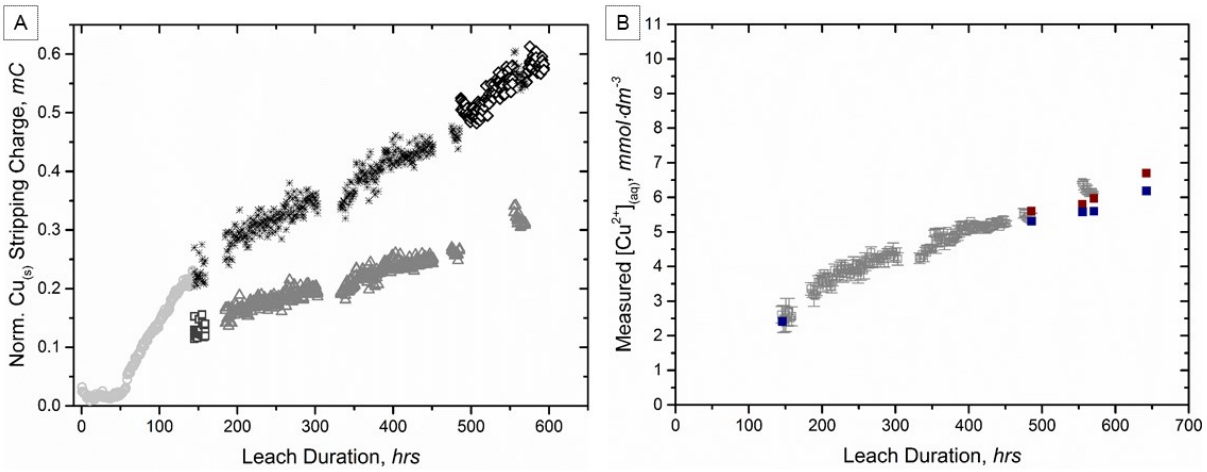


▲ Figure 4.18 – (A) Normalised ASV stripping charge profile for $CuFeS_{2(s)}$ dissolution in 450 *mmol·dm⁻³* $NH_4{\cdot}HSO_{4(aq)}$. (B) ASV $[Cu^{2+}]_{(aq)}$ measurements obtained from still solution (○) in comparison to ICP-AES derived [Cu] (●) and [Fe] (●). (t_{dep}: 300 *s* ○, 120 *s* □, 60 *s* ◇, 30 *s* ○, 30 *s* [unstirred] □).

ICP-AES $[Fe^{2+}]_{(aq)}$ measurements show that Cu^{2+} and Fe^{2+} are extracted in equal amounts. This extraction ratio of $[Fe^{2+}]$:$[Cu^{2+}]$ is variable and the exact factors affecting its magnitude are unclear. A hypothesis, which explains this effect is outlined in more detail in section 5.5.3. As discussed, EEs are highly dependent on $[Cu^{2+}]_{(aq)}$, varying approximately linearly over the experimental timeframe in the range of 0-40 *%* in stirred solution and 0-15 *%* in unstirred solution. D_{Cu} is estimated as 2.4 x 10^{-10} $m^2{\cdot}s^{-1}$ ± 28.9 *%* (*cf.* [7.14 x 10^{-10} $m^2{\cdot}s^{-1}$][21]; figure 4.8A), which is a good estimate considering the limitations of assuming Cottrellian behaviour.

4.6.3.2 450 *mmol·dm⁻³* $[C_4Him][HSO_4]_{(aq)}$

Figure 4.19 presents analogous data for automated electrochemical monitoring of $CuFeS_{2(s)}$ dissolution in 450 *mmol·dm⁻³* $[C_4Him][HSO_4]_{(aq)}$. The reconstructed Cu^{2+} recovery profile (figure 4.19A) indicates different leaching behaviour. An ~ 50 *hr* (passive) induction regime is identified before finite rate $Cu^{2+}_{(aq)}$ extraction commences. It is important to note that this significant feature would be challenging to detect and represent accurately via other methodologies, for example via intermittent ICP-AES $[Cu^{2+}]_{(aq)}$ measurements (figure 4.19B). Furthermore, presence of such a feature may also introduce major errors into the estimation of dissolution rates. Regardless, *in situ* ASV is proven capable of high accuracy rate measurements, which (at least) matches the performance of ICP-AES with regard of measuring the extent of $CuFeS_{2(s)}$ dissolution; additionally providing a more convenient, hand-off, *in situ*, real-time approach to quantification of the extent of $CuFeS_{2(s)}$ dissolution throughout the leaching operation.

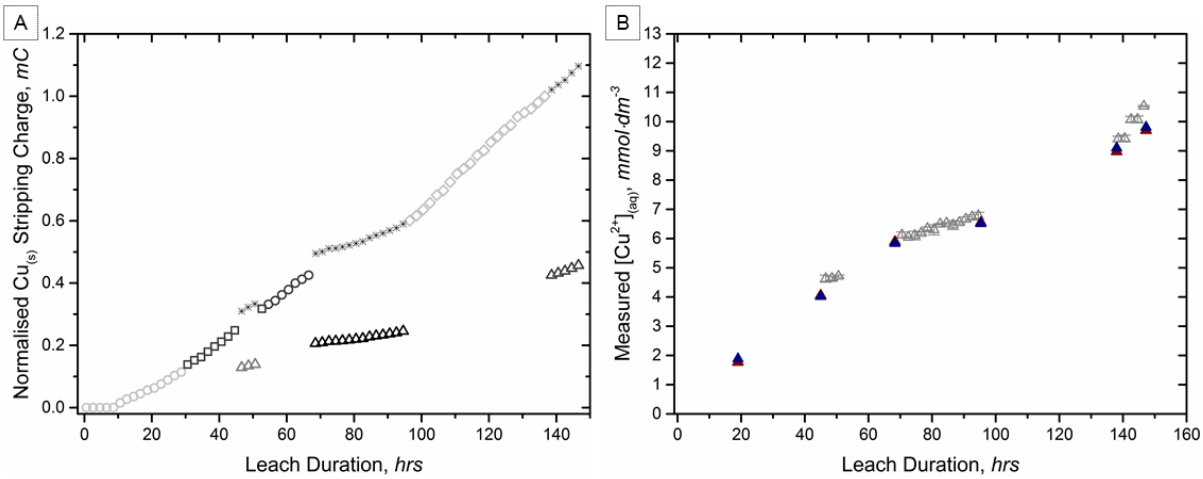


▲ Figure 4.19 - (A) Normalised ASV stripping charge profile for $CuFeS_{2(s)}$ dissolution in 450 *mmol·dm*$^{-3}$ $[C_4Him][HSO_4]_{(aq)}$. (B) ASV $[Cu^{2+}]_{(aq)}$ measurements obtained from still solution (□) in comparison to ICP-AES derived [Cu] (■) and [Fe] (■). (t_{dep}: 300 *s* ○, 300 *s* [unstirred] □, 120 *s* [unstirred]△, 120 *s* ◇)

Once again, D_{eff} can be used to effectively reconstruct the full ASV charge profile in an analogous process to the one which is described in section 4.6.2 (✳ - figure 4.19A). The fully reconstructed plot effectively illustrates that 120 *rpm* stirring results in highly significant 3.5-fold larger $CuFeS_{2(s)}$ dissolution rates for this $IL_{(aq)}$ medium. Despite equivalent conditions and agitation rates, $CuFeS_{2(s)}$ dissolution rates for $[C_4Him][HSO_4]_{(aq)}$ are, in this case, approximately halved in comparison to equimolar $NH_4{\cdot}HSO_{4(aq)}$ - yet leaching over the first 100 *hrs* is comparable (50-150 *hrs*; figure 4.19A). Stirring was switched off for extended periods of the total 600 *hr* monitored leach duration, which partially explains the reduced overall magnitude of extraction. EE values for *in situ* ASV in 450 *mmol·dm*$^{-3}$ $[C_4Him][HSO_4]_{(aq)}$ were found to be similar to $NH_4{\cdot}HSO_{4(aq)}$ - varying between 0-30 % in stirred conditions and 0-20 % in still conditions (*cf*. figure 4.11B).

4.6.3.3 75 *mmol·dm*$^{-3}$ $H_2SO_{4(aq)}$

Figure 4.20 presents analogous data for automated electrochemical monitoring of $CuFeS_{2(s)}$ dissolution in equivalent acidity 75 *mmol·dm*$^{-3}$ $H_2SO_{4(aq)}$. The Cu^{2+} recovery profile (figure 4.20A) is approximately linear, with rates comparable to $CuFeS_{2(s)}$ dissolution in $NH_4{\cdot}HSO_{4(aq)}$. Stirring at 120 *rpm* leads to a 2.0-fold increase in dissolution rate (*cf*. 1.9-fold; $NH_4{\cdot}HSO_{4(aq)}$). It is noteworthy that the reconstructed profile has a 'sharper' in appearance, with lower apparent error. $Cu_{(s)}$ stripping peaks obtained in 75 *mmol·dm*$^{-3}$ $H_2SO_{4(aq)}$ were of more consistent character. Thus, pick-picking analysis in a custom designed *MatLab*® program (table 3.5) benefited from less ambiguous cord line placement (figure 3.12) in order to measure Q_{strip}.

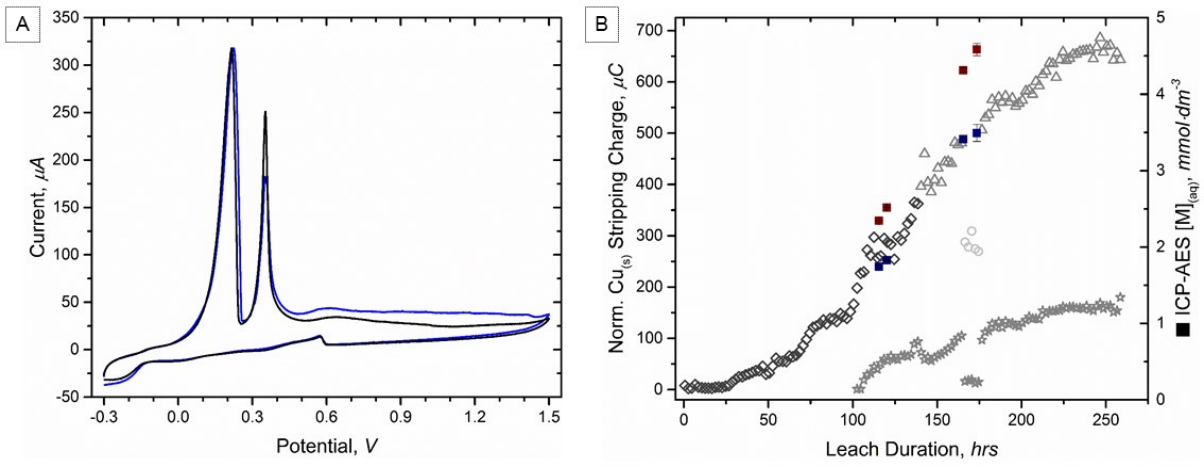


▲ Figure 4.20 – (A) Normalised ASV stripping charge profile for $CuFeS_{2(s)}$ dissolution in 75 *mmol·dm*$^{-3}$ $H_2SO_{4(aq)}$. (B) ASV $[Cu^{2+}]_{(aq)}$ measurements obtained from still solution (△) in comparison to ICP-AES derived [Cu] (▲) and [Fe] (▲). (t_{dep}: 300 *s* ○, 120 *s* □, 120 *s* [unstirred] △, 60 *s* ○, 60 *s* [unstirred] △, 30 *s* ◇, 30 *s* [unstirred] △)

As observed previously for $[C_4Him][HSO_4]_{(aq)}$, a relatively long passive induction period of ~8-10 *hrs* is observed. Interestingly and in contrast to other media studied, EE values appear to rise in the range 0-95 *%* for stirred conditions and 0-60 *%* for still conditions. Unfortunately, (by chance) the experiment was stopped immediately prior to the 100 *%* EE threshold; therefore future work should confirm that EE values do plateau at this limit. Comparison of EE values for all media to those in $CuSO_{4(aq)}$ reference solution reveals good correlation (*cf.* figure 4.11C).

4.6.3.4 450 *mmol·dm*$^{-3}$ $[C_1C_1pz][HSO_4]_{(aq)}$

Figure 4.21 presents preliminary data for the automated electrochemical monitoring of $CuFeS_{2(s)}$ dissolution in 450 *mmol·dm*$^{-3}$ $[C_1C_1pz][HSO_4]_{(aq)}$ - an IL which has not been previously tested and is investigated further in section 6.2. Unfortunately, since this $IL_{(l)}$ was synthesised on a relatively small scale (*Dr O. Kuzmina; Welton Group*), supply was limited and there was not sufficient $IL_{(l)}$ remaining to be able to determine calibration parameters within the available time. Nonetheless, less rigorously treated data is included on account of the presence of some intriguing electrochemical data.



▲ Figure 4.21 - (A) $Cu_{(aq)}$ stripping CV scan showing double peak feature for two independent of *in situ* ASV in 450 *mmol·dm*$^{-3}$ $[C_1C_1pz][HSO_4]_{(aq)}$. (B) all corrected ASV Q_{strip} measurements obtained at various timescales (primary y-axis), compared to ICP-AES values for [Cu] (■) and [Fe] (■) (secondary y-axis). ($Q_{strip,tot}(t_{dep})$: 300 *s* ◇, 120 *s* △, 120 *s* [unstirred] ○; Q_{strip}[peak2] ☆ 30 *s*, 30 *s* [unstirred] △)

Figure 4.21B presents the normalised Q_{strip} measurements (greyscale data; *cf.* panel A - figures 4.18-4.20) featuring a secondary y-axis displaying ICP-AES $[Cu]_{(aq)}$ and $[Fe]_{(aq)}$ measurements (■■). The $Q_{strip}(t)$ measurement profile shows the growth of the expected primary ($Cu_{(s)}$) stripping peak observed throughout all other ASV investigations (V_{peak} = 200 *mV* vs. Ag/AgCl; *cf.* figure 2.22C). Beginning at a leach duration of ~100 *hrs*, electrochemical data shows the growth of a secondary peak in the oxidative stripping scans (V_{peak} = 350-400 *mV* vs. Ag/AgCl; figure 4.21A). Comparing the areas of the peaks in 4.21A, there is a consistent 3:1 ratio (1°: 2°) of total charge associated to each process. The peak can be assigned to Cu(I) with confidence ($E^{\ominus}$= 520 *mV* vs. SHE),[9] which is a fascinating result. Since Cu(I) undergoes 1e$^-$ reduction/oxidation the ratio of $[Cu^+]$:$[Cu^{2+}]$ in electrodeposits is indicated to be 3:2, which could conceivably represent the composition of the $IL_{(aq)}$ leach solution.

Although ICP-AES measurements suggest that $[C_1C_1pz][HSO_4]_{(aq)}$ is not a particularly effective lixiviant solution under the conditions studied, the origin of these intriguing electrochemical results should be further investigated. To the author's knowledge, there is no existing evidence to suggest that Cu(I) is produced in acid-$SO_4^{2-}{}_{(aq)}$ under any condition variations - possibly expressing a key point-of-difference between $H_2SO_{4(aq)}$ and $IL_{(aq)}$-based leaching. However, the cause of Cu(I) involvement in electrodeposits will not be further speculated upon, other than to mention that it may arise from a number of possible sources - *e.g.* differing $Cu_{(aq)}$/$Fe_{(aq)}$ chemistry, differing metal complexation, or IL-electrode interactions. Perhaps the most exciting of these possibilities is that $CuFeS_{2(s)}$ surface-bound Cu(I) may be leached into $IL_{(aq)}$ as Cu(I) in some $IL_{(aq)}$ media, which would be an unprecedented result.

Further work must be undertaken in this $[C_1C_1pz][HSO_4]_{(aq)}$ system to establish the origin of Cu(I) in $[C_1C_1pz][HSO_4]_{(aq)}$-$CuFeS_{2(s)}$ solution. Regardless of the ultimate magnitude of metal extraction in $[C_1C_1pz][HSO_4]_{(aq)}$, studies may be able to decisively confirm that there is an IL-specific $CuFeS_{2(s)}$ dissolution mechanism - a finding which would be in agreement with several independent findings throughout this work and as summarised in section 6.4 - where present knowledge and collated experimental insight from this study are combined in order to propose an $IL_{(aq)}$-$CuFeS_{2(s)}$ leaching mechanism.

4.6.4 Summary of *in situ* ASV Approach

Automated *in situ* monitoring of $CuFeS_{2(s)}$ dissolution provides crucial indications of different $IL_{(aq)}/H_2SO_{4(aq)}$ Cu^{2+} extraction behaviours at equivalent lixiviant solution acidity. Full reconstruction of electrochemical $CuFeS_{2(s)}$ dissolution profiles is a novel analytical approach providing extraordinary levels of detail. Comparison of the typical quality of reconstructed electrochemical extraction curves (figures 4.18-4.20B) and ICP-AES-derived metal extraction curves (figure 5.1-5.4A) highlights that, under similar conditions (*p*H~1.2; 298 *K*; 120 *rpm*), the quality of electrochemical data is of better quality and precision, whereby infrequent anomalous data points are readily identifiable. This is probably a consequence of *ex situ* ICP-AES sampling of inhomogeneous leach solutions and the considerable error introduced in laborious preparation of samples and references for ICP-AES studies (section 2.6.2). Hence, the benefits of this electrochemical automated *in situ* approach are numerous; providing improved accuracy of extraction plot reproduction, rate measurements and identification of important extraction curve features (*e.g.* extended induction periods), all of which are vital for unbiased and accurate comparison of leaches conducted in equivalent conditions.

In addition, it has been shown that electrochemical data may also offer direct insight into dissolution products and solution-borne redox active species. Detection of Cu(I) during leaching in $[C_1C_1pz][HSO_4]_{(aq)}$ suggests that differentiation between metal ions of the same element may be accessible (if present), which is not possible via ICP-AES. Importantly, the concentration of the responsible redox active species is indicated to be of comparable concentration to that of $[Cu^{2+}]_{(aq)}$. In summary, it is indicated that *in situ* ASV may, in some cases, be able to differentiate between metal ions of the same element - which ICP-AES cannot achieve.

Despite relatively large uncertainties (table 4.7), it has also been proven that consideration of D_{eff} and t_{dep} within the Cottrell model allows for Q_{strip} measurements to be normalised effectively in order to produce these continuous $[Cu^{2+}]_{(aq)}$ extraction profiles. This tool could prove invaluable in wider application to metal extraction technologies, should the required electrode-surface confined ASV suited electrochemistry be available for the system of interest.

▼ Table 4.7 – Summary of effective diffusion coefficient values used to transform unstirred ASV data in order to complete continuous charge development profiles for $CuFeS_{2(s)}$ dissolution.

Lixiviant Solution	Agitation Rate, *rpm*	D_{eff}, $cm^2 \cdot s^{-1}$	Uncertainty, *%*
75 $mmol \cdot dm^{-3}$ $H_2SO_{4(aq)}$	0	8.5×10^{-12}	5.2
	120	8.0×10^{-11}	48.8
450 $mmol \cdot dm^{-3}$ $[C_4Him][HSO_4]_{(aq)}$	0	3.1×10^{-12}	19.8
	120	9.6×10^{-12}	6.6
450 $mmol \cdot dm^{-3}$ $NH_4 \cdot HSO_{4(aq)}$	0	1.4×10^{-11}	19.5
	120	3.5×10^{-11}	39.4

4.7 Conclusions

The present chapter has focused upon validation of anodic stripping voltammetry (ASV) as a method suitable for $CuFeS_{2(s)}$ dissolution studies in $H_2SO_{4(aq)}/IL_{(aq)}$ lixiviant solutions.

In addition to previous indications of the prevalence of $[Fe^{2+}]_{(aq)}$, EXAFS studies confirm that $Cu_{(aq)}$ leached from $CuFeS_{2(s)}$ by $H_2SO_{4(aq)}/IL_{(aq)}$ is thermodynamically equivalent to $Cu^{2+}{}_{(aq)}$. Cu-solvation in $IL_{(aq)}$ is affected only by the ILs (dissociated) $SO_4^{2-}{}_{(aq)}$ anion and as such is complexed equivalently to $CuSO_{4(aq)}$ reference solutions as an equilibrated dynamic mixture of hydrates.

Electrochemical indications of an optimum $[IL]_{(aq)}$ for $CuFeS_{2(s)}$ dissolution in $[C_nC_mim][HSO_4]_{(aq)}$ has been verified as a reliable result, which cannot be explained by $Cu^{2+}{}_{(aq)}$ mass transport variations at increased $[IL]_{(aq)}$. $[C_4Him][HSO_4]_{(aq)}$ is indicated as the best performing $[C_nC_mim][HSO_4]_{(aq)}$ system with an optimum $[IL]_{(aq)}$ for maximum leach efficiency at ~450 $mmol \cdot dm^{-3}$ (~10 *%*; 72 *hrs*) - providing dissolution enhancement over $[C_2C_1im][HSO_4]_{(aq)}$ and $[C_4C_1im][HSO_4]_{(aq)}$ at equivalent concentration and acidity.

High confidence limits have been established for ASV-based $[Cu^{2+}]_{(aq)}$ quantification. Application of single calibration parameter sets has been validated with low acceptable errors in the 0-1.5 $mol \cdot dm^{-3}$ $IL_{(aq)}$ concentration range. Conventional ASV has been shown to agree well with Cottrellian theory. When some charge measurement dependencies could not be explained, a mechanism based upon $H^+{}_{(aq)}$ electrocatalysis at $Pt_{(s)}$ surfaces was proposed. This mechanism is not confirmed but has been used to account for several independent and unexpected phenomena, including an inverse square relationship between $[Cu^{2+}]_{(aq)}$ and electrodeposition charge (Q_{dep}).

A range of novel modified ASV procedures have been designed. Specialised '2-vial', '1-vial' and *in situ* ASV procedures have all provided task-specific benefits, ranging from straightforward time economy to improved calibration quality and *in situ* electrochemical monitoring. The adapted '1-vial' ASV procedure accesses 2-3 fold enhancements in $[Cu^{2+}]_{(aq)}$ sensitivity (*cf.* 2-vial ASV) as judged by electrodeposition efficiencies. Reasoning for high order enhancements in the most successful adaptations appears to have origins in non-Cottrellian $Cu^{2+}_{(aq)}$ reduction and longer initial periods of non-diffusion limited analyte electrodeposition.

Automated *in situ* electrochemical monitoring of $CuFeS_{2(s)}$ dissolution has been demonstrated to be a powerful approach to the reconstruction of continuous $Cu^{2+}_{(aq)}$ extraction profiles, allowing more reliable and informed comparisons of lixiviant behaviour. Continuous data functions provide high accuracy rate determinations and visualisation of crucial $CuFeS_{2(s)}$ dissolution profile features, which are difficult to detect via any intermittent sampling technique. Unparalleled access to kinetic detail is provided for $IL_{(aq)}/H_2SO_{4(aq)}$ with high applicability to further metallurgy studies in systems with compatible electrochemistry.

4.8 References

1. J. Castro, P. Pérez Lourido, A. Sousa-Pedrares, E. Labisbal, M. Carabel and J. A. García-Vázquez, *Acta Crystallographica Section C*, 2002, **58**, m65-m67.

2. J.-F. Ma, J. Yang, G.-L. Zheng, L. Li, Y.-M. Zhang, F.-F. Li and J.-F. Liu, *Polyhedron*, 2004, **23**, 553-559.

3. Y.-X. Yuan, T.-C. Niu, M.-M. Xu, J.-L. Yao and R.-A. Gu, *Journal of Raman Spectroscopy*, 2010, **41**, 516-523.

4. B. H. Loo, Y. Tse, K. Parsons, C. Adelman, A. El-Hage and Y. G. Lee, *Journal of Raman Spectroscopy*, 2006, **37**, 299-304.

5. S. Diez-Gonzalez, E. C. Escudero-Adan, J. Benet-Buchholz, E. D. Stevens, A. M. Z. Slawin and S. P. Nolan, *Dalton Transactions*, 2010, **39**, 7595-7606.

6. J. D. Egbert, C. S. J. Cazin and S. P. Nolan, *Catalysis Science & Technology*, 2013, **3**, 912-926.

7. J. M. Hartley, C.-M. Ip, G. C. H. Forrest, K. Singh, S. J. Gurman, K. S. Ryder, A. P. Abbott and G. Frisch, *Inorganic Chemistry*, 2014, **53**, 6280-6288.

8. A. P. Abbott, G. Frisch and K. S. Ryder, *Annual Reports Section "A" (Inorganic Chemistry)*, 2008, **104**, 21-45.

9. P. Aktins and J. de Paula, *Atkins' Physical Chemistry*, Oxford University Press, 8th edn., 2006.

10. D. E. Sayers, E. A. Stern and F. W. Lytle, *Physical Review Letters*, 1971, **27**, 1204-1207.

11. M. Newville, B. Ravel, D. Haskel and E. A. Stern, *Physica B: Condensed Matter*, 1995, 154.

12. E. A. Stern and S. M. Heald, *Basic Principles and Applications of EXAFS - Handbook of Synchrotron Radiaction*, North-Holland, New York, 1983.

13. E. A. Stern, *Contemp. Phys.*, 1978, **19**, 239.

14. E. A. Stern, *Phys. Rev. B*, 1974, **10**, 3027.

15. B. Nyugen, *EXAFS Study of CuFeS2-IL Lixiviant Solutions: A report prepared for the thesis author*, University of Leeds, 2013.

16. M. Tromp, G. P. F. van Strijdonck, S. S. van Berkel, A. van den Hoogenband, M. C. Feiters, B. de Bruin, J. A. van Bokhoven, P. W. N. M. van Leeuwen and D. C. Koningsberger, *Organometallics*, 2010, 3085.

17. J. Chaboy, A. Munoz-Paez, P. J. Merkling and E. S. Marcos, *J. Chem. Phys.*, 2006, 064509.

18. A. J. Bard and L. R. Faulkner, *Electrochemical Methods: Fundamentals and Applications*, Wiley, New York, 2nd edn., 2001.

19. A. P. Abbott, E. I. Ahmed, R. C. Harris and K. S. Ryder, *Green Chemistry*, 2014, **16**, 4156-4161.

20. W. Ji and D. A. Lempe, *Chinese Journal of Chemical Engineering*, 2006, **14**, 770-779.

21. *CRC Handbook of Thermophysical and Thermochemical Data*, CRC Press Inc., Boca Raton, 1994.

22. M. Paunovic and M. E. Schlesinger, *Fundamentals of Electrochemical Deposition*, John Wiley & Sons, New York, 1998.

23. A. P. Abbott, R. C. Harris, F. Holyoak, G. Frisch, J. Hartley and G. R. T. Jenkin, *Green Chemistry*, 2015, **17**, 2172-2179.

24. *American Institute of Physics Handbook*, McGraw Hill, New York, 1972.

25. T. Abe, K. Hirano, Y. Shiraishi, N. Toshima and M. Kaneko, *European Polymer Journal*, 2001, **37**, 753-761.

26. R. Parsons, *Transactions of the Faraday Society*, 1960, **56**, 1340-1350.

27. M. Smiljanic, Z. Rakocevic, A. Maksic and S. Strbac, *Electrochimica Acta*, 2014, **117**, 336-343.

Chapter 5

Up-scaled $IL_{(aq)}$ Leaching Studies

Contents

5.1 Introduction 5-3

5.2 Experiment Design 5-3

5.3 Unprocessed Data 5-4

5.3.1 75 *mmol·dm*$^{-3}$ $H_2SO_{4(aq)}$ 5-4

5.3.2 450 *mmol·dm*$^{-3}$ $IL_{(aq)}$ 5-7

5.4 Analysis and Discussion of Key Leaching Parameters 5-11

5.4.1 Metal Extraction Data 5-12

5.4.2 pH / $[H^+]$ Consumption 5-14

5.4.3 Solution Redox Potential (E_h) 5-16

5.4.4 $[Fe^{2+}]/[Fe^{3+}]$ Implications 5-20

5.4.5 Consideration of $[O_2]_{(aq)}$ 5-22

5.4.6 Proportional Divide Between $CuFeS_{2(s)}$ Dissolution Pathways 5-23

5.5 Surface Studies of Leached $CuFeS_{2(s)}$ Residues 5-25

5.5.1 SEM / EDX 5-26

5.5.2 ToF-SIMS 5-31

5.5.3 Surface Analysis: Conclusions 5-36

5.6 Conclusions 5-39

5.7 References 5-42

Synopsis: Herein, the ambient $CuFeS_{2(s)}$ dissolution activity of best performing screened $IL_{(aq)}$ systems (chapter 6) are studied in further detail in 400 *mL*-scale tank leaching experiments. A kinetic comparison of $IL_{(aq)}$ and equi-acidic $H_2SO_{4(aq)}$ lixiviant power is undertaken, using analysis of key dissolution process parameters ($[M^{n+}]_{(aq)}$; $[H^+]_{(aq)}$; T; E_h; $[O_2]_{(aq)}$) complemented by surface sensitive investigations of leached $CuFeS_{2(s)}$ residues.

5.1 Introduction

As discussed in the outline of project objectives (section 1.10), a low-consumption combinatorial strategy involving the automated electrochemical platform (section 3.2) has been chosen for the identification of the most promising lixiviant activities for $IL_{(aq)}$ systems. A detailed presentation of this aspect of the study can be viewed in chapter 6 (section 6.2). The present chapter studies these promising $IL_{(aq)}$ systems, when up-scaled to larger volume $CuFeS_{2(s)}$ dissolution experiments, in order to verify leach behaviour and parameter variations obtained on a smaller volume scale. As will be introduced and discussed in due course, it was found that there is no apparent distinction between the evolution of *p*H, E_h and T measurements taken during low- and high-volume $CuFeS_{2(s)}$ dissolution experiments. Hence, variations of *p*H and E_h during $IL_{(aq)}/H_2SO_{4(aq)}$-$CuFeS_{2(s)}$ dissolution experiments is considered singularly for continuously monitored physical parameter variations on a 400 *mL*-scale, as the data is deemed significantly more reliable. Therefore, please note that the reversed chronology of the presentation of chapters 5-6, is convenient for introduction to the typical evolution of factors such as *p*H, E_h and T, as applicable to both low- and high-volume $CuFeS_{2(s)}$ dissolution experiments.

This chapter will focus on the larger scale leaching studies, conducted using probe technologies introduced in section 3.2.4.4 and allowing access to the desired typical variation of key physical parameters *p*H, E_h and T throughout the entire leaching process. These 400 *mL*-scale tank leaching experiments were conducted for ~1 *month* durations (700+ *hrs*), in the best performing $IL_{(aq)}$ systems identified within the $NR_4{\cdot}HSO_{4(aq)}$ and $[C_nC_m im][HSO_4]_{(aq)}$ sub-groups studied (sections 6.2.3 and 6.2.4), in comparison with $H_2SO_{4(aq)}$ reference solutions. Unprocessed data is presented for three repeats in each medium.

Unprocessed raw data describing the evolution of leachate composition and conditions ($[M^{n+}]_{(aq)}$; $[H^+]_{(aq)}$; T; E_h) are analysed to fuel a kinetic comparison of $IL_{(aq)}/H_2SO_{4(aq)}$-based $CuFeS_{2(aq)}$ dissolution. Solution and surface-sensitive analytical techniques (ToF-SIMS; SEM/EDX; section 2.8) will additionally be combined, in order to gain an overall picture of the synchronised evolution of surface/solution speciation and in order to judge whether (or not) $IL_{(aq)}$-based $CuFeS_{2(s)}$ dissolution can be rationalised using generally accepted leach mechanics.

5.2 Experiment Design

The described high volume $CuFeS_{2(s)}$ dissolution experiments were conducted in three parallel reactor vessels containing 450 $mmol{\cdot}dm^{-3}$ $[C_4Him][HSO_4]_{(aq)}$, 450 $mmol{\cdot}dm^{-3}$ $NH_4{\cdot}HSO_{4(aq)}$ and 75 $mmol{\cdot}dm^{-3}$ $H_2SO_{4(aq)}$ solutions. Two repeats on each solution were conducted in 500 *mL* round-bottomed flasks (figure 2.26A), sandwiched around a second repeat conducted in custom reaction glassware, with appropriate thermostatic controls (figure 2.26B). The potential influence

of these differing reaction vessels is discussed in conclusion (section 5.6). The customised reactor was specifically designed to allow lixiviant solution contact with massive $CuFeS_{2(s)}$ pieces for time-correlated surface analysis. The perforated sample holders displayed in figure 2.26B allow samples to be easily removed without disruption of leaching in bulk solution, but also to protect the massive $CuFeS_{2(s)}$ samples from the direct effects of stirring and surface abrasion caused by contact with fine particulate $CuFeS_{2(s)}$ present in the main body of the solution. For the purpose of this latter variant of the experiment, 12 massive $CuFeS_{2(s)}$ pieces (1 x 0.5 x 0.5 *cm*) were selected and subjected to SEM/EDX and ToF-SIMS analysis in their unleached states.

Three integrated *p*H, temperature and E_h electrodes (section 2.5.4) were calibrated, before introduction to the reaction vessel containing 400 *mL* neat lixiviant solution, magnetically stirred at 120 *rpm*. Data acquisition from the probes was commenced ~100 *hrs* prior to the addition of any $CuFeS_{2(s)}$ material, to ensure measurement stability prior to the start of the experiment (section 3.2.4.4). A batch of >30 *g* $CuFeS_{2(s)}$ powder was prepared as per standard procedure (section 2.4), for each repeat of the experiment. As such, experiments conducted in parallel (*i.e.* same 'repeat number') are directly comparable, since the powdered $CuFeS_{2(s)}$ material used was equivalent. At t = 0 *hrs*, 10.0 *g* (± 0.05 *g*) powdered $CuFeS_{2(s)}$ was inserted into solution to commence the experiment, alongside (2nd repeat experiment only) addition of four massive $CuFeS_{2(s)}$ samples into the perforated sample holders of each reactor vessel. Leaching was monitored over >700 *hrs* with frequent 2 *mL* ICP-AES sampling with replacement of fresh, equi-thermal lixiviant solution.

During the second set of parallel experiments focusing on synchronous surface analysis, one (different) massive $CuFeS_{2(s)}$ sample was removed from each parallel reactor at leach durations of 24, 72, 240 and 504 *hrs* for immediate surface-sensitive studies via ToF-SIMS (Dr Sarah Fearne, Department of Materials, Imperial College) and SEM/EDX (author). Following 720 *hrs*, all massive $CuFeS_{2(s)}$ pieces were removed before re-examination of the leached surfaces. Unless otherwise stated, all surface analyses discussed in this chapter were undertaken during the second repeat of the experiment; marked in each figure with the symbols of medium tone of colouration. All data analysis was carried out by the author.

5.3 Unprocessed Data

5.3.1 75 *mmol·dm^{-3}* $H_2SO_{4(aq)}$

The acquired raw $CuFeS_{2(s)}$ dissolution data for three rounds of leaching in 75 *mmol·dm^{-3}* $H_2SO_{4(aq)}$ is shown in figure 5.1, presenting ICP-AES $Cu^{2+}_{(aq)}$ and $Fe^{2+}_{(aq)}$ metal extraction in panel A and the evolution of leachate *p*H, temperature and E_h measurements in panels B-D respectively. Data in section 5.3 is presented in unprocessed form, however control experiments have verified that the signal noise presented in panels B-D of figures 5.1-5.4 are a function of the

number of parallel probes data acquisitions. Implications of signal noise is discussed further in the fitting of data (section 5.4).

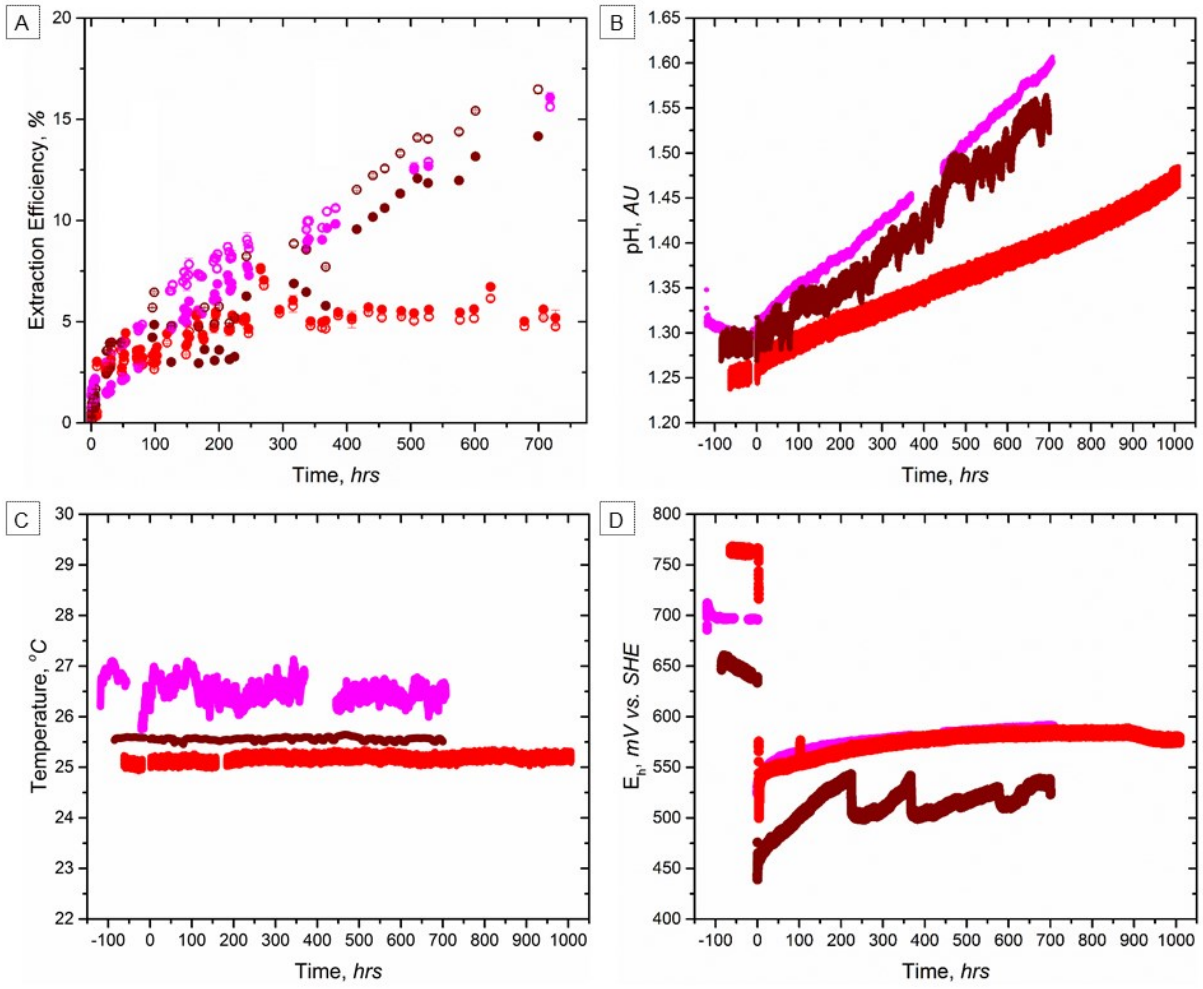
Firstly, examining reaction temperature profiles (figure 5.1C) it can be seen that maintaining 298 *K* throughout the entirety of the reaction proved difficult, since differing thermostatic equipment was available. As expected, the use of a water jacket with a constant flow of thermostatically controlled 298 *K* distilled water provided the most effective control of temperature, with the least effective control afforded by the first repeat, using a silicone oil bath. The maximum measured temperature difference between all experiments was ~2 *K*, where the impact (if any) of this temperature range is also discussed in the fitting of data (section 5.4). Accepting this ~ 2 *K* range of leachate temperatures, initial leachate *p*H is equivalent across all repeats (section 5.4.2).

Metal extraction and unprocessed physical data for $CuFeS_{2(s)}$ dissolution in 75 $mmol \cdot dm^{-3}$ $H_2SO_{4(aq)}$ displays two distinct behaviours (figure 5.1), which are independent of the ~2 *K* temperature difference between repeats. Two experiment repeats in 75 $mmol \cdot dm^{-3}$ $H_2SO_{4(aq)}$ appear to display near-linear extraction kinetics, with the other displaying clear formation of a plateau at ~5 % extraction yield (figure 5.1A). As anticipated from accepted dissolution schemes (E5.1), lixiviant *p*H and metal recoveries are indicated to be linked parameters, with two distinct $H^+_{(aq)}$-consumption rates accounting for realised metal extraction rates (figures 5.1A-5.1B). $H^+_{(aq)}$ consumption is treated further in section 5.4.2.

Metal recovery data for leaching in 75 $mmol \cdot dm^{-3}$ $H_2SO_{4(aq)}$ (figure 5.1A) also gives a calculated [Fe]:[Cu] extraction ratio of between 0.9-1.4. As discussed further throughout chapter 6, values for the [Fe]:[Cu] extraction ratio are inconsistent for all $IL_{(aq)}/H_2SO_{4(aq)}$ media and are likely to be a complex function of factors such as prevalent powdered $CuFeS_{2(s)}$ surface chemistry, lixiviant composition and physical conditions. There are no indications provided in this work that E_h impacts upon [Fe]:[Cu] extraction ratio. Although accepted acid-$SO_4^{2-}{}_{(aq)}$ dissolution schemes (E5.1-E5.3) cannot account for [Fe]:[Cu] ≠ 1, other researchers have detected accelerated initial $[Fe^{2+}]$ extraction rates with respect to $[Cu^{2+}]_{(aq)}$, which is perhaps correlated with Fe-dominated initial (atmospherically) oxidised $CuFeS_{2(s)}$ surfaces (both introduced in section 1.2). [Fe]:[Cu] extraction ratios are discussed further in section 5.5 with respect to observed changes in $CuFeS_{2(s)}$ surface chemistry during leaching.

The grouped behaviours of E_h data does not reflect the discussed grouping of *p*H and metal recoveries. This would appear to indicate that ~100 *mV* E_h variations, on the scale observed in figure 5.1D, is less deterministic of extent of $CuFeS_{2(s)}$ dissolution than *p*H variation under the conditions used. However, since there appears to be little consistency in neat solution E_h ($t<0$ *hrs*; figure 5.1D), these profiles require further analysis as featured in section 5.4.3 - where E_h step-functions at t = 0 *hrs* will also be characterised and discussed.

Increase in signal noise has been proven to be an electronic artefact of data acquisition from three integrated probe systems in parallel. This effect can be visualised in figure 5.1B, where the first repeat (■) was recorded during data acquisition cycle from a single *p*H, E_h, T probe. This aforementioned signal is low noise in comparison to the other repeats, which display ~150 % greater noise, where increased noise is an electronic artefact of monitoring 9 analogue signals in parallel. Control experiments prove that additional noise is sinusoidal in nature, varying symmetrically around the median signal value. Hence, fitted data which tracks this signal median across all leach durations is the best representation of the time-function for noisy unprocessed *p*H, T and E_h data.

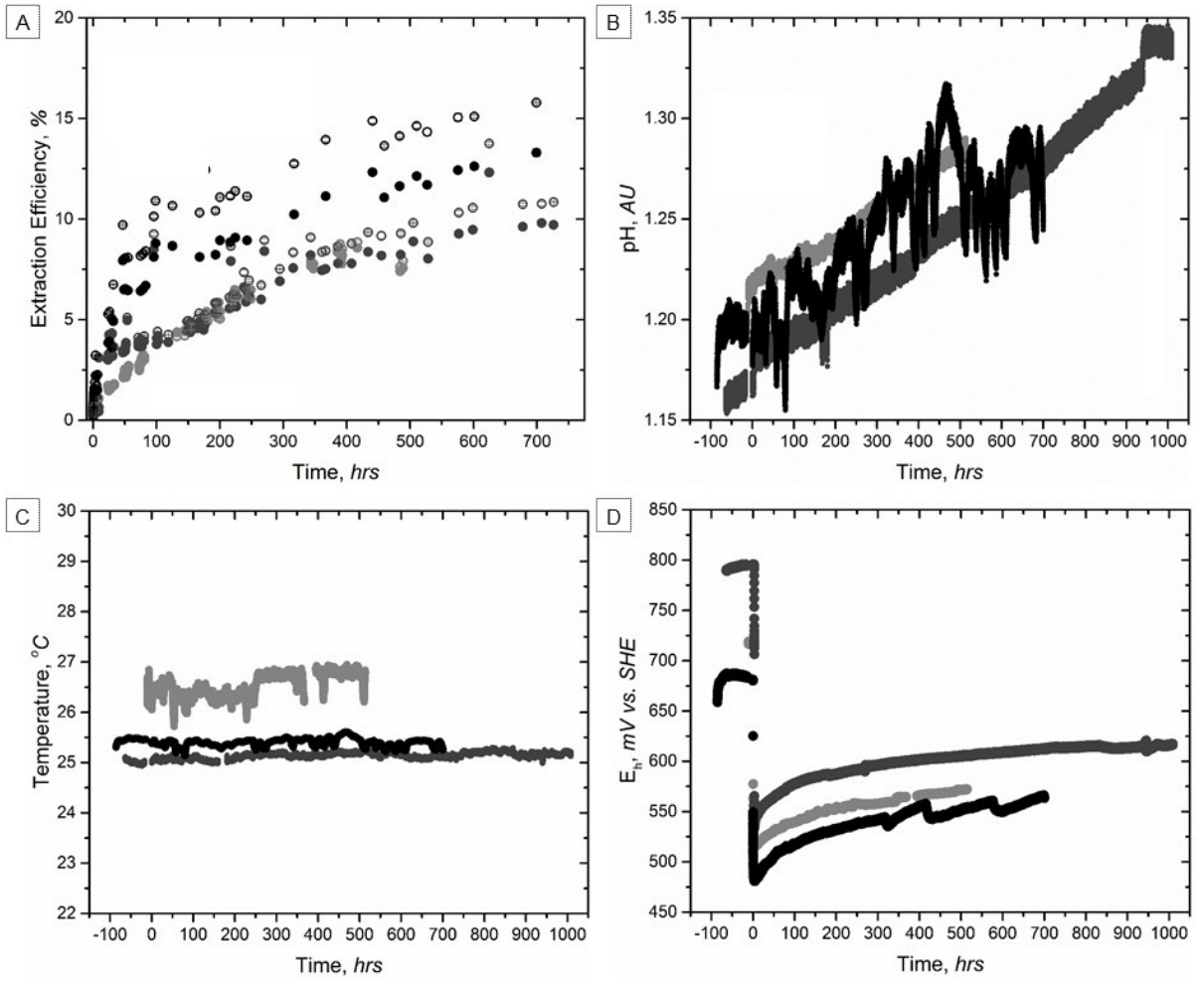


▲ Figure 5.1 - Raw data for 400 *mL*-scale $CuFeS_{2(s)}$ dissolution in 75 *mmol·dm*$^{-3}$ $H_2SO_{4(aq)}$ over extended ~1 *month* ambient leach durations, displaying evolution of (A) ICP-AES $Cu^{2+}_{(aq)}$ (solid markers) and $Fe^{2+}_{(aq)}$ recoveries (open markers) and leachate physical properties. (B) *p*H (C) temperature (D) E_h. (● 1st repeat; ● 2nd repeat; ● 3rd repeat)

5.3.2 450 *mmol·dm*$^{-3}$ $IL_{(aq)}$

Figure 5.2 displays the corresponding raw data for 400 *mL*-scale experiments conducted in 450 *mmol·dm*$^{-3}$ $[C_4Him][HSO_4]_{(aq)}$ solution. Once again, very similar trends in recorded leachate *p*H, temperature and E_h results are observed as discussed in section 5.3.1, albeit with a noticeable increase in spread of third repeat metal extraction data. The cause of periodic 'sinusoidal' *p*H profile for the third repeat in $[C_4Him][HSO_4]_{(aq)}$ (■; figure 5.2B) is unclear and does not reflect the readings provided by the meter during data acquisition. Since data in figure 5.2B shows a consistent $[H^+]_{(aq)}$ consumption rate across three experiment repeats, this effect is justifiably assumed to be an electronic artefact during curve fitting (■; figure 5.6B).

In terms of metal extraction, despite reaching similar recovery magnitudes of 10-15 *%* over ~1 *month* (*cf.* 5-15 *%*; 75 *mmol·dm*$^{-3}$ $H_2SO_{4(aq)}$; figure 5.1A) the geometry of metal extraction profiles are distinct from those received in equi-acidic $H_2SO_{4(aq)}$. Crucially, although metal extraction rates undergo parabolic reduction at leach durations < 100 *hrs,* there is no indication of the formation of dissolution plateaus. Finite metal extraction rates appear to persist across the extended dissolution timescales studies in all three repeats. As with conventional acid-$SO_4^{2-}{}_{(aq)}$ there is no consistency in [Fe]:[Cu] extraction ratio, with each repeat bearing a distinct value between 1.0-1.2, which is consistent across 100-700 *hr* leach durations (section 5.5).

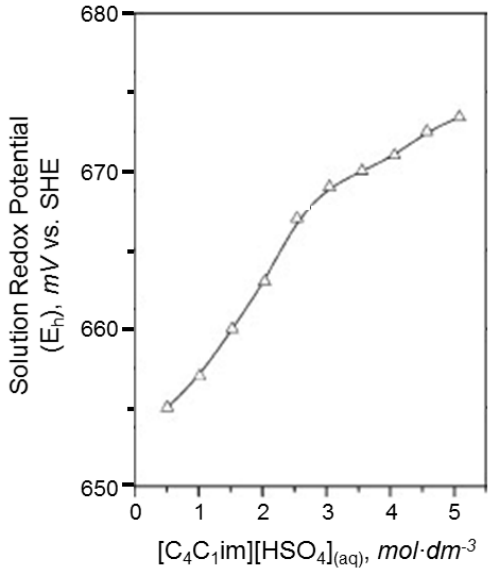


▲ Figure 5.2 - Raw data for 400 *mL*-scale $CuFeS_{2(s)}$ dissolution in 450 *mmol·dm*$^{-3}$ $[C_4Him][HSO_4]_{(aq)}$ over extended ~1 *month* ambient leach durations, displaying evolution of (A) ICP-AES $Cu^{2+}_{(aq)}$ (solid markers) and $Fe^{2+}_{(aq)}$ recoveries (open markers) and leachate physical properties. (B) *p*H (C) temperature (D) E_h. (● 1st repeat; ● 2nd repeat; ● 3rd repeat)

Unprocessed data returned for $CuFeS_{2(s)}$ dissolution in 450 *mmol·dm*$^{-3}$ $NH_4{\cdot}HSO_{4(aq)}$ displays three distinct magnitudes of metal extraction (figure 5.4). The first and last repeats shown in figure 5.4A, give metal extractions which enhance dissolution by ~46 % and ~135 % at equivalent leach durations compared with $H_2SO_{4(aq)}$ lixiviant solution, in directly comparable ambient conditions. $NH_4{\cdot}HSO_{4(aq)}$ exhibits three distinct near-linear *p*H evolution slopes (figure 5.4B), which correlate well visually with the relative rates and magnitudes of metal extraction, again suggestive that $[H^+]_{(aq)}$ is directly linked to metal recoveries (section 5.4). All ICP-AES $Cu^{2+}_{(aq)}$ and $Fe^{2+}_{(aq)}$ measures reflect [Fe]:[Cu] extraction ratios with <10 % deviation from unity, a property of $NH_4{\cdot}HSO_{4(aq)}$ leaching which is in agreement with electrochemical monitoring of $NH_4{\cdot}HSO_{4(aq)}$ (figure 4.18). Later data and discussions (section 6.2.4) will reveal that [Fe]:[Cu] ratio is a function of IL identify for $NR_4{\cdot}HSO_{4(aq)}$ ILs studied with equal conditions.

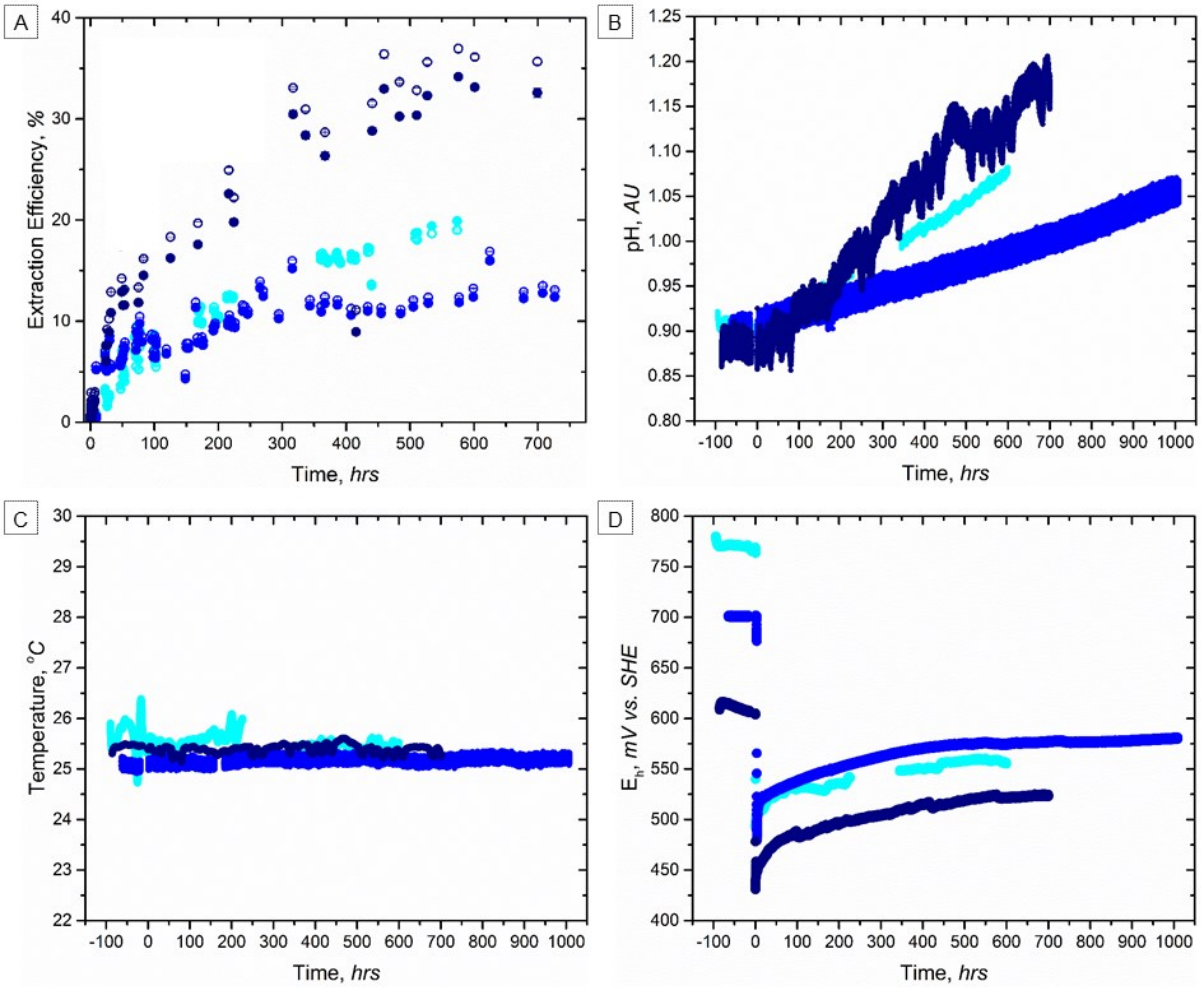
As previously indicated for $[C_nC_mim][HSO_4]_{(aq)}$ leaching (figure 4.6), an optimum $[IL]_{(aq)}$ is later shown to exist for $Cu^{2+}_{(aq)}$ recovery from $NH_4{\cdot}HSO_{4(aq)}$, lying in the vicinity of 450 $mmol{\cdot}dm^{-3}$. This result is verified in chapter 6 through observation in several sets of experimental data across varied leaching conditions (figures 6.4 and 6.5), enhanced $Cu^{2+}_{(aq)}$ recovery rates correlate well with these indications of an optimum $[IL]_{(aq)}$ for $NH_4{\cdot}HSO_{4(aq)}$. However, this non-trivial $[IL]_{(aq)}$ dependency extends further since under certain conditions and for some ILs comparable leaching occurs across all $[IL]_{(aq)}$ in the 0-1.5 $mol{\cdot}dm^{-3}$ range (figure 6.11). Since a weak $[IL]_{(aq)}$ dependence is sometimes observed, a weak effect on initial lixiviant acidity is also a highly interesting finding, where significant $IL_{(aq)}$-$CuFeS_{2(s)}$ leaching occurs for some IL solutions with much lower acidities (*p*H > 1.6; figure 2.13) and 'additive-quantity' $[IL]_{(aq)}$ (50 $mmol{\cdot}dm^{-3}$ *cf.* 450 $mmol{\cdot}dm^{-3}$ $IL_{(aq)}$; figure 6.11). These effects are discussed further in section 6.3.3.

It is worth clarifying that solution E_h evolution is similar in all studied media, with typical solution E_h ranges of ~450-620 *mV* vs. SHE (*cf.* figure 1.8) not expected to produce any $CuFeS_{2(s)}$ active/passive behaviours. Quoting from chapter 1, "direct chemical leaching from $CuFeS_{2(s)}$ typically suffers from slow dissolution kinetics,[1] where dissolution is substantially incomplete after 80 days for typical 'heap' leaching conditions[2]". Figures 1.9 and 1.13 suggest that (typically) a maximum of 25-30 *%* $Cu^{2+}_{(aq)}$ recovery is attainable through chemical leaching over equivalent ~1 *month* leach durations, including additional enhancements from E_h control at 650-700 *mV* vs. SHE. 450 $mmol{\cdot}dm^{-3}$ $NH_4{\cdot}HSO_{4(aq)}$ has been demonstrated to match this performance magnitude (figure 5.4A), without additional aid from optimised E_h conditions (figure 5.4D). As discussed, once again there are indications that E_h variation is not deterministic of metal leaching rates in $IL_{(aq)}$ for the conditions studied. These indications are in agreement with a similar finding by Carlesi *et al*.[3] who very recently reported that differences in $[C_nC_mim][HSO_4]_{(aq)}$-$CuFeS_{2(s)}$ dissolution at varied $[IL]_{(aq)}$ could not be accounted for by approximately unchanged E_h of the $IL_{(aq)}$ medium. To exemplify this, figure 5.3 displays the small neat solution E_h variations observed across the full $[C_4C_1im][HSO_4]_{(aq)}$ concentration range as measured by Dong *et al*.[4], which are representative of the values observed for all $[HSO_4]$-ILs throughout this study. However, E_h is a complex variable and is still a potentially crucial measurement, which must be analysed further (section 5.4.3).



▲ Figure 5.3 - Variation of lixiviant E_h as a function of $[C_4C_1im][HSO_4]_{(aq)}$ concentration. [4]

Importantly, the annotated sections of Klauber's four-stage model of acid-$SO_4^{2-}{}_{(aq)}$ $CuFeS_{2(s)}$ dissolution (figure 1.9)[5] does consider S^0-layer formation to be responsible for parabolic extraction plots equivalent to figures 5.2-5.4A for $IL_{(aq)}$ media. Thus, section 5.5 will use surface-probing studies to investigate whether a similar layer is found on leached $CuFeS_{2(s)}$ residues.



▲ Figure 5.4 - Raw data for 400-*mL* scale $CuFeS_{2(s)}$ dissolution in 450 *mmol·dm*$^{-3}$ $NH_4{\cdot}HSO_{4(aq)}$ over extended ~1 *month* ambient leach durations, displaying evolution of (A) ICP-AES $Cu^{2+}_{(aq)}$ (solid markers) and $Fe^{2+}_{(aq)}$ recoveries (open markers) and leachate physical properties. (B) *p*H (C) temperature (D) E_h. (● 1st repeat; ● 2nd repeat; ● 3rd repeat)

5.4 Analysis and Discussion of Key Leaching Parameters

As mentioned, $CuFeS_{2(s)}$ powder was prepared in large 30 *g* batches (3 x 10 *g*), ensuring equivalency of initial powdered $CuFeS_{2(s)}$ material. Hence, parallel experiments in each medium (i.e. same repeat number) are directly comparable. Unfortunately, the use of differing sources of $CuFeS_{2(s)}$ for each experimental repeat was unavoidable and therefore it is not surprising that differing extraction profiles and physical parameter variations are observed throughout the presented metal extraction data. This section details the processing and analysis of raw leaching data presented in section 5.3, where obtaining accurate, representative fits of experimental data is crucial to further examination of $CuFeS_{2(s)}$ dissolution across all studied media and repeats.

Leachate *p*H, E_h, $[O_2]_{(aq)}$ and metal extraction dynamics are considered in turn below, with particular reference to the relative impact of maximum ~2 *K* temperature difference on each

parameter. Throughout this section curve fitting procedures and resulting parameters are described, in order to produce analytical expressions capable of producing representative values for key leaching parameters at all leach durations (0-700 *hrs*).

The accepted 4-electron acid-$SO_4^{2-}{}_{(aq)}$ oxidative $CuFeS_{2(s)}$ dissolution schemes introduced in section 1.4 are repeated below for reference within this chapter. E5.1-E5.3 also include the rate constant notation used hereafter. As discussed in section 4.2, these reaction schemes feature $Cu^{2+}{}_{(aq)}$ and $Fe^{2+}{}_{(aq)}$ as the thermodynamic products of $CuFeS_{2(s)}$ dissolution. Since results in previous results chapters have confirmed that these thermodynamic dissolution products are common to both $IL_{(aq)}$ and $H_2SO_{4(aq)}$ media, E5.1-E5.3 will be utilised to compare and contrast the dynamics of $CuFeS_{2(s)}$ dissolution in $IL/H_2SO_{4(aq)}$ media. It is also noteworthy that these schemes cannot account for differences in observed $Cu^{2+}{}_{(aq)}$ and $Fe^{2+}{}_{(aq)}$ recovery rate - a factor which is discussed further throughout chapter 6.

$$CuFeS_{2(s)} + 4H^{+}_{(aq)} + O_{2(aq)} \overset{k_1}{\rightarrow} Cu^{2+}_{(aq)} + Fe^{2+}_{(aq)} + 2S^{0}_{(s)} + 2H_2O_{(l)} \quad \text{E5.1}$$

$$CuFeS_{2(s)} + 4Fe^{3+}_{(aq)} \overset{k_2}{\rightarrow} Cu^{2+}_{(aq)} + 5Fe^{2+}_{(aq)} + 2S^{0}_{(s)} \quad \text{E5.2}$$

$$4Fe^{2+}_{(aq)} + 4H^{+}_{(aq)} + O_{2(aq)} \overset{K_3}{\leftrightarrow} 4Fe^{3+}_{(aq)} + 2H_2O_{(l)} \quad \text{E5.3}$$

5.4.1 Metal Extraction Data

5.4.1.1 Influence of Temperature

As discussed in section 1.6.1, Acero *et al.*[6] derived a valuable Arrhenius rate equation, valid for acid-$SO_4^{2-}{}_{(aq)}$ leaching at *p*H 1-3 (E1.26). Since the influence of $[Fe^{3+}]_{(aq)}$ is negated for initial dissolution rates, E1.26 is useful here to estimate the potential impact of a maximum 2 °*C* difference in leachate temperature observed in raw experimental data (section 5.3). With all else equal, and assuming minimal temperature dependence of E_a over this small temperature range, E1.26 suggests 13.8 *%* difference in initial rate at 298 *K* (31.1 $nM{\cdot}s^{-1}$) and 300 *K* (35.4 $nM{\cdot}s^{-1}$). The error introduced in the course of this calculation through assumption will dominate and little can be concluded in this case for such a minimal temperature difference; however, the magnitude of this calculated error emphasises the importance of effective thermal regulation in $CuFeS_{2(s)}$ dissolution experiments.

5.4.1.2 $[Cu^{2+}]_{(aq)}$ Curve Fitting

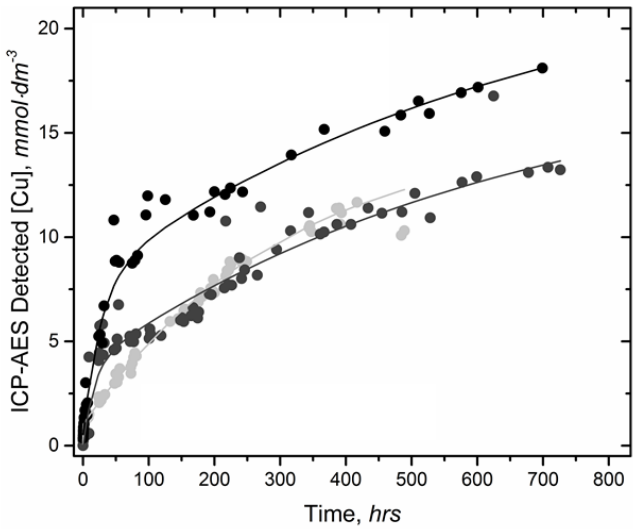
Accurate assessment of initial $[Cu^{2+}]_{(aq)}$ extraction rate is crucial to any kinetic study, however direct measurement from raw data may be complicating by confirmation that $CuFeS_{2(s)}$ dissolution can involve induction periods of significant length (section 4.6). Therefore, chosen

data fitting procedures must allow for such corrections. $Cu^{2+}_{(aq)}$ extraction curves were fitted using standard fit functions in a graphing and data analysis software package (*OriginPro® 2015*; *OriginLab*; table 5.1). A two-term exponential fit function showed good fitting of all extraction profiles (E5.4), with a linear offset term (y_0) allowing induction periods to be measured and corrected for (x=0; $t_{passive}$ - table 5.1). Reduced chi-squared (X^2) values varied over 1 order of magnitude in the range 0.4-4.5 x 10^{-7}.

$$[Cu^{2+}]_t = A_1 e^{-B_1 \cdot t} + A_2 e^{-B_2 \cdot t} + y_0 \qquad \text{E5.4}$$

$$\frac{d[Cu^{2+}]}{dt} = -A_1 \cdot B_1 \cdot e^{-B_1 \cdot t} - A_2 \cdot B_2 \cdot e^{-\frac{1}{B_2} t} \qquad \text{E5.5}$$

Since all $Cu^{2+}_{(aq)}$ extraction data is modelled well by E5.4, this reinforces similarities between observed metal recovery profiles. The form of the gradient function is common to all media and repeats (E5.5). Numeric values can therefore be accessed across all leach durations through the non-linear fitting parameters in table 5.1. Fitted data is further used in the assessment of the proportion of dissolution which occurs via each of the accepted dissolution pathways E5.1-E5.2 (section 5.4.6) and also to generate $[Cu^{2+}]_{(aq)}$ data as a function of time. Figure 5.5 below shows an example of the fitted functions with respect to real $[Cu^{2+}]_{(aq)}$ data.



▲ Figure 5.5 - Example of $[Cu]_t$ non-linear fits of raw data for $CuFeS_{2(s)}$ dissolution in 450 *mmol·dm^{-3}* $[C_4Him][HSO_4]_{(aq)}$ presented in figure 5.2A.

▼ Table 5.1 - Summary of the non-linear fitting of $Cu^{2+}_{(aq)}$ extraction profiles from figures 5.1-5.4 (panel A), using a two-term exponential fit function and standard units - $[Cu]_t = -A_1 \cdot \exp(-B_1 \cdot t) - A_2 \cdot \exp(-B_2 \cdot t) + y_0$.

Medium	Rep.	Non-Linear Fit Parameters (2 *sf*)					$t_{passive}$, *hrs*	Adjusted R^2
		y_0, *mol·dm⁻³*	A_1, *mol·dm⁻³*	B_1, *s⁻¹*	A_2, *mol·dm⁻³*	B_2, *s⁻¹*		
75 *mmol·dm⁻³* $H_2SO_{4(aq)}$	R1	$1.1x10^{-1}$	$2.3x10^{-3}$	$2.3x10^{-5}$	$1.0x10^{-1}$	$7.7x10^{-8}$	---	0.995
	R2	$7.5x10^{-3}$	$1.3x10^{-3}$	$9.9x10^{-6}$	$6.1x10^{-3}$	$2.6x10^{-6}$	---	0.981
	R3	$7.5x10^{-2}$	$3.6x10^{-3}$	$1.3x10^{-5}$	$7.1x10^{-2}$	$9.8\ x10^{-8}$	---	0.998
450 *mmol·dm⁻³* $[C_4Him][HSO_4]_{(aq)}$	R1	$1.5x10^{-2}$	$9.4x10^{-4}$	$1.3x10^{-3}$	$1.4x10^{-2}$	$8.9\ x10^{-7}$	---	0.997
	R2	$1.8x10^{-2}$	$3.9x10^{-3}$	$1.7x10^{-5}$	$1.5x10^{-2}$	$4.3\ x10^{-7}$	0.45	0.992
	R3	$2.4x10^{-2}$	$7.3x10^{-3}$	$1.1\ x10^{-5}$	$1.6x10^{-2}$	$4.1\ x10^{-7}$	---	0.993
450 *mmol·dm⁻³* $NH_4{\cdot}HSO_{4(aq)}$	R1	$8.0x10^{-1}$	$1.1x10^{-2}$	$7.0\ x10^{-6}$	$7.8x10^{-1}$	$1.0\ x10^{-8}$	---	0.996
	R2	$3.4x10^{-2}$	$1.2x10^{-2}$	$6.2x10^{-6}$	$2.2x10^{-2}$	$9.8\ x10^{-8}$	0.82	0.990
	R3	$6.4x10^{-2}$	$2.2x10^{-2}$	$6.0x10^{-6}$	$4.2x10^{-2}$	$3.8\ x10^{-7}$	---	0.996

5.4.2 pH / [H⁺] Consumption

5.4.2.1 Influence of Temperature

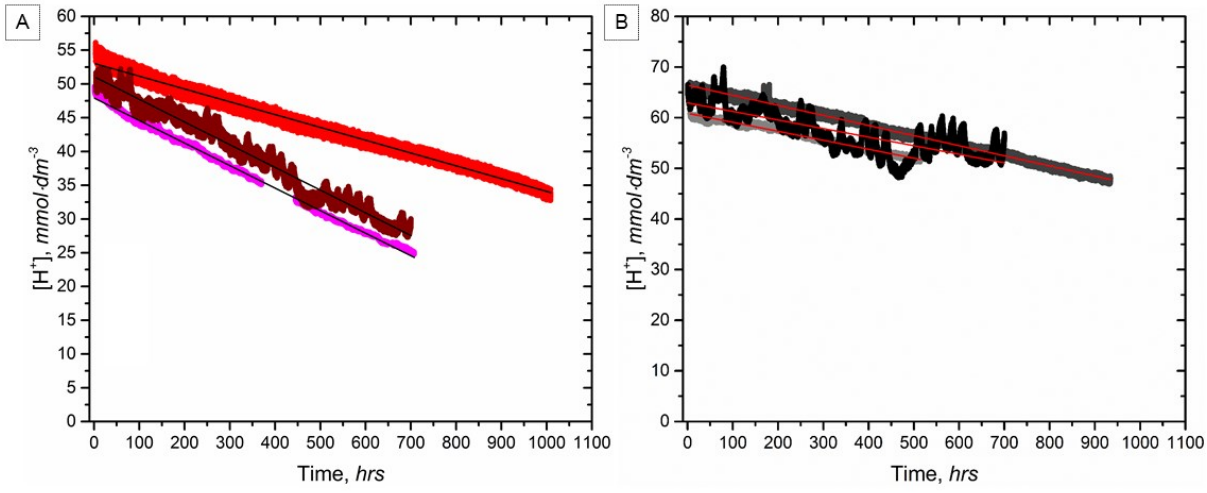
Electrode potential-based *p*H measurement theory is introduced in section 2.3.5. E2.7 contains the Nernstian temperature dependence of *p*H measurement, allowing for consideration of the uncertainty surrounding initial *p*H values. All else equal and assuming $E^{\ominus}$ and $E(V)$ remain approximately constant over the low 2 *K* temperature range, one would expect a maximum initial *p*H uncertainty of ±0.7 *%* as per E5.6. At *p*H 1.2, this corresponds to a *p*H variation of <0.01 *p*H units, which is far outweighed by error induced by small variations in lixiviant concentration. After correcting signals for electronic noise artefacts (see below), all solutions can be regarded as having equivalent starting *p*H within experimental uncertainty of ±0.03 *p*H units. Experimental error was calculated through consideration of the uncertainty generated through $IL_{(aq)}/H_2SO_{4(aq)}$ dilution, with reference to the relevant *p*H variation plots (figure 2.13; figure 6.6B).

$$\frac{\Delta pH}{pH} \cong \frac{(T_2 - T_1)}{T_1} \qquad \text{E5.6}$$

5.4.2.2 $[H^+]_{(aq)}$ Curve Fitting

Since leaching is conducted at low *p*H, the level of free-$H^+_{(aq)}$ consumption during these $CuFeS_{2(s)}$ dissolution experiments is considerable (figure 5.6). Linear fits, summarised in table 5.2, are in excellent agreement with data, with a maximum fitting parameter standard error of 0.33 % for the anomalous, noisy $[C_4Him][HSO_4]_{(aq)}$ curve discussed previously (figure 5.6B).

$[H^+]_{(aq)}$ consumption slopes vary over significant range (0.8-2.4 $\mu mol \cdot dm^{-3} \cdot day^{-1}$; table 5.2), a range that is certainly capable of causing the observed differences in lixiviant activity. However, since lixiviant solution is equivalent across repeats, one must conclude that variations in the $CuFeS_{2(s)}$ source material are responsible for a lack of consistency in the magnitudes of $CuFeS_{2(s)}$ dissolution when using equivalent leachate (*ca*. figure 5.4A). Once again, the fit parameters (table 5.2) are used to access $[H^+]_t$ values which are representative across the entire leach duration.



▲ Figure 5.6 - Plots and linear fits (table 5.2) of free-$[H^+]_{(aq)}$ concentration as a function of time during ~1 *month* $CuFeS_{2(s)}$ dissolution in (A) 75 $mmol \cdot dm^{-3}$ $H_2SO_{4(aq)}$ and (B) 450 $mmol \cdot dm^{-3}$ $[C_4Him][HSO_4]_{(aq)}$.

▼ Table 5.2 - Summary of linear fit parameters for $[H^+]_{(aq)}$ evolution in 400 *mL*-scale extended $CuFeS_{2(s)}$ dissolution experiments, processed from raw data in figures 5.1-5.4 (panel B)

Medium	Repeat	$[H^+]$ Concentration - Linear Fit Parameters		
		$\frac{d[H^+]}{dt}$, *μM·hr⁻¹*	$[H^+]_{t=0}$, *mM*	Adj. Correlation Coefficient (R^2)
75 *mmol·dm⁻³* $H_2SO_{4(aq)}$	R1	-33.4	47.9	0.997
	R2	-19.0	53.0	0.989
	R3	-33.6	51.1	0.976
450 *mmol·dm⁻³* $C_4Him{\cdot}HSO_{4(aq)}$	R1	-17.7	60.9	0.978
	R2	-19.9	66.4	0.991
	R3	-16.9*	62.9*	0.649
450 *mmol·dm⁻³* $NH_4{\cdot}HSO_{4(aq)}$	R1	-67.5	123.9	0.997
	R2	-27.9	125.8	0.974
	R3	-98.5	128.6	0.948
Max. Standard Error:		* = 0.33 %	* = 0.04 %	
Average Standard Error:		0.086 %	0.015 %	

5.4.3 Solution Redox Potential (E_h)

5.4.3.1 Influence of Temperature

As discussed in section 1.6.8, E_h bears a Nernstian temperature dependence, as per E5.7. Since measured E_h is proportional to leachate temperature, the E_h uncertainty caused by maximum ~2 *K* temperature is again proportional to the temperature difference (*cf.* E5.6), with all else equal - giving a low percentage uncertainty of ±0.7 *%* corresponding to a maximum uncertainty of ±5.6 *mV*. This magnitude of error can be neglected since it represents <10 *%* of the observed differences in E_h between equivalent experimental repeats ($\Delta E_{h,max}$ = 90-150 *mV*; figures 5.1-5.4D). The potential causes of shifts in E_h curves are discussed below in section 5.4.3.2.

$$E = E^0 - \frac{RT}{nF} lnQ_r \qquad \text{E5.7}$$

5.4.3.2 Analysis of E_h Curves

Initial visual inspection of the raw E_h curves (figures 5.1-5.4D) reveals similar features; firstly, a high magnitude sharp potential-drop in measured E_h ($-\Delta E_h$), which occurs moments after addition of $CuFeS_{2(s)}$ powder and, secondly, an increase in potential over time ($+\Delta E_h$), with a rate of increase that gradually decays, appearing to converge to a potential asymptote ($E_{h,\infty}$) at high

leach durations. However, aside from these features, there is little consistency between repeats, both in terms of neat solution E_h and the magnitude of key potential changes ($-\Delta E_h$, $+\Delta E_h$, $E_{h,\infty}$). Parameter measurements are summarised in table 5.3.

▼ Table 5.3 - Summary of key measured E_h changes during ~1 *month* 400 *mL*-scale $CuFeS_{2(s)}$ ambient dissolution experiments.

Medium	Repeat	Measured E_h, *mV* (vs. SHE)					
		Neat Medium E_h	$E_{h,min}$ (t ≈ 0 *hrs*)	E_h (t=500 *hrs*)	Potential Drop ($-\Delta E_h$)	Potential Rise ($+\Delta E_h$)	$E_{h,\infty}$ (t = ∞)
75 *mmol·dm^{-3}* $H_2SO_{4(aq)}$	R1	696	524	585	172	61	605
	R2	761	501	581	260	80	586
	R3	641	439	516	202	77	526
450 *mmol·dm^{-3}* $C_4Him{\cdot}HSO_{4(aq)}$	R1	716	527	572	189	45	607
	R2	795	539	595	256	56	627
	R3	683	480	551	203	71	562
450 *mmol·dm^{-3}* $NH_4{\cdot}HSO_{4(aq)}$	R1	765	493	558	278	65	611
	R2	700	489	575	211	86	580
	R3	607	431	519	176	88	537

Since control measurements in E_h reference solutions (*VWR International*) before and after experimentation confirm valid calibration of the integrated probes, one must address the possible causes of difference in measured neat solution E_h. The formal expression for anticipated E_h in acid-$SO_4^{2-}{}_{(aq)}$ media during $CuFeS_{2(s)}$ leaching is repeated for reference purposes (E5.8) alongside a simplified version which applies only to neat lixiviant solution (E5.9). E5.9 uses the half-cell reduction of $H^+_{(aq)}$ by molecular oxygen ($E^{\ominus}$ = +1.23 *V*).[7]

Since proton activity is raised to the fourth power, the observed difference in neat solution E_h may be rationalised through this strong dependence. Calculations using real initial $[H^+]_{(aq)}$, E_h and leachate temperature data reveal that *ln*Q_r (E5.7) varies somewhat unavoidably by 17-25 *%* under the equivalent conditions of this experiment - thus satisfactorily explaining the levels of variability in all E_h characteristics (table 5.3).

$$E_h = E^{\ominus} - \frac{RT}{4F} ln \left[\frac{\{S^0\}^2 \cdot \{H_2O\}^2}{\{CuFeS_2\}} \cdot \frac{\{Cu^{2+}\} \cdot \{Fe^{2+}\}}{\{H^+\}^4 \cdot \{O_2\}} \right] \quad \text{E5.8}$$

$$E_h = E^{\ominus} - \frac{RT}{4F} ln \left[\frac{\{H_2O\}^2}{\{H^+\}^4 \cdot \{O_2\}} \right] \quad \text{E5.9}$$

As discussed in chapter 1 (E1.37), Vilcaez *et al*.[8] concluded that E_h profiles during $CuFeS_{2(s)}$ dissolution are dominated by $[Fe^{2+}]$:$[Fe^{3+}]$, as per E5.10. It is noteworthy that, theoretically speaking, $[Cu^{2+}]_{(aq)}$ has equivalent impact upon measured E_h as $[Fe^{2+}]_{(aq)}$, at nominal concentration, and as such this approach may be too simplistic. However, the approach of using E5.10 as a key simplification is justified by virtue of allowing access to estimates for $[Fe^{3+}]_{(aq)}$ and $[Fe^{3+}]_{(aq)}$ when E_h measurements are considered alongside (total) ICP-AES $[Fe]_{(aq)}$ measures (E5.10-13).

$$E_h = E^0 - \frac{RT}{nF} ln \frac{[Fe^{2+}]}{[Fe^{3+}]} \qquad \Leftrightarrow \qquad \frac{[Fe^{2+}]}{[Fe^{3+}]} = e^{\frac{nF}{RT}(E^0 - E_h)} \qquad \text{E5.10}$$

$$[Fe_{Tot,ICP}] = [Fe^{2+}_{(aq)}] + [Fe^{3+}_{(aq)}] \qquad \text{E5.11}$$

$$\frac{[Fe_{Tot,ICP}]}{[Fe^{2+}_{(aq)}]} = 1 + \frac{[Fe^{3+}_{(aq)}]}{[Fe^{2+}_{(aq)}]} \qquad \text{E5.12}$$

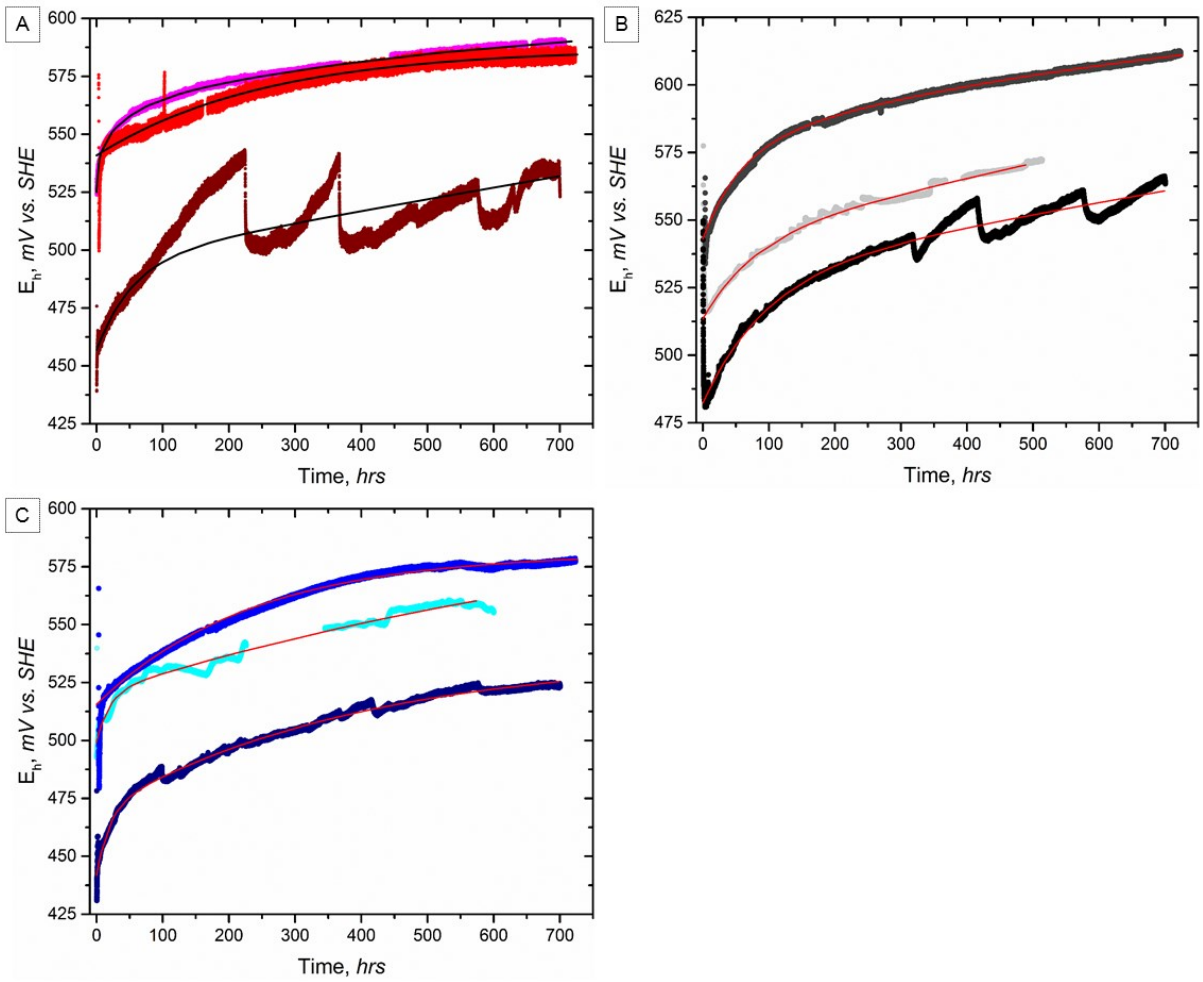
$$[Fe^{2+}_{(aq)}] = \frac{[Fe_{Tot,ICP}]}{1 + \frac{[Fe^{3+}_{(aq)}]}{[Fe^{2+}_{(aq)}]}} \qquad Fe^{3+}_{(aq)} = Fe_{Tot,ICP} - Fe^{2+}_{(aq)} \qquad \text{E5.13}$$

5.4.3.3 E_h Curve Fitting

E_h traces were fitted using the same two-term exponential fitting function within *OriginLab*®, in order to extract redox values that can provide measures of $[Fe^{2+}]$ and $[Fe^{3+}]_{(aq)}$ for all leach durations. Details of the best fitting parameters are provided in table 5.4. In order to achieve a good fit of data, certain problematic curves required significant data exclusion (*ca.* figure 5.1B), therefore standard measures of fit efficacy (*i.e.* reduced X^2) are relatively meaningless. Visualisation of the resulting non-linear fits are shown to give a good overall representation of unprocessed E_h evolution (figure 5.7).

▼ Table 5.4 - Summary of non-linear fitting of raw E_h profiles presented in figures 5.1-5.4 (panel D), using a two-term exponential fit function and standard units - $E_h = -A_1 \cdot \exp(-B_1 \cdot t) - A_2 \cdot \exp(-B_2 \cdot t) + y_0$.

Medium	Repeat	Non-Linear Fit Parameters (2-3 *sf.*)					Goodness of Fit	
		y_0, *V*	A_1, *V*	B_1, s^{-1}	A_2, *V*	B_2, s^{-1}	Red.X^2	Adj. R^2
75 *mmol·dm^{-3}* $H_2SO_{4(aq)}$	R1	0.605	2.2x10^{-2}	1.2x10^{-5}	4.8x10^{-2}	5.3x10^{-7}	9.8x10^{-7}	0.993
	R2	0.586	2.2x10^{-2}	1.1x10^{-6}	2.3x10^{-2}	1.1x10^{-6}	2.7x10^{-6}	0.980
	R3	0.526	7.1x10^{-3}	4.5x10^{-5}	6.5x10^{-2}	2.2x10^{-6}	3.3x10^{-6}	0.993
450 *mmol·dm^{-3}* $C_4Him{\cdot}HSO_{4(aq)}$	R1	0.607	2.7x10^{-2}	2.8x10^{-6}	6.2x10^{-2}	3.1x10^{-7}	5.2x10^{-7}	0.998
	R2	0.627	2.8x10^{-2}	5.3x10^{-6}	5.4x10^{-2}	5.3x10^{-7}	5.3x10^{-7}	0.998
	R3	0.562	1.3x10^{-2}	9.9x10^{-6}	5.9x10^{-2}	1.1x10^{-6}	6.2x10^{-7}	0.998
450 *mmol·dm^{-3}* $NH_4{\cdot}HSO_{4(aq)}$	R1	0.611	1.9x10^{-2}	1.4x10^{-5}	9.1x10^{-2}	2.8x10^{-7}	4.7x10^{-7}	0.979
	R2	0.580	3.3x10^{-2}	1.2x10^{-6}	2.9x10^{-2}	1.2x10^{-6}	1.4x10^{-6}	0.994
	R3	0.53	2.3x10^{-2}	1.5x10^{-5}	6.7x10^{-2}	7.1x10^{-7}	1.9x10^{-6}	0.993



▲ Figure 5.7 - Plots of raw E_h data overlaid with their corresponding non-linear fits (table 5.4) as a function of time during ~1 *month* $CuFeS_{2(s)}$ dissolution in (A) 75 *mmol·dm*$^{-3}$ $H_2SO_{4(aq)}$, (B) 450 *mmol·dm*$^{-3}$ $[C_4Him][HSO_4]_{(aq)}$ and (C) 450 *mmol·dm*$^{-3}$ $NH_4{\cdot}HSO_{4(aq)}$.

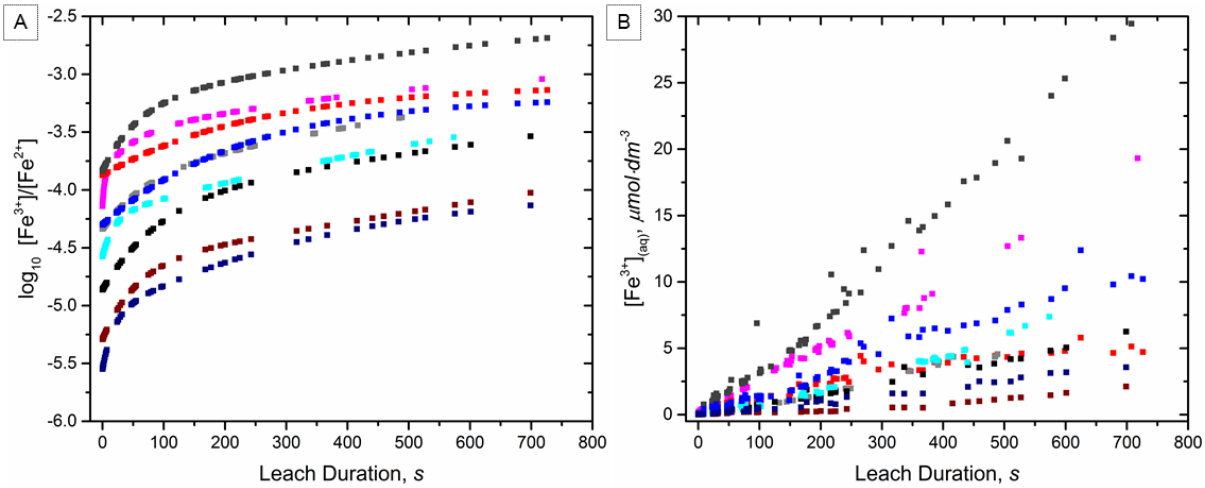
5.4.4 $[Fe^{2+}]/[Fe^{3+}]$ Implications

Through calculations combining E5.10-13, ICP-AES $[Fe]_{(aq)}$ and E_h, plots of the estimated $[Fe^{3+}]/[Fe^{2+}]$ ratio development and free-$Fe^{3+}_{(aq)}$ oxidant production were computed as time-functions (figure 5.8). Magnitude of $\log_{10}[Fe^{3+}]/[Fe^{2+}]$ values (figure 5.8A) agrees well with previous studies, as judged via empirical relation E3.2 (*cf*. $\log_{10}[Fe^{3+}]/[Fe^{2+}] = 10^{-11}$-$10^{-4}$).[9] Values lie on the upper boundary of previously reported values $\log_{10}[Fe^{3+}]/[Fe^{2+}]$ and appear to be convergent, forming an asymptote as leaching rate decays slowly over time. It is noteworthy that over infinite timescales leaching will cease allowing calculation of thermodynamic equilibrium constant K_3 (E5.3). A plot of $\log_{10}[Fe^{3+}]/[Fe^{2+}]$ may, theoretically be observed to converge toward the equilibrium defined $Fe^{3+}/Fe^{2+}_{(aq)}$, which is indicated to be on the order of 10^{-2}-10^{-3}. The required data has been produced in order to calculate K_3 at infinite leach duration when $CuFeS_{2(s)}$ dissolution rate falls to zero. However, after the maximum leach duration range for which data is available (0-1000 *hrs*), predictions of K_3 plotted over time do not show any signs of

convergence. This importantly signifies that leaching rates are still substantial, as implied by metal extraction data and fits.

Having validated the magnitude of $\log_{10}[Fe^{3+}]/[Fe^{2+}]$ inferred from E_h, figure 5.8B estimates free-$[Fe^{3+}]_{(aq)}$ evolution during the $CuFeS_{2(s)}$ dissolution experiments. The rate of $Fe^{2+}_{(aq)}$ oxidation is reported to be comparatively slow in acid-$SO_4^{2-}{}_{(aq)}$ media in comparison to acids with higher Fe-complexing affinity ($PO_4 > Cl^- > SO_4^{2-}$).[10, 11] The process is reportedly catalysed by presence of $Cu^{2+}_{(aq)}$ with a weak $H^+_{(aq)}$ dependence.[11] Huffman *et al.*[11] derived an empirical relation for calculation of rates of $Fe^{2+}_{(aq)}$ oxidation in 0.23-1.0 *mol·dm*$^{-3}$ $H_2SO_{4(aq)}$ (E5.14). Rates calculated from this expression also show good agreement with experimental data in figure 5.8B given the difference in $[H_2SO_4]_{(aq)}$, as neatly presented by linear fit parameters summarised in table 5.5 (*cf.* 18-1960 *nM·hr*$^{-1}$; 1-20 *mmol·dm*$^{-3}$ $Fe^{2+}_{(aq)}$; 226 *mmol·dm*$^{-3}$ $H_2SO_{4(aq)}$; 303 *K*). The linear fit slope parameters can be used to generate representative $[Fe^{3+}]_{(aq),t}$ data for these leach investigations.

$$-\frac{d[Fe^{2+}]}{dt} = \frac{d[Fe^{3+}]}{dt} = l_b \cdot [Fe^{2+}] + l_t \cdot [Fe^{2+}]^2 \qquad \text{E5.14}$$



▲ Figure 5.8 - (A) Variation in $\log_{10}[Fe^{3+}]/[Fe^{2+}]$ and (B) associated (linear) development of free-$[Fe^{3+}]_{(aq)}$ as a function of time during ~1 *month* ambient $CuFeS_{2(s)}$ dissolution, as computed from E_h and $[Fe]_{(aq)}$ measurements. (1st - 3rd repeat; ■■■ H_2SO_4; ■■■ $[C_4Him][HSO_4]$; ■■■ $NH_4{\cdot}HSO_4$)

▼ Table 5.5 - Linear fit parameters for evolution of $[Fe^{3+}]_{(aq)}$ as a function of time during ~1 *month* ambient $CuFeS_{2(s)}$ dissolution in $IL/H_2SO_{4(aq)}$.

Medium	Repeat	Linear Fit Parameters (± Standard Error)		
		$\frac{d[Fe^{3+}]}{dt}$, *nM·hr⁻¹*	Predicted y-intercept, *nM*	Adj. Correlation Coefficient (R^2)
75 *mmol·dm⁻³* $H_2SO_{4(aq)}$	R1	25.0 ± 0.4	112 ± 72	0.984
	R2	8.1 ± 0.3	356 ± 67	0.921
	R3	2.4 ± 0.1	-43.3 ± 24	0.926
450 *mmol·dm⁻³* $C_4Him{\cdot}HSO_{4(aq)}$	R1	9.4 ± 0.2	-129 ± 34	0.975
	R2	41.9 ± 0.7	-432 ± 188	0.976
	R3	8.4 ± 0.1	-35.9 ± 33	0.988
450 *mmol·dm⁻³* $NH_4{\cdot}HSO_{4(aq)}$	R1	11.4 ± 0.2	-144 ± 43	0.982
	R2	15.8 ± 0.3	-9.1 ± 78	0.971
	R3	5.1 ± 0.1	-39.6 ± 21	0.987

5.4.5 Consideration of $[O_2]_{(aq)}$

As discussed in section 1.4.2, pure aqueous environments contain approximately 0.29 *mmol·dm⁻³* $[O_2]_{(aq)}$, where addition of solute such as IL may reduce the molecular oxygen content of an aqueous solution.[3] Typical reference values for $IL_{(l)}$ $[O_2]_{(aq)}$ content have been provided (table 2.2). According to theory, the rate of solubilisation of sparingly-soluble $O_{2(g)}$ is limited by the rate at which it can diffuse across a 'stagnant film' at the surface of the water.[12, 13] An exit coefficient is defined, f =D/x, with D being the aqueous diffusion coefficient of oxygen and x being the stagnant film thickness. The latter factor is significantly reduced by agitation, yet the magnitude of this effect is difficult to quantify.

$$\frac{d[H^+]}{dt} = 4 \cdot \frac{d[O_{2(aq)}]}{dt} \qquad \text{E5.15}$$

Rate analysis of E5.1 and E5.3 allows an expression for the consumption of $[O_2]_{(aq)}$ to be derived (E5.15), under the hypothesis that the process of dissolution bears the dominant influence on varied $[H^+]$ as a function of time. Since the rate of aeration is not easily accessible and is likely to be increasingly complex for moderate $[IL]_{(aq)}$, an alternative method of testing the aforementioned hypothesis has been used. E5.15 has been used to assess the extent to which solution aeration may be a limiting factor in ambient $CuFeS_{2(s)}$ dissolution experiments. $H^+_{(aq)}$ consumption rates in the range of 19-122 *nmol·dm⁻³·hr⁻¹* (section 5.4.2) are 3 orders of magnitude lower than nominal $[O_2]_{(aq)}$, suggesting that exhaustion of $O_{2(aq)}$ could only be possible through combination of a zero re-aeration rate and leach durations of thousands of hours. Additionally, since initially high dissolution rates decay on the order of 20-100 *hrs* as shown in figures 5.1-5.4A, $O_{2(aq)}$

consumption is estimated at an insignificant maximum level of 1.2 *%*. Since 120 *rpm* stirring will additionally re-aerate the lixiviant solution at an increased rate in comparison to still solution, it is reasonable to assume that $[O_2]_{(aq)}$ will remain constant throughout these $CuFeS_{2(s)}$ dissolution studies at its (still) aqueous solubility limit (0.29 *mmol·dm^{-3}*).

5.4.6 Proportional Divide Between $CuFeS_{2(s)}$ Dissolution Pathways

Using the expressions in section 5.4 and the aforementioned hypothesis of dissolution-dominated $[H^+]$ consumption, two approaches have been devised in order to estimate the fraction of $CuFeS_{2(s)}$ dissolution, which occurs via $O_{2(aq)}$-assisted dissolution (x_{k_1}; E5.1) and via $Fe^{3+}{}_{(aq)}$-assisted dissolution (x_{k_2}; E5.2). Firstly, the total $H^+{}_{(aq)}$ consumption rate can be identified with the sum of the rates produced by $O_{2(aq)}$-assisted dissolution - denoted with subscript k_1 - and the oxidation of Fe^{2+} - denoted with subscript K_3 (E5.16). Dividing throughout by the total $H^+{}_{(aq)}$ consumption rate leads to an analytical expression for x_{k_1}, involving the rate of $[Fe^{3+}]_{(aq)}$ generation. Rates of $[Fe^{3+}]_{(aq)}$ is on the scale of *nmol·dm^{-3}·hr^{-3}* with total $H^+{}_{(aq)}$ consumption rates on the order of *µmol·dm^{-3}·hr^{-1}*, hence x_{k_1} is estimated to be >99.7 *%* across all lixiviant media and repeats.

$$\left[\frac{d[H^+]}{dt}\right]_{tot} = \left[\frac{d[H^+]}{dt}\right]_{k_1} + \left[\frac{d[H^+]}{dt}\right]_{K_3} \qquad \text{E5.16}$$

$$1 = \frac{\left[\frac{d[H^+]}{dt}\right]_{k_1}}{\left[\frac{d[H^+]}{dt}\right]_{tot}} + \frac{\left[\frac{d[H^+]}{dt}\right]_{K_3}}{\left[\frac{d[H^+]}{dt}\right]_{tot}} \qquad \text{E5.17}$$

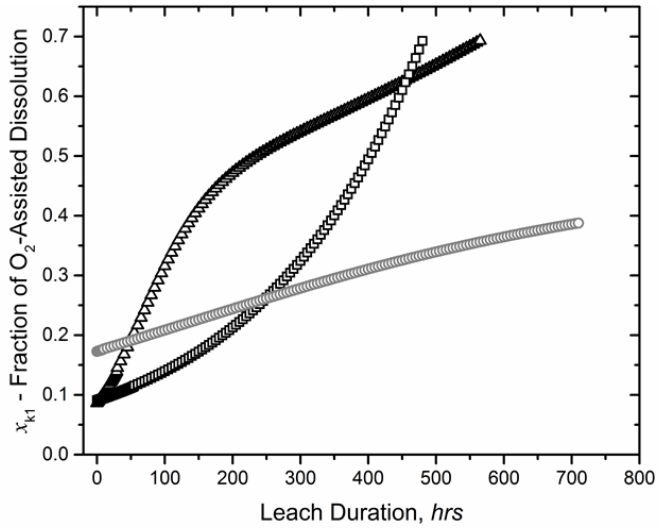
$$x_{k_1} = 1 - \frac{\left[\frac{d[H^+]}{dt}\right]_{K_3}}{\left[\frac{d[H^+]}{dt}\right]_{tot}} \quad \Leftrightarrow \quad x_{k_1} = 1 - \frac{-4 \cdot \left[\frac{d[Fe^{3+}]}{dt}\right]_{K_3}}{\left[\frac{d[H^+]}{dt}\right]_{tot}} \qquad \text{E5.18}$$

In order to verify the magnitude of these values, another x_{k_1} estimation method was prepared. Analysis of the rates suggested by E5.1 reveals that if $O_{2(aq)}$-assisted dissolution were the sole dissolution pathway with null side reactions, the time rate of $H^+{}_{(aq)}$ consumption would be 4-fold larger than the rate of $Cu^{2+}{}_{(aq)}$ recovery (E5.4). Since oxidation of $Fe^{3+}{}_{(aq)}$ from released $Fe^{2+}{}_{(aq)}$ also requires $H^+{}_{(aq)}$ consumption, an equation for calculation of x_{k_1} can be deduced (E5.20).

$$4 \cdot x_{k_1} \cdot \frac{d[Cu^{2+}]}{dt} = -\left[\frac{d[H^+]}{dt}\right]_{k_1} \qquad \text{E5.19}$$

$$x_{k_1} = -\frac{1}{4} \cdot \frac{d[H^+]}{d[Cu^{2+}]} \qquad \text{E5.20}$$

The first derivative of $Cu^{2+}_{(aq)}$ extraction curve fits (table 5.1) and linear rates of $[H^+]_{(aq)}$ variation were used to examine x_{k_1} as a function of time during ~1 *month* ambient $CuFeS_{2(s)}$ dissolution (figure 5.9). At low-moderate dissolution timescales and given that x_{k_2}<0.3 %, x_{k_1}~1 would be expected, corresponding to $H^+_{(aq)}$ consumption mainly via $CuFeS_{2(s)}$-dissolution (E5.1). Values close to this expectation are not achieved across the entire dissolution timescales, with initial x_{k_1} values in the range of 0.1-0.2. This finding indicates that 80-90 % of $H^+_{(aq)}$ consumed in the early stages of $CuFeS_{2(s)}$ dissolution is not used to recover $Cu^{2+}_{(aq)}$. This result is a new perspective of the initial stages of $CuFeS_{2(s)}$ dissolution and is discussed further in section 5.5, where $H^+_{(aq)}$ consumption is linked to significant reductions in surface oxygen content as determined by time-correlated SEM-EDX and ToF-SIMS $CuFeS_{2(s)}$ surface studies.



▲ Figure 5.9 - Plot of the fraction of $O_{2(aq)}$-assisted $CuFeS_{2(s)}$ dissolution (x_{k_1}) as a function of leach duration. (□ 450 *mmol·dm^{-3}* $[C_4Him][HSO_4]_{(aq)}$; △ 450 *mmol·dm^{-3}* $NH_4{\cdot}HSO_{4(aq)}$; ○ 75 *mmol·dm^{-3}* $H_2SO_{4(aq)}$)

Comparison of the plotted data for $H_2SO_{4(aq)}$ and $IL_{(aq)}$ indicates that the $IL_{(aq)}$ dissolution mechanism is very different to that of $H_2SO_{4(aq)}$ with a far higher degree of $CuFeS_{2(s)}$ dissolution occurring via E5.1. $NH_4{\cdot}HSO_{4(aq)}$ lixiviant solution is indicated to have a particularly high x_{k_1} in comparison to other media within 50-400 *hrs* leach duration, which may provide an explanation for increased $Cu^{2+}_{(aq)}$ recoveries in this medium. It is additionally noticeable that the gradient of $x_{k_1}(t)$ is approximately constant for $H_2SO_{4(aq)}$ which appears to correlate well with the greater linearity of raw metal extraction plots (figure 5.1A). Overall, this plot indicates that each solution utilises $H^+_{(aq)}$ in different ways, with strong suggestions of an additional proton consuming reaction at early dissolution timescales, which is currently unaccounted for in the literature. It is important to note that since maximum dissolution rates are observed on the order of <100 *hrs*, explanation of $H^+_{(aq)}$ consumption in the early stages of $CuFeS_{2(s)}$ dissolution may hold the key to

later onset of significant rate retardations and the cause of parabolic $Cu^{2+}_{(aq)}$. The implications of this finding will be discussed in suggestions for further work (chapter 7).

5.5 Surface Studies of Leached $CuFeS_{2(s)}$ Residues

Several researchers have highlighted the requirement to conduct examinations of inhomogeneous surfaces (*e.g.* $CuFeS_{2(s)}$) using two complementary, yet independent approaches. In this fashion, corroborative evidence provided by each spectroscopic source minimises any uncertainty over the results attained. ToF-SIMS (section 2.8.2) is a highly surface-sensitive technique (*~pm*), however significant disadvantages of this choice are instrument time limitations and low surface sampling rates. SEM/EDX (section 2.8.1) is chosen as convenient complementary surface analysis technique. Despite being many orders of magnitude less surface sensitive by comparison (~10 *μm*), SEM/EDX spectra are rapidly acquired in combination with high resolution imaging benefits, which may help to direct the user to interesting surface locations.

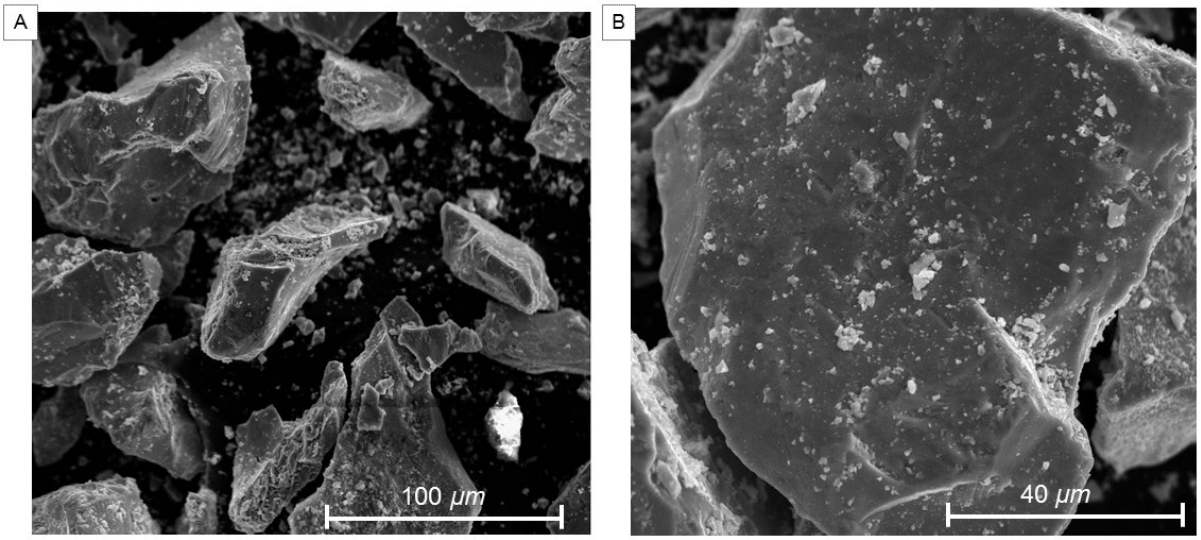
As introduced in section 1.2, surface oxidation of $CuFeS_{2(s)}$ in atmospheric/aqueous conditions or via direct chemical action results in complex and variable surface transformations. During leaching in conventional acid-$SO_4^{2-}{}_{(aq)}$ media these surface evolutions are reported by some to result in the development of kinetically hindering over-layers, composed of sulfurous species left behind by metal ion release. The surface studies presented aim to investigate the composition and structure of $CuFeS_{2(s)}$ surfaces before and after extended periods of leaching. An attempt will then be made to compare the surface composition evolved in $H_2SO_{4(aq)}$ solution to that produced by $IL_{(aq)}$ lixiviant activity.

As illustrated in figure 2.26, the custom design of the perforated sample holders allows for lixiviant-$CuFeS_{2(s)}$ contact, with protection from significant abrasion due to the motion of powdered $CuFeS_{2(s)}$ suspended in solution. The 12 massive $CuFeS_{2(s)}$ samples (~1.0×0.5x0.5 *cm*) placed in these holders and powdered $CuFeS_{2(s)}$ residues (initially $38 \leq x \leq 75$ *μm*) were subjected to surface analyses before experimentation, at time intervals during (24, 72, 240, 504 *hrs*) and after 720 *hrs* of ambient dissolution in 75 $mmol{\cdot}dm^{-3}$ $H_2SO_{4(aq)}$ / 450 $mmol{\cdot}dm^{-3}$ $IL_{(aq)}$. For reference, the corresponding physical and metal recovery data recorded during this experiment is shown as the plots marked with medium tone of colouration in figures 5.1-5.4 (*i.e.* ■, ■, ■). The $CuFeS_{2(s)}$ samples were correlated with the composition of the leach solution and the duration of the leach.

5.5.1 SEM / EDX

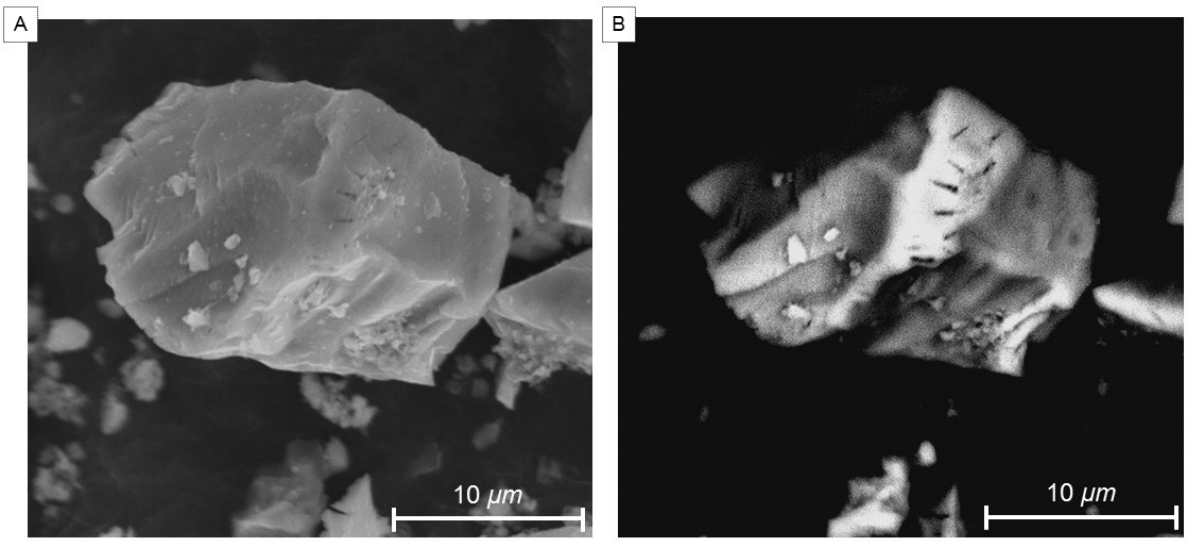
5.5.1.1 Approach to EDX Spectral Acquisition

SEM imaging and EDX analyses were conducted on 38 ≤ x ≤ 75 *μm* size fractioned $CuFeS_{2(s)}$ before and after 30 *days* (720 *hrs*) of ambient leaching in the tank leaching experiments discussed above. Carbon was omitted from element intensity spectra, as it cannot be quantified reliably due to the mounting of samples on $C_{(s)}$ adhesive tape. Figure 5.10 shows typical images of the powder prior to insertion into the leaching vessel, where many small particles can be seen to adhere to the surface of larger particles. Some particles were found to exceed quoted size fraction range, since the upper-level sieve mesh can pass any particle with a maximum cross-sectional diameter of <75 *μm* across the thinnest dimension of the particle.



▲ Figure 5.10 - High resolution SEM images of unleached 38 ≤ x ≤ 75 *μm* size fractioned $CuFeS_{2(s)}$ mounted on conductive $C_{(s)}$ adhesive tape with image sizes of (A) 250x250 *μm* and (B) 100x100 *μm*.

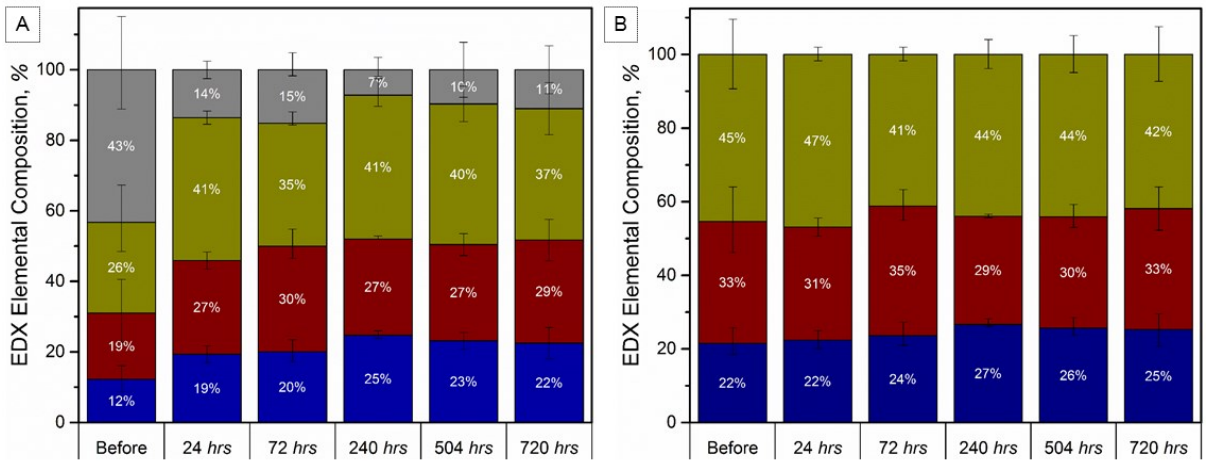
At all EDX sampling points for massive and powdered $CuFeS_{2(s)}$, surface compositions of relatively large and flat powdered $CuFeS_{2(s)}$ surfaces were examined to obtain (20+) surface compositions averaged over large areas. Secondly, topographical secondary electron images (figure 5.11A) were compared to backscattered electron images (figure 5.11B), the latter of which are sensitive to varying crystallographic orientation. Comparison of these SEM modes allowed for further spectra to be acquired at higher magnification, on an *ad hoc* basis, guided by apparent interesting features. Analogous sampling of the massive $CuFeS_{2(s)}$ surfaces was conducted at each sampled leach duration (24, 72, 240, 504 *hrs*).



▲ Figure 5.11 - 30 μm^2 SEM images of a milled $CuFeS_{2(s)}$ particle following 720 *hrs* ambient dissolution in 450 $mmol \cdot dm^{-3}$ $[C_4Him][HSO_4]_{(aq)}$. (A) Primary backscattered image (B) Secondary electron image.

5.5.1.2 EDX Data: Low Magnification

Following the above approach, a large quantity of spectra were obtained for all massive $CuFeS_{2(s)}$ samples, using relatively low-magnification (*ca.* x100-400). Data presented in figure 5.12 shows the SEM/EDX Cu-Fe-S-O surface stoichiometry after 0, 24, 72, 240, 504 and 720 *hr* leach durations. It is important to note that SEM/EDX has a surface depth sensitivity of ~10 *μm* (figure 2.27) as discussed further later. Unleached $CuFeS_{2(s)}$ surfaces appear to feature high oxide compositions (25-70 %), with even higher amounts found with more surface sensitive ToF-SIMS data (figure 5.16). Contact of $CuFeS_{2(s)}$ with all lixiviant media results in an average of ~73 % reduction in surface oxide, with no influence of lixiviant identity or leach duration within experimental error. As such, oxygen contributions were removed from the analysis in order to isolate the stoichiometry of Cu, Fe and S at the surface for later comparison to ToF-SIMS data (figure 5.12B). Unleached and all leached $CuFeS_{2(s)}$ surfaces show similar stoichiometries within experimental uncertainty, with good agreement with the expected elemental stoichiometry $CuFeS_{2(s)}$ over the relatively large ~0-10 *μm* probe depths. Hence, it can be concluded that SEM/EDX examination over large $CuFeS_{2(s)}$ surface areas is unable to distinguish between $CuFeS_{2(s)}$ surfaces produced by dissolution in the studied $IL_{(aq)}$ and $H_2SO_{4(aq)}$ media. Data obtained at higher magnification is discussed below.

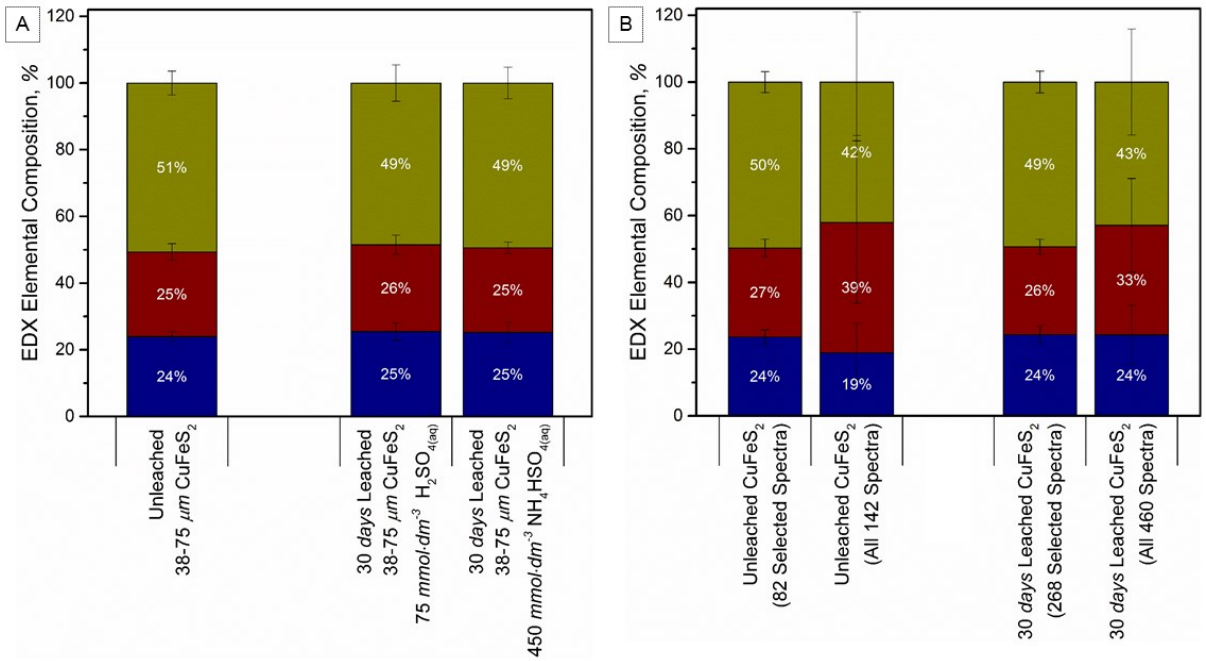


▲ Figure 5.12 - (A) EDX elemental surface compositions obtained at low magnification for large areas of massive $CuFeS_{2(s)}$, averaged over all samples leached in 450 $mmol \cdot dm^{-3}$ $IL_{(aq)}$ and 75 $mmol \cdot dm^{-3}$ $H_2SO_{4(aq)}$ with and (B) without inclusion of surface oxide contributions (Cu ■; Fe ■; S ■; O ■).

5.5.1.3 EDX Data: Moderate-High Magnification

Attention will now be turned to the EDX examination of leached $CuFeS_{2(s)}$ residues ($38 \leq x \leq 75$ *μm*) and massive $CuFeS_{2(s)}$ samples under moderate-high magnifications (>400 fold). It should be briefly mentioned that results for powdered $CuFeS_{2(s)}$ are analogous to those observed at lower magnifications (figure 5.13A). However, EDX data for extended $CuFeS_{2(s)}$ surfaces at higher magnification shows clear variation in the average composition, but also in some cases increased experimental error. Since there is little to discuss regarding the average composition when surfaces exhibit clear inhomogeneity, the source of inhomogeneity was further explored.

EDX spectra obtained at high magnification before and after 720 *hrs* leaching were split into two further categories as explained below. Please note that since there was not sufficient evidence to suggest distinction between the $CuFeS_{2(s)}$ surfaces produced by $IL_{(aq)}/H_2SO_{4(aq)}$ leaching, all spectra obtained following 720 *hrs* leach duration were analysed as a single data of all spectra in order to examine any experimental indications available from a global overview of acid-$SO_4^{2-}{}_{(aq)}$ leaching at *p*H~1.2. Prior to leaching, 57.8 *%* of recorded spectra indicate the expected $CuFeS_{2(s)}$ stoichiometry with previously observed low experimental error, with 58.0 *%* doing so after 30 *days* of ambient $CuFeS_{2(s)}$ dissolution. Spectra exhibiting the nominal $CuFeS_{2(s)}$ stoichiometry (±5 *%* for each element) were grouped into a single column ('selected'; figure 5.13B). Comparing these 'selected' spectra to the complete dataset at high magnification shows that the source of stoichiometric variability lies in the remaining ~42 *%* of spectra.

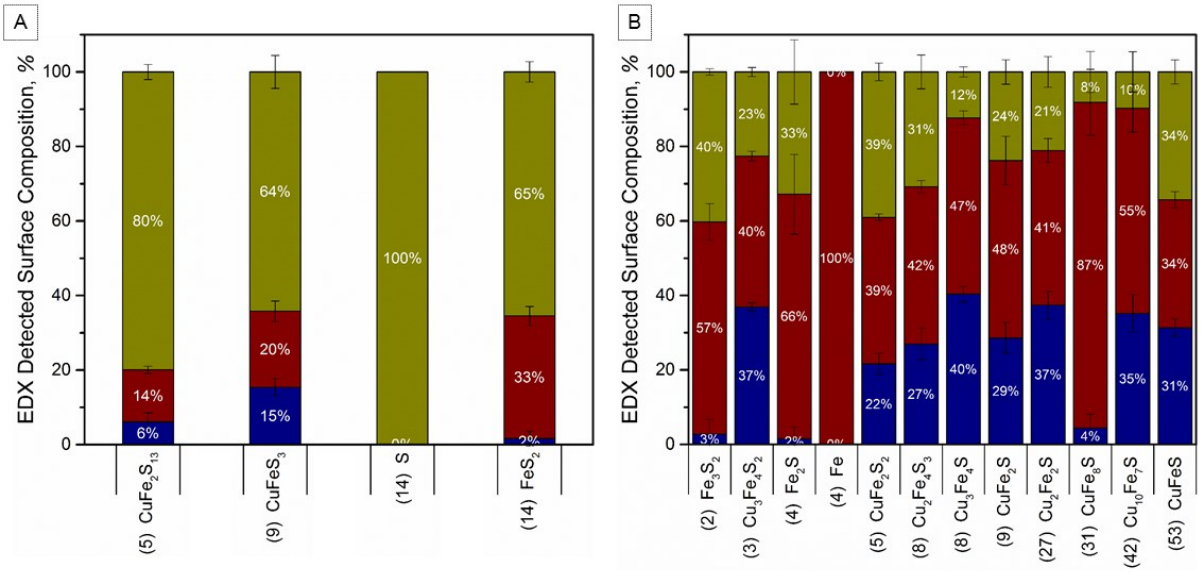


▲ Figure 5.13 - High magnification EDX elemental surface compositions before and after the 30 *day* leaching of (A) 38-75 *μm* $CuFeS_{2(s)}$ powder and (B) 1.0x0.5x0.5 *cm* $CuFeS_{2(s)}$ samples in $IL_{(aq)}/H_2SO_{4(aq)}$ media (Cu ■; Fe ■; S ■; O ■).

The ~42 % spectra displaying different surface stoichiometries were further grouped, revealing high numbers of spectra with similar stoichiometries (figure 5.14). It is noteworthy that, since 'abnormal' features were pursued in high magnification studies, no comment can be made regarding the relative proportion of the $CuFeS_{2(s)}$ surface which displays deviating non-stoichiometric composition. However, since low magnification EDX suggests the expected $CuFeS_{2(s)}$ stoichiometry with relatively low error, this fraction much be very low and overwhelmed by high rates of X-ray photoemission for large area EDX examinations (section 5.5.1.2). In view of the reported role of sulfur species in acid-$SO_4^{2-}{}_{(aq)}$ $CuFeS_{2(s)}$ dissolution, indicated non-$CuFeS_{2(s)}$ surface stoichiometries recorded after 720 *hrs* leaching have been further categorised into moieties with elevated sulfur content and diminished sulfur content in figure 5.14A and B respectively. In each plot, suggested moieties are placed in ascending order by the number of spectra indicating the presence of the phase.

Evidence for elevated surface sulfur levels after leaching in $IL_{(aq)}/H_2SO_{4(aq)}$ was relatively scarce in comparison to low S-phases. Unexpectedly, elevated S concentrations were only apparent in 9.1 % of all recorded spectra. However, four phases were identified, which were independent from the others in terms of error magnitudes. Importantly, a 100 % sulfur phase was identified as a surface phase following both $H_2SO_{4(aq)}$ and $IL_{(aq)}$ lixiviant activity but with low occurrence rate (14 spectra). FeS_2 was also indicated by an equivalent number of surface spectra. Figure 5.14B shows the relatively large quantity of non-$CuFeS_{2(s)}$ surface stoichiometries with diminished-S content. The high frequency of deminished-S phases (82.3 %) in comparison to elevated-S

phases (17.7 %) is somewhat surprising. This observation raises concerns that loss of volatile sulfur compounds[15-17] may occur under the UHV conditions of the microscope sample chamber, which has been reported at room temperature and is accelerated at low pressures. However, these concerns are somewhat allayed by the infrequent observation of 100 % sulfur phases. It will later be found that the outer-surface of $CuFeS_{2(s)}$ does in fact contain significant S (via ToF-SIMS). The fact that SEM/EDX appears not to be able to detect sulfur at equivalent leach durations is a significant drawback to the technique and is discussed further below.



▲ Figure 5.14 - EDX elemental composition of non-stoichiometric moieties presented at the surface of massive $CuFeS_{2(s)}$ leached for 720 *hrs* in $IL_{(aq)}/H_2SO_{4(aq)}$, with number of corroborating spectra given in brackets. (A) Surface phases with elevated sulfur %. (B) Surface phases with diminished sulfur %. (Cu ■; Fe ■; S ■; O ■)

Diminished-S phases are numerous and are likely a consequence of complex surface reconstructions; perhaps as a result of leaching, although some may also be due to differing mineral phases which are intergrown into the $CuFeS_{2(s)}$ structure and possibly revealed by the action of leaching. Interestingly, many of these spectra were recorded in regions bearing a low contrast darkened appearance on the microscope display. This darkening was not related to $CuFeS_{2s)}$ surface topography and was not observed in $CuFeS_{2(s)}$ samples pre-leaching. Additionally, upon collection of EDX spectra in such sulfur depleted regions, X-ray photoemission rates were severely restricted (>10^1), where the origin of this effect remains unexplained when surrounded by large expanses of high-contrast $CuFeS_{2(s)}$ surface. It is possible that these 'darkened' low-sulfur features may be linked to similar findings in ToF-SIMS studies (section 5.5.2), however these effects require further study. A summary of this section is provided later (section 5.5.3.2), in conjunction with ToF-SIMS data presented in section 5.5.2.

5.5.2 ToF-SIMS

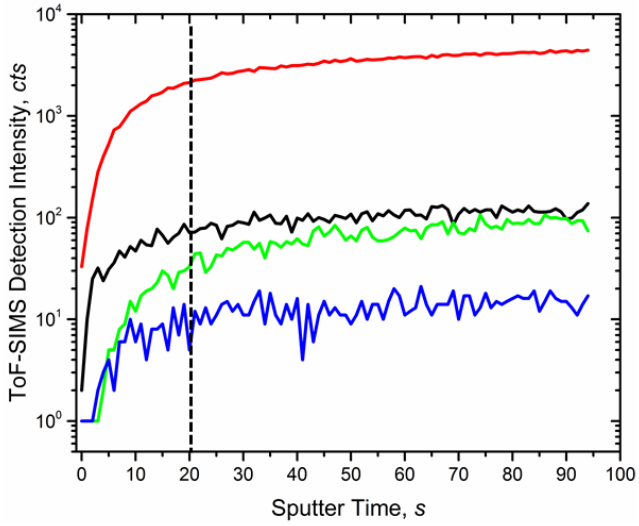
5.5.2.1 Details of Procedure

The objectives of SIMS experiments were two fold - namely, to investigate potential differences in the outer surface layers of $CuFeS_{2(s)}$ with improved surface sensitivity, and to investigate the depth of surface layers overlaying the homogeneous bulk composition, as indicated (*cf.* 10 *μm*; SEM/EDX). Samples were washed several times in still distilled water, before drying with low-pressure $N_{2(g)}$. Minimal contact between the sample and any manipulation tools was maintained throughout. Dynamic SIMS has been performed with the use of a rastered Bi^+ ion beam (25 *keV*; 1 *pA*), with depth profiles obtained from point-sputtering of $CuFeS_{2(s)}$ surface using a Cs^+ ion beam (25 *keV*). For the purposes of this thesis and to simplify data handling/presentation, only the negative ion spectrum is discussed. As discussed in section 1.2, the prevalent ionic state of bulk $CuFeS_{2(s)}$ is $Cu^+Fe^{3+}(S^{2-})_2$. Although the negative ion spectrum may misrepresent surface metal content, it is deemed more insightful to examine the negative ion fragment spectrum since it would include O and S species - where each has been proposed as responsible for kinetic hindrance of $CuFeS_{2(s)}$ dissolution in previous studies, as discussed earlier in section 1.8.

Interfacial depth before reaching bulk composition is determined using static-SIMS and plots of ionic fragment mass detection intensity ($cts \cdot s^{-1}$) as a function of ion beam sputter time. An exemplar plot is shown in figure 5.15, where 20 *s* sputter time (SpT) is required to sputter away sufficient surface layers to reach a stable bulk composition. Conversion of sputter time to physical depth profiles is strongly material dependent and thus non-trivial.[18-20] It may be achieved, in principle, by utilising differential sputter rates to reconstruct accurate 3D depth profiles, but this is not done here. Therefore, in absence of the appropriate conversion relation, interfacial depths will mainly be discussed with reference to sputter timescales, since approximately equivalent depth penetration would be expected for all massive $CuFeS_{2(s)}$ samples.

However, a crude relationship between sputter time and depth penetration has been calculated as follows. Massive $CuFeS_{2(s)}$ samples were selected and used as received possessing an atmospherically oxidised surface. As discussed in section 1.2.4, other researchers have reported ~1-3 *nm* depths of oxidised material at the interface,[21] which overlays bulk $CuFeS_{2(s)}$ composition - 2 *nm* depths will be used for estimation purposes. During this study a typical interface depth corresponds to an average sputter time of 5 *s* (between ~ 4-6 *s*), with 5 *s* selected for calculation purposes. This results in a sputtering rate of roughly 1.5 $Å \cdot s^{-1}$. Using the $CuFeS_{2(s)}$ unit cell dimensions as a reference (figure 1.2) this appears a reasonable value, since a single bulk monolayer has an approximate 1 *Å* thickness and ToF-SIMS is generally applied to examine the first few surface monolayers. However, this value should be treated with

appropriate caution and should be used merely as a rough approximation for the reference of the reader.



▲ Figure 5.15 - Selected ion fragment intensity signals (static ToF-SIMS) as a function of Cs^+ ion sputter time for atmospherically oxidised yet unleached $CuFeS_{2(s)}$ (S^- ●; O^- ●; CuS^- ●; FeS^- ●).

5.5.2.2 ToF-SIMS Data: Unleached $CuFeS_{2(s)}$

As discussed in section 1.2.4, the surface chemistry of unleached $CuFeS_{2(s)}$ is extremely complex, exhibiting a wide range of oxidation products and reconstructed surface phases. ToF-SIMS interrogation of unleached massive $CuFeS_{2(s)}$ reveals high oxide content within the first few surface monolayers, where ~75 *%* of sputtered negative ion fragments are from oxygen-derived moieties (*cf.* ~43 *%*; figure 5.12). As illustrated in the leftmost columns of each panel of figure 5.16, these high oxide levels extend over large $CuFeS_{2(s)}$ penetration depths, as described by (high) static SIMS sputter times of ~20 *s* (figure 5.15).

The key moieties found in relative abundance throughout all dynamic SIMS spectra were: C^-, O^-, OH^-, O^{2-}, Cu^-, CuS^-, CuH^-, CuO^-, $CuOH^-$. Fe^-, FeS^-, FeH^-, FeO^-, FeO^{2-}, S^-, SO^- and SOH^-. Unless specifically discussed, relative surface compositions of each of the above moieties can be considered consistent with the unleached massive $CuFeS_{2(s)}$ sample. ToF-SIMS data is generally presented as summed contributions from all Cu, Fe, S, O and C negative ionic moieties for reasons of clarity of presentation and comparability to SEM/EDX plots (section 5.5.1).

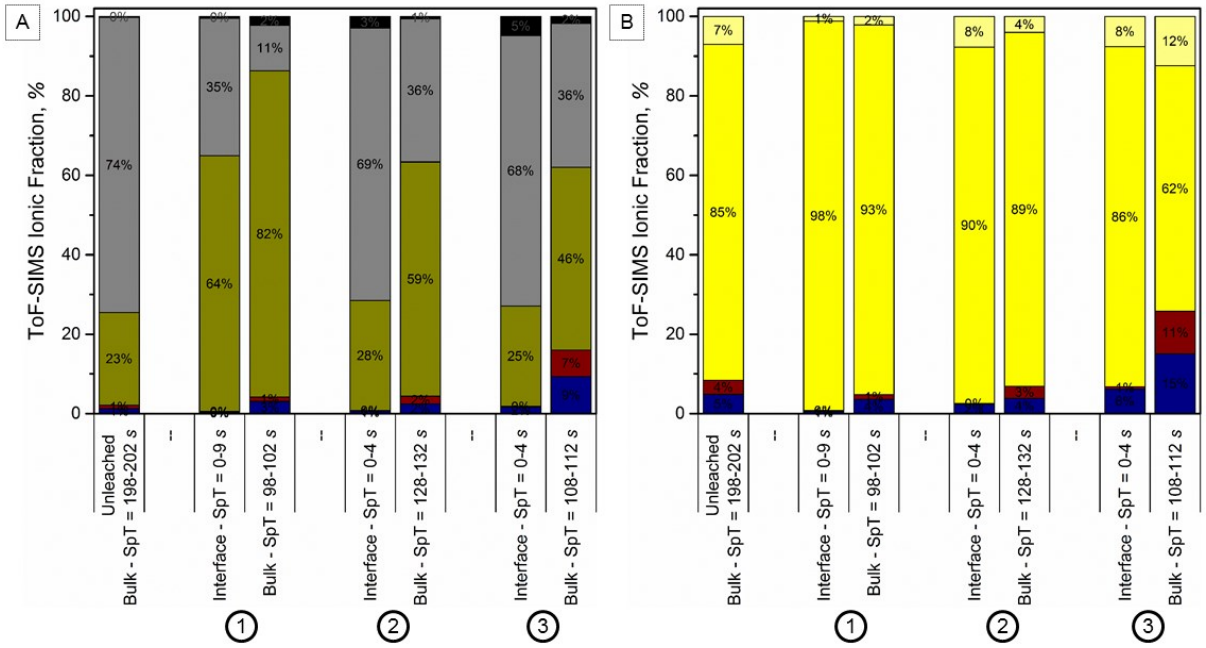
5.5.2.3 ToF-SIMS Data: 240 *hrs* Leached $CuFeS_{2(s)}$

Figure 5.16 features ToF-SIMS data recorded following 240 *hrs* leaching in $NH_4{\cdot}HSO_{4(aq)}$, $[C_4Him][HSO_4]_{(aq)}$ and $H_2SO_{4(aq)}$ compared to representative data for unleached $CuFeS_{2(s)}$. As previously observed during EDX analysis (figure 5.12), detected oxygen levels at the $CuFeS_{2(s)}$ surface significantly decrease due to lixiviant activity. Dynamic SIMS revealed a change in the

relative contributions of each element with increasing sputter times, revealing a distinct outer layer probed by sputter times on the order of 0-6 *s* ("interface") before a second homogeneous layer was observed at higher sputter times ("bulk" - figure 5.16). Where observed metal fractions are sufficiently high, surfaces present with [Cu]:[Fe] > 1.4. This observation correlates well with similar observed [Fe]:[Cu] extraction ratios discussed above for figures 5.1-5.4A. Further information regarding specific [Fe]:[Cu] extraction ratios for different ILs is included in section 6.2.

Inspecting the contribution to Cu-Fe-S stoichiometry in the first few monolayers allows for plots, which are comparable to those for SEM/EDX work, to be produced (figure 5.16B). The overall sulfur content within the first few monolayers is quite high (75-98 *%*), compared to an average of 92 *%* S for unleached $CuFeS_{2(s)}$ at large sputter times (198-202 *s*). Due to the high percentage of S-species (■; figure 5.16A), the sulfur data is further split into S^- (■) and the remaining S-M/S-O contribution (■; figure 5.16B).

Since ToF-SIMS studies were completed after SEM/EDX studies without further lixiviant solution contact, the high S-content at the interface confirms that EDX analysis does not have sufficient surface sensitivity to accurately represent the outermost surface of leached $CuFeS_{2(s)}$ residues. When the S species are further sub-divided, S^- is shown to represent >90 *%* of surface bound S species. However, since the magnitudes of O are also high yet the relative levels of SO^- are low this does question the mode/nature of oxygen- and sulfur- binding at the surface, which may be through linkages which are only apparent from the positive ion spectrum.



▲ Figure 5.16 - Dynamic ToF-SIMS relative surface elemental composition at the indicated sputter times (SpT) for massive $CuFeS_{2(s)}$ samples leached for 240 *hrs* in $IL_{(aq)}/H_2SO_{4(aq)}$. Panel A includes contributions from carbon and oxygen. Panel B excludes carbon and oxygen and divides the high total S-derived fraction into the ionic fraction for S^- and remaining S_{tot} contribution (S_{tot} - S^-). (Cu_{tot}; Fe_{tot}; S_{tot}; O_{tot}; C_{tot}; S^-; [S_{tot} - S^-]) ([1] 450 *mmol·dm*$^{-3}$ $NH_4{\cdot}HSO_{4(aq)}$; [2] 450 *mmol·dm*$^{-3}$ $[C_4Him][HSO_4]_{(aq)}$; [3] 75 *mmol·dm*$^{-3}$ $H_2SO_{4(aq)}$)

In the case of $[C_4Him][HSO_4]_{(aq)}$ leaching, a thin interface (SpT = 4-5 *s*) was uncovered where fragment intensity profiles beyond this time show good agreement with the outer layers of unleached $CuFeS_{2(s)}$. The interface was found to be rich in contributions from O^-, CuH^-, and S^- moieties, in comparison to unleached $CuFeS_{2(s)}$, with longer sputter times showing growth of FeS^- and CuS^- signals and thus indicating bulk $CuFeS_{2(s)}$ character. Several further $[C_4Hiim][HSO_4]_{(aq)}$-leached $CuFeS_{2(s)}$ surfaces were found to present a distinct initial layer, comprised principally of SO^-, OH^- and S^-, but with small enhancements in CuH^- and CuS^-.

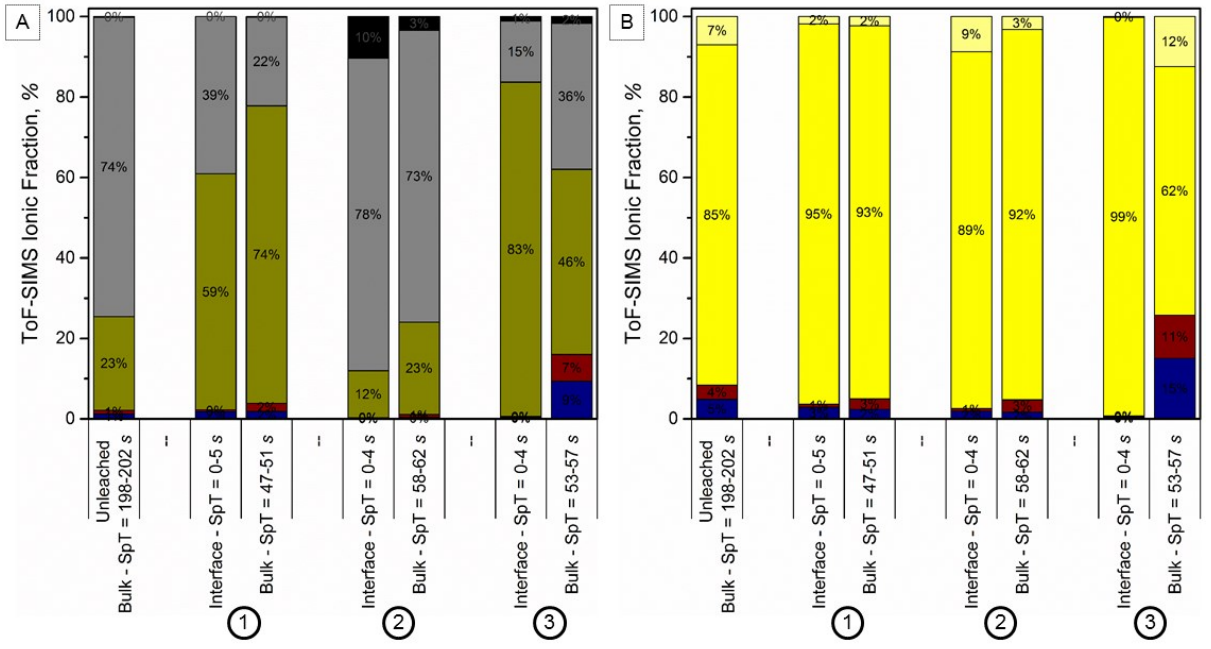
Following 240 *hrs* leaching in 450 *mmol·dm*$^{-3}$ $NH_4{\cdot}HSO_{4(aq)}$, a significantly thicker interface (SpT = 0-11 *s*) was indicated in static SIMS mode. Dynamic SIMS suggests such interfaces are once again dominated by S^- OH^- and O^{n-}, while Fe^-, FeH^- and FeO^- are depleted in comparison to unleached references. Interestingly, oxygen levels in the sampled surfaces are found to be 50-65 % lower than for alternative media - although this indication is stated only tentatively in view of the observed variability of surface oxides levels across all data. S^- once again dominates the total ionic fraction for all S-species, however there is a 100-200 % increase in other ionic S-fragments, which may be specific to the surface produced by $CuFeS_{2(s)}$ dissolution in $[C_4Him][HSO_4]_{(aq)}$.

In contrast, samples leached in $H_2SO_{4(aq)}$ presented 2-3-fold higher metal composition in both the outer and inner surface layers (figure 5.16). Where found, the outer surface layer is again low

depth (SpT < 3 *s*) and comparatively rich in O and S-related fragments. Beyond this outer layer there was a large increase in M-S^- ionic fragments, suggesting that after 240 *hrs* leaching in 75 *mmol·dm*$^{-3}$ $H_2SO_{4(aq)}$ bulk compositions lie significantly closer to the surface. This latter observation is discussed further below.

5.5.2.4 ToF-SIMS Data: 720 *hrs* Leached $CuFeS_{2(s)}$

The corresponding data for 720 *hrs* $CuFeS_{2(s)}$ dissolution is displayed in figure 5.17. ToF-SIMS data generally exhibits similar trends to data for 240 *hrs*, requiring little additional discussion. Interfaces are once again shown to be dominated by O and S oxidation products. There are again equivalently large decreases in O-contributions to surfaces following leaching. Additionally, overlaying oxidised layers contain higher oxide levels compared to bulk, as expected. Sputter times of ~6-11 *s* prove adequate to break through the distinct outer oxidised surface of $IL_{(aq)}$-leached $CuFeS_{2(s)}$, with smaller times required in the case of $H_2SO_{4(aq)}$ yet once again give way to a phase which is dominated by O and S - especially in the case of $IL_{(aq)}$-leached samples, as mentioned above. In the absence of any further compelling evidence, the conclusions of SEM/EDX and ToF-SIMS surface analyses are summarised in section 5-360.



▲ Figure 5.17 - Dynamic ToF-SIMS relative surface elemental composition at the indicated sputter times (SpT) for massive $CuFeS_{2(s)}$ samples leached for 720 *hrs* in $IL_{(aq)}/H_2SO_{4(aq)}$. Panel A includes contributions from carbon and oxygen. Panel B excludes carbon and oxygen and divides the high total S-derived fraction into the ionic fraction for S^- and remaining S_{tot} contribution (S_{tot} - S^-). (■ Cu_{tot}; ■ Fe_{tot}; ■ S_{tot}; ■ O_{tot}; ■ C_{tot}; ■ S^-; ■ [S_{tot} - S^-]) ([1] 450 *mmol·dm*$^{-3}$ $NH_4{\cdot}HSO_{4(aq)}$; [2] 450 *mmol·dm*$^{-3}$ $[C_4Him][HSO_4]_{(aq)}$; [3] 75 *mmol·dm*$^{-3}$ $H_2SO_{4(aq)}$)

5.5.3 Surface Analysis: Conclusions

5.5.3.1 SEM/EDX Conclusions

Via SEM/EDX and ToF-SIMS studies, oxide levels are found to be high for unleached $CuFeS_{2(s)}$ appearing to reduce to a relatively consistent level of 7-15 % following contact with lixiviant solutions. Large surface area EDX studies are unsuitable to highlight surface variations, where the surface composition is shown to vary significantly over small distances. No evidence of the impact of leaching was observed for large surface area EDX studies of powdered or massive $CuFeS_{2(s)}$ samples, with the former likely to be as a result of far greater exposure of mechanical abrasion and the effects of solution agitation.

Via SEM/EDX and ToF-SIMS studies it has been determined that surface oxygen levels are reduced considerably in <24 *hrs*. Since unleached $CuFeS_{2(s)}$ is atmospherically oxidised (section 1.2.2), surface metal-oxides are formed which are rapidly solubilised in the initial stages of dissolution (section 6.4). Excluding the oxide fraction, SEM/EDX indicates equivalent $CuFeS_{2(s)}$ bulk compositions over probe depths of 0-10 *μm* for all solutions and leach durations, when examining large $CuFeS_{2(s)}$ areas.

At higher magnifications, ~40 % of recorded spectra indicated stoichiometry that is different from $CuFeS_{2(s)}$. Many potentially interesting, diminished-S and elevated-S phases have been identified on leached $CuFeS_{2(s)}$ solutions. However, since $CuFeS_{2(s)}$ ore is intergrown with related metal sulfides it is unclear and difficult to judge the significance of these phases. Although they are undoubtedly signs of significant surface inhomogeneity and are frequently observed, their low relative fraction in $CuFeS_{2(s)}$ surfaces indicates that they may be a result symptomatic of lixiviant activity.

However, the most important conclusion for SEM/EDX studies is that the general approach is not sufficiently surface sensitive for examination of any kinetically hindering phase. This conclusion is verified by low apparent abundance of sulfur-rich surface moieties via SEM/EDX, followed by detection of oxide and sulfur dominated surfaces on the same samples immediately after, via ToF-SIMS. Among the different stoichiometric phases discussed above, S-rich non-stoichiometric phases are found to be ~80 % less prevalent than S-depleted areas.

It appears that sulfur bound in bulk $CuFeS_{2(s)}$ is typically detected via SEM/EDX. Hence, the reasons for a lack of sulfur detection in oxidised surface phases and moieties with irregular stoichiometries is unclear and further work is required. This finding may have very important implications for the reliability of SEM/EDX when applied to $CuFeS_{2(s)}$ dissolution studies. For example, in Klauber's conceptual four-stage model for conventional acidic $CuFeS_{2(s)}$ dissolution (figure 1.13) attribution of an S^0 peeling phase was precluded by the detection of no sulfur via

SEM/EDX. The findings confirm that SEM-EDX is not sufficiently surface sensitive to detect such factors in the conditions studied.

5.5.3.2 ToF-SIMS Conclusions

As a technique, ToF-SIMS often suffers from a poor ability to sample surfaces in a representative manner due to instrument time limitations. Thus, with those restrictions in mind, one cannot be certain of how representative the spectroscopic data is with respect to the surface chemistry of the samples. Additional concerns arise from the significant degree of inhomogeneity that is indicated via SEM/EDX. Further studies are required to combine both positive and negative ion data, in an effort to obtain a more comprehensive understanding of the $CuFeS_{2(s)}$ surface composition and chemistry.

Additionally, it is challenging to process the high volumes of data produced from a single site, including consideration of both the positive and negative ion data and to link them together - which is necessary for a complete picture of the dominant surface chemistry. Due to time constraints this procedure has not been attempted and conclusions are appropriately tentative.

For example, negative ion fragment data contains information about distinct interfacial over-layers dominated by sulfur species and oxides. The layers contain the products of atmospheric oxidation for unleached $CuFeS_{2(s)}$ samples and the dissolution products for samples leached in $IL_{(aq)}/H_2SO_{4(aq)}$. As mentioned above, there is a considerable decrease in oxide species during the initial stages of $CuFeS_{2(s)}$ dissolution, which appear to occur over similar equivalent initial dissolution times and correlate with significant H^+-consumption. As discussed in section 5.4.6, these findings cannot be reconciled easily with current understanding of the initial stages of dissolution.

As discussed further in section 6.4, it is proposed that $H^+_{(aq)}$ consumption during leaching and decreases in surface-bound oxides are a manifestation of the initial stages of $CuFeS_{2(s)}$ dissolution that have yet to be characterised in full. Since $CuFeS_{2(s)}$ dissolution during this initial phase occurs at high rates, more attention should be focused on understanding the underlying process(es) that link(s) these two observations. Protons are good oxygen acceptor species - therefore, it is further proposed that these observed parameter variations may be explained by a process involving $H^+_{(aq)}$-assisted solubilisation of surface metal-oxides from (atmospherically oxidised) $CuFeS_{2(s)}$ surfaces. Metal-oxides are known to dominate atmospherically oxidised surfaces (section 1.2), where considerable metal-oxide solubility in acidic solution is likely to translate to enhanced initial metal extraction rates and may also account for unexplained $H^+_{(aq)}$ consumption (section 6.4).

From ToF-SIMS data, it can be concluded that thin oxidation-product-rich interfaces - dominated by S and O moieties - are produced on $CuFeS_{2(s)}$ that has been leached in $H_2SO_{4(aq)}$ as well as $IL_{(aq)}$ solutions. This product layer requires sputter times on the order of 4-11 *s* to be removed, in order to reveal a phase that resembles unleached $CuFeS_{2(s)}$. However, from the perspective of surface analysis, one key finding is that $CuFeS_{2(s)}$ samples leached in $IL_{(aq)}$ (SpT = 6-11 *s*) appear to form up to 3-fold thicker oxidised surface layers than for $H_2SO_{4(aq)}$ (SpT = 3-6 *s*). Thicker interfacial layers for $IL_{(aq)}$ could be indicative of a greater extent of metal extraction which has been confirmed for $NH_4{\cdot}HSO_{4(aq)}$ (figure 5.4) in comparison to $H_2SO_{4(aq)}$ (figure 5.1). In accordance with this reasoning, bulk metal compositions are shown to be present at smaller penetration depths in the case of $H_2SO_{4(aq)}$ when compared to $IL_{(aq)}$. This finding appears to indicate that there may be a rate-limiting hindrance to $H_2SO_{4(aq)}$-$CuFeS_{2(s)}$ leaching, which is less apparent for some $IL_{(aq)}$ lixiviant solutions. Equally importantly, $IL_{(aq)}$ and $H_2SO_{4(aq)}$ lixiviant solutions seem to form interfaces with surface chemistries which are distinguishable via ToF-SIMS for ambient leaching (see above for details), which again points to different leaching mechanisms in the two media.

Metal extraction results shown in section 5.3 indicate that [Fe]:[Cu] is often in the range 1-1.4. The offset between extracted levels of each metal is maintained across long leach durations (*e.g.* ●○; ~50-700 *hrs*; figure 5.2A), confirming that the offset is caused by preferential Fe-leaching in the initial stages of dissolution (<50 *hrs*; figure 5.2A) - an effect that has also been reported previously.[4] On the basis of ToF-SIMS data, it has been demonstrated that $CuFeS_{2(s)}$ surfaces display a complementary surface stoichiometry of up to 1.4. This stoichiometric imbalance in surface-bound metals for leached $CuFeS_{2(s)}$ ([Cu]:[Fe] > 1) accounts for both surface metal ratios in unleached $CuFeS_{2(s)}$ ([Cu]:[Fe] = 1) and preferential initial metal extraction rates ([Fe]:[Cu] > 1). It is proposed that since Fe content of unleached $CuFeS_{2(s)}$ surfaces is dominated by Fe-oxides[21] (*e.g.* Fe(III)O-OH; Fe_2O_3; section 1.2.2), more rapid solubilisation of these species in the early stage of leaching is responsible for initial preferential Fe extraction.

These indications may help explain differential $IL_{(aq)}$/$H_2SO_{4(aq)}$ leaching rates at equivalent *p*H, which are explored further in chapter 6 and are in agreement with existing knowledge that identity of the acid can cause formation of different leached surfaces with distinct properties - *e.g.* the enhanced porosity of sulfurous deposits at the surface of $CuFeS_{2(s)}$ leached in $HCl_{(aq)}$ lixiviant solution compared with.$H_2SO_{4(aq)}$ (sections 1.6.6 and 1.8.2). The above surface studies are however unable to provide further insight into the apparent kinetic hindrance of the leaching process.

As discussed in section 1.8, much research in the field of $CuFeS_{2(s)}$ dissolution has focussed on the role of sulfur and its derivatives at the surface. However, little to no attention has been paid to oxygen levels and the rationalisation of binding to sulfur rich phases. Oxide levels were shown

to be reduced in a concerted process in the early stage of leaching, yet still exists in high proportion, meaning that oxygen containing species which remain at the surface could also be strong kinetic hindrance candidates. This key indication is used further in section 6.4 in order to propose a mechanism for $IL_{(aq)}$-based $CuFeS_{2(s)}$ leaching, where parabolic rates are hypothesised to be the ramification of this effect. Differing interface lengths have been suggested to form for $CuFeS_{2(s)}$ dissolution in $IL_{(aq)}/H_2SO_{4(aq)}$, each comprised of >90 *%* S and O moieties. There is evidence that the oxide layer extends to far greater depths for $IL_{(aq)}$-based $CuFeS_{2(s)}$ dissolution and correspondingly higher metal contents are held near to the surface for $H_2SO_{4(aq)}$-based leaching.

5.6 Conclusions

400 *mL*-scale tank leaching experiments have been used to assess whether (or not) the best performing $IL_{(aq)}$ systems can enhance ambient $CuFeS_{2(s)}$ dissolution, with respect to conventional acid-$SO_4^{2-}{}_{(aq)}$ of equal *p*H. Operating in up-scaled conditions, with satisfactory thermal regulation at ~298 *K* and equally handled 30 *g* batches of powdered $CuFeS_{2(s)}$ - providing good conditions for direct comparison of ambient $IL_{(aq)}/H_2SO_{4(aq)}$ lixiviant activity.

Key unprocessed metal extraction data (figure 5.4A), reveals that some ILs can indeed enhance metal recoveries, with respect to equi-acidic $H_2SO_{4(aq)}$. Significant enhancements in $Cu^{2+}{}_{(aq)}$ recoveries (*e.g.* 46 *%*, 135 *%*) were achieved for independent repeats of ~1 *month* leach durations in 450 $mmol{\cdot}dm^{-3}$ $NH_4{\cdot}HSO_{4(aq)}$, with respect to $H_2SO_{4(aq)}$. Recovery of up to 40 *%* $Cu^{2+}{}_{(aq)}$ in $IL_{(aq)}$ is a high value when considering leaches were conducted for 30 *days*, using ambient conditions, without application of corrections for ~90 *%* purity $CuFeS_{2(s)}$, E_h optimisation, unprocessed $CuFeS_{2(s)}$ ore and in absence of chemical oxidant assistance. Quoting from the literature regarding $CuFeS_{2(s)}$ hydrometallurgy, "….[even at elevated temperatures, present lixiviant systems provide] substantially incomplete dissolution after 80 days leaching":[5, 22] The most effective $IL_{(aq)}$ lixiviant systems trialled in this work provide ambient metal recoveries that defy this cited quotation. Additionally, further improvements may be accessible through incorporation of the aforementioned dissolution aids through system optimisation.

In contrast to all observed $IL_{(aq)}$-related dissolution behaviour, some repeats using $H_2SO_{4(aq)}$ are observed to plateau sharply at 5 *%* extraction, highlighting the potential issues faced for kinetically hindered conventional systems (figure 5.1). Crucially, this effect has not been observed for any $IL_{(aq)}$-based lixiviant system across all studies in this thesis, under the ambient unaided dissolution conditions chosen.

Key physical parameter variations (*p*H, E_h, T) have been detailed, with applicability to all low- and high- volume $H_2SO_{4(aq)}/IL_{(aq)}$-$CuFeS_{2(s)}$ dissolution experiments throughout this study. Data has been fitted effectively by standard exponential and linear fit functions for use in further analysis.

In contrast to the accepted view of acid-$SO_4^{2-}{}_{(aq)}$, E_h variations on the order of ~100 *mV* between repeats (figure 5.1D) are found to not be leach rate-determining for the conditions studied. A requirement for E_h control / enhancement due for E_h has not been observed at any point during these up-scaled studies. In fact, extent of dissolution was often seen to decrease upon typical ~100 *mV* relative increase in E_h. For example, low E_h of 450 *mV* vs. SHE is typical of the conditions in which optimal $IL_{(aq)}$ lixiviant behaviour was observed. Conversely, the size of $H^+{}_{(aq)}$-consumption rates (19-122 $nmol \cdot dm^{-3} \cdot hr^{-1}$) is found to be deterministic/symptomatic of $CuFeS_{2(s)}$ dissolution rates.

Analysis of E_h data allowed for consideration of $[Fe^{2+}]$:$[Fe^{3+}]$ throughout extended leach durations, where the choice of analytical approach was validated by reference to key literature values. $[Fe^{2+}]$:$[Fe^{3+}]$ was found to vary in the range 10^3-10^6, with subsequent $Fe^{3+}{}_{(aq)}$ generation rates of 2.4-41.9 $nM \cdot hr^{-1}$ in good agreement will previous studies.

In absence of a viable transition state model to base a comprehensive kinetic study upon, only limited kinetic analysis is appropriate. The fraction of $CuFeS_{2(s)}$ dissolution, which occurs via each accepted dissolution scheme has been calculated, indicating key differences in the usage of $H^+{}_{(aq)}$ at different stages of leaching in $H_2SO_{4(aq)}$/$IL_{(aq)}$ (figure 5.9). Metal extraction rates cannot reconcile $H^+{}_{(aq)}$ consumption in the early stages of $CuFeS_{2(s)}$ leaching in $IL_{(aq)}$/$H_2SO_{4(aq)}$. Specifically, 80-90 % of $H^+{}_{(aq)}$ consumed in the early stages of $CuFeS_{2(s)}$ dissolution is not used to recover $Cu^{2+}{}_{(aq)}$. It was found that oxidation via $Fe^{3+}{}_{(aq)}$ could not be neglected despite low $[Fe^{3+}]_{(aq)}$ throughout leach durations (<30 $\mu mol \cdot dm^{-3}$; table 5.5). It has been calculated that $H^+{}_{(aq)}$ consumption dynamics can only account for the use of ~1 % equilibrated $[O_{2(g)}]_{(aq)}$ and, thus, are not rate-determining in $IL_{(aq)}$/$H_2SO_{4(aq)}$.

Two independent surface techniques determine sulfur and oxide dominated (oxidised) surfaces before and after leaching; crucially, both methods indicate a large reduction in oxide level in the initial stages of $CuFeS_{2(s)}$ dissolution. SEM/EDX has observed high levels of sample inhomogeneity on leached $CuFeS_{2(s)}$. SEM/EDX has also been indicated to have poor detection capabilities toward S at the oxidised surface, however the technique has identified some potentially interesting stoichiometries that do not reflect a $CuFeS_{2(s)}$ surface. [Fe]:[Cu] metal extraction ratios of between 0.9-1.4 (*e.g.* figure 5.4A) have been rationalised by reciprocal ratios in the surface chemistry of leached $CuFeS_{2(s)}$ surfaces, via ToF-SIMS. Typical ToF-SIMS data suggests that different surface chemistries develop on extended $CuFeS_{2(s)}$ surfaces during the course of leaching in $IL_{(aq)}$/$H_2SO_{4(aq)}$. ToF-SIMS data also highlights key differences in the oxidised surface composition for $H_2SO_{4(aq)}$/$IL_{(aq)}$. Surfaces leached in the best performing $IL_{(aq)}$ system are indicated to have an up to 3-fold thicker depth of oxidised layer before the homogeneous bulk is detected. Further indications reveal that $H_2SO_{4(aq)}$-leached surfaces may

hold more metal content closer to the interface, perhaps suggesting a specific barrier to its release from the surface.

5.7 References

1. N. Hiroyoshi, M. Arai, H. Miki, M. Tsunekawa and T. Hirajima, *Hydrometallurgy*, 2002, **63**, 257-267.
2. D. L. Pool, D. C. Thompson and L. E. Schultze, 1989.
3. C. Carlesi, E. Cortes, G. Dibernardi, J. Morales and E. Muñoz, *Hydrometallurgy*, 2016, **161**, 29-33.
4. T. Dong, Y. Hua, Q. Zhang and D. Zhou, *Hydrometallurgy*, 2009, **99**, 33-38.
5. C. Klauber, *International Journal of Mineral Processing*, 2008, **86**, 1-17.
6. P. Acero, J. Cama and C. Ayora, *European Journal of Mineralogy*, 2007, **19**, 173-182.
7. P. Aktins and J. de Paula, *Atkins' Physical Chemistry*, Oxford University Press, 8th edn., 2006.
8. J. Vilcáez and C. Inoue, *Minerals Engineering*, 2009, **22**, 951-960.
9. P. C. Singer and W. Stumm, *Oxygenation of Ferrous Iron: The Rate-Determining Step in the Formation of Acidic Mine Drainage*, Harvard University, 1968.
10. W. Stumm and G. F. Lee, *Industrial & Engineering Chemistry*, 1961, **53**, 143-146.
11. R. E. Huffman and N. Davidson, *Journal of the American Chemical Society*, 1956, **78**, 4836-4842.
12. A. L. Downing and G. A. Truesdale, *Journal of Applied Chemistry*, 1955, **5**, 570-581.
13. L. W. Winkler, *Berichte der deutschen chemischen Gesellschaft*, 1888, **21**, 2843-2854.
14. B. E. Kimball, J. D. Rimstidt and S. L. Brantley, *Applied Geochemistry*, 2010, 972-983.
15. D. A. Young, *Phase Diagrams of the Elements*, Laurence Livermore Laboratory, University of Calfornia, 1975.
16. G. C. Vezzoli, F. Dachille and R. Roy, *Inorganic Chemistry*, 1969, **8**, 2658-2661.
17. R. P. Tucker, *Industrial & Engineering Chemistry*, 1929, **21**, 44-47.
18. S. Hofmann, *Applied Physics*, 1977, **13**, 205-207.
19. S. Hofmann, *Applied Physics*, 1976, **9**, 59-66.
20. A. J. Taylor, D. J. Graham and D. G. Castner, *Analyst*, 2015, **140**, 6005-6014.
21. R. P. Hackl, D. B. Dreisinger, E. Peters and J. A. King, *Hydrometallurgy*, 1995, **39**, 25-48.
22. H. R. Watling, *Hydrometallurgy*, 2013, **140**, 163-180.

Chapter 6

$IL_{(aq)}$ Screening & Mechanistic Insights

Contents

6.1 Introduction 6-3

6.2 $IL_{(aq)}$ Screening Studies 6-3

6.2.1 Assessing Sample-to-Sample Variability 6-3

6.2.2 Effect of Mass:Volume Ratio 6-5

6.2.3 Screening of Heterocyclic IL Cations 6-7

6.2.4 Screening of $NR_4 \cdot HSO_{4(aq)}$ ILs 6-8

6.3 $IL_{(aq)}$ Leaching Insights 6-10

6.3.1 Effect of $[SO_4^{2-}]_{(aq)}$ 6-10

6.3.2 Effect of Base 6-11

6.3.3 Effect of $[IL]_{(aq)}$ 6-13

6.3.4 Effect of $IL_{(aq)}$ Identity 6-14

6.3.5 Potential IL-$CuFeS_{2(s)}$ Interactions 6-16

6.3.6 Effect of $p\{O_{2(g)}\}$ and $p\{Ar_{(g)}\}$ 6-18

6.3.7 Base Leaching 6-19

6.4 Conclusions 6-20

6.4.1 Proposal of an $IL_{(aq)}$-$CuFeS_{2(s)}$ Leaching Mechanism 6-22

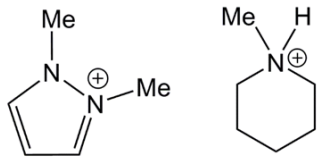
6.5 References 6-24

Synopsis: $IL_{(aq)}$ systems are screened for $CuFeS_{2(s)}$ dissolution activity. Specific key process parameters, such as pulp density, $[O_2]_{(g)}$, $[IL]_{(aq)}$, IL identity and sample-to-sample variability are examined by individually designed assays with reference to conventional $H_2SO_{4(aq)}$ leaching. New IL-based experimental insights arising from screening assays are combined with the outcomes of key physical parameter variations (*p*H, E_h, T), kinetic studies and surface analyses (chapter 5) in order to propose an IL-specific $CuFeS_{2(s)}$ dissolution mechanism.

6.1 Introduction

$IL_{(aq)}$-based $CuFeS_{2(s)}$ dissolution enhancements are indicated to be largely independent of E_h (section 5.6), yet high $[H^+]_{(aq)}$-consumption rates appear symptomatic of the rate of $CuFeS_{2(s)}$ dissolution in $IL_{(aq)}/H_2SO_{4(aq)}$ (figures 5.1-5.4B). However, with oxidant $[Fe^{3+}]_{(aq)}$ concentrations also low, a purely *p*H-dependent mechanism for leaching is not compatible with two aspects of $IL_{(aq)}$ leaching which have been observed so far. Firstly, *p*H alone cannot explain indications of a non-trivial dependence of extent of $CuFeS_{2(s)}$ dissolution upon $[IL]_{(aq)}$ (figure 4.6A). Secondly, *p*H cannot explain differences in the leaching ability of ILs at nominal $[HSO_4]_{(aq)}$ and equivalent *p*H (figure 4.6B; figures 5.1-5.4A). Hence, the challenge to researchers is to explain $IL_{(aq)}$-based leaching enhancements for equivalent *p*H and E_h conditions. Experiments in this chapter are therefore designed to align with this objective, with reference to the E_h variations summarised previously (figures 5.1-5.4D; table 5.3).

As discussed in chapter 2, ILs occupy a large chemical space. Use of a high-performance automated electrochemical screening platform, complemented by intermittent ICP-AES sampling, provides an ideal basis to explore the effect of change in process parameters and to explore wider $IL_{(aq)}$ lixiviant activity. The author's gratitude is extended to Dr Olga Kuzmina for synthesis and characterisation of the HSO_4-ILs with untested moieties based on the pyrazolium ($C_nC_m$pz) and piperidinium cations ($C_n$pip - figure 6.1) for the express purpose of $IL_{(aq)}$ screening documented in section 6.2.3. The lixiviant activity of these HSO_4-ILs will be compared to $NH_4{\cdot}HSO_{4(aq)}$ and $[C_4Him][HSO_4]_{(aq)}$ as the most promising $IL_{(aq)}$ lixiviant systems within their respective classes, compared to $H_2SO_{4(aq)}$ reference solutions.



▲ Figure 6.1 - Cationic structures for N,N-dimethylpyrazolium [C_1C_1pz] and 1-methylpiperidinium [C_1pip], utilised for HSO_4-$IL_{(aq)}$ lixiviant systems.

6.2 $IL_{(aq)}$ Screening Studies

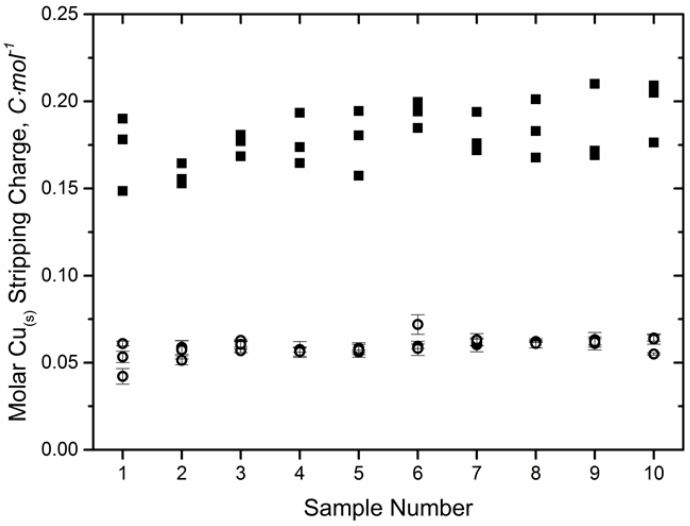
6.2.1 Assessing Sample-to-Sample Variability

Application of ASV as a combinatorial technique in conjunction with the presented automated workstation has been validated (section 3.3) with further optimisations of the ASV procedure achieving significantly enhanced $[Cu^{2+}]_{(aq)}$ detection sensitivities (2-3 fold; section 4.5). Having verified the integrity of this approach, the final validation work required to contextualise data returned in rounds of combinatorial $IL_{(aq)}$ screening is to make an assessment of typical sample-

to-sample variability of ambient $CuFeS_{2(s)}$ dissolution experiments in $IL_{(aq)}/H_2SO_{4(aq)}$ systems. Hence, the significance of different leaching performances based upon variation of conditions can be calculated with respect to expected sample-to-sample variability for equivalent conditions.

The sensitivity of electrochemical ASV to sample-to-sample variability for equivalent $IL_{(aq)}$-$CuFeS_{2(s)}$ dissolution has been assessed as a key control experiment toward larger $IL_{(aq)}$ sample array. 1-vial ASV was used to monitor $[Cu^{2+}]_{(aq)}$ during the parallel leaching of ten equivalent samples containing 450 $mmol{\cdot}dm^{-3}$ $NH_4{\cdot}HSO_{4(aq)}$ lixiviant (4 *mL*). Figure 6.2 displays $Cu_{(s)}$ stripping data normalised to molar $[Cu]_{(s)}$ - effectively normalising ASV data by the quantity of $Cu^{2+}{}_{(aq)}$ present in the active $CuFeS_{2(s)}$ leached sample. This process has been done to demonstrate that 1-vial ASV data is once again indicated to be significantly more sensitive to $[Cu^{2+}]_{(aq)}$, despite experiments being conducted in active leachate solution. In contrast, the 2-vial procedure is non-useful for screening of real leached samples.

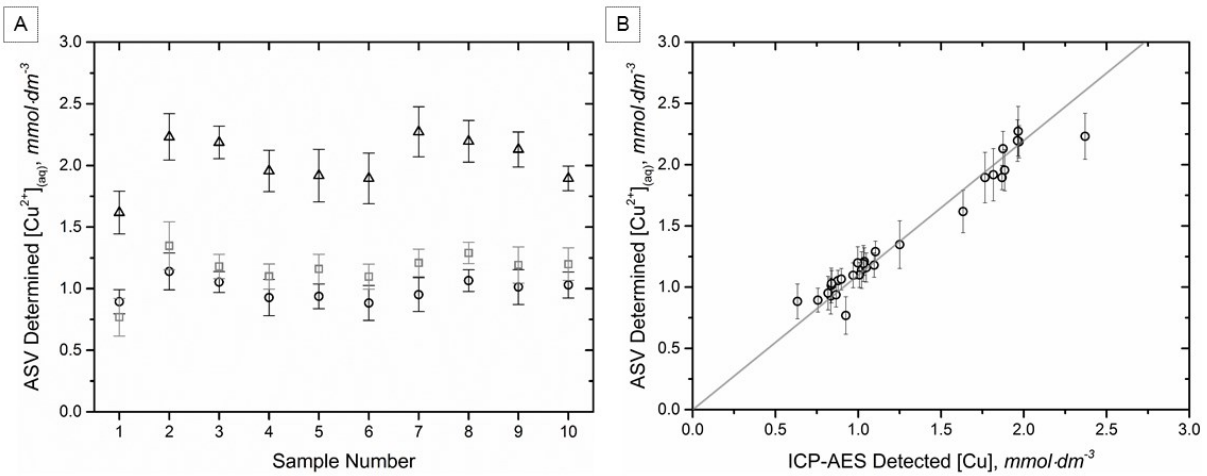
Discarded first repeat data (2-vial format) yields a wide range of possible molar stripping charges, whereas subsequent repeats converge to a consistent value of 59 ± 5 $mC{\cdot}mol{\cdot}dm^{-3}$ with low dataset variance (rel.σ^2 = 0.04 %). This low uncertainty numeric value is in excellent agreement with the calibration slope for 450 $mmol{\cdot}dm^{-3}$ $NH_4{\cdot}HSO_{4(aq)}$ (*cf.* 56.6 ± 0.6 $mC{\cdot}mol{\cdot}dm^{-3}$ - table 4.4), proving that calibration of 1-vial ASV data (rel. $\sigma^2_{R2\text{-}4}$ = $4.3x10^{-4}$) is a low uncertainty process, in contrast to that of 2-vial ASV which incurs significant error due to an order of magnitude increase in relative dataset variance (rel. σ^2_{R1} = $1.6x10^{-3}$).



▲ Figure 6.2 - Molar $Cu_{(s)}$ stripping charge suggested by normalisation of ASV data by independently verified ICP-AES $[Cu^{2+}]_{(aq)}$ measurements for (discarded) first repeat data (■) and repeats 2-4 (O).

Independent ASV and ICP-AES $[Cu^{2+}]_{(aq)}$ measurements were obtained after leach durations of 72, 120 and 216 *hrs*, with the former data shown in figure 6.3A. During extraction, the [Cu]:[Fe] ratio was equal to one, similar to other findings for $NH_4{\cdot}HSO_{4(aq)}$ (figure 4.18; figure 6.7). The

correlation plot for $[Cu^{2+}]_{(aq)}$ quantification (figure 6.3B) once again shows strong agreement between $[Cu^{2+}]_{(aq)}$ quantification methods, with <10 % discrepancy (m = 1.09 ± 0.14; R^2 = 0.994). Sample-to-sample variation for equivalent leaching was ultimately found to be small, with relative variances in the range of 0.7-2.1 % (table 6.1), providing adequate scope to distinguish between lixiviant performance and inter-sample variability within a screening assay.



▲ Figure 6.3 - (A) ASV-determined $[Cu^{2+}]_{(aq)}$ for 10 equivalent $IL_{(aq)}$-$CuFeS_{2(s)}$ samples (4 *mL*; 450 *mmol·dm*$^{-3}$ $NH_4{\cdot}HSO_{4(aq)}$; 298 *K*; unagitated) obtained at 72 (O), 120 (□) and 216 *hrs* (△) leach durations. (B) $[Cu^{2+}]_{(aq)}$ quantification correlation plot for independent ASV and ICP-AES measurements.

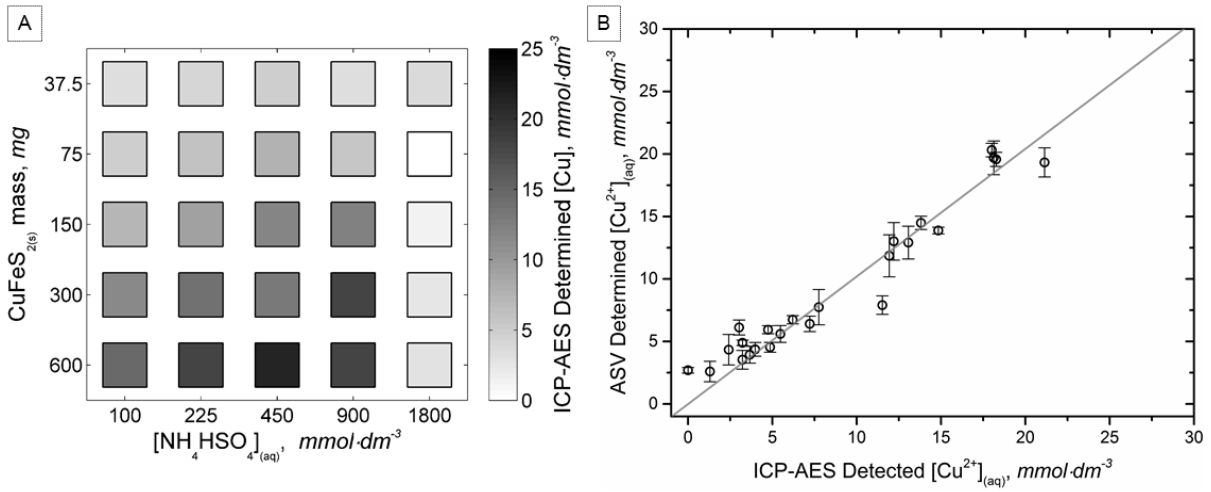
▼ Table 6.1 – Analysis of sample-to-sample variation for 10 samples leached in parallel under equivalent conditions (4 *mL*; 450 *mmol·dm*$^{-3}$ $NH_4{\cdot}HSO_{4(aq)}$; 298 *K*; unagitated)

t, *hrs*	Average Concentration, *mmol·dm*$^{-3}$ ± σ		
	ICP-AES $[Fe_{tot}]_{(aq)}$	ICP-AES $[Cu^{2+}]_{(aq)}$	ASV $[Cu^{2+}]_{(aq)}$
72	0.89 ± 0.08	0.85 ± 0.08	0.99 ± 0.08
120	1.07 ± 0.09	1.05 ± 0.09	1.15 ± 0.16
216	1.91 ± 0.20	1.91 ± 0.19	2.03 ± 0.21

6.2.2 Effect of Mass:Volume Ratio

In a similar experiment, a medium-scale array of 25 samples was screened to investigate the effect of $[IL]_{(aq)}$ (0.1-1.8 *mol·dm*$^{-3}$) and mass:volume ratio (12.5-200 *g·dm*$^{-3}$) on ambient $NH_4{\cdot}HSO_{4(aq)}$ leaching - as a 'proof-of-concept' precursor to larger scale $IL_{(aq)}$ screening experiments. 3 *mL* samples were leached for 264 *hrs* in equivalent conditions (298 *K*; unagitated) with $[Cu^{2+}]_{(aq)}$ quantification at 72, 164 and 216 hrs via ASV and ICP-AES (figure

6.4A). Once again, ICP-determined $[Fe]_{(aq)}$ measurements fall within ±5 % of their respective $[Cu^{2+}]_{(aq)}$ values, averaging 101.3 ± 1.7 % of extracted $[Cu^{2+}]_{(aq)}$ levels, as with figure 4.18 and figure 6.7.



▲ Figure 6.4 - (A) Colour-coded vial diagram expressing ICP-AES determined $[Cu^{2+}]_{(aq)}$ following 264 *hrs* leaching of 3 *mL* $NH_4{\cdot}HSO_{4(aq)}$ samples with varied $[IL]_{(aq)}$ and mass:volume ratio. (B) Correlation plot for first repeat (■) and later repeat (○) electrochemical $[Cu^{2+}]_{(aq)}$ measurements against corresponding ICP-AES values.

Regions of high lixiviant performance (dark areas) are highlighted by all techniques, at the maximum mass:volume ratio but at intermediate ~450 $mmol{\cdot}dm^{-3}$ $[IL]_{(aq)}$, in agreement with previous and current work (figure 4.6; figures 6.5-6.6), and confirming that peak $IL_{(aq)}$ lixiviant activity is not an artefact of mass transport, as concluded previously from ASV simulation (section 4.4). In section 4.4, ASV confident limits were proven sufficient to allow application of a single set of calibration parameters across varied system conditions. For simplicity, a single set of calibration parameters (table 4.4) were applied to all samples, despite the range of $[IL]_{(aq)}$. This process is possible due to a vast reduction in medium-specificity of calibration plots brought about by adaptation to a 1-vial procedure (figure 4.10). This decision is justified by retaining an excellent correlation between $[Cu^{2+}]_{(aq)}$ measurements *cf.* figure 6.4B ($m = 1.02 \pm 0.04$; $R^2 = 0.963$) and figure 6.4A.

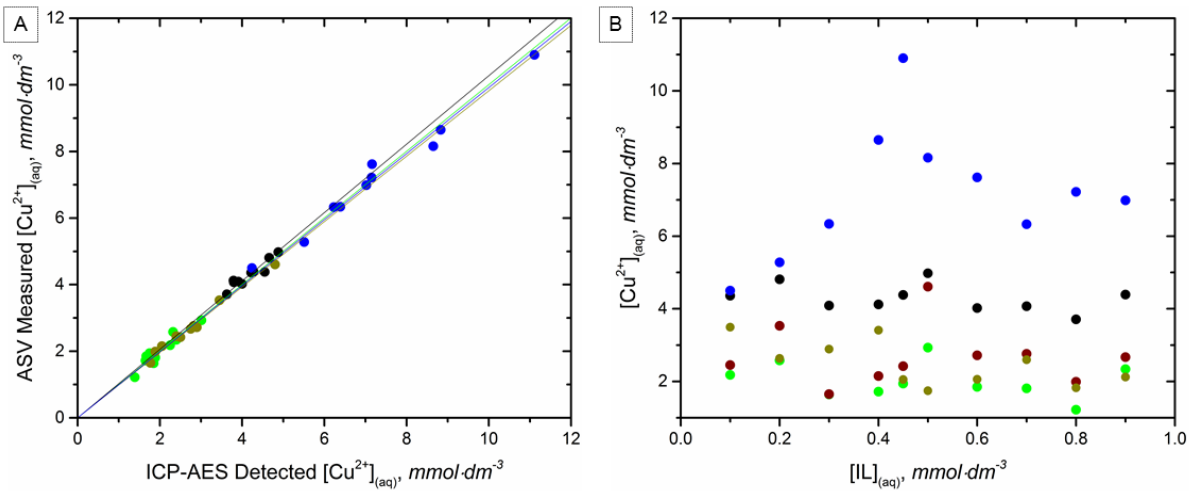
Importantly, within this 25 sample array, 2 orders of magnitude difference are observed in the leaching performance of the best (450 $mmol{\cdot}dm^{-3}$; 600 *mg*) and worst (1800 $mmol{\cdot}dm^{-3}$; 75 *mg*) performing systems. On comparison of the relative variance of the dataset with respect to measured sample-to-sample variability (70-320 *% cf* rel.σ^2 - table 6.1), enhancement is evaluated to be at least 35-fold larger than sample-to-sample variability. Thus, the success of this electrochemical combinatorial approach in distinguishing IL lixiviant performance and inter-sample variability is proven, whereby the relative size of a positive result and an average result is separated by many orders of magnitude.

Remarkably, the results of this medium-scale assay also support the presence of an optimum $[IL]_{(aq)}$ for $NH_4{\cdot}HSO_{4(aq)}$-$CuFeS_{2(s)}$ leaching, in agreement with previous findings for $[C_nC_m im][HSO_4]_{(aq)}$ ILs in terms of $[IL]_{(aq)}$ (figure 4.6A). Despite earlier indications of a strong *p*H effect for $IL_{(aq)}$-$CuFeS_{2(s)}$ dissolution (figure 5.6), since neat solution $[H^+]_{(aq)}$ is significantly increased upon rise in $[IL]_{(aq)}$ (figure 6.6B), factors other than $H^+_{(aq)}$-consumption (*cf*. E1.12) must also play a crucial role in the $IL_{(aq)}$ leaching process. This non-trivial $[IL]_{(aq)}$ dependence is later explained to be related to $SO_4^{2-}{}_{(aq)}$-based rate limitations (section 6.2.4) and is a crucial piece of information used to propose a mechanism for $IL_{(aq)}$ leaching (section 6.4).

6.2.3 Screening of Heterocyclic IL Cations

Lixiviant activity of $[C_nC_m im][HSO_4]_{(aq)}$, $[C_1C_1 pz][HSO_4]_{(aq)}$ and $[C_1 pip][HSO_4]$ ILs has been compared at equal concentration (450 *mmol·dm*$^{-3}$). As discussed in sections 2.3.5-2.4, $[C_nC_m im][HSO_4]_{(aq)}$ solutions have equivalent free-$[H^+]_{(aq)}$ activity at nominal $[HSO_4^-]_{(aq)}$,[1] which extends to the treatment of all of the aforementioned ILs with various N-heterocyclic cations (figure 2.13B).

Figure 6.5 compares the results of 165 *hrs* still, ambient leaching in the above IL systems, with respect to that of the lead $IL_{(aq)}$ lixiviant system $NH_4{\cdot}HSO_{4(aq)}$. Once again, electrochemical $[Cu^{2+}]_{(aq)}$ estimates show good agreement with independent ICP-AES measures (figure 6.5A), with <4.5 % discrepancy indicated for each medium. $[Fe^{2+}]_{(aq)}$ extraction reflects the appearance of figure 6.5B; however, interestingly, the [Fe]:[Cu] extraction ratio is highly medium dependent - ranging from 0.94-1.78 (± 30 %) for $NH_4{\cdot}HSO_{4(aq)}$ and $[C_1 pip][HSO_4]_{(aq)}$ respectively. This aspect is discussed further in section 6.2.4. $NH_4{\cdot}HSO_{4(aq)}$ is once again shown to be the most efficient IL lixiviant system, with the optimum 450 *mmol·dm*$^{-3}$ $[IL]_{(aq)}$ outperforming higher $[NH_4{\cdot}HSO_4]_{(aq)}$ by 35-60 %, extracting 4.0 % $Cu^{2+}_{(aq)}$ from $CuFeS_{2(s)}$ over the full reaction timescale. Across all 50 samples, 0.5-1 order of magnitude difference in lixiviant activity is observed. The remaining lixiviant solutions extract significant quantities of $Cu^{2+}_{(aq)}$ at low $[IL]_{(aq)}$ (2.1-4.4 *mmol·dm*$^{-3}$) with further extraction indicated to be effectively independent of $[IL]_{(aq)}$ increases - a pattern which is consistently observed (section 6.3.3).

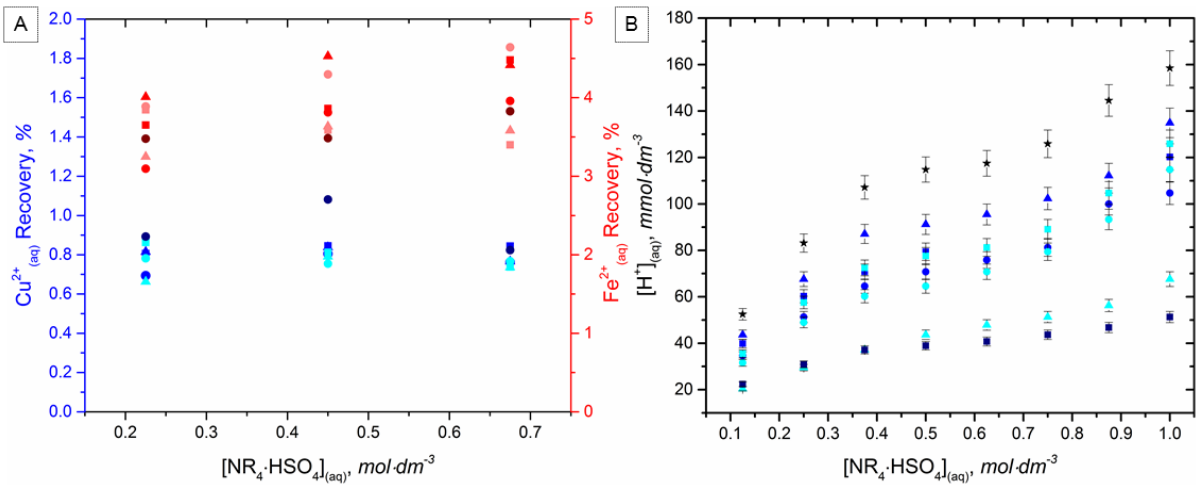


▲Figure 6.5 - (A) $[Cu^{2+}]_{(aq)}$ correlation plot for ICP-AES and ASV screening of 450 *mmol·dm*$^{-3}$ $IL_{(aq)}$ solutions following 165 *hrs* ambient leaching. (B) $Cu^{2+}_{(aq)}$ extraction as a function of $[IL]_{(aq)}$. (● $NH_4{\cdot}HSO_4$; ● $[C_4Him][HSO_4]$; ● $[C_2C_1im][HSO_4]$; ● $[C_1pip][HSO_4]$; ● $[C_1C_1pz][HSO_4]$)

6.2.4 Screening of $NR_4{\cdot}HSO_{4(aq)}$ ILs

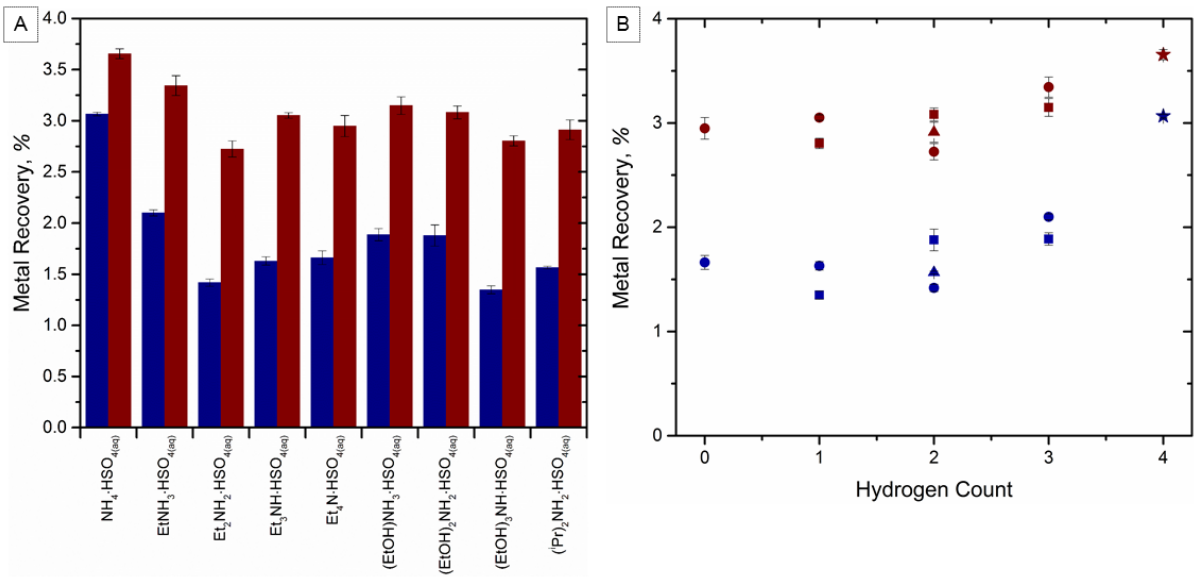
In experiments analogous to the previous section, a range of mono-, di- and tri-substituted $NR_4{\cdot}HSO_{4(aq)}$ lixiviant solutions were screened for $CuFeS_{2(s)}$ dissolution activity over 72 *hrs* (R = H, Et, EtOH, ^{i}PrOH). Figure 6.6A requires two independent axes to effectively display metal extraction data, since $Fe^{2+}_{(aq)}$ recovery is 3.2-6.0 fold larger than that of $Cu^{2+}_{(aq)}$. In contrast to the screening of heterocyclic IL variants (section 6.2.3), a protic NR_4^+-based IL possesses additional contributions to *p*H, such that $IL_{(aq)}$ *p*H is dependent upon the relative basicity of the conjugate base, NR_3 (*i.e.* $pK_a(NH_3)$ = 41; $pK_a(HNEt_2)$ = 21.4).[2, 3] However, despite the considerable difference in free-$[H^+]_{(aq}$ of NR_4^+ ILs (figure 6.6B), there is low impact of $[IL]_{(aq)}$ on metal recoveries. A focused examination of the influence of $[IL]_{(aq)}$ can be found in section 6.3.3, with important implications for process economy.

To verify the above and provide further information, the leaching experiment was repeated in two homologous series of $NR_4{\cdot}HSO_{4(aq)}$, using a single concentration and 150 *hrs* leach duration (450 *mmol·dm*$^{-3}$; R = H, Et, EtOH). Once again, the ranking of $IL_{(aq)}$ lixiviant solutions does not match with acidity data (figure 6.6B). For example, 450 *mmol·dm*$^{-3}$ $Et_3NH{\cdot}HSO_{4(aq)}$ extracts significantly less $Fe^{2+}_{(aq)}$ and $Cu^{2+}_{(aq)}$ despite ~40 % higher $[H^+]_{(aq)}$ than other NR_4^+-IL variants. Data also demonstrates a [Fe]:[Cu] extraction ratio in the range 1.2-2.1, which appears to be a function of specific IL identity. Replotting these metal recoveries as a function of ammonium-bound hydrogen count (NH_nR_{4-n} - figure 6.7B) appears to show the emergence of a systematic variation of leaching ability and highlights that the presence of a protic IL cation (n=0) is unnecessary for leaching.



▲ Figure 6.6 - (A) ICP-AES determined Cu^{2+} (blue) and Fe^{2+} recoveries (red) for screening of $NR_4{\cdot}HSO_{4(aq)}$ systems following 72 *hrs* ambient $CuFeS_{2(s)}$ leaching. (B) Associated free-$[H^+]_{(aq)}$ for screened $NR_4{\cdot}HSO_{4(aq)}$ systems. (★ = NH_4; ● = mono-; ■ = di-; ▲ = tri-substituted; ●● Et_n; ●● $(EtOH)_n$; ●● $(^iPrOH)_n$)

Since proton lability appears unimportant to lixiviant activity in $NR_4{\cdot}HSO_{4(aq)}$ ILs it is possible that specific $IL_{(aq)}$-$CuFeS_{2(s)}$ interactions may be responsible for observed differences in leaching. This conclusion is perhaps supported by the presence of an optimum $[IL]_{(aq)}$ in some experiments and a lack of $[IL]_{(aq)}$ influence in others, where low $[IL]_{(aq)}$ leaches considerable metal. The effect of $[IL]_{(aq)}$ is considered in further detail in section 6.3.3.



▲ Figure 6.7 - ICP-AES $Cu^{2+}_{(aq)}$ (blue) and $Fe^{2+}_{(aq)}$ (red) recoveries for 150 *hrs* ambient $CuFeS_{2(s)}$ dissolution in 450 *mmol·dm*$^{-3}$ $NR_4{\cdot}HSO_{4(aq)}$ solution - presented in (A) a bar chart representation and (B) as a function of the ammonium-bound hydrogen atom count (n; ★ = NH_4; ● = Et_{4-n}; ■ = $(EtOH)_{4-n}$; ▲ = $(^iPrOH)_{4-n}$).

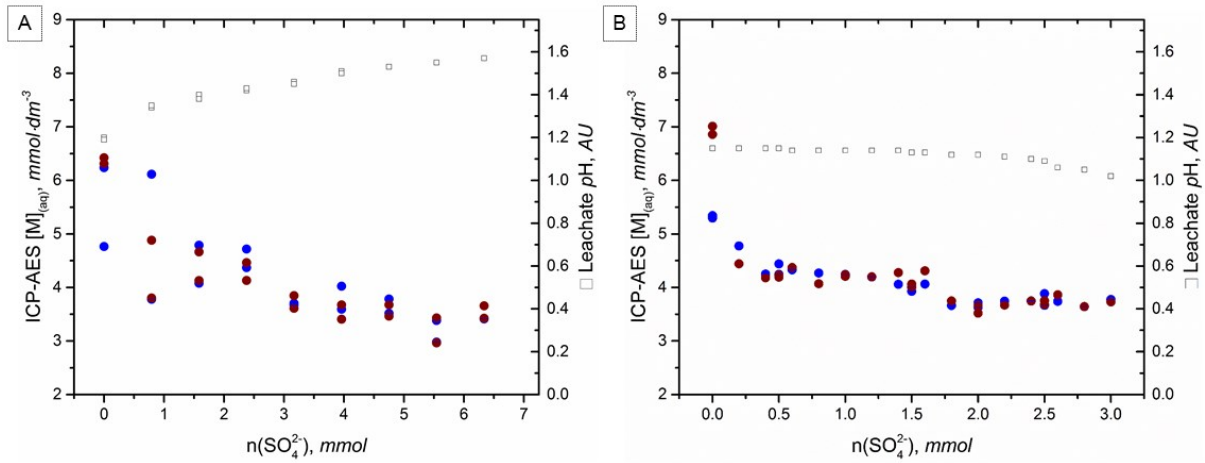
In discussion of $NH_4{\cdot}HSO_{4(aq)}$, the $IL_{(aq)}$ system is consistently indicated to be the most efficient lixiviant system at nominal $[HSO_4^-]_{(aq)}$. The majority of investigations were conducted with

concentrations close to that of a confirmed optimum $[IL]_{(aq)}$ for $NH_4{\cdot}HSO_{4(aq)}$ (Cu) leaching (figures 6.4 and 6.6). Throughout this data, and other sources (*cf. in situ* ASV; figure 4.18), [Fe]:[Cu] extraction ratio is close to 1:1, whereas the same ratio appears to be a function of NR_4^+-IL identity. This point of difference between closely related $NR_4{\cdot}HSO_{4(aq)}$ systems should be investigated further, with the author suggesting the application of *in situ* ASV to monitor leach progression electrochemically (section 4.6). $HNEt_3{\cdot}HSO_{4(aq)}$ may be a particularly good choice, since it bears the largest difference in observed [Fe]:[Cu] across both experiments in the present section, where the electrochemical response to greatly increased proportions of $Fe^{2+}{}_{(aq)}$ should be examined.

6.3 $IL_{(aq)}$ Leaching Insights

6.3.1 Effect of $[SO_4^{2-}]_{(aq)}$

Dutrizac[10] found that high $[SO_4^{2-}]_{(aq)}$ contributed to reduced $CuFeS_{2(s)}$ dissolution rates in conventional acid-SO_4^{2-} media. Since $[HSO_4^-]_{(aq)}$ is relatively high in these systems, dissociation of the acidic $[HSO_4]^-$ anion (pK_a ~1.99) will form large quantities of $[SO_4^{2-}]_{(aq)}$, which may impose limits on $CuFeS_{2(s)}$ dissolution in HSO_4-ILs. This effect was investigated further using ICP-AES measurements following 120 *hrs* of ambient $CuFeS_{2(s)}$ dissolution in 450 *mmol·dm*$^{-3}$ $[C_4Him][HSO_4]_{(aq)}$ with the addition of 0-6.5 *mmol* $Na_2SO_{4(aq)}$ (figure 6.8A).



▲ Figure 6.8 - (A) ICP-AES determined $Cu^{2+}{}_{(aq)}$ (blue) and $Fe^{2+}{}_{(aq)}$ (red) following 120 *hrs* $CuFeS_{2(s)}$-leaching in 450 *mmol·dm*$^{-3}$ $[C_4Him][HSO_4]_{(aq)}$ upon addition of $Na_2SO_{4(aq)}$ with recorded leachate *p*H (□).
(B) Repeat of experiment with HSO_4/SO_4 *p*H buffered solutions.

Addition of $[SO_4^{2-}]_{(aq)}$ did indeed curtail the degree of metal extraction by $[C_4Him][HSO_4]_{(aq)}$ (figure 6.8A). However, the addition of $[SO_4^{2-}]_{(aq)}$ also had the effect of reducing leachate acidity, as shown. Since it was impossible to know which of the latter effects was responsible for reduced leaching, the experiment was repeated in HSO_4-SO_4 buffered solution (*p*H 1.15 ± 0.01), producing similar results (figure 6.8B).

As discussed in section 1.6.5, NaCl has previously been used to increase kinetically hindering S-layer porosity and maintain high active surface area.[11] With regard to the different leaching behaviours of $H_2SO_4/HCl_{(aq)}$ solutions (section 1.6.6), surface-specific $Cl^-_{(aq)}$ desorption is an accepted enhancement-causing influence. Hence, $Na^+_{(aq)}$ may not be expected to show involvement in the leaching process; however, Carneiro *et al*.[11] discuss a possible surface-specific enhancement arising from $Na^+_{(aq)}$. Regardless, since this would manifest as a positive influence on $CuFeS_{2(s)}$ dissolution, the data shown in figure 6.8B and obtained at buffered *p*H proves that high $[SO_4^{2-}]_{(aq)}$ is responsible for reduced lixiviant activities.

Since any negative role of $Na^+_{(aq)}$ has been rejected, it can therefore be calculated that leaching is curtailed by 48 *%* through addition of 5.5 *mmol* $[SO_4^{2-}]_{(aq)}$ (275 *mmol·dm^{-3}*) relative to leaching with no additional $[SO_4^{2-}]_{(aq)}$. Increased $SO_4^{2-}{}_{(aq)}$ is determined to retard $IL_{(aq)}$-$CuFeS_{2(s)}$ leaching at a rate of 17.5 *%* per 100 *mmol·dm^{-3} [IL]$_{(aq)}$*, ultimately limiting HSO_4-$IL_{(aq)}$ lixiviant power and explaining the formation of an optimum $[IL]_{(aq)}$. For further work, alternative AIL options should be investigated; in particular, mixed anion systems or DESs may be a potentially fruitful area of study. Furthermore, it would be practically useful to study the effect of $[SO_4^{2-}]_{(aq)}$ in greater detail to gain access to this key performance-determining relationship. Further discussion of the implications of this crucial finding can be found throughout this section and are also included in section 6.3.1.

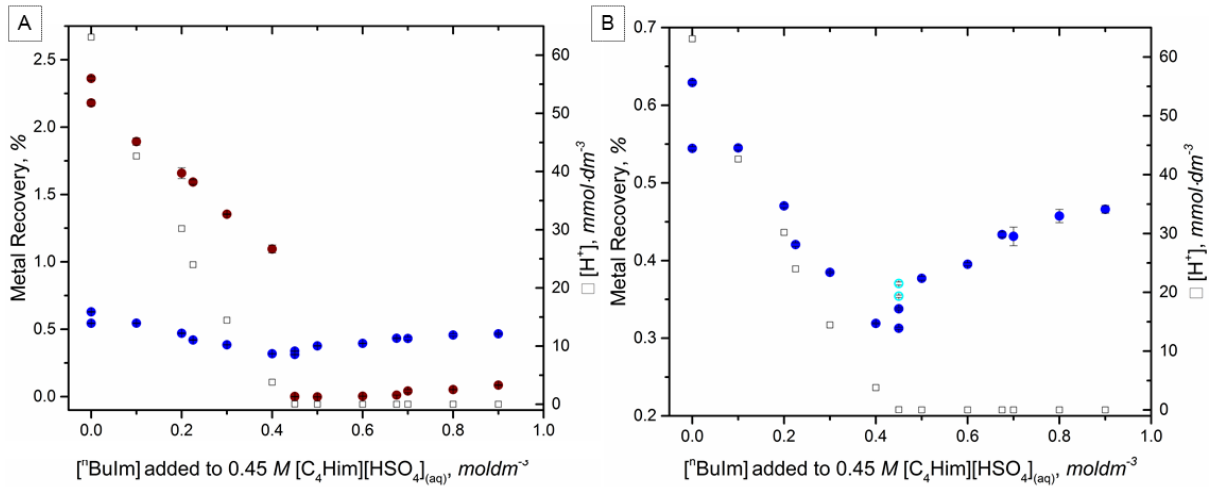
6.3.2 Effect of Base

As outlined in section 2.6.4, $Cu^{2+}_{(aq)}$ complexation in IL lixiviant has been shown to be dependent upon *p*H (*cf.* figure 2.25); it was also shown that at moderate *p*H the quantity of free base is high and comparable to leachate metal compositions (*p*H 4.5; $[C_4im]$ ≈ 9 *mmol·dm^{-3}*; table 2.11). An experiment was designed to investigate the effect of *p*H on $IL_{(aq)}$ leaching, whilst avoiding the introduction of species which are not involved in *p*H determining equilibria in the reference system. $CuFeS_{2(s)}$ was leached for 331 *hrs* in 450 *mmol·dm^{-3}* $[C_4Him][HSO_4]_{(aq)}$ with addition of 0-900 *mmol·dm^{-3}* $C_4im_{(aq)}$ producing the metal recoveries presented in figure 6.9.

As base is added *p*H is decreased with respect to the $[C_4Him][HSO_4]_{(aq)}$ reference solution. As [base]:[IL] approaches a value of 1 (centre of plot; $[C_4im]$ = 450 *mmol·dm^{-3}*), $Fe^{2+}_{(aq)}$ recovery is strongly reduced in proportion to free-$[H^+]_{(aq)}$. A sigmoidal change in solution *p*H occurs about the point where [base]:[IL] = 1, at which point free-$[H^+]_{(aq)}$ has reduced by 3 orders of magnitude (*p*H = 4.3; $[H^+]_{(aq)}$ ~ 50 *µmol·dm^{-3}*). The sharp reduction in acidity produces a 'stepped-reduction' in $[Fe^{2+}]_{(aq)}$ recovered, whereby as $[H^+]$ tends to 0, $Fe^{2+}_{(aq)}$ extraction is switched off. This observation indicates $Fe^{2+}_{(aq)}$ extraction to be controlled by *p*H (figure 6.9A).

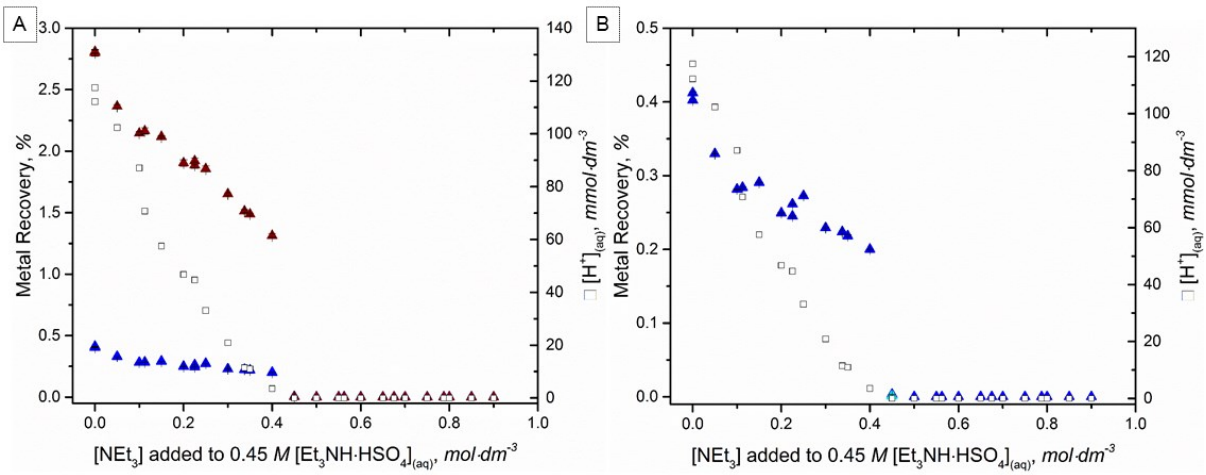
Figure 6.9B magnifies the $Cu^{2+}_{(aq)}$ extraction data from panel A, reflecting a similar dependence on leachate *p*H when [base]:[IL] < 1. With the addition of further base (*i.e.* [base]:[IL] > 1),

$Cu^{2+}_{(aq)}$ and $Fe^{2+}_{(aq)}$ recoveries begin to increase once more indicating the presence of a base leaching mechanism for each metal during $CuFeS_{2(s)}$ dissolution. This conclusion is supported by significant 0.35 *%* $Cu^{2+}_{(aq)}$ recovery using 450 *mmol·dm*$^{-3}$ $C_4im_{(aq)}$ in isolation (●; figure 6.9B).



▲ Figure 6.9 - (A) ICP-AES determined $Cu^{2+}_{(aq)}$ (blue) and $Fe^{2+}_{(aq)}$ (red) recoveries following 331 *hrs* $CuFeS_{2(s)}$-leaching in 450 *mmol·dm*$^{-3}$ $[C_4Him][HSO_4]_{(aq)}$ with variation of added $[C_4im]$, with neat solution free-$[H^+]_{(aq)}$ shown (□). (B) Magnification of $Cu^{2+}_{(aq)}$ recoveries showing $Cu^{2+}_{(aq)}$ recovery using 450 *mmol·dm*$^{-3}$ $[C_4im]_{(aq)}$ (●).

The corresponding experiment for 120 *hrs* leaching in 450 *mmol·dm*$^{-3}$ $Et_3NH{\cdot}HSO_{4(aq)}$ with addition of 0-900 *mmol·dm*$^{-3}$ $NEt_{3(aq)}$ supports these conclusions (figure 6.10). Similar reduction slopes and 'step-reduction' in metal extraction are observed upon addition of $NEt_{3(aq)}$ for [base]/[IL] ≤ 1. However, in contrast to the previous experiment there is no increase in metal recoveries for conditions in which [base]:[IL] > 1. Since (unlike $C_4im_{(aq)}$) 450 *mmol·dm*$^{-3}$ $NEt_{3(aq)}$ (▲) exhibits zero metal leaching, there is no corresponding increase in metal extractions in basic conditions. Since some bases appear to extract Cu and others do not, screening and further discussion of $CuFeS_{2(s)}$ dissolution by nitrogenous bases is featured in section 6.3.7 below.



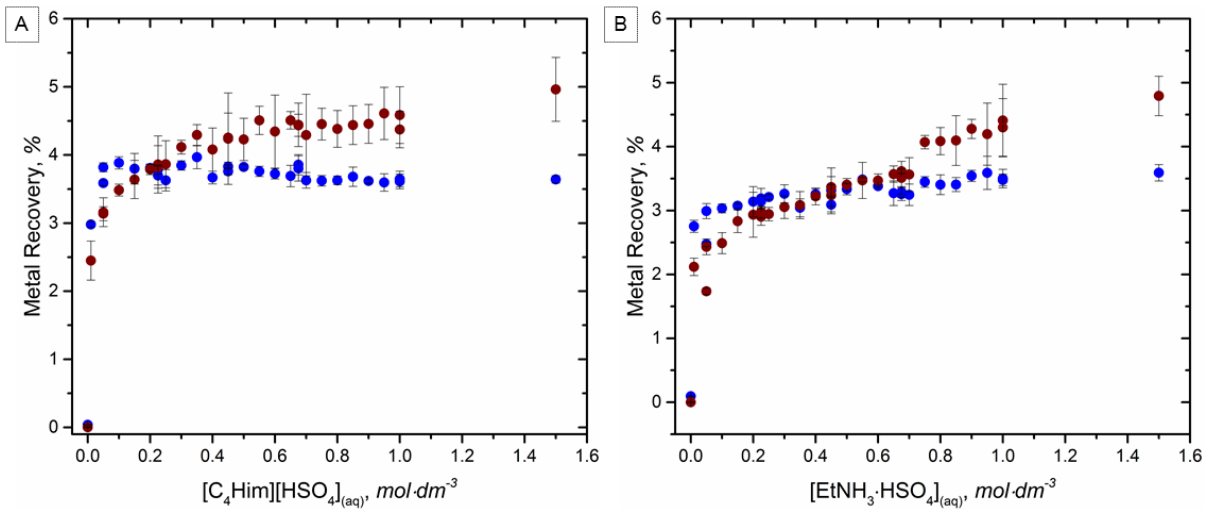
▲ Figure 6.10 - (A) ICP-AES determined $Cu^{2+}_{(aq)}$ (blue) and $Fe^{2+}_{(aq)}$ (red) recoveries following 120 *hrs* $CuFeS_{2(s)}$-leaching in 450 *mmol·dm*$^{-3}$ $Et_3NH{\cdot}HSO_{4(aq)}$ with variation of added [NEt_3], with free-$[H^+]_{(aq)}$ shown before leaching (□). (B) Magnification of $Cu^{2+}_{(aq)}$ recoveries showing $Cu^{2+}_{(aq)}$ recovery using 450 *mmol·dm*$^{-3}$ $NEt_{3(aq)}$ (▲).

6.3.3 Effect of $[IL]_{(aq)}$

Data featured in figures 4.6 and 6.6 is suggestive of the low impact of $[IL]_{(aq)}$ for most trialled IL identities, with/without the indicated presence of an optimum $[IL]_{(aq)}$ for $CuFeS_{2(s)}$ dissolution (*e.g.* figures 4.6 *cf.* figure 6.11). A strong effect of retardation of metal recovery rates at high $[IL]_{(aq)}$ has been demonstrated to explain these effects (section 6.3.1). Data in figure 6.11 presents a similar investigation of the effect of $[IL]_{(aq)}$, this time focusing on low $[IL]_{(aq)}$.

The effect of $[IL]_{(aq)}$ was studied over 132 *hrs* $CuFeS_{2(s)}$ leaching, using solution compositions within the 0-1.5 *mol·dm*$^{-3}$ $[IL]_{(aq)}$ range for $[C_4Him][HSO_4]_{(aq)}$ and $EtNH_3{\cdot}HSO_{4(aq)}$, respectively (figure 6.11A-B). ICP-AES $[Cu^{2+}]_{(aq)}$ measurements obtained following $CuFeS_{2(s)}$ dissolution, show relatively high power metal extraction when $[IL]_{(aq)} \leq 0.1$ *mol·dm*$^{-3}$ for both $Cu^{2+}_{(aq)}$ and $Fe^{2+}_{(aq)}$ extraction. Thereafter, further $[IL]_{(aq)}$ increase appears to provide a weak near-linear enhancement of $Fe^{2+}_{(aq)}$ recovery of 1-2 *%·mol*$^{-1}$*·dm*^{3} for each studied $IL_{(aq)}$ media.

As inferred by previous results, at $[IL]_{(aq)} > 0.05$ *mol·dm*$^{-3}$ there is effectively no dependence of $[IL]_{(aq)}$ due to the apparent competition between $[SO_4^{2-}]_{(aq)}$ inhibition of $CuFeS_{2(s)}$ dissolution (section 6.3.1) and the enhancing effect of raised $[H^+]_{(aq)}$ as proven in section 6.3.2. Since $pK_a(HSO_4^-) = 1.99$,[12] both $[H^+]_{(aq)}$ and $[SO_4^{2-}]_{(aq)}$ have equivalent activity in solution. Hence it is noticeable from figure 6.11 that the rate of $[H^+]_{(aq)}$ promotion of dissolution and the rate of $[SO_4^{2-}]_{(aq)}$ retardation of dissolution appear also to be equal and opposite. These observations seem to indicate that $NR_4{\cdot}HSO_{4(aq)}$ based enhancement of $CuFeS_{2(s)}$ dissolution are determined by the additional *p*H contribution of the cation since, in contrast to the IL anion, $H^+_{(aq)}$ can be released into solution from the cation (crucially) without simultaneous release of $SO_4^{2-}{}_{(aq)}$.



▲ Figure 6.11 - ICP-AES determined $Cu^{2+}_{(aq)}$ (blue) and $Fe^{2+}_{(aq)}$ (red) recovery following 132 *hrs* $CuFeS_{2(s)}$ dissolution in varied concentrations of (A) $[C_4Him][HSO_4]_{(aq)}$ (B) $EtNH_3{\cdot}HSO_{4(aq)}$.

Although this seems to explain the dependence of $[IL]_{(aq)}$ at high concentrations, several over indications of figure 6.11 are more difficult to explain. It is clear from figures 6.9-6.10 that *p*H is an important parameter in determining leaching efficiency. However, the present data appears to indicate that $[IL]_{(aq)}$ as low as 10 $mmol{\cdot}dm^{-3}$ extracts large metal quantities when relatively unaided by low acidities (*p*H~2) and in a low concentration, where $[SO_4^{2-}]_{(aq)}$ would be expected to be far less significant.

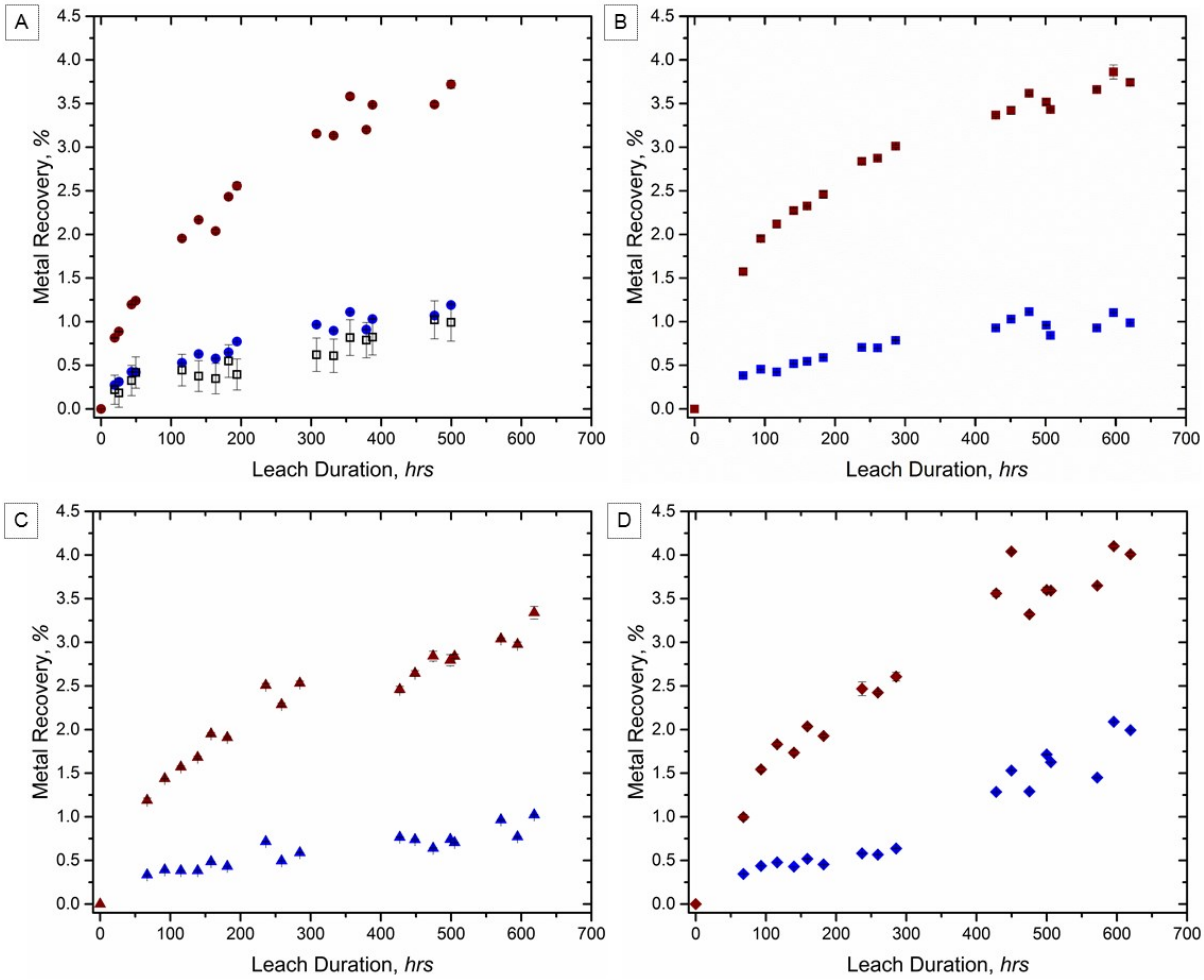
Resolving the mechanism by which ILs extract metals are low $[IL]_{(aq)} < 50$ $mmol{\cdot}dm^{-3}$ will be key. Investigation of the use of HSO_4-$IL_{(aq)}$ lixiviants as low concentration lixiviants appears a very promising possible application. These 'additive-level' concentrations represent a probable effective supplement to established/new hydrometallurgic systems with high metal extraction in *green* high dilution solution. Once again it is noteworthy that these $SO_4^{2-}{}_{(aq)}$-based limitations to $IL_{(aq)}$ lixiviant activity apparently do not apply to $CuFeS_{2(s)}$ flotation concentrates, highlighting an interesting point of difference.

In summary, it appears that competition between $H^+_{(aq)}$-promotion and $SO_4^{2-}{}_{(aq)}$-retardation of $CuFeS_{2(s)}$ dissolution are key to determining metal extraction. The supporting arguments thus far, however, fail to rationalise the different leaching behaviours of non-protic heterocyclic ILs at nominal $[HSO_4^-]_{(aq)}$ (*e.g.* figures 4.6 and 6.5) which is the subject of further discussions in section 6.3.4 below.

6.3.4 Effect of $IL_{(aq)}$ Identity

To aid clarification of the overall dominance of $IL_{(aq)}$-based $CuFeS_{2(s)}$ dissolution profiles long-duration low-volume experiments were conducted for three equivalent acidity $IL_{(aq)}$ systems and compared with $H_2SO_{4(aq)}$ at equal acidity. Figures 2.13 and 6.6B show an equivalence between

the measured free-$[H^+]_{(aq)}$ concentrations for 450 *mmol·dm*$^{-3}$ $[C_4Him][HSO_4]_{(aq)}$, $[C_2C_1im][HSO_4]_{(aq)}$, $EtNH_3{\cdot}HSO_{4(aq)}$ and 75 *mmol·dm*$^{-3}$ $H_2SO_{4(aq)}$ ($pH_{t=0}$ = 1.19 ± 0.01). The metal extraction profiles, which cover leach durations of 0-620 *hrs*, are displayed in figure 6.12A-D. Samples of 450 *mmol·dm*$^{-3}$ $[C_4Him][HSO_4]_{(aq)}$ were utilised for UV-visible leached-$[Cu^{2+}]_{(aq)}$ measurements (□ - figure 6.12A) using an average $\varepsilon_{Cu,800nm}$ collected for IL references (12.2 ± 0.8 *L·mol*$^{-1}$*·cm*$^{-1}$; figure 2.24). These independent measures are shown to be equivalent to ICP-AES measurements when taking account of modest experimental error.



▲ Figure 6.12 - ICP-AES determined $Cu^{2+}_{(aq)}$ (blue) and $Fe^{2+}_{(aq)}$ recoveries for 450 *mmol·dm*$^{-3}$ $IL_{(aq)}$ (A) $[C_4Him][HSO_4]_{(aq)}$ - showing independent UV-visible spectroscopic $[Cu^{2+}]_{(aq)}$ measurements (□) (B) $[C_2C_1im][HSO_4]_{(aq)}$ (C) 75 *mmol·dm*$^{-3}$ $H_2SO_{4(aq)}$ (D) $EtNH_3{\cdot}HSO_{4(aq)}$.

As shown in figure 6.12, dissolution profiles are similar at 0-300 *hrs*, with 0.5-0.75 *%* $Cu^{2+}_{(aq)}$ and 2.5-3 *%* $Fe^{2+}_{(aq)}$ recovered. Over this initial period $[C_nC_mim][HSO_4]_{(aq)}$ ILs are indicated as the best performing media, extracting ~50 *%* more $Cu^{2+}_{(aq)}$ and ~20 *%* more $Fe^{2+}_{(aq)}$. However, during the subsequent 300-600 *hrs* leach duration, $EtNH_3{\cdot}HSO_{4(aq)}$ exhibits a higher leaching rate to match $Fe^{2+}_{(aq)}$ extraction in all other leachates (4 *%*; within error) but to exceed the $Cu^{2+}_{(aq)}$ of all other media by ~100 *%* (2.1 *% cf.* ~1 *%*). In section 6.2.4 it was highlighted that higher-order

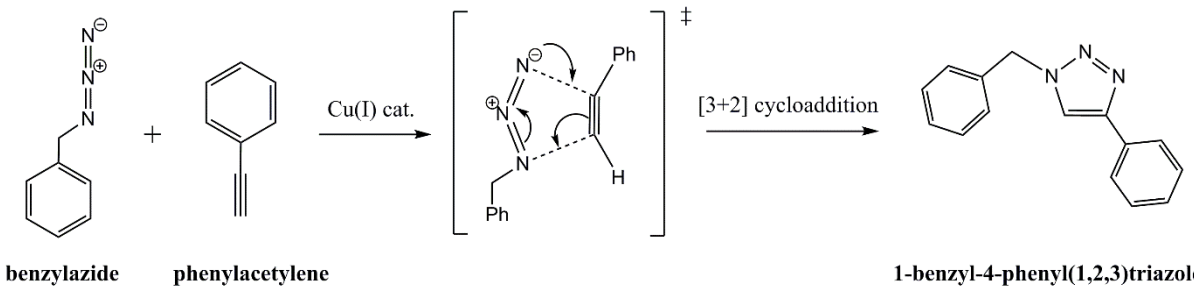
protic $NR_4{\cdot}HSO_{4(aq)}$ exhibit [Fe]/[Cu] extraction ratios that are closer to 1 (figure 6.7), where figure 6.12D seems to suggest that an early stage $Cu^{2+}_{(aq)}$ recovery deficit with respect to $Fe^{2+}_{(aq)}$ is recouped at longer leaching times, showing distinct behaviour within the stated leach duration range.

From equivalent starting *p*Hs, $[H^+]_{(aq)}$-consumption over the course of 620 *hr* leaching was measured as 4-6 $mmol{\cdot}dm^{-3}$, with the highest values attributed to 450 $mmol{\cdot}dm^{-3}$ $EtNH_3{\cdot}HSO_{4(aq)}$ samples - correlating with superior metal leaching observed in this medium. Interestingly, all $IL_{(aq)}$ media exhibit comparable $Cu^{2+}_{(aq)}$ recovery with respect to low $[H_2SO_4]_{(aq)}$ solution; however, $Fe^{2+}_{(aq)}$ is determined to be ~23 *%* higher in all $IL_{(aq)}$ solutions. Therefore, general $IL_{(aq)}$ leaching is indicated to have a stronger influence on $Fe^{2+}_{(aq)}$ extraction, with respect to conventional acid-$SO_{4(aq)}$ leaching at nominal *p*H, with $Cu^{2+}_{(aq)}$ extraction a product of specific IL identities. It is also crucial to note that data from figure 6.11 suggests that comparable $[Cu^{2+}]_{(aq)}$ would be produced from leaching with $[IL]_{(aq)}$ in leaching additive quantities as low as 50 $mmol{\cdot}dm^{-3}$. In summary, it is clear that *p*H is not the dominant effect for $IL_{(aq)}$ lixiviant activity, where specific $IL_{(aq)}$ identities are capable of enhancing $Cu^{2+}_{(aq)}$ recoveries.

6.3.5 Potential IL-$CuFeS_{2(s)}$ Interactions

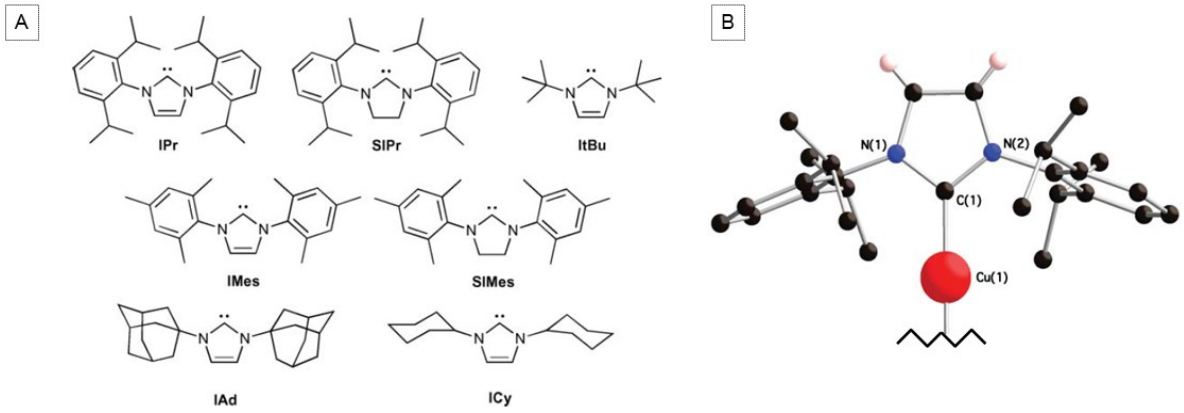
An interesting body of work has recently emerged in the field of Cu(I)-N-heterocyclic carbenes, $[(NHC)Cu]^+$, which exhibit excellent catalytic properties towards the hydrosilylation of ketones and 'click chemistry' [3+2] cycloaddition of azides and terminal alkynes.[13, 14] It is relevant to $IL_{(aq)}$-$CuFeS_{2(s)}$ leaching that carbenes have been observed to form alongside dissolution of metal oxides in $[C_nC_m im]^+$ IL solutions.[15]

With this in mind, several experiments were undertaken to test for the presence of Cu-NHCs as a possible intermediate in an $IL_{(aq)}$ leaching mechanism. Powdered $CuFeS_{2(s)}$ (200 *mg*; 38 ≤ x ≤ 75 *μm*) was placed into $[C_4Him][HSO_4]_{(aq)}$ solution (4 *mL*; 450 $mmol{\cdot}dm^{-3}$), containing benzylazide and phenylacetylene (30 $mmol{\cdot}dm^{-3}$ each). The reaction mixture was allowed to stir for 5 *days*, before filtration and analysis via ^{13}C and ^{1}H NMR and ESI-MS (see appendices for spectra). No evidence was found in several experimental repeats to suggest that any cyclised triazole had formed, whilst NMR characterisation proved that the linearised hydrolysis products had not formed.[16, 17] However, in light of the observation of Cu(I) species as part of the electrodeposit (section 4.6.3), this technique may provide valuable information regarding the origin of the Cu(I) species and should therefore be repeated in solutions containing both $[C_1C_1pz][HSO_4]_{(aq)}$ and the necessary reagents (figure 6.13).



▲ Figure 6.13 - Mechanism for 'click' [3+2] cycloaddition of benzylazide and phenylacetylene, where detection of product 1-benzyl-4-phenyl(1,2,3)triazole is indicative of the presence of Cu(I) carbene reaction catalyst.

The mechanism for the reaction of benzylazide and phenylacetylene - simplified in figure 6.13 - is a stepwise regioselective Huisgen cycloaddition process, which is extremely slow in ambient non-catalysed conditions.[18, 19] _ENREF_25 Effective NHC ligands have been produced via deprotonation at the imidazolium-C_2 position by strong base (figure 6.14A) - where the resulting NHC is stabilised by bulky N,N-substituents (*e.g.* t-butyl, mesityl or 2,5-diisopropylbenzene) prior to coordination to Cu(I), as shown for [(IPr)CuR] in figure 6.14B.



▲ Figure 6.14 - (A) Imidazolium-based N-heterocyclic carbene (NHC) ligands, containing bulky substituents stabilising the carbene species. (B) Ball and stick representation of NHC-Cu(I) complex (IPr)CuR].[13]

In follow-up studies, Dr Claire Ashworth and Dr Tricia Hunt (Imperial College) began DFT investigations of potential dissolution promoting metal-$[C_nC_m\text{im}][HSO_4]_{(aq)}$ interactions, which may occur at the $CuFeS_{2(s)}$ mineral interface. It was in fact found, in preliminary results, that IL moieties interact moderately with Cu but a far stronger interaction with Fe was indicated.[20] In future work, the result of DFT calculations could help rationalise high $[Fe^{2+}]$:$[Cu^{2+}]$ extraction ratios observed throughout this thesis. Additionally, $Fe^{2+}_{(aq)}$ extraction in $IL_{(aq)}$ has often been observed to be a stronger function of $[IL]_{(aq)}$ than for $Cu^{2+}_{(aq)}$ extraction for equivalent experiments (*e.g.* figure 6.11). One possible rationale for this observation is that the IL has a complexing role with regard to surface- or solution-bound Fe; a hypothesis which would require much further work.

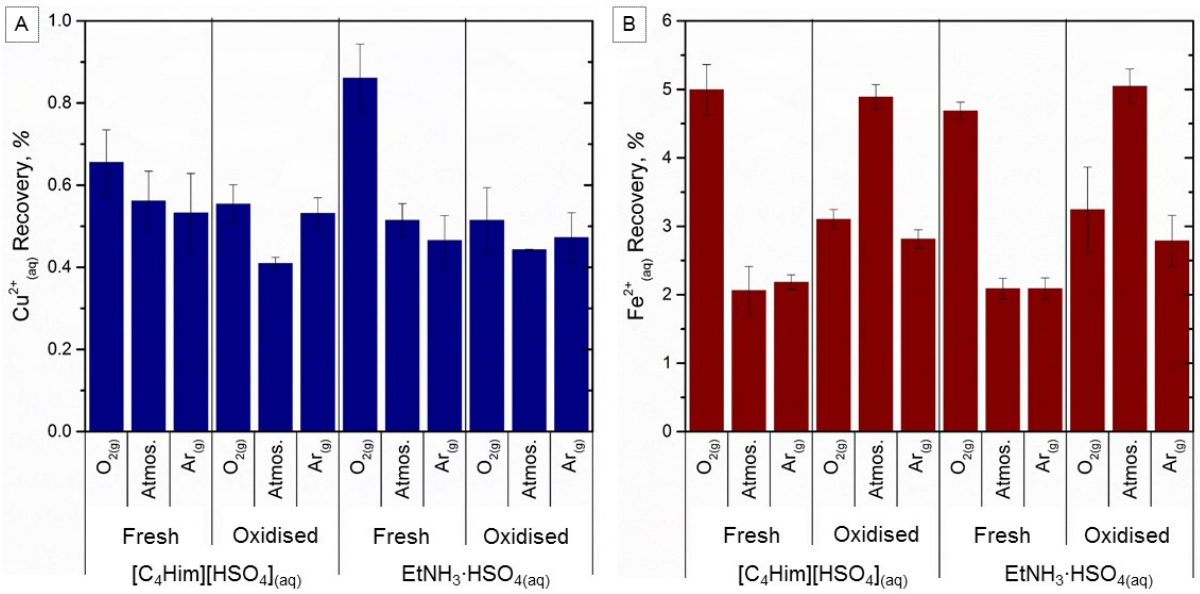
6.3.6 Effect of $p\{O_{2(g)}\}$ and $p\{Ar_{(g)}\}$

In section 5.6, it is highlighted that the best performing media in 400 *mL*-scale tank leaching studies is able to achieve $Cu^{2+}_{(aq)}$ recovery levels that match the performance of advanced conventional acid-$SO_4^{2-}{}_{(aq)}$ systems, for which significant proportions of their total performance is attributable to E_h control enhancements (figure 1.9). In other words, for $IL_{(aq)}$ systems E_h is not the dominant factor - however, it is clear that further enhancements may be achieved through E_h control in $IL_{(aq)}$ lixiviant solutions.

Figures 5.1-5.4D highlight that there is significant scope to increase E_h before one would expect to reach the onset of passivation potential (E_{pp}; figure 1.8). However, referring to figure 5.3 as a reference point for the typical E_h measured for neat $IL_{(aq)}$ solutions, an insignificant variation of E_h (<10 *mV*) in the 0-1.5 $mol{\cdot}dm^{-3}$ $[IL]_{(aq)}$ range is indicated. Thus, investigations presented so far have not significantly varied E_h. In light of $[SO_4^{2-}]_{(aq)}$ hindrance to $IL_{(aq)}$-$CuFeS_{2(s)}$ dissolution, extremes of $[IL]_{(aq)}$ cannot be used to investigate E_h dependence either. Therefore, an alternative approach was designed, based upon $[O_2]_{(aq)}$ availability.

In section 1.4, the accepted effect of the $O_{2(g)}$-$O_{2(aq)}$ equilibrium on acid-$SO_4^{2-}{}_{(aq)}$ leaching was discussed, concluding that $[O_2]_{(aq)}$ has a strong dependence on metal recoveries, since so-called non-oxidative dissolution is extremely slow at ambient temperatures and pressures (E1.5-E1.6). The effect of $[O_2]_{(aq)}$ on $IL_{(aq)}$ based dissolution was investigated using normal atmospheric $O_{2(g)}$ exchange and two extremes of $[O_2]_{(g)}$ availability: namely, via exclusion of $O_{2(g)}$ by high purity $Ar_{(g)}$ sparging and, conversely, maximisation of $O_{2(g)}$ using pure $O_{2(g)}$ sparging. Additionally, two types of $CuFeS_{2(s)}$ were used to investigate the effect of surface oxidation. A large batch of $CuFeS_{2(s)}$ powder was prepared as per standard procedure, before half was stored under $Ar_{(g)}$ (following 45 minutes sparging) and half was left open to air evenly dispersed on the sieve desk to undergo atmospheric oxidation over 3 weeks. 3 *mL* scale leaching reactions were conducted in equiacidic 450 $mmol{\cdot}dm^{-3}$ $[C_4Him][HSO_4]_{(aq)}$ and $EtNH_3{\cdot}HSO_{4(aq)}$ (*ca.* section 6.3.4). 5 *mL* reaction vessels (~2 cm^3 headspace) were used, with 45 *mins* sparging prior to airtight sealing and unagitated ambient leaching for 120 *hrs* (figure 6.15).

Figure 6.15 shows the $Cu^{2+}_{(aq)}$ (panel A) and $Fe^{2+}_{(aq)}$ (panel B) recoveries averaged over three repeats of each category of conditions. Focusing firstly on data for fresh $CuFeS_{2(s)}$ powder $O_{2(g)}$ sparging is observed to enhance $[Cu^{2+}]_{(aq)}$ and $[Fe^{2+}]_{(aq)}$ by 20-70 *%* and 130-150 *%* respectively in comparison to atmospheric conditions. There is a surprisingly low impact of inert $Ar_{(g)}$ atmosphere, with comparable leaching of each metal with respect to atmospheric conditions when the significant magnitude of error is accounted for.



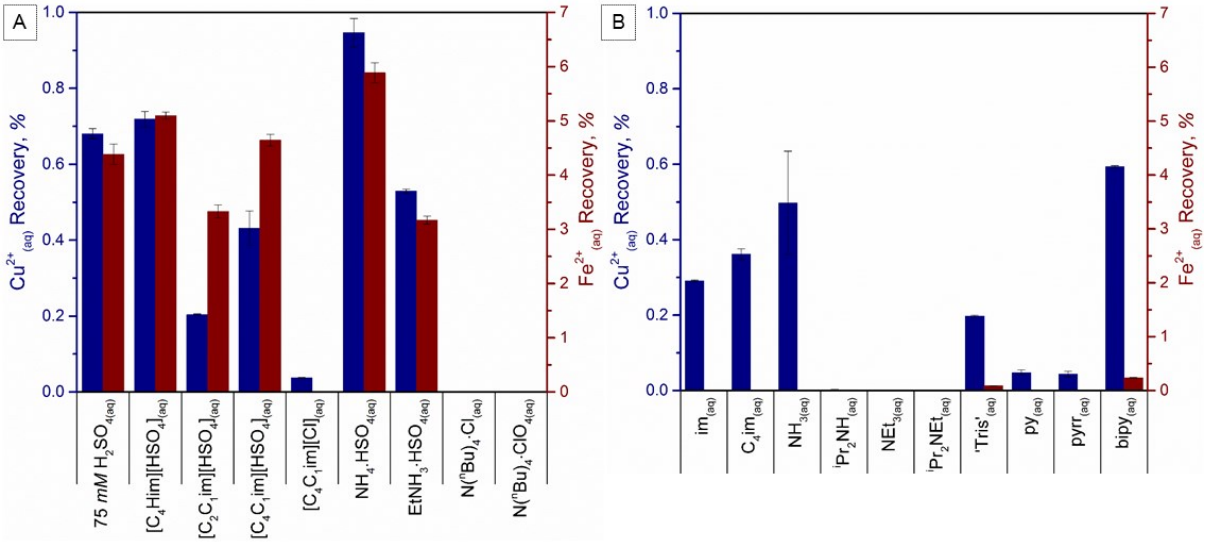
▲ Figure 6.15 - ICP-AES $Cu^{2+}_{(aq)}$ (blue) and $Fe^{2+}_{(aq)}$ (red) metal recoveries for 120 *hrs* $CuFeS_{2(s)}$ dissolution from 450 *mmol·dm*$^{-3}$ $[C_4Him][HSO_4]_{(aq)}$ and $[EtNH_3{\cdot}HSO_4]_{(aq)}$ lixiviant solution in varied atmospheric conditions ($O_{2(g)}$ sparged; $Ar_{(g)}$ sparged; natural atmosphere) and with freshly fractured and 3 week old oxidised $CuFeS_{2(s)}$.

Moving on to discussion of data for atmospherically oxidised $CuFeS_{2(s)}$, the overall trends are quite unexpected and appear to indicate a very different leach mechanism from that of conventional acid-$SO_4^{2-}{}_{(aq)}$. $Cu^{2+}_{(aq)}$ extraction across all three gaseous conditions is comparable after consideration of error magnitudes - suggestive of a $Cu^{2+}_{(aq)}$ leaching mechanism that is independent of $[O_2]_{(aq)}$ availability. The trend observed in $Fe^{2+}_{(aq)}$ recovery is that leaching under atmospheric conditions reaches the equivalently high $Fe^{2+}_{(aq)}$ levels of $O_{2(aq)}$ sparged, unoxidised $CuFeS_{2(s)}$. This latter observation may be expected since atmospheric $CuFeS_{2(s)}$ oxidation may condition the surface to promote release of large quantities of ions from the pre-oxidised surface. However, it is challenging to explain the fact that $Fe^{2+}_{(aq)}$ recoveries are not at least matched or further enhanced in high $[O_2]_{(aq)}$ conditions. In fact, the $Fe^{2+}_{(aq)}$ extraction is not significantly higher than under $Ar_{(g)}$ sparged conditions - constituting negligible difference between leaching under the high and low extremes of $[O_2]_{(aq)}$. Further work is required to understand this effect, however it appears that there may be an optimum $[O_2]_{(aq)}$ for $Fe^{2+}_{(aq)}$ leaching of surface oxidised $CuFeS_{2(s)}$. Ultimately these effects in combination suggest that there are distinctions between the E_h dependence for effective $CuFeS_{2(s)}$ dissolution, whereby the exact E_h required is a function of the extent of atmospheric oxidation of $CuFeS_{2(s)}$ surfaces. It is noteworthy that E_h variation is well-suited to a combinatorial approach and should be studied in further work.

6.3.7 Base Leaching

Previously, in section 6.3.2, it was seen that addition of $C_4im_{(aq)}$ to 450 *mmol·dm*$^{-3}$ $[C_4Him][HSO_4]_{(aq)}$ resulted in a 'V'-shaped plot of $Cu^{2+}_{(aq)}$ recovery (figure 6.9B), where non-zero $Cu^{2+}_{(aq)}$ leaching by $C_4im_{(aq)}$ apparently takes over from the suppressed activity of

$[C_4Him][HSO_4]_{(aq)}$. This effect was seemingly confirmed by the analogous experiment involving combinations of $NEt_{3(aq)}$ and $Et_3NH{\cdot}HSO_{4(aq)}$, where $Cu^{2+}{}_{(aq)}$ did not recover and was switched off when $[H^+]_{(aq)}$ dropped to low levels, since $NEt_{3(aq)}$ did not leach any $Cu^{2+}{}_{(aq)}$ in isolation. Following on from these positive indications of a base leaching mechanism for $Cu^{2+}{}_{(aq)}$, a range of amine bases were screened for $CuFeS_{2(s)}$ dissolution activity. The two panels of figure 6.16 compare leaching of focal 450 *mmol·dm*$^{-3}$ HSO_4-$IL_{(aq)}$ (panel A) with that of 450 *mmol·dm*$^{-3}$ concentrations of screened bases (panel B) for equivalent $CuFeS_{2(s)}$ starting material.



▲ Figure 6.16 - $Cu^{2+}{}_{(aq)}$ (blue) and $Fe^{2+}{}_{(aq)}$ (red) recoveries from 150 *hrs* of $CuFeS_{2(s)}$ leaching in (A) 450 *mmol·dm*$^{-3}$ $IL_{(aq)}$ and (B) a selection of (partially water miscible) 450 *mmol·dm*$^{-3}$ amine bases.

Figure 6.16 firstly indicates that there is negligible $Fe^{2+}{}_{(aq)}$ extraction in trialled base solutions, with the exception of tris(hydroxymethyl)aminomethane ("tris") and 2,2'-bipyridine ("bipy"), aside from the results of section 6.3.2 (as expected). With respect to $Cu^{2+}{}_{(aq)}$ leaching all moderately water-miscible bases afforded comparable recoveries to that of the focal $IL_{(aq)}$ systems and 75 *mmol·dm*$^{-3}$ $H_2SO_{4(aq)}$. It is therefore established that there is a significant base leaching route to $CuFeS_{2(s)}$ extraction.

6.4 Conclusions

First and foremost, HSO_4-$IL_{(aq)}$ systems have been observed to enable higher hydrometallurgic metal recoveries than conventional acid-$SO_4^{2-}{}_{(aq)}$ media of equivalent acidity, although the level of enhancement at nominal acidity (if any) is dependent upon the IL system in question and appears to be a complex function of $CuFeS_{2(s)}$ surface chemistry, $[H^+]_{(aq)}$, $[SO_4^{2-}]_{(aq)}$ and potentially even free-[base]. Combinatorial electrochemical screening of $IL_{(aq)}$ systems for $CuFeS_{2(s)}$ dissolution has proven a successful approach for data gathering, facilitating the sampling of many $IL_{(aq)}$ systems and parameter variations under equivalent conditions.

A newly uncovered non-trivial dependence of $CuFeS_{2(s)}$ dissolution on $[IL]_{(aq)}$ and IL identity has been revealed at nominal acidity (e.g. figure 6.5B). In several independent experiments, $NH_4{\cdot}HSO_{4(aq)}$ has been identified as the IL medium which promotes the greatest metal recoveries from $CuFeS_{2(s)}$, with an indicated 'optimal' $[IL]_{(aq)}$ concentration in the vicinity of 450 $mmol{\cdot}dm^{-3}$ (see below). However, several other $IL_{(aq)}$ systems based on the NR_4, $[C_nC_mim]$, $[C_nC_mpz]$ and $[C_npip]$ cations have been observed to affect differing metal recoveries at nominal $[HSO_4]$, and therefore nominal acidity. Screening within various homologous series of ILs has highlighted $NH_4{\cdot}HSO_4$ and $[C_4Him][HSO_4]$ as 'lead' systems within their respective classes.

Furthermore, many results within this chapter have reinforced a non-linear relationship to degree of medium acidity. HSO_4-$IL_{(aq)}$ system performance is shown to be restricted by $[SO_4^{2-}]_{(aq)}$ at elevated $[IL]_{(aq)}$, which is a possible explanation for observations of two distinct $[IL]_{(aq)}$ dependences - namely, one which results in little effect of $[IL]_{(aq)}$ above a (low) threshold concentration, and a more complex $[IL]_{(aq)}$ dependence producing an 'optimum' $[IL]_{(aq)}$ for $CuFeS_{2(s)}$ dissolution (e.g. figure 6.5B). The latter $[IL]_{(aq)}$ dependency appears to be particularly apparent in experiments involving $NH_4{\cdot}HSO_{4(aq)}$, where the optimum $[IL]_{(aq)}$ lies in the vicinity of 450 $mmol{\cdot}dm^{-3}$.

An interesting theme of the lower volume studies undertaken, is the common mismatch in $Cu^{2+}_{(aq)}$:$Fe^{2+}_{(aq)}$ extraction levels. Extents of $Fe^{2+}_{(aq)}$ recovery are commonly several times larger than that of $Cu^{2+}_{(aq)}$ (e.g. figure 6.6A), with the origin of this result unclear. In addition, the extent of $Fe^{2+}_{(aq)}$ extraction appears to have an increased dependence upon $[IL]_{(aq)}$ and/or *p*H with respect to $Cu^{2+}_{(aq)}$ extraction. As discussed above, this evidence - alongside tentative indications from DFT studies that IL experiences far stronger interactions with surface bound Fe in comparison to surface bound Cu - suggests that $IL_{(aq)}$ lixiviants have a directed influence on $Fe^{2+}_{(aq)}$ solvation, whereby $Cu^{2+}_{(aq)}$ release is indirectly mediated. Further study is required to clarify these indications, with suggestions for follow-up investigations provided in section 7.4.

The specific influences of base and SO_4^{2-} addition on the lixiviant medium has been investigated in detail. This study highlights a dissolution retarding effect of excess free-$[SO_4^{2-}]_{(aq)}$ in *p*H buffered solution (~18 *%* per 100 $mmol{\cdot}dm^{-3}$ $[SO_4^{2-}]_{(aq)}$; *cf.* section 6.3.1). The implications of this finding are discussed further below, with respect to the proposal of a mechanism for $IL_{(aq)}$-$CuFeS_{2(s)}$ dissolution (section 6.4.1). It has been established that that many common (water-soluble) bases are, firstly, capable of facilitating completely selective $Cu^{2+}_{(aq)}$ recovery from $CuFeS_{2(s)}$ at basic *p*H (figure 6.16) and, secondly, of producing a 'V'-shaped $Cu^{2+}_{(aq)}$ recovery plots when modifying acidity from high-moderate-low (figure 6.9B). Crucially, effective bases for $Cu^{2+}_{(aq)}$ leaching include analogues of the IL cations studied (e.g. C_4im), leading to the possibility of transient free-base contribution to $Cu^{2+}_{(aq)}$ recovery. In otherwise equivalent conditions, this latter result suggests that the action of free-base allows $Cu^{2+}_{(aq)}$ recoveries far beyond

expectation, given the lowered medium acidity. The possibility of transient free-base involvement in $CuFeS_{2(s)}$ dissolution mechanisms is discussed further below.

It has been shown that in contrast to conventional $SO_4^{2-}{}_{(aq)}$ media, $IL_{(aq)}$ leaching is relatively insensitive to natural E_h variations under the condition studied. Instead, lixiviant acidity and, specifically, observed levels of $H^+{}_{(aq)}$ consumption has a far greater deterministic influence on unassisted leaching. However, studies which varied the availability of $O_{2(g)}$, to high and low extremes, resulted in variable leaching performance. This finding aligns well with previous studies, where a moderate 'Goldilocks' E_h potential is found to be optimal for control of predominant solution and surface speciation which is favourable to acidic $CuFeS_{2(s)}$ dissolution.

6.4.1 Proposal of an $IL_{(aq)}$-$CuFeS_{2(s)}$ Leaching Mechanism

A proposal for the mechanism for HSO_4-$IL_{(aq)}$ dissolution of $CuFeS_{2(s)}$ is outlined below, combining the opposing dissolution influences of $[H^+]_{(aq)}$ and $[SO_4^{2-}]_{(aq)}$. An initial $[H^+]_{(aq)}$ consuming reaction is a result of proton-assisted solvation of surface metal oxides and is common to all acidic hydrometallurgies. High initial dissolution rates are a result of the oxidative preparation of $CuFeS_{2(s)}$ by the powdering process. Over time, the activity of this oxidised outer surface is quenched and the system is henceforth limited by the rate of oxidation of the surface. It is plausible that this rate of surface oxidations may be a function of IL identity and $[IL]_{(aq)}$, such that $[IL]_{(aq)}$ of *ca*. 450 $mmol{\cdot}dm^{-3}$ tends to accelerate this process.

It is proposed that the ratio of $[H^+]$:$[SO_4^{2-}]$ may control the extent of dissolution at high $[HSO_4]$ and at longer leach durations, *i.e.* when free-$[SO_4^{2-}]_{(aq)}$ becomes prohibitive to further extraction. As a consequence it is suggested that protic NR^+-ILs are able to access dissolution enhancements due to higher $[H^+]$:$[SO_4^{2-}]$ (>1), relative to $[C_nC_m\text{im}][HSO_4]$ for which $[H^+]=[SO_4^{2-}]_{(aq)}$. It is further proposed that differences in the relative rates of enhancement/retardation arising from $[H^+]$:$[SO_4^{2-}]$ is an IL-specific property, which can explain differing IL dissolution activities and also the formation of a peak-optimum in $[IL]_{(aq)}$. The highlighted dissolution retarding effect of excess free-$[SO_4^{2-}]_{(aq)}$ (~18 *%* per 100 $mmol{\cdot}dm^{-3}$ $[SO_4^{2-}]_{(aq)}$; *cf.* section 6.3.1) is proposed to be responsible for counteracting increased acidity upon raising $[IL]_{(aq)}$, which plausibly explains the (variable) 'flat-line'/'peak forming' character of metal recovery plots as a function of $[IL]_{(aq)}$.

One must also reconcile a further key effect of $[IL]_{(aq)}$. Relatively large metal recoveries are observed at low $[IL]_{(aq)}$, despite the fact that $[H^+]_{(aq)}$ is reduced by ~1 order of magnitude (*p*H~2) and $[SO_4^{2-}]_{(aq)}$ is on the order of ~10 $mmol{\cdot}dm^{-3}$. As mentioned above, the retardation effect of $[SO_4^{2-}]_{(aq)}$ has been indicated to be ~18 *%* per 100 $mmol{\cdot}dm^{-3}$ $[SO_4^{2-}]_{(aq)}$ (*cf.* section 6.3.1), which can be assumed to be negligible in this case. Referring to table 2.11 it can be seen that a change in *p*H in the range 1-2, results in ~10^2 increase in [base]:[baseH^+]. On this basis, it is proposed that transient free-base may also participate in $IL_{(aq)}$-$CuFeS_{2(s)}$ dissolution and

therefore provide $IL_{(aq)}$ specific $Cu^{2+}_{(aq)}$ leaching enhancements, as suggested by several study findings (e.g. figure 6.9B). However, it must be noted that since free-base concentrations are low there may be an alternative explanation.

6.5 References

1. T. Q. To, PhD, Imperial College of Science & Technology, 2012.
2. F. G. Bordwell and X. M. Zhang, *Journal of the American Chemical Society*, 1994, **116**, 973-976.
3. F. G. Bordwell, G. E. Drucker and H. E. Fried, *The Journal of Organic Chemistry*, 1981, **46**, 632-635.
4. Z.-F. Cao, H. Zhong, Z.-H. Qiu, G.-Y. Liu and W.-X. Zhang, *Hydrometallurgy*, 2009, 2.
5. Z.-F. Cao, H. Zhong, G.-Y. Liu, Y.-R. Qiu and S. Wang, *Journal of Taiwan Institute of Chemical Engineers*, 2010, 338.
6. Z.-F. Cao, H. Zhong, T. Jiang, S. Wang, G.-Y. Liu and L.-Y. Xia, *Journal of Chemical Technology & Biotechnology*, 2012, 938.
7. C. Gupta, *Extractive Metallurgy of Molybdenum*, Taylor & Francis, 1992.
8. A. J. Bard and L. R. Faulkner, *Electrochemical Methods: Fundamentals and Applications*, Wiley, New York, 2nd edn., 2001.
9. P. Gouzerh and M. Che, *L'Actualité Chimique*, 2006, 1.
10. J. E. Dutrizac, *Metallurgical Transactions B*, 1981, **12**, 371-378.
11. M. F. C. Carneiro and V. A. Leão, *Hydrometallurgy*, 2007, **87**, 73-82.
12. P. Aktins and J. de Paula, *Atkins' Physical Chemistry*, Oxford University Press, 8th edn., 2006.
13. S. Diez-Gonzalez, E. C. Escudero-Adan, J. Benet-Buchholz, E. D. Stevens, A. M. Z. Slawin and S. P. Nolan, *Dalton Transactions*, 2010, **39**, 7595-7606.
14. J. D. Egbert, C. S. J. Cazin and S. P. Nolan, *Catalysis Science & Technology*, 2013, **3**, 912-926.
15. S. Wellens, N. R. Brooks, B. Thijs, L. Van Meervelt and K. Binnemans, *Dalton Trans.*, 2014, 3443.
16. M. K. Denk, J. M. Rodezno, S. Gupta and A. J. Lough, *Journal of Organometallic Chemistry*, 2001, **617–618**, 242-253.
17. O. Hollóczki, P. Terleczky, D. Szieberth, G. Mourgas, D. Gudat and L. Nyulászi, *Journal of the American Chemical Society*, 2011, **133**, 780-789.
18. V. V. Rostovtsev, L. G. Green, V. V. Fokin and K. B. Sharpless, *Angewandte Chemie International Edition*, 2002, **41**, 2596-2599.
19. A. Tudose, L. Delaude, B. André and A. Demonceau, *Tetrahedron Lett.*, 2006, 8529.
20. C. A. Ashworth, personal communication.

Chapter 7

Conclusions and Future Work

Contents

7.1 Summary of Literature Survey 7-2

7.2 Summary of Key Aims 7-3

7.3 Summary and Evaluation of Key Achievements 7-4

7.4 Suggestions for Further Work 7-7

Synopsis: This brief chapter is intended to provide a summary of key project achievements, evaluation of the level of success in attainment of project objectives and details of suggestions for further work.

7.1 Summary of Literature Survey

Efforts to decrease reliance on traditional high-consumption $CuFeS_{2(s)}$ pyrometallurgy from flotation concentrates, has focused on delivering hydrometallurgic solutions to the beneficiation of sulfide ores. Typically aggressive conventional acid-oxidant chemical leaching systems, including the commonly employed $Fe_2(SO_4)_3$-$H_2SO_{4(aq)}$ system, are established and cheap. However, maintaining initially rapid $CuFeS_{2(s)}$ dissolution rates and treatment of low grade ore feedstocks has proven challenging - a problem that is exacerbated by reduced kinetics at ambient temperatures and pressures. $IL_{(aq)}$-based hydrometallurgy is investigated as a promising contender to supersede conventional acid-$SO_4^{2-}{}_{(aq)}$ systems.

A recent surge in ionic liquid (IL) applications has driven research of ILs in the context of Cu extraction from $CuFeS_{2(s)}$, with some promising studies focusing on lixiviant activity toward flotation concentrates. ILs have subsequently been proposed as a potentially higher performance and more benign solution, but the sheer number of IL variants complicates the search for the most efficient systems. Although first generation $IL_{(aq)}$ systems based on the $[C_4C_1im][HSO_4]$ give promising indications of superior performance with respect to acid-$SO_4^{2-}{}_{(aq)}$ dissolution of Cu concentrates, IL leaching mechanisms, kinetics and unprocessed ore applicability remain understudied. The primary focus of this study is the $Cu^{2+}{}_{(aq)}$-leaching performance of hydrogensulfate $IL_{(aq)}$-$CuFeS_{2(s)}$ systems and associated fundamental leaching mechanisms and kinetics. This study examines these factors, with particular emphasis on the comparing $IL_{(aq)}$ lixiviant activity with that of $H_2SO_{4(aq)}$ references under ambient conditions.

7.2 Summary of Key Aims

- Build and validate an automated screening platform capable of high throughput analysis of varied $IL_{(aq)}$-$CuFeS_{2(s)}$ systems.

- Develop anodic stripping voltammetry (ASV) as a tool for *in situ* Cu quantification applicable to $CuFeS_{2(s)}$ dissolution in aqueous/IL environments.

- Screen for and identify $IL_{(aq)}$ lead systems showing promising $CuFeS_{2(s)}$ dissolution activity and compare metal recoveries with $H_2SO_{4(aq)}$ reference solutions.

- Determine whether $IL_{(aq)}$-based leaching operates with differing leach mechanisms and kinetics in comparison to $H_2SO_{4(aq)}$ reference solutions.

- Examine $IL_{(aq)}$ leaching in up-scaled conditions, monitoring key process parameters (*p*H, T, E_h).

- Examine $CuFeS_{2(s)}$ residues leached in $IL_{(aq)}$ and $H_2SO_{4(aq)}$ media using surface-sensitive SEM/EDX and ToF-SIMS in order to identify surface compositions and prevalent species.

7.3 Summary and Evaluation of Key Achievements

This section is intended only as a brief summary of the study to meet the objectives set out in section 1.10. Extended conclusions can be found at the end of each respective chapter.

The setup of an automated electrochemical platform has been described - offering high performance high-throughput, low-volume screening capabilities, with proven applicability to $IL_{(aq)}$ systems and $CuFeS_{2(s)}$ hydrometallurgy. Base motorised functions have been integrated with a range of probe systems (potentiostat, analogue probes, UV-visible spectroscopy, pipetting robot) for one-touch execution of 200 sample-scale experiments. Electrochemical (ASV) screening of $IL_{(aq)}$ sample arrays has been demonstrated with minimal chemical consumption and high precision $[Cu^{2+}]_{(aq)}$ measurements.

It was found that the detection capabilities of cupric ion-selective electrodes (ISE) were insufficient to detect $Cu^{2+}_{(aq)}$ in solution in the presence of ILs during the initial stages of the leach ([Cu] < ~1 *mM*). Conventional ASV can achieve an order of magnitude improvement in the detection limits, however additional optimisation led to a further 2-fold increase in $[Cu^{2+}]_{(aq)}$. Demonstration of the power of this approach was observed in the result of a medium-scale 25 sample screening assay. ASV was used to prove that $IL_{(aq)}$ samples with differing $[IL]_{(aq)}$ and $CuFeS_{2(s)}$ mass contents exhibited >2 orders of magnitude difference in lixiviant activity - values that are at least 35-fold larger than measured sample-to-sample variability.

Automated *in situ* electrochemical monitoring of 120 *mL*-scale $CuFeS_{2(s)}$ dissolution has been demonstrated for several $IL_{(aq)}$ systems alongside $H_2SO_{4(aq)}$ media. Experiments indicate that IL identity has a large impact on $CuFeS_{2(s)}$, with (lead system) 450 $mmol{\cdot}dm^{-3}$ $NH_4{\cdot}HSO_{4(aq)}$ and 75 $mmol{\cdot}dm^{-3}$ $H_2SO_{4(aq)}$ showing high rate, linear extraction profiles over 6 *days* continuous $[Cu]_{(aq)}$ sensing. In contrast, further $HSO_{4(aq)}$-ILs with differing cationic structures ($[C_1C_1pyr]$; $[C_4Him]$) yield reduced, parabolic rates at nominal $[HSO_4]_{(aq)}$ and equivalent *p*H. Fully reconstructed $Cu^{2+}_{(aq)}$ extraction profiles have allowed access to previously omitted dissolution curve features, including extended dormant induction periods (up to 50 *hrs*) and precise rate variations. The luxury of the provision of additional electrochemical insight beyond the primary focus of $[Cu]_{(aq)}$ quantification is shown through the observation of Cu(I) presence in electrodeposits obtained from $[C_1C_1pyr][HSO_4]_{(aq)}$ potentially becoming a further indication of different leaching mechanisms for $IL_{(aq)}$ media in comparison to $H_2SO_{4(aq)}$.

We demonstrate that the aforementioned electrochemical combinatorial approach is indeed a powerful tool for screening and improving $Cu^{2+}_{(aq)}$ extraction performance of HSO_4-$IL_{(aq)}$ lixiviants. Proof-of-concept screening experiments have proven successful in the highlighting of complex dependencies. A large degree of variability in lixiviant activity has been uncovered at nominal $[HSO_4]_{(aq)}$ (and *p*H) for closely structurally-related ILs - where many $[C_nC_mim][HSO_4]_{(aq)}$ and

$[NR_4{\cdot}HSO_{4(aq)}]_{(aq)}$ IL variants have been screened. It has been demonstrated that variations of alkyl substituents (n,m) for equivalent *p*H $[C_nC_m im][HSO_4]_{(aq)}$ solutions yields vastly differing $Cu^{2+}{}_{(aq)}$ recovery efficiencies, indicating $[C_4Him][HSO_4]_{(aq)}$ as the best performing solution within the $[C_nC_m im]$ IL class. Improved relative recoveries are provided by the NR_4 $HSO_{4(aq)}$ class. [Fe]: [Cu] extraction ratios have been shown to be variable and deterministic to extents of $Cu^{2+}{}_{(aq)}$ recovery. For example, NR_4 ILs extract similar amounts of $Fe^{2+}{}_{(aq)}$ for consistent leach durations, however there is significant variability in $Cu^{2+}{}_{(aq)}$ recovery within the class, indicative of differing acid dependencies for each metal ion. $NH_4{\cdot}HSO_{4(aq)}$ was found to be the lead system in terms of $Cu^{2+}{}_{(aq)}$ recovery, combining high recoveries for both $Fe^{2+}{}_{(aq)}$ and $Cu^{2+}{}_{(aq)}$ in close to equivalent quantities.

HSO_4-$IL_{(aq)}$ systems have been observed to enhance $CuFeS_{2(s)}$ dissolution with respect to conventional acid-$SO_4^{2-}{}_{(aq)}$ media of equivalent acidity, although the level of enhancement appears to be a complex function of $CuFeS_{2(s)}$ surface chemistry, $[H^+]_{(aq)}$, $[SO_4^{2-}]_{(aq)}$ and potentially even free-[base]. Fundamentally, HSO_4-$IL_{(aq)}$ system performance appears restricted by $[SO_4^{2-}]_{(aq)}$ at elevated $[IL]_{(aq)}$, which manifests as two distinct $[IL]_{(aq)}$ dependences - namely 'flat-line' dependence and 'peak-forming' dependence .

A mechanism for HSO_4-$IL_{(aq)}$ dissolution of $CuFeS_{2(s)}$ has been outlined, combining the opposing influences of $[H^+]_{(aq)}$ and $[SO_4^{2-}]_{(aq)}$. It is proposed that the ratio of $[H^+]$:$[SO_4^{2-}]$ controls the extent of dissolution at high $[HSO_4]$, *i.e.* when $[SO_4^{2-}]_{(aq)}$ becomes prohibitive to further extraction. It is therefore a consequence that protic NR^+-ILs are able to access enhancements due to higher $[H^+]$:$[SO_4^{2-}] > 1$, relative to $[C_nC_m im][HSO_4]$ for which $[H^+]=[SO_4^{2-}]_{(aq)}$. It is further proposed that differences in the relative rates of enhancement/retardation arising from $[H^+]$:$[SO_4^{2-}]$ is an IL-specific property, which can explain the formation of a peak-optimum in $[IL]_{(aq)}$. A measured retardation effect of $[SO_4^{2-}]_{(aq)}$ (~18 *%* per 100 $mmol{\cdot}dm^{-3}$ $[SO_4^{2-}]_{(aq)}$; *cf.* section 6.3.1) could certainly be comparable to enhancements provided by increased $[IL]_{(aq)}$, which could explain the 'flat-line'/peak forming appearance of metal recovery plots as a function of $[IL]_{(aq)}$.

Large scale experiments (400 *mL*) strongly indicate that $NH_4HSO_{4(aq)}$ enables the greatest $Cu^{2+}{}_{(aq)}$ and $Fe^{2+}{}_{(aq)}$ recoveries for the conditions studied. It has been indicated that IL leaching mechanisms differ from that of conventional acid-$SO_4^{2-}{}_{(aq)}$, particularly with respect to the proportion of $CuFeS_{2(s)}$ oxidation, which occurs via each accepted route. There is strong indication of a further acid consuming stage in early stages of $CuFeS_{2(s)}$ dissolution, which appears to be connected to large scale reduction of surface bound oxide.

Surface sensitive techniques have suggested key differences in the surface chemistry of massive $CuFeS_{2(s)}$ surfaces leached in $IL_{(aq)}$ and $H_2SO_{4(aq)}$. SEM/EDX has observed dominance of $CuFeS_{2(s)}$ consistent surface stoichiometries over 0-10 *μm* probe depths and development of increased non-$CuFeS_{2(s)}$-like surface stoichiometries upon leaching - however the technique was

not sufficiently surface sensitive to detect elemental composition variations between $IL_{(aq)}$ and $H_2SO_{4(aq)}$ over ~1 *month* ambient leach durations. ToF-SIMS has confirmed the dominance of sulfur and oxygen species at the immediate interface, with oxygen fractions decreasing significantly in the early stages of aqueous lixiviant contact. Significant depths of oxidised dissolution products are found for all media, with key differences in depth and composition indicated for $IL_{(aq)}$ and $H_2SO_{4(aq)}$ respectively. High $H^+_{(aq)}$ and surface oxide consumption during the early stages of leaching have been proposed to be correlated to a single specific process during which (initial) dissolution rates remain high. Crucially, following extended leaching in $H_2SO_{4(aq)}$ bulk metal quantities are indicated to lie closer to the interface with respect to $IL_{(aq)}$ leached residues, suggestive of a specific rate curtailing effect. In contrast, $NH_4{\cdot}HSO_{4(aq)}$ leached residues are indicated to have a much deeper interface (~3-fold), yet leaching appears less restricted. In conjunction with detection of sulfur dominated outer layers it is proposed that $NH_4{\cdot}HSO_{4(aq)}$ has a specific role in control of $CuFeS_{2(s)}$ surfaces.

7.4 Suggestions for Further Work

In light of the key achievements of this work, general suggestions for new project directions are provided below, with more specific suggestions referred to, where relevant throughout the text.

- Robotic Workstation

Formalise strategy for integration of UV-visible spectroscopy onto the robotic platform as a more rapid second independent, complementary $[Cu^{2+}]_{(aq)}$ measurement approach. If successful, explore simple 'Quadrant DoE'-style experiments to begin validation of the instrument for potential multivariable analysis derived from these two on-line independent measures.

- *in situ* ASV experiments:

Monitor further NR^{+}-ILs with *in situ* approach to observe the electrochemical response to fundamentally different [Cu]:[Fe] extraction ratios. $[C_1C_1pz][HSO_4]_{(aq)}$ should be reinvestigated in conjunction with outer approaches in order to resolve the origin of the observed Cu(I) species. It would be a powerful option to apply this *in situ* technique in up-scaled condition, although, not at the expense of equipment such as the *p*H, E_h and T probe. Control experiments may be required in order to assess whether there is interference of the two probe systems if placed in the same reactor. Trial the *in situ* method for use in elevated temperatures $CuFeS_{2(s)}$ dissolution monitoring. Determine whether two independent electrochemical probe systems can be used in conjunction in a single leaching reactor - control experiments will be necessary to determine whether there is 'cross-talk' coupling of the probes.

- $NH_4{\cdot}HSO_{4(aq)}$

Aim to clarify the nature of the optimum in $[IL]_{(aq)}$ for maximum $CuFeS_{2(s)}$ dissolution. Screen $[NH_4{\cdot}HSO_4]_{(aq)}$ with low concentration sampling intervals. Resolve the 'exact' position of the optimum $[IL]_{(aq)}$, which may help shed further light on its physical origin and/or causes.

- Low-Volume Electrochemical Screening of IL-$CuFeS_{2(s)}$

Screen arrays in which E_h has been manipulated between samples with order conditions held equal.. Further rounds of screening with the (most promising) NR_4^{+}-IL system and further protic cation variants. Update the model for a desirable IL system (acidic, not dominated by $[HSO_4^{-}]$ etc.). Design screening rounds based on the model system. Based on the proposed mechanism, the author suggests exploration of mixed anion $AIL_{(aq)}$ systems, *p*H adjusted $[Cl^{-}]$-ILs, trial of DESs and basic ILs. Explore E_h control through screening of oxidising conditions. Screen the addition of commonly employed mild oxidants, probably beginning with $FeCl_{3(s)}$.

- High-volume Studies

Extend analogous kinetic studies to the temperature dependence of ILs, beginning with $NH_4{\cdot}HSO_{4(aq)}$ media. Confirm indications of lower E_a dissolution of $CuFeS_{2(s)}$ via Arrhenius and 'shrinking-core' kinetic studies. Combine current system with an $[O_2]_{(aq)}$ probe (DO) and $[O_2]_{(g)}$ meter seeking to establish rates of aeration in $IL_{(aq)}/H_2SO_{4(aq)}$ and to implement system for $O_{2(g)}$-influx E_h control. Combined use of two equivalent reactors leaching in parallel to accommodate an additional electrochemical system if 'cross-talk' coupling of probes proves to be an issue. Combine automated electrochemical profiling with *p*H, T, E_h and $[O_2]_{(aq)}$ measurements in up-scaled reactor.

- $IL_{(aq)}$ as a leach enhancing additive

Investigate the lower limit of $[IL]_{(aq)}$ based recoveries with a focus on *p*H and E_h. Design a screening assay for investigation of $IL_{(aq)}$ additives to complement extraction from established Fe^{3+}-acidic hydrometallurgy systems.

- Mechanistic studies

Using the mechanism proposed in this text as a starting point, design studies that will test the hypothesis. Investigate the specific origins of $CuFeS_{2(s)}$ induction periods.

Surface techniques

Conduct analogous 400 *mL*-scale experiments whilst leaching at elevated temperatures, with a view to producing an exaggerated picture of the surface chemistries that govern $CuFeS_{2(s)}$ dissolution to compare and contrast with weaker indications from low temperature surface chemistries.

- Alternative metallurgies

Assess the result of $NH_4{\cdot}HSO_{4(aq)}$ applied to $CuFeS_{2(s)}$ concentrate. Screen ILs with regard to lixiviant activity in further metallurgies such as rare earths (Re, Mo, etc.).

Appendices

Contents

A. Appendix 1 – Full Arduino Codes A-1

a) Main Motor Control Code A-1

b) Emergency Stop Killswitch Operating A-9

B. Appendix 2 – NI LabView VIs B-1

C. Appendix 3 – MatLab Programming for ASV C-1

a) Extract, Plot and Save Ivium Data to .txt File – ExtractandPlotIvium.m C-1

b) Electrodeposition Batch Analysis - ASV_ED_Analysis.m C-3

c) Stripping Peak Batch Analysis – ASV_ST_Analysis.m C-5

d) ASV Analysis Functions C-7

D. Appendix 4 - IL Characterisation Spectra D-1

a) NMR Spectrum D-1

Synopsis: Appendix material provides additional insight into specific methods of programming, characterisation and analysis not suitable for full-length feature in the main text.

A. Appendix 1 – Full Arduino Codes

a) Main Motor Control Code

```
/* Authors: Daniel Godfrey & James Bannock
For use with Permission and appropriate training only

Instructions:
- ICE use Emergency Stop button
- A back-up copy of the code can be found here: Desktop > Arduino > Backup
- Once the firmware has been uploaded (below), LabView Vis exist for functions below:
- All subvi-s are located at Desktop > LabView VIs....
e.g.
- Go to any vial from any stored position using:        'GoToVial.vi'
- Motor speeds can be changed using a sub-vi called:    'ChangeSpeed.vi'
- Perform auto-homing procedure to set (0,0,0):         'AutomaticHoming.vi'

Arduino Serial Port Assignment:
- Start > Control Panel > System > Device Manager > Ports (COM & LPT)
- Find the "CNC Motors" port on the instrument control box and detach the USB cable
- In device manager, one port will disappear labelled "COMX"
- Plug USB back in and confirm that "COMX" reappears in the list

Firmware Upload:
- Check for "Arduino Uno on COMX" with correct port (found above) at bottom-right of window
- If incorrect, go to Tools > Board... and Tools > Serial Port...
- Once correct, upload the firmware using the appropriate controls above

Set (0,0,0) Reference Position:
- (After uploading firmware...)
- Open the Serial Command window, type @ ('at' symbol) and hit the Return key
- The probe will automatically find and save a consistent reference position
- Make sure the sample holder is correctly positioned below the probe mount

Functions: (Advanced Users Only)

X,Y,Z
- Moves motors to X,Y,Z position relative to 0,0,0
- e.g. 5000,_,5000
- Do not exceed maximum values
- Maximum values are 32500,22000,8000
- '_' character is used to maintain last axis position (e.g. in above command y will not
move)
- Firmware returns '1' when 3 motor motions are complete

&X,Y,Z
- Virtual movement
- e.g. &5000,5000,5000
- Stores X,Y,Z as new position with no physical movement
- Returns '1' instantly

!float
- Adjust motor speed (float = 0.1 – 1; Default = 0.2)
- e.g. !0.95
- Decimal (float) number of 2dp is accepted.
- ,,,\n is returned if correctly set

?int
- Adjust acceleration steps (int = 0-1000[+]; Default = 100)
- e.g. ?100
- Integer must be entered
- ,,,\n is returned if correctly set

#
```

```
- Write current probe positions to Serial buffer
- Used for troubleshooting only - of no use in LabView
e.g. - when # is sent over the Serial Command window the followings is returned
X = 1000
Y = 2050
Z = 7000

@
- Use limit switches to activate automatic procedure to set (0,0,0) position
*/

// Access EEPROM Memory, Maths Functions and I/O Options
#include <EEPROM.h>
#include <math.h>
#include <stdio.h>

// Set wired digital pins from Arduino to Motor Drivers - X, Y, Z
const int dir[] = {10, 7, 4, 2};
const int stepp[] = {9, 6, 5, 3};
const int limitp[] = {13, 12, 8};

// Define and initialise some global variables
int moveto = -1;
int command = 0;
float vel = 0.2;
float vel1 = 0;
int acc = 100;
int acc1 = 0;

// Configuration options run once upon firmware upload
void setup() {

  // Activate pins for all 4 motors (for loop with zero-indexed integer i)
  for (int i = 0; i < 4; i++)
  {
    pinMode(dir[i], OUTPUT);
    pinMode(stepp[i], OUTPUT);
  }

  //Activate pins to read limit switches for automatic 0,0,0 positioning
  for (int k = 0; k < 3; k++)
  {
    pinMode(limitp[k], INPUT);
  }

  // Begin serial communication with 9600 baud rate
  Serial.begin(9600);

}
// Setup(): Closed

// Main Program: Open
void loop()
{
  // Initialise common variables
  int value = 0;
  int denom = 0;

  // Look for data on the serial buffer
  if (Serial.available() > 0)
  {

    // Isolate character commands for special functions e.g. auto-homing, change speed etc.
    if (Serial.peek()=='!'||Serial.peek()=='?'||Serial.peek()=='@'||Serial.peek()=='#')
    {

      // Set rotation direction for auto-homing & initialise reading parameters to zero
```

```
int choice = Serial.read();
vel1 = 0;
acc1 = 0;
int rotdir[] = {-2, 2, 2};

// If you find the ASCII character for '#' - Print the stored position
if (choice == 35)
{
  int hash = Serial.read();
  int mot[] = {0,0,0};
  int powers_[] = {10000, 1000, 100, 10, 1};

  for (int n = 0; n < 5; n++)
  {
    mot[0] = (EEPROM.read(3 * n) * powers_[n]) + mot[0];
    mot[1] = (EEPROM.read((3 * n) + 1) * powers_[n]) + mot[1];
    mot[2] = (EEPROM.read((3 * n) + 2) * powers_[n]) + mot[2];
  }

  Serial.print("\nX = ");
  Serial.print(mot[0]);
  Serial.print("\nY = ");
  Serial.print(mot[1]);
  Serial.print("\nZ = ");
  Serial.print(mot[2]);
  Serial.print("\n");

  // Flush the serial port - Serial.flush() doesn't work
  byte w = 0;

  for (int i = 0; i < 10; i++)
  {
    while (Serial.available() > 0)
    {
      char k = Serial.read();
      w++;
      delay(1);
    }
    delay(1);
  }

}

// If you find the ASCII character for '@' – Auto-define zero using limit switches
if (choice == 64)
{
  int at = Serial.read();

  //Drive each axis until limit switch engages
  for (int j = 0; j<3; j++)
  {
    boolean lim = false;
    digitalWrite(limitp[j], LOW);
    delay(200);

    while (lim == false)
    {
      lim = (digitalRead(limitp[j]) == HIGH)? true : false;
      rotate(rotdir[j], 0.3, stepp[j + 1], dir[j + 1]);
    }

    delay(200);

      // When Y-axis limit is reached, move 24520 steps in -ve direction
      if (j==1)
      {
        for (int y = 0; y < 24520; y++)
```

```
          {
            rotate(-rotdir[j], 0.3, stepp[j + 1], dir[j + 1]);
          }
        }

        // When Z-axis limit is reached then move 7800 steps in the -ve direction
        if (j==2)
        {
          for (int z = 0; z < 7800; z++)
          {
            rotate(-rotdir[j], 0.3, stepp[j + 1], dir[j + 1]);
          }
        }
      delay(200);
    }

    // Write these new found positions to EEPROM memory
    for (int n = 0; n<5; n++)
    {
      EEPROM.write(3*n,0);
      EEPROM.write(3*n+1,0);
      EEPROM.write(3*n+2,0);
    }

    // Send a command to LabView to signify completed action
    Serial.print("_,_,_\n");

    // Flush the serial port - Serial.flush() doesn't work
    byte w = 0;

    for (int i = 0; i < 10; i++)
    {
      while (Serial.available() > 0)
      {
        char k = Serial.read();
        w++;
        delay(1);
      }
      delay(1);
    }

  }

  // If you find the ASCII character for '!' - Change Motor Speed
  if (choice == 33)
  {
      int ex = Serial.read();
      while(!Serial.available());
      vel1 = Serial.parseFloat();
      delay(10);

      // Change Motor Speed and send a command to LabView to signify completed action
      if (vel1 > 0) {
        Serial.print("_,_,_\n");
        vel = vel1;
      }
      else {
      }

      // Flush the serial port - Serial.flush() doesn't work
      byte w = 0;

      for (int i = 0; i < 10; i++)
      {
        while (Serial.available() > 0)
        {
          char k = Serial.read();
```

```
            w++;
            delay(1);
          }
          delay(1);
        }

    }

    // If you find the ASCII character for '?' - Change Acceleration Steps
    if (choice == 63)
    {

        int qu = Serial.read();
        while(!Serial.available());
        acc1 = Serial.parseInt();
        delay(10);

        // Change Acceleration and send a command to LabView to signify completed action
        if (acc1 > 0) {
          Serial.print("_,_,_\n");
          acc = acc1;
        }
        else {
        }

        // Flush the serial port - Serial.flush() doesn't work
        byte w = 0;

        for (int i = 0; i < 10; i++)
        {
          while (Serial.available() > 0)
          {
            char k = Serial.read();
            w++;
            delay(1);
          }
          delay(1);
        }

    }

}

// Instructions if command does not start with ? or !
else
{

    if (Serial.available() > 2)
    {

      // Initialise arrays for positions / multipliers / virtual movements
      int counter = 0;
      int delta = 0;
      unsigned int post[] = {0, 0, 0};
      int powers_[] = {10000, 1000, 100, 10, 1};
      int mot[] = {0, 0, 0};
      int stay[] = {0, 0, 0};
      int disc = 0;
      int virt = 0;

      // If command starts with '&' - discard '&' and mark it as a virtual movement
      if (Serial.peek() == '&')
      {
        disc = Serial.read();
        virt = 1;
      }
```

```
else{
}

// Recall current probe position from EEPROM memory
for (int n = 0; n < 5; n++)
{
  mot[0] = (EEPROM.read(3 * n) * powers_[n]) + mot[0];
  mot[1] = (EEPROM.read((3 * n) + 1) * powers_[n]) + mot[1];
  mot[2] = (EEPROM.read((3 * n) + 2) * powers_[n]) + mot[2];
}

//Construct position to move to in each axis (for loop with zero-indexed integer m)
for (int m = 0; m < 3; m++)
{

  int feed[] = {-1, -1, -1, -1, -1};
  int value = 0;
  int t = 0;

  //  Extract  desired  X,Y,Z  positions  with  up  to  5  digits  (ignore  LF  and  ,)

  for (t; t < 5; t++)
  {
    delay(5);
    value = Serial.read();
    if (value == ',' || value == 10)
    {
      break;
    }
    if (t == 4)
    {
      int handle2 = Serial.read();
    }
    if (m == 2 && t == 4)
    {
      int handle2 = Serial.read();
    }

    //If X,Y or Z is '_' then write 1 to 'stay' array (marker for no movement req.)
    if (value == '_')
    {
      stay[m] = 1;
    }

    // Convert ASCII array to numeric array
    feed[t] = value - 48;

  }

  int pos = 0;
  int j = 0;

  // Compile t (0-5) elements of the feed command into a number (using multipliers)
  switch (t)
  {

      case 5:
        pos = 10000*feed[0] + 1000*feed[1] + 100*feed[2] + 10*feed[3] + feed[4];
        break;

      case 4:
        pos = 1000 * feed[0] + 100 * feed[1] + 10 * feed[2] + feed[3];
        break;

      case 3:
        pos = 100 * feed[0] + 10 * feed[1] + feed[2];
        break;
```

```
      case 2:
        pos = 10 * feed[0] + feed[1];
        break;

      // '_' changes stay[m] to 1 i.e. use current position – check for this first
      case 1:
      {
        if (stay[m] > 0)
        {
          pos = mot[m];
        }
        else{
          pos = feed[0];
        }
        break;
      }

      case 0:
        break;

  }

  // Recompile desired position (post = X | Y | Z)
  post[m] = pos;

}
// Movement in each axis closed

// Flush the serial port - Serial.flush() doesn't work
byte w = 0;

for (int i = 0; i < 10; i++)
{
  while (Serial.available() > 0)
  {
    char k = Serial.read();
    w++;
    delay(1);
  }
  delay(1);
}

int del[] = {0, 0, 0};

// For each axis, calculate movement required - del[q] (zero for virtual/stay)
for (int q = 0; q < 3; q++)
{
  del[q] = post[q] - mot[q];

  // Set positional change to zero for virtual movements and '_' axis commands
  if (stay[q] > 0 || virt == 1)
  {
    del[q] = 0;
  }

  // If a 'real' movement is required, turn the motors appropriately
  if (del[q] != 0)
  {

    for (int y = 0; y < abs(del[q]); y++)
    {

      // Setup speed-dependent accel., accel. parameters and minimum motor speed
      int acc2 = acc * (vel/0.2);
      float min_vel = 0.05;
      float cur_vel = 0;
```

```
            int decel_y = abs(del[q]) - acc2;

            // If too many acceleration steps required use slow constant speed of 0.2
            if (2*acc2 >= abs(del[q]))
            {
              cur_vel = 0.2;
            }

            // Otherwise define velocity at all time points
            else
            {
              cur_vel = (y<acc2)? vel*((float)y + 1)/(float)acc2 : vel;
              cur_vel         =         (y>decel_y-1)?         vel*((float)acc2-((float)y-
(float)decel_y))/(float)acc2:cur_vel;

              // Enforce velocity limits
              cur_vel = (cur_vel < min_vel)? min_vel : cur_vel;
              cur_vel = (cur_vel > vel)? vel : cur_vel;
            }

            //Employ 'rotate' function to turn motors - 2 µsteps = below 32,767 int limit
            if (del[q] > 0)
            {
              rotate(2, cur_vel, stepp[q + 1], dir[q + 1]);
            }
            else{
              rotate(-2, cur_vel, stepp[q + 1], dir[q + 1]);
            }

          }

        }

      }

      // Print '1' when movement is complete (virtual or real)
      Serial.print(1);

      int temp;

      // Write new position to EEPROM memory - overwriting previous location data
      for (int n = 0; n < 4; n++)
      {

        temp = floor(post[0] / powers_[n]);
        EEPROM.write(3 * n, temp);
        post[0] = post[0] - temp * powers_[n];

        temp = floor(post[1] / powers_[n]);
        EEPROM.write(3 * n + 1, temp);
        post[1] = post[1] - temp * powers_[n];

        temp = floor(post[2] / powers_[n]);
        EEPROM.write(3 * n + 2, temp);
        post[2] = post[2] - temp * powers_[n];

        // For the final digit write remainder of position / 10 using modulo operator
        if (n == 3)
        {

          EEPROM.write(3 * (n + 1), floor(post[0] % 10));
          EEPROM.write(3 * (n + 1) + 1, floor(post[1] % 10));
          EEPROM.write(3 * (n + 1) + 2, floor(post[2] % 10));

        }

      }
```

```
      }
      // Serial.Available() > 2: Closed

    }
    // Else Statement: Closed

  }
  // Serial.Available() > 0: Closed

}
// Main Program: Closed


// Configuration of custom function: 'rotate' (no data returned)
void rotate(int steps, float s_vel, int step_pin, int dir_pin)
{

  // Set direction of motion and write to direction pin
  int dir = (steps > 0) ? HIGH : LOW;
  digitalWrite(dir_pin, dir);

  // Set absolute number of steps (direction independent)
  steps = abs(steps);

  // Set delay times to define motor speed
  for (int i = 0; i<steps;i++)
  {

    digitalWrite(step_pin, HIGH);
    delayMicroseconds(round((1 / s_vel) * 70));

    digitalWrite(step_pin, LOW);
    delayMicroseconds(round((1 / s_vel) * 70));

  }


}
```

b) Emergency Stop Killswitch Operating

```
//Configuration Loop
void setup()
{
  // Pin 10 is Reset Pin - Write HIGH in setup
  digitalWrite(10, HIGH);
  pinMode(10,OUTPUT);

  // Pin 2 monitors 'Emergency Stop' switch
  pinMode(2,INPUT);

  // Initialize serial communication at 9600 baud rate
  Serial.begin(9600);

}


// Main Program Loop
void loop()
{

  int lim = digitalRead(2);
```

```
  delay(10);
  Serial.println(lim);
  delay(1000);

  // Write LOW to RESET
  if (lim == 0)
  {
    digitalWrite(10,LOW);
    delay(100);
  }

}
```

B. Appendix 2 – NI LabView VIs

It is impractical to publish graphical coding materials here. Materials may be requested from the author.

C. Appendix 3 – MatLab Programming for ASV

a) Extract, Plot and Save Ivium Data to .txt File – ExtractandPlotIvium.m

```
%{
Instructions:
1. Extracts Data from Ivium Data Files and Dataset Files (.idf & .ids).
2. Construct 'filelist' externally and call this function.
3. Saves MatLab figures and writes data to .txt file.
%}

clear;
close all;
format long;

FileList = dir('*.ids');
k1 = size(FileList,1);

for m1 = 1:k1;

    %Extract data from files one file at a time
    [m,cyc] = ExtractIviumData(FileList,k1,'ids');

    [n p] = size(m);

    %Get handle to filename
    namefig = Filelist(m1).name;

    %Setup plot area
    set(0,'Units','pixels');
    scnsize = get(0,'ScreenSize');      %screensize is [1,1,11440,900]
    figure(1);
    f1 = figure(1);
    position = get(f1,'Position');       %[440 378 560 420]
    outerpos = get(f1,'OuterPosition');  %[432 370 576 512]
    borders = outerpos - position;       %[-8 -8 16 92]
    edge = -borders(1)/2;
    g = [scnsize(3)*(1/20),edge,scnsize(3)*0.95,scnsize(4)-edge]; %[left bottom
width height]
    set(f1,'OuterPosition',g);
    d1 = axes;
    set(d1,'FontSize',14);
    hold on;
    c1 = scatter(m(:,1),m(:,2),8,'s');
    hold off;
    title(namefig,'FontSize',20,'FontWeight','bold','Interpreter','none');
    xlabel('Potential (V)','FontSize',18,'FontWeight','bold');
    ylabel('Current (A)','FontSize',18,'FontWeight','bold');

    savefig(f1,namefig);

    G1 = strcat(namefig(1:end-4),'.txt');
```

```
    % Create 1st Results File & Print Column Titles
    resultsfile = fopen(G1,'w');
    fprintf(resultsfile, '%s', 'Col1');
    fprintf(resultsfile, '\t');
    fprintf(resultsfile, '%s', 'Col2');
    fprintf(resultsfile, '\t');
    fprintf(resultsfile, '%s', 'Col3');
    fprintf(resultsfile, '\r\n');

    % Write Results Line-by-Line to Output File
    for m2=1:n

        fprintf(resultsfile, '%.6E', m(m1,1));
        fprintf(resultsfile, '\t');
        fprintf(resultsfile, '%.6E', m(m2,2));
        fprintf(resultsfile, '\t');
        fprintf(resultsfile, '%.6E', m(m2,3));
        fprintf(resultsfile, '\r\n');

    end

    clearvars m cyc m2 n p;
    clear axes;
    close(f1);

end;

close all;
```

b) Electrodeposition Batch Analysis - ASV_ED_Analysis.m

Note: ExtractIviumData.m is a custom build function also featured in these appendicies.

```
%{
Instructions:
1. Run this code in a directory containing Ivium electrodeposition traces
2. Files should have .idf extension
3. User is prompted to give title to results file (any string, no extension)
4. Produces a .txt results file containing:
    - 'File ID':    File Identifier
    - 'ED Time':    Total Electrodeposition Time (s)
    - 'Istart':     First Current Measured (A)
    - 'Iend':       Current Measured at 'ED Time' (A)
    - 'Qtot':       Total Charge Integral Under i-t Trace (C)
    - 'Qnet':       'Qtot' (as above) Minus Rectangular Background
                    i.e. (0,0)-(Iend,0)-(Iend,ED Time)-(0,ED Time)
%}

clear;
close all;
format long;

% Ask user for Results File name
G = input('Please Name the Results File...[any string]: ','s');

% Compile List of Electrodeposition Files and Generate For Loop Count k
FileList = dir('*.idf');
k = size(FileList,1);

% Initialise Array to Populate with Results
results = zeros(k,5);

% Main Program Loop
for m1 = 1:k;

    % Extract Data from Each File
    ExtractIviumData(FileList,m1,'idf');

    % Define Output Parameters
    EDtime = M(X{1},1);
    Istart = M(1,2);
    Iend = M(X{1},2);
    I = M(:,2);
    int = M(2,1) - M(1,1);
    Qtot = int*trapz(I);
    Iadj = I-Iend;
    Qnet = int*trapz(Iadj);

    % Populate Appropriate Line of Results Array
    results(m1,1) = EDtime;
    results(m1,2) = Istart;
    results(m1,3) = Iend;
    results(m1,4) = Qtot;
    results(m1,5) = Qnet;
```

```
end;

% Create Results File & Print Column Titles
resultsfile = fopen(G,'w');
fprintf(resultsfile, '%s', 'File ID');
fprintf(resultsfile, '\t');
fprintf(resultsfile, '%s', 'ED Time');
fprintf(resultsfile, '\t');
fprintf(resultsfile, '%s', 'Istart');
fprintf(resultsfile, '\t');
fprintf(resultsfile, '%s', 'Iend');
fprintf(resultsfile, '\t');
fprintf(resultsfile, '%s', 'Qtot');
fprintf(resultsfile, '\t');
fprintf(resultsfile, '%s', 'Qnet');
fprintf(resultsfile, '\r\n');

% Write Results Line-by-Line to Output File
for m1=1:k

    fprintf(resultsfile, '%s', FileList(m1).name);
    fprintf(resultsfile, '\t');
    fprintf(resultsfile, '%.0f', results(m1,1));
    fprintf(resultsfile, '\t');
    fprintf(resultsfile, '%.3E', results(m1,2));
    fprintf(resultsfile, '\t');
    fprintf(resultsfile, '%.3E', results(m1,3));
    fprintf(resultsfile, '\t');
    fprintf(resultsfile, '%.3E', results(m1,4));
    fprintf(resultsfile, '\t');
    fprintf(resultsfile, '%.3E', results(m1,5));
    fprintf(resultsfile, '\r\n');

end

% Close Results File
fclose(resultsfile);
close all;
```

c) Stripping Peak Batch Analysis – ASV_ST_Analysis.m

Note: OnePeak.m and TwoPeak.m are similar custom functions, the former of which is featured in these appendicies.

```
%{
Instructions:
1. Run this code in a directory containing Ivium CV stripping datasets
2. Files can be analysed for key peak statistics for up to two peaks
2. Files should have .ids extension
3. User is prompted to give title to results file (any string, no extension)
4. Produces (up to) two .txt results file containing:
    - 'File ID':          File Identifier
    - 'Int. Method':      Choice of peak-picking method (auto/1-point/2-point)
    - 'Peak V':           Potential of maximum current (in reference to baseline)(V)
    - 'Peak I':           Value of current at Vmax (in reference to baseline)(A)
    - 'Peak Area':        i-V peak area (AV)
    - 'Peak Charge':      i-t integral of peak to give stripping charge (C)
%}

clear;
close all;
format long;

% Ask user for Results File name
G1 = input('Please Name the Primary Results File...[any string]: ','s');
G2 = input('Please Name the Secondary Results File...[any string]: ','s');

% Compile List of CV Dataset Files and Generate For Loop Count k
FileList = dir('*.ids');
k = size(FileList,1);

% Initialise Arrays to Populate with Results
results = zeros(k,4);
results1 = zeros(k,4);

% Main Program Loop
for m1 = 1:k;

    % 1st Peak: Visual trace and pick peak
    OnePeak

    % Ask the user if there is another peak to analyse [y/n]
    z1(m1) = input('Another Peak? [y/n] - ','s');

    % If affirmative, 2nd Peak: Visualise trace and pick peak
    if z1(m1) == 'y';

        TwoPeak

    end;

end

% Create 1st Results File & Print Column Titles
```

```
resultsfile = fopen(G1,'w');
fprintf(resultsfile, '%s', 'File ID');
fprintf(resultsfile, '\t');
fprintf(resultsfile, '%s', 'Int. Method');
fprintf(resultsfile, '\t');
fprintf(resultsfile, '%s', 'Peak V');
fprintf(resultsfile, '\t');
fprintf(resultsfile, '%s', 'Peak I');
fprintf(resultsfile, '\t');
fprintf(resultsfile, '%s', 'Peak Area');
fprintf(resultsfile, '\t');
fprintf(resultsfile, '%s', 'Peak Charge');
fprintf(resultsfile, '\r\n');

% Write Results Line-by-Line to Output File
for m1=1:k

    fprintf(resultsfile, '%s', FileList(m1).name);
    fprintf(resultsfile, '\t');
    fprintf(resultsfile, '%s', a1(m1));
    fprintf(resultsfile, '\t');
    fprintf(resultsfile, '%.3f', results(m1,1));
    fprintf(resultsfile, '\t');
    fprintf(resultsfile, '%.3E', results(m1,2));
    fprintf(resultsfile, '\t');
    fprintf(resultsfile, '%.3E', results(m1,3));
    fprintf(resultsfile, '\t');
    fprintf(resultsfile, '%.3E', results(m1,4));
    fprintf(resultsfile, '\r\n');

end

fclose(resultsfile);

% Create 2nd Results File & Print Column Titles
resultsfile1 = fopen(G2,'w');
fprintf(resultsfile1, '%s', 'File ID');
fprintf(resultsfile1, '\t');
fprintf(resultsfile1, '%s', 'Int. Method');
fprintf(resultsfile1, '\t');
fprintf(resultsfile1, '%s', 'Peak V');
fprintf(resultsfile1, '\t');
fprintf(resultsfile1, '%s', 'Peak I');
fprintf(resultsfile1, '\t');
fprintf(resultsfile1, '%s', 'Peak Area');
fprintf(resultsfile1, '\t');
fprintf(resultsfile1, '%s', 'Peak Charge');
fprintf(resultsfile1, '\r\n');

% Write Results Line-by-Line to Output File
for m1=1:k

    fprintf(resultsfile1, '%s', FileList(m1).name);
    fprintf(resultsfile1, '\t');
    fprintf(resultsfile1, '%s', z1(m1));
    fprintf(resultsfile1, '\t');
```

```
    fprintf(resultsfile1, '%.3f', results1(m1,1));
    fprintf(resultsfile1, '\t');
    fprintf(resultsfile1, '%.3E', results1(m1,2));
    fprintf(resultsfile1, '\t');
    fprintf(resultsfile1, '%.3E', results1(m1,3));
    fprintf(resultsfile1, '\t');
    fprintf(resultsfile1, '%.3E', results1(m1,4));
    fprintf(resultsfile1, '\r\n');

end

fclose(resultsfile1);
close all;
```

d) ASV Analysis Functions

i) Extract All Electrochemical Data – ExtractIviumData.m

```
%{
Instructions:
1. Extracts Data from Ivium Data Files and Dataset Files (.idf & .ids)
2. Construct 'filelist' externally and call this function
%}

function [M,SW] = ExtractIviumData(filelist,counter,filetype)

    p = inputParser;

    defaultFileType = 'idf';
    validFileType = {'idf','ids'}
    checkFileType = @(x) any(validatestring(x,validFileType));

    addRequired(p,'filelist',@ischar);
    addRequired(p,'counter',@isnumeric);
    addRequired(p,'filetype',defaultFileType,checkFileType);

    parse(p,filelist,counter,filetype);

    % Read in Ivium data using matched inputs
    filename = filelist(counter).name;
    CNCfile = fopen(filename);

    % Read Whole File Line-By-Line for Data-start Marker Search
    HL = textscan(CNCfile,'%s','delimiter','\n');
    HL2 = [HL{:}];

    % Define Data-start Marker & format into Character Array
    PDt = 'primary_data';
    Ad = char(PDt);

    % Find the Lines Containing the Data Marker
    PD = strfind(HL2, Ad);
```

```
    sPD = size(PD);
    oPD = ones(sPD);
    strPD = num2str(oPD);
    csPD = cellstr(strPD);
    PD2 = strcat(PD,csPD);
    PD3 = strcmp(PD2,csPD);
    PD4 = +PD3;

    % Define the correct markers & column formats to use (.idf/.ids)
    if filetype = 'idf';
        NC = find(PD4==0, 1, 'first');
        col = '%f%f%f%s';
    end;
    if filetype = 'ids';
        NC = find(PD4==0);
        NC = NC(2:);
        col = '%f%f%f';
    end;

    % Define Number of lines to Read & Header Lines to Data
    NL = NC + 1;
    ND = NC + 2;

    % Define number of Sweeps
    [Sw NA] = size(NC);
    M = [0 0 0];

    % For Each Sweep Go back to the Top of the File and Read in the Data
    for v = 1:SW;

        frewind(CNCfile);
        NCact = textscan(CNCfile,'%f', 1, 'HeaderLines', NC(v));
        frewind(CNCfile);
        X = textscan(CNCfile,'%f', 1, 'HeaderLines', NL(v));
        frewind(CNCfile);
        data2 = textscan(CNCfile, col, X{1}, 'HeaderLines', ND(v), 'delimiter',
'/t');%Read data by using number of lines to read and calc'd data header lines
        data1 = data2(:,1:3);
        data = cell2mat(data1);

        M = vertcat(M,data)

    end

    fclose(CNCfile);

end
```

ii) Flexible CV Peak Picking Function – OnePeak.m

```
%{
Instructions:
Use as part of ASV_ST_Analysis.m and duplicate/use TwoPeak.m to find multiple peaks
per file
%}

function OnePeak(filelist,counter,filetype)

    l = inputParser;

    defaultFileType = 'idf';
    validFileType = {'idf','ids'}
    checkFileType = @(x) any(validatestring(x,validFileType));

    addRequired(l,'filelist',@ischar);
    addRequired(l,'counter',@isnumeric);
    addRequired(l,'filetype',defaultFileType,checkFileType);

    parse(l,filelist,counter,filetype);

    % Extract all data from Ivium dataset file
    ExtractIviumData(filelist,counter,filetype);

    bgdata = M(53:253,1:2);
    p1 = M(203,1:2);

    % Visualise 1st Sweep Data in plot
    h = figure(1);
    set(h, 'Position', [1200 50 500 900])
    h1 = plot(M(:,1),M(:,2));
    title(filename,'interpreter','none');
    xlim([-0.3 1.2]);
        hold on;
    coef_fit = polyfit(bgdata(:,1),bgdata(:,2),1);
    y_fit = polyval(coef_fit,M(:,1));
    h2 = plot(M(:,1),y_fit,'r');

    % User Input of Peak-Picking Method
    e1 = false;

    while e1 == false;

        a2(m1) = input('Method: a = Auto; m = Manual; t = TwoPoint - ','s');
        a1(m1) = a2(1,m1);

        if a1(m1) == 'a' || a1(m1) == 'm' || a1(m1) == 't';

            e1 = true;

        end

    end
```

```
% User input of Parameters for Peak Picking
userhappy= false;

if a1(m1) == 'a';

    userhappy = true;

end

while userhappy == false;

    if a1(m1) == 'm';

        [p1V p1I] = ginput(1);
        h3 = scatter(p1V,p1I);

        a2 = input('Continue? ','s');

    end

    if a2 == 'y';

        userhappy = true;

    end;

end;

if a1(m1) == 't';

[pV pI] = ginput(2);
h3 = scatter(pV,pI);

a2 = input('Continue?','s');
if a2 == 'y';

    userhappy = true;

end
end


    end;
        hold off;

    if a1(m1) == 'a';
    AutoPeak;
    end
    if a1(m1) == 'm';
    ManualPeak;
    end
    if a1(m1) == 't';
    TwoPointV1;
    end
    results(m1,1) = peakposition;
    results(m1,2) = peakheight;
```

```
        results(m1,3) = Vwidth;
        results(m1,4) = peakarea;
        results(m1,5) = peakcharge;

end
```

iii) Automatic Peak Picking Code – AutoPeak.m

```
%{
Instructions:
Section of code for automatic peak picking using red line guide.
User is given the option in ASV_ST_Analysis of using:
-   AutoPeak.m - (This code block) finds nearest point to intersection of red line
-   ManualPeak.m - Uses same start position as AutoPeak but allows user to define
                   upper boundary of integration
-   TwoPoint.m - Uses a straight line drawn between two user-defined points to
                 define integration area
%}

if a1(m1) == 'a';

    sub1(:,1) = M(:,1);
    sub1(:,2) = abs(M(:,2)-y_fit);
    peakregion1 = sub1(403:1502,1:2);

    [c1 c2] = getNElements(peakregion1(:,2),10);

    inters1(:,1) = c2;
    inters1(:,2:3) = peakregion1(c2,:);
    [d1 d2] = min(inters1(:,2));

    p2 = inters1(d2,2:3);
    xdata1 = [p1(1) p2(1)]';
    ydata1 = [p1(2) p2(2)]';

    %find maximum I in 0-300mV peak region to define extrapolation area
    [r1 r2] = max(M(403:403+inters1(d2,1),1));
    peakloc1 = r2;
    extradata1 = M(peakloc1:1800,1:2);

    %Fit P1 and P2 with Line
    y1 = polyfit(xdata1,ydata1,1);
    linepeak = polyval(y1,r1);

    %locate p2 (intersection)
    p2x = peakloc1 + 403;
    p2real = M(p2x,1:2);

    %Define region to use trapz then use
    peakdata2 = M(51:p2x,1:2);
    peakdata3 = peakdata2(:,2);
    p1real = peakdata2(1,:);
    Qtot = 0.02*trapz(peakdata3);

    %calculate area of background trapezium
    fullVwidth = p2real(1) - p1real(1);
    twidth = fullVwidth/0.05;
    area = 0.5*twidth*(p1real(2)+p2real(2));

    %calculate peak height etc. height is r1
    peakV = extradata1(1,:);
```

```
    peaksize = peakV(2) - linepeak;

    %Define final parameters
    peakcharge = Qtot - area;
    peakarea = peakcharge/20;
    peakposition = peakV(1,1);
    peakheight = peaksize;
    Vwidth = 0;

    clearvars coords;

    end;
```

iv) One-point Peak Picking Code – ManualPeak.m

```
%{
Instructions:
Section of code for 1-point peak picking using red line guide.
User is given the option in ASV_ST_Analysis of using:
-   AutoPeak.m - finds nearest point to intersection of red guide line
-   ManualPeak.m - (This code block) Uses same start position as AutoPeak but
                   allows user to define upper boundary of integration
-   TwoPoint.m - Uses a straight line drawn between two user-defined points to
                 define integration area
%}

if a1(m1) == 'm';

    p2 = [p1V p1I];
    xdata = [p1(1) p2(1)]';
    ydata = [p1(2) p2(2)]';

    %find maximum I in 0-300mV peak region to define extrapolation area
    peakregion = M(303:603,1:2);
    [r1 r2] = max(peakregion(:,2));
    peakloc = r2+303;
    extradata = M(peakloc:1800,1:2);

    %Fit P1 and P2 with Line
    y1 = polyfit(xdata,ydata,1);
    linepeak = polyval(y1,r1);

    %get all values x,y of line in intersection region at 1mV intervals
    coords(:,1) = extradata(:,1);
    coords(:,2) = (coords(:,1)*y1(1))+y1(2);

    %subtract, take absolute and find minimum
    sub = abs(extradata(:,2)-coords(:,2));
    [s1 s2] = min(sub);

    %locate p2 (intersection)
    p2x = peakloc + s2;
    p2real = M(p2x,1:2);

    %Define region to use trapz then use
    p2Ind = round((p1V/0.001)+3);
    peakdata1 = M(51:p2x,1:2);
    peakdata = peakdata1(:,2);
    p1real = peakdata1(1,:);
    Qtot = 0.02*trapz(peakdata);

    %calculate area of background trapezium
    fullVwidth = p2real(1) - p1real(1);
    twidth = fullVwidth/0.05;
    area = 0.5*twidth*(p1real(2)+p2real(2));

    %calculate peak height etc. height is r1
    peakV = extradata(1,:);
```

```
    peaksize = peakV(2) - linepeak;

    %Define final parameters
    peakcharge = Qtot - area;
    peakarea = peakcharge/20;
    peakposition = peakV(1,1);
    peakheight = peaksize;
    Vwidth = 0;

        close all;


    clearvars coords;

end
```

v) Two-point Peak Picking Methodology – TwoPoint.m

```
%{
Instructions:
Section of code for 2-point peak picking without using red line guide.
User is given the option in ASV_ST_Analysis of using:
-   AutoPeak.m - finds nearest point to intersection of red line
-   ManualPeak.m - Uses same start position as AutoPeak but allows user to define
                   upper boundary of integration
-   TwoPoint.m - (this code block) Uses a straight line drawn between two user-
                 defined points to define integration area
%}

if a1(m1) == 't';

    p1 = [pV(1) pI(1)];
    p2 = [pV(2) pI(2)];
    xdata = [p1(1) p2(1)]';
    ydata = [p1(2) p2(2)]';

    extradata = M(1:903,1:2);

    %Fit P1 and P2 with Line
    y1 = polyfit(xdata,ydata,1);
    alldata(:,2) = (M(1:903,1)*y1(1))+y1(2);
    alldata(:,1) = M(1:903,1);
    %Fit line for full visual spectrum

    %%%%%Find Intersection Afterpeak (P2)%%%%
    %subtract, take absolute and find minima (multiple)
    sub1(:,1) = alldata(:,1);
    sub1(:,2) = abs(extradata(:,2)-alldata(:,2));
    [s1 s2] = getNElements(sub1(:,2),10);

    %Match with the intersections closest to p1 & p2
    inters(:,1) = s2;
    inters(:,2:3) = M(s2,:);

    [c1 c2] = min(abs(inters(:,2)-p1(1)));
    [d1 d2] = min(abs(inters(:,2)-p2(1)));

    p1real = inters(c2,:);
    p2real = inters(d2,:);

    %Define region to use trapz then use
    peakregion = M(p1real(1):p2real(1),1:2);
    peakdata = peakregion(:,2);
    Qtot = 0.02*trapz(peakdata);

    %calculate area of background trapezium
    fullVwidth = p2real(2) - p1real(2);
    twidth = fullVwidth/0.05;
    area = 0.5*twidth*(p1real(3)+p2real(3));

    [r1 r2] = max(peakregion(:,2));
```

```
    peakloc = r2+p1real(1);
    peak = peakregion(r2,:);

    %calculate peak height etc. height is r1
    linepeak = polyval(y1,peak(1));
    peaksize = peak(2) - linepeak;

    %Define final parameters
    peakcharge = Qtot - area;
    peakarea = peakcharge/20;
    peakposition = M(p1real(1)+r2,1);
    peakheight = peaksize;
    Vwidth = 0;

    close all;


    clearvars coords;

end
```

Published with MATLAB® R2015a

D. Appendix 4 - IL Characterisation Spectra

a) NMR Spectrum

